UNIVERSITÀ DEGLI STUDI DI NAPOLI FEDERICO II

SCUOLA POLITECNICA E DELLE SCIENZE DI BASE

DIPARTIMENTO DI INGEGNERIA CHIMICA, DEI MATERIALI E DELLA PRODUZIONE INDUSTRIALE

PHILOSOPHY DOCTOR DISSERTATION

IN

INGEGNERIA DEI PROCESSI E PRODOTTI INDUSTRIALI
XXXIII CICLO

NO_x ADSORPTION AND NTP DESORPTION-REDUCTION

Advisory board

Prof. Amedeo Lancia

Prof. Francesco Di Natale

Prof. Wamadeva Balachandran

Doctoral Candidate

Luigi Amato

ACCADEMIC YEARS 2018/2021

GLOSSARY

LIST OF SYMBOLS

a_v	Specific mass transfer area
c	Gas concentration
c_0	Gas initial concentration
$c_{p,w}$	Specific heat of the wall
D	Fluid-phase diffusion coefficient
D_e	Effective diffusion coefficient
d_g	Gap distance
d_{int}	Adsorbent bed diameter
d_p	Particle diameter
D_L	Fickian axial dispersion coefficient
e	Electron charge
E_{act}	*Activation Energy*
E_b	*Breakdown electric field*
E_e	*Free-electron kinetic energy*
E_S	*Corona onset electric field*
f^*	Packed bed friction factor
$F_{S,0}$	*Initial adsorbate mass flow rate per specific area*
$F_{S,OUT}$	*Outlet adsorbate mass flow rate per specific area*
h_f	Film heat transfer coefficient between the gas and the adsorbent
h_w	Internal convective heat coefficient
j	Current density
k_i	*Reaction rate constant for the production of the species "i"*

k_i^o	*Pre-exponential factor of the reaction rate constant*
k_a	*Adsorption rate constant*
k_B	Boltzmann constant
k_d	*Desorption rate constant*
K_e	*Equilibrium constant*
K_L	*Langmuir constant*
K_f	*Overall mass transfer coefficient*
$k_{f,ext}$	*External mass transfer coefficient*
$k_{f,int}$	*Internal mass transfer coefficient*
K_F	Freundlich constant
K_H	Henry constant
K_{BET}	B.E.T constant
k_s	mass transfer coefficient based on the adsorbate difference driving force
K_s	Overall mass transfer coefficient based on the adsorbate difference driving force
L_T	Total adsorbent bed length
LUB	Length of Unused Bed
m_e	Electron mass
n_e	Electron density
$n_{i,n}$	Negative ion concentration
$n_{i,p}$	Positive ion concentration
N_v	Total molar flow rate
NTP	Non-Thermal Plasma
P	Gas pressure

$P°$	Saturation pressure
Pe_p	Peclet number (particle-based)
PFD	Process Flow Diagram
q	Surface charge density
r_a	*Adsorption rate*
r_d	*Desorption rate*
R	*Universal gas constant*
R_L	Separation factor
Re	Reynolds number
Re^*	Reynolds number for a packed bed
S_b	Cross-bed section
Sc	Schmidt number
t^*	Theoretical adsorption time
t_b	Time of breakpoint
T_g	Electronic temperature
T_g	Gas temperature
T_s	Solid temperature (adsorbent)
T_W	Wall temperature
T_∞	External air temperature
u	Gas velocity
U	overall heat transfer coefficient
V_b	Breakdown voltage
v_e	Free-electron velocity

v^*_e	Free-electron drift velocity
$v^*_{i,n}$	Drift velocity of negative ions
$v^*_{i,p}$	Drift velocity of positive ions
V_{pore}	*Volume of the pores*
$x°$	Ratio between the equilibrium and the saturation pressure of adsorbate

GREEK SYMBOLS

α_w	Ratio of the internal surface area to the volume of the column wall
α_{wL}	Ratio of the logarithmic mean surface area of the column shell to the volume of the column
ε	Bed porosity
ΔH_{ads}	Adsorption heat
ε_e	Electron mean energy
ε_p	Adsorbent porosity
λ_L	axial heat dispersion coefficient
μ_g	Gas viscosity
ρ_b	Adsorbent bed density
ρ_g	Gas density
ρ_p	Particle density
ρ_w	Wall density
φ_s	Correction factor for the deviation from linear equilibrium
ω_b	Specific amount of solute adsorbed at the breakpoint
ω_e	Adsorption capacity (Equilibrium)
$\omega_{e,i}$	Adsorption capacity for the species “i”
ω_s	Specific amount of solute adsorbed at the saturation
ω_{max}	Monolayer adsorption capacity

EQUATION LIST

$$-\frac{d}{dt}[NO] = +\frac{d}{dt}[NO_2] = 2\,k_{NO_2}[NO]^2[O_2] \qquad \textit{(Eq. 1-1)}$$

$$k_{NO_2} = k^o_{NO_2} e^{-\frac{E_{act}}{RT}} \qquad \textit{(Eq. 1-2)}$$

$$V_{pore} = \frac{\varepsilon_p}{\rho_p} \qquad \textit{(Eq. 2-1)}$$

$$\omega_e = \omega_e(P) \qquad or \qquad \omega_e = \omega_e(c) \qquad \textit{(Eq. 2-2)}$$

$$\omega_{e,i} = \omega_{e,i}(P_i) \qquad or \qquad \omega_{e,i} = \omega_{e,i}(c_i) \qquad \textit{(Eq. 2-3)}$$

$$r_a = k_a c(\omega_{max} - \omega_e) \qquad \textit{(Eq. 2-4)}$$

$$r_d = k_d \omega_e \qquad \textit{(Eq. 2-5)}$$

$$k_a c(\omega_{max} - \omega_e) = k_d \omega_e \qquad \textit{(Eq. 2-6)}$$

$$\omega_e = \frac{k_a c \omega_{max}}{k_d + k_a c} \qquad \textit{(Eq. 2-7)}$$

$$K_e = \frac{k_a}{k_d} \qquad \textit{(Eq. 2-8)}$$

$$\omega_e = \omega_{max} \frac{K_L c}{1 + K_L c} \qquad \textit{(Eq. 2-9)}$$

$$R_L = \frac{1}{1 + K_L c_0} \qquad \textit{(Eq. 2-10)}$$

$$\frac{1}{\omega_e} = \frac{1}{\omega_{max} K_L} \frac{1}{c} + \frac{1}{\omega_{max}} \qquad \textit{(Eq. 2-11)}$$

$$\omega_e = K_F c^{\frac{1}{n}} \qquad \textit{(Eq. 2-12)}$$

$$\log(\omega_e) = \log(K_F) + \frac{1}{n} \log(c) \qquad \textit{(Eq. 2-13)}$$

$$\omega_e = \omega_{max} \frac{K_e c^{\frac{1}{n}}}{1 + K_e c^{\frac{1}{n}}} \qquad \textit{(Eq. 2-14)}$$

$$\omega_e = K_H c \qquad \textit{(Eq. 2-15)}$$

$$K_H = K_L \omega_{max} \qquad \textit{(Eq. 2-16)}$$

$$\omega_e = \omega_{max} \frac{K_{BET} x^\circ}{[1 - x^\circ][1 + x^\circ(K_{BET} - 1)]} \qquad \textit{(Eq. 2-17)}$$

$$x^\circ = \frac{P}{P^\circ} \qquad \textit{(Eq. 2-18)}$$

$$F_{S,0} = u c_0 \qquad \textit{(Eq. 2-19)}$$

$$u c_0 t^* = L_T \rho_b (\omega_s - \omega_0) \qquad \textit{(Eq. 2-20)}$$

$$t^* = \frac{L_T \rho_b (\omega_s - \omega_0)}{u c_0} \qquad \textit{(Eq. 2-21)}$$

$$\rho_b = (1-\varepsilon)\rho_p \qquad \textit{(Eq. 2-22)}$$

$$F_{S,0} - F_{S,OUT} = L_T \rho_b \frac{d\omega}{dt} \qquad \textit{(Eq. 2-23)}$$

$$(uc_0 - uc)dt = L_T \rho_b d\omega \qquad \textit{(Eq. 2-24)}$$

$$\omega(t) = \frac{u}{L_T \rho_b} \int_{t_0}^{t} (c_0 - c\,)dt \qquad \textit{(Eq. 2-25)}$$

$$\omega(t) = \frac{uc_0}{L_T \rho_b} \int_{t_0}^{t} \left(1 - \frac{c}{c_0}\right) dt \qquad \textit{(Eq. 2-26)}$$

$$LUB = L_T \left(1 - \frac{\omega_b}{\omega_s}\right) \qquad \textit{(Eq. 2-27)}$$

$$LUB = L_T \left(1 - \frac{\int_0^{t_b} \left(1 - \frac{c}{c_0}\right) dt}{\int_0^{t_s} \left(1 - \frac{c}{c_0}\right) dt}\right) \qquad \textit{(Eq. 2-28)}$$

$$\int_0^{t_b} \left(1 - \frac{c}{c_0}\right) dt \approx 1 \cdot t_b \qquad \textit{(Eq. 2-29)}$$

$$\int_0^{t_s} \left(1 - \frac{c}{c_0}\right) dt \approx 1 \cdot t^* \qquad \textit{(Eq. 2-30)}$$

$$LUB = L_T \left(1 - \frac{t_b}{t^*}\right) \qquad \textit{(Eq. 2-31)}$$

$$uc - u(c + dc) = dL\rho_b \frac{\partial \omega}{\partial t} + \varepsilon dL \frac{\partial c}{\partial t} \qquad \textit{(Eq. 2-32)}$$

$$-u\frac{\partial c}{\partial L}=\rho_b\frac{\partial \omega}{\partial t}+\varepsilon\frac{\partial c}{\partial t} \qquad \textit{(Eq. 2-33)}$$

$$\rho_b\frac{d\omega}{dt}=K_f a_v(c-c^*) \qquad \textit{(Eq. 2-34)}$$

$$a_v=\frac{6\,(1-\varepsilon)}{d_p} \qquad \textit{(Eq. 2-35)}$$

$$\frac{1}{K_f}=\frac{1}{k_{f,ext}}+\frac{1}{k_{f,int}} \qquad \textit{(Eq. 2-36)}$$

$$k_{f,int}=\frac{10\,D_e}{d_p} \qquad \textit{(Eq. 2-37)}$$

$$\rho_b\frac{d\omega}{dt}=K_s a_v(\omega^*-\omega) \qquad \textit{(Eq. 2-38)}$$

$$k_s a_v=\rho_b 15\varphi_s D_e/(d_p)^2 \qquad \textit{(Eq. 2-39)}$$

$$-u\frac{\partial c}{\partial L}+\varepsilon D_L\frac{\partial^2 c}{\partial L^2}=\rho_b\frac{\partial \omega}{\partial t}+\varepsilon\frac{\partial c}{\partial t} \qquad \textit{(Eq. 2-40)}$$

$$\frac{D_L}{D}=\gamma_1+\gamma_2\frac{d_p u}{D}=\gamma_1+\gamma_2\frac{Re\,Sc}{\varepsilon} \qquad \textit{(Eq. 2-41)}$$

$$\frac{1}{Pe_p}=\frac{\gamma_1\varepsilon}{Re\,Sc}+\gamma_2 \qquad \textit{(Eq. 2-42)}$$

$$\varepsilon c c_{p,g}\frac{\partial T_g}{\partial t}+c c_{p,g}\frac{\partial u T_g}{\partial L}=\rho_b(-\Delta H_{ads})\frac{\partial \omega}{\partial t}-\rho_b c_{p,s}\frac{\partial T_s}{\partial t}+\varepsilon\lambda_L\frac{\partial^2 T_g}{\partial L^2}+\frac{4h_w}{d_{int}}\left(T_g-T_w\right) \qquad \textit{(Eq. 2-43)}$$

$$\rho_p c_{p,s} \frac{\partial T_s}{\partial t} = \frac{6h_f}{d_p}\left(T_g - T_s\right) + \rho_p(-\Delta H_{ads})\frac{\partial \omega}{\partial t} \quad \textit{(Eq. 2-44)}$$

$$\rho_w c_{p,w} \frac{\partial T_w}{\partial t} = \alpha_w h_w\left(T_g - T_w\right) - \alpha_{wl} U(T_w - T_\infty) \quad \textit{(Eq. 2-45)}$$

$$u = \frac{1}{S_b}\frac{N_v R T_g}{P} \quad \textit{(Eq. 2-46)}$$

$$-\frac{\partial P}{\partial L} = 150\frac{\mu_g(1-\varepsilon)^2}{\varepsilon^3 {d_p}^2}u + 1.75\frac{(1-\varepsilon)}{\varepsilon^3 d_p}\rho_g u^2 \quad \textit{(Eq. 2-47)}$$

$$f^* = \frac{150}{Re^*} + 1.75 \quad \textit{(Eq. 2-48)}$$

$$Re^* = \frac{d_p \rho_g u}{\mu_g(1-\varepsilon)} \quad \textit{(Eq. 2-49)}$$

$$-\frac{\partial P}{\partial L} = f^*\frac{\rho_g\ (1-\varepsilon)^2}{d_p \varepsilon^3}u^2 \quad \textit{(Eq. 2-50)}$$

$$E_e = \frac{1}{2}m_e v_e^2 \quad \textit{(Eq. 3-1)}$$

$$q = en_e dx_e - en_{i,p}dx_{i,p} + n_{i,n}dx_{i,n} \quad \textit{(Eq. 3-2)}$$

$$j(x) = \frac{dq}{dt} = en_e {v^*}_e - en_{i,p}{v^*}_{i,p} + en_{i,n}{v^*}_{i,n} \quad \textit{(Eq. 3-3)}$$

$$j = \int j(x)dx \quad \textit{(Eq. 3-4)}$$

$$V_b = \frac{BPd_g}{C + log\, Pd_g} \qquad \textit{(Eq. 3-5)}$$

$$C = log\left[\frac{A}{log\left(1+\frac{1}{\gamma}\right)}\right] \qquad \textit{(Eq. 3-6)}$$

$$\frac{E_b}{P} = \frac{B}{C + log\, Pd_g} \qquad \textit{(Eq. 3-7)}$$

$$E_b = 3000d_g + 1.35 \quad [10^6\, V/m] \qquad \textit{(Eq. 3-8)}$$

$$E_S = E_0 m_v \left(\delta + 0.0308\sqrt{\frac{\delta}{R_0}}\right) R_0 \ln\frac{D_w}{R_0} \qquad \textit{(Eq. 3-9)}$$

$$\delta = \frac{T_s P}{P_s T} \qquad \textit{(Eq. 3-10)}$$

$$\sigma_{\alpha\to\beta}(E) = \int_0^{E_{max}} dT_2 \int d\omega_1 d\omega_2 \frac{k_1 \cdot k_2}{4\pi \cdot k_\alpha} \left| f_\beta^{av}(\omega_1, \omega_2, \omega_1 T_2 \right|^2 \qquad \textit{(Eq. 3-11)}$$

$$\varepsilon_e = \frac{3}{2} k_B T_e \qquad \textit{(Eq. 3-12)}$$

$$\omega(t) = \frac{u}{L_T \rho_b} \sum_{i=1}^{n-1} \left(c_o - \frac{c_i + c_{i+1}}{2}\right) \Delta t_i \qquad \textit{(Eq. 4-1)}$$

$$\omega_{NO}^*(t) = \frac{u}{L_T \rho_b} \sum_{i=1}^{n-1} \left(c_{NO}^{ss} - \frac{c_{NO,i} + c_{NO,i+1}}{2}\right) \Delta t_i \qquad \textit{(Eq. 4-2)}$$

$$\omega^{*}_{NO_2}(t) = \frac{u}{L_T \rho_b} \sum_{i=1}^{n-1} \left(c^{SS}_{NO_2} - \frac{c_{NO_2,i} + c_{NO_2,i+1}}{2} \right) \Delta t_i \qquad \textit{(Eq. 4-3)}$$

$$\sigma(t) = \frac{u}{L_T \rho_b} \sum_{i=1}^{n-1} \left(\frac{c_{NO_x,i} + c_{NO_x,i+1}}{2} \right) \Delta t_i \qquad \textit{(Eq. 6-1)}$$

NUMERICAL ANALYSIS EQUATIONS

$$\nabla \cdot \boldsymbol{E} = \frac{\rho}{\varepsilon_0} \qquad \textit{(Eq. 5-1)}$$

$$\nabla \; x \; \boldsymbol{E} = 0 \qquad \textit{(Eq. 5-2)}$$

$$-\nabla V = \boldsymbol{E} \qquad \textit{(Eq. 5-3)}$$

$$-\nabla \cdot \nabla V = \frac{\rho}{\varepsilon_0} \qquad \textit{(Eq. 5-4)}$$

$$\rho_P = -\nabla \cdot \boldsymbol{P} \qquad \textit{(Eq. 5-5)}$$

$$\nabla \cdot \boldsymbol{E} = \frac{\rho + \rho_P}{\varepsilon_0} \qquad \textit{(Eq. 5-6)}$$

$$\nabla \cdot (\varepsilon_0 \, \boldsymbol{E} + \boldsymbol{P}) = \; \rho \qquad \textit{(Eq. 5-7)}$$

$$\boldsymbol{D} = \varepsilon_0 \, \boldsymbol{E} + \boldsymbol{P} \qquad \textit{(Eq. 5-8)}$$

$$\nabla \cdot \boldsymbol{D} = \rho \qquad \textit{(Eq. 5-9)}$$

$$\boldsymbol{P} = \varepsilon_0 \, \chi_e \, \boldsymbol{E} \qquad \textit{(Eq. 5-10)}$$

$$\boldsymbol{D} = \varepsilon_0 \, \boldsymbol{E} + \boldsymbol{P} = \; \varepsilon_0 \, \boldsymbol{E} + \varepsilon_0 \, \chi_e \, \boldsymbol{E} = \varepsilon_0 \, (1 + \chi_e) \, \boldsymbol{E} \qquad \textit{(Eq. 5-11)}$$

$$\boldsymbol{D} = \varepsilon_0 \varepsilon_r \, \boldsymbol{E} \qquad \textit{(Eq. 5-12)}$$

$$-\nabla \cdot (\varepsilon_0 \varepsilon_r \nabla V) = \rho \qquad \textit{(Eq. 5-13)}$$

$$\boldsymbol{D} = \varepsilon_0 \varepsilon_r \boldsymbol{E} \quad \textit{(Eq. 5-14)}$$

$$\boldsymbol{n} \cdot (\mathbf{D_1} - \mathbf{D_2}) = \rho_s \quad \textit{(Eq. 5-15)}$$

$$\frac{d\rho_s}{dt} = \boldsymbol{n} \cdot \boldsymbol{J_i} + \boldsymbol{n} \cdot \boldsymbol{J_e} \quad \textit{(Eq. 5-16)}$$

$$\boldsymbol{n} \cdot \boldsymbol{D} = 0 \quad \textit{(Eq. 5-17)}$$

$$V_{app} = -V_0 \cdot \sin(\omega_0 \cdot t) \quad \textit{(Eq. 5-18)}$$

$$\omega_0 = 2\pi \cdot f_0 \quad \textit{(Eq. 5-19)}$$

$$\frac{\partial n_e}{\partial t} + \nabla \cdot [-n_e(\mu_e \cdot \boldsymbol{E}) - \boldsymbol{D}_e \cdot \nabla n_e] = R_e \quad \textit{(Eq. 5-20)}$$

$$\frac{\partial n_\varepsilon}{\partial t} + \nabla \cdot [-n_\varepsilon(\mu_\varepsilon \cdot \boldsymbol{E}) - \boldsymbol{D}_\varepsilon \cdot \nabla n_\varepsilon] + \boldsymbol{E} \cdot [-n_e(\mu_e \cdot \boldsymbol{E}) - \boldsymbol{D}_e \cdot \nabla n_e] = S_{en} \quad \textit{(Eq. 5-21)}$$

$$\bar{\varepsilon} = \frac{n_\varepsilon}{n_e} \quad \textit{(Eq. 5-22)}$$

$$T_e = \frac{2}{3}\,\bar{\varepsilon} \quad \textit{(Eq. 5-23)}$$

$$\mu_e = \frac{3.74 \cdot 10^{24}}{N}\,\left(\frac{E}{N}\right)^{-0.25} \quad \textit{(Eq. 5-24)}$$

$$\boldsymbol{D}_e = \mu_e T_e \quad \textit{(Eq. 5-25)}$$

$$\boldsymbol{D}_{\varepsilon} = \mu_{\varepsilon} T_e \qquad \textit{(Eq. 5-26)}$$

$$\mu_{\varepsilon} = \frac{5}{3}\mu_e \qquad \textit{(Eq. 5-27)}$$

$$\boldsymbol{n} \cdot \boldsymbol{\Gamma}_e = \frac{1 - r_e}{1 + r_e}\left(\frac{1}{2} v_{e_{th}}\, n_e\right) - \sum \gamma_i (\boldsymbol{\Gamma_i} \cdot \boldsymbol{n}) \qquad \textit{(Eq. 5-28)}$$

$$\boldsymbol{n} \cdot \boldsymbol{\Gamma}_{\varepsilon} = \frac{1 - r_e}{1 + r_e}\left(\frac{5}{6} v_{e_{th}}\, n_{\varepsilon}\right) - \sum \varepsilon_i \gamma_i (\boldsymbol{\Gamma_i} \cdot \boldsymbol{n}) \qquad \textit{(Eq. 5-29)}$$

$$v_{e_{th}} = \sqrt{\frac{8 k_b T_e}{\pi m_e}} \qquad \textit{(Eq. 5-30)}$$

$$\boldsymbol{n} \cdot \boldsymbol{\Gamma}_e = 0 \qquad \textit{(Eq. 5-31)}$$

$$\boldsymbol{D} = \varepsilon_0\, \varepsilon_i\, \boldsymbol{E} \qquad \textit{(Eq. 5-32)}$$

$$n \cdot (D_1 - D_2) = \sigma_s \qquad \textit{(Eq. 5-33)}$$

$$\frac{d\sigma_s}{dt} = n \cdot J_i + n \cdot J_e \qquad \textit{(Eq. 5-34)}$$

$$V_{dst} = V_{src} \qquad \textit{(Eq. 5-35)}$$

$$R_e = \sum_{j=1}^{M} x_j k_j N n_e \qquad \textit{(Eq. 5-36)}$$

$$N_2^+ \rightarrow N_2 \qquad \textit{(Eq. 5-37)}$$

REACTION LIST

$NO_z + O_2 \rightarrow NO_{z-1} + O_3$ *(R 1-1)*

$2\,NO \rightleftharpoons (NO)_2$ *(R 1-2)*

$N_2 + O_2 \rightleftharpoons 2\,NO$ *(R 1-3)*

$2\,NO + O_2 \rightleftharpoons 2\,NO_2$ *(R 1-4)*

$NO \rightleftharpoons ½\,N_2O + ¼\,O_2$ *(R 1-5)*

$(NO)_2 + O_2 \rightarrow 2\,NO_2$ *(R 1-6)*

$NO + O_2 \rightleftharpoons NO_3$ *(R 1-7)*

$NO_3 + NO \rightarrow 2\,NO_2$ *(R 1-8)*

$NO + O_3 \rightleftharpoons NO_2 + O_2$ *(R 1-9)*

$VOC + OH \rightarrow \cdot RO_2 + products$ *(R 1-10)*

$\cdot RO_2 + NO \rightleftharpoons NO_2 + \cdot RO$ *(R 1-11)*

$radicals \rightarrow HO_2 + products$ *(R 1-12)*

$HO_2 + NO \rightleftharpoons NO_2 + OH$ *(R 1-13)*

$NO_2 + hv\ (\lambda = 420nm)\ \rightarrow\ NO + O\ (\ ^3P)$ *(R 1-14)*

$O\ (\ ^3P) + O_2 \rightarrow\ O_3$ *(R 1-15)*

$2\ NO_2 \rightleftharpoons N_2O_4$ *(R 1-16)*

$2\ NO_2 + H_2O \rightarrow HNO_2 + HNO_3$ *(R 1-17)*

$3\ NO_2 + H_2O \rightarrow 2\ HNO_3 + NO$ *(R 1-18)*

$4\ NO + 4\ NH_3 + O_2 \rightarrow 4\ N_2 + 6\ H_2O$ *(R 1-19)*

$2\ NO_2 + 4\ NH_3 + O_2 \rightarrow 3\ N_2 + 6\ H_2O$ *(R 1-20)*

$4\ NO + 2\ CO(NH_2)_2 + O_2 \rightarrow 4\ N_2 + 2\ CO_2 +\ 4\ H_2O$ *(R 1-21)*

$2\ NO_2 + 2\ CO(NH_2)_2 + O_2 \rightarrow 3\ N_2 + 2\ CO_2 +\ 4\ H_2O$ *(R 1-22)*

$2\ SO_2 + O_2 \rightarrow 2\ SO_3$ *(R 1-23)*

$2NH_3 + SO_3 +\ H_2O \rightarrow (NH_4)_2SO_4$ *(R 1-24)*

$NH_3 + SO_3 +\ H_2O \rightarrow NH_4HSO_4$ *(R 1-25)*

$BaO + NO +\ O_2 \rightarrow Ba(NO_2)_2$ *(R 1-26)*

$BaO + NO_2 \rightarrow BaO\ NO_2$ *(R 1-27)*

$BaO\ NO_2 \rightarrow BaO_2 + NO$ *(R 1-28)*

$BaO_2 + 2\ NO_2 \rightarrow Ba(NO_3)_2$ *(R 1-29)*

$NO + NO_2\ + 2\ NH_3 \rightarrow 2\ N_2\ + 3\ H_2O$ *(R 1-30)*

$NO + O_3\ \rightarrow\ NO_2\ + O_2$ *(R 1-31)*

$N_2 + e^- \rightarrow 2\ N + e^-$ *(R3-1)*

$N_2 + e^- \rightarrow N_2^+ + 2\ e^-$ *(R3-2)*

$N_2 + e^- \rightarrow N^+ + N + 2\ e^-$ *(R3-3)*

$N_2 + e^- \rightarrow N^* + N + e^-$ *(R3-4)*

$N_2 + e^- \rightarrow N_2(A) + e^-$ *(R3-5)*

$N^+ + e^- \rightarrow N + hv$ *(R3-6)*

$N_2^+ + e^- \rightarrow N^* + N$ *(R3-7)*

$N_3^+ + e^- \rightarrow N^* + N_2$ *(R3-8)*

$N_4^+ + e^- \rightarrow N_2(A) + N_2$ *(R3-9)*

$N_2 + e^- \rightarrow N_2(A) + e^-$ *(R3-10)*

$N_2 + e^- \rightarrow N_2(a) + e^-$ *(R3-11)*

$N_2 + e^- \rightarrow N_2(B) + e^-$ *(R3-12)*

$N_2 + e^- \rightarrow N_2(C) + e^-$ *(R3-13)*

$N_2 + e^- \rightarrow 2\,N + e^-$ *(R3-14)*

$N_2 + e^- \rightarrow N_2^+ + 2\,e^-$ *(R3-15)*

$N_2(A) + N_2(a) \rightarrow N_4^+ + e^-$ *(R3-16)*

$2\,N_2(a) \rightarrow N_4^+ + e^-$ *(R3-17)*

$2\,N \rightarrow N_2^+ + e^-$ *(R3-18)*

$N_4^+ + e^- \rightarrow 2\,N_2$ *(R3-19)*

$N_2^+ + e^- \rightarrow 2\,N$ *(R3-20)*

$2\,N + N_2 \rightarrow 2\,N_2$ *(R3-21)*

$N_2(A) + N_2 \rightarrow 2\,N_2$ *(R3-22)*

$N_2(A) + N \rightarrow N_2 + N$ *(R3-23)*

$N_2(B) + N_2 \rightarrow N_2(A) + N_2$ *(R3-24)*

$N_2(B) \rightarrow N_2(A)$ *(R3-25)*

$N_2(a) + N_2 \rightarrow N_2(B) + N_2$ *(R3-26)*

$N_2(C) \rightarrow N_2(B)$ *(R3-27)*

$N_2(C) + N_2 \rightarrow N_2(a) + N_2$ *(R3-28)*

$N_2^+ + 2\,N_2 \rightarrow N_4^+ + N_2$ *(R3-29)*

$N_4^+ + N_2 \rightarrow 2\,N_2 + N_2^+$ *(R3-30)*

$N_2 + e^- \rightarrow N_2(a'1\Sigma_u^-) + e^-$ *(R3-31)*

$N_2(a'1\Sigma_u^-) + NO \rightarrow N + O + N_2$ *(R3-32)*

$N + NO \rightarrow N_2 + O$ *(R3-33)*

$O + NO \rightarrow NO_2$ *(R3-34)*

$O + NO_2 \rightarrow NO + O_2$ *(R3-35)*

$N + NO_2 \rightarrow N_2O + O$ *(R3-36)*

$O + O_2 + M \rightarrow O_3 + M$ *(R3-37)*

$NO + O_3 + M \rightarrow NO_2 + O_2 + M$ *(R3-38)*

$O + O_3 \rightarrow 2\,O_2$ *(R3-39)*

PLASMA REACTIONS

$e^- + A_2 \rightarrow A_2^+ + e^-$ *(PR1)*

$e^- + A_2 \rightarrow A^+ + A + 2\,e^-$ *(PR2)*

$e^- + A_2 \rightarrow A_2^-$ *(PR3)*

$e^- + A_2 \rightarrow A^- + A$ *(PR4)*

$e^- + A_2 \rightarrow A_2^* + e^-$ *(PR5)*

$h\nu + A_2 \rightarrow A_2^*$ *(PR6)*

$e^- + A_2^* \rightarrow A_2^+ + 2\,e^-$ *(PR7)*

$h\nu + A_2 \rightarrow A_2^+ + e^-$ *(PR8)*

$h\nu + S \rightarrow S^+ + e^-$ *(PR9)*

$M^* + A_2 \rightarrow A_2^+ + M + e^-$ *(PR10)*

$A + B \rightarrow AB^+ + e^-$ *(PR11)*

$A^\pm + B \rightarrow A + B^\pm$ *(PR12)*

$e^- + AB^+ \rightarrow (AB)^* \rightarrow A + B^*$ *(PR13)*

$2\,e^- + A^+ \rightarrow A^* + e^-$ *(PR14)*

$e^- + A^+ \rightarrow A^* \rightarrow A + hv$ *(PR15)*

$A^+ + B^- \rightarrow AB$ *(PR16)*

$A^+ + B^- \rightarrow A^* + B$ *(PR17)*

$A^+ + B^- + M \rightarrow A + B + M$ *(PR18)*

$A + B + M \rightarrow AB + M$ *(PR19)*

FIGURE LIST

TABLE LIST

ABSTRACT

NO_x emissions have multi-fold hazards for both environment and human health, due to their role in the formation of fine particles, ozone smog, acid rain and eutrophication. The increasing level of emissions and the improved comprehension of NO_x toxicity have led to a progressive reduction of allowed emissions from stationary and mobile anthropic sources. NO_x emissions can be controlled by altering the combustion process (e.g. Selective Non-Catalytic Reduction) or by post-combustion treatment of the flue gases (e.g. Selective Catalytic Reduction). These two technologies are the most commonly used for industrial processes in a wide range of applications. SCR has a higher capital cost than SNCR but allows a superior reduction of NO_x concentration and it is the preferred technique in many industrial applications when high-quality standards are required.

Due to the recent stricter European regulations for NO_x emissions, SNCR is almost inadequate for the new standards, and cost-effective and alternative methods to SCR are under investigation.

The NO_x adsorption and non-thermal plasma desorption/reduction strategy was proposed and it is investigated in this thesis. The process consists of the adsorption of NO_x on a sorbent material followed by the sorbent regeneration using non-thermal plasma in N_2 flushing. The presence of the plasma has the double effect of promoting the NO_x desorption from the sorbent surface and reducing the NO_x desorbed to N_2 and O_2. A further reduction of NO_x can be performed in a DBD plasma reactor. The desorption and reduction are promoted by the high reactive nitrogen gas discharge particles that react with NO_x.

A granular activated carbon (GAC) was investigated for NO_x adsorption from simulated flue gases. The adsorption capacity for NO_x was negligible (less than 4mg/g) if a mixture of NO diluted in N_2 was considered; however, it was possible to calculate the adsorption isotherms at 30 and 120°C. A great improvement in the adsorption capacity was calculated as oxygen was fed (up to 66mg/g). The tests demonstrated that part of the NO was catalytically oxidized to NO_2 in the presence of oxygen, with a consequent improvement in NO_x adsorption. Even the adsorbent impregnation with copper (GAC-Cu) played a positive role in the NO oxidation, hence improving the capacity to remove NO_x from the gas stream.

Dielectric Barrier Discharge reactors demonstrated a high efficiency (up to 100%) in NO_x reduction. The configurations with one and two dielectrics were investigated, highlighting the high performance of the one dielectric barrier discharge reactor and the high flexibility of the two dielectric barriers discharge. A numerical analysis was performed to model the plasma condition promoted in the

realistic reactors. The results in terms of electric parameters were consistent with those estimated in the gas discharge, e.g. electric field, electron density and electron temperature.

Cyclic tests of adsorption and sorbent regeneration plasma-assisted demonstrated the effectiveness of the process by using GAC-Cu for NO_x removal. The amount of NO_x adsorbed during the adsorption stage was desorbed and converted during the desorption plasma-assisted process. Higher effectiveness (≈100%) was estimated in the case of GAC-Cu of commercial size (1.5-3mm), while the effectiveness decreased in the case of lower granular size (0.3-0.6mm).

The possibility to perform the process at low temperature makes this technology suitable for those gas treatment plants that require a retrofit to accomplish the new regulations. The gas would be treated with the designed reactor to obtain further NO_x reduction, without risks of ammonia slip that represents the main problem of high-efficiency conventional technologies.

PREMISES AND AIM OF THE WORK

One of the main worldwide challenges in the 21st century is emission control for environmental protection. The climate changes and the ever-increasing global mean temperature are making the countries very sensitives to environmental protection. Around 200 countries, which are part of the United Nations Framework Convention on Climate Change (UNFCCC), meet annually to discuss climate changes and seek to reduce the atmospheric concentrations of greenhouse gases to prevent dangerous anthropogenic interference with the earth's climate system. Nick Nuttall, the Spokesperson at the 21st yearly session of the Conference of the Parties (COP21), during a Student Conference at Tongji University in Shanghai said: "The question is not if the world is moving to address climate change and also realize the Sustainable Development Goals. The question is now scale and also speed if we are to avoid potentially catastrophic climate impacts, hand on a healthy planet to the next generations and seize the opportunities of a different kind of development path". The "Paris Agreement" signed in 2016 by all the UNFCCC members represents a crucial deal to protect the environment. The goal is to keep the increase in global temperature below 2°C above pre-industrial levels and pursuing efforts to limit it to 1.5°C. It also aims to strengthen countries' ability to deal with the impacts of climate change and support them in their efforts. Greenhouse gases are the main liable for increasing the global temperature. The primary greenhouse gases are water vapour, carbon dioxide, methane, nitrogen oxides, chlorofluorocarbons, and ozone. Even if the water vapour has the largest concentration in gas emission, it represents a small fraction of the water vapour naturally present on the earth. About the carbon oxides (CO_2, CO) there exist many literature studies that analyse their role as CH4 and promote containment of emissions, for example by replacing carbon-based fuels with free-carbon ones like hydrogen. Hydrogen has been considered by Snam CEO, Marco Alverà, "the small molecule that will save the world"; however, even if the carbon dioxide represents a cause of global warming, its emission from the exhaust gas is not regulated. The other pollutants, instead, are subjected to regulations that allow reducing the emission in the atmosphere and reduce the environmental impact.

This thesis focuses the attention on nitrogen oxides (NO_x). NO_x is a class of species that represents one of the most important gaseous pollutants due to its role in the formation of fine particles, smog, acid rain and in eutrophication phenomena; furthermore, the NO_x species are very harmful to humans. Nitrogen oxides are primary pollutants, as they are directly released into the atmosphere, both from combustion processes and fertilization. The combustion processes can occur in stationary sources

(power plants, industrial combustion, domestic heating) and transportation. Strategies to reduce the amount of NO_x produced during combustion consist of a controlled mixing of air/oxygen and fuel to optimize the combustion, or a controlling of the chamber temperature by feeding inert species/exhaust gases. Their application strongly depends on the specific process, the temperature required, and the design of the combustion chamber. In a few cases, these strategies can be enough to obtain the NO_x emissions below the threshold value. In many other cases, a post-treatment unit is required to reduce the NO_x coming from the combustion chamber to comply with the regulations. There exist many strategies that can offer a NO_x reduction with high efficiency. They can be classified in wet or dry technologies, with or without catalyst, that could require the use of reducing species for NO_x removal. The selection of the most appropriate technology mainly depends on the specific process, the NO_x concentration, the NO_x efficiency required, the operating temperature, the presence of other pollutants, moisture, and particulates. Last but not least, the choice of the post-treatment process, depends on the space required by the reactor: in the transports, e.g., size and weight are crucial to define the best strategy for pollutant removal.

The most common post-combustion De-NO_x strategies for stationary plants are the Selective Non-Catalytic Reduction (SNCR), Selective Catalytic Reduction (SCR), for industrial applications, and NO_x Storage and Reduction (NSR), for transportation.

The first two technologies allow reducing NO_x by using urea or ammonia as reducing species. SNCR does not require an extra unit for the treatment as the reducing species is injected directly in the combustion chamber. This technology is widely used where the NO_x removal efficiency required is below 80%. If higher efficiency is required, SCR technology is used for NO_x removal. The NO_x conversion takes place on the catalyst surface in the SCR reactor. This technology allows NO_x conversion with an efficiency up to 95-98%. The disadvantage of this process consists of the high temperature required to activate the catalyst (200-400°C) and the deactivation of the catalyst in the presence of sulphur species (SOx).

The NSR, also known as the three-way catalyst process, consists of three stages: NO_x adsorption at low temperature, NO_x desorption at a higher temperature (sorbent regeneration) and NO_x reduction with hydrocarbons over the catalyst. In the more recent applications an ammonia-based reductant is injected over the catalyst to improve the NO_x reduction. The critical stage of the process is represented by the sorbent regeneration and NO_x reduction that occurs as the temperature increases and reducing species (hydrocarbons e.g.) are fed. This condition is guaranteed by rich combustion in the case of gas coming from engines. Although the NSR process is the most common technology applied to the

vehicle sector, its limitations, in terms of temperature transient between the two stages and non-selective NO_x conversion in the regeneration stage, make the NSR process less suitable for big-scale applications.

In the last 30 years, the better comprehension of the charges transport in a gas phase and the capability to produce commercially high potential currents extended the applicability of Non-Thermal Plasma (NTP) processes. The NTP, historically used for ozone production, is founding a lot of new applications like plasma printing, virus modification, clean air, environmental solutions. Some researchers have proposed the NTP for the conversion of NO_x to N_2 and O_2. This application can offer an alternative method for the NO_x conversion without the use of a reducing species (urea, ammonia, hydrocarbons, e.g.) at room temperature. This result was confirmed by some experiments performed and discussed in this thesis. However, oxygen-free gas is mandatory to obtain the NO_x reduction with plasma technology. In this thesis, we studied a three-stage process for NO_x removal. This process takes inspiration from the NSR process in which the NO_x adsorbs on the sorbent surface in the first stage. The sorbent regeneration (2^{nd} stage) is promoted from NTP and it occurs at room temperature in nitrogen gas. The NO_x desorbed and concentrated in N_2 can then be reduced in an NTP reactor (3^{rd} stage). This technique offers an alternative to the high-temperature regeneration in the NSR process and avoid using further chemical reducing species.

The NO_x adsorption and plasma desorption-reduction process is explored in this thesis and its application to a lab-scale, combined with the numerical simulations, allowed to design of a pilot-scale reactor for industrial applications. The possibility to perform the process at low temperature makes this technology suitable for that gas treatment plant that requires a retrofit to accomplish the new regulations. The gas composition and temperature that is taken into account in this thesis would simulate the exhaust gas having the stack of industrial plants such as cement factory or waste incinerator. This gas would be treated with the designed reactor to obtain a further NO_x reduction, without risks of ammonia slip that represents the main problem of high-efficiency conventional technologies.

This thesis would give the bases for the NO_x adsorption and NTP desorption-reduction reactor design that could be built and installed tail-end the gas treatment units to further reduce the NO_x emissions.

The ever increasing strategies for the production of green electric energy allows reconsidering the efficacy of those applications that were normally considered as competitive due to their high electric demand, e.g. NTP technologies.

This thesis work has been based on an experimental and numerical analyses aimed to investigate the adsorption of NO_x on a selected sorbent and the features of non-thermal plasma regeneration.

The choice of the adsorbent is the first step for the design of the NO_x adsorption and NTP desorption-reduction reactor. An intensive literature research and review have been performed for the investigation of sorbent materials that could fit the process under scrutiny, looking at both the NO_x adsorption and the plasma-assisted desorption stages. A carbon based sorbent impregnated with copper was selected, and a wide experimental campaign defined the adsorption capacities of the sorbent in different experimental conditions. An experimental campaign was performed in order to investigate the plasma power and the capability to reduce the NO_x emissions as it was diluted in nitrogen gas. These experimental campaigns get the basis for the development of a lab-scale reactor and cyclic tests were performed to demonstrate the effectiveness of the process.

Further efforts are needed to define plasma power required for the application of the process in a scale-up reactors. For this reason, numerical analyses have been performed to estimate the electrical parameters for the DBD reactors under investigations. A first approach to the numerical analysis was made by solving the Gauss' Law for the electric field using the scalar electric potential as the dependent variable. Since it was considered not accurate enough to describe the plasma physics and chemistry, the chemical reactions were introduced and the Boltzmann Equation for the calculation of the electrons drift diffusion were coupled to the electrostatics study.

The thesis work is divided in three main sections. The first (Chapter 1, 2 and 3) provides a review on the NO_x pollution and it describes the main features of adsorption and plasma processes. The second section (Chapter 4) provides the experimental setup and the results for the adsorption investigation. In Chapter 5 the reduction of NO_x diluted in N_2 was investigated both in numerical analysis and experimental campaigns. Lastly, the proof of the concept of the NO_x adsorption and NTP desorption and reduction was proposed in Chapter 6.

1. INTRODUCTION TO NO_X POLLUTION CONTROL

Nitrogen oxides (NO_x) are one of the most harmful classes of pollutants for the high risks related to human health, vegetation, environment. This chapter will discuss the characteristics of NO_x pollution focusing on the physical and chemical aspects of the most relevant species, describing their negative aspects focusing on human health. Moreover, a collection of the data for the NO_x emissions and the legislation will be described to give an idea of the size of the problem and the weakness in NO_x emissions. At the end of the chapter, the conventional and alternative methods for NO_x removal will be described and the scope of the work will be presented.

1.1 Nitrogen Oxides properties

Nitrogen oxides refer to a class of pollutants usually produced from the reaction among nitrogen and oxygen. Although the nitrogen oxides are commonly represented by NO_x ($NO + NO_2$), they can be classified as a group of 7 substances in which the nitrogen can assume an electronic valence from 1 to 5 (N_2O, NO, N_2O_2, N_2O_3, NO_2, N_2O_4, N_2O_5) where oxygen ions are always at valence minus 2. Depending upon the number of oxygen atoms, NO_x can react to either deplete or enhance ozone concentrations [1]–[3].

$$NO_z + O_2 \rightarrow NO_{z-1} + O_3 \qquad \textit{(R 1-1)}$$

The stability and the relative concentration of NO_x species in exhaust gases and atmosphere depends on several phenomena and reactions take place whenever NO_x:

i. is hit with a photon of ionizing radiation (UV or a shorter wavelength light);
ii. is hit with enough photons that together transfer enough energy to change its ionization level;
iii. is catalysed;
iv. is stimulated sufficiently by thermal (IR) energy;
v. reacts with a chemically oxidizing or reducing radical (an ionized fragment of a molecule);
vi. reacts with a chemically oxidizing or reducing ion (an atom with unbalanced electrical charge).

In addition to their contribution to ozone production in troposphere and ozone depletion in the stratosphere, the nitrogen oxides contribute to nutrient enrichment problems (eutrophication). The eutrophication occurs in bodies of water when the availability of either nitrates or phosphates become too large. As a result, the ratios of nitrogen to phosphorus, silicon, iron and other nutrients are altered. This alteration may induce changes in phytoplankton, produce noxious or toxic brown or red algal blooms (which are called “red tides”), or stimulate other plant growth. The algal blooms and plant growth limit the amount of sunlight that penetrate in water and cause the death of other plants in the water, which depletes the oxygen content of the water (hypoxia) when the plants die, sink, and decay. Such eutrophication can make the bottom strata of water uninhabitable for both animals (such as fish and shellfish) and aquatic plants. The process is likely to occur both in marine and inland waters [1]. When nitrogen oxides dissolve in water and decompose, they form nitric acid (HNO_3) or nitrous acid (HNO_2). Nitric acid forms nitrate salts when it is neutralized. Nitrous acid forms nitrite salts. Thus, NO_x and its derivatives exist and react either as gases in the air, as acids in droplets of water, or as a

salt. These gases, acid gases and salts together contribute to pollution effects that have been observed and attributed to acid rain.

Commonly, NO_x emissions are referred to the NO_2 concentration because NO is rapidly converted to NO_2, and N_2O has such a long life because it is not highly reactive. However, this choice is not always accepted as due to their role in forming ozone, both NO and NO_2 should be considered. For environmental purposes, NO_x emissions are considered as the sum of NO and NO_2 and they are expressed in NO_2 equivalent. N_2O is largely biogenic, and as such was not subject to regulation.

The NO_x regulations upgrade impose their emissions even smaller to preserve the environment and global warming. New regulations followed the COP21 act to reduce the threshold emission for those pollutants that contribute to global warming. For the first time, N_2O is introduced as a pollutant, but it is still not clear how and when it could be regulated. The physical and chemical properties of NO and NO_2 are described deeply below to better understand their role as pollutants.

1.1.1 Nitrogen monoxide (NO)

Nitric oxide (NO), or nitrogen monoxide, is a colourless toxic gas with a sharp, sweet odour. It is the most heat-stable among the other oxides of nitrogen, with a decomposition temperature above $1000°C$; it is non-combustible but supports and accelerates the burning of combustible materials. It has a boiling point of $-152°C$ (at $1atm$) and a molecular weight of $30g/mol$ [4]. At room temperature and 1 atm partial pressure, its maximum solubility in water is $67mg/L$, slightly higher than oxygen; NO is a lipophilic molecule and possesses a $6 \div 8$ fold higher solubility in non-polar solvent and lipid membranes compared to water. NO has an unpaired electron and formally it is an unstable free-radical species; for that reason, it is often referred to as "NO·" or "NO". The $N - O$ bond distance in the monomer is approximately 1.151 Å. Theoretical studies confirm that the unpaired electron of nitrogen monoxide resides in a π^* orbital and does not reside completely on the nitrogen, but it is shared between the nitrogen and the oxygen. The molecular orbitals obtained by simple combination of the nitrogen and oxygen atomic orbitals are reported in Figure 1.1.

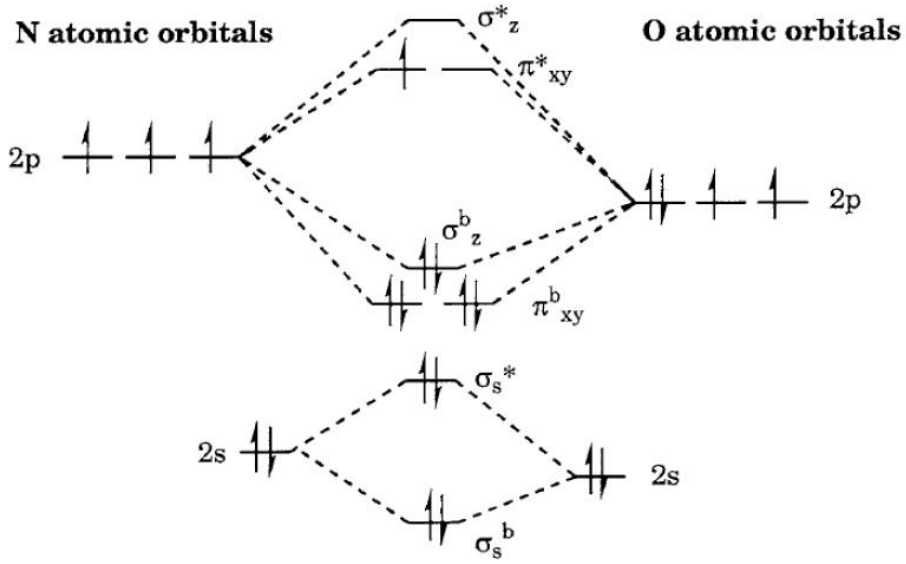

Figure 1.1 - Molecular orbital diagram.

At room temperature, NO has a little propensity to react with itself in a radical-radical dimerization process, forming the dimer O=N − N=O.

$$2\,NO \rightleftharpoons (NO)_2 \qquad (R\ 1\text{-}2)$$

The N-N bond in the dimer is extremely long (2.263 Å); the interaction is considerably weaker than a covalent bond and cannot be entirely explained by van der Waals interactions. Moreover, the NO dimer presents a symmetric planar cis-conformation, favoured because of orbital overlap between the oxygens giving a weak O − O bond Figure 1.2.

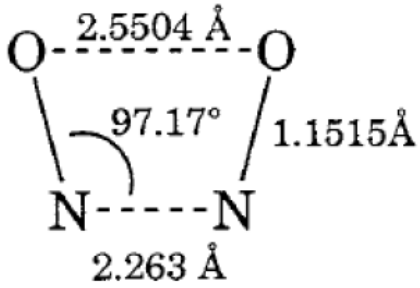

Figure 1.2 - Structure of the NO dimer.

This indicates that the electrons in the N − N bond of the dimer are delocalized over the entire dimer structure. The bond weakness can be attributed to a variety of effects including the weak attractive forces of the delocalized electrons in the π^* molecular orbitals as well as electronic repulsion of the lone pair electrons on the adjacent, bonding nitrogen. However, since there is no net gain in overall

bonding and entropy would favour the monomer, at room temperature and pressure NO exists primarily as a monomeric species [5].

Even though it is a toxic gas, in biology NO has also the function of key signalling molecule in vertebrates: its free-radical nature makes it much more reactive than other signalling molecules and its small size enables it to diffuse through cell membranes and walls to perform a range of signalling functions in various body systems. Furthermore, nitric oxide is a powerful vasodilator and it plays an important role in regulating blood flow and pressure; for this reason, it is used by modern medicine in several ways.

The path of nitrogen to emissions of NO_x is characterized by formation and destruction reactions with overlapping sets of homogeneous and heterogeneous catalysed and non-catalysed reactions. The nitrogen can both come from fuel or air. Due to the high energy of the triple bond between the two atoms in molecular nitrogen (940 kJ/mol), the nitrogen oxidation to nitric oxide is an endothermic reaction.

$$N_2 + O_2 \rightleftharpoons 2\,NO \qquad \textit{(R 1-3)}$$

The Reaction (R *1-3)* occurs in the combustion processes, mainly. where the valence electrons of the nitrogen have enough energy to break the triple blond and link to the oxygen atoms. The nitrogen oxidation was first proposed the Russian physicist Yakov Borisovich Zel'dovich and it is known as Zeldovich mechanism. There exist other mechanisms for the NO_x generation that cannot be explained with the Zeldovich mechanism [6].

The nitrogen valence in the nitric oxide is +2. Although the NO is a stable molecule, the nitrogen valence may change in depending on the atoms of oxygen linked. The atmosphere NO can react with the air oxygen to produce NO_2, assuming a valence equal to +4.

$$2\,NO + O_2 \rightleftharpoons 2\,NO_2 \qquad \textit{(R 1-4)}$$

The Reaction (R *1-4)* is exothermic and the NO oxidation is encouraged by the thermodynamics at room temperature. Moreover, the abundance of oxygen in the air encourages the oxidation of NO to NO_2.

The NO oxidation occurs as the nitric oxide is diluted in air. The third more stable among the nitrogen oxides is the nitrous oxide (N_2O). Although the nitrous oxide is mainly produced by the HCN

oxidation and NCO reduction, it is important to consider the homogeneous reaction with NO to consider the equilibrium between NO, NO_2 and N_2O.

$$NO \rightleftharpoons ½\ N_2O + ¼\ O_2 \qquad (R\ 1\text{-}5)$$

In the Reaction *(R 1-5)*, the nitrogen reduces its valence from +2 to +1.

The equilibrium reactions for the NO production and its conversion to NO_2 and N_2O was proposed by Svoboda et al. [7], whose results are shown in Figure 1.3.

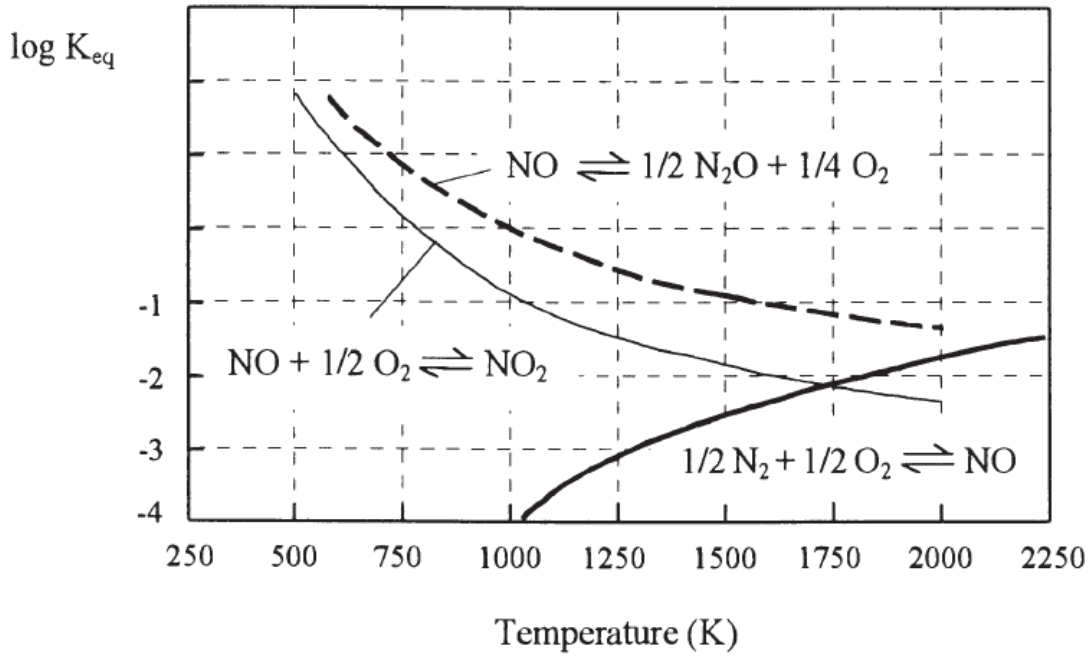

Figure 1.3 - Equilibrium constants of nitrogen reactions as functions of temperature [7].

In terms of the logarithm of the equilibrium constant for the homogeneous reactions that involve the stable nitrogen oxide species.

The nitric oxide production from N_2 and O_2 become relevant as the temperature is higher than 1000K. The higher the temperature, the higher is the conversion to NO. Once the NO is produced, the molecules can oxidize to NO_2. Figure 1.3 shows that the NO oxidation is encouraged at low temperatures while the equilibrium shifts to the NO production as the temperature increases. The equilibrium constant for N_2O production is also higher at low temperature.

1.1.2 Nitrogen dioxide (NO_2)

Nitrogen dioxide (NO_2) is a reddish-brown toxic gas (or yellow liquid) that has a characteristic biting, acrid odour. NO_2 has a boiling point of 21°C (at 1 atm) and a molecular weight of 46 g/mol. The vapour density is 1.58 times that of air. The odour threshold is 0.1–0.4 ppm (0.2–0.8 mg/m^3) [8]. Nitrogen dioxide is produced from the NO oxidation in which the nitrogen assume the valence +4. The oxidation of NO to NO_2 can occur from three pathways: reaction with oxygen, reaction with ozone, reaction with VOCs.

The oxidation with O_2 was proposed in the previous section at the Reaction (R *1-4)*. The equilibrium is strongly temperature-dependent as it was shown in Figure 1.3. A less relevant dependence was found by Epling et al. [9].

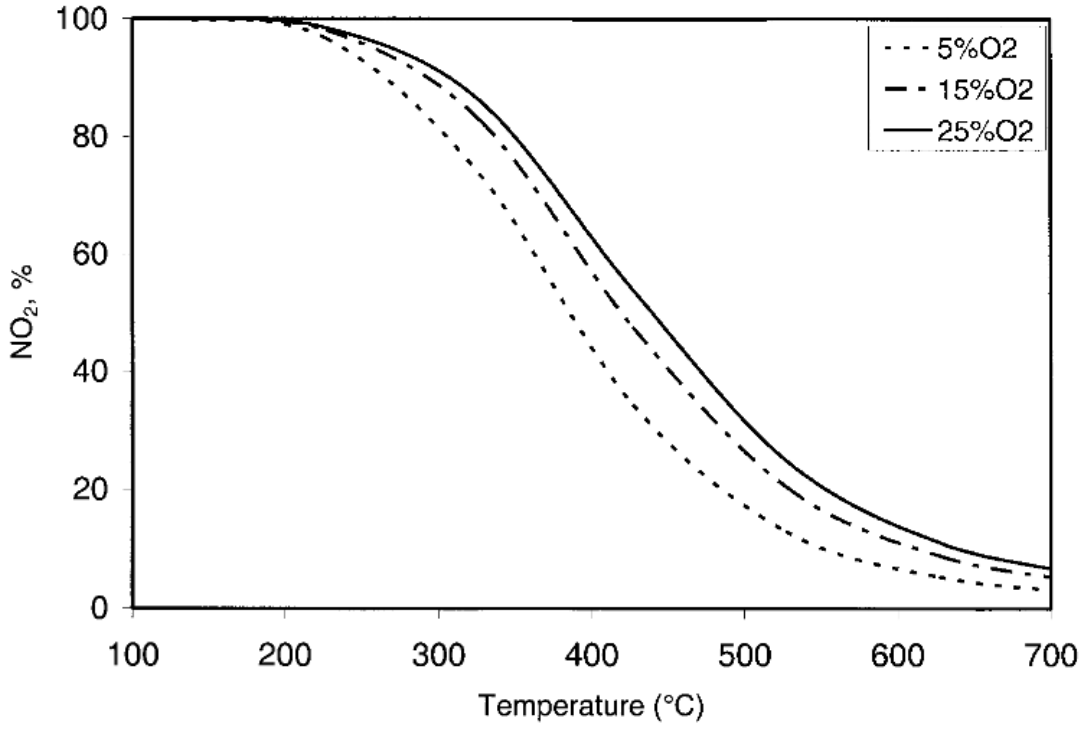

Figure 1.4 - Thermodynamic NO/NO_2 equilibrium in the function of temperature and oxygen concentration.

The oxidation of NO to NO_2 become less relevant as the temperature is higher than 150°C and the equilibrium in Reaction (R *1-4)* shifts to the left. The oxidation is weakly affected by the oxygen concentration as it varies between 5 and 25% at fixed NO_x concentration of 250 ppm as shown in Figure 1.4.

Since the Reaction (R *1-4)* is a homogeneous gas-phase reaction, it does not necessarily require the participation of a solid surface. It proceeds as a third-order reaction:

$$-\frac{d}{dt}[NO] = +\frac{d}{dt}[NO_2] = 2\,k_{NO_2}[NO]^2[O_2] \qquad \textit{(Eq. 1-1)}$$

The kinetic constant k_{NO_2} can be estimated experimentally. Most of the kinetic studies agree that the rate constant k_{NO_2} in (Eq. 1-1) is independent of total pressure; furthermore, the kinetics of this reaction has a peculiarity as it has been observed that the reaction rate decreases with an increase in temperature. The temperature dependence of k_{NO_2} in the temperature range $273 \div 600\ K$ is acknowledged to be represented by an Arrhenius-type equation:

$$k_{NO_2} = k^o_{NO_2} e^{-\frac{E_{act}}{RT}} \qquad \textit{(Eq. 1-2)}$$

The reduction of the rate constant with increasing temperature implies negative activation energy and its value, divided by the ideal gas constant R, has been estimated to be $E_{act}/R = -530K$. Other features of the reaction that are still a subject of disagreement, particularly the presence of other gasses and humidity. A collection of data about the rate constant for the NO oxidation can be found in the paper of Tsukahara et al. [10].

Tsukahara et al. have proposed three different mechanisms:

i. Thermolecular reaction

According to this view, two molecules of NO and one O_2 molecule simultaneously collide and form a transient complex, which then takes a single step to form two molecules of NO_2. Kassel calculated the frequencies of three-body collisions for this reaction and concluded that, although the frequency is not high, it is sufficiently high to explain the observed rates of the reaction and that the rate via the termolecular collisions could decrease with increasing temperature [11].

Alternatively to the termolecular reaction, the two-step mechanism can be considered. Persuasiveness of a two-step mechanism hinges on the demonstration of the existence of an intermediate.

ii. Preequilibrium mechanism with the dimer of NO as intermediate

The dimer $(NO)_2$, that is produced by the equilibrium Reaction (R 1-2) react with oxygen to produce NO_2:

$$(NO)_2 + O_2 \rightarrow 2\,NO_2 \qquad \textit{(R 1-6)}$$

The Reaction (R 1-2) is very fast compared with NO_2 production in the Reaction (R 1-6), which therefore is the rate-determining step. Since the O_2 concentration is only 0.041 mol/L even in pure oxygen at atm and 298 K, the reaction rate of the overall reaction coincides with the Equation (Eq. 1-1).

iii. Preequilibrium mechanism with NO_3 as intermediate

Although the NO_3 is highly unstable, it was detected in the NO oxidation to NO_2. Hence the following mechanism was proposed:

$$NO + O_2 \rightleftharpoons NO_3 \qquad \textit{(R 1-7)}$$

$$NO_3 + NO \rightarrow 2\,NO_2 \qquad \textit{(R 1-8)}$$

The Reaction (R 1-7) is very fast compared with NO_2 production in the Reaction (R 1-8), which therefore is the rate-determining step. Even in this case, it is possible to demonstrate that the oxidation rate of NO to NO_2 can be expressed as in Equation (Eq. 1-1).

Both mechanisms are compatible with the experimental fact that the rate of Reaction (R 1-4) decreases with increasing temperature. Both pathways are more probable than the termolecular reaction, which requires three-body collisions.

Other possible roots of NO oxidation to NO_2 are the reaction with ozone and with organic peroxy radicals collectively called RO_2 [12], [13].

$$NO + O_3 \rightleftharpoons NO_2 + O_2 \qquad \textit{(R 1-9)}$$

$$VOC + OH \rightarrow \cdot RO_2 + products \qquad \textit{(R 1-10)}$$

$$\cdot RO_2 + NO \rightleftharpoons NO_2 + \cdot RO \qquad \textit{(R 1-11)}$$

$$radicals \rightarrow HO_2 + products \qquad \textit{(R 1-12)}$$

$$HO_2 + NO \rightleftharpoons NO_2 + OH \qquad (R\ 1\text{-}13)$$

All these reactions happen in the troposphere that is the lowest layer of the atmosphere. The presence of pollutants in this area have multi-fold hazards for environment and human health. Great attention must be given to the ozone concentration in the troposphere. The ozone reacts with NO to produce nitrogen dioxide as in the Reaction (R 1-9). However, this reaction is discouraged in the presence of VOCs as the Reactions (R 1-11) and (R 1-13) become more relevant.
In such cases, NO_2 can produce ozone due to its photodissociation [12].

$$NO_2 + h\nu\ (\lambda = 420nm) \rightarrow NO + O\ (^3P) \qquad (R\ 1\text{-}14)$$

$$O\ (^3P) + O_2 \rightarrow O_3 \qquad (R\ 1\text{-}15)$$

Where *hν* is the light radiation and λ the wave-length. It may be that NO, NO_2 and O_3 coexist in a photo-strationary equilibrium. Daniel J. Jacob proposed the following equilibrium between the species [13]:

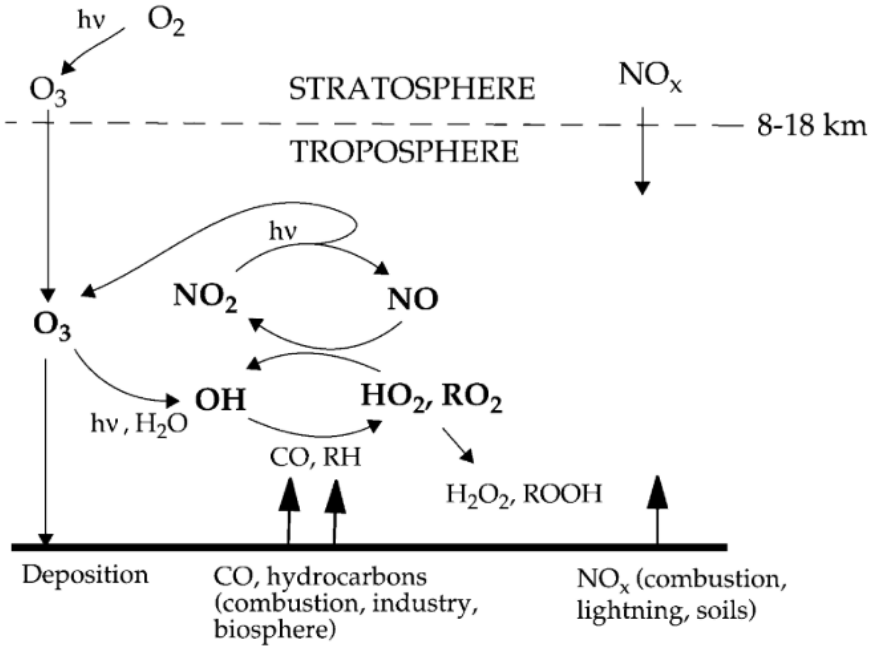

Figure 1.5 - Schematic of tropospheric chemistry for NO_x, O_3, HO_x and RO_2 [13].

When released into the atmosphere, NO is rapidly oxidised to NO_2 through processes involving ozone (O_3) and, in highly polluted areas radicals, such as peroxy-radicals (RO_2) and the hydroperoxy radical

(HO_2). Oxidation by radicals is very fast and may cause high concentrations of nitrogen dioxide at roadsides. In the presence of sunlight, NO_2 is photolytically decomposed back to NO with the subsequent formation of O_3: This leads to the photo-stationary state where the rate of oxidation of NO is balanced by its reformation by the photolytic dissociation of NO_2. This balance is disturbed by the presence of VOC and other compounds which may be oxidised to peroxy radicals, and net ozone production may occur. At night the oxidation of NO by O_3 proceeds to completion, i.e. until either NO or O_3 is totally depleted, with a consequent NO_2 concentration increasing.

It is important to note that the ozone that we want to minimize is that present in the troposphere that is ozone in the ambient air that we breathe. We are not talking about stratospheric ozone in the upper atmosphere that we cannot breathe. Stratospheric ozone protects us and the troposphere from ionizing radiation coming from the sun.

Furthermore, high concentrations of free radicals $\cdot RO_2$ and HO_2 react in presence of NO_2 generating peroxy alkyl nitrates, peroxyacetyl nitrate (PAN) and peroxy benzoyl nitrate (PBN) [14].

Like NO, nitrogen dioxide has a free-radical nature due to an unpaired electron delocalised throughout the molecule, as shown in Figure 1.6; for this reason, it is often referred to as '$\cdot NO_2$'.

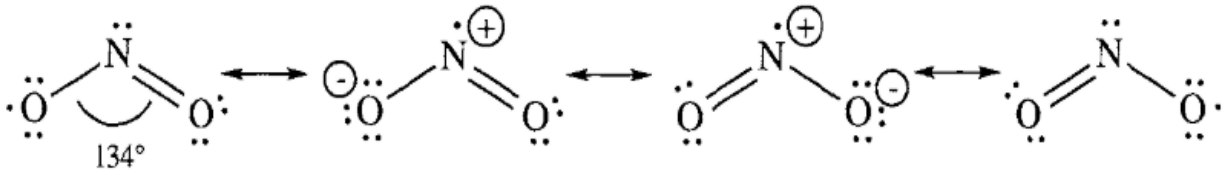

Figure 1.6 - Lewis dot depiction and resonance forms of NO_2.

Due to its radical nature, it can react with other radical species, including itself or nitrogen monoxide. In fact, NO_2 exists in equilibrium with its dimeric form, that is the colourless gas dinitrogen tetroxide:

$$2\,NO_2 \rightleftharpoons N_2O_4 \qquad (R\ 1\text{-}16)$$

NO_2 is predominant at higher temperatures, while it tends to convert to N_2O_4 below $-11.2°C$.

Due to the weakness of the N − O bond, NO_2 is a strong oxidizing agent and it causes corrosion; it combusts, sometimes explosively, with many compounds, such as hydrocarbons.

The NO_2 hydrolysis is widely studied for many applications. The NO_2 reacts with water to produce acid nitrous and/or nitric acid, contributing to the acid rains problem:

$$2\,NO_2 + H_2O \rightarrow HNO_2 + HNO_3 \qquad (R\ 1\text{-}17)$$

$$3\,NO_2 + H_2O \rightarrow 2\,HNO_3 + NO \qquad \textit{(R 1-18)}$$

The disproportionation, sometimes called dismutation, of NO_2 in Reaction (R 1-17) occurs mainly in cold water; while the NO_2 hydrolysis is promoted at higher temperatures, Reaction (R 1-18).
Although the NO_2 have multi-fold hazard problems, it is used as a nitrating and oxidizing agent, in rocket fuels, in the manufacture of haemostatic cotton and other oxidized cellulose compounds, and in bleaching flour. Moreover, both NO and NO_2 are intermediate compounds in the industrial process for the production of nitric acid.

1.2 Toxicology

Nitrogen oxides are primary pollutants, as they are directly released into the atmosphere. They impact on the environment by promoting the ozone production in the troposphere, acid rains and eutrophication of soil and water; furthermore, the N_2O is a greenhouse gas and it contributes to global warming. Lastly, nitrogen oxides readily react with common organic chemicals, and even ozone, to form a wide variety of toxic products, some of which may cause DNA mutations.

In addition to air pollution, nitrogen oxides are highly toxic gases, which can cause serious damages to human health [15].

Exposure to even low concentrations can irritate eyes, nose, throat and lungs, leading to coughing, shortness of breath, tiredness and nausea. Classified as irritant asphyxiant gases, at high levels they mainly impact on respiratory conditions, causing severe inflammations in the air passages and lungs: many of them dissolve in the moisture on any moist tissue surfaces, forming strong acids or alkalis which then burn the delicate tissues; fluid from damaged lung tissue pours out into air spaces preventing air from getting to deeper lung and causing asphyxia. Department of Health and Human Services (DHHS), the International Agency for Research on Cancer (IARC) and the United States Environmental Protection Agency (EPA) have not classified nitrogen oxides for potential carcinogenicity in humans, but exposure of pregnant animals has resulted in toxic effects in developing foetuses and it has been observed that NO and NO_2 can cause changes in the genetic material of animal cells [16].

Due to their toxicity, the NO_x emissions are strictly regulated worldwide. In the European Union, the Scientific Committee on Occupational Exposure Limits (SCOEL) that was set up in 1995 by the Commission to evaluate the potential health effects of occupational exposure to chemicals, contributes to the defining of Occupational Exposure Limit Values (OELVs) for the protection of workers from chemical risks, to be set at UE level pursuant to the Chemical Agents Directive (Directive 98/24/EC) and to the Carcinogens and Mutagens Directive (Directive 2004/37/EC). The SCOEL recommendation for nitric oxide [4] and nitrogen dioxide [8] are summarized in Table 1.1.

Substance	CAS No.	TWA IOELV		STEL IOELV	
		ppm	mg/m^3	ppm	mg/m^3
NO	10102-43-9	2	2.5	-	-
NO_2	10102-44-0	0.5	0.96	1	1.91

Table 1.1 - Occupational Exposure Limit Values for NO and NO_2 recommended by SCOEL.

Table 1.1 reports the Indicative Occupational Exposure Values (IOELVs) for nitric oxide and nitrogen dioxide. The numbers represent the threshold limit values a worker can be exposed to, day after day for a working lifetime without adverse effects. For the NO, it is reported the Time Weighted Average (TWA) value that represents the mean exposure concentration based on 8 h/day, 5 days/week work in terms of part per million (ppm), and mg/m^3. For the NO_2, the Short-Term Exposure Limit (STEL) is reported in addition to the TWA. The STEL represents the threshold limit value a worker can be exposed to, for a duration of 15 min no more than 4 times per day with at least 60 min between exposure periods.

For what concerns the nitrous oxide (N_2O), tit was not possible to find any EU documentation that expresses its occupational exposure limit value. The data collected and the tests performed are not able to define a threshold for this chemical specie. However, data on N_2O has been found in the Irish Health and Safety Authority (H&SA) published the "2020 Code of Practice for the Safety, Health and Welfare at Work (Chemical Agents) Regulations (2001-2015) and Safety, Health and Welfare at Work (Carcinogens) Regulations (2001-2019)". This code of practice provides practical guidance about occupational exposure limit values (OELVs) not only for those chemical species currently legally binding under the Chemical Agents Regulations and Carcinogens Regulations (which have been assigned an IOELV), but also for those chemical species which OELVs derives from authoritative sources other than EU Commission Directives. Moreover, they included information about the NO and NO_2 limit values for the underground mining and tunnelling sector. This information can be considered in addition to the SCOEL recommended values [17].

Substance	CAS No.	TWA IOELV		STEL IOELV	
		ppm	mg/m^3	ppm	mg/m^3
NO	10102-43-9	2 (25)	2.5 (30)	- (35)	- (45)
NO_2	10102-44-0	0.5 (3)	0.96 (5)	1 (5)	1.91 (9)
N_2O	10024-97-2	50[1]	90[1]	-	-

Table 1.2 - Occupational Exposure Limit Values for NO, NO_2 and N_2O from (H&SA).

In addition to the SCOEL recommended values, the 2020 Code of Practice, include information about the limit values apply to underground mining and tunnelling sector only until 21 August 2023, within brackets. Furthermore, the Code provides a list of advisory (OELVs) including nitrous oxide for which the TWA is equal to 50 ppm (90 mg/m^3).

[1] Advisory OELVs derived from authoritative sources other than EU Commision Directives.

1.3NO_x emissions and legislation

Significant amounts of NO_x also exist in the troposphere with global production estimates of ~48 TgN/year (10^{12} grams of Nitrogen per year) [18]. Tropospheric NO_x is generated by high-temperature reactions involving N_2 and O_2. These are mainly anthropogenic and include combustion of fossil fuels and biomass burning. On average, some 90% of tropospheric NO_x resides in the boundary layer, where it is a precursor to lower tropospheric ozone.

The major natural sources of tropospheric NO_x are soil emissions and lightning [19]. In the upper troposphere, the lightning source dominates. In the mid-upper troposphere, lightning dissociates N_2 and O_2, into free N and O within the extremely hot flash channel. These in react with ambient N_2 and O_2 to produce NO, which remains after the lightning channel cools. During the conversion between NO and NO_2, ozone is generated in the presence of HO_2 and RO_2. Ozone is sensitive to lightning NO_x amounts, which are believed to be responsible for 35–45% of global free-tropospheric ozone [20].

Biogenic NO_x emissions from soils are a large natural source with substantial uncertainties in global bottom-up estimates (ranging from 4 to 15 Tg N yr−1) [19]. Soil NO_x is produced primarily by biotic processes and it is mainly in the form of NO; a secondary generation pathway for soil NO is the abiotic chemical decomposition of HNO_2 that occurs under low pH and high organic matter content. The aforementioned biotic processes are microbial processes that occur in many natural and agricultural ecosystems and consists of nitrification and denitrification reactions carried out by soil bacteria. Nitrification is the oxidation of ammonium ($NH4^+$) to nitrite (NO_2^-) and nitrate (NO_3^-) by a specialized group of bacteria that gain carbon from carbon dioxide rather than from the consumption of organic compounds. NO is produced during the reduction of NO_2^-, which is an intermediate in the oxidation process from $NH4^+$ to NO_3^-, as shown in Figure 1.7.

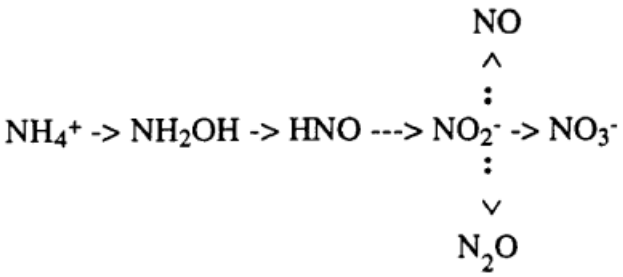

Figure 1.7 - Pathway of chemoautotrophic nitrification [21].

Denitrification consists of a sequence of reactions in which nitrate and nitrite are reduced to NO, N_2O and N_2:

$$NO_3^- \rightarrow NO_2^- \rightarrow NO \rightarrow N_2O \rightarrow N_2$$

Figure 1.8 - NO_x denitrification in soils.

Denitrifying bacteria survive under anaerobic conditions by using nitrogen oxides as their electron acceptors in place of oxygen. Production and emissions from soils are controlled by environmental variables and soil characteristics, including nutrient availability, water-filled pore space and soil temperature. Those variables are affected by agricultural management practices, such as fertilization and irrigation.

The role of agricultural practices on environmental quality has been examined in the past two decades because of the links between increased agricultural productions accompanied by deterioration of environmental quality. In developing countries, intensive agricultural production systems have increased the use of nitrogen-based fertilizer as an effort to produce and sustain high crop yields. Consequently, nitrogen losses have also increased with the passage of time [16].

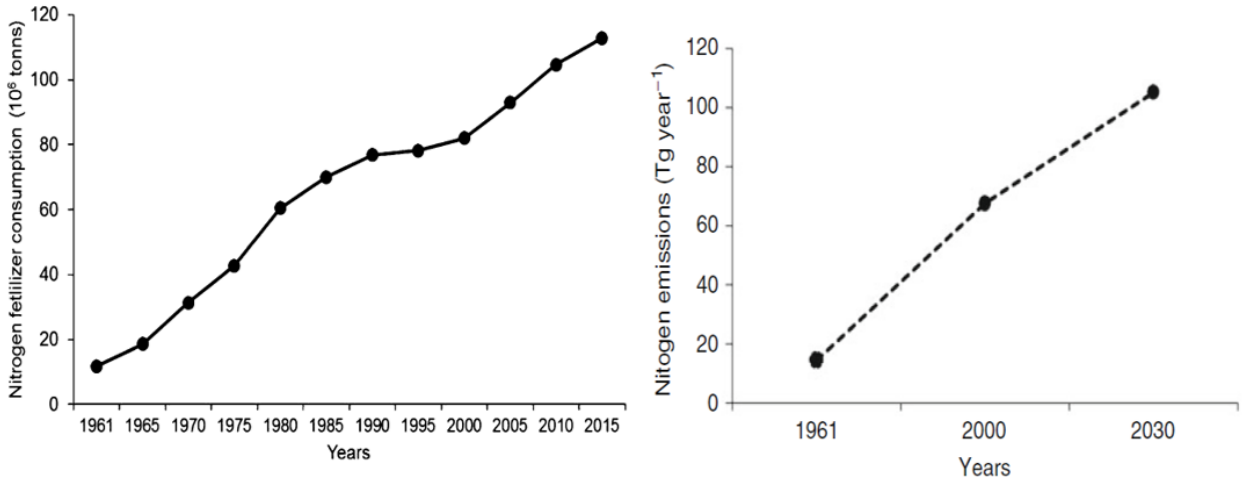

Figure 1.9 - Historical and predicted nitrogen fertilizer consumption in global agriculture (left) and emission of anthropogenic reactive nitrogen in the global environment (right) [16].

The increased use of nitrogen-based fertilizers has led to increased nitrogen losses from agroecosystems and recovery of nitrogen in the global crop production system [22] and rest may be lost into the atmosphere, accumulate in the soil or enter surface or subsurface water bodies through leaching or runoff.

The agriculture NO_x emissions are both correlated to biogenic emissions (nitrification and denitrification) and anthropogenic emissions (fertilization). NO_x from agriculture corresponds only to a small part of the total NO_x anthropogenic emissions. The anthropogenic (man-made) NO_x is

produced mainly from combustion processes. During the combustion, the nitrogen present in the air and/or in the fuel oxidizes to NO_x. This mechanism was well investigated by Zel'dovich; furthermore, the high-temperature combustion promotes radicals that contribute to the NO_x production.

1.3.1 Anthropogenic NO_x emissions

The Organization for Economic Co-operation and Development (OECD) has collected data on man-made emissions of major air pollutants for member countries. The OECD is an intergovernmental economic organisation with 36 member countries, founded in 1961 to stimulate economic progress and world trade. These data come from two sources: Convention on Long-Range Transboundary Air Pollution (LRTAP Convention) in UNECE-EMEP emissions Database (June 2018); National Inventory Submissions 2018 (June 2018) to the United Nations Framework Convention on Climate Change (UNFCCC).

The nitrogen oxides data for Europe have been used to derive the emission trend from 1990 to 2018, taking into account that these data exclude international aviation and maritime transport emissions (even if they are one of the main sources of NO_x). In addition to the NO_x European trend, the percentage of the Italian contribution to the NO_x emissions has been reported in Figure 1.10 [23].

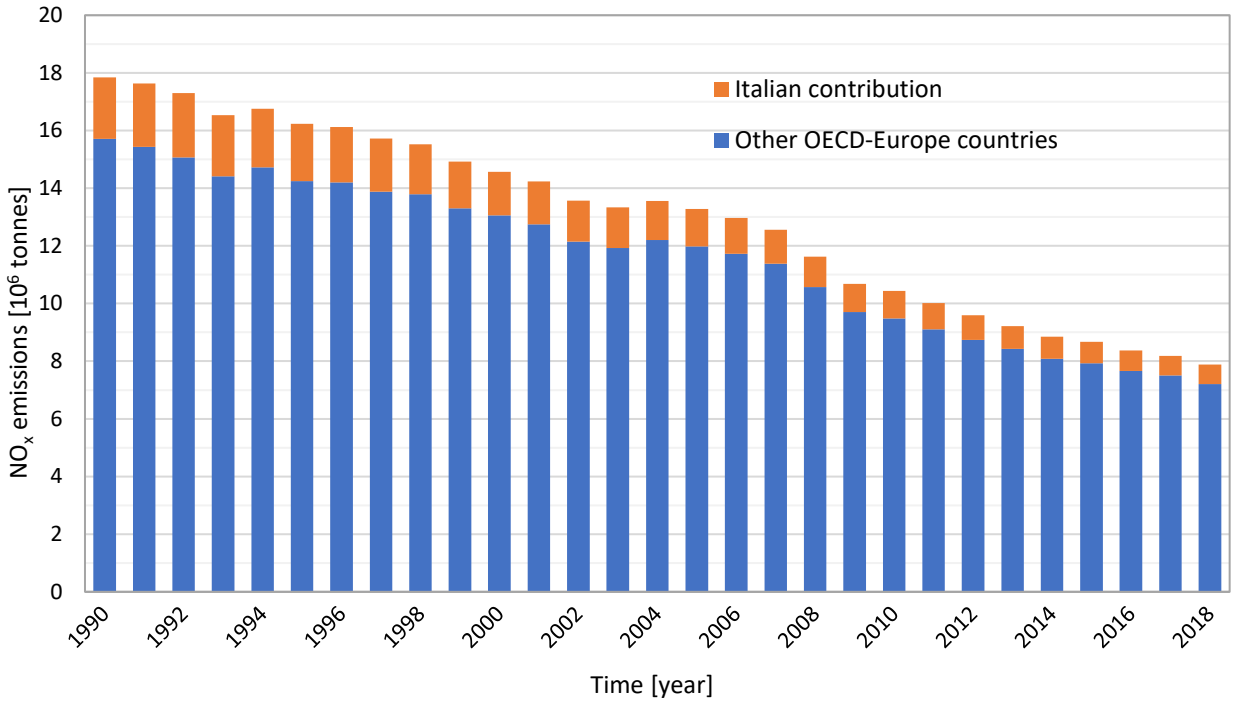

Figure 1.10 - Total man-made NO_x emissions from 1990 to 2018 for the OECD-Europe countries and Italian contribution.

Figure 1.10 shows that the NO_x emissions for the OECD members, that include Europe countries, constantly decreases among the last two decades. Furthermore, the Italian contribution decreased constantly from a value of 2.1 megatonnes (11.9%) in 1990 to 670 thousand tonnes (8.5%) in 2018. The drop of the NO_x emission in the last twenty years is due to the even more stringent regulations that aim to control the NO_x emission in the different fields. These regulations assume further importance if we consider that industrial production, road transport and the total energy consumption are increasing constantly [24]–[26]. To comply with the emission standards, an improvement of the flue-gas abatement techniques was required, resulting in an overall reduction of NO_x emissions.
Nitrogen oxides are commonly measured in $\mu g/m^3$ or part per million (ppm) of NO_2 as the NO_x chemistry leads mostly to the nitrogen dioxide species. 1 ppm of NO_2 is equal to 1180 $\mu g/m^3$ at room temperature and pressure. Annual mean nitrogen dioxide concentrations in urban areas throughout the world are generally in the range of 20–90 $\mu g/m^3$ (0.01−0.05 ppm). The maximum hourly mean value may be several times the annual mean. It is known that nitrogen dioxide concentrations are highly correlated with population, and population worldwide continues to grow. A proposal for the new air quality limit values was based on the recommendations of the World Health Organization (WHO) health assessment, i.e. the update and revision of the Air Quality Guidelines (AQGs) for Europe [27]. The European air quality standards, set by the Ambient Air Quality Directive (EU, 2008) for the protection of human health, and the air quality guidelines (AQGs) set by the WHO for nitrogen dioxide (NO_2) are summarized in Table 1.3.

Air quality standards for protecting human health from NO_2

Pollutant	Averaging period	Standard type and concentration	Comments
NO_2	1 hour	EU limit value: 200 $\mu g/m^3$	Not to be exceeded on more than 18 hours per year
		WHO AQG: 200 $\mu g/m^3$	
		EU alert threshold: 400 $\mu g/m^3$	To be measured over 3 consecutive hours over 100 km^2 or an entire zone
	Calendar year	EU limit value and WHO AQG: 40 $\mu g/m^3$	

Table 1.3 - Air quality standards for the protection of human health for NO_2 [28].

Ambient Air Quality Directive (EU, 2008) requires the member countries to adopt and implement air quality plans and meet standards in order to protect human health and the environment. The calendar year limit value for the protection of human health corresponds to the WHO (World Health Organization) air quality guidelines, designed to offer guidance in reducing the health impacts of air pollution. The Ambient Air Quality Directive (EU, 2008) also sets targets for the protection of

vegetation at the annual limit value of 30 µg/m^3. These guidelines are based on expert evaluation of current scientific evidence and they are currently under review.

All the EEA-39 countries (except Greece, Kosovo and Liechtenstein) and Andorra submitted NO_2 data in 2017 with a minimum coverage of 75 % of valid data from 3260 stations for the annual limit value and 3078 stations for the hourly limit value. Sixteen of the EU Member States and four other reporting countries recorded concentrations above the annual limit value (and the identical WHO AQG value).

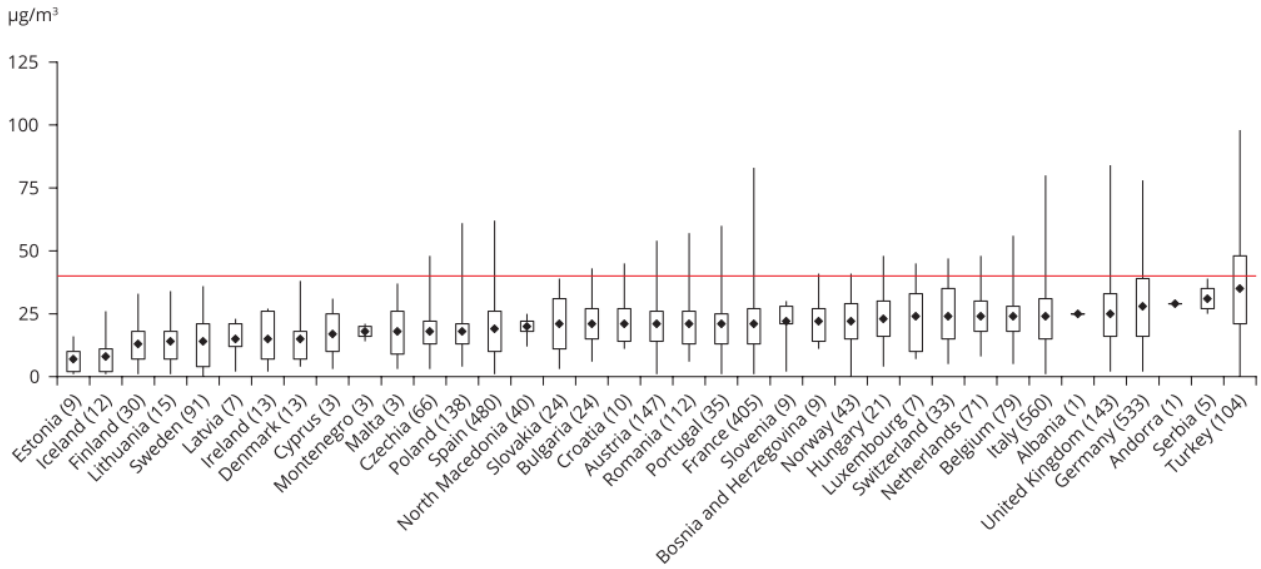

Figure 1.11 - NO_2 concentrations in relation to the annual limit value in 2017 and the number of stations considered for each country [28].

The graph is based on the annual mean concentration values. For each country, the number of stations considered (in brackets) and the lowest, highest and average values (in µg/m^3) recorded at its stations are given. The rectangles mark the 25th and 75th percentiles. At 25 % of the stations, levels are below the lower percentile; at 25 % of the stations, concentrations are above the upper percentile. The limit value set by EU legislation (which is equal to that set by the WHO AQG) is marked by the horizontal line that corresponds to 40 µg/m^3. The maximum and minimum limit values recorded are represented by the vertical lines. Most of the countries recorded NO_x emissions above the limit. Concentrations were above the annual limit value at 10 % of all stations measuring NO_2. The map in Figure 1.12 shows that stations with concentrations above the annual limit value were widely distributed across Europe in 2017 [28].

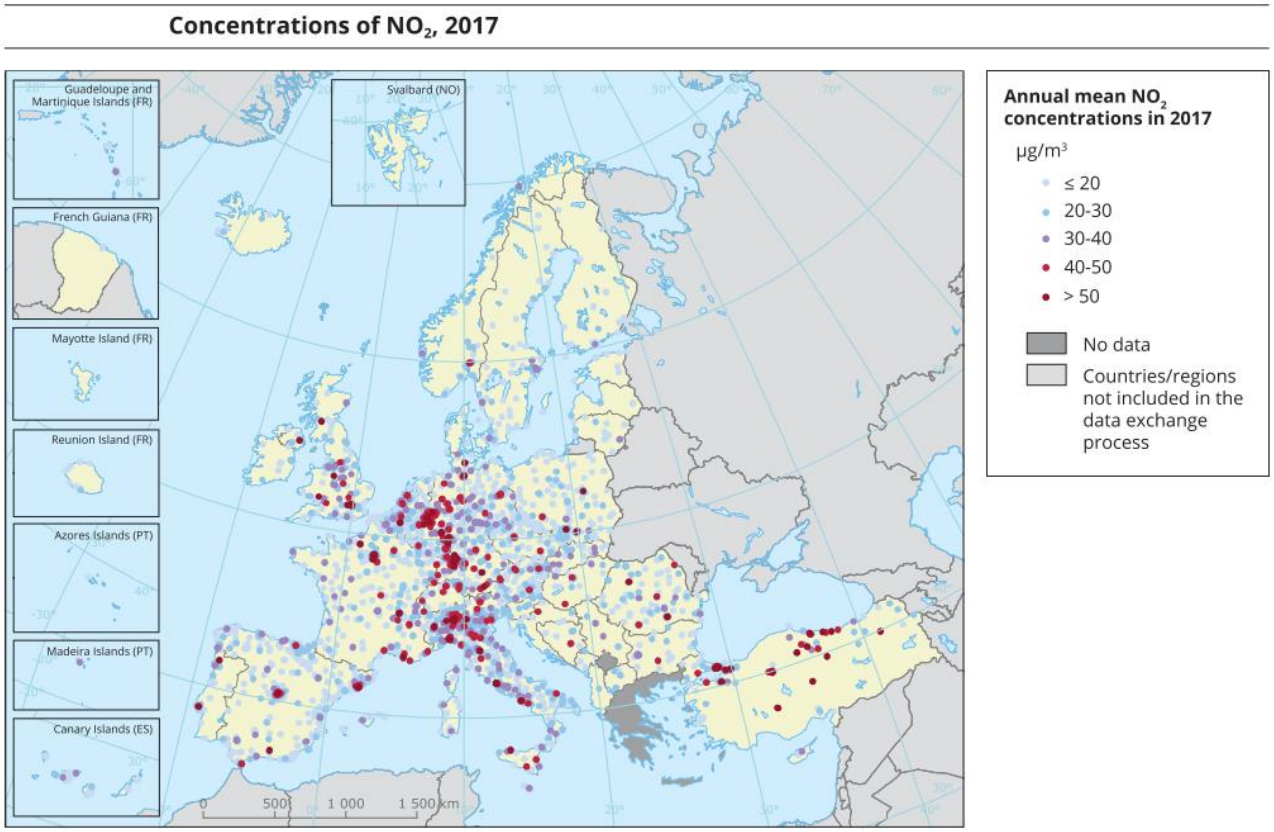

Figure 1.12 - Map of the countries and their annual mean NO_2 concentration recorded in 2017 [28].

Figure 1.12 reports the observed concentrations of NO_2 in 2017. Dots in the last two colour categories correspond to values above the EU annual limit value and the identical WHO AQG (40 µg/m3). Only stations with more than 75 % of valid data have been included in the map. The peaks can be observed mainly across the largest cities and close to the industries.

The information about pollutant emissions collected from the Europen countries, and their sources, are collected by the European Environment Agency (EEA). Also, on the EEA website, it is possible to found the pollutant emissions for each country per kind of pollutant, emission source and per year [29]. The data in Figure 1.13 reports the evolution of the emissions of NO2 per sector in EU countries.

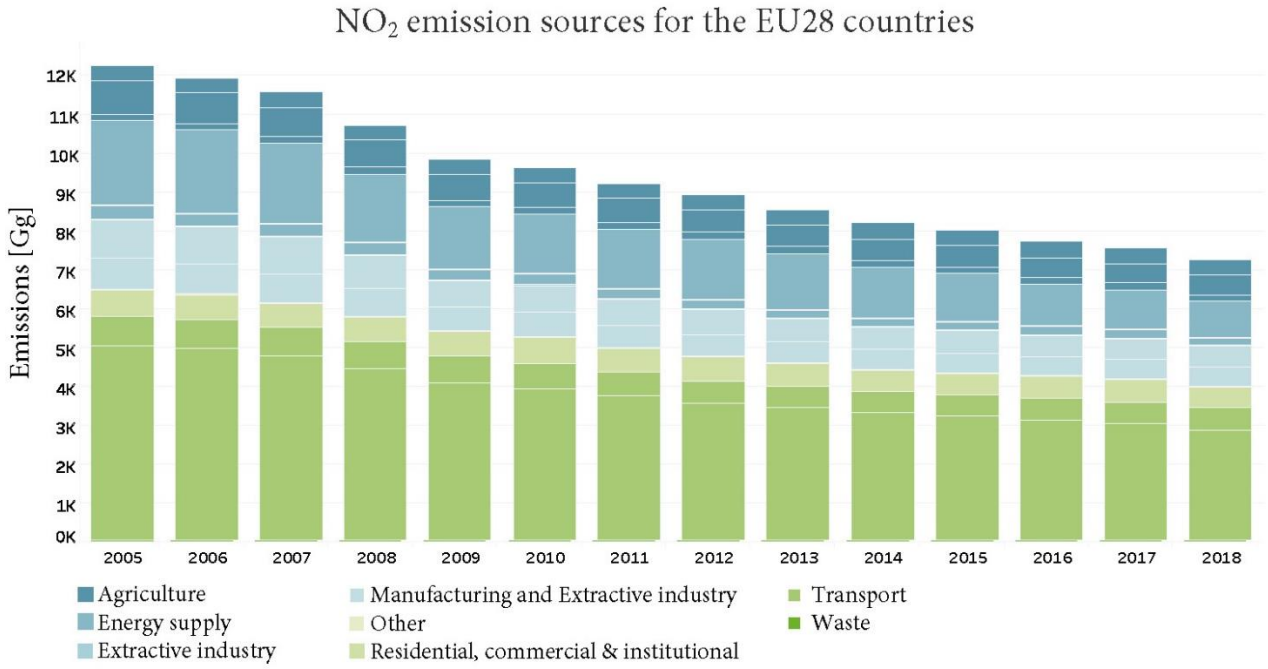

Figure 1.13 - NO_2 emission sources for the EU28 countries [29].

The data in Figure 1.13 shows the NO_2 amount produced per year in the 28 European countries, distinguishing the emission sources. These data can be compared with those of the Organization for Economic Co-operation and Development (OECD) that includes 36 countries, most of them part of the EU [23]. Figure 1.13 shows that the amount of NO_2 emitted from anthropogenic sources in Europe is constantly decreasing as it was discussed from the OECD data in Figure 1.10. However, the EEA data include national navigation and international aviation that was not considered from OECD. The details of the emission sources in Europe and Italy in 2018 are reported in Table 1.4.

Country Name	Pollutant	EEA Sector	EEA Sub-Sector	NO_2 [Gg]
EU28	**NO_x**	Energy supply	Energy production	919.45
			Fuel processing	0.74
			Fuel production and processing	199.69
			Other energy	-
		Extractive industry	Extractive industry	9.77
		Manufacturing and extractive industry	Heavy industry	559.96
			Light industry	492.11
		Residential, commercial, institutional	Residential, commercial & institutional	561.09
		Transport	Non-road transport	572.79
			Road-transport	2832.80
		Agriculture	Crops	417.65
			Energy use	485.30
			Livestock	173.71
		Waste	Waste management	44.77
			Wastewater treatment	0.01
		Other	Other	2.33
		National total for the entire territory (based on fuel sold)		**7272.17**
Italy	**NO_x**	Energy supply	Energy production	28.25
			Fuel processing	-
			Fuel production and processing	18.10
			Other energy	-
		Extractive industry	Extractive industry	0.21
		Manufacturing and extractive industry	Heavy industry	51.78
			Light industry	16.43
		Residential, commercial, institutional	Residential, commercial & institutional	75.39
		Transport	Non-road transport	85.84
			Road-transport	290.82
		Agriculture	Crops	29.35
			Energy use	49.24
			Livestock	21.68
		Waste	Waste management	2.08
			Wastewater treatment	-
		Other	Other	-
		National total for the entire territory (based on fuel sold)		**669.16**

Table 1.4 - Anthropogenic NO_x emission from different sectors in Europe and Italy for the year 2018.

The NO_x emissions are expressed as Gg (10^6 g of NO_2). The higher percentage of NO_x emissions comes from transport either in Italy and in Europe. The road-transport includes passenger cars, heavy-duty vehicles, moped and motorcycles; the non-road transport includes national navigation, railways, international aviation, international shipping, domestic aviation and all the other transports. The data reported in Table 1.4 are shown as pie charts in Figure 1.14.

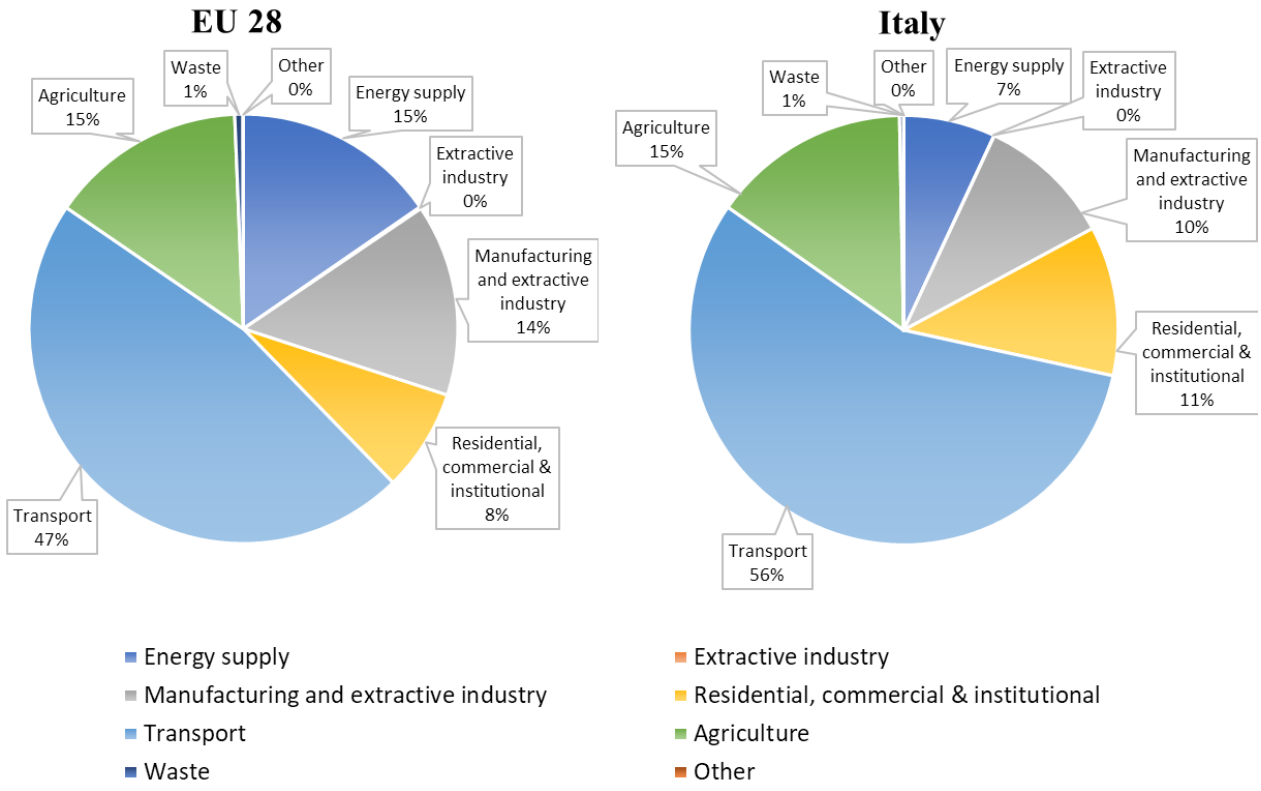

Figure 1.14 - Anthropogenic NO_x emission from different sectors in Europe and Italy for the year 2018.

More than half of the NO_x was emitted by transports in Italy. This percentage is higher than the European mean emission for the same source. NO_x emissions from residential, commercial and institutional sources cover 11% of the total emissions, while it is 8% in Europe. These difference are correlated to the lower capacity of Italy to produce electricity and consequentially, a lower amount of NO_x is produced from the energy supply sector.

1.3.2 NO_x regulations

Great attention was paid to vehicles emissions for both NO_x and Particulate Matters (PM) in the last decades due to their impact on the environment. Petroleum-derived liquid fuels currently provide around 95% of transport energy and roughly 60% of crude oil produced is used to make transport fuels [30], [31]. The demand for transport fuels across the world is huge, being around 4.9 billion litres each for gasoline and diesel and 1.3 billion litres for jet fuel daily, with an expected yearly growth of around 1% [32]. Changes in the transport sector are occurring mostly because of:

- an increasing demand driven by increasing population and prosperity;
- the need to ensure energy security;
- control Greenhouse Gases (GHG) emissions;
- improve local air quality;
- in response to consumer preferences and demands

The importance of each of these "drivers for change" is differ in different countries and at different times in rich countries [33]. New strategies have been proposed and commonly adopted to the new vehicles, while circulation limits are introduced in some circumstances to mitigate the air pollutions. Figure 1.15 provides a summary of the current and future regulatory introduction timings for both on-road and off-road engines and vehicles [34].

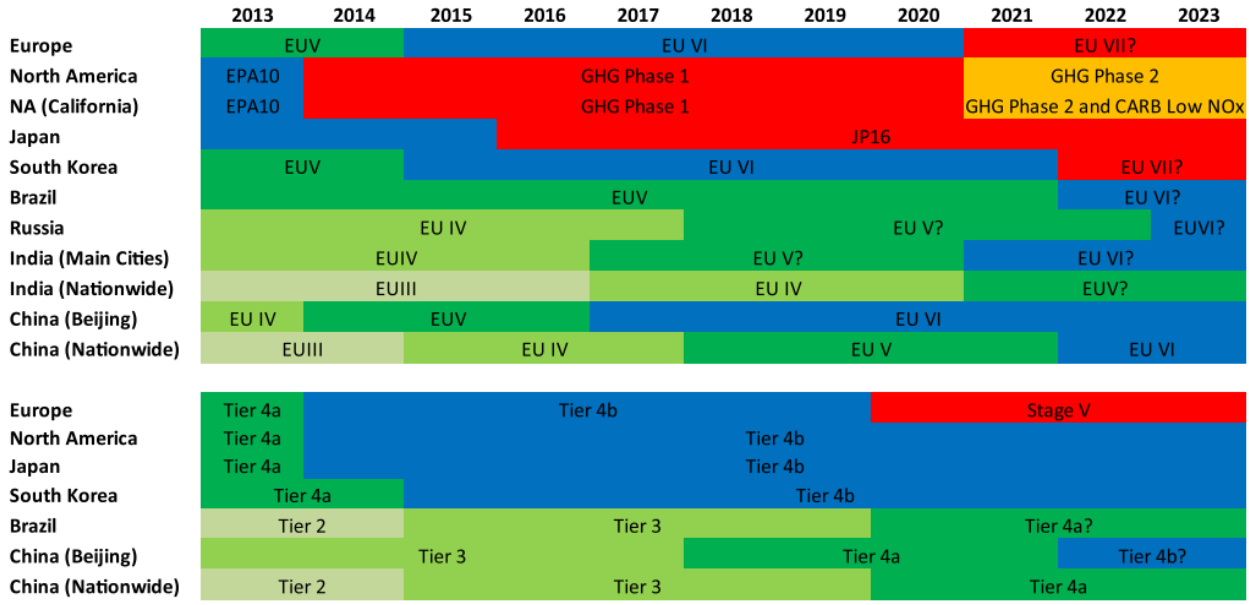

Figure 1.15 - Summary of the introductory timings of current and future regulations in the on-road and non-road engines [34].

The European (EU IV-VI) and the North American (EPA10) regulations are included in Figure 1.15 for on-road vehicles/engines; while the non-road Stage IV/Tier 4 was adopted for the non-roads. These regulations impose even more stringent emissions for PM and NO_x among the years. Figure 1.16 reports the pollutants limit emissions according to the regulations introduced for the Heavy-Duty Diesel engines.

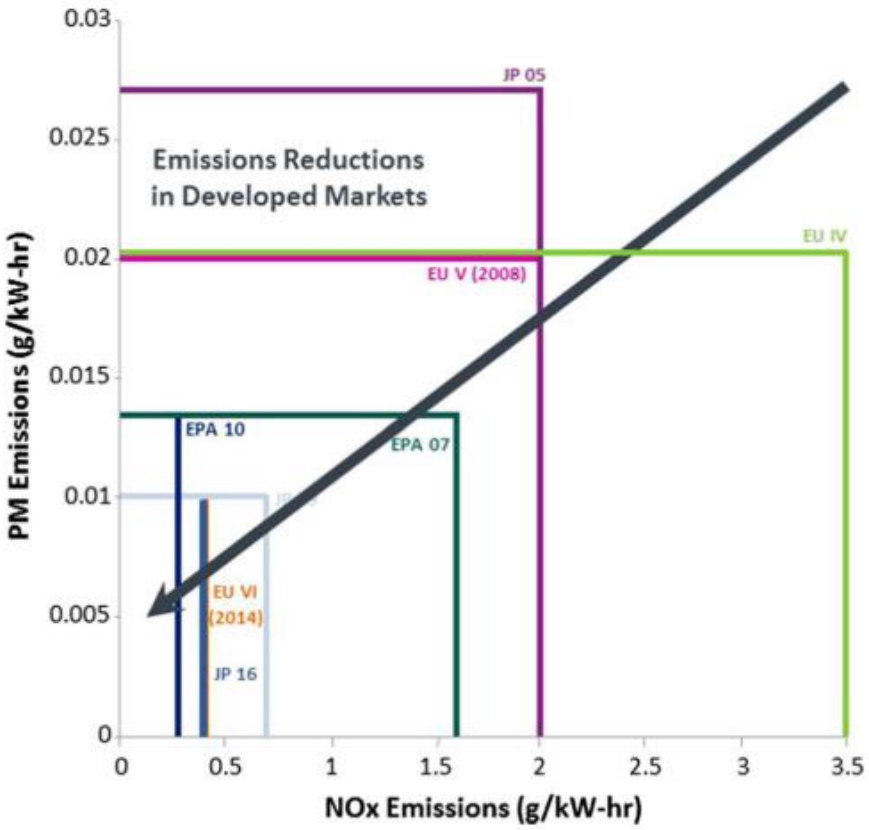

Figure 1.16 - Evolution of the PM and NO_x emission regulations for HDD engines in Europe, North America and Japan [34].

The latest regulation in Europe is EU6 introduced on 31/12/2013 with the limits of 10 mg/kWh and 400 mg/kWh for PM and NO_x respectively. In North America, the EPA'10 was introduced on 01/01/2010. This imposes the limits of 13 mg/kWh and 270 mg/kWh for PM and NO_x respectively. For what concerns the non-road areas the Stage IV/Tier 4f was introduced in 2014, imposing the limit emissions of 25 and 400 mg/kWh for PM and NO_x respectively.

Figure 1.15 and Figure 1.16 show the active regulatory evolutions in several countries and highlight, indirectly, how the evolution of technology allowed a reduction of NO_x emissions requirement.

For what concern the stationary sources, new standards in terms of pollutant emissions have been imposed by the governmental organizations. NO_x emissions from energy supply, manufacturing and extracting industries represented 29% and 17% of the total NO_x anthropogenic emissions in Europe and Italy respectively, in 2018 (Figure 1.14). The standards are strictly correlated to the innovative techniques for production and gas treatment. The European Integrated Pollution Prevention and Control (IPPC) Bureau (EIPPCB) was set up in 1997 to organise an exchange of information between member states, industry and non-governmental organisations promoting environmental protection on Best Available Techniques (BAT), associated monitoring and developments in them. With the entry

into force of the Industrial Emissions Directive (IED, 2010/75/EU), the EIPPCB organises and coordinates the exchange of information that leads to the drawing up and review of BAT reference documents according to the dispositions of a guidance document on the exchange of information (Commission Implementing Decision 2012/119/EU). The European IPPC Bureau is an output-oriented team which produces reference documents on Best Available Techniques, called BREFs. BREFs are the main reference documents used by competent authorities in member states when issuing operating permits for the installations that represent a significant pollution potential in Europe. There are about fifty thousands of these installations in Europe. In the international context, the European information exchange on best available techniques is considered to be an EU contribution to the global process initiated in 2002 at the World Summit on Sustainable Development so that non-EU countries can also reap the benefits of this ambitious work. The most updated BREF are available on the EIPPCB web site [35].

The most innovative techniques consolidated in the literature are described in the BREFs. The reference documents provide information on the techniques, their applicability and the limit emissions for new plants and pre-existing plants; in such cases, the existing plants have to introduce new techniques or revamp the existing ones, to accomplish the new regulations. The most common techniques for the NO_x reduction in stationary sources are the Selective Non-Catalytic Reduction (SNCR) and the Selective Catalytic Reduction (SCR). The average abatement efficiency and the emission levels associated with the use of the different techniques are reported in the BREFs for each specific productive sector and production technologies.

The NO_x emission limit for the cement industry and the waste incineration e.g. can be found in their BREFs updated in 2013 and 2019 respectively [36], [37]. The limit values are reported in Table 1.5.

		BAT-AEL (daily average value) $[mg/Nm^3]$		Comments
Cement industry	**Kiln type**			
	Preheater kilns	$< 200 - 450$		The upper level is 500 mg/Nm^3 if the initial NO_x level after primary techniques is $> 1000\ mg/Nm^3$.
	Lepol and long rotary kiln	$400 - 800$		Depending on initial levels and NH_3 slip.
Waste incineration	**Parameters**	**New plants**	**Existing plants**	
	NO_x	$50 - 120$	$50 - 150^{(1)}$	(1) The higher end is 180 mg/Nm^3 where SCR is not applicable.
	CO	$10 - 50$	$10 - 50$	
	NH_3	$2 - 10$	$2 - 10^{(2)}$	(2) For existing plants fitted with SNCR without wet abatement techniques, the higher end is 15 mg/Nm^3.

Table 1.5 - NO_x emission limits from the cement industries and waste incineration.

From the comparison of the NO_x emission limits in the two BREFs, it is possible to note that the waste incineration regulations are more stringent than the cement industry. For what concerns cement industry, existing kiln system design, fuel mix properties including waste and raw material burnability (e.g. special cement or white cement clinker) can influence the ability to remain within the range. Referring to preheater kilns, levels below 350 mg/Nm^3 are achieved at kilns with favourable conditions when using SNCR: in 2008, the lower value of 200 mg/Nm^3 has been reported as a monthly average for three plants using SNCR.

The waste incineration BREF document reports that the daily average of NO_x emission is 80-180 mg/Nm^3 when the SNCR is adopted, by maintaining the NH_3 emissions below 6 mg/Nm^3, depending on dosing rate, waste, and combustor type. When SCR is adopted, the daily average of NO_x emission is in the range 40-150 mg/Nm^3, by maintaining the NH_3 emissions below 10 mg/Nm^3. Besides, if specifically designed (extra catalyst layer, higher operating temperature), SCR can also catalytically destroy PCDD/F. SCR and SNCR technologies will be described in the "pollution control

technologies" of this thesis. It will be described the role of ammonia/urea and the importance to maintain low the emissions of secondary pollutants as ammonia (NH_3) and carbon monoxide (CO).
Based on the BREFs standards and their developments, the European Parliament and the Council of the European Union approved the directive 2010/75/EU on industrial emissions (integrated pollution prevention and control). With this directive, the Commission established guidance on: energy industries, production and processing of metals, mineral industry, chemical industry, waste management and others. This directive is the reference for the majority of the industrial applications for pollution prevention and control. The EU states members have approved national directives based on 2010/75/EU act to regulate the emissions in the different applications.
Following the Paris climate conference (COP21), the European Green Deal was established. in 2019, The European Green Deal is a set of policy initiatives by the European Commission with the goal to make Europe climate neutral by 2050. For what concern pollutants, the European Parliament and the Council of the European Union approved the Directive (EU) 2016/2284 on the reduction of national emissions of certain atmospheric pollutants, amending Directive 2003/35/EC and repealing Directive 2001/81/EC. This Directive includes the pollutant emission reduction commitment for the EU members, with a focus on the greenhouse gases. A table for the national emission reduction commitments for NO_x is included in annex II and part of it is reported in Table 1.6

Country	**NO_x emissions reduction compared to year 2005**	
	From year 2020 to year 2029	From year 2030
Belgium	41%	59%
Germany	39%	65%
Greece	31%	55%
Spain	41%	62%
France	50%	69%
Italy	40%	65%
United Kingdom	55%	73%
EU28	42%	63%

Table 1.6 - NO_x emission reduction commitments for some EU members compared to the year 2005.

Table 1.6 reports information on some of the European countries. The full list that includes the totality of the State members can be found in the directive. The reductions are referred to the total NO_x emission compared to the States emission in the year 2005. The countries must introduce new regulations that allow the NO_x emissions reduction in all the more critical field to meet the European regulation. Table 1.6 shows that Italy, e.g., has to reduce the NO_x emission of 40% than in 2005 for any year from 2020 to 2029 and a further 25% reduction from 2030.

The industrial companies are looking with even more interest toward new processes for NOx reduction. In fact, while in many cases, the installed technologies allow accomplishing the new regulations by controlling the reagents or the operative conditions, in other processes, the installed technologies are inadequate to achieve the threshold imposed.

1.4Pollution control techniques

The NOx removal strategies can be classified in the two main groups:

I. Pre-combustion strategies;

II. Post-combustion strategies.

The pre-combustion strategies, or primary methods, consist of a group of intervents that reduces the amount of nitrogen oxidation to NO_x during the combustion process. The post-combustion strategies, or secondary methods, are used to reduce the NO_x produced, converting the oxides to nitrogen and oxygen hopefully or trapping them. Particular attention must be paid to the secondary pollutants and/or secondary waste that can be produced from the treatment, such as CO, NH_3, N_2O, sorbent, water, etc; both for pre- and post-combustion strategies.

There exist many strategies for NO_x control in literature, either for pre-combustion and post-combustion. Most of them are well-known and widely adopted in industrial applications; some others are still under scrutiny. Most of the innovative strategies combine multidisciplinary engineering competences to promote NO_x conversion or trapping.

For the reduction or controlling of NO_x emissions, one or a combination of primary and/or process-integrated and secondary techniques are considered suitable. The most common strategies and some innovative techniques are described below.

1.4.1 Pre-combustion strategies

For environmental/safety and economic reasons, the NO_x reduction process should preferably start with the implementation of general primary techniques. These ensure that a minimum amount of pollutants are produced. If these strategies are not enough, the post-treatment process will guarantee the respect of the NO_x threshold. In many cases, the pre-combustion strategies must be taken into account during the design of the combustion chamber, as they require specific geometries or mixing of air with fuel.

NO_x production can be reduced using furnace control measures that:

- prevent an oversupply of air (i.e. prevent the supply of additional nitrogen);
- prevent the use of unnecessarily high furnace temperatures (including local hot spots);
- optimise combustion control for the homogenisation of the combustion conditions and to avoid sharp temperature gradients.

CHOICE OF THE FUEL

Nitrogen oxides production is correlated to the amount of nitrogen in the combustion chamber. This nitrogen can come from either the fuel and the nitrogen present in the air. In such cases, the choice of fuel can be a strategy to reduce the amount of NO_x produced. If the chamber conditions do not encourage high temperatures, the thermal NO_x is low. On the contrary, fuel NO_x can represent an important fraction of the total NO_x. Zero fuel NO_x emissions can be achieved only when N-free fuel is used. At the same time, fuel with a moderate calorific value is suggested to control the peak temperature. In such cases, e.g. the incinerators, the quality of the fuel cannot be controlled and hence the nitrogen content in the fuel. The wastes have a heterogeneous composition that can lead to peaks of temperature and nitrogen content in the combustion chamber [36], [37]. The homogenisation of the fuel and raw material feedings can reduce the amount of NO_x produced and consequently its emission.

LOW EXCESS AIR COMBUSTION AND GAS MIXING

The use of a well-distributed air supply to avoid the uneven temperature gradients that result in high-temperature zones and, hence, increased NO_x production is a widely adopted and important primary technique for the reduction of NO_x production. Although sufficient oxygen is required to ensure that organic materials are oxidised (giving low CO and VOC emissions), the oversupply of air can result in additional oxidation of atmospheric nitrogen, and the production of additional NO_x [38], [39]. The importance of mixing was demonstrated by many authors among the years. The mixing encourages the contact between fuel and oxygen and consequently, a lower excess of air is required.

In the last two decades, a new concept of Flameless or Mild combustion have been introduced. Flameless oxidation [40] or Mild combustion [41] is a technology that emits very low pollutant emissions, especially thermal NO_x and CO are lowered to residual values while maintaining a high thermal performance of the system. Under the special conditions of the combustion regime, the reactions take place in a volume sustained by the hot medium above the self-ignition temperature, and it is not possible to observe any visible flame or luminous effect; that is why the regime was named ‘‘Flameless oxidation”. An important advantage of burners that operate under the flameless regime is their ability to burn fuels of changing and fluctuating quality, or LCV fuels.

OXYGEN INJECTION

Nitrogen present in the air can react in the combustion chamber at a temperature above 1300°C to produce thermal NO_x. The pollutant emission can be controlled by reducing the amount of molecular nitrogen contained in the air. The injection of either pure oxygen or oxygen-enriched air provides a means of supplying the oxygen required for combustion while reducing the supply of additional nitrogen that may contribute to additional NO_x production. This strategy does not require any modification of the combustion chamber and allows to produce the heat required without promoting the thermal NO_x production. In many cases, the separation of air is not economically sustainable and this strategy is not attractive; while it assumes relevance in those applications where an oxygen-enriched air is produced from other processes and this gas can be used to burn the fuel.

FLUE GAS RECIRCULATION

When the fuel has a high calorific value, peaks of temperature are achieved in the combustion chamber, in the flame region. Flue gas recirculation (FGR) is one of the strategies that contain the increasing of temperature. This strategy allows reducing the excess of air required to obtain a full burned fuel, as the unburned species recirculates in the combustion chamber promoting the combustion. This technique involves the replacement of around 10–20 % of the secondary combustion air with recirculated flue-gases. NO_x reduction is achieved because the supplied recirculated flue-gases have a lower oxygen concentration and therefore lower flue-gas temperature which leads to a decrease of the nitrogen oxide levels. It has been pointed out that FGR can reduce NO_x emission levels and fuel consumption [42], [43].

FGR usually includes two types, external and internal recirculation. In the external recirculation (EFGR), flue gas is recirculated outside of the furnace and added to the combustion air; hence, the equipment may become larger and more expensive. In the internal flue gas recirculation (IFGR), combustion products are recirculated inside the furnace back to the burner and added into the flame; hence, the equipment can be compact and costs a little. Thus, IFGR becomes an ideal method to reduce the NO_x emissions, particularly for small boilers which have been widely adopted in industries owing to higher boiler efficiency and economically optimal operation according to need [44].

STEAM INJECTION

Water injection was initially proposed to reduce emissions of nitrogen oxides (NO_x). Since the latent heat of water evaporation is large, the maximum in-chamber temperature will be reduced remarkably with water injection, which is good for reducing NO_x emissions. However, with water injection, the combustion will be greatly suppressed with the consequence of unburned species in the exhaust [45], [46]. In some studies, it was expressed that when the fuel-water mixture increases, smoke and particulate matter (PM) emissions also increase [47], [48].

Steam was initially injected into the combustion chamber directly. Although the particulate emissions, this strategy was widely adopted in marine diesel engines to contain the NO_x emission. The unburned species issue was greatly avoided by the steam indirect injection that was introduced later. The water vapour is mixed with fuel to produce an emulsion that is fed at high pressure in the combustion chamber. NO_x, CO, soot, SO_2 and PM strongly depend on the emulsion injection pressure. The higher is the pressure, the faster is the combustion rates, resulting in high gas temperatures. This tends to vaporize the fuel spray so quickly that the liquid fuel cannot penetrate deeply into the chamber. Therefore, the initial combustion with the spray is restricted to a small region near the injector, and the flame spreads around the chamber through slow propagation [49], [50].

LOW NO_x BURNERS

Low NO_x burners are those units that allow the production of a low amount of NO_x due to their design, the controlled temperature and the well-distributed oxygen along the chamber. The basic ideas are to create an O_2-deficient stoichiometric condition (especially during the early part of the combustion process), reduce peak flame temperature, or to vary the residence time within various parts of the combustion zone to reduce NO_x formation and increase re-conversion of NO_x to N_2 and O_2.

Low NO_x burners are designed to reduce the primary air portion which leads to lower NO_x formation whereas common multi-channel burners are operated with a primary air portion of 10 to 18 % of the total combustion air. The higher portion of the primary air leads to a short and intensive flame by the early mixing of hot secondary air and fuel. This results in high flame temperatures along with a creation of a high amount of NO_x formation which can be avoided by using low NO_x burners. The primary air proportion in the low NO_x burners, instead, is reduced to some 6–10% of that required for stoichiometric combustion. These burners are useful for reducing the flame temperature and thus reducing thermal and (to some extent) fuel derived NO_x.

The net effect of this burner design is to produce very early ignition, especially of the volatile compounds in the fuel, in an oxygen-deficient atmosphere, and this will tend to reduce the formation of NO_x. Such techniques require effective air/gas mixing in the secondary zone to ensure CO (and other products of incomplete combustion) are maintained at low levels.
There exist many low NO_x burner configurations. The distribution of the air along the chamber and the mixing strategies are strongly correlated with the chamber design. Many patents propose low NO_x burners; the choice should be dependent on the process, the fuel and the power [51]–[54].

Pre-combustion strategies can be considered as precautions either inside or outside the combustion chamber. These strategies allow NO_x reduction with a relatively low-cost intervents. These strategies are strongly recommended for new plants to reduce the amount of NO_x produced in the combustion chamber. The main cross-media effects of these strategies are the reduction of the heat produced and the production of unburned species as CO, PM, etc.

1.4.2 Post-combustion strategies

Post-combustion strategies take place once the pre-combustion strategies are not able to limit the NO_x emission below the threshold value. The post-combustion methods allow reducing NO_x content from the exhaust gas through physical and/or chemical processes. There exist many kinds of post-combustion strategies to reduce NO_x emissions. They can be classified as:

i. NO_x separation;
ii. NO_x conversion.

NO_x separation includes those techniques that separate the NO_x from the exhaust, by reducing the NO_x content in the gas. An example of these strategies is the NO_x adsorption on a sorbent surface or the NO_x absorption in a liquid phase. The main drawback of these techniques is transferring the NO_x from flue gas to another medium and thus in many cases generating waste which has to be treated then. NO_x conversion, instead, promotes chemical reactions that involve the nitrogen oxides species, generating inert species (hopefully nitrogen and oxygen gases). The most common post-treatment techniques for the NO_x conversion are the direct decomposition, the Selective Non-Catalytic Reduction (SNCR), the Selective Catalytic Reduction (SCR) and the NO_x Storage and Reduction (NSR).
The most common and some of the innovative techniques are described below.

1.4.2.1 NO_x separation strategies

NO_x from combustion process usually represents 0.1% of the total exhaust or less. The separation as well as the conversion of these species, diluted in a gas mainly made of nitrogen, oxygen, carbon dioxide and water vapour, requires a technology that is selective toward NO_x. Thus, focusing on the NO_x physical and chemical properties many strategies have been introduced for the NO_x removal.
The most common strategies for NO_x removal by separation processes are the NO_x absorption (in a liquid phase) and the NO_x adsorption. As the molecules move from the gas phase toward a liquid phase (absorption) or toward a solid surface that traps them (adsorption) Both the processes need a post-treatment as the liquid and the solid are secondary wastes of the $DeNO_x$ process, specific after-treatments are needed to compute the process.

NO_X ABSORPTION

Gas absorption is a unit operation in which soluble components of a gas mixture are dissolved in a liquid. The gas passing through a liquid matrix leads to a physical or chemical transfer of gas molecules to the liquid phase. The higher is the affinity between the liquid and the gas molecules, the higher is their solubility. The affinity consists of chemical bonds or physical interactions between the gas molecules and the bulk liquid. Hence, when these bonds or interactions are strong enough, the gas molecules are “trapped” in the bulk liquid and their concentration in the gas decreases.
During the past decades, the capture of NO_x by liquid-phase absorption process has drawn much attention for its advantages of low cost and co-capture of other pollutants. Although more of 90% of the NO_x from combustion processes are insoluble in water, the NO oxidation into soluble NO_2 makes this process competitive with other $DeNO_x$ strategies.
Wet methods for removal of NO_x are limited by the relatively inert nature of NO and thus it is necessary the addition of reagents for promoting its removal. The wet oxidative processes are mainly based on three types of principles: gas-phase oxidation of NO to NO_2, liquid-phase oxidation and metal-chelate systems. When NO is oxidized to NO_2, the solubility of the NO_x is increased mainly due to the formation of N_2O_3 and N_2O_4. Gas-phase oxidation can be done with a strong oxidizer such as O_3 or ClO_2.
NO can also be directly absorbed in a solution containing a very strong oxidizing agent. Nitrogen oxides are oxidized to nitrite and then to nitrate depending on the composition of the solution. The typical oxidative absorbents proposed by literature are hydrogen peroxide (H_2O_2) [55], [56]; iron (II)

EDTA (Fe(II)-EDTA) [57], [58]; sodium chlorite ($NaClO_2$) [59], [60]; sodium persulfate ($Na_2S_2O_8$) [61], [62] or potassium ferrate (K_2FeO_4) [63], [64].

Most of these researches studied the simultaneous absorption of NO and SO_2 having the scope to simulate the effect of NO on the SO_2 absorption. In fact, the wet processes are widely used for the SO_2 removal from exhausts. In its PhD dissertation, Ing. Flagiello from the University of Napoli "Federico II" has investigated the absorption of NO_x (90% NO and 10% NO_2) in a solution of water and sodium chlorite. The use of $NaClO_2$ allowed reaching up to complete removal of NO_x, compared to the use of freshwater or alkaline water (seawater), for which the removal efficiencies were very low (of the order of 2 - 7%).

Being a separation process, the absorption allows removing the NO_x from the exhaust, concentrating it in the liquid phase. The liquid represents a secondary waste after-treatment and strategies for the nitrates recovery are under investigation in recent years.

NO_X ADSORPTION

Adsorption technique is widely used in gas and wastewater treatments. The effectiveness of the process consists of the capability to remove with an efficiency of up to 100% molecules diluted in a gas or liquid phase. The adsorption is commonly used for the removal of organic compounds, pollutants, biological water purification, etc.

Adsorption takes place when molecules from gas or liquid bind themselves to the surface of a solid substance. Electrical forces or chemical bonds can link the molecules to the solid by cleaning the gas/liquid. The selectivity of the solid toward a species is correlated to the functional groups dispersed on its surfaces called sites. As the molecules reach the sites, the interactions occur and the molecules adsorb on the solid surface that is hence called sorbent or adsorbent; while the molecules attached are called adsorbate. In addition to the selectivity of the sites towards the molecules of interest, the solid porosity is relevant for the adsorption efficiency. The higher is the porosity, the higher is the specific sorbent surface exposed to the molecules. However, an extremely high specific surface means that the pore sizes become very small making the sorbate diffusion into the pores slower. The larger is the molecule size, the larger must be the pore size required to allow the penetration of the molecules in the sorbent.

The adsorption process will be described in more details in Chapter 2 of this thesis.

Commercial adsorbents are highly porous, with pore surface areas ranging from about 100 to 1,200 m^2/g. The most common solids used for the adsorption, that has a high specific surface, are carbon-

based materials (from coal, lignocellulosic biomass, e.g.), mineral adsorbents (zeolites, silica gels) and synthetics. The sorbent can be impregnated with metal oxides to increase the catalytic conversion of the sorbate, improving the affinity between sorbate and sorbent. The impregnation is usually about 3-10% wt of the sorbent mass and it is obtained from a liquid treatment of the sorbent.

The adsorption is usually performed at low temperatures. In fact, being an exothermic process, the molecule trapped can desorb as the temperature increases. A similar consideration can be made also on the pressure. The higher is the pressure, the higher is the probability that the molecules meet the active sites on the sorbent surface. However, the impregnation can make the adsorption more effective at higher temperature due do the catalytic conversion of the sorbate to a more affine molecule with the sorbent. This is the case of the nitric oxide adsorption from the gas phase. The NO_x adsorption is widely investigated in the literature mainly on a zeolite or activated carbon surface. The NO_x adsorption capacity depends on many factors like the adsorbent characteristics, the operative settings (pressure, temperature) and the gas composition. The interaction with the SO_2 is commonly investigated as the sulphur dioxide (hazardous molecule) can be removed from the exhaust operating the adsorption. It was found from many authors that the presence of the SO_2 plays a positive role in the NO adsorption and vice-versa. In fact, the NO and SO_2 themselves exist in interaction during the adsorption process, which would enhance each other adsorption ability, in such cases. However, increasing concentrations of SO_2 in the feed would result in increasing amounts of its adsorption on the sorbent active sites, which would strongly desorb the NO from the active sites and restrain the NO adsorption on the sorbent active sites [65], [66]. Even the percentage of oxygen in the gas stream affects the NO adsorption, more than SO_2. The adsorption of NO can increase ten-folds as the oxygen concentration increases. It was demonstrated that the activated carbon plays a double role in the NO_x adsorption as the gas contains oxygen. The NO adsorption competes with the NO oxidation to NO_2. Once the NO_2 is produced, it can adsorb on the sorbent surface with a capacity higher than NO [66], [67]. Zhang et al. [67] have found that the NO_2 adsorption and NO_2 release start only after the carbon surface was rapidly oxidized during the early stage of adsorption. Once the NO adsorption sites achieve the saturation, the NO_2 continues to be produced and adsorbed on the sorbent sites. Hence, even if only NO is fed, the NO_2 is catalytically produced and the amount of NO plus NO_2 at the exit of the sorbent bed is equal to the NO fed, once the saturation is achieved. The NO and NO_2 adsorption capacity on activated carbon is mainly attributed to the presence of basic sites that are more selective for NO_2 than NO due to the polarity of the molecule [68].

Although the NO_x adsorption can achieve an efficiency of 100%, NO_x concentration increases as the sorbent sites progressively have been occupied. Once the NO_x concentration in the treated gas achieves the threshold limit, the sorbent must be replaced or treated to regenerate the active sites. The most common treatment for sorbent regeneration is the high-temperature desorption. Being an exothermic process, the reverse of the adsorption process occurs as the temperature increases. The NO_x particles desorb from the sorbent surface and pass in the gas phase with a high concentration. When desorption is properly carried out, NO_x desorbs with a gaussian-like profile whose peak is much higher than its concentration in the adsorption process. The gas from regeneration must be treated to convert the NO_x desorbed. Hence, the adsorption is a high-performance process with the production of a secondary wastes. Both the exhaust sorbent and the concentrated purge NO_x from desorption require further treatment.

1.4.2.2 Conventional NO_x conversion strategies

The most studied and consolidated technologies for the post-treatment De-NO_x are

- Direct Decomposition;
- Selective Non-Catalytic Reduction (SNCR);
- Selective Catalytic Reduction (SCR);
- NO_x Storage and Reduction (NSR).

These strategies are described below and the most prompt innovations are reported.

DIRECT DECOMPOSITION

Nitrogen oxidation to NO_x occurs as the nitrogen reacts with oxygen at high temperature, according to the Reaction (R *1-3)* and (R *1-4)*. Looking at the thermodynamic, the reverse of the Reaction (R *1-3)* is encouraged as the temperature is lower than 1000°C, Figure 1.3; the Gibbs free energy is equal to -86 kJ/mol at room temperature. Although the NO reduction is a spontaneous process at room temperature, the kinetics is very low as the activation energy of homogeneous decomposition is very high. For this reason, industrial processes are carried out using catalysts, which allow achieving NO_x reduction within a reasonable timescale. The process of NO_x reduction to N_2 and O_2, with the support of a catalyst, is called Direct Decomposition.

In the 1920s, it was reported that direct NO decomposition proceeded on the surface of platinum (Pt) at above 800°C [69], but research in this direction fell away because the catalytic activity was insufficient and alternative catalysts to platinum were not forthcoming. In the early 1990s, however,

it was found that Cu ion-exchange zeolites (Cu-ZSM-5), $Pd/MgAl_2O_4$, perovskite-type oxides, and Ag/Co_3O_4 showed high NO_x decomposition activities. Since then there has been a significant increase in research activity on direct NO decomposition catalysts, with pyrochlore-type and rare earth oxides additionally found to have NO decomposition activities [70]–[75]. Both the efficiency and the operating temperature depend on the material-based catalyst and the other species in the gas phase. The temperature can vary from 400 to 1000°C; while the efficiency can achieve 90% when no oxygen is present It was proposed that NO_2 formed during the reaction of NO with O_2 was an intermediate in the NO decomposition. At high temperatures, the decomposition of NO_2 into NO and O_2 is thermodynamically favoured [76].

Direct decomposition of NO_x is versatile and economic because no reductants are required. However, the catalytic activities of conventional catalysts are insufficient, particularly in the presence of other gases such as O_2 and CO_2. In recent years, however, the investigation of different catalyst structures and compositions has led to enhanced catalytic activity; in particular, significant advances have been made in improving the tolerance of the catalyst to coexisting gases [77]. Furthermore, the recent advances in nanomaterial technology gave a significant contribution to increasing the decomposition yields [78], [79].

SELECTIVE NON-CATALYTIC REDUCTION (SNCR)

Stationary sources, such as industrial process furnaces, necessarily generate flue gases in which O_2 is an order of magnitude greater than NO, or higher. Both NO and O_2 are oxidising agents, but O_2 is well known to be generally more reactive than NO, thus it is easier to reduce O_2 in the presence of NO. It is also possible to reduce both NO and O_2 by using massive quantities of a reducing agent, but it would clearly be desirable to find means to selectively reduce NO in the presence of O_2. The expense of a reducing agent in such a 'selective' reduction of NO would correspond to the small amounts of NO. Although NO_x is made of nitrogen and oxygen, its decomposition does not occur easily either at high or low temperature without the use of catalyst. The catalyst has many drawbacks such as the poisoning, ageing, temperature sensitivity and selectivity. For this reason, other chemical pathways were investigated for NO_x conversion among the years. The reactivity of many reducing species with nitrogen oxides was investigated and the most prompt results were achieved with ammonia.

Wendt et al. (1972) discussed a method of 'non-catalytic' pollution abatement in which they injected ammonia (NH_3) into the post-flame gas and observed a reduction of NO. However, they got a very

little reduction of NO until they had added enough NH_3 to completely consume the O_2 present, thus non-selective reduction of NO and O_2 was achieved. They suggested that NH_3 might have been pyrolysed to H_2 and N_2 due to the very hot stainless-steel injector, before it entered the combustion effluent. Thus, they argued that hydrogen may have been the reducing agent causing non-selective NO_x reduction [80]. The overall reactions for NO_x conversion with ammonia are:

$$4\,NO + 4\,NH_3 + O_2 \rightarrow 4\,N_2 + 6\,H_2O \qquad (R\ 1\text{-}19)$$

$$2\,NO_2 + 4\,NH_3 + O_2 \rightarrow 3\,N_2 + 6\,H_2O \qquad (R\ 1\text{-}20)$$

Reactions (R *1-19)* and (R *1-20)* highlight that ammonia reacts either with nitrogen oxides and molecular oxygen to produce water vapour hopefully; in fact, nitrogen can oxidize to NO_x as the temperature increases.

The SNCR is a conceptually simple process for NO_x control. At temperatures between 875 °C and 1150 °C, ammonia is injected and thoroughly mixed in a flue gas stream containing NO_x. A rapid gas-phase homogeneous reaction occurs such that in spite of the presence of excess oxygen generally required in the furnace, the reagent selectively reduces NO leaving oxygen largely untouched [81]. The schematic of the SNCR concept is elaborated in Figure 1.17.

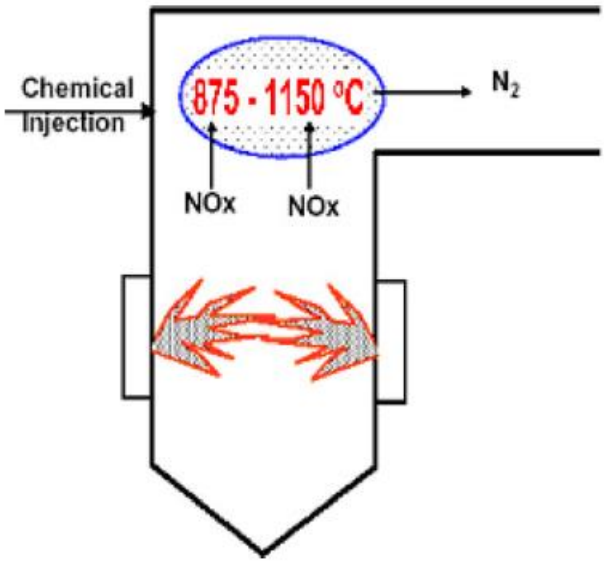

Figure 1.17 - Schematic of SNCR concept [81].

The range of temperature in which the reaction takes place causing a net reduction of NO is termed as the temperature window. This is a narrow interval because below 800 °C the reaction is too slow

to give any reduction and most of the injected NH_3 remains un-reacted. At higher temperatures (i.e. greater than 1200 °C) NH_3 tends to oxidise to form NO rather than to reduce it. A typical trend of NO_x emissions in the function of the SNCR temperature at fixed ammonia/NO_x ratio is reported in Figure 1.18.

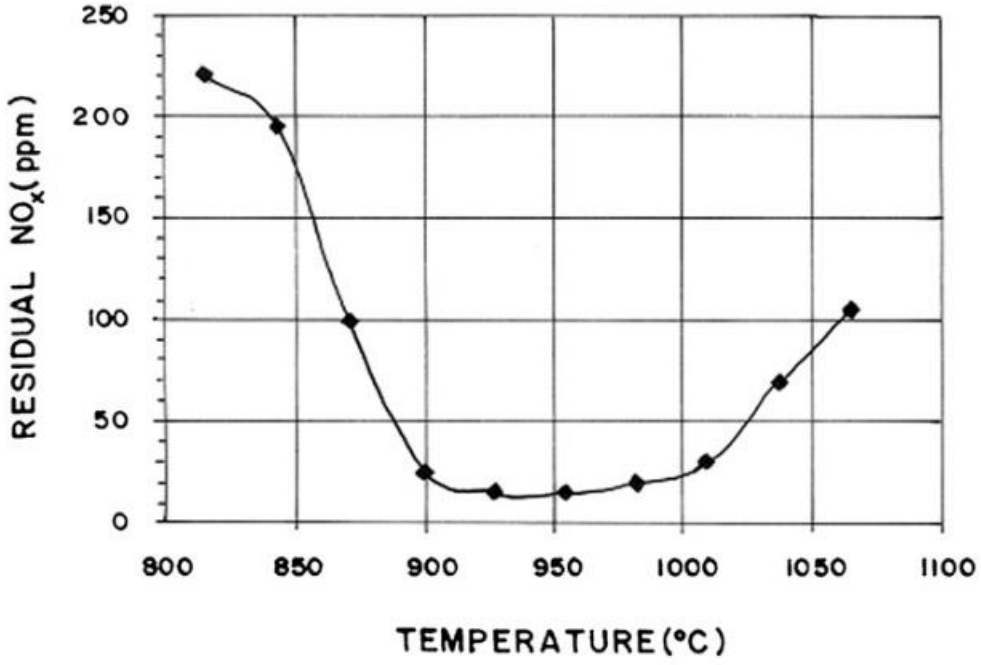

Figure 1.18 - Temperature window of SNCR process using ammonia at molar ratio (NH_3/NO^{IN})=1.5 [81].

The NO_x conversion becomes relevant in an operating window within 900-1050°C.

In most full-scale applications, the reagents of choice are either NH_3 or urea ($CO(NH_2)_2$). The mechanism of selective non-catalytic reduction using ammonia gas shows that NH_3 first converts to amidogen (NH_2), by reacting with hydroxyl (OH) radical, (NH_2) then reacts with NO in the flue gas stream to reduce it. Thus molecular radical species such as amidogen (NH_2) and hydroxyl (OH) dominate the reduction chemistry [81]. Salimian and Hanson [82] proposed that a compound such as urea might rapidly decompose to give amidogen radicals directly. They performed modelling calculations based on their very first reaction mechanism, which showed that the peak efficiency of NO removal was comparable to that of NH_3 injection. They suggested the need to characterise the urea as an alternative source of NH_2. There may be a number of advantages of using urea, in place of NH_3, as it is a solid, inert, non-corrosive material which is easily handled, safely stored and can be readily introduced into a combustion gas stream either as a solid or in solution.

The overall reactions for NO_x conversion with urea are:

$$4\,NO + 2\,CO(NH_2)_2 + O_2 \rightarrow 4\,N_2 + 2\,CO_2 + 4\,H_2O \qquad \textit{(R 1-21)}$$

$$2\,NO_2 + 2\,CO(NH_2)_2 + O_2 \rightarrow 3\,N_2 + 2\,CO_2 + 4\,H_2O \qquad \textit{(R 1-22)}$$

Although the facilities of urea, it was demonstrated in the following years, that urea has a higher temperature window and a lower efficiency for NO_x conversion [83]. In particular, even if the conversion efficiency peaks are comparable, the applications using urea must work at a higher temperature to reduce the amount of ammonia slip and consequently the efficiency achievable decreases. Ammonia plays a positive role in NO_x conversion, but is a greenhouse gas and it is classified a pollutant more dangerous than NO_x. For this reason, it is important to prevent the amount of ammonia emitted in the exhaust gas (ammonia slip). The higher is the temperature, the higher is the ammonia/urea degradation, the higher is the amount of hydrogen that can react with NO_x. However, when the temperature rises to value above 1200-1400 °C, the amount of NO_x produced from ammonia/urea considerably increases [83]. For this reason, a balance must be found between the amount of ammonia/urea fed, the gas temperature, the NO_x conversion and the ammonia slip.

The injector design has a significant effect on process performance. The reducing agent is commonly fed from pipe injectors having purposely designed hydraulic spray nozzle at high pressure. The high feeding velocity encourages both the atomization of ammonia/urea molecules and the amidogen production. Moreover, the injection pipes are radially-placed at different heights along the reactor to avoid local reactants accumulation and they are commonly provided with a retractable system controlled via an actuator. Good mixing of additives and NO_x in flue gas, at the optimum reaction temperature, is essential to reach high NO_x reduction. CFD modelling has its role to play along with the reaction chemistry to improve the overall performance, by maximizing mixing rate in the chamber [84], [85].

The SNCR efficiency is commonly lower than 60% even if peaks of 90% can be achieved in particular circumstances, where the gas temperature is higher than 1000°C and the gas mixing is optimized as it is shown in Table 1.7 [86].

Industry and Units	% Reduction	
	Ammonia-Based	Urea-Based
Cement Kilns	12-77	25–90
Chemical Industry	NA[a]	35–80
Circulating Fluidized and Bubbling Bed Boilers	76–80	NA
Coal, Wood and Tire Fired Industrial and IPP/Co-Generations Boilers	NA	20–75
Coal-Fired Boilers	38–83	20–66
Gas- and Oil-Fired Industrial Boilers	30–75	NA
Glass Melting Furnaces	51–70	NA
Steel Products Industry	NA	42.9–90
Municipal Waste Combustors	45-70	16–87
Oil- and Gas-Fired Heaters	45–76	NA
Process Units	NA	40–85
Pulp and Paper Industry	NA	20–62
Refinery Process Units and Industrial Boilers	NA	20–75
Stoker-Fired and Pulverized Coal-Fired Boilers	50–83	NA
Stoker-Fired Wood-Fueled Boilers	40–75	NA
Vapor, Sludge and Hazardous Waste Incinerators	65–91	NA

Table 1.7 - SNCR NO_x reduction efficiency by industry and reagent type [86].

The technology is attractive due to its simplicity, catalyst-free system (and hence free of associated problems), ease of installation on existing plants, applicability to all types of stationary-fired equipments, lower capital and operating cost, the fact that it is largely unaffected by fly ash and usability with other NO_x emission control technologies. The range over which any significant NO_x removal rates can be achieved from one system to the other depending on the system parameters such as flue gas constituents, flue gas velocity gradients and system geometry which influences the mixing between the reagent and the flue gas [81].

Selective Catalytic Reduction (SCR)

The ammonia/urea was confirmed as the best reducing agent for NO_x removal among the last 50 years for its selectivity and a good compromise of costs. The NO_x reduction to nitrogen and water occurs as the nitrogen oxides react with oxygen and ammonia or urea according to the Reactions (R *1-19)*(R *1-20)* and (R *1-21)*(R *1-22)* respectively. These reactions can occur with an efficiency higher than 90% as the temperature is higher than 1000°C and an amount of reducing specie higher than the

stoichiometric value is used. The higher is the amount of reducing agent used, the higher is the ammonia slip that is itself a pollutant. NO_x removal efficiency in the Selective Non-Catalytic Reduction (SNCR) reactors is rarely above 70% as the ratio NH_3/NO_x is lower than 1. Furthermore, many combustion processes produce gases at a temperature below 1000°C and for this reason, the SNCR is not applicable.

The use of catalyst was introduced to overcome the limits of SNCR processes. The selective reactions can be promoted on the catalytic surface, reducing the operative temperature and increasing the NO_x reduction efficiency. This process is called Selective Catalytic-Reduction (SCR).

Selective catalytic reduction (SCR) has been applied to fossil fuel-fired combustion units, for emission control since the early 1970s and is currently being used in whole the world. SCR is typically implemented on stationary source combustion units requiring a higher level of NO_x reduction than achievable by selective non-catalytic reduction (SNCR) or combustion controls. Theoretically, SCR systems can be designed for NO_x removal efficiencies above 98%. In practice, commercial coal-, oil-, and natural gas-fired SCR systems are often designed to meet control targets of over 90 per cent [87].

Figure 1.19 shows a simplified process flow schematic for SCR.

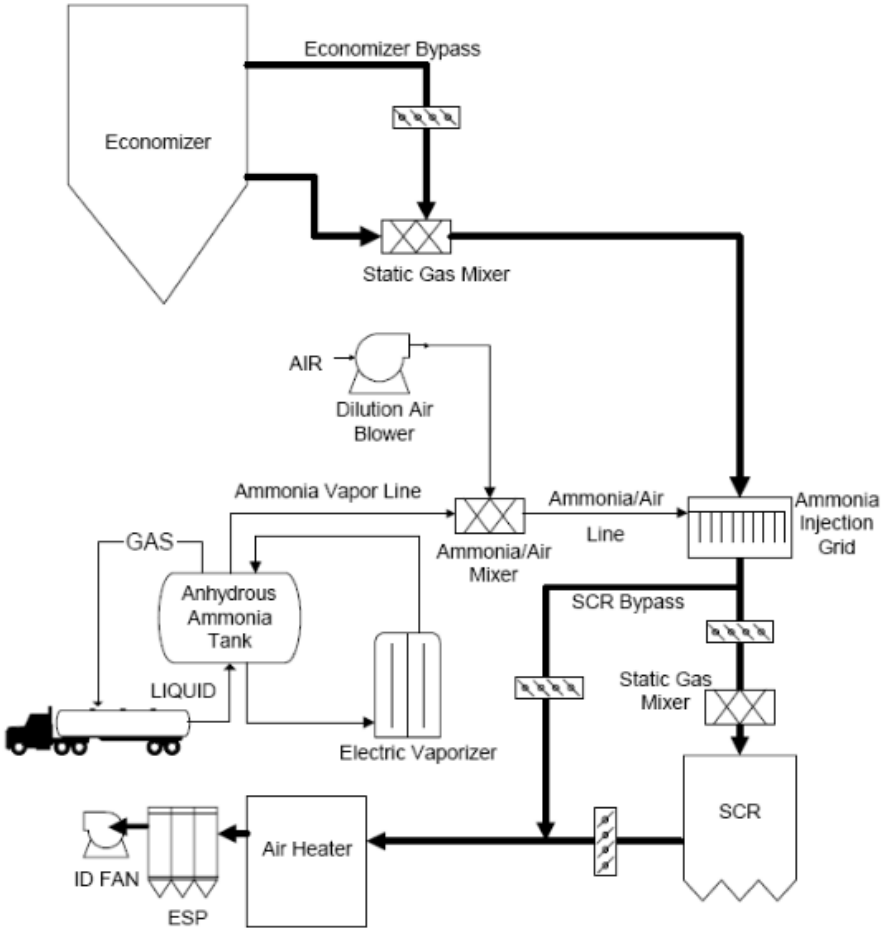

Figure 1.19 - SCR Process Flow Diagram [87].

Reagent is injected into the flue gas downstream of the combustion unit and economizer through an injection grid mounted in the ductwork. The reagent is generally diluted with compressed air or steam to aid injection. The reagent mixes with the flue gas, and both components enter a reactor chamber containing the catalyst. As the hot flue gas and reagent diffuse through the catalyst and contact activated catalyst sites, NO_x in the flue gas chemically reduces to nitrogen and water. The heat of the flue gas provides energy for the reaction. The nitrogen, water vapour, and any other flue gas constituents then flow out of the SCR reactor. As discussed for the SNCR, also in the SCR the reagent mixing is crucial to avoid the ammonia slip. The mixing takes place before the catalyst, at a certain distance. Usually, a distribution layer is placed above the catalysts to encourage the mixing and equalize the flow. The ammonia injection pipes and the first catalytic layer should be spaced enough to grant good reactants mixing, but this is optimize to contain the plant size; for this reason, a static mixer is preferred to the direct injection in the new plants.

Below the distributor, catalyst layers are placed along the reactor. they are arranged as sequential monolayer modules, with a defined interspace between them in order to ensure good reactants mixing that enhances catalyst efficiency as shown in Figure 1.20.

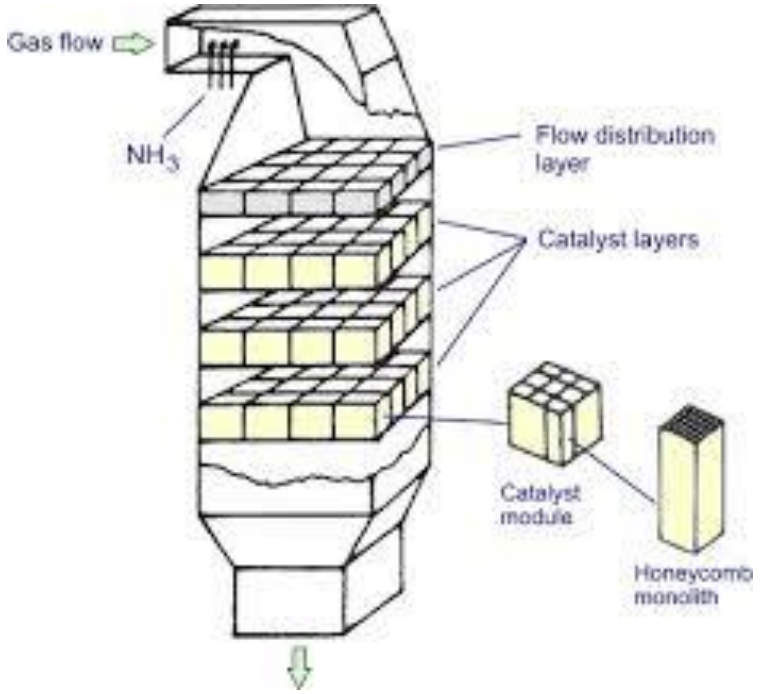

Figure 1.20 - SCR catalytic layers.

Catalyst elements placed in a frame form a catalyst module. The modules stack together in multiple layers to create a reactor bed of the total required catalyst volume. A typical module is 1 m x 2 m and 1 m in height. The size of the SCR depends on the residence time required to achieve the conversion desired. Higher residence times generally result in higher NO_x removal rates. Temperature also affects the required residence time. The required residence time decreases as the temperature approaches the optimum temperature for the reduction reaction. The optimal residence time for an SCR system is a function of the number of active catalyst sites available for the reduction reaction and the gas flow rates within those active sites (interstitial flow rate). For coal-fired boilers, typical specific surface areas range from 300 to 1200 square meters per cubic meters [m^2/m^3] [87]. Increasing the catalyst specific surface area increases the NO_x removal for a given flue gas flow rate. This can be accomplished by either increasing the catalyst volume, which increases the reactor size or increasing the pore space of the catalyst, which generally increases the catalyst cost.

The most common catalysts used in SCR are V_2O_5-based, supported on TiO_2 monolith (or iron oxides). The amount of V_2O_5 varies generally between 0.5 and 3% wt/wt while TiO_2 is used in weight-percentage of 80-85% to provide a high surface area (40-100 m^2/g). Furthermore, tungsten oxide

(WO_3) and molybdenum oxide (MoO_3) may be added as structural elements to improve thermal stability, while aluminium silicates and glass fibres enhance catalyst mechanical properties. The higher is the vanadia concentration, the higher is the catalytic activity. Lietti et al. studied the NO conversion in an SCR by varying the catalyst composition [86]. The NO conversion and N_2 selectivity are reported in Figure 1.21.

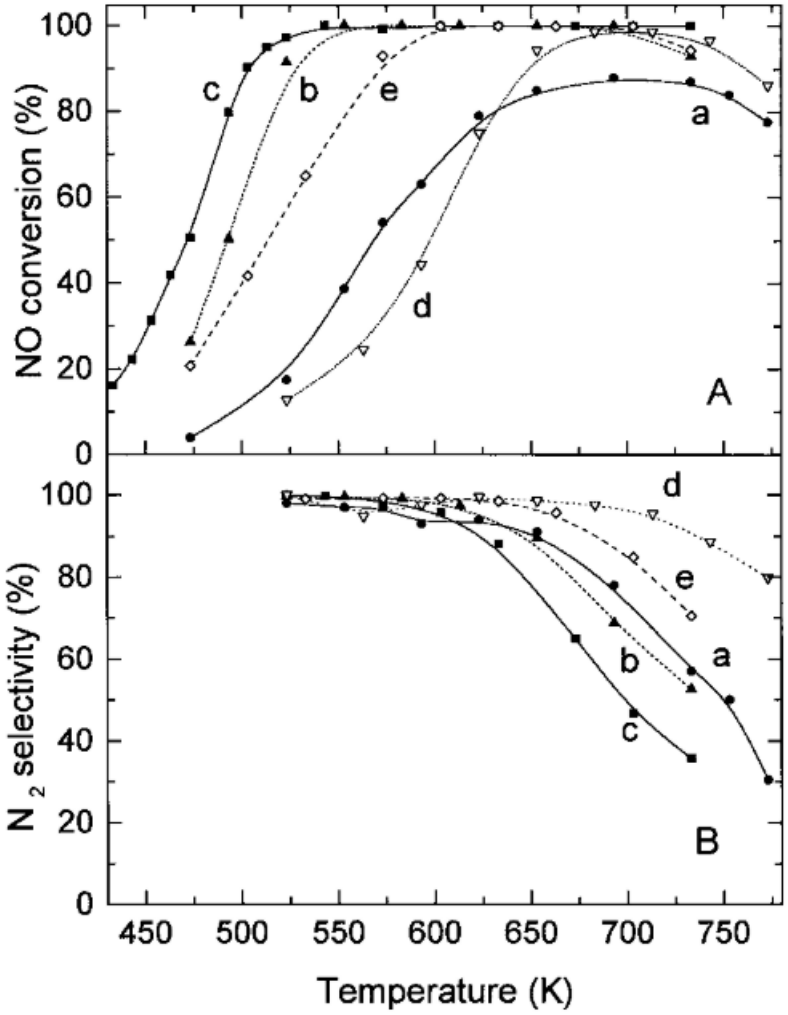

Figure 1.21 - Results of catalytic activity runs performed over the V_2O_5(x)-MoO_3(6)/TiO_2 samples and over reference V_2O_5(x)/TiO_2 samples. (A) NO conversion vs temperature; (B) N_2 selectivity vs temperature. (a) MoO_3(6)/TiO_2; (b) V_2O_5(0.8)-MoO_3(6)/TiO_2 ; (c) V_2O_5(1.5)-MoO_3(6)/TiO_2 ; (d) V_2O_5(0.8)/TiO_2 ; (e) V_2O_5(1.5)/TiO_2 c

Figure 1.21 shows that the temperature required to achieve 50% NO conversion is progressively lowered from ~570 K down to 470 K on increasing the vanadium loading from 0 to 1.5% wt/wt (curves a, b, and c, respectively). For the samples with the highest vanadium content, appreciable NO conversions are attained at temperatures as low as 420 K. At the highest investigated temperatures,

the NO conversion decreases due to the occurrence of the NH_3 oxidation reaction: as a matter of fact, the NH_3 conversion (not reported in the figure) is equal to or only slightly higher than that of NO in the whole temperature range, but is always complete in the high-temperature region. The N_2 selectivity is nearly complete for all the investigated samples in the low-temperature region but declines at high temperatures due to the formation of N_2O. The decrease of the N_2 selectivity at high temperatures is more evident for the sample with the highest V_2O_5 loading (curve c). It is noted that the temperature window for the reaction (i.e., the temperature range where high NO conversion and high N_2 selectivity are simultaneously achieved) is widened and shifted towards lower temperatures by adding vanadium due to the increased activity of the catalysts in the low-temperature region. The reactivity of the ternary catalysts is significantly higher than that of the corresponding binary samples, having the same vanadium loading, as seen by comparing curves d-b and e-c. This effect is particularly evident in the case of the samples with V_2O_5=0.8% wt/wt where the NO conversion curve is shifted 100 K towards lower temperatures. This is a clear indication that the presence of molybdenum increases the activity of V_2O_5/TiO_2 catalysts.

Although the catalyst efficiency is correlated to the vanadium percentage, it is commonly lower than 3% wt/wt. Further to the NO_x reduction, V_2O_5 catalyses also the oxidation of SO_2 to SO_3:

$$2\,SO_2 + O_2 \rightarrow 2\,SO_3 \qquad \textit{(R 1-23)}$$

In the presence of ammonia and moisture, the sulphur trioxide can produce ammonium sulphate:

$$2NH_3 + SO_3 + H_2O \rightarrow (NH_4)_2SO_4 \qquad \textit{(R 1-24)}$$

At very low operating temperatures (< 200°C), made possible by the high intrinsic activity of the catalyst, ammonium sulphate deposition can cause catalyst deactivation (reversible). The deposition of ammonium sulphates can be prevented by operating at higher temperatures (300-400°C), but deposition in the cooler parts of the down-stream waste heat boiler can cause serious fouling and corrosion [88]. The formation and deposition of ammonium sulphates depend upon a number of catalyst parameters, such as SO_2 oxidation activity and pore size distribution, as well as on the exact operating conditions, such as temperature and NH_3 and SO_3 partial pressures. The ammonium sulphate production competes with the ammonium bisulphate (ABS) NH_4HSO_4:

$$NH_3 + SO_3 + H_2O \rightarrow NH_4HSO_4 \qquad \textit{(R 1-25)}$$

Ammonium sulphate production, Equation (R *1-24)*, compete with the ammonium bisulphate production, Equation (R *1-25)*, as both the reactions occur as the sulfur trioxide reacts with ammonia in the presence of moisture. Ammonium bisulphate (ABS), as the ammonium sulphate, can cause the catalytic deactivation. ABS, being a gluey liquid, it sticks on the catalyst causing an irreversible deactivation. This means that the ammonium bisulphate production must be avoided more than the ammonium sulphate. The amount of SO_3 produced from the oxidation, as in the Equation (R *1-23)* is 0.5-2% of SO_2 concentration in the flue gas; depending on the amount of SO_3, it is possible to set the concentration of NH_3 and the operating temperature in order to avoid ABS and promote ammonium sulphate instead. A useful graph that allows setting the operating condition to prevent the formation of ABS is presented in Figure 1.22.

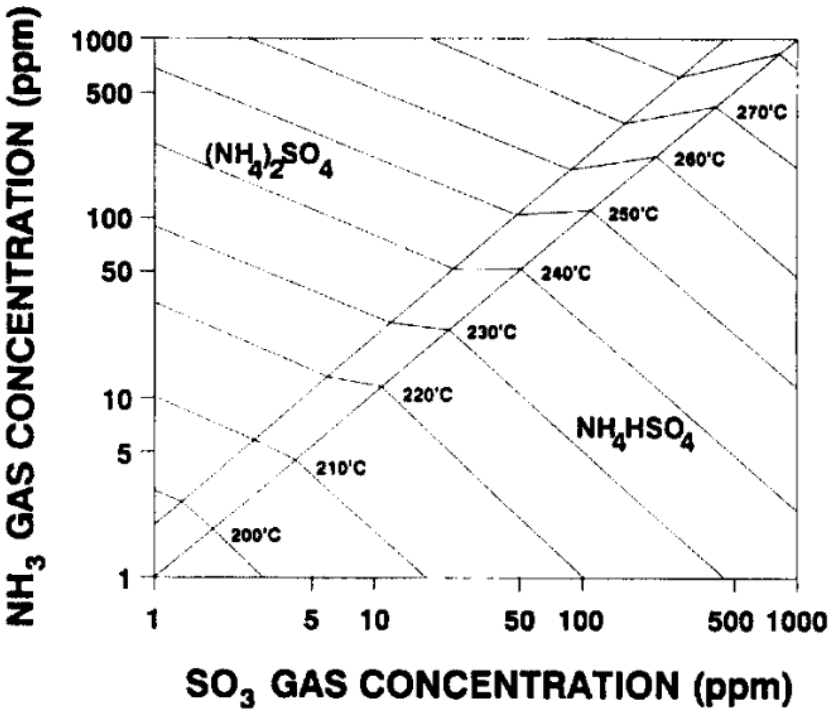

Figure 1.22 - Ammonium sulphate and bisulphate equilibrium in the function of the temperature and the NH_3 , SO_3 concentrations [88].

The parametric lines define the equilibrium conditions above of them the ammonium sulphate production is encouraged. The higher the ammonia concentration, the higher the ammonium sulphate production as the stoichiometric ratio with ammonia is 1:2; while it is 1:1 for ABS:NH_3.

Often, the SCR follows the DeSOx process to preserve the catalyst in the NO_x process. However, DeSOx is mainly a wet process and consequently, the gas must be reheated to achieve the operating temperature in the SCR. Once the SOx can not be removed totally, the operating temperature in the

SCR must be chosen considering either the ammonia slip and the ABS production cross factors. Also, the amount of ammonia injected must meet the efficiency requirements, the ammonia slip and the ABS production. The higher the ammonia feed, the higher is the NO conversion as discussed before; however, the ratio NH_3/NO_x is commonly in the range 0.6-0.85 to prevent the ammonia slip. On the contrary, the low amount of ammonia promotes the formation of ABS more than the ammonium bisulphate, irreversibly poisoning the catalyst. The choice of the operating temperature can mitigate ABS production, as the conversion to ammonium bisulphate is promoted at high temperature. Usually, the operating temperature is below 400°C to prevent the sintering of the vanadium and reduce the amount of energy provided to the gas after the wet DeSOx process.

The use of a catalyst results in two primary advantages of the SCR process over SNCR. The main advantage is the higher NO_x reduction efficiency. In addition, SCR reactions occur within a lower and broader temperature range. However, the decrease in reaction temperature and the increase in efficiency is accompanied by a significant increase in capital and operating costs. The capital cost increase is mainly due to the large volumes of catalyst required for the reduction reaction. Operating costs for SCR mostly depends on the replacement catalyst and on the ammonia costs, and while historically, the catalyst replacement cost has been the largest, the reagent cost has become the most substantial portion of operating costs for most SCR [89].

NO_X STORAGE AND REDUCTION

NO_x Storage and Reduction is relatively new compared with the traditional $DeNO_x$ SNCR and SCR processes. The first application was developed by Toyota researchers in 1995 for diesel engines. Although the age of this technology, it was included in the conventional technologies as its application is widely spread especially for those mobile NO_x sources and the process is well known. Over the last several years, nitrogen oxides (NO_x) storage/reduction (NSR) catalysts, also referred to as NO_x adsorbers or lean NO_x traps, have been developed as an aftertreatment technology to reduce NO_x emissions from lean-burn power sources.

NSR catalyst technology reduces NO_x performing a cyclic process: the lean combustion and rich combustion. During the lean part of the cycle, NO_x particles are trapped on a catalyst that plays also the role of sorbent for the NO_x storage. Intermittent rich excursions are used to reduce the NO_x trapped to N_2 and restore the original catalyst surface; lean operation then resumes. The catalyst has a certain NO_x trapping capacity; and once this capacity approaches some level of saturation, unacceptable amounts of NO_x will slip through the catalyst. At or before this point, the catalyst is exposed to a rich

environment or exhaust, which induces NO_x release from the surface and reduction to N_2 [9]. An example of the cycle is illustrated in Figure 1.23

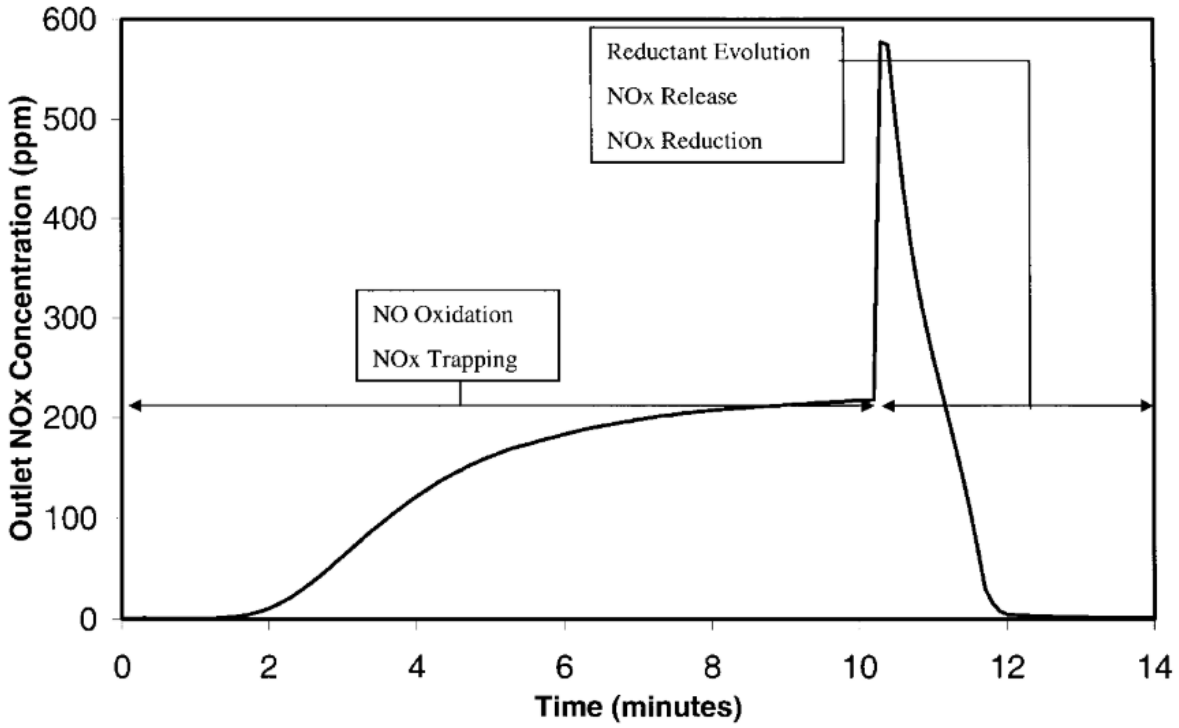

Figure 1.23 - A representative NO_x breakthrough and release profile for an NSR cycle [9].

In the representative cycle described in Figure 1.23, the lean period occurs in the first 10 minutes; then the rich period begins at 10 minutes into the cycle and occurs for 2 minutes. The rich event also results in the recovery of some or all of the original trapping capacity of the surface. The nearly complete removal of NO_x for some time period, almost 2 minutes for the data shown in Figure 1.23, is one of the primary characteristics that makes NSR catalysts a leading candidate for lean-burn aftertreatment systems.

The overall principle of catalyst operation during the cycle can be described by these five reaction steps:

I. NO oxidation to nitrogen dioxide (NO_2);
II. NO or NO_2 sorption on the surface in the form of nitrites or nitrates;
III. reductant evolution when the exhaust is switched to the rich condition;
IV. NO_x release from the nitrite or nitrate sites;
V. NO_x reduction to N_2.

Such operation of the catalyst requires a combination of strong basic properties to accomplish storage of NO and NO_2 (step 2), and red-ox catalytic properties to facilitate all of the steps. Thus, NSR catalysts are typically composed of at least one alkali or alkaline-earth component (e.g. Ca, Ba, K, Na, Mg) and at least one precious-metal component (e.g. Pt, Rh, Pd), which are supported on a high surface area refractory oxide (e.g. γ-Al_2O_3). For example, the most common formulation studied in the literature includes Pt and Ba supported on γ-Al_2O_3, commonly designated as $Pt/BaO/Al_2O_3$. The alkali-alkaline-earth metal has the role of storage component, due to their highly basic properties; the precious metal, instead, participate in the red-ox reactions for the NO oxidation in the lean stage and NO_x reduction in the reach period. A simplified mechanism of Storage and Reduction is reported in Figure 1.24.

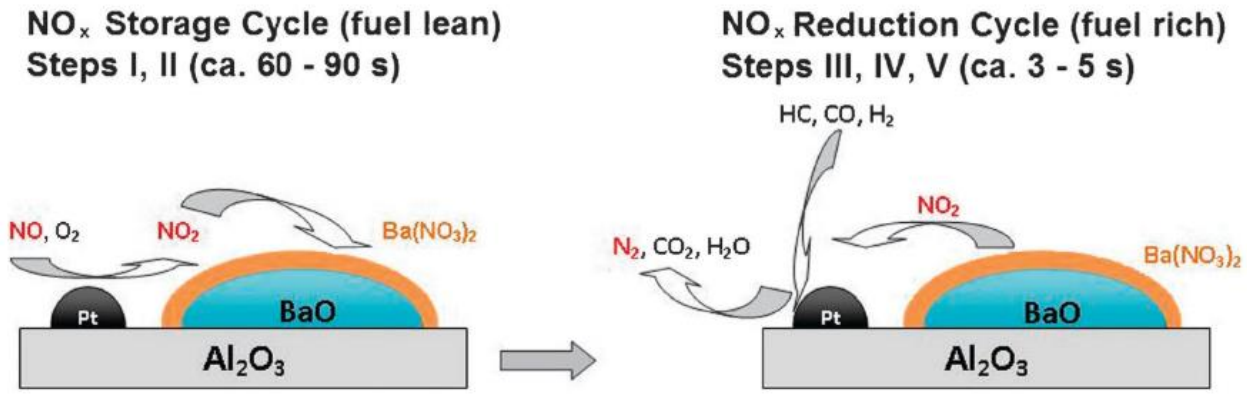

Figure 1.24 - Illustration of a possible NO_x Storage and Reduction (NSR) mechanism on a typical $Pt/BaO/Al_2O_3$ [90].

During the lean stage, NO converts to NO_2 in the presence of oxygen on the platinum surface (I stage). The NO_x adsorb mainly on the BaO sites due to their affinity (II stage). During the reach period, the evolution of reducing species occurs, such as HydroCarbons (HC), hydrogen and carbon monoxide (III stage). Meanwhile, NO_x desorbs from the nitrite or nitrate sites as the effect of the rich condition (IV). The reducing species participate in red-ox reactions on the platinum surface to reduce the NO_x to N_2 (V stage). Nearly sites of Pt and BaO encourage either the NO_x oxidation/adsorption under the lean condition and the NO_x desorption/reduction under the rich condition. Ammonia and nitrous oxide are byproducts of the reactions and their concentration should be contained to reduce their emissions in the exhaust.

The capability to adsorb NO_x on the catalyst surface is crucial for the effectiveness of the mechanism. The adsorption capacity of the NSR catalysts was widely investigated in these years. Although the $Pt/BaO/Al_2O_3$ seems to be the best catalyst, the effects of other metals such as Cerium and Zirconium

on the NO_x removal was investigated in the last years, as well as the effect of the concentration of the metals [9], [91], [92]. The NO_x conversion efficiency strongly depends on the activation temperature of the catalyst. It is about 400°C for the $Pt/BaO/Al_2O_3$ catalyst while it decreases to 230°C for the $Pt/CeO_2/Al_2O_3$ catalyst.

Focusing on the $Pt/BaO/Al_2O_3$, two different adsorption simultaneous mechanisms were proposed:

a. Nitrite production [93],

   The NO adsorbs on the barium oxide sites as nitrite, in the presence of oxygen. The oxidation is catalyzed by the platinum sites under the lean condition and the following disproportionation occurs,

$$BaO + NO + O_2 \rightarrow Ba(NO_2)_2 \qquad \textit{(R 1-26)}$$

b. Nitrate production [94],

   The NO oxidation leads to the formation of NO_2, then it adsorbs in the form of nitrate, due to the interaction between Pt and BaO sites,

$$BaO + NO_2 \rightarrow BaO\ NO_2 \qquad \textit{(R 1-27)}$$

$$BaO\ NO_2 \rightarrow BaO_2 + NO \qquad \textit{(R 1-28)}$$

$$BaO_2 + 2\ NO_2 \rightarrow Ba(NO_3)_2 \qquad \textit{(R 1-29)}$$

   that release one molecule of nitric oxide every two molecules of nitrate adsorbed.

The two pathways are summarized in Figure 1.25.

Figure 1.25 - Two different pathways for the NO oxidation and the NO_x trapping on the $Pt/BaO/Al_2O_3$ catalyst [90].

The NO can either oxidize to NO_2 and adsorbs as nitrate or interact with oxygen and adsorb as nitrite. In the nitrite route, it is proposed that NO is oxidized on platinum sites and directly trapped by nearby BaO sites to form Ba-nitrites. The Ba-nitrites are finally oxidized to Ba-nitrates.

Although the NO conversion and adsorption is encouraged at high temperature ~ 400°C, the catalyst is affected by thermal deterioration and metal sintering. As platinum sinters at high temperature, fewer sites become available for NO and O_2 adsorption and reaction. As a result, the rate of catalytic NO oxidation decreases. Thermal ageing can lead to a decrease of the surface area, which reduces the NO_x storage. However, the loss of barium-containing NO_x storage components due to the reaction with Al_2O_3 imposes a more noticeable influence on the NO_x storage efficiency. Recently it has been reported that the addition of Fe-compound to the NSR catalyst can improve thermal stability [76].
The catalyst can be also affected by sulphur poisoning. For example, the $Pt/BaO/Al_2O_3$ activity is inhibited by the presence of SO_2 in the flue-gas stream; this deactivation occurs more rapidly during rich-conditions rather than lean conditions, due to the reducing species, and it is attributed to the formation of barium sulphate (which blocks the reaction with NO_x) and of PtS species. Furthermore, there could be competitive adsorption between NO_x and SO_2. Recent studies reported that a quaternary mixed oxide material, in the form of $BaO/ZrO_2/TiO_2/Al_2O_3$ functionalized with platinum, reduces the poisoning effect due to the presence of SO_x [95].

1.4.2.3 Alternative NO_x conversion strategies

Each of the conventional technologies has a number of inherent strengths and weaknesses. The most critical issues of the conventional technologies described above are high temperature and sulphur

poisoning for the catalysts applications, ammonia slip, low efficiency and high temperature for the non-catalytic strategies.

The SNCR has been widely adopted in the past, due to the absence of the catalyst and the consequently low capital and operating costs (compared with the catalytic technologies). The SNCR allowed meeting the past regulations in many application fields. On the contrary, the new regulations introduced imposes new standards ever more stringent. In most of the applications, the SNCRs are not able to meet the new standards for NO_x and NH_3 emissions and the innovative alternative technologies are gaining of interest for those applications where the SCRs are not applicable or economically unfeasible. Among the innovative technologies, the most important ones are the SCR with enhanced NO_2 reduction and the NOx adsorption and NTP desorption-reduction.

SCR WITH ENHANCED NO_2 REDUCTION

The Selective Catalytic Reduction (SCR) strategy, that was described in the previous section, offers the most effective technology for the NO_x removal known so far. Although the improvements in finding more attractive catalysts, the SCRs intrinsically suffer for the activation temperature of the catalyst, the residence time of the gas in the catalyst region, the catalyst sulphur sensitivity.

The residence time depends on the reaction rates for the NO_x reduction. The maximum reduction efficiency is a function of the temperature and the catalyst properties.

In most cases, around 90% of nitrogen oxides contained in exhaust gases is NO (more than 90% of NO_x), and NO_2 content is very small. This means that the Reactions (R *1-19)* and (R *1-21)* are favoured than (R *1-20)* and (R *1-22)* ones. According to the literature, a higher concentration of NO_2 improves the NO_x reduction via ammonia on a V_2O_5 catalyst [96], [97]. The reaction

$$NO + NO_2 + 2\,NH_3 \rightarrow 2\,N_2 + 3\,H_2O \qquad (R\ 1\text{-}30)$$

is faster than Reactions (R *1-19)* and (R *1-20)* at low temperature. Consequently, SCRs can maintain the same efficiency operating at low temperature or reducing the time of contact with the catalysts.

Thus, the NO oxidation is preliminary to the NO_x reduction. The oxidation is commonly promoted by the ozone injection in the SCR or upstream of it. The NO oxidation is faster than the reductions reactions and it occurs according to the mechanism in Figure 1.26.

$$NO + O_3 \rightarrow NO_2 + O_2 \qquad (R\ 1\text{-}31)$$

The rate constant is 2.59×10^9 exp(-3.176/RT) where R is 1.987 kcal/mol K and T is in K [98].

Mok et al. found that Above 150°C, there was an optimum NO_2 content for the efficient NO_x reduction, which was about 50% NO_2 in NO_x. On the other hand, at lower temperatures below 120°C, the NO_x reduction was found to keep increasing with the NO_2 content. The injection of ozone increased NO_x removal efficiencies from 51, 67, 76, 93% at temperatures 423, 443, 473 and 503 K up to 80, 86, 90 and 97%, respectively [96].

The low temperature of the SCR with ozone makes the Non-Thermal Plasma (NTP) technology suitable for ozone production. The oxygen from the exhaust gas easily oxidizes to ozone as it passes through an NTP reactor [99], [100]. The high electric field in NTP leads to the production of free electrons, ions and radicals that recombine to produce metastable species such as ozone. Once the ozone is produced, the oxidation Reaction (R *1-31)* occurs, leading to NO_2 production. The ozone production and the consequent NO oxidation to NO_2 can occur either by applying the NTP directly on the exhaust gases; or indirectly, applying the NTP on oxygen stream and then the ozone produced meets the exhaust [101]. The high-content NO_2 gas stream, from NTP reactor, is sent to the SCR reactor for the NO_x reduction. Due to the high NO_2 content in the exhaust, the SCR in the combined process NO oxidation – NO/NO_2 reduction operates at a lower temperature than conventional SCR by maintaining the same efficiency.

Besides the NO oxidation to NO_2 through the ozone from the NTP reactor, the plasma can also oxidize the particulate matters to CO_2 according to the literature [102]–[104].

An example of SCR improved by non-thermal plasma application is represented in Figure 1.26.

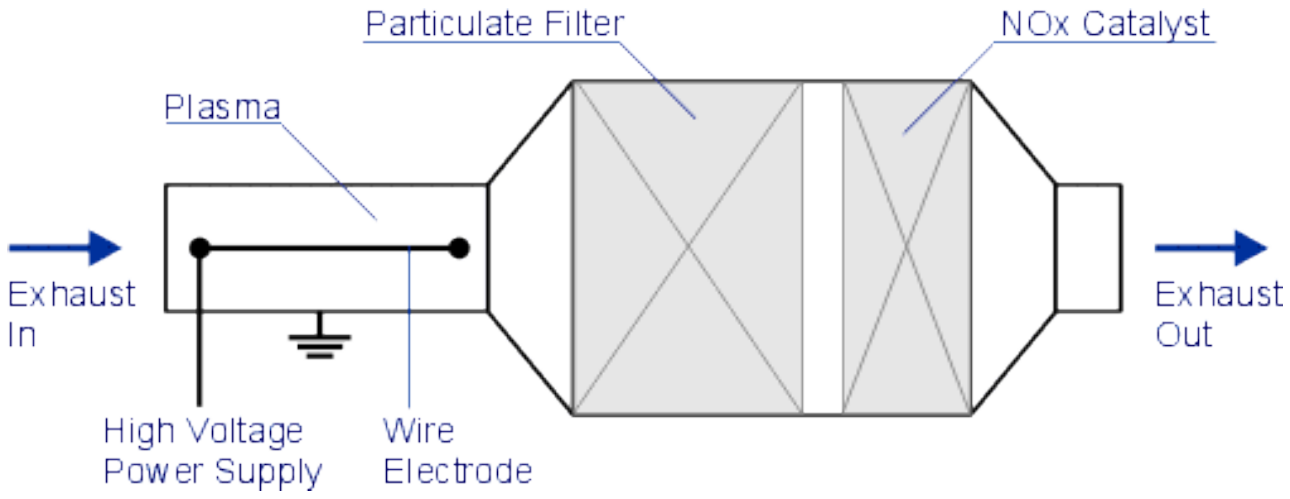

Figure 1.26 - Integrated NTP-SCR system for NO_x removal.

The ozone produced in the plasma reactor oxidize NO to NO_2 and partially oxidize the particulate matters to CO_2. A particulate filter follows the NTP reactor for a further PM trapping before the catalyst for the NO_x reduction (SCR).

NO_x Adsorption and NTP Desorption-Reduction

Among the pollutant removal technologies, the use of NTP is growing of interest in the 21st century. The production of metastable oxidizing species can be useful for the ozone generation, NO oxidation, PM oxidation, etc, as NTP is applied in a rich oxygen gas stream. The NTP applications are increasingly proceeding with scientific and technological innovations. The physics of the NTP, its applications and the generation techniques are widely described in Chapter 3. New researches investigate the possibility to reduce NO_x with NTP without the use of a catalyst by applying NTP directly on the exhaust gas. The presence of oxygen inhibits the NO_x reduction and the NO oxidation occurs on the contrary. The oxidation is much higher as the oxygen concentration in the exhaust increases. Further to the NO oxidation to NO_2, the ozone is also a secondary waste from the NTP application and it represents a pollutant more dangerous than NO itself [105].

On the contrary, when no oxygen is present and the NTP is applied to an NO diluted in N_2 gas stream, the NO reduction occurs and the amount of NO_2 produced is negligible. Penetrante was first to study the kinetics of NO reduction when diluted in N_2 in a plasma condition [106], [107]. After them, many other authors performed NTP reactors for the NO reduction in a free-oxygen environment achieving a NO reduction efficiency of 93-98% [108], [109]. Although the effectiveness of the NTP for the NO reduction, in absence of oxygen, this technology alone is low of interest in realistic applications as all the combustion processes contain oxygen in the exhausts. Okubo et al. proposed a new strategy for NO_x removal from the exhaust that combines the adsorption process to the NTP sorbent regeneration [110]. The process consisted of the two stages process in which NO_x, contained in the exhaust, was adsorbed in the first phase; once the sorbent achieved the saturation, the NTP was promoted in the corresponding of the sorbent leading to the NO_x desorption and its concentration in the gas phase. Once the capability of the NTP to restore the adsorbent capacity was confirmed, the nitrogen was used as a carrier gas for the NO_x desorption. The NO_x concentrated in N_2 was consequently reduced to N_2 and O_2 thanks to the NTP, in accordance with the literature. Hence the NTP offers an alternative for the sorbent regeneration that simultaneously desorb and reduce the NO_x to N_2 [111].

A schematic diagram of the combined adsorption and NTP desorption is represented in Figure 1.27.

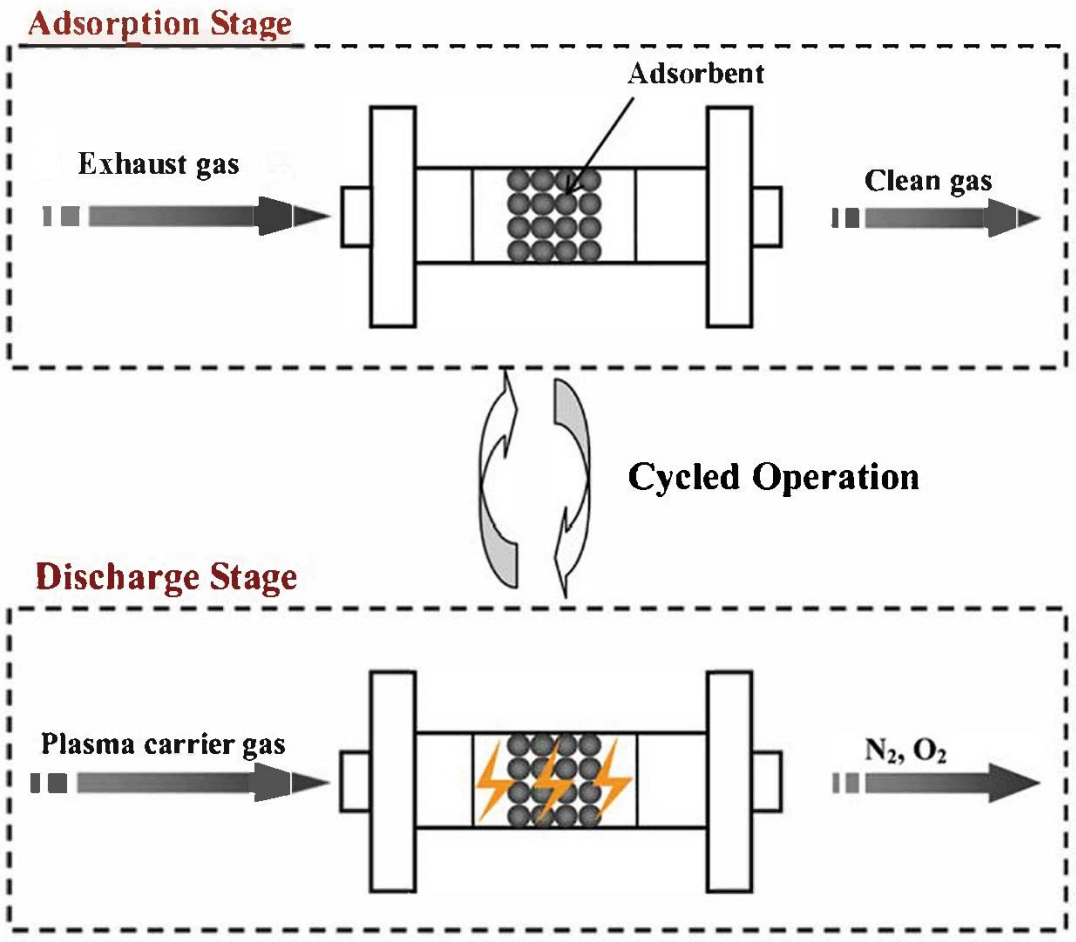

Figure 1.27 - Schematic diagram of the combined adsorption and NTP desorption process [112].

The NO_x adsorption is a low-cost process in which the gas passes through the sorbent material and the gas molecules are trapped on its surface. The results of the trapping is a cleaned gas that exit from the adsorbent bed. Once the sorbent achieves the saturation, it cannot trap any more molecules and the NO_x in the outlet is equal to the NO_x fed to the sorbent bed. Before the saturation, the discharge stage is initiated: a reducing carrier gas (N_2 e.g.) flushes into the sorbent bed simultaneously to the NTP generation. Hence, the NO_x trapped desorbs and the molecules convert to N_2 and O_2 as the effect of the non-thermal plasma. The adsorption capacity of the sorbent restores as the effect of the regeneration and the renewed available sites can guest NO_x molecules anew. Two reactors can provide a continuous process. A schematic diagram of the two reactors in parallel for the NO_x adsorption and plasma desorption-reduction are reported in Figure 1.28.

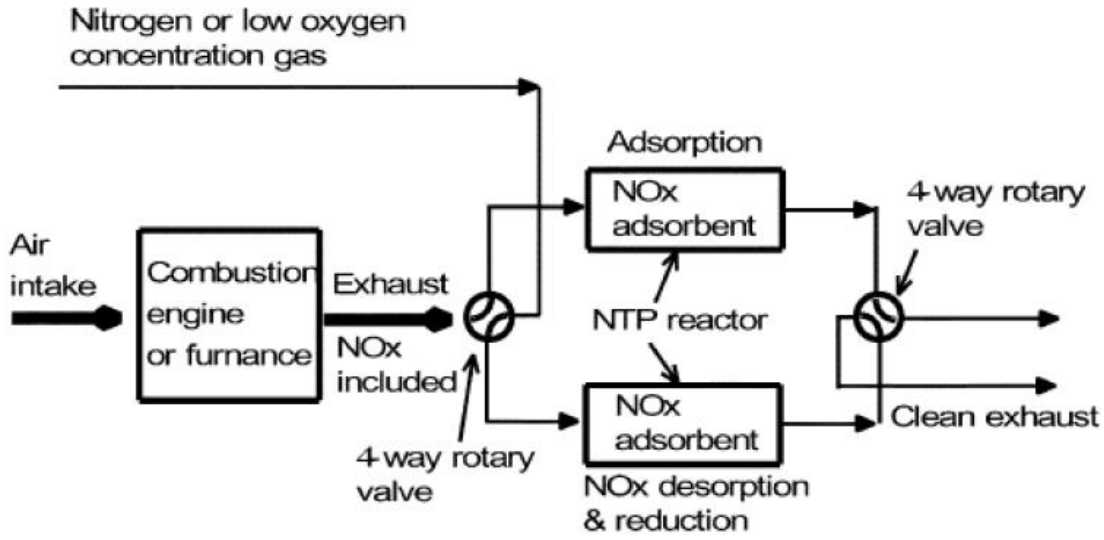

Figure 1.28 - Schematic diagram of the adsorption and plasma desorption-reduction for a continuous process [111].

The exhausts are treated in the reactor operating in the adsorption mode while the other reactor is working in the desorption mode. Once the sorbent has to be regenerated, the exhaust gas is switched to the other reactor, filled with the regenerated sorbent. The cyclic operation of the reactors allows the continuous adsorption of the NO_x in the exhaust and their reduction during the discharge stage. The discharge gas contains the N_2 generated by the NO_x reduction.

The adsorption and NTP desorption-reduction represents a prompt technology for gas treatment. The most attractive aspect is the possibility to perform the process at low temperature. In fact, the adsorption as well as the plasma regeneration can be processed at a temperature below 120°C. Being an exothermal process, the adsorption is encouraged at low temperatures, while the desorption is promoted at high temperature. However, the NTP regeneration allows reducing the operating temperature, promoting the NO_x desorption at a lower temperature than the thermal desorption. The NTP is easily controlled at low temperature, as the energy is provided to small particles like electrons by maintaining a low gas temperature. The higher the temperature, the higher the velocity of the high-weight molecules in the gas and hence an exponentially increasing of the gas temperature. Its low-temperature range of operation makes this technology applicable also down-stream the wet processes, for acid gas absorption, without the necessity to reheat the gas.

One of the main aspects of NO_x reduction in the adsorption and NTP desorption-reduction is the absence of reducing species such as ammonia, urea, hydrocarbons, etc. This characteristic makes the process very attractive for the NO_x abatement. In fact, the managing of reducing species and their mobility represent the higher cost for conventional $DeNO_x$ technologies. Also, there are some

applications where the installation of reactant reservoirs represents a limit such as for the ship equipment where the free spaces are limited and the weight of the units represent a further cost for the ship. Although no reducing species are required, the discharge stage occurs in an environment free of oxidizing species like nitrogen. The nitrogen gas is cheaper to be produced, managed and stored.

For what concern the drawbacks, Yu et al. [112] have measured the concentration of other secondary pollutants from the discharge stage such as nitrous oxide. As the discharge occurs in a gas that is free of oxidizing species, the metastable species produced in the NTP can lead to the N_2O production further to the NO_x reduction to N_2.

1.4.2.4 Post-treatment combined techniques for NO_x abatement

The conventional and/or alternative techniques in such cases are not able to reduce the NO_x concentration in the exhausts up to the threshold value. Although the most used and the most prompt innovative techniques have been described above, other strategies can further reduce the NO_x amount in a gas stream. These are the cases of combined strategies where the strengths of the techniques match each other by improving the overall NO_x separation or conversion. A schematic presentation of the most common post-treatment techniques for NO_x conversion and their combination are reported in Figure 1.29

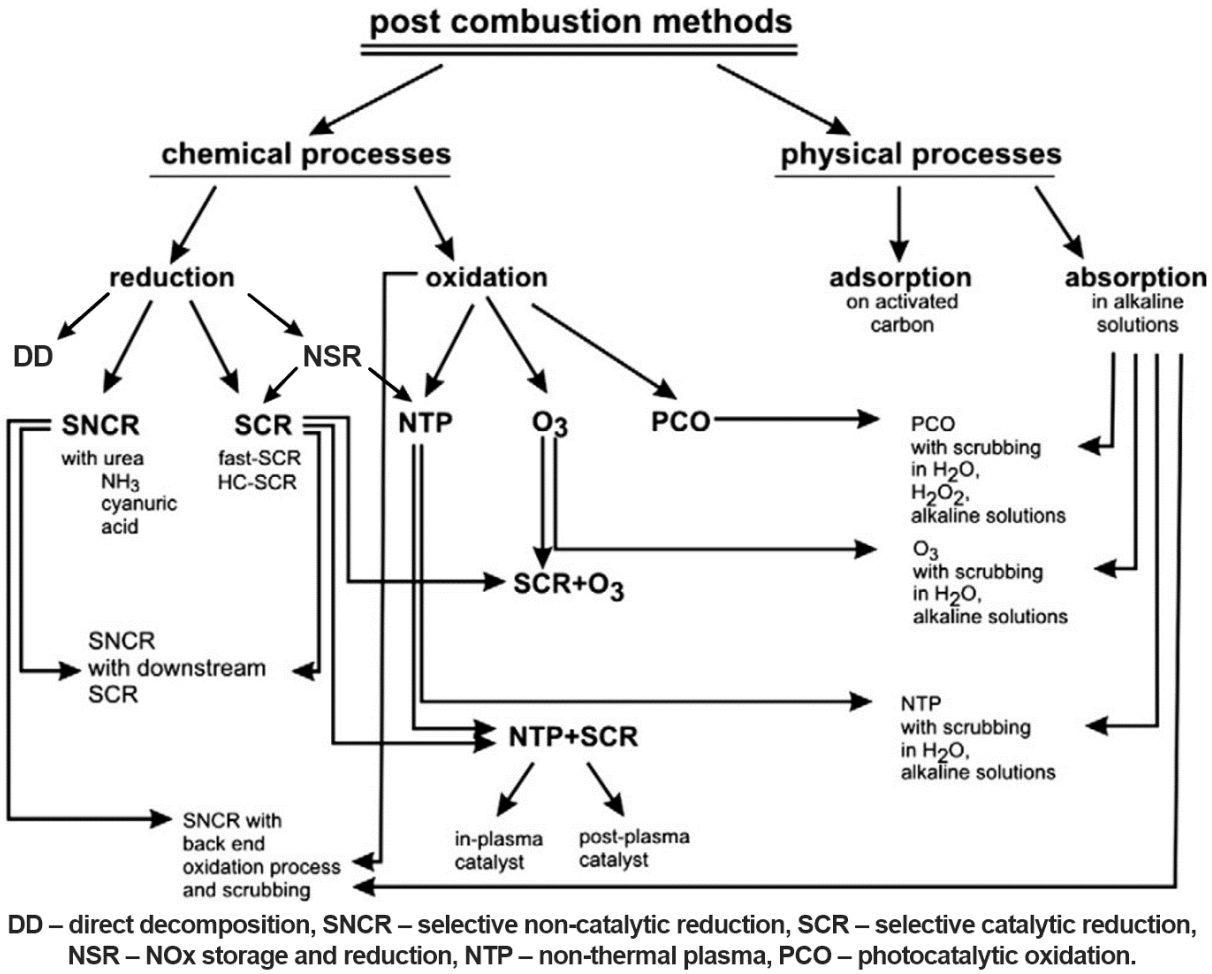

Figure 1.29 - Schematic presentation of NO_x abatement post-combustion methods [113].

The main post-treatment strategies for the De-NO_x are Direct Decomposition (DD), Selective Non-Catalytic Reduction (SNCR), Selective Catalytic Reduction (SCR), NO_x Storage and Reduction (NSR), adsorption, absorption.

For those plants where SNCR is used but their performances do not allow to accomplish the new regulations, an SCR can be installed in cascade for a further NO_x conversion. An alternative to the SCR could be the NO oxidation and scrubbing that follows the SNCR.

The NO_x Storage and Reduction (NSR) during the rich combustion might produce CO and NH_3. A cascade NSR-SCR can be designed that allows to increase the NO_x abatement and reduces the ammonia slip. The NH_3 released from the rich stage in the NSR is helpful to selectively reduce NO_x in the SCR.

The absorption process, described above, has a good NO_x removal efficiency once an alkaline-water solution is used. However, the NO_x abatement efficiency is much higher as the NO_2 concentration increases. The NO_x oxidation to NO_2 can be performed via NTP processes, via contact with O_3, via

photocatalytic oxidation processes. Even the SCR efficiency improves as the NO_x are in the form of NO_2 than NO. Hence, the cascade NTP-SCR improves SCR efficiency; in fact, both methods are dry processes and they occur at low temperatures compared to SNCR. In the end, the NTP can be used in reducing environment to reduce the NO_x to N_2 in the gas phase directly. An application of this process is the adsorption and NTP desorption-reduction.

2. STATE OF THE ART ON NO_X ADSORPTION PROCESS

Innumerable physical, chemical and biological processes take place at the boundary between two phases, while others are initiated at that interface. The change in concentration of a given substance at the interface as compared with the neighbouring phases is referred to as adsorption. Depending on the type of phases in contact, we can consider this process in the following systems: liquid-gas,
Liquid-liquid, solid-liquid and solid-gas. The major development of adsorption processes on a large, industrial scale deal mainly with the solid-gas and solid-liquid interfaces [114].

This chapter describes the adsorption process focusing the attention on the gas-solid systems. The real adsorption system can be defined as including the adsorbent (solid) being in contact with the gas bulk phase and the so-called interfacial layer. This layer consists of two regions: the part of gas residing in the force field of the solid surface and the surface layer of the solid. The material in the adsorbed state is defined as the "adsorbate", but that in the bulk gas or vapour phase prior to being adsorbed is called the "adsorptive". Since the adsorption is a mechanism that initiates at the interface gas-solid, it is a function of the gas density and the partial pressure of the adsorptive species. Porous solid are generally preferred as adsorbents. The high porosity increases the specific interface area (exposed surface per unit of volume or weight) of the sorbent; hence, the amount of adsorbate per unit of volume or weight is higher for porous materials than non-porous ones.

The development of adsorption processes is described in terms of thermodynamic and kinetics. The thermodynamic determine the equilibrium condition that represents the limit where the system behaves ideally, and it is independent of the mass transfer and the kinetic limitations. The kinetics determine the efficiency of the real process and the development of the system toward the equilibrium. Kinetics includes the rate factors, mass and heat-transfer limitations and hydrodynamic dispersion resulting from the velocity distribution across the bed and from mixing and diffusion in the interparticle void space.

This chapter would give an overview of the adsorption process and its application for gas molecules. The first part describes the properties that characterize an adsorbent material and its activation and impregnation. Then the thermodynamic and the kinetic aspects of the adsorption process are illustrated. Lastly, the state of the art of the NO_x adsorption is reported.

2.1Adsorbent properties

The performance of the adsorption process is strongly correlated to the adsorbent affinity with the gas molecules to be adsorbed. The size of the adsorptive molecules and their chemistry would prefer the interaction with an adsorbent having active sites with proportional size and chemical affinity. To better understand the choice of the adsorbent, some physical and chemical properties of the solid used for the adsorption process are described below.

A first characterization of the adsorbent is based on surface properties, such as the specific surface area and polarity. The specific surface area would indicate the surface of solid per unit of volume or weight. The higher is the surface area, the higher is the number of sites available for the adsorption. The increasing of the specific surface area leads to an increasing of the porosity with the consequence of ever small pore size.

The pores volume V_{pore} can be defined from the particle density ρ_p and the adsorbent porosity ε_p:

$$V_{pore} = \frac{\varepsilon_p}{\rho_p} \qquad \textit{(Eq. 2-1)}$$

The adsorbent porosity ε_p represents the fraction of intra-particle void space and it differs from the inter-particle void fraction ε.

The value of ε_p provides a macroscopic description of the internal structure of porous substances. However, most of the solid adsorbents possess a complex porous structure that consists of pores of different shapes and dimensions, depending on the nature of the adsorbent and the method by which it is obtained.

It is possible to classify pores according to their sizes [115]:

- macropores, with widths exceeding about 50 nm;
- mesopores, with intermediate size width between 2 nm and 50 nm;
- micropores, with widths not exceeding about 2 nm.

Macropores represents the bigger pores of the sorbent. They are consistently larger than the gas molecules size, hence the macropores play solely the role of transport pores. Adsorption on the surface of macropores is usually negligible.

Mesopores represents a wide range of pore size. They can play the role of transport pores if their size is larger than adsorptive molecules, or adsorbent surface if they are comparable. The adsorptive

molecules transport in the mesopore channels toward the smallest pores. The adsorption occurs by filling the active sites in the mesopores leading to the so-called “layer coverage”.

The micropores have a dimension comparable with gas molecules. The adsorption occurs in the pore-end of the channels. The adsorbate molecules move deeply into the pores, as the effect of the concentration gradient, by breaking and remaking bonds with the adsorbent surface.

If we consider that the radii of isolated neutral atoms are in the range between 30 and 300 pm (10^{-12} m), the micropores have a size comparable with gas molecules. The nitrogen molecule size e.g. has a Van der Waals radius of 155 pm. Because sizes of micropores are comparable to those of adsorbate molecules, all atoms or molecules of the adsorbent can interact with the adsorbate species. Consequently, the adsorption in micropores may easily develop in a pore-filling process in which their volume is the main controlling factor.

An approximation of pore size distribution of some common adsorbents is shown in Figure 2.1.

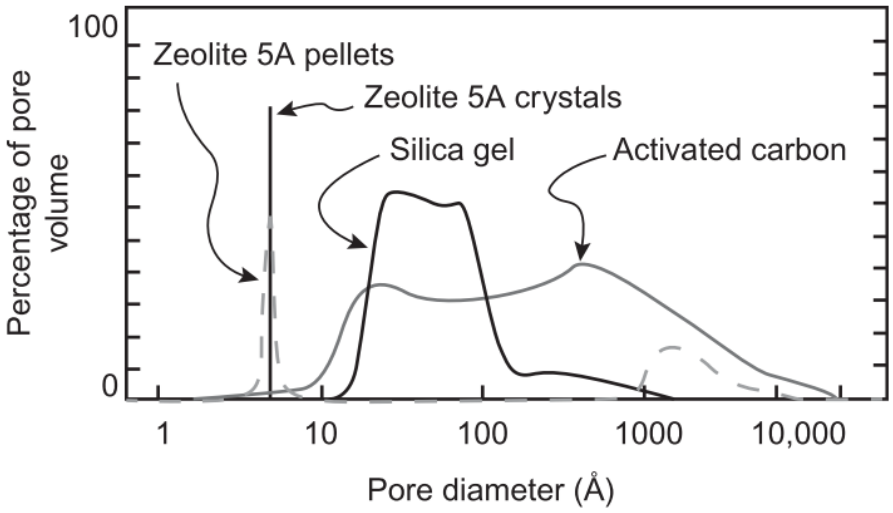

Figure 2.1 - Pore size distribution of several adsorbents [116].

Zeolite materials are characterized by a high number of micropores (pore diameter <20Å), the silica gels by mesoporous and activated carbons are characterized by a wide distribution of pore sizes.

For what concern the selectivity of the sorbent toward the molecules would be adsorbed, the effectiveness depends on the interactions between the adsorptive molecules and the sorbent active sites at the interface. The interactions are due mainly to electrical forces; the functional groups are commonly classified as acidic or basic. The functional group kinds depend on the nature of the adsorbent and the technique used for the activation of the sorbent.

Among the practical solids used in industries, activated carbon (AC) is one of the most complex solids but it is the most versatile because of its extremely high surface area and micropore volume. Activated

carbon is widely used for the pollutant removal through adsorption technique [117], [118]. ACs are the solid products of the pyrolysis processes that fit really well in the circular economy concept. The waste pyrolysis process for energy production e.g. produces syngas used as fuel and biochar as a secondary waste. The biochar can then activated and used as an adsorbent for a wide kind of species, reducing the environmental impact and increasing the sustainability of the process.

ACTIVATED CARBONS

Activated carbons (ACs) are commonly used as adsorbent material for either organic and inorganic species. The structure of activated carbon is complex and it is basically composed of an amorphous structure and a graphite-like microcrystalline structure. The graphitic unit in activated carbon usually is composed of about 6-7 layers and the average diameter of each unit is about 10 nm.
Typical characteristics of activated carbon are listed below.

True density	2.2 g/cc
Particle density	0.73 g/cc
Total porosity	0.71
Macropore porosity	0.31
Micropore porosity	0.40
Macropore volume	0.47 cc/g
Micropore volume	0.44 cc/g
Specific surface area	1200 m^2/g
Mean macropore radius	800 nm
Mean micropore half width	1 - 2 nm

Figure 2.2 - Typical characteristics of activated carbon [119].

The volume of macropore is usually in the order of 0.2-0.5 cc/g and the area contributed by the macropore is usually very small, of the order of 0.5 m^2/g, which is negligible compared to the area contributed by the micropore. Macropores, therefore, are of no significance in terms of adsorption capacity but they act as transport pores to allow adsorbate molecules to diffuse from the bulk into the particle interior. The volume of mesopore is usually in the range of 0.1 to 0.4 cc/g and the surface area is in the range of 10-100 m^2/g. Mesopore contributes marginally to the capacity at low pressure and significantly in the region of capillary condensation. Like macropores, mesopores act as transport pore when capillary condensation is absent and they act as a conduit for condensate flow in the capillary condensation region. The micropores are slit-shaped and because of their high dispersive

force acting on adsorbate molecule they provide space for storing most of the adsorbed molecules and the mechanism of adsorption is via the process of volume filling.

ACs are made by thermal decomposition of carbonaceous raw materials followed by an activation process to remove tarry carbonization products formed during pyrolysis, thereby opening the pores.

Activated carbon is made from raw materials which are usually rich in oxygen and therefore many functional groups on activated carbon have oxygen atom; moreover, oxygen also is introduced during the course of preparation. Oxygen carrying functional groups can be classified into two main types: acidic group and basic group. The functional groups of activated carbon can be increased by treating it with some oxidizing agents or decreased by exposing it to a vacuum environment at a very high temperature.

ACs may be produced as byproducts from a large variety of raw materials e.g. agro-industries (wood waste, palm and coconut oil production e.g.), oil and gas industries (petroleum pitch) or coal. The carbon produced is then treated to increase its adsorption capacity. The so-called "activation process" is a thermal treatment that allows increasing the porosity of the sorbent and the number of functional groups on the sorbent surface. The raw materials are first pyrolyzed and carbonized to remove the volatile fraction and small molecular products. The residual carbonaceous material is subject to the oxidizing action of a gas stream, such as steam, carbon dioxide, air or a mixture of these. The optimum carbonization temperature range is 400-800 °C while the activation temperature range is 600-900°C. During the activation, the carbon is partially gasified to CO_2 and a porous highly activated carbon skeleton is produced. Hence, the vacancies due to the gasification can host gas/liquid molecules during the adsorption.

In order to increase the sorbent selectivity and the adsorption capacity, the sorbent "impregnation" can follow the activation process. The impregnation can be defined as the fine distribution of chemicals and/or metal particles in the pores of AC. The impregnation methods can be either dry or wet depending on the way desired chemical is added onto the surface of the adsorbent. In dry impregnation method, the fixed quantity of solvent is added in such a way that the pores of the adsorbent are just filled, whereas in wet impregnation solvent more than the volume of the pores are added and after filling the pores, the excess chemical is dried and the loading of the chemical species can be controlled [120].

Most ACs contain some oxygen complexes which arise from chemical adsorption of air (oxidation) either during the activation stage or during storage. Those surface complex add a polar nature to the ACs and exist mainly in the form of four different acidic surface oxides:

I. strong carboxylic groups;
II. weak carboxylic groups, which exist as lactone groups combined with the neighbouring carbonyl groups;
III. phenolic hydroxyl groups;
IV. carbonyl groups, which form lactone groups with weak carboxyl groups.

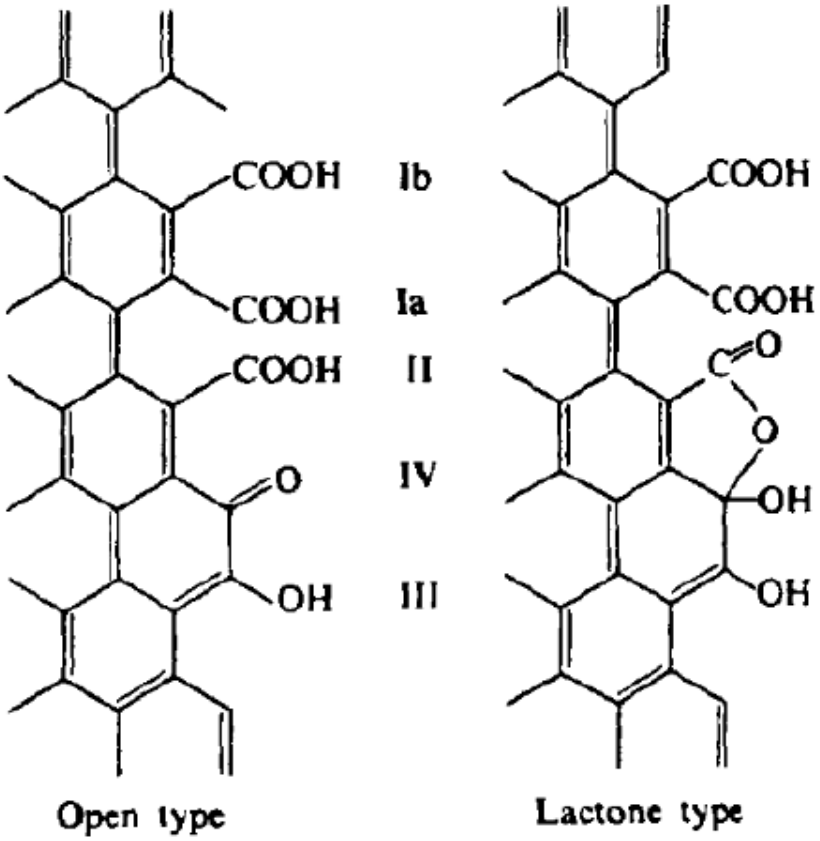

Figure 2.3 - Surface oxides on the carbon surface.

The four surface groups, shown in Figure 2.3, can be removed by heat treatment in an inert atmosphere or under vacuum conditions. The first group has been indicated as Ia and Ib as the different vicinal functional groups. Once the carboxylic group is isolated (Ib), it is required more energy to break the bond with the carbon; while the presence of neighbour polar molecules such as another carboxylic group or a carbonyl group can contribute to the molecule removing. The molecule Ia can be removed at a temperature of 200°C; while 325°C are required for the removal of isolated carboxylic molecules (Ib).

Oxygen, hydrogen, sulfur and nitrogen are generally present in ACs in the form of functional groups and/or atoms chemically bonded to the structure. In the carbon structure, the main functional groups which, in general, are considered to be responsible for uptake of pollutants include carboxyl,

carbonyl, phenols, lactones, quinones besides others. The unique adsorption properties of ACs can be significantly influenced by these functional groups. The functional groups on carbon surface mainly derived from activation process, precursor(s), thermal treatment and post chemical treatment. The nature and concentration of surface functional groups may be modified by suitable thermal or chemical treatments to improve the performance of AC for specific contaminants removal.

2.2Adsorption equilibrium and thermodynamics

The process of adsorption of molecules on the adsorbent surface consists of interactions between the adsorbate and adsorbent surface. It is possible to distinguish two types of adsorption phenomena:

- Physical adsorption or physisorption;
- Chemical adsorption or chemisorption.

In physisorption, the interactions are electrostatic forces such as Van der Waals forces for permanent dipoles and London forces for temporary ones. They are week interactions and they are characterized by low bond energies that make the adsorption process reversible; thus, the adsorbate species can desorb and leave the adsorbent surface.

In chemisorption, the adsorbate is linked chemically with the adsorbent surface. The chemical bonds are stronger than the electrostatic forces that make the adsorption irreversible: the adsorbate can not desorb by physical processes.

However, there are many intermediate situations for which it is not easy to make this classification. The main features of the two types of adsorption are shown in Table 2.1 [121].

Physisorption	**Chemisorption**
Low adsorption heat ($\leq 5\ kJ/mol$)	High adsorption heat ($20 - 100\ kJ/mol$)
Non specific	Highly specific
Monolayer or multilayer	Monolayer only
No dissociation of adsorbed species	May involve dissociation
Only significant at relatively low temperatures	Possible over a wide range of temperature
Non-activated, rapid, reversible	Activated, may be slow and irreversible
No electron transfer although polarization of sorbate may occur	Electron transfer leading to bond formation between sorbate and surface

Table 2.1 - Physical and chemical adsorption properties.

The heat of adsorption provides a direct measure of the strength of the bonding between adsorbate and adsorbent surface. Physical adsorption from the gas phase is invariably exothermic, as may be shown by a simple thermodynamic argument. Since the adsorbed molecule has at most two degrees of translational freedom on the surface and since the rotational freedom of the adsorbed species must always be less than that of the gas phase molecule, the entropy change on adsorption ($\Delta S=S_{ads}-S_{gas}$)

is necessarily negative. In order for significant adsorption to occur, the free energy change on adsorption (ΔG) must also be negative and since ΔG=ΔH-TΔS, this requires ΔH negative that means exothermic adsorption.

The amount of adsorbate per unit of adsorbent is proportional to the number of active sites and their distribution on the adsorbent surface. Furthermore, the capacity of the adsorbent to link the molecules depends on the gas physical/chemical properties. Thermodynamic properties such as temperature and pressure affect the internal energy of the gas molecules and their capacity to penetrate the adsorbent in the micropores, as well as the adsorptive concentration in the gas phase. The equilibrium condition between the gas molecules and the amount of adsorbate is expressed by the "adsorption capacity":

$$\omega_e = \omega_e(P) \qquad or \qquad \omega_e = \omega_e(c) \qquad \textit{(Eq. 2-2)}$$

If we consider the capacity of an adsorbent to link the gas molecules of a species i, the Equations (Eq. *2-2)* become:

$$\omega_{e,i} = \omega_{e,i}(P_i) \qquad or \qquad \omega_{e,i} = \omega_{e,i}(c_i) \qquad \textit{(Eq. 2-3)}$$

The adsorption capacity for the species i ($\omega_{e,i}$) can be expressed in the function of its partial pressure (P_i), in the gas phase, or its concentration (c_i). The adsorption capacity is generally expressed as mole or mass of adsorbate per mass of solid adsorbent; while the concentration is expressed as mole or mass of adsorptive in the gas volume.

Being the adsorption a function of the gas temperature, the curves are parametric in the temperature and isotherms curve can be estimated. The adsorption isotherm can be derived assuming thermodynamic equilibrium between surface and bulk phases, which means equality of chemical potentials of a given component in coexisting phases; its analytical form depends on the assumed model of the adsorption system and the complexity is related to the heterogeneity of the solid surfaces [114].

The higher is the partial pressure of the i-th species in the gas phase, the stronger is the driving force toward the active sites. Due to the high porosity of the adsorbent materials, high partial pressure encourages the gas molecules to achieves the active sites in the micropores. Many models have been proposed among the years to estimate the adsorption capacity in the function of the partial pressure (or gas concentration).

Five types of adsorption isotherms have been recognised, as shown in Figure 2.4.

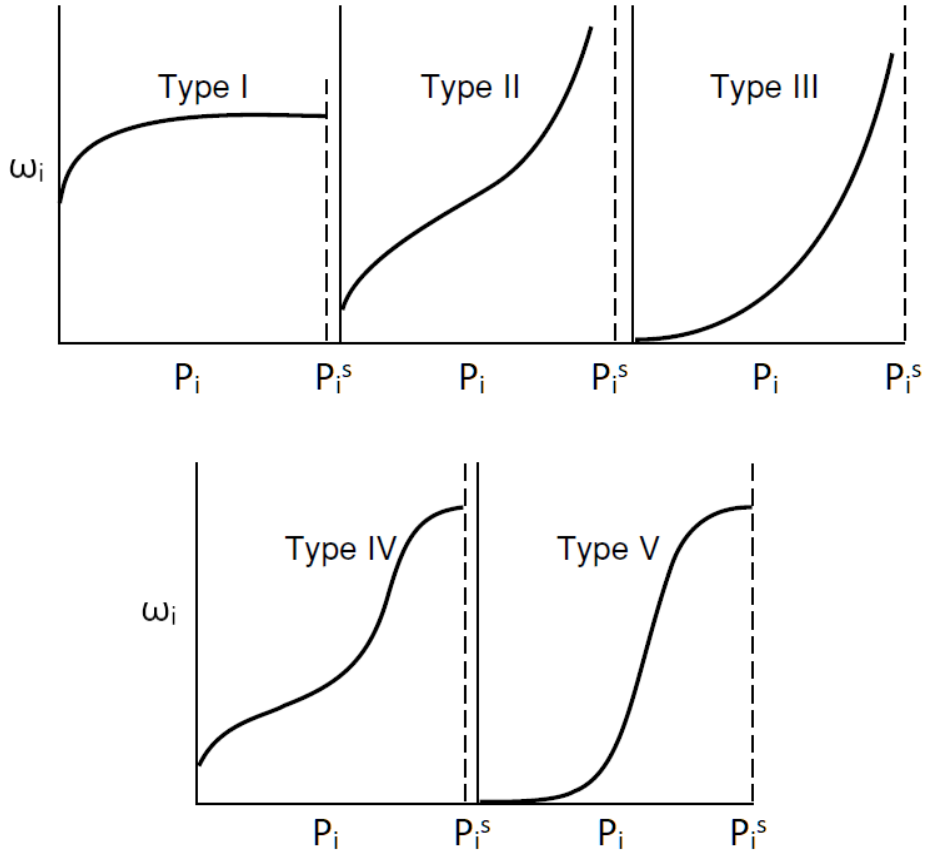

Figure 2.4 - Representative adsorption isotherm types.

The adsorption capacity rises as the partial pressure increases. The increasing is rarely linear as it is possible to see from Figure 2.4. Isotherms that are concave downward are usually called “favourable” because a high adsorption capacity can be obtained at low concentration of the adsorbate in the fluid phase; while an isotherm that is concave upward (this shape is rare) is called “unfavourable” because relatively low adsorption capacities are obtained.

The isotherm type I, in Figure 2.4, is called “Langmuir isotherm”. It describes monolayer adsorption which is characterized by a fast initial increase of the adsorption capacity with the partial pressure of the adsorbate. A large number of active sites are easily accessible even at low partial pressure and they define a “layer”. Since the partial pressure increases, few other sites can be available for the adsorption. This leads the curve to an asymptotic-like pattern as the maximum number of active sites are occupied.

The type II is the S-shaped (or sigmoid) isotherm and it shows a large deviation from the Langmuir model: the flat region indicates the formation of a monolayer, but the number of active adsorption sites available increases as the adsorption proceeds, generating multilayers.

The type III isotherm describes multi-layer adsorption that occurs without the generation of the intermediate monolayer as the adsorption capacity increases exponentially. The adsorption is not encouraged at low concentration and the number of sites available increase exponentially.

Types IV and V are also typical of multi-layer adsorption which reaches a saturation level. The layers are represented by the flat region of the adsorption curves. The multi-layer can be explained with the capillary condensation of the gas.

In literature, the adsorption process is described by many different thermodynamic models. The most acknowledged ones refer to three different theories:

a) Capillary condensation theory;
b) Polanyi potential theory;
c) Langmuir theory.

The capillary condensation theory is mainly used for the adsorption of vapours at high partial pressure: the adsorption on porous adsorbent materials occurs as multi-layer adsorption and the smallest pores are filled with adsorbate at liquid state. The Capillary condensation phenomenon was discovered by Zsigmondy who investigated the update of water vapour by silica materials [122]. Zsigmondy proved that condensation of physisorbed vapours could occur in narrow pores below the standard saturated vapour pressure. The main condition, for the existence of capillary condensation, is the presence of a liquid meniscus in the adsorbent capillaries. For cylindrical pores, with the pore width in the range 2-50 nm i.e. for mesopores/micropores, this phenomenon is relatively well described by the Kelvin equation [123].

The Polanyi potential theory hypothesises a force field in the proximity of the adsorbent surface, which is characterized by an adsorption potential. This potential is defined as the work done by the adsorption forces to bond a molecule and it corresponds to the species free energy variation between its state in the fluid bulk and the condition of adsorbed molecule. Consequentially, the adsorbate volume depends on the potential according to the relation expressed by the adsorption isotherm. The adsorption phenomenon occurs when the force field can compress the adsorbate on the surface with a partial pressure which determines its condensation (if vapour); the process occurs throughout a progressive filling of the pore volume. This theory is valid for physical adsorption and non-polar adsorbate.

The Langmuir adsorption theory is used to describe the equilibrium between adsorbate and adsorbent system, where the adsorbate adsorption is limited to one molecular layer at or before a relative pressure of unity is reached. Although the isotherm initially proposed by Langmuir in 1918 is

generally suitable for describing the chemisorption process when ionic or covalent chemical bonds are formed between the adsorbent and the adsorbate, the equation is obeyed in many systems with moderately low coverage and can be easily extended to describe the behaviour of the binary adsorption system. For those systems in which low concentration of adsorptive species (ppm-range or ppb-range) in the gas phase adsorbs, the Langmuir theory offers a good approximation of experiments.

Taking inspiration from the Langmuir theory, the most common gas-solid models are:

- Langmuir model;
- Freundlich model;
- Langmuir-Freundlich model;
- Henry model;
- Brunauer-Emmett-Teller model

LANGMUIR MODEL

According to the Langmuir model, the adsorption is considered as a chemical reaction between the adsorbate molecules and a finite number of active sites on the adsorbent surface. The theory is based on the following assumptions:

i. the adsorption takes place in well-defined local sites on the adsorbent surface;
ii. the adsorbent surface is flat and homogeneous;
iii. all the sites are iso-energetic (energetically equivalent);
iv. each site can hold at most one adsorbate molecule (monolayer adsorption);
v. there are no interactions between molecules adsorbed on adjacent sites.

Being a chemical reaction, the grade of adsorption can be expressed by an "adsorption rate":

$$r_a = k_a c(\omega_{max} - \omega_e) \qquad \textit{(Eq. 2-4)}$$

where k_a represents the adsorption rate constant, c is the gas concentration, ω_{max} and ω_e represent monolayer adsorption capacity and the adsorption capacity that is in equilibrium with c, from the Equation (Eq. *2-2)*. The grade of adsorption is thus proportional to the gas concentration and the active sites available.

The adsorbate species can desorb, leaving the sites occupied. The grade of desorption can be calculated as:

$$r_d = k_d \omega_e \qquad \textit{(Eq. 2-5)}$$

where k_d is the desorption rate constant.

At steady state, the number of adsorbed molecules is equal to the number of desorbed molecules over time; thus, Equations (Eq. 2-4) and (Eq. 2-5) are equivalent:

$$k_a c(\omega_{max} - \omega_e) = k_d \omega_e \qquad \textit{(Eq. 2-6)}$$

or:

$$\omega_e = \frac{k_a c \omega_{max}}{k_d + k_a c} \qquad \textit{(Eq. 2-7)}$$

The ratio between the adsorption rate and the desorption rate constants, define the equilibrium constant:

$$K_e = \frac{k_a}{k_d} \qquad \textit{(Eq. 2-8)}$$

The equilibrium constant in the adsorption processes is also known as Langmuir constant K_L.

Hence the Equation (Eq. 2-7) becomes:

$$\omega_e = \omega_{max} \frac{K_L c}{1 + K_L c} \qquad \textit{(Eq. 2-9)}$$

The Equation (Eq. 2-9) is well known as the "Langmuir isotherm" for the calculation of the adsorption capacity. K_L and ω_{max} depend mainly on the thermodynamic conditions and the adsorbent properties respectively. The essential characteristics of the Langmuir isotherm can be expressed by a dimensionless constant called the separation factor R_L:

$$R_L = \frac{1}{1 + K_L c_0} \qquad \textit{(Eq. 2-10)}$$

where c_0 is the initial concentration in the gas phase. R_L values indicate the adsorption to be unfavourable when $R_L>1$, linear when $R_L=1$, favourable when $0<R_L<1$, and irreversible when $R_L=0$.

The Equation (Eq. 2-9) can be expressed in the linear form:

$$\frac{1}{\omega_e} = \frac{1}{\omega_{max} K_L} \frac{1}{c} + \frac{1}{\omega_{max}} \qquad \textit{(Eq. 2-11)}$$

The Langmuir is the most common model used to interpret the adsorption results for a low adsorptive concentration in the gas phase.

FREUNDLICH MODEL

The Freundlich adsorption isotherm is an empirical model, used for monolayer adsorption that occurs on rough and energetically heterogeneous surfaces. This isotherm gives an expression which defines the surface heterogeneity and the exponential distribution of active sites and their energies. The basic assumption of the model is that the energy distribution follows a decaying exponential law: the active sites with low activation energy are the most common ones. The higher is the activation energy, the lower is the number of the related active sites. The active sites are filled decreasingly in relation to their activation energy.

The Freundlich isotherms are represented by:

$$\omega_e = K_F c^{\frac{1}{n}} \qquad \textit{(Eq. 2-12)}$$

Where K_F is the Freundlich constant and 1/n represents the adsorption intensity. The coefficient 1/n is a function of the bond energy and its value ranges between 0 and 1. At high pressure, 1/n=0, hence the adsorption becomes independent of pressure. If 1/n=1 there is a linear dependence between the adsorption capacity and the gas concentration, and K_F is a "partition coefficient".

Similarly to the partition coefficient for the partition of a chemical between non-miscible liquids, The partition coefficient can be derived for the partition of a chemical between a fluid and a solid adsorbent. In the case of adsorption, the partition coefficient is the ratio of the amount of adsorbate, per mass of adsorbent, to the amount of adsorptive per gas volume.

The Equation (Eq. 2-12) can be expressed in the linear form:

$$\log(\omega_e) = \log(K_F) + \frac{1}{n} \log(c) \qquad \textit{(Eq. 2-13)}$$

In such cases, the Freundlich model is combined with the Langmuir model. This combined model is called "Langmuir-Freundlich".

LANGMUIR-FREUNDLICH MODEL

The Langmuir-Freundlich model combines the decaying energy distribution of the active sites to the adsorption process seen as a chemical reaction between the adsorbate and adsorbent surface. Starting from the chemical reaction consideration made in the Langmuir model, the equivalence of adsorption and desorption reaction led to the Equation (Eq. 2-9). If the iii. assumption of the Langmuir model decay (the sites does not have the same energy), the concentration c can be replaced by the power-law as in the Freundlich model. The isotherm equation becomes:

$$\omega_e = \omega_{max} \frac{K_e c^{\frac{1}{n}}}{1 + K_e c^{\frac{1}{n}}} \qquad \textit{(Eq. 2-14)}$$

In this case, the parameters must be estimated become three.

HENRY MODEL

The Henry adsorption isotherm is valid for the adsorbate-adsorbent systems where the concentration of the adsorbate approaches to zero (infinite dilution); in this case, each adsorbate molecule can be considered isolated from the others and not influenced by their presence.
The Henry isotherm expression may be written as:

$$\omega_e = K_H c \qquad \textit{(Eq. 2-15)}$$

where K_H is the Henry constant.
The Henry model can be used only in the case of partial coverage of the adsorbent surface and as the adsorptive concentration is very low. The Henry isotherm can be derived from both Langmuir and Freundlich models. In the case of infinite dilution, c tends to zero and the value $K_e c$ in the Equation (Eq. 2-9) tends to zero too, being K_e a finite value. The Henry constant thus can be estimated from the Langmuir parameters:

$$K_H = K_L \omega_{max} \qquad \textit{(Eq. 2-16)}$$

In the Freundlich model, the condition of iso-energetical adsorption sites is represented by 1/n=1 and the Equation (Eq. 2-12) is reduced to the Henry isotherm.

BRUNAUER-EMMETT TELLER MODEL

The Brunauer–Emmett–Teller (BET) theory aims to explain the physical adsorption of gas molecules on a solid surface even if it is referred to the condensation condition. The B.E.T. isotherm is a model meant to describe multi-layer adsorption and it is based on the same hypothesis of Langmuir model of the adsorbent surface with a limited number of active sites. The formation of the first layer is assumed to occur according to the Langmuir model, while the subsequent layers build up with a mechanism similar to condensation. Hence, the adsorption enthalpy related to the formation of the first layer differs from the adsorption enthalpy related to the formation of the subsequent layers; the first layer follows the Langmuir model, the latter is assumed to equal to the liquefaction enthalpy of the adsorbate.

The B.E.T. isotherm is commonly expressed in the function of the partial pressure:

$$\omega_e = \omega_{max} \frac{K_{BET} x^\circ}{[1 - x^\circ][1 + x^\circ(K_{BET} - 1)]} \qquad \textit{(Eq. 2-17)}$$

where x° is the ratio between the equilibrium and the saturation pressure of adsorbate:

$$x^\circ = \frac{P}{P^\circ} \qquad \textit{(Eq. 2-18)}$$

BET adsorption isotherms have a trend similar to the type II or type III in Figure 2.4.

The BET model is widely used to measure the adsorbent surface properties. standard BET analysis is most often conducted at the boiling temperature of N_2 (77 K) [124].

2.3Adsorption kinetics in a fixed bed reactor

The Equilibrium condition between the adsorptive and the adsorbate species is achieved once the number of molecules adsorbed coincide with the amount desorbed. This condition is guaranteed by the totality of the active sites occupied by adsorbate as the sorbent achieves the saturation.

If the saturation represents the capacity of an adsorbent to trap the gas molecules, it does not give information about the mass transfer and the number of molecules desorbed and/or slipped during the transition period between the adsorbent "virgin" and "saturated" condition. The rate factors and the kinetics are described by the mass transfer phenomena of the molecules from the gas bulk toward the adsorbent surface and them adsorption.

A mass transfer mechanism for the adsorption is widely proposed as the following five steps:

1) fluid mixing;
2) external mass transfer;
3) pore diffusion;
4) surface diffusion;
5) reaction kinetics at phase boundary.

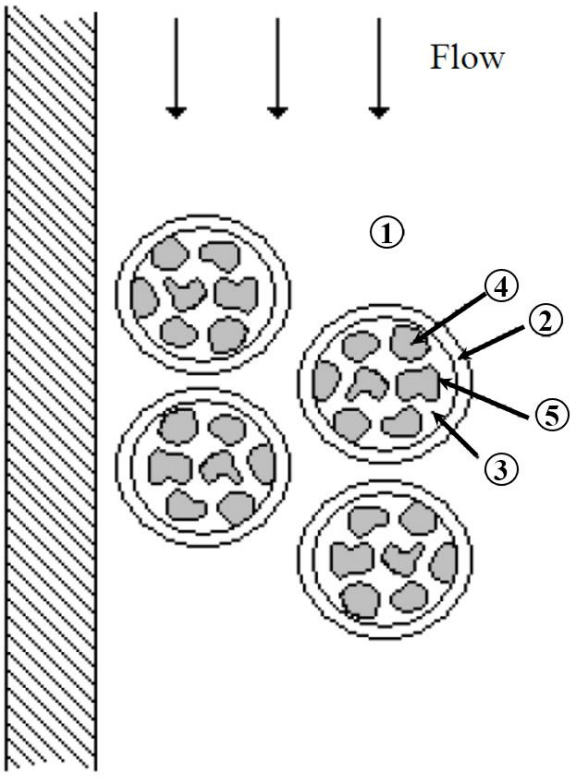

Figure 2.5 - Mass transfer mechanism: 1) fluid mixing, 2) external mass transfer, 3) pore diffusion, 4) surface diffusion, 5) reaction kinetics at the phase boundary.

Fluid mixing represents the transport of the species in the gas bulk. The well-mixing condition leads to the homogeneous concentration of the gas species in the bulk region, far from the adsorbent. External mass transfer occurs between the external surfaces of the adsorbent particles and the surrounding fluid phase. The driving force is the concentration difference across the boundary layer that surrounds each particle. Pore diffusion or macropore diffusion occurs as the gradient in concentration between the external surface and the gas in the pores. The pores are sufficiently large that the adsorbing molecules escape the force field of the adsorbent surface and the driving force is a purely gradient in concentration. Surface diffusion is the diffusion in pores sufficiently small that the diffusing molecule never escapes the force field of the adsorbent surface. The transport occurs through interactions of near adsorption sites. The driving force for the process can thus be approximated by the gradient in concentration of the species in its adsorbed state. Reaction kinetics, at the phase boundary, are generally controlled by mass transfer within the pore network rather than by the kinetics of sorption at the surface.

A schematic representation of pore diffusion and surface diffusion is shown in Figure 2.6.

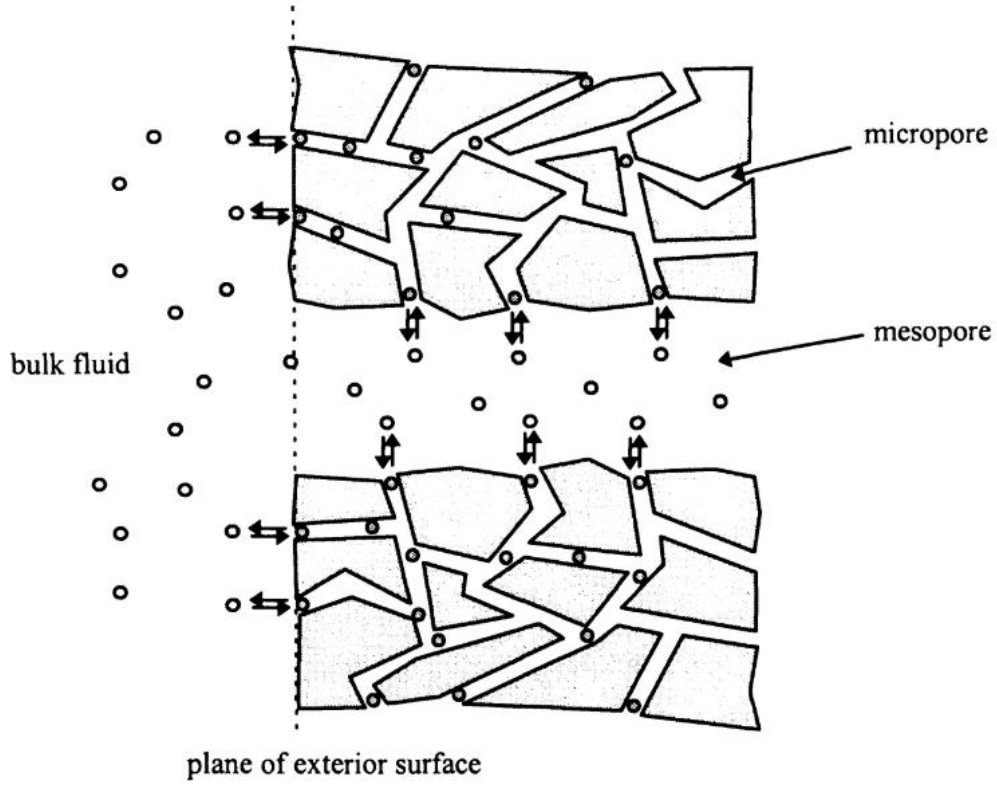

Figure 2.6 - Pore diffusion and surface diffusion of particles in the adsorbent pores [119].

The macropores and mesopores are greatly larger than gas molecules. This confirms the hypothesis of the pure diffusion model into the pores as a few interactions with active sites can occur. On the contrary, the dimension of the micropores is comparable with the gas molecules. Hence, the gas molecules in the micropores can diffuse as a gradient in concentration but only by electrical interactions between the near active sites.

Molecules are attracted to surfaces as the result of two types of forces: dispersion-repulsion forces (also called London or van der Waals forces) such as described by the Lennard-Jones potential for molecule-molecule interactions; and electrostatic forces, which exist as the result of a molecule or surface group having a permanent electric dipole or quadrupole moment or net electric charge. If a surface is polar, its resulting electric field will induce a dipole moment in a molecule with no permanent dipole and, through this polarization, increase the extent of adsorption. Similarly, a molecule with a permanent dipole moment will polarize an otherwise nonpolar surface, thereby increasing the attraction.

The typical adsorption reactor consists of a cylindrical column in which the sorbent is placed determining the so-called “adsorption bed”. Referring to a sorbent bed made of granular particles, it can be either fixed or fluidised depending on the velocity and the direction of the gas flowing, as shown in Figure 2.7.

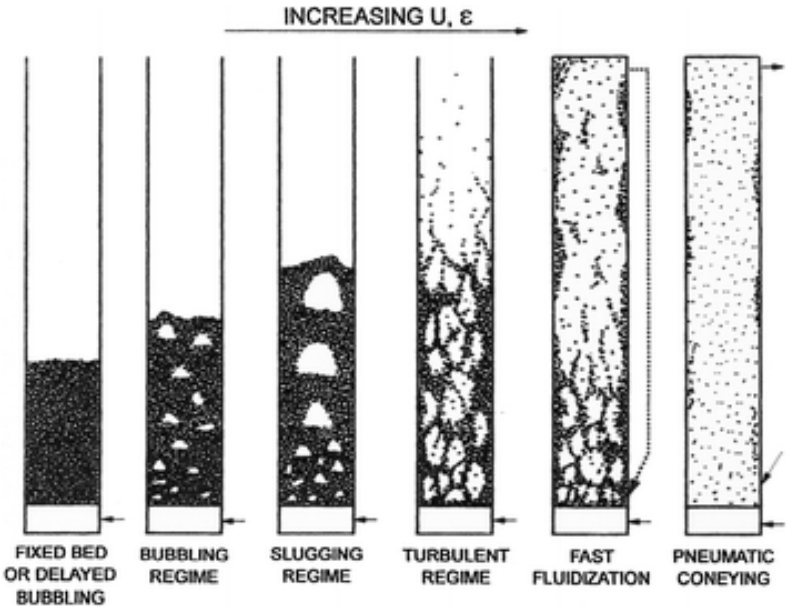

Figure 2.7 - Adsorption bed design in the function of the gas velocity: fixed bed (left), fluidised bed (right) [125].

In the fixed bed configuration, the sorbent particles do not move each other into the reactor; the gas passes within the vacuum between the grains and into the pores. If the gas moves upward above a

characteristic velocity named "minimum fluidisation velocity", u_{mf}, the bed is fluidised, and several hydrodynamic regimes are observed by increasing the velocity above u_{mf} (Figure 2.7). If the gas moves horizontally or downward or if its velocity is below u_{mf}, the bed behaves as a fixed bed unit.
The main fixed bed disadvantage is the discontinuity of the process; in fact, when the sorbent is saturated or it is achieved the target of the sorbate concentration in the outlet gas, it becomes necessary either to regenerate the adsorbent or to dispose of it. In the fluidised bed configuration, the gas passes through the sorbent granular particles at high enough velocity to suspend the solid and cause it to behave as though it is a fluid. The main advantages of this configuration are the uniform particle mixing and the ability to operate the regeneration in a continuous state. In fact, due to the intrinsic fluid-like behaviour of the solid material, fluidised beds do not experience poor mixing as in packed beds. Furthermore, the fluidised bed nature of these reactors allows for the ability to continuously withdraw the product and introduce new sorbent material into the reaction vessel. The sorbent removed, may be regenerated in an additional unit before to reintegrate it into the adsorption chamber. The main disadvantages of the fluidised bed reactor, compared with the fixed bed, are the pumping requirements, the particle entrainment, the production of ashes and the erosion of the internal components due to the frictions between the solid particles and the wall of the vessel.
In fixed-bed adsorption, the concentrations in the fluid and solid phases change with the time and with the position in the bed. If the solid contains no adsorbate at the start or it has most of the active sites available for the adsorption, the gas molecules adsorb near the inlet of the bed, where the fluid first contacts the adsorbent. The adsorptive concentration in the fluid drops rapidly with the distance along the sorbent bed; while the adsorbed concentration increases. If the mass transfer from the fluid toward the adsorbent surface is strong enough and the adsorbent bed is far from the saturation, the adsorptive concentration in the outlet can reach zero. Since the adsorbed species occupies most of the active sites available, tracks of adsorptive species can be detected at the end of the bed. This condition is called "breakpoint" and the bed become less effective. The breakpoint occurs when the concentration of the fluid leaving the bed spikes as unadsorbed solute begins to emerge. Usually, a breakpoint composition is set to be the maximum amount of solute that can be acceptably lost, typically something between 1 and 5 percent. The "saturation", instead, represents the condition of total ineffective of the adsorbent. No more molecules can be adsorbed and the concentration at the outlet of the bed is equal to the feed. The concentration profiles along the adsorbent bed and parametric in the time, and the breakthrough curve are represented in Figure 2.8.

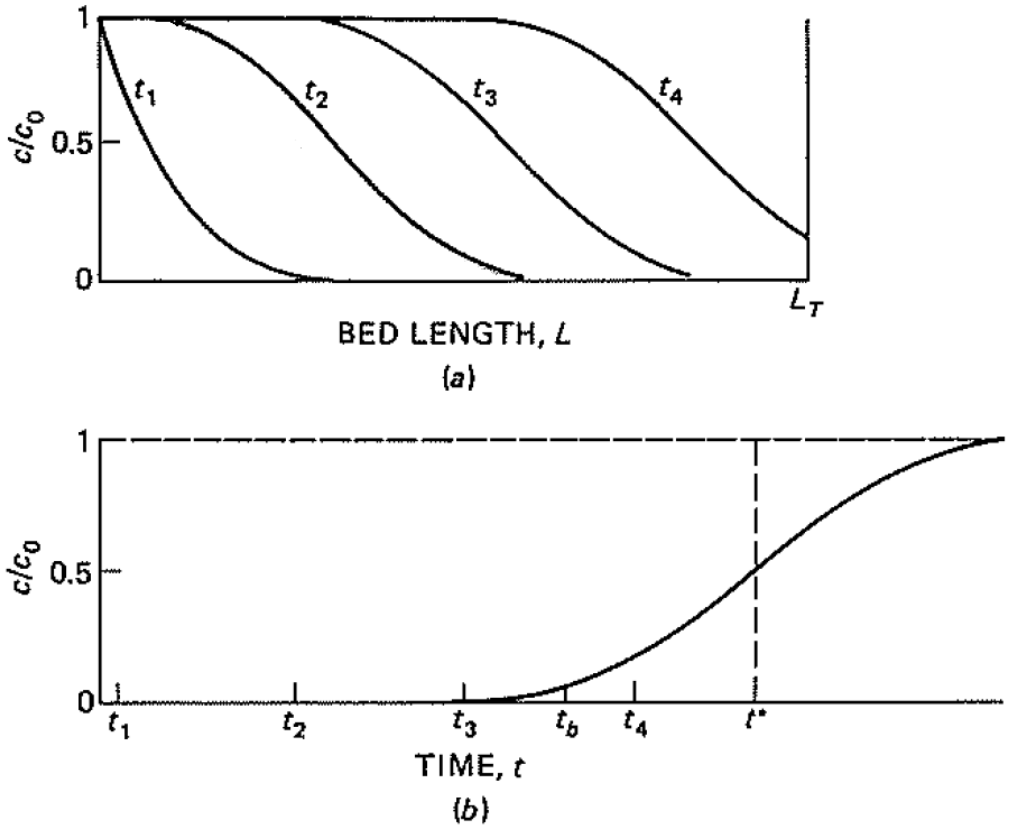

Figure 2.8 - Concentration profiles (a) and breakthrough curve for adsorption in a fixed bed (b) [126].

Figure 2.8 shows the normalized concentration of an adsorptive species, where c_0 represents the feed concentration and L_T the bed length. At the time t_1, the concentration drops exponentially along the reactor and it rich zero for a length lower than L_T (chart a). From time t_2, the concentration profiles become S-shaped and their shape is constant and shifts on the right with the time. Hence the S-shaped cannot reach zero before the L_T, the concentration rises in the outlet gas up to the feed once the saturation condition occurs. The concentration profile in the function of the time at the end of the adsorbent bed is called "curve of breakthrough" and it is shown in Figure 2.8 (b). From the breakthrough curve, it is possible to estimate the amount of solute adsorbed in the function of the time and consequently the amount of adsorbent saturated. In most of the cases, the breakthrough has an S-shape and is symmetric. This means that the time t^*, that represents the time at which c/c_0 is equal to 0.5, coincides with the stoichiometric capacity of the adsorbent to adsorb the gas molecules, and it can be obtained by a simple material balance.

For a unit area of bed cross-section, the solute feed rate is the product of the superficial velocity and the feed concentration:

$$F_{S,0} = uc_0 \qquad \textit{(Eq. 2-19)}$$

For an ideal breakthrough curve, all the solute fed in time t^* is adsorbed, and the concentration on the solid has increased from the initial value ω_0 to the equilibrium or saturation value ω_s. Thus,

$$uc_0 t^* = L_T \rho_b (\omega_s - \omega_0) \qquad \textit{(Eq. 2-20)}$$

or

$$t^* = \frac{L_T \rho_b (\omega_s - \omega_0)}{uc_0} \qquad \textit{(Eq. 2-21)}$$

where ρ_b is the bulk density of the packed bed that represents the mass of the adsorbent in the bed volume. It is proportional to the particle density ρ_p and the reciprocal of the void fraction of packing ε:

$$\rho_b = (1 - \varepsilon)\rho_p \qquad \textit{(Eq. 2-22)}$$

The initial amount of adsorbate ω_0 is equal to zero if the adsorbent is virgin or it is totally regenerated. The amount of adsorbate on the adsorbent surface is a function of the adsorption time and it can be calculated from a mass balance as the concentration profile in the function of the time (breakthrough curve) is known.
From a mass flow on the adsorbed bed referred to the solute:

$$F_{S,0} - F_{S,OUT} = L_T \rho_b \frac{d\omega}{dt} \qquad \textit{(Eq. 2-23)}$$

where $F_{S,0}$ and $F_{S,OUT}$ are the inlet and outlet mass flow per unit of area of bed cross section.
Multiply for dt and replacing the solute rate as in the Equation (Eq. *2-19)*, the Equation (Eq. *2-23)* becomes:

$$(uc_0 - uc)dt = L_T \rho_b d\omega \qquad \textit{(Eq. 2-24)}$$

Hence, the adsorption capacity can be calculated in the function of the time since the profile of the outlet concentration in the function of the time is known. In fact, being the other parameters constant in the time, the Equation (Eq. *2-24)* becomes:

$$\omega(t) = \frac{u}{L_T \rho_b} \int_{t_0}^{t} (c_0 - c\,) dt \qquad \textit{(Eq. 2-25)}$$

In the case the inlet concentration is constant, the Equation (Eq. *2-25)* becomes:

$$\omega(t) = \frac{u c_0}{L_T \rho_b} \int_{t_0}^{t} \left(1 - \frac{c}{c_0}\right) dt \qquad \textit{(Eq. 2-26)}$$

The adsorbate amount is proportional to the mass flow and to the area overlapped the breakthrough curve. The break-point time t_b is always lower than t^*, and the actual amount of solute adsorbed at the breaking point can be determined by integrating the breakthrough curve up to the time t_b, as shown in Figure 2.9.

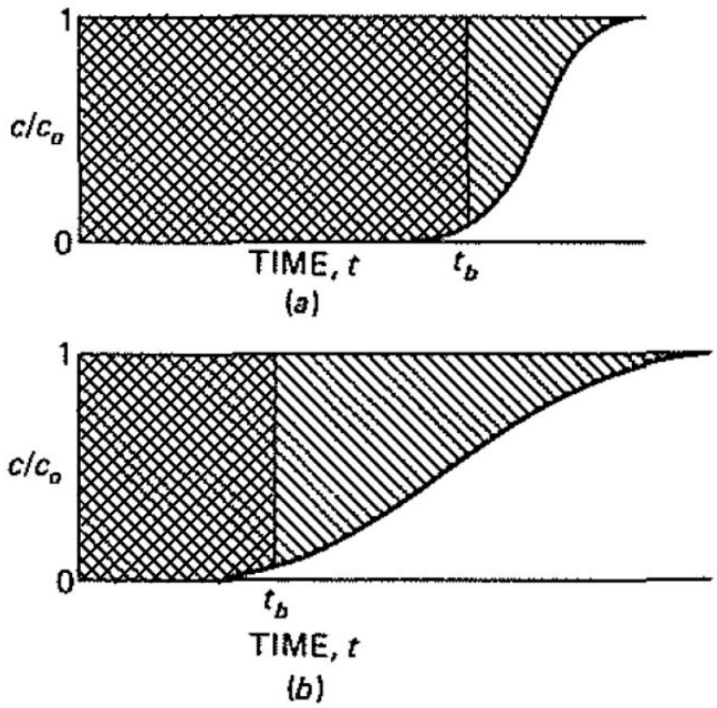

Figure 2.9 - Breakthrough curves for a strong (a) and weak (b) mass-transfer.

The area overlapped the curve between zero and t_b represents the integral in the Equation (Eq. *2-26)* for the calculation of the adsorbate amount in the breakpoint condition. As it is possible to see from Figure 2.9, the number of molecules trapped in the corresponding of the breakpoint condition depends on the breakthrough curve shape. In Figure 2.9 (a), the slope of the S-shaped curve is higher than in Figure 2.9 (b). The difference is due to the stronger mass transfer in the first case than in the latter. An improved mass transfer leads the adsorptive species to adsorb as soon they are in contact with the

adsorbent surface. In the ideal case of no mass-transfer resistance, the breakthrough curve would be a vertical line from 0 to 1 when all the solid was saturated. In this case, all the adsorbent bed is saturated and the time of the breakpoint coincides with the saturation time. In realistic applications, the presence of a mass transfer resistance makes part of the adsorbent unused. This phenomenon is well described in the concentration profile in the function of the bed length and parametric in the time Figure 2.8 (a). The slope of the curves depends mainly on the mass transfer between fluid and solid. The curves at the time t_2, t_3, t_4 have the same shape but it is shifted to the right. This means that, after a transient period, the mass transfer can be considered constant. The portion of the bed on the left of the curves is saturated and the adsorbent is in equilibrium with the feed ($c/c_0=1$); while the portion on the right is in its initial state ($c/c_0=0$). The portion of the bed where a concentration is between zero and the feed is called "Mass Transfer Zone" MTZ. Within the mass-transfer zone, the fluid-phase concentration drops from the feed value to zero. Equilibrium with the feed is not attained in this region. As a result, because an adsorption bed must typically be removed from service shortly after breakthrough begins, the full capacity of the bed is not utilized. Obviously, the broader that the mass-transfer zone is, the greater will be the extent of unused capacity.

The bed profiles in the corresponding of the breakpoint condition and breakthrough curve are shown in Figure 2.10.

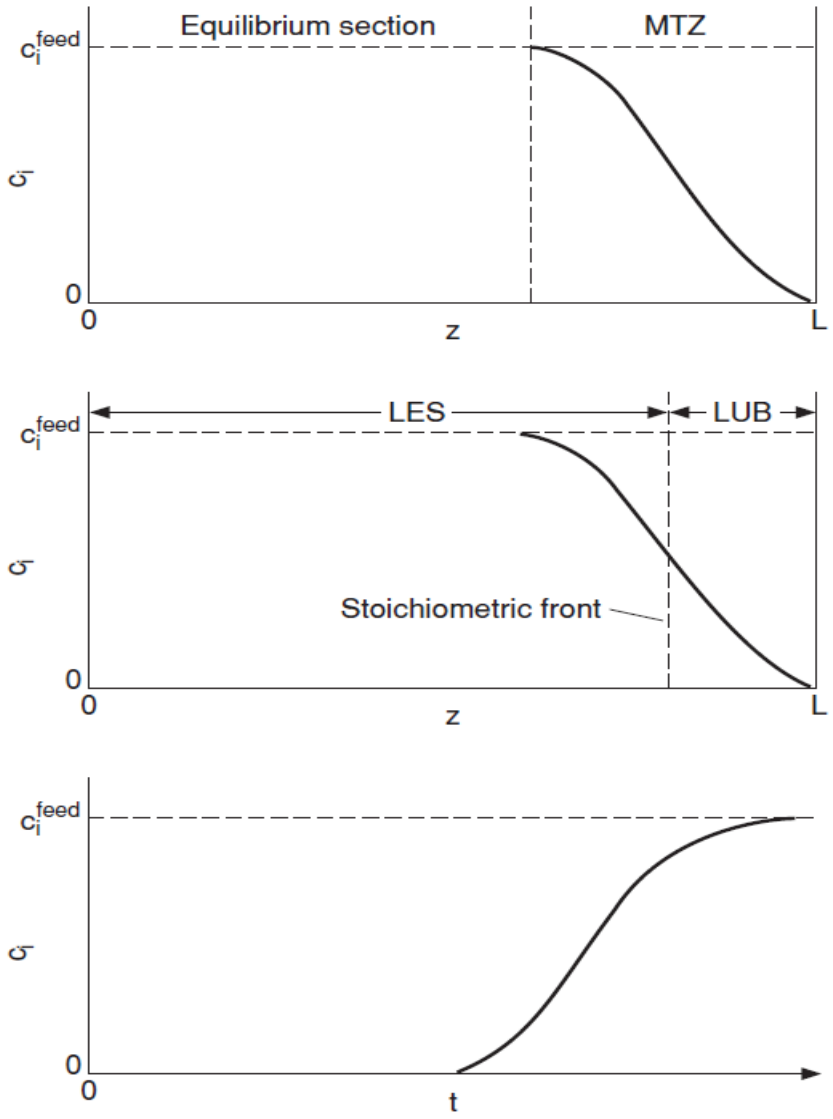

Figure 2.10 - Bed profiles (top and middle) and breakthrough curve (bottom) at the breakpoint condition [127].

The bed profiles show the mass transfer zone (MTZ) and equilibrium section at breakthrough.

The stoichiometric condition, that is represented with t^* in the breakthrough curve (Figure 2.8), is represented by the stoichiometric front in the bed profile (Figure 2.10). This corresponds to $c/c_0=0.5$ if the S-shaped curve is symmetric. The stoichiometric front divides the MTZ into two parts with contributions to the Length of the equivalent Equilibrium Section (LES) and the Length of the equivalent Unused Bed (LUB). The lower is the mass transfer zone, the lower is the LUB, the higher is the adsorbent bed utilization. For systems with a favourable isotherm, the concentration profile in the mass-transfer zone soon acquires a characteristic shape and width that do not change as the zone moves down the bed. Thus, tests with different bed lengths give breakthrough curves of the same

shape, but with longer beds, the mass transfer zone is a smaller fraction of the bed length and a greater fraction of the bed is utilized.

To calculate the length of the unused bed from the breakthrough curve, the total solute adsorbed up to the breakpoint and the adsorption capacity must be determined from the Equation (Eq. *2-26)* for $t=t_b$ and $t=t_s$ respectively. The ratio of these two quantities is the fraction of the bed capacity utilized at the breakpoint, and 1 minus this ratio is the unused fraction. The unused fraction is converted to an equivalent length of the bed (LUB) multiply it for the bed length.

$$LUB = L_T\left(1 - \frac{\omega_b}{\omega_s}\right) \qquad \textit{(Eq. 2-27)}$$

Replacing the amount of the adsorbate in the breakpoint and the saturation conditions, the Equation (Eq. *2-27)* becomes:

$$LUB = L_T\left(1 - \frac{\int_0^{t_b}\left(1 - \frac{c}{c_0}\right)dt}{\int_0^{t_s}\left(1 - \frac{c}{c_0}\right)dt}\right) \qquad \textit{(Eq. 2-28)}$$

Where the integral represents the area overlapped the breakthrough curve from time zero to the breakpoint and the saturation conditions. If we consider the breakthrough curve symmetric and the breakpoint condition as $c/c_0 \rightarrow 0$, the integrals can be approximated as follows:

$$\int_0^{t_b}\left(1 - \frac{c}{c_0}\right)dt \approx 1 \cdot t_b \qquad \textit{(Eq. 2-29)}$$

$$\int_0^{t_s}\left(1 - \frac{c}{c_0}\right)dt \approx 1 \cdot t^* \qquad \textit{(Eq. 2-30)}$$

From Figure 2.8 (b) it is clear that the integrals can be approximated as the rectangle areas having high 1 and length t_b and t^* respectively.

Hence the Length of Unused Bed can be calculated as:

$$LUB = L_T\left(1 - \frac{t_b}{t^*}\right) \qquad \textit{(Eq. 2-31)}$$

In the ideal case, the mass transfer resistance is zero, thus the mass transfer zone becomes negligible and $t_b=t_s=t^*$. From the Equation (Eq. *2-31)* the LUB is zero as the totality of the adsorbent is saturated when the concentration in the outlet passes from zero to c_0 instantaneously. In a realistic scenario, if the total bed length is long enough that the MTZ is constant, in the proximity of the end of the bed, the scale-up of the reactor can be designed looking at the LUB. In fact, LUB has been defined as half of the MTZ, thus it is constant too. From the breakthrough curve, it is possible to calculate the LUB and the stoichiometric time t^*. When the total bed length increases, the LUB remains constant, thus the LES is equal to the total length of the bed minus the LUB, Figure 2.10 (middle). Knowing the LES, it is possible to calculate the stoichiometric time and consequently the time of breakpoint for the scaled-up bed.

The gas concentration and temperature change along the reactor as the adsorption occurs. Before saturation, the adsorptive species passes from the gas phase to adsorbed form with a release of heat. The mass and energy balances can be made on a differential length of the adsorbent bed to calculate the mass and energy transfers. The differential calculations, then, can be integrated for the total length.

MASS BALANCES

The mass transfer resistance can be evaluated from a mass balance. In a fixed bed reactor, the mass transfer is estimated by making a mass balance on a section of the bed for a length of dL, as in Figure 2.11.

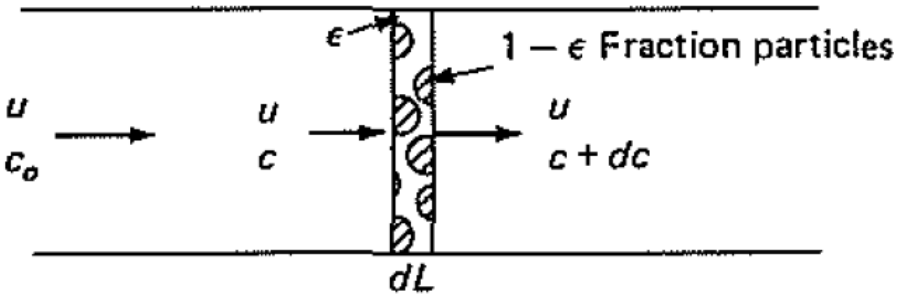

Figure 2.11 - Mass balance for a section dL of a fixed bed [126].

The difference between the amount of solute entering in the cross-section and the output is equivalent to the amount of solute adsorbed plus that in the gas phase. The mass balance per unit area of bed cross-section on the solute can be written as:

$$uc - u(c + dc) = dL\rho_b \frac{\partial \omega}{\partial t} + \varepsilon dL \frac{\partial c}{\partial t} \qquad \textit{(Eq. 2-32)}$$

or:

$$-u\frac{\partial c}{\partial L}=\rho_b\frac{\partial \omega}{\partial t}+\varepsilon\frac{\partial c}{\partial t} \qquad \textit{(Eq. 2-33)}$$

Being ε the external void fraction of the bed, the first term on the right in the Equation (Eq. *2-33)* includes the amount of solute dissolved in the pore fluid as ρ_p is proportional to (1-ε) from the Equation (Eq. *2-22).* For adsorption from a gas, the first term in Equation (Eq. *2-33),* the accumulation in the fluid, is usually negligible compared to the accumulation on the solid [126].
The mechanism of transfer to the solid includes diffusion through the fluid film around the particle and diffusion through the pores to internal adsorption sites. The actual process of physical adsorption is practically instantaneous, and equilibrium is assumed to exist between the surface and the fluid at each point inside the particle. The transfer process is approximated using an overall volumetric coefficient and an overall driving force. Suzuki proposed two different models by considering the solute concentration and the adsorbate amount as Linear Driving Force (LDF) [128]:

i. LDFC model

LDFC model is based on concentration difference:

$$\rho_b\frac{d\omega}{dt}=K_f a_v(c-c^*) \qquad \textit{(Eq. 2-34)}$$

where the concentration c^* is the value that would be in equilibrium with the average concentration ω in the solid, K_f is the overall mass transfer coefficient based on the fluid phase concentration difference as the driving force, and a_v is the specific mass transfer area. The parameter a_v is taken as the external surface of the particles. In the case of sphere particles,

$$a_v=\frac{6\,(1-\varepsilon)}{d_p} \qquad \textit{(Eq. 2-35)}$$

Where d_p is the diameter of the particle.
The overall coefficient K_f depends on the external coefficient $k_{f,ext}$ and on an effective internal coefficient $k_{f,int}$.

$$\frac{1}{K_f} = \frac{1}{k_{f,ext}} + \frac{1}{k_{f,int}} \qquad \textit{(Eq. 2-36)}$$

Diffusion within the particle is an unsteady-state process and the value of $k_{f,int}$ decreases with time, as solute molecules must penetrate further and further into the particle to reach adsorption sites. An average coefficient can be used to give an approximate fit to uptake data for spheres:

$$k_{f,int} = \frac{10\ D_e}{d_p} \qquad \textit{(Eq. 2-37)}$$

where D_e is the effective diffusion coefficient and it depends on the particle porosity, the pore diameter, the tortuosity, and the nature of the diffusing species.

The value of k_f can be estimated from available correlations in terms of the Sherwood number, Sh, and the Schmidt number, Sc. For packed-bed operations, Perry's chemical engineer handbook, recommends the correlations in Table 2.2 [127].

Equation	*Re*	Phase	Ref.
$Sh = 1.15\left(\frac{Re}{\varepsilon}\right)^{0.5} Sc^{0.33}$	$Re > 1$	Gas/liquid	Carberry, *AIChE J.*, **6**, 460 (1960)
$Sh = 2.0 + 1.1\ Re^{0.6} Sc^{0.33}$	$3 < Re < 10^4$	Gas/liquid	Wakao and Funazkri, *Chem. Eng. Sci.*, **33**, 1375 (1978)
$Sh = 1.85\left(\frac{1-\varepsilon}{\varepsilon}\right)^{0.33} Re^{0.33} Sc^{0.33}$	$Re < 40$	Liquid	Kataoka et al., *J. Chem. Eng. Japan*, **5**, 132 (1972)
$Sh = \frac{1.09}{\varepsilon} Re^{0.33} Sc^{0.33}$	$0.0015 < Re < 55$	Liquid	Wilson and Geankoplis, *Ind. Eng. Chem. Fundam.*, **5**, 9 (1966)
$Sh = \frac{0.25}{\varepsilon} Re^{0.69} Sc^{0.33}$	$55 < Re < 1050$	Liquid	Wilson and Geankoplis, *Ind. Eng. Chem. Fundam.*, **5**, 9 (1966)

Table 2.2 - External mass transfer coefficients in adsorption beds.

This model is suitable for those cases where fluid-to-particle mass transfer is a dominant mass transfer resistance. In such cases, K_f can be replaced by the external coefficient $k_{f,ext}$.

ii. LDFQ model

LDFQ model is based on the adsorbate amount difference:

$$\rho_b \frac{d\omega}{dt} = K_s a_v (\omega^* - \omega) \qquad \textit{(Eq. 2-38)}$$

where ω^* is the adsorbate amount that would be in equilibrium with the gas concentration c, Ks is the overall mass transfer coefficient based on the adsorbate difference driving force.

This model is suitable for those cases where the intraparticle diffusion is a dominant mass transfer resistance. When intraparticle diffusion is the only rate-determining step of mass transfer, $K_s a_v$ can be replaced by particle-phase mass transfer coefficient, $k_s a_v$, which is related to the intraparticle diffusion parameters as:

$$k_s a_v = \rho_b 15 \varphi_s D_e / (d_p)^2 \qquad \textit{(Eq. 2-39)}$$

where φ_s is a correction factor for the deviation from linear equilibrium.

LDFC and LDFQ models are identical when the adsorption isotherm is linear ($\omega = K_{eq} c$), setting $K_{eq} = K_f a_v / K_s a_v$. For non-linear equilibrium systems, the two models indicate considerably different concentration profiles. Better approximation is possible by considering that LDFC model and LDFQ model are valid, respectively, at fluid-to-particle mass transfer and at intraparticle diffusion.

More complex kinetics adsorption models on activated carbons can be found in the Largitte et al. overview [129]. They evaluated 10 kinetic models considering the rate-determining step the external mass transfer, the internal diffusion or the adsorption at the phase boundary.

The mass balance evaluated in the volume having a length dL as in Figure 2.11, is valid under the hypothesis of a fully developed velocity profile. This hypothesis is valid if the wall effect is negligible as the gas is in a turbulence state and the void fraction of packing ε is low. The effects of flow nonuniformities, in particular, can be severe in gas systems when the ratio of bed-to-particle diameters is small. If the flow is nonuniform, an axial dispersion of the gas occurs.

Hence, in the case of axial dispersion not negligible, the Equation (Eq. *2-33)* becomes:

$$-u \frac{\partial c}{\partial L} + \varepsilon D_L \frac{\partial^2 c}{\partial L^2} = \rho_b \frac{\partial \omega}{\partial t} + \varepsilon \frac{\partial c}{\partial t} \qquad \textit{(Eq. 2-40)}$$

where D_L is a Fickian axial dispersion coefficient. The axial dispersion coefficient must account not only for nonuniformities in the fluid velocity across the packed bed but also for molecular diffusion and convective mixing. As such, the axial dispersion coefficient is best determined experimentally for each specific contactor.

Neglecting flow nonuniformities, the contributions of molecular diffusion and turbulent mixing arising from stream splitting and recombination around the sorbent particles can be considered additive; thus, the axial dispersion coefficient D_L is given by:

$$\frac{D_L}{D} = \gamma_1 + \gamma_2 \frac{d_p u}{D} = \gamma_1 + \gamma_2 \frac{Re\ Sc}{\varepsilon} \qquad \textit{(Eq. 2-41)}$$

or in terms of particle-based Peclet number ($Pe_p = d_p\, u/D_L$), by:

$$\frac{1}{Pe_p} = \frac{\gamma_1 \varepsilon}{Re\ Sc} + \gamma_2 \qquad \textit{(Eq. 2-42)}$$

where D is the fluid-phase diffusion coefficient, Re and Sc represent the Reynolds and the Schmidt numbers respectively, considering the particle diameter as a characteristic linear dimension.

The first term on the right in the Equation (Eq. *2-41)* and (Eq. *2-42)* accounts for molecular diffusion, and the second term accounts for mixing. The molecular diffusion depends on the bed porosity; it varies between 0.64-0.73 for typical void fractions, ε=0.35-0.5. The coefficients can be estimated as in Table 2.3.

γ_1	γ_2	Ref.
0.73	$0.5\left(1 + \frac{13\gamma_1\varepsilon}{ReSc}\right)^{-1}$	Edwards and Richardson, *Chem. Eng. Sct.*, **23**, 109 (1968)
Nonporous particles: 0.7 Porous particles: ≤20/ε	0.5	Wakao and Funazkri, *Chem. Eng. Sct.*, **33**, 1375 (1978)
1	$\frac{3}{4}\varepsilon + \frac{\pi^2\varepsilon(1-\varepsilon)}{6} \ln(ReSc)$	Koch and Brady, *J. Fluid Mech.*, **154**, 399 (1985)
0.714	$\frac{\sigma_v^2}{2} + (1+\sigma_v^2)\left\{\gamma(1-p)^2 + \gamma^2 p(1-p)^3\left[e^{-\frac{1}{\gamma p(1-p)}} - 1\right]\right\}$ with $\gamma = 0.043\ ReSc/(1-\varepsilon)$ $p = 0.33 \exp(-24/Re) + 0.17$	Gunn, *Chem. Eng. Sct.*, **2**, 363 (1987)

Table 2.3 - Coefficients for Axial Dispersion Correlations in Packed Beds Based on Equations (Eq. 2-41*) and (Eq.* 2-42*) [127].*

ENERGY BALANCES

Since adsorption is generally accompanied by the evolution of heat, the rate of heat transfer between the adsorbent particles and the fluid phase may be important. In addition, heat transfer can occur across the column wall in small diameter beds and is important in energy applications of adsorption. In gas adsorption systems, even with highly porous particles, the controlling heat transfer resistance is generally associated with extra particle transport, so that the temperature within the particles is essentially uniform.

The bed temperature rise of 10 to 50°C may result when treating vapours with only 1% adsorbable component [126]. In small-diameter beds, heat loss will limit the temperature rise, but a large unit

will operate almost adiabatically, and significant differences in performance could result. In such cases, a large-diameter pilot column should be used, or detailed calculations made to account for heat release and heat transfer in the bed. A detailed description of the energy balance can be found in the Dantas et al. paper [130]. The heat absorbed from the gas is equivalent to the heat transferred from the solid, the axial dispersion less than the heat exchanged with the wall.

$$\varepsilon c c_{p,g} \frac{\partial T_g}{\partial t} + c c_{p,g} \frac{\partial u T_g}{\partial L} = \rho_b (-\Delta H_{ads}) \frac{\partial \omega}{\partial t} - \rho_b c_{p,s} \frac{\partial T_s}{\partial t} + \varepsilon \lambda_L \frac{\partial^2 T_g}{\partial L^2} + \frac{4 h_w}{d_{int}} (T_g - T_w) \qquad \textit{(Eq. 2-43)}$$

where $c_{p,g}$ and $c_{p,s}$ are the molar specific heat of the gas and the solid phases respectively, T_g, T_s, T_w are the temperature of the gas, of the solid and the wall respectively, ΔH_{ads} is the adsorption heat at zero coverage, λ_L is the axial heat dispersion coefficient, h_w is the internal convective heat coefficient between the gas and the wall and d_{int} is the bed diameter. The gas temperature is correlated to the solid and the wall temperatures from the energy balance on the solid phase and on the column wall respectively:

$$\rho_p c_{p,s} \frac{\partial T_s}{\partial t} = \frac{6 h_f}{d_p} (T_g - T_s) + \rho_p (-\Delta H_{ads}) \frac{\partial \omega}{\partial t} \qquad \textit{(Eq. 2-44)}$$

$$\rho_w c_{p,w} \frac{\partial T_w}{\partial t} = \alpha_w h_w (T_g - T_w) - \alpha_{wl} U (T_w - T_\infty) \qquad \textit{(Eq. 2-45)}$$

where h_f is the film heat transfer coefficient between the gas and the adsorbent, ρ_w and $c_{p,w}$ are the column wall density and specific heat respectively, α_w is the ratio of the internal surface area to the volume of the column wall, α_{wl} is the ratio of the logarithmic mean surface area of the column shell to the volume of the column, U is the overall heat transfer coefficient between the column wall and the external air, and T_∞ is the external air temperature.

For an adiabatic system, the last term of Equation (Eq. *2-45)* must not be considered as the wall does not exchange heat with the outside of the reactor.

The mass and the energy balances, proposed in this section, include convective and diffusive/conductive contributions. The convective terms are a function of the gas velocity that can be approximated constant for a mass/energy balances on a bed length dL.

The gas velocity can be expressed as:

$$u = \frac{1}{S_b}\frac{N_v R T_g}{P} \qquad \textit{(Eq. 2-46)}$$

Where S_b is the cross bed section, N_v is the total molar flow rate, R is the universal gas constant and P is the gas pressure.

The gas temperature can be estimated from the energy balances; while the gas pressure in the packed bed reactors is usually calculated from the Ergun equation:

$$-\frac{\partial P}{\partial L} = 150\frac{\mu_g(1-\varepsilon)^2}{\varepsilon^3 {d_p}^2}u + 1.75\frac{(1-\varepsilon)}{\varepsilon^3 d_p}\rho_g u^2 \qquad \textit{(Eq. 2-47)}$$

where μ_g is the viscosity of the fluid flowing through the packed bed. The total pressure drop due to the adsorbent bed can be calculated from the integral of the Equation (Eq. *2-47)* in the bed length L_T. In laminar flow conditions, pressure drop does not depend on the fluid density and has a linear relationship with the superficial velocity; under turbulent flow conditions, the second component of the Ergun equation dominates so that pressure drop increases with the square of the superficial velocity and has a linear dependence on the density of the fluid.

Additionally, the Ergun equation can also be expressed through the use of a packed bed friction factor f*, which is defined as follows:

$$f^* = \frac{150}{Re^*} + 1.75 \qquad \textit{(Eq. 2-48)}$$

Where Re* is the Reynolds number for a packed bed:

$$Re^* = \frac{d_p \rho_g u}{\mu_g(1-\varepsilon)} \qquad \textit{(Eq. 2-49)}$$

Thus, the Eq. (Eq. *2-47)* can be expressed in the form:

$$-\frac{\partial P}{\partial L} = f^*\frac{\rho_g\ (1-\varepsilon)^2}{d_p \varepsilon^3}u^2 \qquad \textit{(Eq. 2-50)}$$

2.4Overview of the NO_x adsorption over Activated Carbons

The adsorption is a process that operates in continuous up to the reaching of the adsorbent saturation. In the fixed bed a certain amount of adsorbent is preliminary load in the reactor, before the beginning of the process. Once the process starts, fluid passes through the adsorbent bed and the adsorptive species transfer from the fluid to the adsorbent surface. The maximum adsorbate amount can be estimated from the equations in Section 2.3 of this chapter; while the mass transfer defines the gas concentration profile in the outlet gas.

The higher is the solute feed rate, the faster is the adsorbent saturation (at adsorbent bed length). Once the saturation occurs, the process stops and the adsorbent must be regenerated or replaced. This makes the adsorption process suitable for those applications where the adsorptive concentration and/or the fluid velocity are limited, in order to reduce the dead time due to adsorbent regeneration (or replacement).

The NO_x concentration in the exhaust depends on many factors but rarely exceeds the 1000 ppm. Due to its versatility, the low operating temperature, the possibility to place a column at the tail-end of the gas treatment plant, make the adsorption an alternative strategy for NO_x removal; especially for the retrofit of the existing plants.

For all reported studies, the experimental campaign has been carried out in a fixed bed adsorber made of Activated Carbon (AC). Before each test, a gas stream containing an inert gas species has been used to pre-treat the adsorbent material to remove traces of volatile compounds, vapours and moisture which might influence the adsorption process. The gas composition, the operating temperature and the adsorbent characteristics seems to be the most relevant features that influence the NO_x adsorption capacity.

In the following the effect of specific parameters have been analysed for NOx adsorption over activated carbon:

- impact of O_2 concentration
- impact of temperature;
- impact other interacting species;
- impact of adsorbent impregnation.

2.4.1 Impact of O_2 concentration

The effect of the presence of oxygen in the inlet gas stream is the most studied features of the NO_x adsorption processes. If nitric oxide (NO) and oxygen (O_2) coexist in the gas stream, the capacity of the adsorbent to separate the nitric oxide is higher than in absence of oxygen. Oxigen presence, in the gas stream, leads to the NO oxidation on the adsorbent surface and thus the activation of new sites for the NO_x adsorption. Yet, for what concerns the adsorption on carbonaceous adsorbents, there are still some disagreements on the reaction mechanism due to high variability of the adsorbent composition.

Rubel et al. [131] carried out an experimental campaign of NO and NO_2 adsorption on ACs that are originating from different raw materials. They noticed a great increase of the NO adsorption capacity in presence of O_2: the weight increase of the adsorbent material after the adsorption is 10 times higher, compared to the case of adsorption without O_2. Furthermore, they carried out an experimental campaign exposing the adsorbent material to O_2 by itself and then exposing it to NO without O_2: the pre-saturation with O_2 improves the adsorption capacity of NO by 50%, in comparison to the case of adsorption in absence of O_2 and without the pre-saturation; indeed, no improvements were observed in comparison to the adsorption of NO + O_2. Repeating the same tests for the adsorption of NO_2, it has been found that the adsorption capacity is not influenced by either the presence of O_2 or the pre-saturation with O_2. The adsorbent capacity to adsorb NO_2 has been estimated to be slightly higher than the capacity to adsorb NO in the presence of O_2.
The analysis of heat of adsorption for the adsorption of NO + O_2 revealed that the oxidation of NO may only occur at the surface or within the pores of the carbon, rather than in the gas phase. The proposed adsorption mechanism in presence of O_2 is shown in Figure 2.12

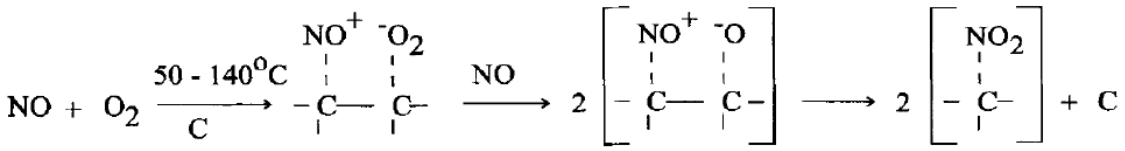

Figure 2.12 - The proposed mechanism for the adsorption of NO in presence of O_2, by Rubel et al.[131].

From the infrared spectroscopic analysis of adsorbed NO, the presence of NO^+ has been detected. The presence of vicinal oxygen leads to an ion pair formation of NO_2. The oxidation could be assisted by the pore structure of the carbon.

Kong et Cha [132] performed an investigation on NO_x adsorption processes at room temperature using char produced from sub-bituminous coal. Firstly, they carried out some adsorption tests with O_2 only, finding out that the adsorption capacity of O_2 increases with temperature, but its value remains negligible at room temperature. To investigate the effect of O_2, each experimental run has been carried out changing time by time the oxygen concentration in the inlet gas sample within the range 5-21%. Increasing the O_2 concentration, more NO is converted to NO_2 in the gas phase; the time of the NO breakpoint increases while those of NO_2 decreases. Moreover, it has been observed that, at saturation, the NO_2 concentration in the outlet gas is higher than that in the inlet gas, while less NO is found in the outlet gas: this means that, even if there is no further adsorption, part of the NO is still oxidized to NO_2 on the char surface. It may be concluded that char acts as a catalyst for the oxidation of NO in presence of O_2. Yet, the NO_x removal was found independent of the O_2 concentration as more than 5% O_2 is in the inlet gas.

Neathery et al. [133] examined the possibility to increase the NO_x removal efficiency using AC at different operating conditions. When the gas stream contains either NO and O_2, the oxidation of NO to NO_2 competes with the NO adsorption. It has been observed that the formation and the adsorption of NO_2 could be influenced by the dimensions and the distribution of the adsorbent pores. The authors performed the adsorption of 2% of NO in the presence of 5% of O_2, at different gas pressures. The adsorption capacity increases as the partial pressure increases. The adsorption isotherm shape is shown in Figure 2.13, expressed as condensed NO_2 volume over micropores volume in the function of the gas pressure.

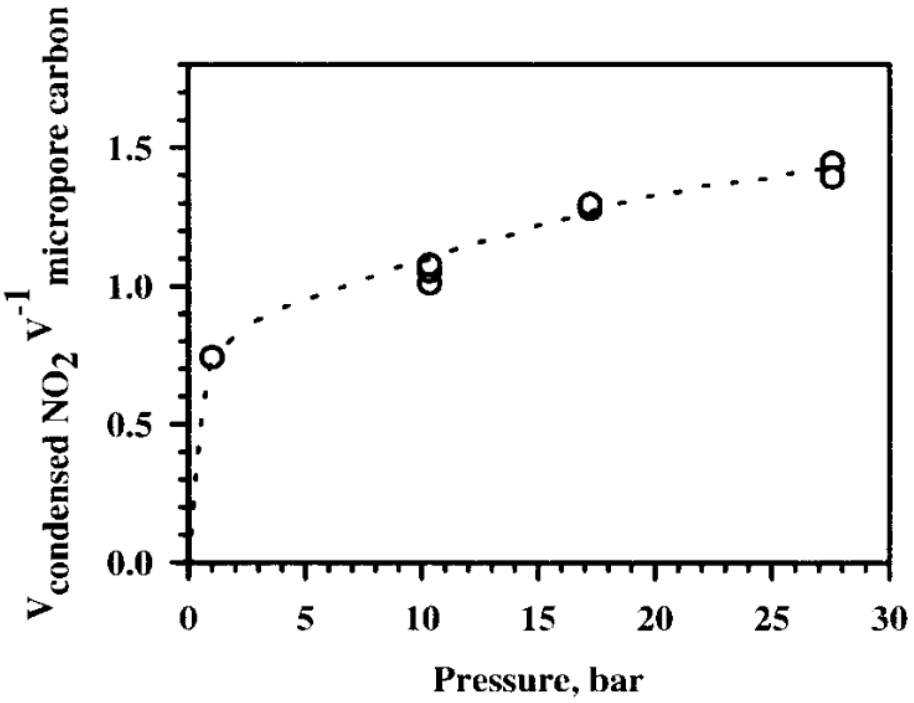

Figure 2.13 – Adsorption isotherm. Conditions: 2% NO, 5% O_2, 15% CO_2, balance He;at 70°C [133].

The adsorption isotherm is favourable and has the typical type I shape shown in Figure 2.4. Even if the Langmuir model is not suitable for multi-layer adsorption that occurs during the pore filling process, the experimental data have been examined using both the Langmuir and the BET models, obtaining identical conclusions: a monolayer of NO_2 has been formed within the carbon micropores. The proposed adsorption mechanism is the same of the one hypothesized by Rubel et al. [131] (Figure 2.12), which involves the co-adsorption of NO and O_2 on char, with the subsequent reaction between the adsorbed species that leads to the formation of an adsorbed NO_2-like species.

Lee et al. [68] studied the NO_x adsorption processes on coconut shell-based GAC impregnated with KOH. In their study, the NO_x was made mainly of NO_2 rather than NO in the inlet gas. They verified that oxygen plays a positive role even in the NO_2 adsorption. The breakthrough curves obtained for the adsorption process performed without or with oxygen is shown in Figure 2.14.

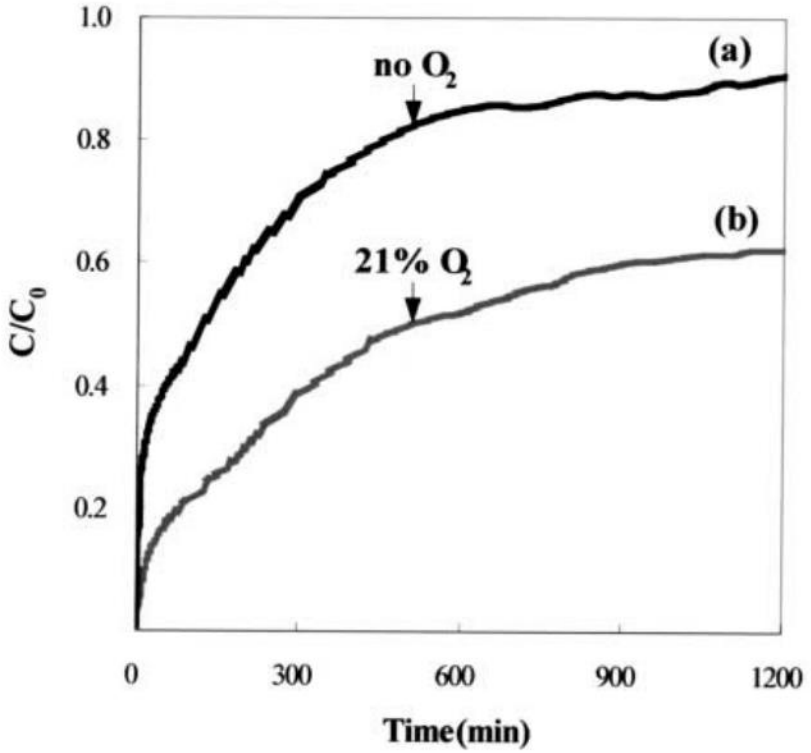

Figure 2.14 - NO_x breakthrough curves for about 150ppm of NO_2 , 4ppm of NO at 130°C, without O_2 (a) or with 21% O_2 (b) [68].

In the presence of O_2, the NO_x adsorption capacity increases 2.5 times compared to the adsorption without O_2. This improvement was attributed by the NO oxidation to NO_2 in the presence of oxygen; while the NO_2 converts partially to NO in the absence of oxygen. The higher capacity of the adsorbent to link NO_2 rather than NO makes the process more effective in the presence of oxygen.

A surface characterization realized through a ToF-SIMS (time of flight secondary ion mass spectrometry) study revealed that nitrites and nitrates are generated on the GAC surface after the adsorption, bonded on the surface with K^+ and producing crystals of KNO_2 and KNO_3. The reaction mechanism proposed by Lee et al. is shown in Figure 2.15, where it is possible to note the nitrite and the nitrate species on the carbon surface desorb as NO and NO_2 in the equilibrium condition.

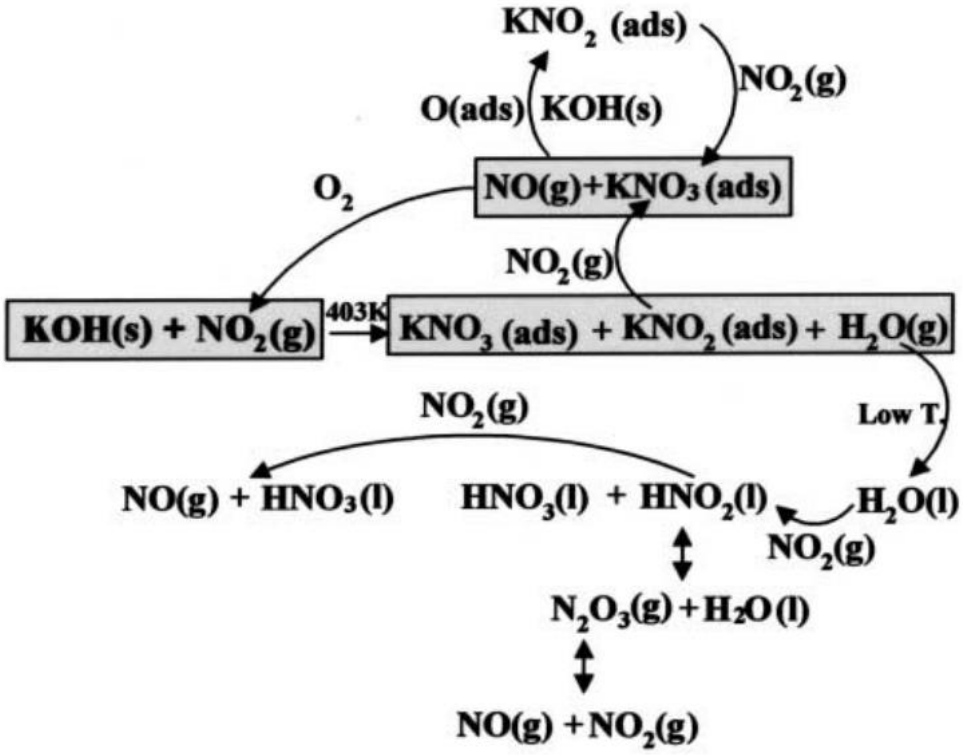

Figure 2.15 - Proposed reaction mechanism for the NO_2 adsorption on a K-IAC, by Lee et al. [68].

López et al. [134] conducted a study on the NO adsorption on ACs derived from sub-bituminous coal at room temperature. The experimental campaign has been carried out comparing the performances of activated carbon (AC) containing 7%wt of mineral matters and metals (Na, K, Ca and Fe); a demineralized activated carbon (DAC) and a DAC loaded with copper. The authors performed a detailed characterization of the surface complex, analysing the activated carbon after the NO adsorption without or with O_2 by XPS (X-ray photoelectron spectroscopy). The most important nitrogen-complexes found on a carbon surface are shown in Figure 2.16.

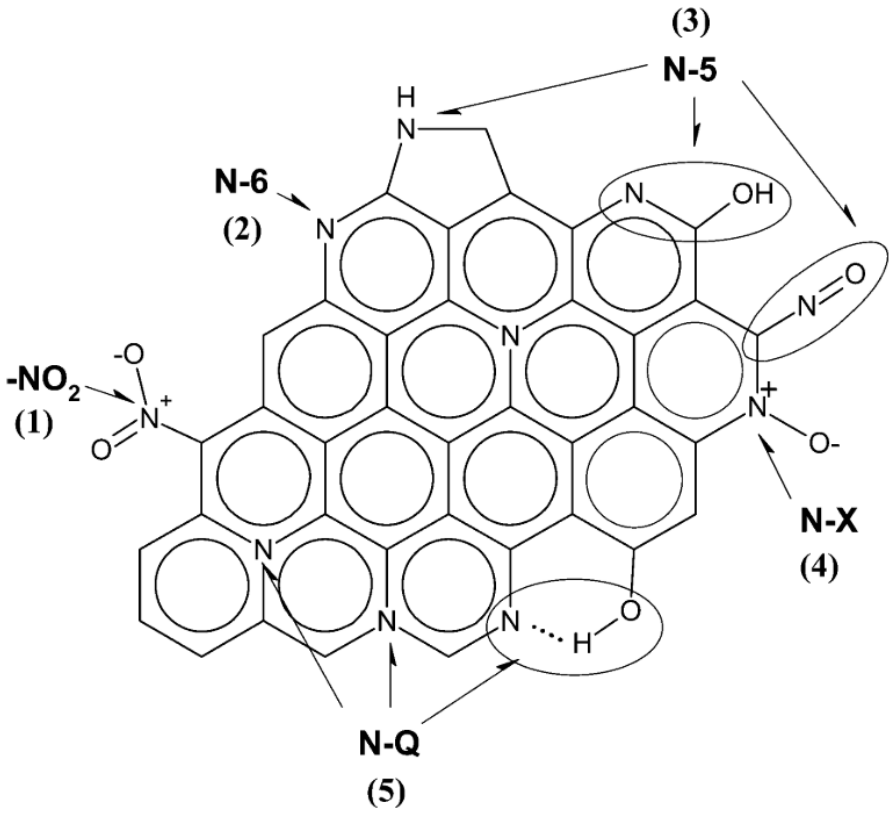

Figure 2.16 - Schematic representation of common nitrogen surface complexes found on carbon by López et al. [134].

The nitrogen-complexes detected by the authors are:

(1) nitro-type complexes (NO_2^-)

(2) the pyridinic complex (N−6);

(3) N−5 complexes (e.g. pyrrolic, pyridone, and nitroso);

(4) pyridine-N-oxide complexes (N−X);

(5) quaternary-N complexes (N−Q).

The nitrate complexes (NO_3^-) are not shown as they have been considered to constitute part of the mineral matter present in the carbon.

After NO adsorption without O_2, both the AC and the DAC show an increase of the surface nitrogen complexes. N−X and NO_3^- complexes increase in the activated carbon; while N−Q and NO_2^- complexes increase in the demineralized activated carbon. Furthermore, a reduction of the oxygen surface complexes due to the gasification of carbon material has been observed for both types of AC. After NO adsorption, in the presence of O_2, the number of surface nitrogen complexes increases for the AC and decreases for the DAC. This could be due to the blocking effect of oxygen in the active sites where NO was firstly adsorbed. On the other hand, the number of surface oxygen complexes

increases for both the types of AC. This may suggest that the O_2 is firstly chemisorbed on the surface and then NO reacts with it to form NO_2 complexes.

Zhang et al. [67] studied NO adsorption process on activated carbons with varied porous textures(5-12Å). The experimental results suggest that, in presence of O_2, the homogeneous oxidation of NO in the gas phase occurs, hence improving the adsorption capacity of the materials; however, a pre-adsorption of O_2 does not affect the NO adsorption. For these reasons, it may be concluded that the adsorbent material acts as a catalyst for the oxidation of NO in presence of O_2. No direct relationship between NO conversion and the number of surface oxygen groups has been identified, yet higher amounts of surface oxygen groups seem to accelerate the release of NO_2, even if its concentration lowers. The dependences of NO conversion on NO and O_2 concentrations have been derived and they are shown in Figure 2.17.

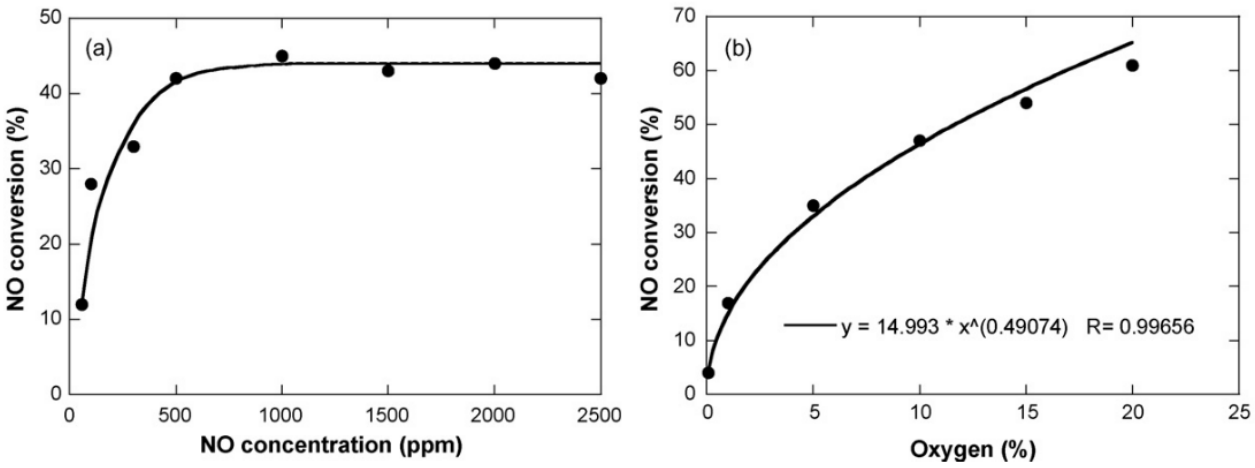

Figure 2.17 – The dependence of steady-state NO conversion on NO concentration at 10% O_2 (a), and on O_2 concentration at 500 ppm NO in feed gas at 25°C [67].

Experiments revealed that the NO conversion increased with NO concentration up to 500 ppm and it is constant above this level; while the NO conversion (and, correspondingly, the reaction rate) is proportional to the square root of O_2 concentration.

NO adsorption on activated carbons in the presence of oxygen is a complex and dynamic process involving physical adsorption of NO, co-adsorption of oxygen, reaction of NO and O_2 in narrow micropores, reaction of formed NO_2 with carbon leading to NO chemisorption and oxidation of carbon surface. For all the tested adsorbent materials, the NO_2 concentration begins to rise while the NO concentration is close to steady-state.

From a TPD (temperature-programmed desorption) analysis, it emerged that the carbon surface is not oxidized by either NO or O_2 alone at ambient temperature, while significant oxidation of the surface has been detected after the simultaneous exposure to NO and O_2. To examine the species adsorbed on carbon during the NO adsorption process, TPD tests were run after adsorption for 5 min, 30 min, 1 h, 2.5 h, and 24 h in a gas mixture of 500 ppm NO and 10% O_2. Figure 2.18 shows the total amount of desorbed NO, NO_2, O_2, CO and CO_2 during TPD as a function of adsorption time.

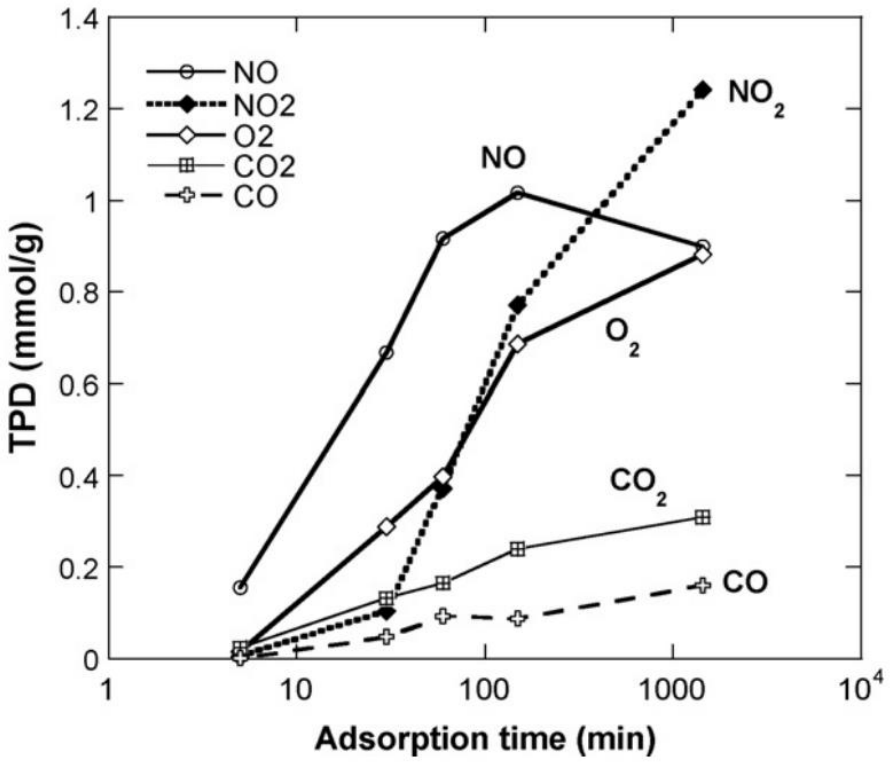

Figure 2.18 - Variation of the total amount of desorbed species during TPD as a function of the adsorption time [67].

The amount of desorbed NO increases linearly with time up to 1 h and then it is almost constant. NO_2 desorption starts at about 5 min and increases slowly before 30 min. After 30 min, the amount of desorbed NO_2 increases rapidly with the adsorption time.

Zhang et al, estimated that 90% of the consumed gaseous NO became adsorbed NO species on the carbon surface during the first 5 min of adsorption. After 5 min, some of the gaseous NO was converted into adsorbed NO_2 species. During the first 30 min, 75% of the consumed gaseous NO converted to adsorbed NO, 12% to adsorbed NO_2 and 4% to gaseous NO_2, respectively. The percentage of gaseous NO_2 increases dramatically after 30 min. The authors have assumed that the absence of NO_2 during the initial period is due to its instability on the carbon. Once NO_2 is formed in the micropores, it may migrate to the active carbon sites and oxidize them, leaving NO adsorbed on

the surface. After these sites have been oxidized, the NO_2 becomes stable on the carbon surface either as adsorbed species or is released as gas. Therefore, the delayed breakthrough curve is not due to the selective adsorption of NO_2, but mainly to its decomposition.

Yi et al. [66] studied the adsorption of NO on metal-modified coconut shell activated carbon at 50°C. They have found that the amount of NO adsorbed copper-impregnated activated carbon was 0.02 mmol/g. The adsorption capacity increased of one order of magnitude in the presence of other gas species like SO_2, NO, CO_2, O_2; however, O_2 has been considered the key to co-adsorption as its good oxidation capacity. An adsorption mechanism has been proposed in the case of co-adsorption and it is described below where the influence of other interacting species is presented.

2.4.2 Impact of temperature

The adsorption is generally an exothermic process and, as such, it should be enhanced by low values of the operating temperature. Yet, the adsorption on carbonaceous material involves reactions between the adsorbate and the adsorbent surface which could show different behaviours with the variation of the operating temperature, mainly depending on the composition of the adsorbent surface and the pore size volume and distribution. In such cases, physical/chemical interactions between the NO_x and the active sites could be improved by an increase in temperature. Some chemical reactions can become relevant at high temperature, promoting adsorption paths that are negligible at low temperature.

In their study, Neathery et al. [133] have found that the capacity of the ACs to remove NO_x is inversely proportional to the operating temperature. They found that the NO_x adsorbed decreases linearly with the temperature in the range 20-140°C. This trend is in accordance to the thermodynamic of the process. Being exothermic, the process is encouraged at low temperature and the adsorption capacity decreases with the temperature.

Lee et al. [68], instead, have found that the adsorption capacity increases with the temperature. They performed the adsorption of NO_x (NO_2 mainly) on KOH-GAC at different operating temperature, i.e. 30, 80 and 130°C in presence of oxygen. The breakthrough curves obtained are shown in Figure 2.19.

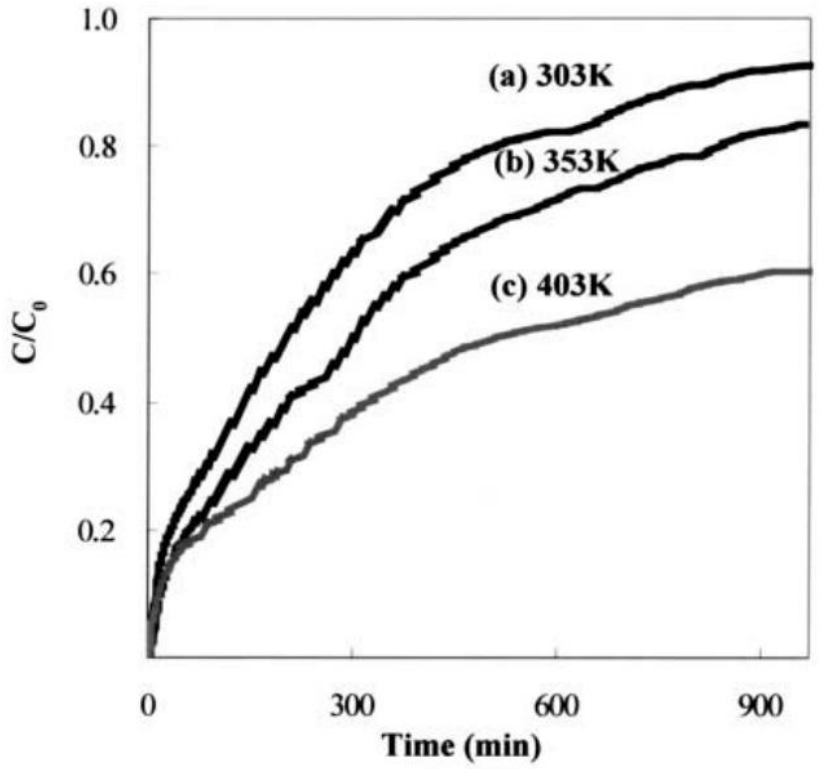

Figure 2.19 - NO_x breakthrough curves over K-IAC for about 150ppm of NO_2 , 4ppm of NO, 21% of O_2, balanced in N_2 at the temperature of 303K (a), 353K (b), 403K (c), by Lee et al. [68].

The breakthrough curves of the NO_x shift on the right as the temperature increases and this effect is more remarkable within the range 353-403K. The slower is the breakthrough curve, the higher is the adsorbent capacity. In fact, the adsorption capacity is proportional to the area above the breakthrough curve, as in the Equation (Eq. *2-26).*

The unpredicted results have been explained by the authors by considering the three aspects:

i. enhanced oxidation of NO to NO_2;
ii. higher adsorption efficiency of NO_2;
iii. physical evaporation of HNO_3.

The dissociative chemisorption of O_2 is encouraged at high temperature, leading to a higher oxidation rate of NO to NO_2. The NO_2 adsorption is encouraged by the potassium impregnation. The NO_2 interaction with KOH, present on the adsorbent surface, become stronger as the temperature rising, with the consequence of improved adsorption efficiency. Lastly, the condensation of water vapour as HNO_3 on the surface of the adsorbent material, which may lead to a blocking of micropores, is deterred at high temperature.

The three aspects contribute separately to an increasing of the NO_x adsorption that is hence encouraged at high temperature.

Klose and Rincon [135] conducted an experimental campaign to investigate the effect of temperature on the NO adsorption in presence of oxygen using a palm shell-based AC. Their tests were performed at the temperatures of 100, 120 and 150°C. The authors have found that the adsorption capacity is inversely proportional to the temperature, in accordance with Neathery et al. results [133].
The breakthrough curves at the three different temperatures are shown in Figure 2.20.

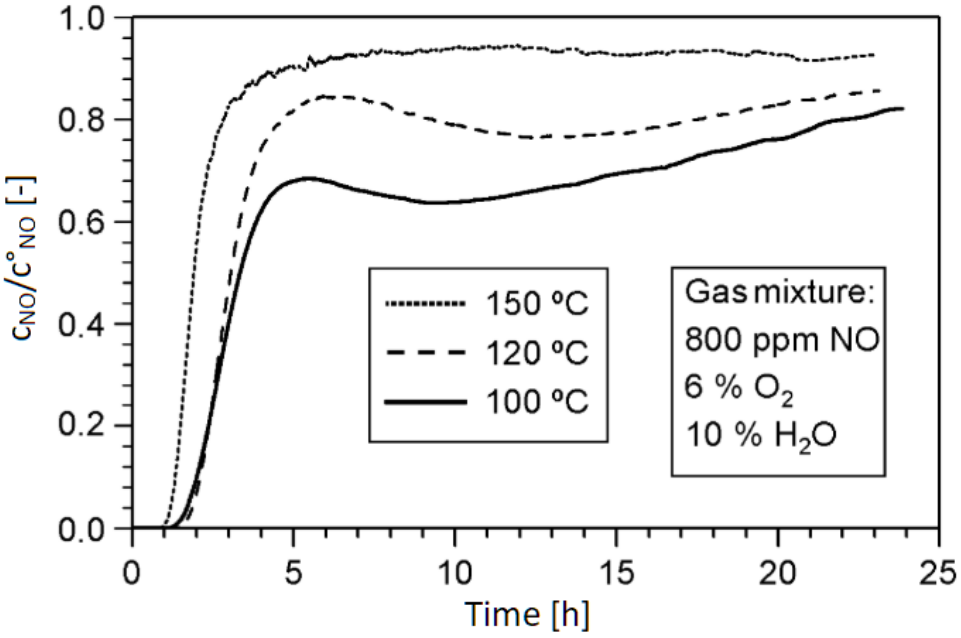

Figure 2.20 - Breakthrough curves at 100, 120, 150°C, by Klose and Rincon [135].

All the curves represented in Figure 2.20 show a sharp rise of the NO concentration, which is more enhanced for 150°C; yet, the curve profiles obtained at 100 and 120°C differ from the one obtained at 150°C, as a decrease in the NO concentration is noticed. This phenomenon has been attributed to an acceleration of the NO conversion at lower temperatures, that does not occur as the operating temperature increases. The NO oxidation to NO_2 leads to a reduction of the NO emissions and the breakthrough curve decreases. Moreover, the higher NO_2 concentration improves the NO_x adsorption efficiency due to the higher NO_2 affinity with the adsorbent than NO; hence, the saturation time is higher at low temperature.
The peak in concentration at 100°C was found also at the other NO concentrations i.e. 400 and 1200ppm. The peak disappears as the temperature increases and the saturation is achieved faster (Figure 2.20). A similar trend has been obtained at the NO concentration of 400 and 1200ppm.

Sumathi et al. [136] have investigated the NO adsorption on a Cerium-supported palm shell activated carbon in the range 100-300°C. They found that the adsorption capacity does not decreases monotonically with the increasing of the temperature.
The breakthrough curves at the different temperatures are shown in Figure 2.21.

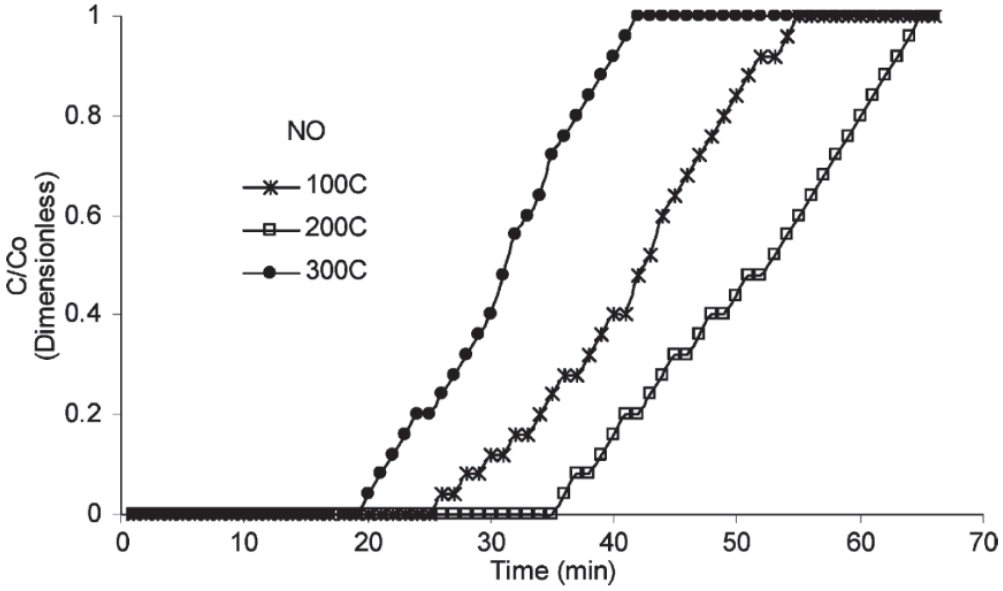

Figure 2.21 - NO Breakthrough curves for 500ppm of NO, 2000ppm of SO_2 , 10% of O_2, balanced in N_2 at the temperature of 100, 200 and 300°C, by Sumathi et al. [136].

The highest breakpoint and the saturation times have been obtained at 200°C, with the consequence of a peak in adsorption capacity as the process proceeds at 200°C.
Lower temperature (below 200 °C) enhances the Ce-doped AC for higher catalytic activity because of the disassociation of NO chemisorption, accompanied by N_2O and N_2 evolution and oxygen accumulation on the catalyst surface. At a temperature of 300°C, NO starts deterring. This is because of the oxygen-containing group formed on the surface of the activated carbon, which is likely to attach to the carbon group of the adsorbent to form CO and CO_2. Moreover, temperatures above 300 °C also develop the burnout phenomena that hinder any type of reaction.

Even Zhu et al. [65] have found that the adsorption capacity increases with temperature and then it decreased as the gas temperature was above 120°C. They considered the adsorption capacity as the sum of the NO and SO_2 trapped on the adsorbent surface.

2.4.3 Impact of other interacting species

NO_x adsorption is mainly studied in the literature, to simulate those industrial processes in which NO_x would be removed from the exhaust gas coming from a combustion process. For this reason, in such cases, the model flue gas could include other species, different from NO and O_2, that can be found in the burned-exhaust gases. The most common species found in the flue gases that could affect the NO_x adsorption are H_2O, CO_2 and SO_2.

For what concerns the effect of the presence of water vapour in the inlet gas, the common result is that H_2O does not have any influence of the adsorption of NO, as reported by Rubel et al. [131]. On the contrary, Takeuchi et al. [137] found out that NO_2 adsorption increases if there is moisture in the model gas. In the presence of water vapour, NO_2 reacts with H_2O, in the carbon pores, to produce adsorbate nitric acid (HNO_3). This effect was evident in the case of adsorption on activated carbon impregnated with potassium. The authors proposed the mechanism shown in Figure 2.22

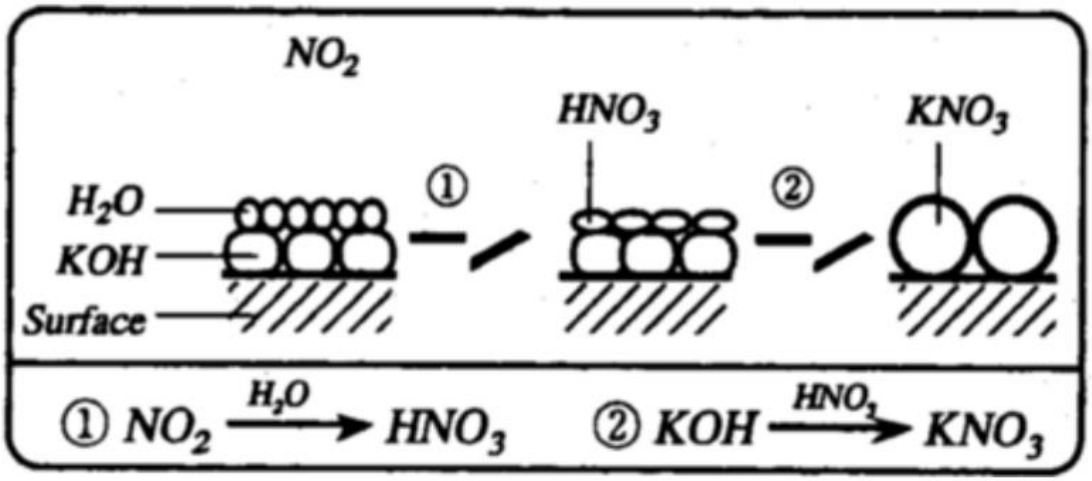

Figure 2.22 - Schematic diagram of the removal mechanism of NO_2 by the K-CA, by Takeuchi et al. [137].

The nitric acid produced in the corresponding of the potassium sites reacts to produce adsorbed nitrate potassium.

Kong and Cha [132] carried out an experimental campaign at room temperature, changing the moisture content in the inlet gas within the range 0.23−0.95% (by volume). They have found that water vapour does not adsorb on char significantly. In the presence of NO_x, however, much more water vapour uptake on char was observed. They assumed that some of the water vapour reacted with NO_2 to produce HNO_3 which was then adsorbed. Furthermore, they highlighted that the heat

generated for the adsorption of H_2O enhances O_2 adsorption, while on the other hand water may inhibit the oxidation of NO due to the blocking of micropores and reaction sites.

The presence of CO_2 in the gas seems to not influence the NO_x adsorption. These considerations have been made by Yi et al. [66], Ruber et al. [131] and Neathery et al. [133] in their works.

The most studied interacting species in the NO_x adsorption, apart from O_2, is the SO_2. Being the adsorption strategy attractive for the SO_2 as well as for the NO_x, the coadsorption of NO_x and SO_2 is widely investigated in the literature.
Most of the authors have found that SO_2 and NO_x (NO and NO_2) are competitive in the adsorption [133], [136], [138]. Being the SO_2 molecule much larger than NO_x, it can block the adsorption sites avoiding the NO_2 adsorption. Sumathi et al. [136] have found that the time of breakpoint for the SO_2 and the NO decreases as the concentration of the other pollutant increases. They evaluated the time of breakpoint for the NO as a function of the SO_2 concentration, and the results are shown in Figure 2.23.

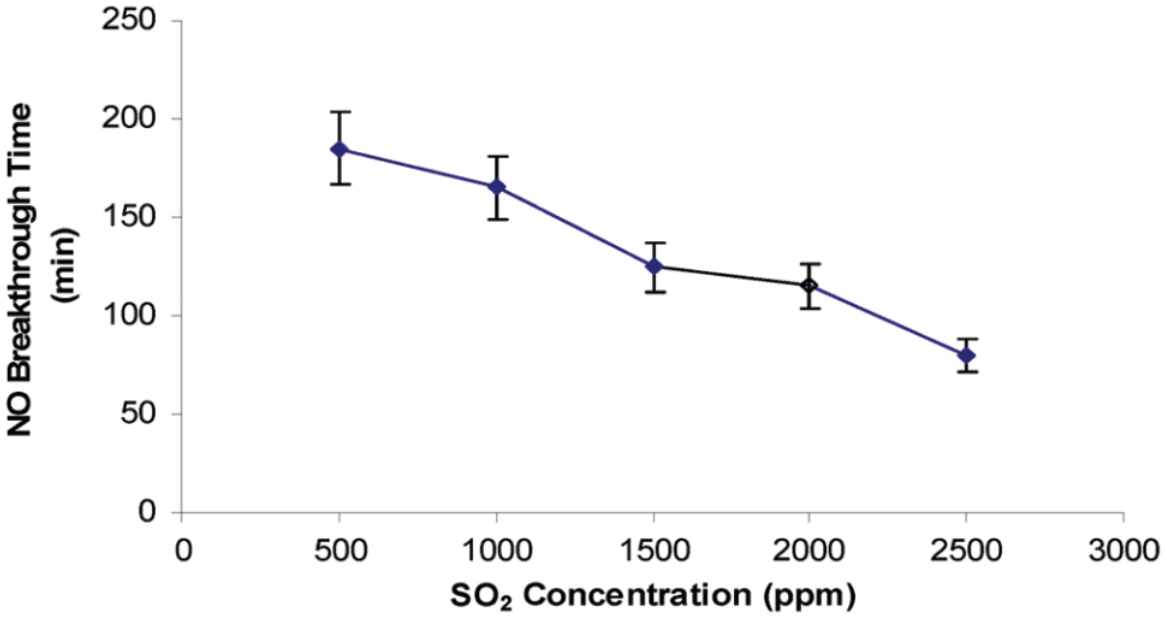

Figure 2.23 – Time of breakpoint for 500 ppm of NO over cerium impregnated AC at 100°C in the function of the SO_2 concentration(500-2,500ppm), in the presence of 10% O_2, balanced in N_2, by Sumathi et al. [136].

The breakthrough curves shifts on the left as the time of breakpoint decreases. This means that the higher is the SO_2 concentration in the gas stream, the lower is the NO adsorption capacity.

Davini et al. [138] found out that the carbonaceous material adsorbs larger amounts of SO_2 and lower amounts of NO_x when both SO_2 and NO_x are present in the flue gas, compared to the adsorption of the species separately.

Zhu et al. [65] have found out that the NO adsorption capacity increased for low concentration of SO_2 in the gas stream, up to 50ppm. For SO_2 concentration above 50ppm, the NO adsorption capacity decreased constantly, as it is shown in Figure 2.24.

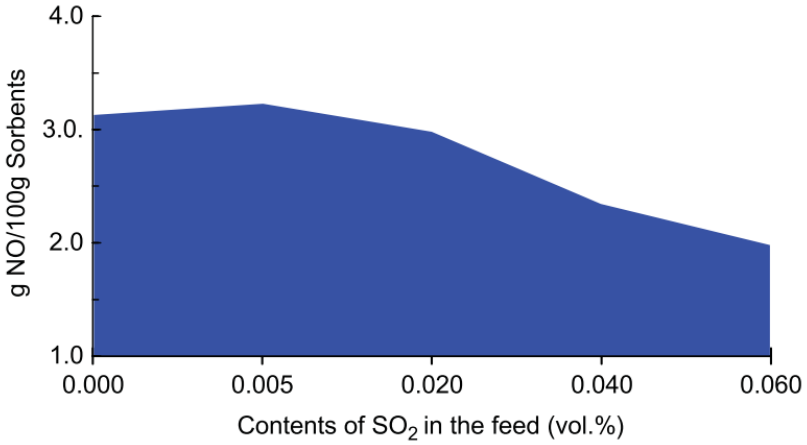

Figure 2.24 – Amount of NO adsorbed over Na-K impregnated AC at 120°C in the function of SO_2 concentration (0-600ppm), in the presence of 10% O_2, 14% CO_2, 300ppm CO, by Zhu et al. [65].

The authors proposed a co-adsorption mechanism for NO and SO_2 in the presence of oxygen:

$$SO_2 + * \rightarrow SO_2^*$$
$$NO + O_2 + * \rightarrow NO_2^*$$
$$O_2 + * \rightarrow O_2^*$$
$$NO + O_2^* + SO_2^* \rightarrow [(NO_2)(SO_3)^*] + *$$
$$NO_2^* + SO_2^* \rightarrow SO_3^* + NO + *$$

Figure 2.25 - NO and SO_2 co-adsorption mechanism proposed by Zhu et al. [65].

In addition to the adsorption of the gas molecules, NO and SO_2 themselves exist in interaction during the adsorption process, which would enhance each other adsorption ability. However, according to the adsorption mechanism, increasing concentrations of SO_2 in the feed would result in increasing amounts of the adsorbed species SO_2^*. Simultaneously, SO_2^* would strongly desorb the NO from the active sites and restrain the NO adsorption on the sorbent active sites, with the consequence of a reducing NO adsorbed amount, as in Figure 2.24.

Yi et al. [66] have considered the adsorption of NO and the coadsorption of NO and SO_2 in absence of oxygen. They found that the NO adsorption is 2.5 higher as 1,000ppm of NO and 2,000ppm of

SO_2, balanced in N_2 are fed; while it increases of one order of magnitude as 10% of CO_2 and 5% of O_2 were added.

2.4.4 Impact of adsorbent impregnation

The activation of the adsorbent materials has been described as the process that enhances the adsorption capacity as the exposed surface of the adsorbent increases. This process can be defined as a physical process in which gas molecules release the adsorbent surface, as the effect of the temperature, leaving vacancies in the adsorbent structure. Those vacancies become active sites where the adsorptive species can sit during the adsorption process. In addition to the activation process, the adsorbent can be impregnated with chemicals. Usually, the impregnation adds metals on the adsorbent surface, generating new sites where chemical reactions or electron exchanges could happen. The nature of the metals impregnated on the adsorbent surface would affect the selectivity of the adsorbent toward the adsorptive species.
Many researchers carried out experimental investigations to evaluate the effect of the impregnation on the NO_x adsorption over activated carbons.

Takeuchi et al. [137] tested samples of coconut shell-based AC which differ for the chemical impregnation, such as Li, K and Rb hydroxides. For all the different impregnation, the NO adsorption is strongly enhanced compared to the non-impregnated AC. An increasing of the impregnated metal amount leads to a higher NO_2 adsorption capacity. The optimum amount was estimated to be about 400 mol/kg; while NO_2 adsorption is deterred at a higher amount of impregnation as the blockage of micropores during the impregnation. Among the impregnated activated carbon tested by the authors, the one treated with KOH showed the highest performances in the NO_x adsorption, due to the high reactivity of the potassium, as reported in Figure 2.22. KOH provides strong basic functional groups to the AC, which play the role of selective adsorption sites for NO_x.

The positive effect of the potassium hydroxide has been confirmed by Lee et al. [68]. They found that the NO_x adsorption capacity over impregnated AC was four times higher than the non-impregnated AC.

Zhu et al. [65] investigated the optimum percentage of potassium and sodium impregnation. They used different solutions containing different concentrations of sodium carbonate (Na_2CO_3) and potassium hydroxide (KOH) during the adsorbent preparation. They have found that a good balance

in NO and SO_2 adsorption capacity was obtained as 4% and 2.5% by weight of Na_2CO_3 and KOH were used to prepare the adsorbent, respectively.

Davini et al. [138] used AC impregnated with Fe oxides, finding out that NO_x adsorption is favoured by the presence of iron, due to its catalytic activity in the process of transforming the NO_x in other species with higher stability, that can be strongly adsorbed on carbonaceous material. The amount of NO_x adsorbed increases with increasing the amount of iron on the carbon surface, in the range 0-1.5% by weight of Fe.

López et al. [134] investigated the effect of copper impregnation over demineralized activated carbon (DAC). During the adsorption of NO, without any other interacting species, the Cu-DAC showed an increase of the surface oxygen complexes. The authors attributed this effect to the dissociative chemisorption of NO. This explanation was supported by the XPS analysis which points out that only Cu^{2+} was present on the carbon surface before the adsorption, while Cu^{+} was detected on the carbon after the adsorption, suggesting the redox role of the copper on the adsorbent surface during the adsorption of NO. The NO dissociative chemisorption occurs on the adsorbent surface with the oxygen and nitrogen atoms being transferred to the carbon by a spillover mechanism, that is reported in Figure 2.26.

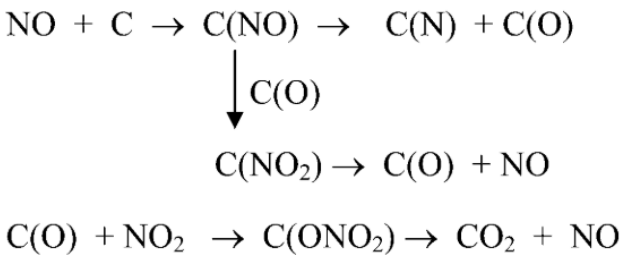

Figure 2.26 - Dissociative chemisorption of NO over Cu-AC surface, by López et al. [134].

NO dissociates on the adsorbent surface, as the effect of the copper, by producing N-adsorbed and O-adsorbed species. The oxidized sites can react with NO to produce NO_2 adsorbed, and hence, improving the NO_x adsorption. The NO dissociative chemisorption have been found more intense in the presence of molecular O_2 in the gas stream. A TPD analysis showed two peaks in the desorption profile for the impregnated carbon, which represents the adsorption of NO in the form of nitrites (NO_2^-) and nitrates (NO_3^-). This suggests that the copper has a catalytic effect on the transformation of NO into species that can be strongly adsorbed on the carbon. The catalytic effect of the copper contributes also to the NO_x adsorption capacity. By performing the adsorption NO and O_2 for longer

times, it has been observed an increase of the NO_2 concentration after NO reached a steady-state concentration. The authors proposed that the NO_2 is formed from the oxidation of NO with the oxygen complexes formed on the surface on the carbon.

The positive effect of copper impregnation on the NO_x adsorption have been verified also by Yi et al. [66]. In their study, the authors have found that the copper impregnation improved the adsorption more than the calcium, magnesium and zinc. The improvement due to the copper impregnation increased in the case of co-adsorption of NO with SO_2 and O_2. The confirmed the co-adsorption mechanism proposed by Zhu et al. [65] and shown in Figure 2.25.

Sumathi et al. [136] investigated the effect of the Cerium impregnation over the activated carbon in NO_x adsorption. According to their previous study, the Cerium showed a better adsorption capacity than the Ni, [139]. They have found a similar efficiency in terms of NO_x adsorption; however, the SO_2 adsorption was greatly encouraged in the case of Cerium impregnation, in the range of temperature 100-300°C. They have tested different activated carbons impregnated with Cerium having a metal percentage of 0, 5, 8, 10, 12 by weight. The best adsorbent material was that having $10\%_{wt}$ of Cerium for either NO_x and SO_2 absorption. The Cerium improved the NO oxidation to NO_2, that is easier to adsorb. Although they have found that the NO_x adsorption has a peak at 200°C, they performed most of the results at the temperature of 100°C as the NO_x adsorption improved slightly with an increase of the temperature; while SO_2 adsorption decreased significantly.

3. PLASMA

Plasma (from Ancient Greek πλάσμα, meaning "mouldable substance") is one of the four fundamental states of matter and was first described by Chemist Irving Langmuir in the 1920s.
Nearly all the ordinary matter in the universe exists in a plasma state, both by mass and volume. Astrophysical plasma is observed in most of the Sun and stars, as well as in the interplanetary and interstellar space; while, in our atmosphere, examples of plasma are the lightning or aurora borealis.
Plasma is a fully or partially ionised gas, which exists in a mixed form of electrons, ions and neutrals in both ground and excited states. Since plasma contains a high number of charged particles, its behaviours can be affected by long-range electrical and magnetic fields.
The main difference between gas and plasma are summarized in Table 3.1.

Properties	Gas	Plasma
Electrical conductivity	Low	High
Acting species	Molecules	Electrons, ions, radicals, neutral species
Interactions	Binary, Three-body	Long-range interactions through the electric and magnetic forces.

Table 3.1 - Gas and Plasma main physical differences.

Although the gas, such as air, could be characterized by a relatively low amount of free charges, it is an insulator, overall. On the contrary, the high concentrations of electrons and ions make the plasma electrically conductive. The interactions in the plasma are numerous and most of them include the electrons, such as molecule ionization, attachment, electron recombination, charge transfer, neutral recombination, ion recombination, decompositions etc. Long-range electric and magnetic fields dominate the behaviour of the ions, thus the number of interactions is strongly dependent on the electric and magnetic forces. The physics and chemistry of the plasma are described in this chapter. In particular, the attention is focused on the Non-Thermal Plasma (the plasma of non-equilibrium) for its application in promoting chemical reactions unfavoured at low temperatures.

3.1Plasma Physics

Plasma can be considered as a gas coupled with a high level of energy, above the limit that retains the gas molecules in the ground-state. Hence, atomic reactions occur, and the gas molecules convert from neutral to radicals, ions and electrons.

In solar and stellar plasmas, the ionization process occurs by nuclear fusion reactions. In the ionosphere, ionization is accomplished not through heating of the plasma, rather by far-ultraviolet and x-rays from the Sun. For example, there are about 1000 positive and negative ions per cubic centimetre in the stratosphere.

Depending on the energy source and the amount supplied, the plasma may show different properties in terms of electron density and relative temperature of electrons, ions and neutral species

Plasma states are so classified in:

- equilibrium plasma (Thermal Plasma);
- non-equilibrium plasma (Non-Thermal Plasma).

In the equilibrium plasma, the electrons, ions, radicals and molecules are in the thermodynamic equilibrium at the temperatures of 10^4-10^7 (1-1,000eV); thus it is also called “Thermal Plasma”. The electrons density is extremely high, up to 10^{26} m^{-3}. At these conditions, the high number of free electrons in the plasma promote atomic reactions. In extreme conditions of energy, the temperature and the electron density is so high that nuclear reactions occur.

Examples of moderate and extreme thermal plasma are the electric arc and the stellar plasma (solar plasma e.g.), as shown in Figure 3.1.

Figure 3.1 - Examples of thermal plasma: electric arc (left), solar explosion (right).

Non-equilibrium plasma, instead, is characterized by electrons that are in not equilibrium with ions, radicals and molecules. The electron temperature is much higher than the temperature of heavy species (ions and neutrals), which are near the room temperature; thus the plasma is also called "Non-Thermal Plasma" (NTP). The electrons in non-thermal plasma can reach temperatures of 10.000–100.000K (1–10eV). The electron temperature and ionization rate are lower in non-thermal plasma, compared to the thermal one. The plasma temperature is largely lower than the electron temperature, as in the NTP the majority of the discharge energy leads to the production of electrons rather than ions and neutrals heating.

An example of NTP is the gas-discharge lamp.

Figure 3.2 – Gas discharge lamps as an example of Non-Thermal Plasma.

Gas discharge lamps consist of a glass (or quartz) tube or bulb that contains a gas at low pressure. Once a differential potential is applied at the two ends of the lamp, free electrons promote ionization reactions producing photons that emit the light. The colour of the light produced depends on the emission spectra of the atoms making up the gas, as well as the pressure of the gas, current density, and other variables.

Non-thermal plasmas have a great interest for those applications that requires a high conductive gas or a highly reactive gas as the effect of free electrons, ions and radicals produced in NTP. The study of plasma physics is crucial for non-thermal plasma comprehension. Plasma properties are determined by the nature of its constituents, the interaction between the species and how they are affected by an external electric (or magnetic) field.

3.1.1 Plasma constituent elements

Plasma is made of neutral and charged particles that generate and recombine changing in density and conductivity. Non-thermal plasma can be generated imposing an electric field strong enough to ionize neutral gas. The number of charged particles increases by increasing the electric field and the gas

transform from electrically neutral to conductive. The ionized species move toward the cathode and the anode, depending the so-called “gas discharge”.
The particles can be found in the plasma are:

i. photons;
ii. electrons;
iii. ground-state atoms (or molecules) and excited atoms (or molecules);
iv. positive and negative ions.

To better clarify the plasma physics, it is important to understand the properties of these species and their behaviour in gas discharge [140].

PHOTONS

Photons are elementary particles which can transmit electromagnetic interactions with atoms or plasma. Photons collisions can cause excitation or ionization of neutral atoms, which has important implications in a gas discharge.
The emission and absorption of light can be considered as photon interaction with atoms or plasma or the collision between them. Photons are the carrier of optical radiation that represents a form of energy. When light irradiated an atom, this would be excited or ionized. This phenomenon is interpreted as “collision” of photons and atoms. During this collision, the atom absorbs the photon by increasing its internal energy. After absorption of a photon of energy, the atom at a lower energy state will transit to a higher energy state, with a reversible process. When returning to a low energy state from a higher energy state, atom radiate another photon.
Photons can excite or ionize atoms and the necessary condition is that the photon energy *hv* must be greater than, or at least equal, to the excitation energy or ionization energy of the atom. Photoluminescence excitation and photoionization are not exclusively caused by external radiation. Photons emitted by excited atoms can also cause themselves excitation or ionization of neutral atoms, which has important implications in the gas discharge. When photon energy is more than the ionization energy of gas molecules, the excess photon energy will release in the form of less-energy photons, or convert into kinetic energy of newly generated electrons after photoionization.
During the gas discharge process, the photons excite or ionize neutral atoms (or molecules), increasing their level of energy. Meanwhile, the excited or ionized species can release photons, by reducing their level of energy. The photon transfer, from species in a gas discharge process,

encourages the production of excited or charged species that absorb or emit energy. Furthermore, electrons can be released from ions or neutral molecules as the effect of the photoionization process. Photons are greatly relevant at the beginning of the gas discharge as they increase the number of seed electrons that initiate the gas discharge. Seed electrons are those electrons generated from the high-voltage electrode as the impact of the photons on it. The seed electrons, emitted from the cathode, move toward the anode as the effect of the external electric field and they are the precursors of the gas ionization.

ELECTRONS

The electron moves around the nucleus by the electromagnetic attraction of the protons in the nucleus. The nucleus attraction strength is not always the same. When two different atoms are drawn closer together under certain conditions (e.g., temperature increases), the velocity of the electrons in the outer orbitals increases and the electron is attracted to the more attractive nucleus and it might escapes from the original nucleus to form a free electron. External conditions (e.g., temperature increases) also improve the ability of electronic movement. The large collisional energy exchange during molecular impacts at higher temperature eventually promote the production of free electrons and the molecular ionization.

A similar effect take place when a molecule is accelerated in a strong electric field. The formation of free electrons and positive ions is called ionization. Under normal circumstances, the outermost atomic electron ionizes first, because of the weakest binding by the nucleus.

Although in the gas discharge process many kinds of positive and negative ions may exist, the electronic effects usually dominate. Since the electronic mass is much smaller than the gas particles, during the elastic collision, the electrons' kinetic energy loss is low. Because in gas discharge, the elastic collision probability is much larger than that of the inelastic collision, in the case of the presence of external fields, the electron's thermal average kinetic energy is much bigger than that of neutral particles. The electron's kinetic energy is also relevant to the electric field strength E.

The free-electron energy can be approximated by its kinetic energy:

$$E_e = \frac{1}{2} m_e v_e^2 \qquad \textit{(Eq. 3-1)}$$

Where m_e and v_e represents the mass and the velocity of the electron, respectively.

GROUND-STATE ATOMS (OR MOLECULES) AND EXCITED ATOMS (OR MOLECULES)

Atom is the smallest unit of ordinary matter that forms a chemical element; it cannot be divided in a chemical reaction. The atom consists of a nucleus and an extranuclear part, so it is a nuclear structure. The nucleus is dense and it is characterized by a positive charge, while several negatively charged electrons orbiting around the nucleus.

A Molecule consists of several atoms by covalent bonding electron pairs connected together. It may consist of atoms of the same chemical element or different elements. The fundamental difference between molecules and atoms is that in a chemical reaction a molecule can be divided, but an atom cannot.

Electron energy is different, and the track is also different. Typically, the smaller the orbit radius is, the smaller the energy is. The energy of the electrons can only take a series of discrete certain values. The atomic potential energy (internal energy) depends on where the energy of the electrons is, which depends on the mutual configuration of the atomic nucleus and electrons.

Atoms are usually in a stable energy level called the "ground-state". When valence electrons obtain additional energy from outside, they can jump to a level with higher energy. The atom energy is higher than the ground-state, thus the atom is "excited". The energy required for the electron jump is called "excitation energy". Sometimes it is preferred to refer to the "excitation potential", that is defined as the potential difference, through which an electron should be accelerated to acquire the value of excitation energy.

An average life expectancy in the excited state of the atom is very short, often only 10^{-7}-10^{-8}s in magnitude, and then it spontaneously transits to the ground state or another low excitation level, and radiates additional energy in the form of photons. However, the atom may also have a so-called metastable excited state, and the metastable level lifetime is longer 10^{-4}-10^{-2}s. Metastable atoms can transit in a different electron level of energy only colliding with other particles or a wall.

The energy transferred to an atom that moves from the ground-state to excited-state of metastable-state is less than the energy required by the electrons to escapes from the atom completely and become a free electron; that is called "Ionization Energy". This means that the excited and metastable atoms absorb energy without losing electrons. They can lose their exciding energy in the form of photons coming back to their ground-state; or they can absorb further energy, in the form of photons, achieving the ionization energy. When the energy of an electron is higher than the ionization energy, the electron escapes from the atom completely and become a free electron, and the atom becomes a positive ion; this process is called "Ionization".

A molecule is generally composed of several atoms. Due to the interaction among these atoms, the molecular level is more complex than the atomic level, and excitation and ionization of a molecule is also different with gas atoms. In addition to electron energy, molecular internal energy includes vibrational and rotational energy. Especially the vibration energy affects the reaction a lot, and these energy levels are also discrete. Molecular energy levels' marks are rather complicated, but they can still be represented by the energy level diagram. The definition of the molecular level of degeneracy is similar to the corresponding definition for atoms [140].

POSITIVE AND NEGATIVE IONS

Ions are active gas molecules/atoms that have lost electrons (positive ions) or that have absorbed an electron (negative ions). Depending on external factors, atom makes one or more electrons escape from theshackles of the nucleus (an electron is far from the nucleus so there is actually no interaction with the nucleus) and the formation of free electrons and positive ions is called ionization of atoms. A so-called positive ion is an atom which has lost one or several electrons Attachment of an electron to certain atoms or molecules (especially if the outer electron shell is nearly full) forms a negative ion; the process is called "attachment". Negative ion energy is equal to the ground state energy of the atom or molecule plus electron binding energy. The ionization and the attachment process are reversible; the charged ion and electrons can release energy and come back to their ground-state.
When positive ion and negative ion/electron collide and transfer the charge, the neutralization can occur and the process is called "recombination", which can occur both int the gas space and the vessel wall. Positive and negative ions recombine to form two molecules. Therefore, the energy released is the difference between the ionization energy and electron energy consumed by deprivation from the anion, which is usually released in the form of photons.
Another important recombination is that occur on the wall. In gas discharge, positive ions in the electric field move to the cathode, while negative ions move to the anode. When they meet the electrodes the anions release electrons and go back to their ground-state. The impact of positive ions with the cathode transfers kinetic energy to the electrode and electrons can be released from the metal. The positive ion can recombine with an electron and the rest become free electrons.

3.1.2 Movement of charged particles in gas discharge

The plasma produced from a gas discharge has a great interest due to its applications. In gas discharge, the collision process is a very important source of generating charged particles. Charged particles move and collide with either neutral and other charged particles to produce ionization or recombination processes. Their initial velocity can be an arbitrary direction. Thus, the trajectory of charged particles changes direction because of collisions. Between the two collisions, the path is bent toward the direction of the field of a parabola, gradually from one electrode toward the other electrode, forming a directional movement. Charged particles are accelerated by an electric field increasing their energy. In the electric field charged particles initially have low speed, then gradually increase; however, the collisions with other molecules reduce the kinetic energy of the charged species. It is possible to define an average velocity of charged particles in an electric field direction that can be observed as the kinetic energy obtained from the electric field is exactly equal to the kinetic energy of the loss because of collisions [140].

Among the particles constituting the plasma, the charged particles have a directional movement as the effect of the external field, while neutral or excited particles rarely are affected by the external field. Positive ions move toward the cathode directions, while electrons and negative ions move toward the anode, under a uniform electric field. If electrons, positive and negative ions move dx_e $dx_{i,p}$ and $dx_{i,n}$ in time dt, respectively, the surface charge density generated on the electrode can be calculated as:

$$q = en_e dx_e - en_{i,p} dx_{i,p} + n_{i,n} dx_{i,n} \qquad \textit{(Eq. 3-2)}$$

where n_e, $n_{i,p}$ and $n_{i,n}$ are the concentrations of electrons, positive and negative charged particles, respectively and e is the charge of one electron. Then, the current density at the distance x from the cathode is:

$$j(x) = \frac{dq}{dt} = en_e v^*_e - en_{i,p} v^*_{i,p} + en_{i,n} v^*_{i,n} \qquad \textit{(Eq. 3-3)}$$

Where v^*_e, $v^*_{i,p}$ and $v^*_{i,n}$ is the drift velocity of electrons, cations and anions. The drift velocity represents the particles mean velocity in an external electric field that leads to a directional movement of the particles.

An example of positive charge motion in the case of the presence of an external field is shown in Figure 3.3.

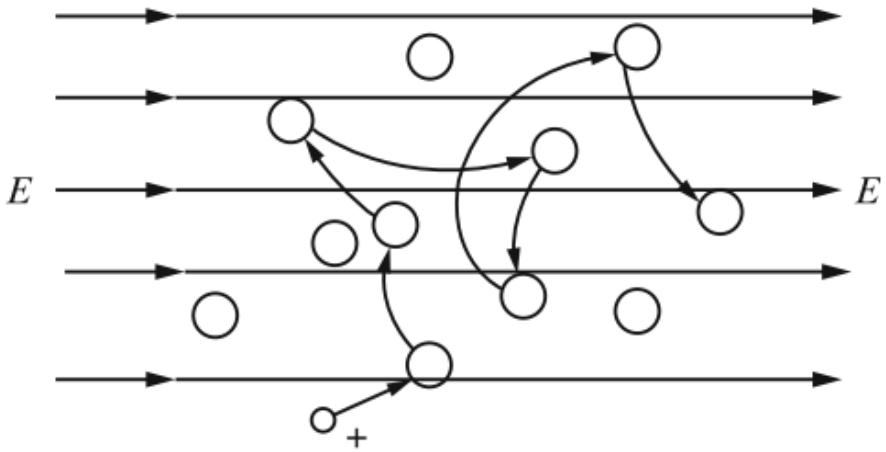

Figure 3.3 - Positive ion motion diagram, in the case of the presence of an external field.

Charged particles have directional motion according to the electric field, as it is possible to see from Figure 3.3. Although the collisions with other molecules/atoms/ions that change the direction, the overall movement of the space charges is in according with the external electric field.

In the outer loop, the total current density is calculated from the integral of the current density long the distance between the electrodes:

$$j = \int j(x)dx \qquad \textit{(Eq. 3-4)}$$

In the gas discharge there exist electrons and ions at the same time. Since the electron's drifting velocity is larger than the ion's by a magnitude of 3-4, so it can be considered that the main discharge current is the result of electron drift motion. Due to their charge per mass, much higher than ions ($<10^{-3}$ times the ions), electron mobility changes with the field strength, even in a weak electric field. The energy of the electron obtained in the external electric field will be greater than their average thermal kinetic energy; thus, the drift velocity of electrons will be greater than their average velocity in random motion, but also much larger than the ion drift velocity. Mobility is related to a gaseous state and ionic species. The higher the gas pressure is, or the larger the ion mass is, the smaller its value is. The mobility of positive and negative ions does not differ a lot in gas.

3.1.3 Gas breakdown

Under normal state, gas that is isolated from a variety of external ionization is not conductive. The density of free charges and ions in the atmosphere e.g. is so low that the air can be considered an electrically insulating medium. Even in the case of an external electric field, these charged particles do not be affected about of it and they continue to move in their random motion. However, when the electric field is strong enough, these charged particles moving along the direction of the electric field form a conduction current. The process of the insulating state mutated to the conductive state is called breakdown. When the breakdown occurs the conductance increases, and it is usually accompanied by light and sound. The minimum voltage at which the breakdown occurs is called breakdown voltage V_b. In a uniform electric field, the ratio of the breakdown voltage and gap distance is called the breakdown strength E_b; it reflects the resistance of electric capacity, namely the dielectric strength of the gas.

When the breakdown occurs, the charged particles move in the direction of the external electric field. The movement of charged particles promotes an increase of the current transferred in the gas gap, between the electrodes. This phenomenon is called Gas discharge and its intensity and form depend on many factors, electrical power, gas pressure, electrode shape, e.g. Gas discharge can be created and sustained through the application of an electric field to a dielectric gas. This electric field may be set up by a potential difference from hundreds of V to tens of kV, depending on the other factors. The environment pressure for non-thermal plasma can vary from few mbar up to atmospheric pressure. The pressure above the atmosphere is strongly not recommended as the ions and radicals can recombine easily, leading to an increasing of the gas temperature and hence turning the system toward the thermal plasma.

When an electric potential difference is applied to a gas, the charged particles move according to the electric field and they accelerate up to their drift velocity. Since the migration velocity of electrons is larger than that of positive ions (by two orders of magnitude) and their size is much smaller than ion size, electrons accelerate greatly more than ions. The electron size is six orders of magnitude smaller than ions, thus their free path is greatly higher than that of ions. Hence positive ions remain in their original position (moving little), so relatively to the electrons, they can be regarded as stationary. When the electric field is strong enough to cause electrons to reach a sufficient kinetic energy value, impact ionization occurs. Newly generated electrons from molecular ionization generate further ionization, triggering chain reactions of molecule ionization. The electrons produced from the chain

reactions move toward the cathode simultaneously, forming the so-called “avalanche of electrons”. A schematic diagram of the cascade gas ionization is shown in Figure 3.4.

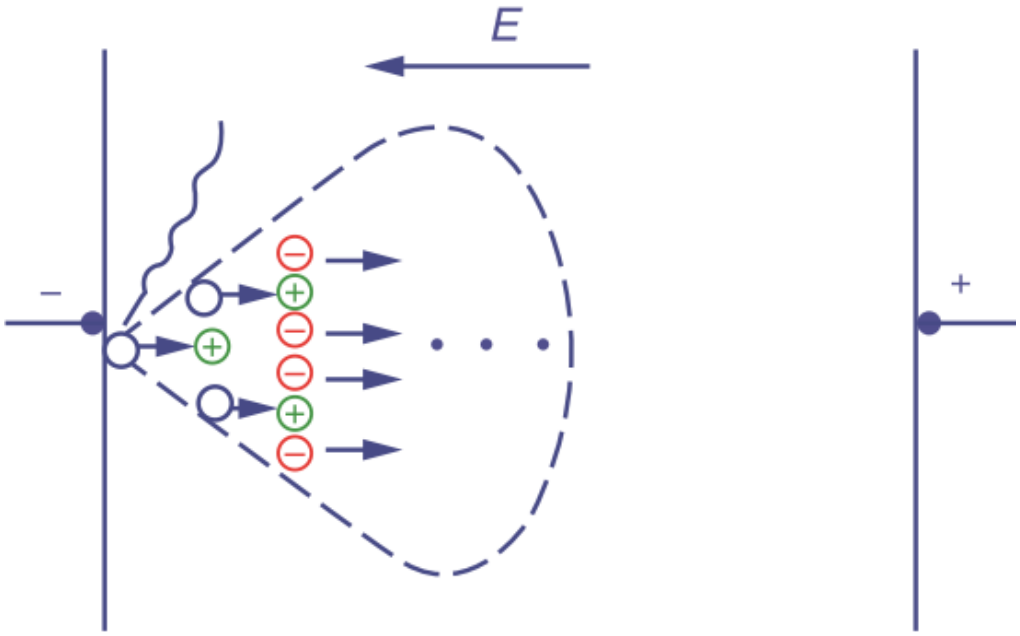

Figure 3.4 - Schematic diagram of the avalanche of electrons [140].

Considering a neutral gas, without free charges, under the effect of an external electric field, no directional movement of the particles occurs. When a photon (curved line in Figure 3.4) impact the cathode with enough energy, it can generate a seed electron. The seed electron acceleration, toward the anode, is proportional to the external electric field. If the electron energy is above the ionization energy, the collision with a neutral particle generates a positive ion and an electron that is called “second generation electron”. The two electrons (seed and 2nd generation) accelerate in the direction of the external field and once they impact two neutral particles with an energy higher than the ionization energy, they generate two new electrons, for a total of four free electrons as it is shown in Figure 3.4.

When free charges are already present in the gas (atmospheric air e.g.) they directionally move as the effect of the external field. This means that the ionization is encouraged and it does not necessary starts from the cathode. The avalanche of electrons occurs as soon as the electrons, moving toward the anode, produce effective ionization reactions in a chain mechanism.

The number of electrons produced and the avalanche intensity mainly depends on the strength of the external field. When the external potential is so high that the avalanche of electrons reaches the anode, the breakdown occurs. The longer is the distance between the two electrodes, the higher is the energy

lost in the electrons' impact during they travel toward the anode. Hence long distances require a high intensity of the external field. The correlation between the breakdown voltage and the distance between the electrodes is expressed by Paschen's law, according to the Townsend mechanism [140]. Paschen's law can be expressed as:

$$V_b = \frac{BPd_g}{C + log\, Pd_g} \qquad \textit{(Eq. 3-5)}$$

where:

$$C = log\left[\frac{A}{log\left(1 + \frac{1}{\gamma}\right)}\right] \qquad \textit{(Eq. 3-6)}$$

The breakdown voltage V_b is a function of the gas pressure P, the gap distance between the electrodes d_g, and γ that is the electrode surface ionization coefficient of positive ions, i.e. the average number of secondary electrons overflowing when positive ions from the cathode surface strike the cathode. The constant A and B are relative to gas and can be determined by experiments; they represent the saturation ionization in the gas and the excitation/ionization energies, respectively. Sometimes it is referred to the minimum electric field that allows the gas breakdown:

$$\frac{E_b}{P} = \frac{B}{C + log\, Pd_g} \qquad \textit{(Eq. 3-7)}$$

The breakdown voltage can be expressed in the function of the product Pd_g , parametric in the kind of gas. The calculation of V_b by Equation (Eq. *3-5)*, with experimentally determined constants, gives a satisfactory agreement with experiments [141]. The constants for the most common ionized gas are reported in Table 3.2.

Gas	A	B	E/p	C	D	E/p
	$cm^{-1}Torr^{-1}$	$V/(cm \cdot Torr)$	$V/(cm \cdot Torr)$	$cm^{-1}Torr^{-1}$	$V/(cm \cdot Torr)^{1/2}$	$V/(cm \cdot Torr)$
He	3	34	20–150	4.4	14	100
Ne	4	100	100–400	8.2	17	250
Ar	12	180	100–600	29.2	26.6	700
Kr	17	240	100–1000	35.7	28.2	900
Xe	26	350	200–800	65.3	36.1	1200
Hg	20	370	150-600			
H_2	5	130	150-600			
N_2	12	342	100–600			
N_2	8.8	275	27–200			
Air	15	365	100–800			
CO_2	20	466	500–1000			
H_2O	13	290	150–1000			

Table 3.2 - Constants in the formulas for the ionization coefficient and regions of applicability [141].

The data in Table 3.2 are empirical. They represent a good approximation in a specific electric field range as it is reported in the fourth column in Table 3.2. The experimental curves $V_b(Pd_g)$, the so-called Paschen curves, are plotted in Figure 3.5.

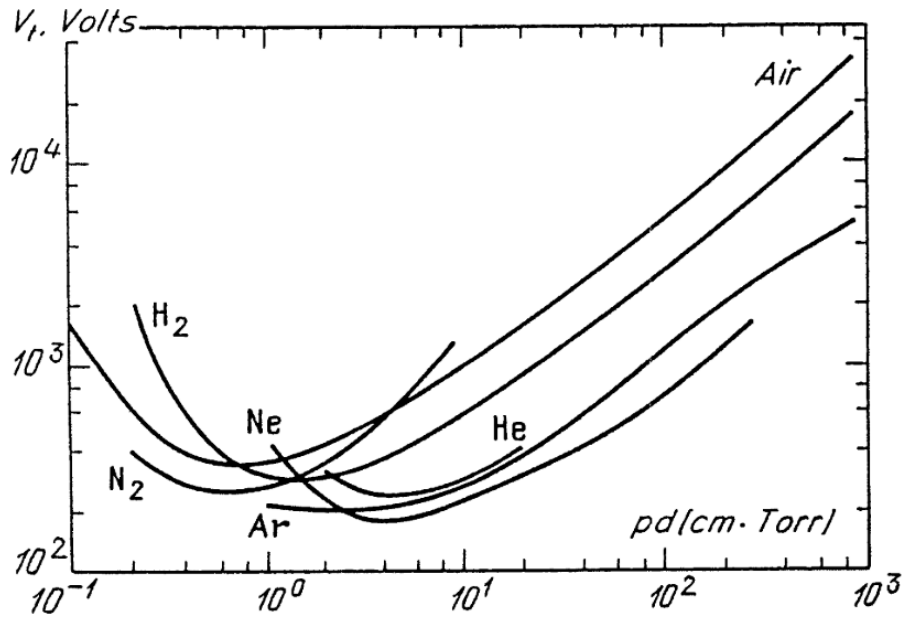

Figure 3.5 - Breakdown potentials in various gases over a wide range of Pd_g values (Paschen curves) [141].

The breakdown voltage varies by three orders of magnitude as the gas pressure and/or the distance between the electrodes change. The effect of the pressure can be explained by evaluating the mean free path of the electrons in the gas phase. When the pressure is high, which leads to a short mean free path, the electrons do not have the time to be properly accelerated by the applied electric field before they hit heavy particles and lose energy. In this case, the distance between electrodes needs to be short so that the high pressure is balanced and the breakdown is achieved. On the other hand, if the pressure is low, which relates to a long mean free path, then the probability of the electron collisions will decrease, favouring a higher distance between electrodes (at a fixed external field). The higher is the distance, the higher is the energy that must be provided to the electrons. Generally, the distance between the electrodes is at least a few centimetres to limit the breakdown potentials below 100kV.

The breakdown voltage changes in the function of the product Pd_g and has a minimum that is different for each gas (Figure 3.5). This minimum corresponds to "Stoletov's point" that represents the maximum capability of electrons to ionize the gas.

Experiments have demonstrated that in a uniform electric field applied to air at atmospheric temperature and pressure, the minimum electric field that allows the gas breakdown is:

$$E_b = 3000 d_g + 1.35 \quad [10^6\ V/m] \qquad \textit{(Eq. 3-8)}$$

Where the electrode distance d_g is expressed in meters and the equation is valid for the millimetric gaps [140].

The gas breakdown occurs as the external field is high enough to promote the gas ionization. The breakdown voltage strongly depends on the nature of the gas, the gas pressure and the electrodes' distance. Furthermore, the breakdown voltage is influenced by:

- gas impurities;
- nature and shape of the electrodes;
- electric field distribution;
- external ionization source.

IMPACT OF GAS IMPURITIES

When two kinds of gases are mixed in the discharge tube, the breakdown voltage can not simply use the mixing method to be calculated according to the concentration of the mixed gas. In such cases, the breakdown potential for a mixture of two gases e.g. can be smaller than that of the single gas.

This is the case of a mixture of nitrogen and hydrogen. The Paschen curves for a mixture of N_2 and H_2 are shown in Figure 3.6.

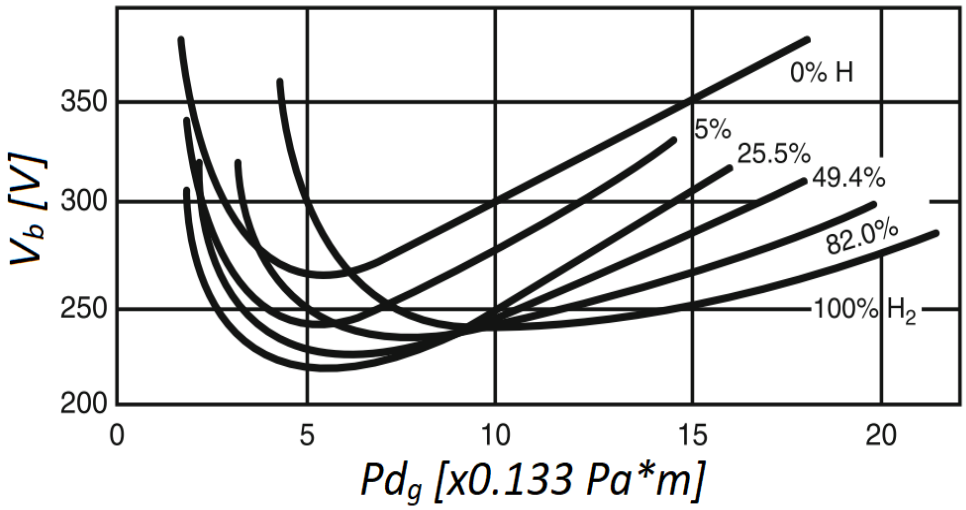

Figure 3.6 - Breakdown potentials in the function of N_2-H_2 gas composition, at low Pd_g values [140].

For such condition of pressure and gap distance, the breakdown potential could be lower in the case of the gas mixture than in pure nitrogen or pure hydrogen. Mixing nitrogen with some concentration of hydrogen, the breakdown potential of the gas mixtures decreases; while mixing with some other concentration, it will raise. The minimum breakdown potential (about 220V) was found for hydrogen content of 25.5% at Pd_g equal to about 0.7 Pa*m; that is lower than the minimum breakdown potential for the pure gases.

Similar behaviour can be found in the case of water vapour in the air. The breakdown potential slightly decreases as air contains tens of ppm of water vapour. A further increase of moisture content leads to an increase of the breakdown potential.

In the case of traces of water vapour, the water molecules break down into hydrogen and oxygen, which leads to the appearance of a small amount of hydrogen. Figure 3.6 shows that the breakdown potential decreases for nitrogen that contains small amounts of hydrogen. A further increase of water vapour content in the air leads to the formation of negative ions. Due to the slow velocity of negative ions in the electric field, the ionizing ability is extremely small, so it appears to reduce the effective number of electrons participating in the formation of avalanches. Thus, the breakdown curve has a minimum due to the reducing of the hydrogen producing rate and the improvement in negative ion production [140].

IMPACT OF ELECTRODES' NATURE AND SHAPE

Nature and shape of the electrodes have a great influence on breakdown voltage. The cathode surface roughness has a positive role in the gas ionization up to 3-4 times higher than the smooth electrode. The distortion of local space charges near the rough electrode makes the electric field very high. The higher the electric field near the cathode, the higher the ion density and the number of secondary electrons released from the cathode, as the effect of the ion impact with the metal. In addition, the electrode materials, especially the shape of the electrode surface, influence the generation of the secondary electrons from the cathode. Impurities on the cathode surface such as oil slick, oxide film dust and other insulation particles reduce the number of secondary electrons generated from the positive ion bombardment of the cathode. On the contrary, the presence of alkaline/alkaline-earth metals encourages the secondary emission of electrons from the cathode, more than transition metals. The higher is the capability of electrodes to release secondary electrons, the higher is the Townsend constant γ that is hidden in the C constant in the Paschen law, Equations () (). The constant γ is relevant in the Paschen law equation for low Pd_g values, while it becomes negligible as the pressure or the gap distances increase; in fact, the secondary electrons generated in the gas phase become more relevant than those generated from the positive ion bombardment of the cathode. An example of the electrode nature influence on the breakdown voltage is shown in Figure 3.7.

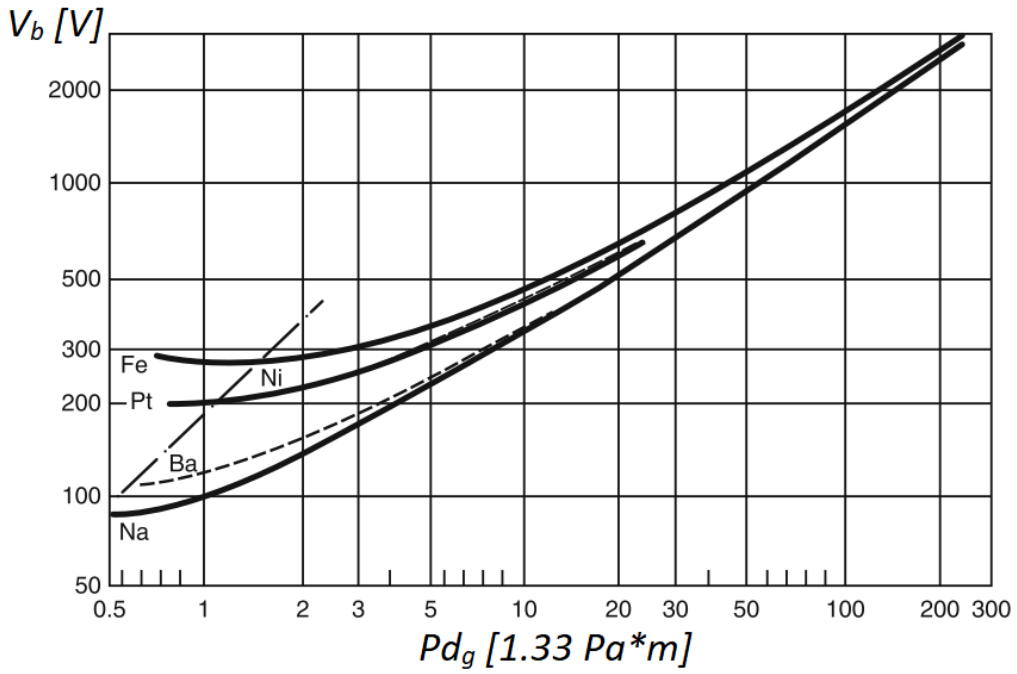

Figure 3.7 - Breakdown voltage curves of Ar between planar electrodes with different cathode materials.

Figure 3.7. shows the breakdown voltage curves of Ar between planar electrodes in the case of a cathode made of different metals. It is possible to note that the breakdown voltage at low pressure or gap distance changes strongly for different electrode materials. At high Pd_g values, the nature of the electrodes becomes irrelevant on the gas breakdown process.

IMPACT OF ELECTRIC FIELD DISTRIBUTION

Electrode structure and polarity determine the electric field distribution in the electrode gap before breakdown. The electric field distribution plays a decisive role in the generation of secondary electrons either in the gas phase and close to the electrode, which therefore has a great influence on gas breakdown potential.

If we consider a uniform electric field among parallel plates, the electric field close to the electrodes is the same in the positive and negative electrodes. The electric field distribution between the electrodes in a coaxial cylindrical electrode system is non-uniform. When the inner electrode has a positive potential, the electric field near the cathode (external electrode) is weaker and the breakdown voltage is relatively high. When the inner electrode has negative potential, the electric field near the cathode is quite strong and the breakdown voltage is relatively low.

An example of breakdown voltage for Ar and Ne in a coaxial cylinder system for different polarities, is shown in Figure 3.8.

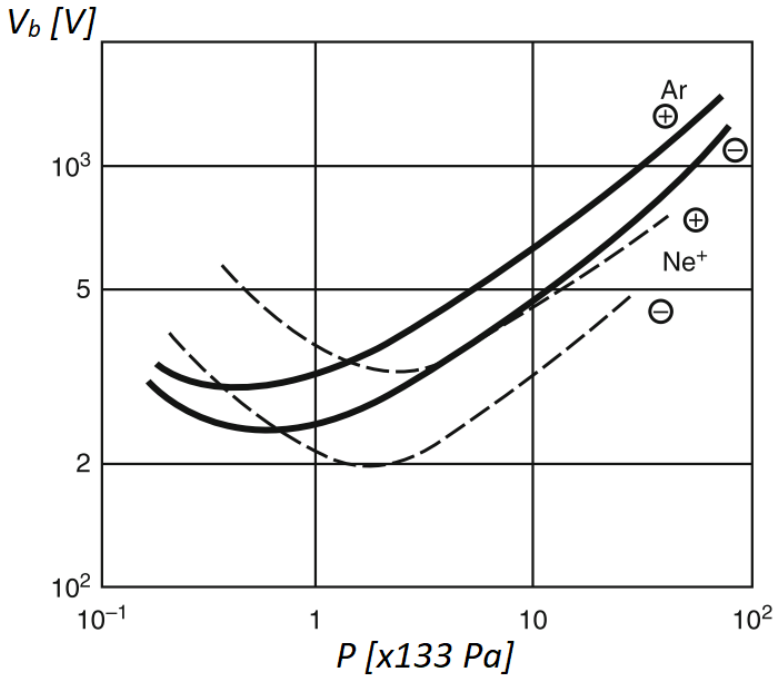

Figure 3.8 - Breakdown voltage for Ar and Ne in a coaxial cylinder system, for different polarities.

The solid lines in Figure 3.8 show the breakdown voltage for the Ar; while the dotted lines are referred to the Ne. The positive and negative symbols denote the use of the inner electrode either as an anode or a cathode respectively. The breakdown voltage is always lower in the case of the inner electrode having a negative charge. When the inner electrode is the cathode, the electric field strength is higher in the region with a higher density of charge. When the outer electrode is the cathode, the primary and secondary electrons generated at the electrode surface are distributed on a higher surface (the curved surface of the cylinder).

IMPACT OF EXTERNAL IONIZATION SOURCE

The breakdown voltage can be correlated to the capacity to promote ionization in the gas. If the gas is globally and locally neutral, the gas particles are not significantly influenced by the external field and their movement is random. The ignition of the gas discharge consists of promoting free electrons that are the precursors of the electron avalanche. The most probable phenomenon that can generate primary electrons is the photon impact with the cathode that provide energy to the metal promoting the detachment of an electron called “seed electron”.

Further to the natural phenomena, the detachment of an electron from the cathode can be promoted by the following operations:

i. heating the cathode;
ii. irradiating the cathode by ultraviolet light;
iii. placing a radioactive substance near the discharge zone;
iv. producing high-frequency sparks in the discharge zone.

These strategies encourage the production of primary electrons with the consequence of a reduced breakdown voltage [140].

3.1.4 Classification of gas discharges

The gas breakdown leads to the generation of ionized gas. When the potential is high enough, the charged particles accelerate in the direction of the external electric field, promoting a gas discharge. Depending on the electrical power, gas pressure, electrode shape and other factors, various form of gas discharge can be generated.

The gas discharges can be classified in the three groups:

- Glow discharges;
- Spark discharges;
- Arc discharges.

Glow discharges are characterized by a homogeneous breakdown of the gas that occurs between two smooth electrodes (parallel plates e.g.). When the voltage is high enough, a luminous phenomenon suddenly appears in the whole space between the cathode and the anode. The glow discharge has a small discharge of current density, in the range of mA. Glow discharges occur preferentially in the low-pressure gases where the charged particles density are relatively low and the avalanches of electrons are scattered in the gas volume. The glow is made up of individual electron avalanches which trigger successive avalanches at nearby locations. The total current from the electrode is relatively steady, but it is composed of many tiny pulses.

The discharge region generally occupies the entire space between the electrodes. The neon tube discharge is an example of glow discharge. The emitting light colours are dependent on the filling gases in the tube. An example of glow discharge is shown in Figure 3.9.

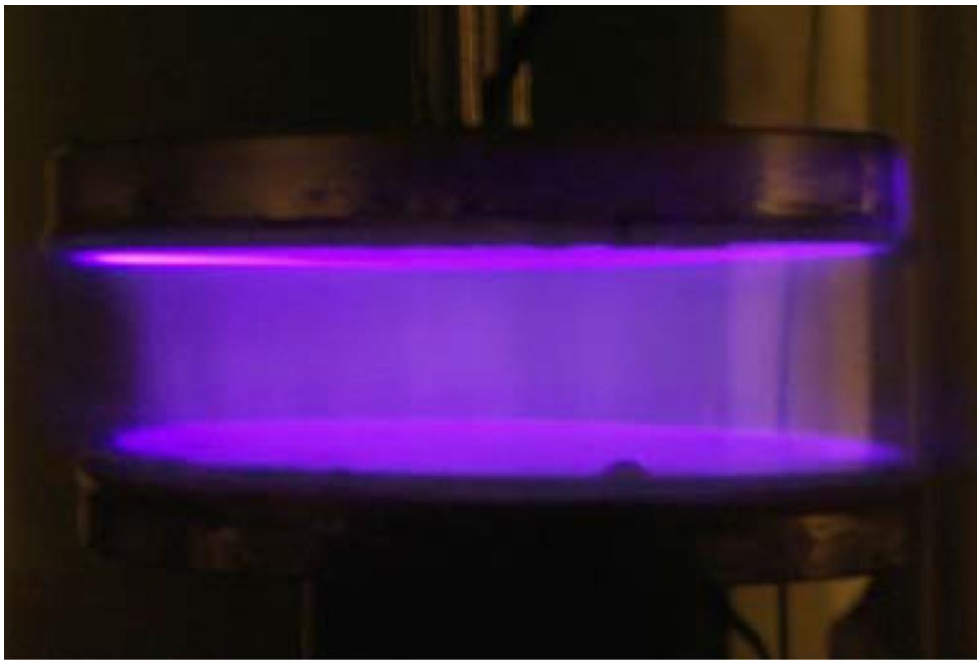

Figure 3.9 - Low-pressure glow discharge in parallel plate electrodes.

Glow discharges are also called volume discharges as the uniformity of the discharge in whole the volume between the two electrodes, as it is shown in Figure 3.9. However, when the two electrodes are far enough, the volume discharge can turn to surface discharge and a bright layer cover the high voltage electrode. If the voltage is above the breakdown voltage, the discharge occurs but the

avalanche of electrons reaching the anode could not be enough to sustain the volume plasma. Moreover, when increasing the gas pressure, the plasma volume is gradually smaller and the discharge no longer fills the entire space between the electrodes. At higher pressure (e.g., atmospheric pressure), the plasma channel is gradually smaller and the discharge no longer fills the entire space between the electrodes. Surface discharges are typical for smooth electrodes in high pressure.

If the radius of curvature of the high voltage electrode decreases, the electric field is not uniform anymore. The high-intensity electric field at of the electrode surface increases the localized charged particle density. The increased energy of electrons moving toward the anode generate fast avalanches of electrons that leave on their back positive ionized particles. Due to the fast development of the charged species, they can be considered stationary in the space compared to the electron mobility, forming a channel of high density charged particles called “streamer”. Gas discharge in the form of streamers is also called “Spark discharge”. Streamers appear as intermittent thin bright sparks between the electrodes. The reason for the intermittent spark discharge is that the form of the streamer makes the current suddenly increase, as the highest charge density of the streamer is the head of the streamer itself. The increasing of current leads to an increasing in the impedance voltage of the external circuit; so the gap voltage is reduced at the same time. The spark cannot be maintained and extinguished. This makes the circuit impedance voltage drop again, so the gap will form a spark breakdown again. This makes the formation of the intermittent spark discharge. An example of spark discharge is shown in Figure 3.10.

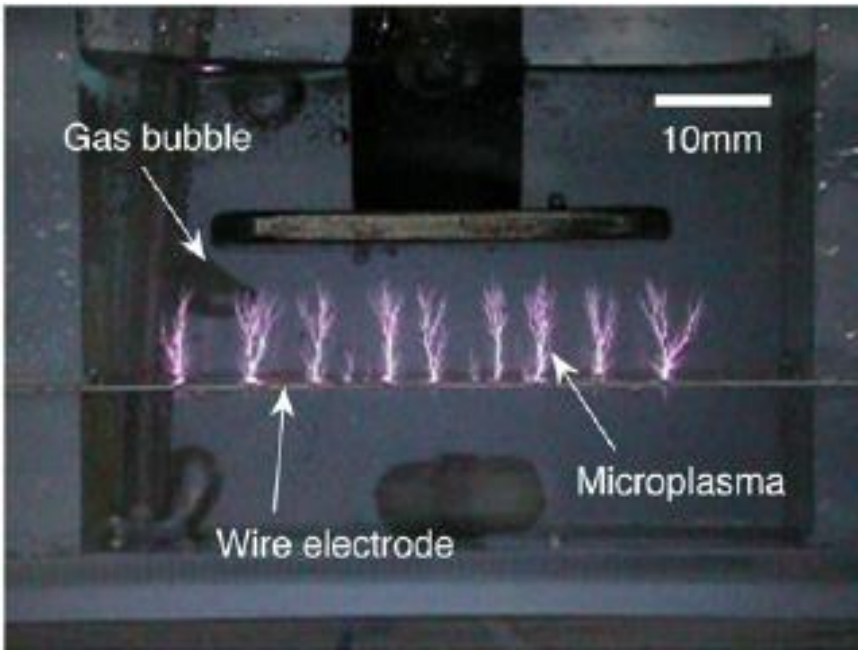

Figure 3.10 - Spark discharges in wire-plate electrode configuration.

The streamers can be considered as microchannels made of high density charged particles. Hence the plasma volume can be identified as the sum of the streamers' volume. The streamers occur as the voltage of the external field is higher than the breakdown voltage.

If the outer loop impedance is small, that is, the power supply is large enough, a bright discharge channel with high conductance forms in the gas gap and the charge immediately transfer between the electrodes. This phenomenon is called "arc discharge". When the arc discharge occurs, the electric potential can not be sustained and the transferred current in the gas gap increases exponentially. The temperatures of the arc channel and the electrode are both high with great current density. Usually, the arc discharge is an undesired phenomenon and it happens when the electric potential is too high that an instantaneous breakdown of the gas occurs. The energy from the arc discharge is released in the form of heat. An example of the arc discharge is shown in Figure 3.11.

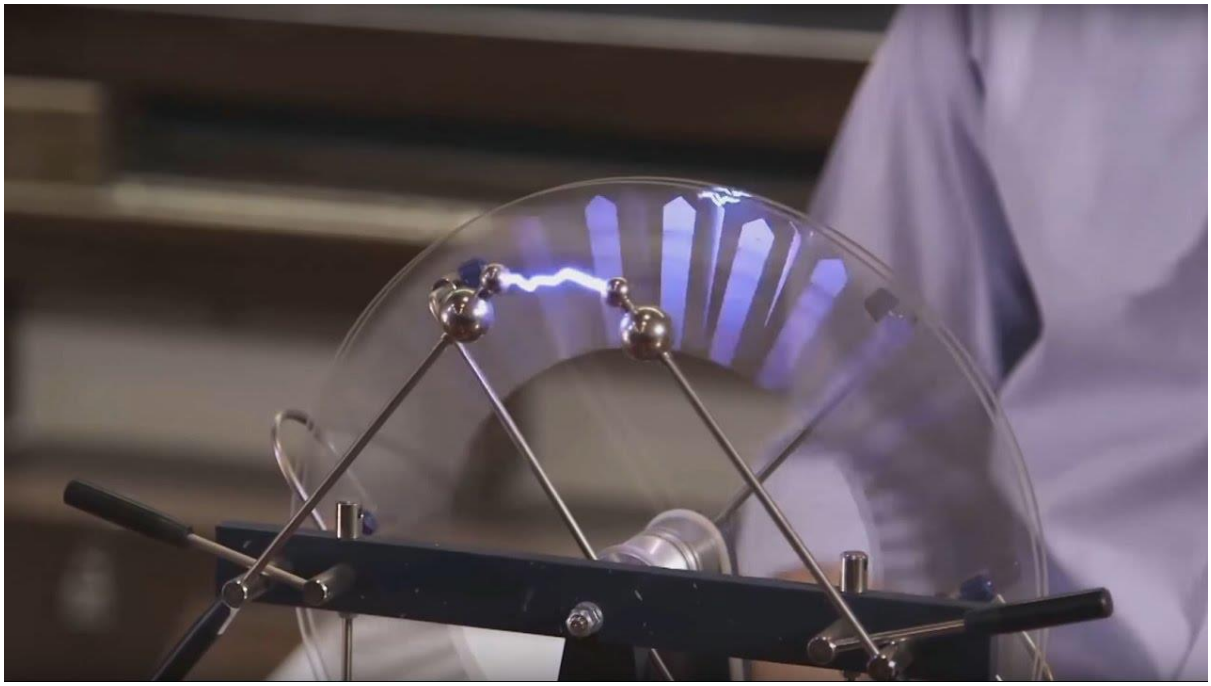

Figure 3.11 - An example of arc discharge.

Also in the case of a low-pressure system, the arc discharge can be promoted. The glow discharge occurs at a voltage slightly lower than the breakdown, as the effect of the self-sustaining mechanism [140]. The current transferred in a glow discharge mechanism can vary in the range 10^{-4}-10^{-1}A. A further increase of the external potential leads to an exponential increasing of the discharge current, promoting the so-called abnormal glow discharge. When the discharge current continues to increase, the discharge converts to an arc discharge.

There exist many techniques for non-thermal plasma production. Although the discharges can be classified as above, the high-intensity electric field can be promoted in different ways. The most common and conventional examples of gas discharges are represented by “Corona Discharge” and the “Dielectric Barrier Discharge”. Also, gas discharges can be promoted by electron beams and microwave.
A detailed description of the common techniques for gas discharge can be found in this section.

CORONA DISCHARGE PHYSICS

Corona discharges are relatively low power electrical discharges that take place at or near atmospheric pressure. The corona discharge is inhomogeneous and it can be generated by strong electric fields associated with small diameter wires, needles, or sharp edges on an electrode. The other electrode is

grounded and it can be a plate or a cylindrical surface that surrounds the high voltage electrode placed along the axis.

The most common way to produce corona discharge is by a direct pulsed current; however, alternating current can be also used. The mechanism generating the corona discharge depends on the polarity applied to the electrode. The corona will be called “positive” or “negative” as the polarity of the high voltage electrode. Even if the mechanism of propagation of the electron avalanches are similar in the two coronas, there are few differences in terms of charged particles distribution and ions and electrons current density. Schematic mechanisms of the gas ionization in the case of positive corona and negative corona are shown in Figure 3.12 a and b, respectively.

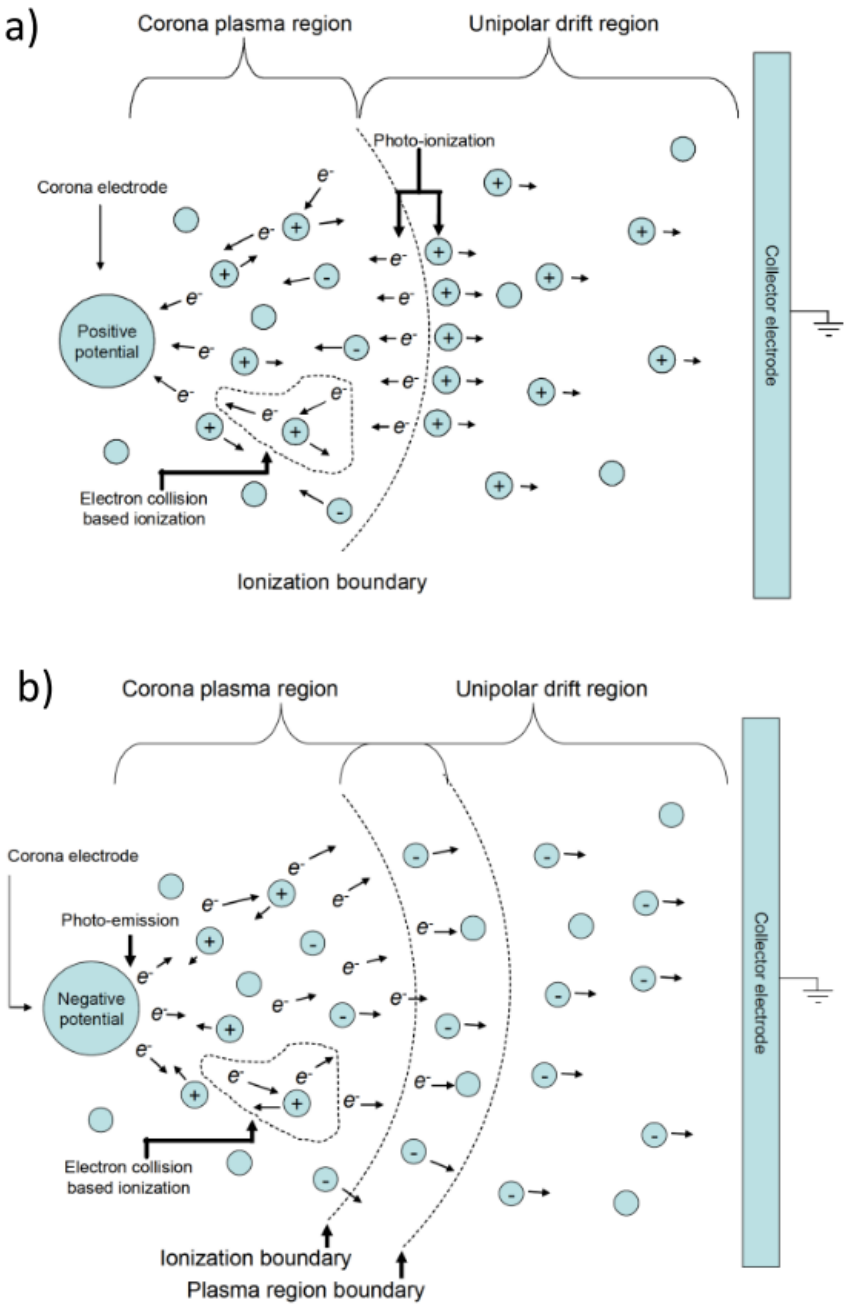

Figure 3.12 - Schematic presentation of a positive (a) and negative corona discharge (b) [142].

Figure 3.12 shows the positive and negative coronas for a wire-plate system. The wire is connected with the high voltage output of the power supply, while the plate is grounded. When the load is positive, the wire assumes the role of the anode and the corona is positive; when the load is negative, the wire is the cathode and the corona is negative.

Seed electrons, produced in natural ionisation events in the inter-electrode space, accelerate in the direction of the electric field. The density of seed electrons is higher near the high voltage electrode as the high intensity of the electric field. Most of the seed electrons are produced by photoionization

of neutral particles of by a photon impact with the electrode, as it is described in section 3.1.1. In the vicinity of the high voltage electrode surface, named ionization region, inelastic collisions of electrons and neutral gas molecules result in electrons breaking free of the molecules. Secondary electrons accelerate in the direction of the electric field and they promote the avalanche of electrons.

In the case of positive potential, the electrons move toward the high voltage electrode and the molecules' ionization is encouraged than the attachment as the high-intensity electric field within the ionization region. Near the corona electrode, electrons have average energies high enough to sustain their net production; however, at an increasing distance, the ionisation rate decreases and the attachment rate increases. The location where the ionisation rate equals the attachment rate defines the boundary of the ionisation region. This boundary lies very close to the high-voltage electrode, at a distance of a few of its radius of curvature. Out of the ionization region, the electric field is not enough to produce ionization and few electrons are available for ion recombination; thus positive ions displace on the boundary and they direct toward the grounded plate. The outer region consists almost entirely of the slowly migrating massive positive ions, moving toward the grounded-electrode. Positive ions are responsible for all current beyond the active ionisation region, whereas negative ions move towards the corona electrode. The region within the ionization boundary is known as the plasma region, the outer as the unipolar region.

The positive corona mechanism, described above, is valid for the configurations: wire-plate, needle-plate, wire-pipe, coaxial cylinder. If the ratio between the curvature radius of the electrode and the electrode distance is large, that means the electric field is uniform; when the voltage rises to a certain value, the entire gap will break down suddenly. Hence the plasma appears as a tight sheath around the electrode (glow discharge). Conversely, if the ratio between the curvature radius of the electrode and the electrode distance is small, that means the electric field is non-uniform; when the voltage rises to a certain value, at first the electrode surface appears as a light-emitting layer. As the voltage increases, the light-emitting layer expands and the discharge current also increases. A further increase in the electric potential produces a spark discharge.

A representation of the positive corona forms, in a pulsed DC voltage, is shown in Figure 3.13.

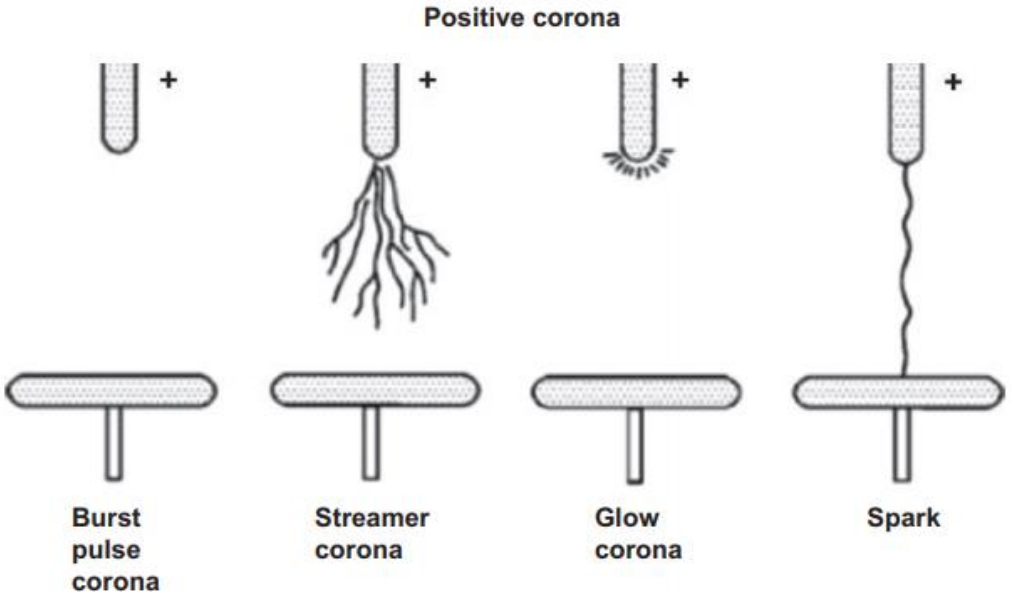

Figure 3.13 - Various discharge types for positive coronas in a needle-plate electrode configuration [143].

For positive corona in the needle-plate electrode configuration, discharges initiate as a burst pulse corona and proceed to the streamer corona, glow corona, and spark discharge as the applied voltage increases.

In the case of negative potential, secondary electrons sustaining negative corona are produced primarily by photo-emission from the corona electrode surface, as it is shown in Figure 3.12 b. The general movement of electrons in a negative corona is outward from the curved electrode. A negative corona can be divided into three radial areas around the sharp electrode. In the inner area, called "ionization region", high-energy electrons collide with neutral atoms and cause avalanches. In this region, the production of new electrons by electron-impact ionization prevails over the attachment of electrons or recombination. In the intermediate region, attachment prevails over ionization and the number of electrons gradually diminishes as the electric field decreases. However, in contrast to positive corona, electrons just beyond the ionisation boundary are of sufficient number and energy to drive electron-impact reactions. Electron attachment and ion recombination occur in this region. Thus, the corona plasma region extends beyond the ionisation region. Differently, in positive corona, the two regions coincide. Out of the corona plasma region, only negative ions are present as their energy is not strong enough to promote atoms/molecules ionization. In the outer region only a flow of negative ions and free electrons occur toward the positive electrode, and their concentration decrease radially, as the effect of their recombination/neutralization. The inner two regions are known

as the corona plasma. The inner region is an ionizing plasma, the middle a non-ionizing plasma, the outer is known as the unipolar region.

In contrast to the uniform positive corona discharge, negative corona discharges appear as discrete points or tufts along the high-voltage electrode. Near the corona onset voltage, only a few tufts appear. They are irregularly spaced along the electrode and preferentially appear at imperfections on the surface. As the voltage is increased, the number of tufts increases and their distribution becomes more uniform.

For negative corona in the needle-plate electrode configuration, discharges initiate as a Trichel pulse corona, followed by pulseless corona and spark discharge as the applied voltage increases. A representation of the negative corona forms, in a pulsed DC voltage is shown in Figure 3.14.

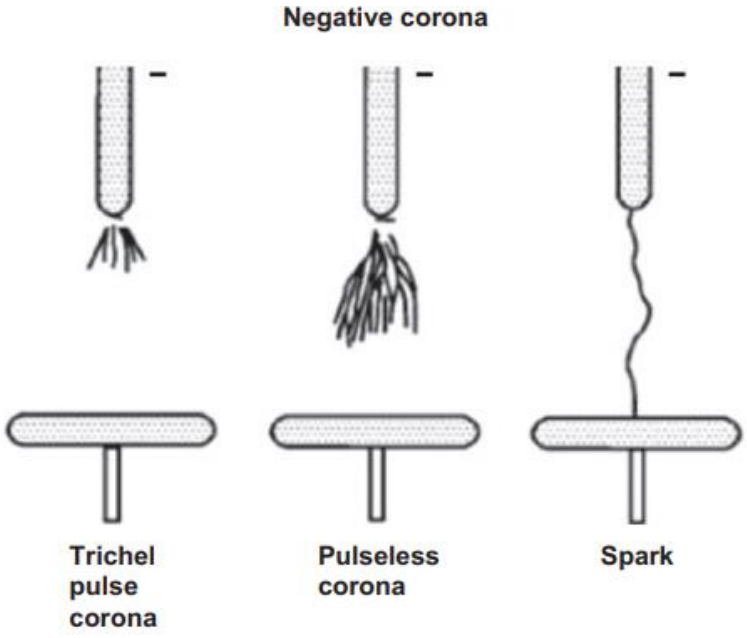

Figure 3.14 - Various discharge types for negative coronas in a needle-plate electrode configuration [143].

The main difference between positive and negative coronas is that in a positive corona, the secondary electrons are generated by the gas surrounding the plasma region and they travel inward the ionization region; whereas in a negative corona, the secondary electrons are released by the electrode itself and they travel outward. This means that the nature of the cathode and its capacity to promote a secondary electron emission contributes significantly to the plasma intensity.

As a consequence of the different process of ionization, even with the same geometry and voltages, the positive corona appears a little smaller than the corresponding negative corona, due to the lack of a non-ionising plasma region between the inner and outer regions. The total number of electrons and the electron density are much greater in the negative corona than in the corresponding positive corona.

The ionisation region of a positive corona is characterised by a dim and uniform glow over the electrode surface, while the brush or tuff-like discharges of a negative corona are characterised by intermittent Trichel pulses. A representation of positive and negative coronas is shown in Figure 3.15.

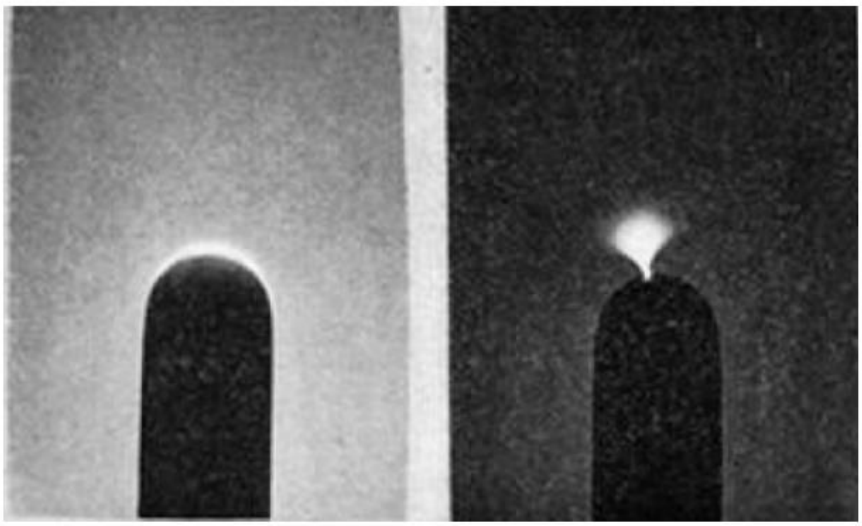

Figure 3.15 - Visualization of positive corona glow (left) and a negative corona discharge (right) [142].

In Figure 3.15 it is possible to see the different light produced by a positive corona (left) and the negative corona (right). The positive corona generates a bright layer that surrounds the edge of the electrode. The thickness of this layer is greatly smaller than the radius of the discharge in the negative corona. In the case of negative corona, the discharge is localized in one point and the light spread out in the direction of the anode.

The minimum electric field required to initiate a visible corona discharge, i.e. the "corona onset", depends on the electrode properties, the gap distance and the gas density. The most important equation for the empirical calculation of the corona onset voltage is the Peek's Law. Peek's law defines the electric field necessary for triggering a corona discharge between two wires and it can be written as:

$$E_S = E_0 m_v \left(\delta + 0.0308 \sqrt{\frac{\delta}{R_0}} \right) R_0 \ln \frac{D_w}{R_0} \qquad \textit{(Eq. 3-9)}$$

where E_S is the corona onset electric field intensity on the discharge electrode surface in [V/m], E_0 is the disruptive electric field and it is usually considered to be about $3\text{-}3{,}2 \cdot 10^6$ [V/m], m_v is the dimensionless surface parameter, R_0 is the radius of the wire in [m], D_w is the distance between the centre of the wires, and δ is the relative density of gas with respect to the normal condition of 273.15K.

$$\delta = \frac{T_s P}{P_s T} \qquad \textit{(Eq. 3-10)}$$

In this equation T_s and T are 273.15K and local temperature, respectively, and P_s and P are 101,325Pa and local pressure, respectively.

The Peek's Law can be extended to the wire-cylinder configuration replacing D_w with the outer radius of the cylinder. In the case of the wire-plane configuration, the parameter D_w must be replaced with the double of the distance between wire and plane. In fact, the configuration can be considered as two wires charged with the same voltage, with the plane placed in the middle of them and orthogonal to the line passing through the centres of the two wires.

The coefficient m_v is a roughness factor, which takes into account the state of the conductor surface. For rough or weathered conductors, the corona starts at lower voltages than if the conductor is perfectly smooth. The parameter m_v is equal to 1 for a smooth conductor, and when the conductor is dirty, the roughness factor is usually taken between 0.5 and 0.7.

The gas density plays a key role in the corona discharge. Either the gas temperature and pressure affect the gas density and hence the onset voltage. The higher is the gas density, the shorter is the mean free path of charged particles. When the particle density increases, the number of interactions increases with the consequence of higher energy released by the electrons. The electrons having low internal energy cannot effectiveness impact neutral particles and ionize them. The attachment reactions prevail and the electron avalanches extinguish.

The condition of small particle number concentration can be achieved either operating at low pressure or high temperature. Experimental investigations showed that at high temperature (above 500°C) the onset condition is obtained for a voltage always lower than that calculated by the Peek's Law [144], [145]

DIELECTRIC BARRIER DISCHARGE (DBD) PHYSICS

When an electric discharge occurs in a configuration that includes at least one dielectric between the electrodes, the discharge is called "Dielectric Barrier Discharge" DBD. The DBD is a highly transient, low-temperature non-equilibrium discharge formed from electrons of high mean energy which exists in a broad range of pressures. Because of the presence of at least one dielectric barrier, these discharges require the adoption of high AC voltage; being the dielectric an insulator, it cannot pass a direct current. The time derivative of the applied voltage, the dielectric constant and its thickness

determine the amount of displacement current that can be passed through the dielectric(s). To transport current (other than capacitive) in the discharge gap the electric field has to be high enough to cause a breakdown in the gas. During the discharge development, charge carriers accumulate on the dielectric(s) reducing the field strength in the discharge area and hence quenching the discharge. As in the case of corona discharge, even the dielectric barrier discharge can be classified in volume discharge, surface discharge and a combination of both. The type of discharge strongly depends on the configuration design. A classification of the DBD types can be summarized as in Figure 3.16.

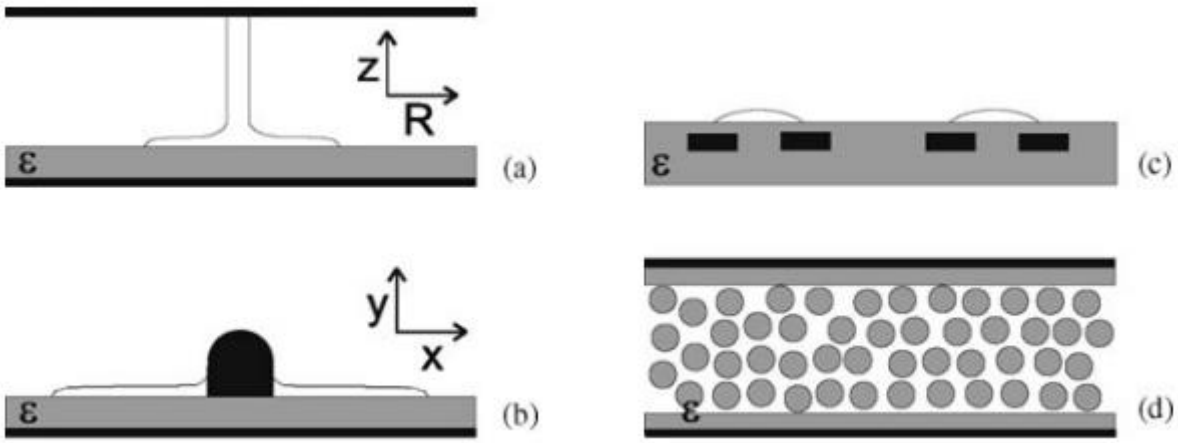

Figure 3.16 - Simplified representation of the volume discharge (a), the surface discharge (b), a combination of them in a coplanar arrangement (c), and a packed bed (d) [146].

Looking at a planar arrangement, for simplicity, the volume dielectric barrier discharge occurs as the two electrodes, represented by two parallel plates, have at least one dielectric between them and the gas gap is at least of a few millimetres. The discharge appears as a luminous filament, called "streamer", that bridges the gas gap and is partially spread on the dielectric surface (Figure 3.16 a). When the plates are too close to each other or the electrodes are both in contact with the dielectric, the discharge occurs on the dielectric surface and is called "surface discharge". The Surface discharge appears as a bright light layer that covers the dielectric surface (Figure 3.16 b). There are many possible combinations of these basic configurations. In the case of plasma display panels, e.g., both the electrodes are inside the dielectric, while the discharge occurs on its surface (Figure 3.16 c). In such applications, such as chemical reactions, dielectric pellets or spheres fill the gas gap. The discharge occurs in the void spaces between the particles and the plasma intensity is higher than in the case of empty DBD (Figure 3.16 d).

The planar arrangement considerations can be extended to other configurations. Looking at the volume barrier discharge, the most common configurations are shown in Figure 3.17.

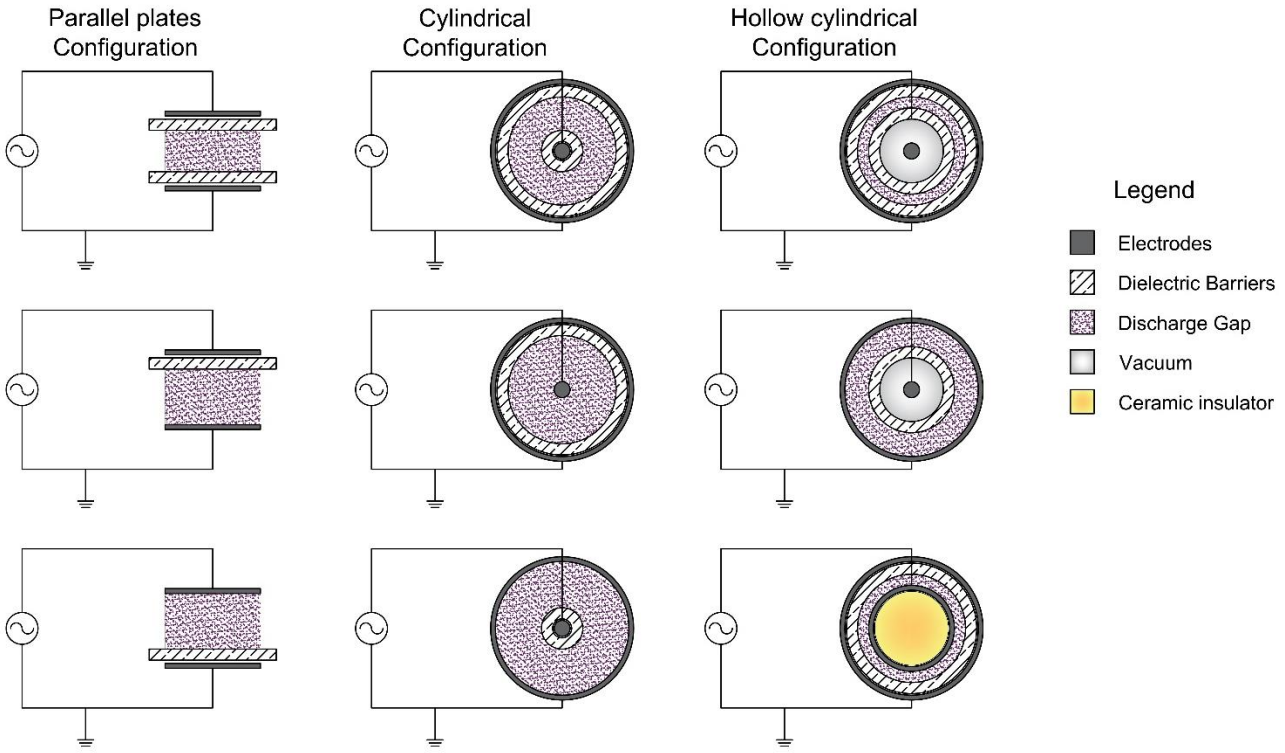

Figure 3.17 - Common configurations of volume DBDs: parallel plates (left), cylindrical (centre) and hollow cylindrical (right).

The most common DBD configurations are parallel plates, cylindrical and hollow cylindrical. In parallel plates, the electrodes consist of two plates, one charged, the other grounded. A dielectric plate can be placed near one of the two electrodes or two dielectrics can be designed near both. The gas passing through the electric field can breakdown as the electric field is strong enough. Being the gas gap usually small, in the range of 10^{-4}-10^{-2} m, more plates can be placed in parallel and they are alternately charged. In the cylindrical configuration, a metal cylinder represents an electrode (usually the ground) and the other electrode is placed along the axis (high voltage electrode). The dielectrics in the cylindrical configuration are dielectric tubes that can either be placed near one dielectric or both the dielectrics. In this case, the discharge is radial and the gas passes through the annulus surface area defined by the dielectrics or the electrode and dielectric. Rarely the cylindrical configurations have a gas gap radius higher than few centimetres as the breakdown potential increases significantly. The hollow cylindrical configuration allows to increases the annulus surface area with the consequence of a higher gas flow rate, by maintaining the same gas velocity and breakdown voltage. Increasing the ground cylinder diameter the cross sectional area can be maintained equivalent to the cylindrical configuration, by using a dielectric cylinder having a bigger diameter, or replacing the high voltage electrode with a cylinder. In the first case, the vacuum condition must be created inside

the glass tube, to reduce the electric resistance; the high voltage electrode in the latter configuration is usually placed on the surface of a ceramic cylinder.

When the electrodes are close enough, the gas spaces bounded by one or two dielectrics have practically the same breakdown voltage as if they were between metal electrodes. The typical ratio $\Delta V/d_e$, that promotes the breakdown is about 10^6 Vm^{-1}; where ΔV is the potential displacement and d_e is the distance between the electrodes. However, the ratio increases when the d_e is higher than 1cm and/or the dielectric(s) thickness became comparable to the gas gap. For atmospheric pressure discharges gap spacings of a few millimetres are common, thus requiring alternating driving voltages with peak intensity typically of tens of kV.

The presence of the dielectric(s) precludes DC operation; hence, alternating or pulsating current is used to breakdown the dielectric and generate the plasma. DBD configurations can be operated between line frequency and microwave frequencies, but the most common operating range for most technical DBD applications lies between 500 Hz and 500 kHz. The dielectric limits the average current density in the gas space; it thus acts as a ballast which, in the ideal case, does not consume energy. However, at very high frequencies the current limitation imposed by the dielectric becomes less effective and an electric arc may be generated.

When the electric field in the discharge gap is high enough to cause the breakdown, a large number of short-lived microdischarges are observed at atmospheric pressure (volume discharge) that form a streamer. Each streamer has an almost cylindrical plasma channel, typically of about 100 μm radius, and spreads into a larger surface discharge at the dielectric surface(s), as it is shown in Figure 3.18.

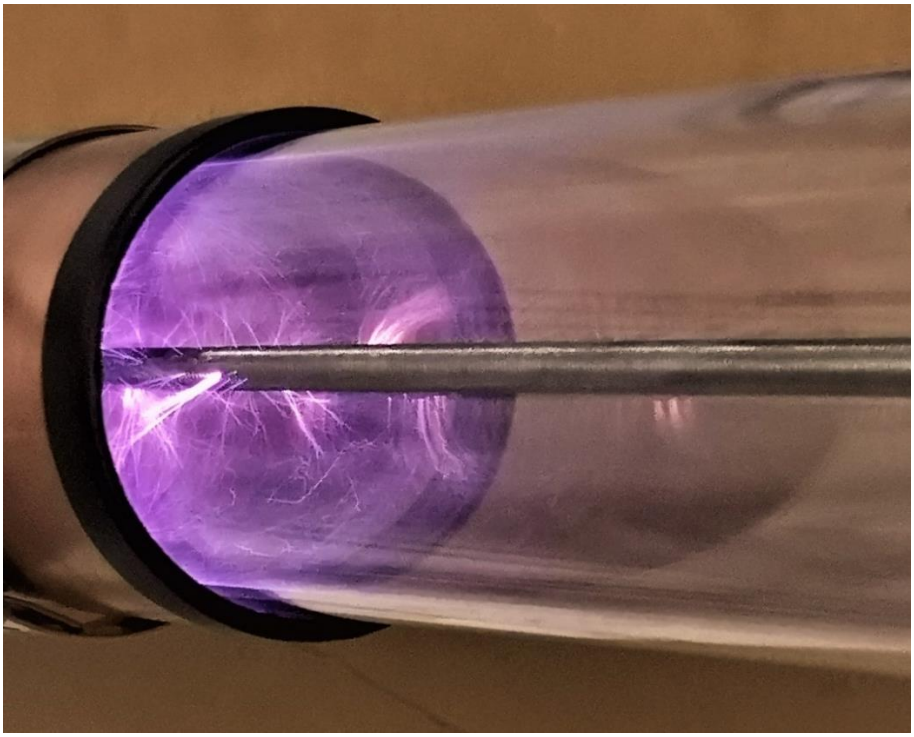

Figure 3.18 - Example of streamers in a cylindric DBD.

Figure 3.18 shows an example of volume plasma promoted in a cylindric DBD. When a potential higher than the breakdown voltage is applied, microdischarges occur and they appear in the form of streamers. The streamers spread along the reactor length and they across the entire gas gap distance. At fixed geometry, the thickness and the frequency of streamers depend mainly on the power load.

lt is important to distinguish the terms streamer and microdischarge. An initial electron starting from some point in the discharge gap (or from the cathode or dielectric that covers the cathode) produces secondary electrons by direct ionization and develops an electron avalanche. If the avalanche is big enough, the cathode-directed streamer is initiated. The streamer bridges the gap in a few nanoseconds and forms a conducting channel of weakly ionized plasma. An intensive electron current flows through this plasma channel until the local electric field collapses. Collapse of the local electric field is caused by the charges accumulated on the dielectric surface and the ionic space charge; ions are too slow to leave the gap for the duration of this current peak. The group of local processes in the discharge gap initiated by an avalanche and developed until electron current termination is usually called a microdischarge.

A schematic diagram of a single streamer and a simple equivalent circuit in a two dielectric barrier discharge is shown in Figure 3.19.

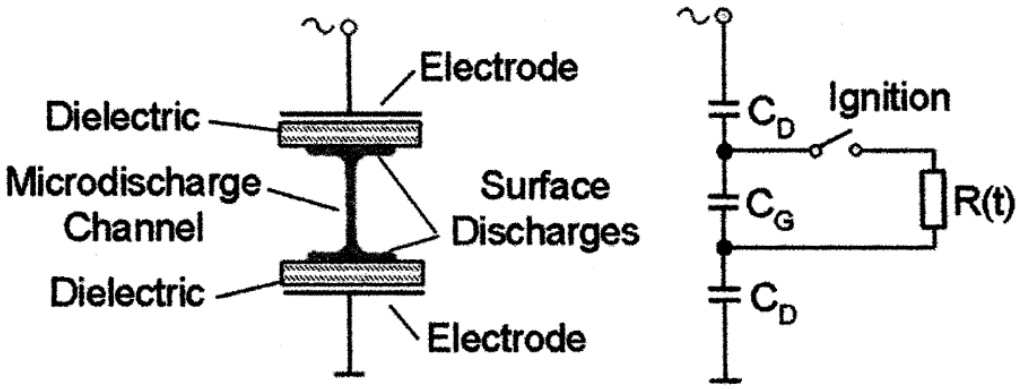

Figure 3.19 - Sketch of streamer and a simple equivalent circuit [147].

The DBD can be schematized as the series of three capacitors: one for the gas and one for each dielectric, and a resistor in parallel with the gas capacitor that works when the streamer occur. The lower the dielectric constants, the lower the total capacitance and the lower the current that passes through the gas gap. Either the increasing of the potential and/or of the frequencies led to an increasing electric field. By applying an electric field larger than the breakdown field, local breakdown in the gap is initiated. In the equivalent circuit, this is symbolized by closing a switch and forcing part of the current through the plasma filament, whose resistance R(t) rapidly change with time. Electron avalanches, starting from the cathode, quickly produce such a high space charge that self-propagating streamers are formed. When the avalanches achieve the anode, an extremely thin cathode fall layer is formed on the dielectric surface. At this moment, a high-intensity current flow through the conductive channel bridging the electrode gap peaks. Subsequently, charge accumulation at the dielectric surface(s) reduces the local electric field to such an extent that ionization stops within a few nanoseconds and the streamer is choked. When the electric field is not any more high enough to sustain the discharge, in the equivalent circuit this is symbolized by closing a switch, avoiding the current to pass through the resistance.

After electron current termination there is no longer an electron-ion plasma in the main part of the microdischarges, but high levels of vibrational and electronic excitation remain in the channel volume, along with charges deposited on the surface and ionic charges in the volume. This allow us to separate this region from the rest of the volume and call it a microdischarge remnant. Positive ions (or positive and negative ions in the case of electronegative gas) of the remnant slowly move to electrodes, resulting in a low and very long (~10μs for a 1mm gap) falling ion current. The microdischarge remnant will facilitate the formation of a new microdischarge in the same spot as the polarity of the applied voltage changes. That is why it is possible to see single filaments in DBD. If

microdischarges would form at a new spot each time the polarity changes, the discharge would appear uniform. The fact that the microdischarge remnant is not fully dissipated before the formation of the next microdischarge is called the “memory effect”.

A snapshot of the microdischarges in a 0.762mm DBD air gap photographed through a transparent electrode is shown in Figure 3.20.

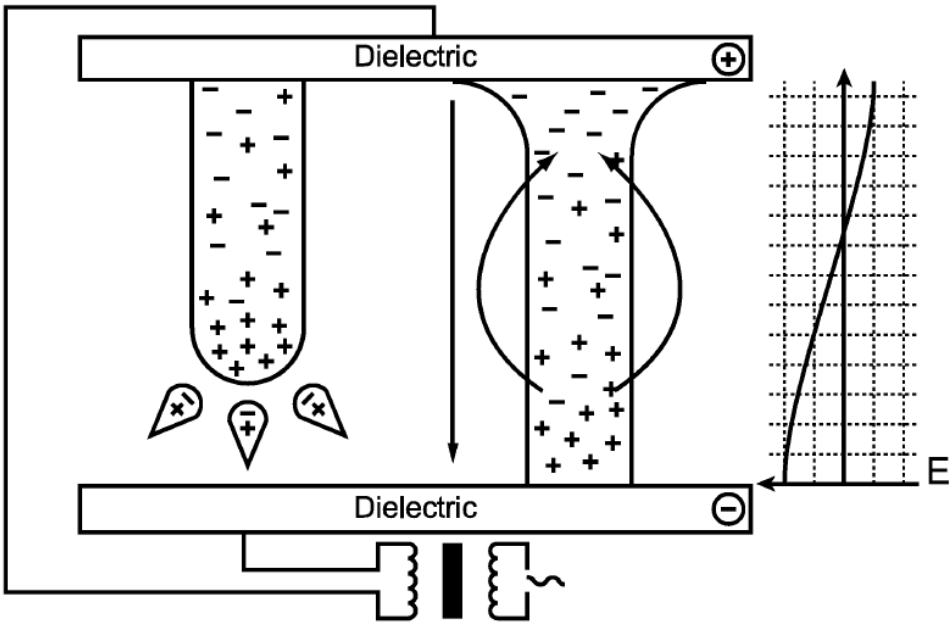

Figure 3.20 - Illustration of the streamer formation (left), plasma channel (middle) and electric field distortion (right) [148].

Figure 3.20 shows an illustration of the interaction between the DBD microdischarges (quasi-repulsion) related to an electric field distortion caused by the microdischarge remnant. Streamer formation (left-hand side) and plasma channel (and microdischarge remnant) electric field distortion (right-hand side) are due to space charges. The figure shows the electric field from the microdischarge, the applied external electric field, and their superposition. In the presence of space positive charge, the electric field is increased at the cathode and decreased at the anode. Charge accumulation on the surface of the dielectric(s) barrier reduces the electric field at the location of a microdischarge. lt results in current termination within just several nanoseconds after the breakdown. The short duration of microdischarges leads to very low overheating of the streamer channel.

According to numerical modelling, the reduced electric field at the streamer head can reach 800 Td (1Td is equivalent to 10^{-17}Vcm^2), that is several times higher than the reduced electric field at the breakdown (about 100 to 300 Td) [149]. The reduced electric field (θ) corresponds to the ratio E/n, where E is the electric field and n is the total gas number density. At atmospheric pressure, the

streamer duration is of about 10ns and electron densities of 10^{14} to $10^{15}cm^{-3}$ are reached in microdischarges. The total charge transferred in the gas gap is proportional to the width of the discharge gap and the relative permittivity, while it is inversely proportional to the dielectric thickness and it does not depend on gas density.

Over a wide range of operating frequencies and voltage shapes, microdischarge properties do not depend on the external driving circuit, but rather by the gas properties, the pressure and the electrode configuration. Raising the power for a given configuration means generating more microdischarges per unit of time and/or per unit of electrode surface area. This characteristic of DBDs is very important because it allows investigating and optimising microdischarge properties for a given application in a fairly small laboratory set-up. Scale-up even to very large electrode surfaces in industrial applications normally does not present a problem if gap spacing and power density are not changed.

Even in the case of volume discharge, a displacement of light can be observed on the dielectric(s) surface, as it is shown in Figure 3.19. The light intensity on the surface of the dielectric belongs to a surface discharge. The shape and the intensity of the surface discharge(s), at the bases of the plasma channel, depend on the voltage applied and its polarity. On the dielectric surface, in the corresponding of the cathode, distinct channels radially propagate from the discharge axis. In the case of the anode, the discharge homogeneously diffuse around the channel axis onto the dielectric surface.

When the gas gap decreases, the surface discharge becomes relevant than the volume discharge. The surface discharge area increases and the volume discharge channel tends to disappear. The form of the surface discharge remains roughly the same than before, and the differences in the function of the electrode polarity remain. The discharge patterns on the dielectric surface of surface discharges in the function of the electrode polarity have been proposed by Gibalov et al. [146] and they are shown in Figure 3.21.

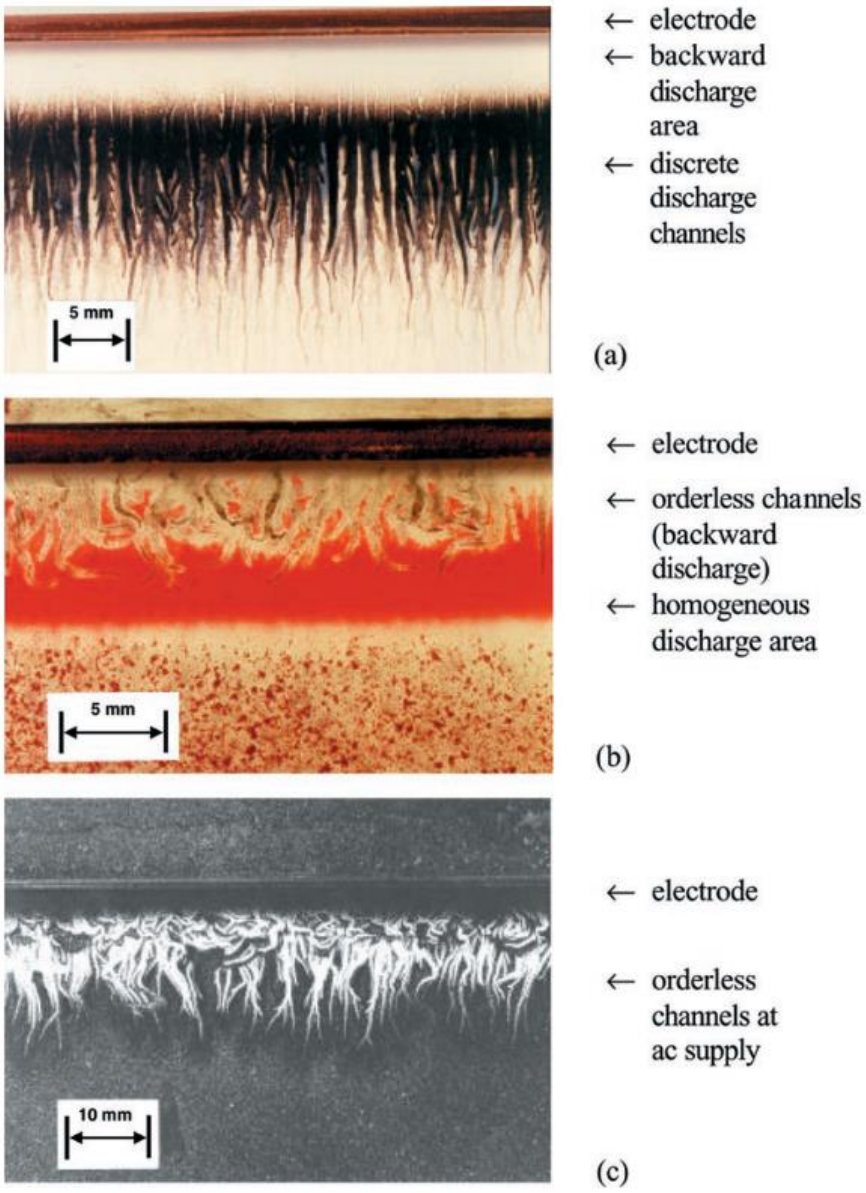

Figure 3.21 - Discharge patterns on the dielectric surface of an SD for a positive voltage pulse (top), negative voltage pulse (middle) and an AC voltage (bottom) [146].

In the case of Surface Discharge (SD) with positive polarity (a positive voltage at the surface electrode), distinct channels appear on the dielectric with widths in the order of magnitude of 1mm (Figure 3.21 a). With the opposite polarity, the discharge is uniformly distributed in a certain area along the electrode (Figure 3.21 b). As the voltage is decreased the potential difference between the surface charges and the electrode reaches breakdown field strength and 'backward' discharges with opposite polarity appear near the electrode. These back discharges have the patterns of the opposite polarity: at positive polarity, they look uniform (Figure 3.21 a); while at negative polarity they consist

of orderless channels (Figure 3.21 b). With an AC voltage, a mixture of both patterns can be observed (Figure 3.21 c).
However, there is a distinct difference between the discharge mechanisms in the volume and surface discharges. In volume discharges, the plasma streamers bridge the gas gap. The charge is transferred through these channels. With increasing voltage the number of microdischarges per period increases. In surface discharges, there is no defined discharge gap. An increase in the voltage leads to an enlargement of the discharged area on the dielectric. In this case, the charge transfer takes place in a thin layer on the dielectric surface.

Even in the case of packed bed reactors presented in Figure 3.16 (d), the surface discharge occurs. When the DBD is packed with pellets or spheres, the plasma physic change. The presence of dielectric particles into the gas gap does not allow the microdischarges to flow freely between the electrodes as the gas gap tortuosity is too high. The dielectric particles refract the electric field, making it non-uniform and stronger than the externally applied field by a factor of 10 to 250 depending on the shape, porosity, and dielectric constant of the pellets. A schematic representation of a cylindrical packed-bed DBD is shown in Figure 3.22.

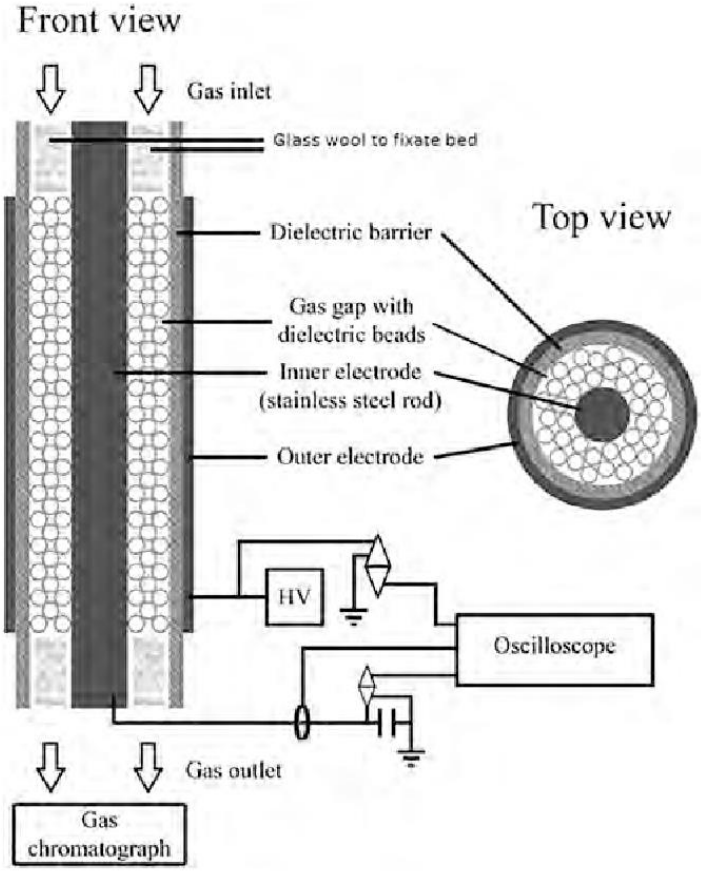

Figure 3.22 - Schematic representation of a cylindrical packed bed DBD.

When a high AC voltage is applied to the inner electrode, generating an electric field higher than the breakdown, a non-thermal plasma in the void spaces between dielectric particles produces. A glow discharge appears on the surface of the particles in the region where the electric field is high enough to allow the gas ionization and the photons emissions. The dielectric tube inhibits direct charge transfer between electrodes and plasma. In some applications, the spheres/pellets of ferroelectric ceramics with high dielectric permittivity (ε>1000) are used. Ceramics based on $BaTiO_3$ are most commonly employed for the discharges. The ferroelectric materials can have a significant dipole moment in the absence of an external electric field. An external AC voltage leads to over polarization of the ferroelectric material and reveals strong local electric fields on the surface, which can stimulate the discharge on the ferroelectric surfaces. The active volume of the ferroelectric discharge is located in the vicinity of the dielectric barrier.

Preferred materials for the dielectric barrier are glass or silica glass, in special cases also ceramic materials, thin enamel or polymer layers. In some applications, additional protective or functional coatings are applied. The dielectric serves a dual purpose: it limits the amount of charge and energy

imparted to an individual micro discharge and, at the same time, distributes the micro discharges over the entire electrode/dielectric area. Intact dielectric guarantee that no spark or arc can occur in the discharge gap.

ELECTRON BEAM

Free electrons in a vacuum can be manipulated by electric and magnetic fields to form a fine beam. The electron beam is known as "particle accelerators" system, where the particles being accelerated are electrons and the beam generated is the equivalent of beta radiation. Although the electron beam is widely used for thermal processes, as the beam collides with the solid-state matter, the ionized gas in the beam region can produce a non-thermal plasma. Electron beam generated plasmas are produced by injecting a high energy electron beam into a gas background, which will ionize, dissociate, and excite atoms or molecules as it traverses the gas volume.

A schematic representation of the electron beam is shown in Figure 3.23

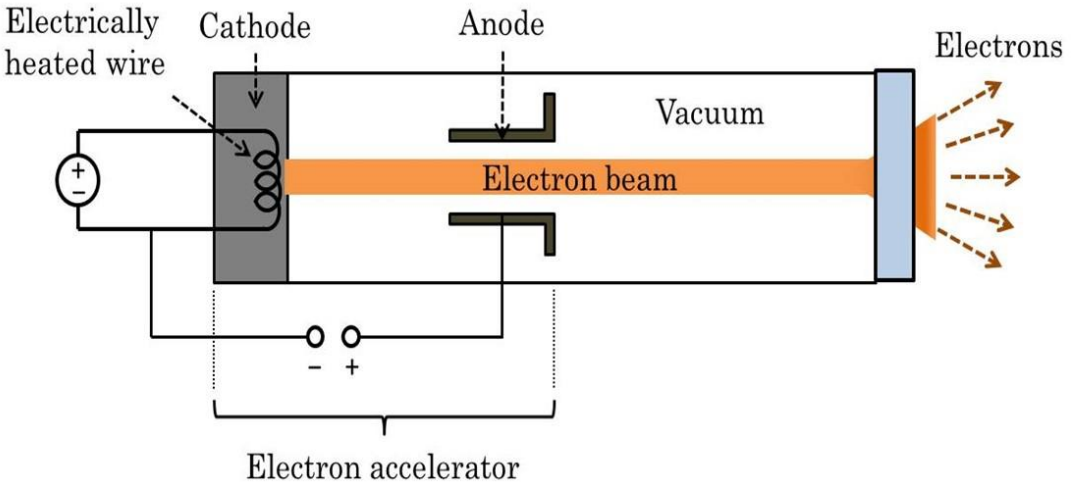

Figure 3.23 - Schematic representation of an Electron beam.

The electron beam source consists of a cylindrical hollow-cathode discharge held a few hundred volts negative with respect to a semi-transparent anode. In an electron beam method, the electrons are accelerated by high voltage in a vacuum region before being injected into a gas processing chamber thorough a thin foil window. This use of a direct high voltage to produce a high-energy electron beam allows the conversion of the input electrical power to beam power at greater than 95%. The energy of the electron beam is directly used for dissociation and ionization the background gas. The electrons released from the beam impact the neutral gas molecules generating the avalanche of electrons and ions that form the plasma. During the ionization by the beam, a shower of ionization electrons is

generated, which further produce a limited volume of plasma. The plasma source region is largely limited to the beam volume, which is particularly well-defined when the beam is magnetically collimated. Essentially, a beam-driven plasma can be viewed as a flowing afterglow, where outside the beam volume, the plasma density and ion composition are almost exclusively determined by diffusion and gas-phase reactions.

MICROWAVE

In addition to both DC and AC techniques, the non-thermal can be generated by RF/microwave. Viewed by a microwave/RF applicator, a plasma is seen as an electrically conductive body. As such, the energy contained in the field is transferred to sustain the plasma. The microwave discharge operates at very high frequencies (0.3-10 GHz) in the range of microwaves, with which only light electrons can follow the oscillations of the electric field. Therefore, this discharge is far from local thermodynamic equilibrium and can be operated in a wide pressure range. Most microwave-induced plasmas are produced in a waveguide structure or resonant cavity, where the microwaves meet the gas which is contained in a gas chamber often made of a dielectric material, such as quartz.
An example of a waveguide-based microwave configuration is shown in Figure 3.24.

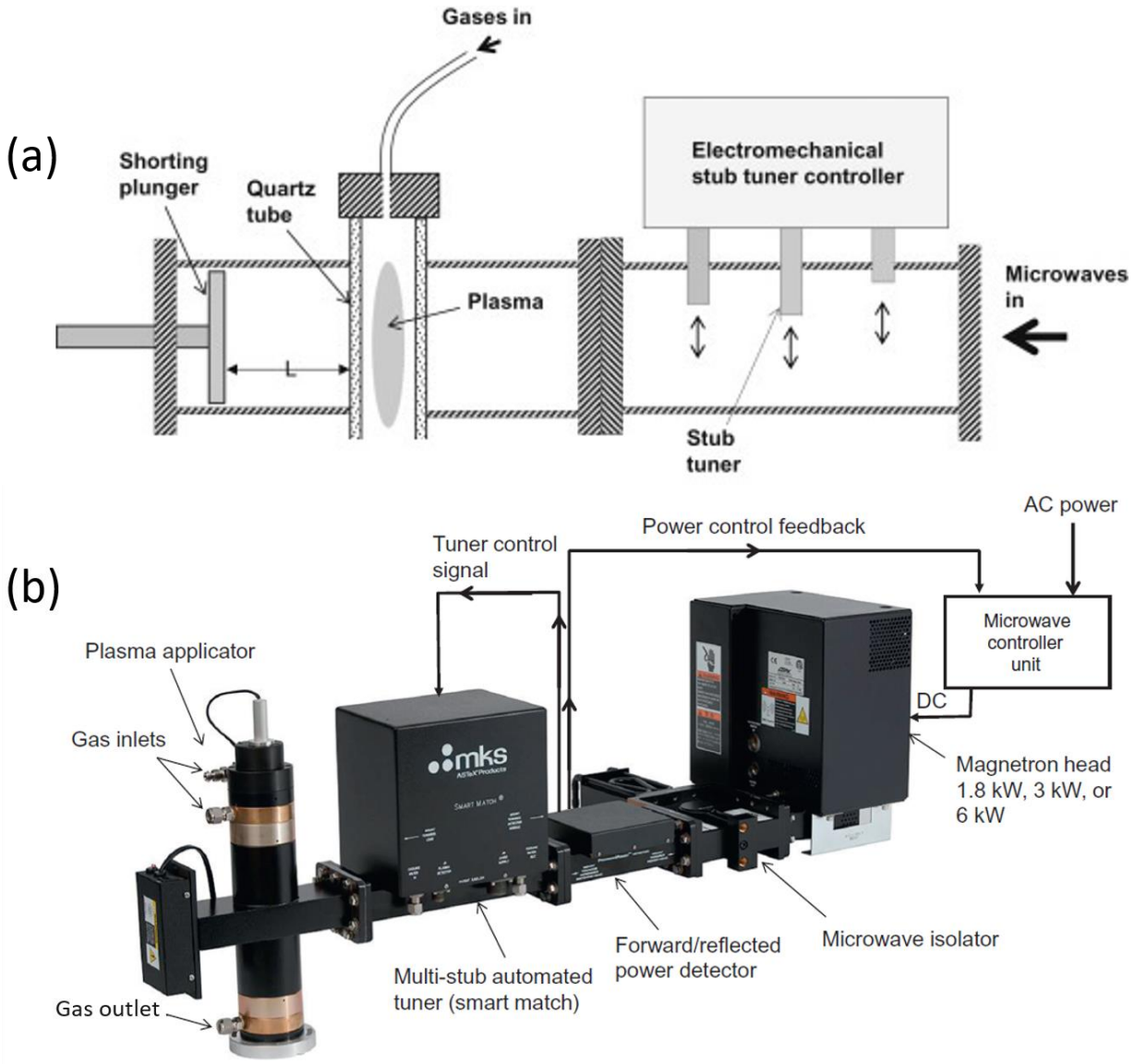

Figure 3.24 - Waveguide-based microwave configuration: a schematic representation (a) and assembled picture (b)[150].

Microwaves are fed from the left, while the gas from the top in Figure 3.24. The plasma is formed in the dielectric tube and its intensity is controlled by the stub tuner controller. Plasmas present a challenge in manual tuning and matching of such system, therefore an automated tune/match system is necessary. A shorting plunger, as shown, is also helpful in aiding the automated matching system. As the dimensions of the cavities diminish when the frequency increases, the maximum microwave frequencies used for discharge applications are usually below 3 GHz. A very common frequency is 2.45 GHz, which is also used in microwave ovens. The performance of microwave discharge mostly depends on the type of microwave power applicators. The microwave generator, driven by a high voltage power supply, produces microwave power via a magnetron. To protect this magnetron from

the damaging effects that reflected power may have, an isolator is needed to allow the microwave power to pass from the generator to the load but not to return to the main source.

3.2Plasma Chemistry

In Section 3.1, the physics of the plasma has been described. The mean characteristic of the non-thermal plasma is the high concentration of free electrons and ions in non-equilibrium that constitute the ionized gas. The gas ionization can be achieved and sustained as the effect of an external field that promotes the gas breakdown. Under the breakdown condition, the energy of electrons is high enough to collide effectively with neutral particles to produce ions, electrons and/or photons. Neutral atoms/molecules thus can either absorb or emit energy to produce excited or charged species (ions). Both excited species and ions have an energy level different from the neutral species and thus they are also more chemically reactive. These species can interact with electrons, excited species, ions or neutral particles promoting chemical reactions that are unfavoured at room temperature and pressure. As in the case of thermochemical reactions, the higher is the energy provided to the reagents, the higher is the probability to obtain the activated complex that are the precursors of the chemical products; also in plasma chemistry, the energy provided in a form of electron energy is proportional to the ions and electrons concentration and thus it is proportional to the reaction yield. The yield of a total plasma-chemical process is due to synergistic contributions of numerous different elementary reactions taking place simultaneously in a discharge system. The extremely high chemical activity of plasmas is based on a high and often super-equilibrium concentration of active species. The active species generated in plasma include chemically aggressive atoms and radicals, charged particles (electron and ions), and excited atoms and molecules. Elementary processes of atoms and radicals are traditionally considered in frameworks of chemical kinetics elementary processes of charged particles. In plasma chemistry, almost the totality of chemical reactions is via electrons or excited/ionized particles [148].

The most common kinds of reactions can be achieved in plasma chemistry are listed in Table 3.3.

Type	Reaction	#
Ionization	$e^- + A_2 \rightarrow A_2^+ + e^-$	*(PR1)*
Dissociative Ionization	$e^- + A_2 \rightarrow A^+ + A + 2\,e^-$	*(PR2)*
Attachment	$e^- + A_2 \rightarrow A_2{}^-$	*(PR3)*
Dissociative Attachment	$e^- + A_2 \rightarrow A^- + A$	*(PR4)*
Excitation	$e^- + A_2 \rightarrow A_2^* + e^-$	*(PR5)*
Photoexcitation	$hv + A_2 \rightarrow A_2^*$	*(PR6)*
Excited ionization	$e^- + A_2^* \rightarrow A_2^+ + 2\,e^-$	*(PR7)*
Photoionization	$hv + A_2 \rightarrow A_2^+ + e^-$	*(PR8)*
Surface Ionization	$hv + S \rightarrow S^+ + e^-$	*(PR9)*
Penning ionization	$M^* + A_2 \rightarrow A_2^+ + M + e^-$	*(PR10)*
Associative ionization	$A + B \rightarrow AB^+ + e^-$	*(PR11)*
Charge transfer	$A^\pm + B \rightarrow A + B^\pm$	*(PR12)*
Dissociative electron-ion recombination	$e^- + AB^+ \rightarrow (AB)^* \rightarrow A + B^*$	*(PR13)*
Three-body electron-ion recombination	$2\,e^- + A^+ \rightarrow A^* + e^-$	*(PR14)*
Radiative electron-ion recombination	$e^- + A^+ \rightarrow A^* \rightarrow A + hv$	*(PR15)*
Ion-ion associative recombination	$A^+ + B^- \rightarrow AB$	*(PR16)*
Ion-ion recombination	$A^+ + B^- \rightarrow A^* + B$	*(PR17)*
Three-body ion-ion recombination	$A^+ + B^- + M \rightarrow A + B + M$	*(PR18)*
Three-body neutral association	$A + B + M \rightarrow AB + M$	*(PR19)*

Table 3.3 - Most common plasma reactions: electron/molecular reactions, atomic/molecular reactions, decomposition and synthesis.

In Table 3.3, the electrons are represented as e^-, A and B are neutral atoms, S is the electrode surface, M is an inert atom/molecule that participates to the reaction, known as "third body", + and – indicate ions with their respective charge symbols, and * indicates an excited or radical species.

The key process in plasma is ionization, which means the conversion of neutral atoms or molecules into electrons and positive ions. Thus, ionization is the first elementary plasma-chemical processes to be considered. The rates of such processes depend on how many electrons have enough energy to do the job. It can be described through the electron energy distribution function (EEDF), which is proportional to the electron temperature. Numerically, in most plasmas under consideration, the mean electron energy is from 1 to 5eV; in rare cases is higher than 5 eV and however lower than 10 eV. In

non-thermal plasma the positive ions rarely are multi-charged, thus their charge is usually equal to +1e ($1.6 \cdot 10^{-19}$C). Usually, the number densities of electrons and positive ions are equal or close in quasi-neutral plasmas, but in "electronegative" gases (like O_2, Cl_2, SF_6, etc.) with high electron affinity, negative ions are also effectively formed.

Negative ions are formed mainly by the attachment reactions, which consists of the generation of a negative ion from an electron and a neutral atom/molecule. Electron attachment leads to the formation of negative ions with charge –1e ($1.6 \cdot 10^{-19}$C). Attachment of another electron and formation of multi-charged negative ions is extremely rare in the gas phase because of electric repulsion. Although the energy distribution functions for negative ions is similar to that for the positive ones, that for ionization reaction is slightly higher. The ionization occurs with a high efficiency near the cathode where the electric field strength is higher; while the attachment becomes relevant in the proximity of the anode where the electron energy decreases and the probability to produce a negative ion increases.

Mechanisms of ionization can be very different in different plasma-chemical systems and it may be subdivided generally into the following five groups:

i. direct ionization by electron impact;
ii. stepwise ionization by electron impact;
iii. ionization by the collision of heavy particles;
iv. photo-ionization;
v. surface ionization.

In the case of direct ionization, the electrons have energy high enough to provide the ionization act in one collision. The ions can be generated according to the plasma reactions (PR1)-(PR4) in Table 3.3, e.g. These processes are the most important in cold or non-thermal discharges, where electric fields and therefore electron energies are quite high, but where the excitation level of neutral species is relatively moderate.

When the density of electrons is greatly higher than the density of neutral atoms/molecules, the probability to produce excited neutral species is quite high, as in the plasma reaction (PR6). The excited species can then be ionized by electron impact (PR7). This mechanism is known as "stepwise ionization by electron impact".

The ionization may occur by the collision of heavy particles as in the reactions (PR10) - (PR12). The ionization occurs as the total energy of the collision partners exceeds the ionization potential.

The chemical energy of colliding neutral species can also contribute to ionization in the so-called associative ionization processes.

Photo-ionization takes place in collisions of neutral species with photons, which result in the formation of an electron-ion pair (PR8). Photo-ionization has a great interest in the propagation of non-thermal plasma discharges such as streamers.

Surface ionization or electron emission is provided by electron, ion, and photon collisions with different surfaces or simply by surface heating (PR9). Surface ionization is most important at the beginning of the gas ionization as it contributes to the generation of free electrons from neutral particles. Surface ionization is crucial in gas ionization starting from the gas free of space charges.

Ion species have an energy that is always higher than neutral particles, thus they are the major players in plasma chemistry. Being the ionization the most probable electron/molecule reaction, a high concentration of positive ions can be found in non-thermal plasma. Their exothermic reactions with neutrals usually have no activation energy, which makes their contribution significant in many specific plasma-chemical processes. In addition to high chemical activity, the ions can have significant kinetic energy that leads to a fast conversion to species having a lower level of energy. Positive ions can recombine with electrons in high exothermic processes. The most common recombination paths are:

- dissociative electron-ion recombination;
- three-body electron-ion recombination;
- radiative electron-ion recombination.

The dissociative electron-ion recombination is the fastest electron neutralization mechanism in molecular gases. The different polarity of electron and ion encourage the recombination. The recombination establishes the neutrality of the intermediately formed molecule ion, with a high energy level. The high energy content leads to the dissociation of the molecule (PR13).

When the electron effectively collides atomic positive ions, the recombination occurs. The excess of energy, from the recombination, is going into the kinetic energy of a free electron which participates in recombination act as “a third-body partner” (PR14). The energy excess can also be emitted in a form of photons as the effect of the electron-ion recombination (PR15).

The positive ions can also recombine with negative ions, forming a neutral molecule (PR16) or transferring the charge without atomic recombination. The energy can go into electronic excitation

of a neutral product (PR17) or into a third body that participates to the reaction (PR18). Lastly, neutral particles can associate without ionization or excitation as in (PR19).

The elementary reactions proposed in Table 3.3 represents the process of elementary charged particles that are the fundament of the plasma chemistry. Being the energetic level of high-vibrational electrons, ions, excited species and radicals, higher than their fundamental state, these species are extremely reactive. They tend to react either with neutral particles or high-content energetic particles, reducing their internal energy. The sequence of transformations of initial chemical substances and electric energy into products and thermal energy is usually referred to as the mechanism of the plasma chemistry. Elementary reaction rates are determined by the micro-kinetic characteristics of individual reactive collisions (like, for example, reaction cross sections or elementary reaction probabilities) as well as by relevant kinetic distribution functions (like the electron energy distribution function [EEDF], or population function of excited molecular states).

The elementary reaction rate is a result of the integration of the reaction cross-section or probability over the relevant distribution function and characterizes the energy or excitation state of reactants. If on one hand, the chemical reaction rates give information about the velocity and the contribution of a reaction participating in a complex mechanism of reactions in a macroscopic view, the cross-section is an atomic-scale analysis that suggests what happens when a reaction occurs. Cross-sections in chemical reactions or scattering is a factor which measures the likelihood of the event when a particular species approach another in a specified way. If we consider for example the ionization reaction (PR1), that is the most common in plasma chemistry, the electron, having kinetic energy greater than the ionization energy, causes an effectiveness reaction that produces a positive ion with the realising of an electron. In a probabilistic view, the ionization event is a statistical process that is summarized in terms of how far an electron travels on average before it takes part in an ionizing collision; this is called the mean free path for ionization. It can be described by considering a volume containing atoms/molecules of the same species, as it is shown in Figure 3.25.

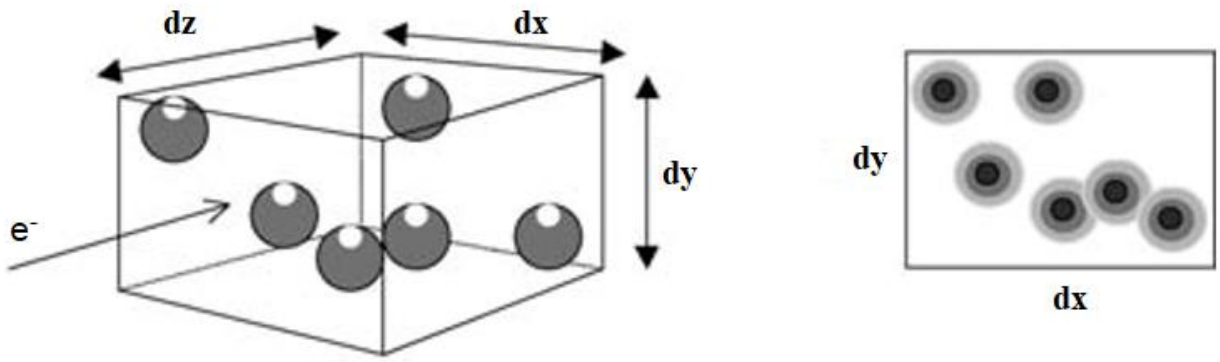

Figure 3.25 - Electron impact in a volume xyz (left) and impact cross-section area (right).

Suppose the volume $dV=dx\cdot dy\cdot dz$, shown in Figure 3.25, contains only atoms/molecules with a density n_g. The electron travels into the volume measuring $dx\cdot dy$ in cross-sectional area, by dz in depth. The number of target atoms of gas in the volume is $n_g\cdot dV$. Each target appears to have a cross-sectional area σ_i, obstructing the electron path. The quantity σ_i conveniently describes the probability of ionizing collisions between the atom/molecule and the electron. For one particular energy of the electron, the whole of the section $dx\cdot dy$ will be obscured by the cross-section of the atoms/molecules and the impact cross-section can be calculated as $\sigma_i=dx\cdot dy/n_g dV$, where dz is equal to the mean free path of the electron.

The ionization impact can be represented as in Figure 3.26

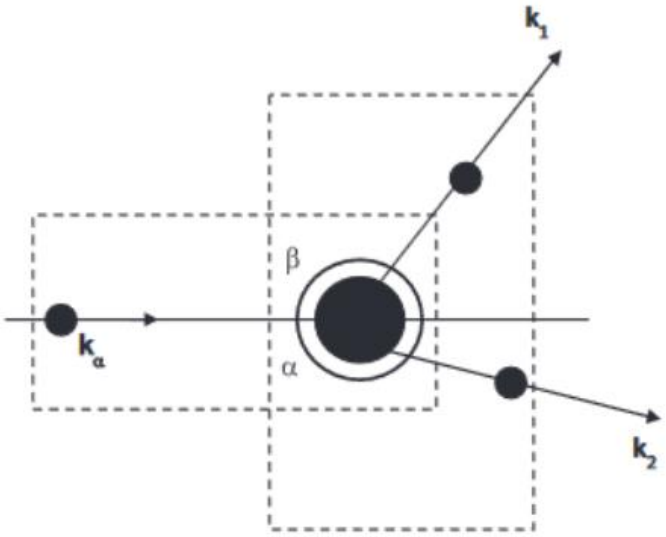

Figure 3.26 - Schematic diagram of the electron collision with a particle, causing the ionization [151].

The incident electron, with momentum represented by the vector k_α, hits the target which is initially in a state α, leaving behind the target in state β and two electrons leaving the interaction zone with

momentum k_1 and k_2, respectively. Accounting for exchange, the spin averaged total ionization cross-section as a function of energy E, $\sigma_{\alpha\to\beta}(E)$, has the form [152]:

$$\sigma_{\alpha\to\beta}(E) = \int_0^{E_{max}} dT_2 \int d\omega_1 d\omega_2 \frac{k_1 \cdot k_2}{4\pi \cdot k_\alpha} \left| f_\beta^{av}(\omega_1, \omega_2, \omega_1 T_2 \right|^2 \qquad \textit{(Eq. 3-11)}$$

where ω_1 and ω_2 are the unit vectors in the direction of respectively k_1 and k_2, T_2 is the energy of the ejected electron and E_{max} is equal to $(E-E_\beta)/2$ where E_β is the energy of the target after the collision when it misses one electron.

Once the reaction cross-section and the distributions are known, they give the rate constant. If the cross-section for a reaction is understood, the reaction is understood [153]. Due to the presence of high energy electrons, in gas discharge, and the low ionization degree, electrons are not at thermodynamic equilibrium with the surrounding gas and obey their own energy distribution function. The latter allows relating the electron mean energy ε_e to the electronic temperature:

$$\varepsilon_e = \frac{3}{2} k_B T_e \qquad \textit{(Eq. 3-12)}$$

where k_B is the Boltzmann constant and T_e is the electronic temperature. Electrical transport properties depend on the electron mean energy. The latter also strongly affects the rate of plasma reactions. The electron energy distribution function and mean energy can be calculated from collision cross-section data and solving the Boltzmann equation. The latter is computationally demanding. As it was explained in the work of Hagelaar and Pitchford [154], a common approach to avoid excessive calculation time is to solve an approximation of the Boltzmann equation for a number of values of the reduced electric field θ and to generate tables of the resulting transport properties and rate coefficients versus the reduced electric field

However, when different reactions occur in a complex plasma chemistry mechanism, the cross-section analysis is extremely complex and the overall reaction rates are thus commonly used.

NO_X conversion in Nitrogen Plasma Chemistry

The kinetic mechanism in an ionized gas subject to a high-intensity electric field is very complex. A high number of reactions involving neutral particles, electrons, ions and radicals occur. Thousands of reactions can be found for the most common ionized gas mixtures. Van Gaens and Bogaerts [155] have made a collection of 1880 reactions with their rate constants and/or cross-sectional data for

atmospheric pressure argon, nitrogen, oxygen and moisture; while a detailed network of reactions for the non-equilibrium discharge in nitrogen-oxygen mixtures can be found in the previous work of Kossyi et al. [156].

With regard to atmospheric nitrogen discharge, Moravej et al. [157] have proposed the following mechanism for the Nitrogen non-thermal plasma at atmospheric pressure:

Reaction	**Rate coefficient** $[cm^3 molecule^{-1} s^{-1}]$	**#**
$N_2 + e^- \rightarrow 2\,N + e^-$	$6.3 \times 10^{-6} {T_e}^{-1.6} e^{-9.8/T_e}$	*(R3-1)*
$N_2 + e^- \rightarrow N_2^+ + 2\,e^-$	$4.7 \times 10^{-13} \sqrt{T_e}(1 + 0.13T_e) e^{-15.7/T_e}$	*(R3-2)*
$N_2 + e^- \rightarrow N^+ + N + 2\,e^-$	$4.0 \times 10^{-14} \sqrt{T_e}(1 + 0.08T_e) e^{-25.5/T_e}$	*(R3-3)*
$N_2 + e^- \rightarrow N^* + N + e^-$	$2.6 \times 10^{-15} \sqrt{T_e}(1 + 0.15T_e) e^{-13.3/T_e}$	*(R3-4)*
$N_2 + e^- \rightarrow N_2(A) + e^-$	$5.8 \times 10^{-13} \sqrt{T_e}(1 + 0.29T_e) e^{-7.1/T_e}$	*(R3-5)*
$N^+ + e^- \rightarrow N + hv$	$1.0 \times 10^{-12} \left(\frac{T_e}{T_g}\right)^{-0.70}$	*(R3-6)*
$N_2^+ + e^- \rightarrow N^* + N$	$2.0 \times 10^{-7} \left(\frac{T_e}{0.03}\right)^{-0.39}$	*(R3-7)*
$N_3^+ + e^- \rightarrow N^* + N_2$	$3.0 \times 10^{-7} \left(\frac{T_e}{0.03}\right)^{-0.40}$	*(R3-8)*
$N_4^+ + e^- \rightarrow N_2(A) + N_2$	$6.0 \times 10^{-7} \left(\frac{T_e}{0.03}\right)^{-0.40}$	*(R3-9)*

Table 3.4 - Nitrogen non-thermal plasma at atmospheric pressure kinetic scheme, proposed by Moravej et al. [157].

The model in Table 3.4 considered the most relevant nitrogen chemical reactions and define the kinetic rate constants as a function of the electronic temperature T_e [K] and the gas temperature T_g [K].

In the following years, De Wilde et al. [158] proposed a more complex model that is reported in Table 3.5.

Reaction	Rate coefficient	Unit	#
$N_2 + e^- \rightarrow N_2(A) + e^-$	$2.4 \times 10^{12-140/\theta}$	$m^3 kmol^{-1} s^{-1}$	*(R3-10)*
$N_2 + e^- \rightarrow N_2(a) + e^-$	$1.9 \times 10^{12-174/\theta}$	$m^3 kmol^{-1} s^{-1}$	*(R3-11)*
$N_2 + e^- \rightarrow N_2(B) + e^-$	$3.8 \times 10^{12-148/\theta}$	$m^3 kmol^{-1} s^{-1}$	*(R3-12)*
$N_2 + e^- \rightarrow N_2(C) + e^-$	$3.8 \times 10^{12-211/\theta}$	$m^3 kmol^{-1} s^{-1}$	*(R3-13)*
$N_2 + e^- \rightarrow 2\,N + e^-$	$3.8 \times 10^{10-350/\theta}$	$m^3 kmol^{-1} s^{-1}$	*(R3-14)*
$N_2 + e^- \rightarrow N_2^+ + 2\,e^-$	$3.0 \times 10^{12-365/\theta}$	$m^3 kmol^{-1} s^{-1}$	*(R3-15)*
$N_2(A) + N_2(a) \rightarrow N_4^+ + e^-$	5.4×10^9	$m^3 kmol^{-1} s^{-1}$	*(R3-16)*
$2\,N_2(a) \rightarrow N_4^+ + e^-$	6.0×10^9	$m^3 kmol^{-1} s^{-1}$	*(R3-17)*
$2\,N \rightarrow N_2^+ + e^-$	6.0×10^8	$m^3 kmol^{-1} s^{-1}$	*(R3-18)*
$N_4^+ + e^- \rightarrow 2\,N_2$	$1.9 \times 10^{14}\sqrt{1/T_e}$	$m^3 kmol^{-1} s^{-1}$	*(R3-19)*
$N_2^+ + e^- \rightarrow 2\,N$	$1.5 \times 10^9\sqrt{1/T_e}$	$m^3 kmol^{-1} s^{-1}$	*(R3-20)*
$2\,N + N_2 \rightarrow 2\,N_2$	$5.0 \times 10^{13} e^{(500/T_g)}$	$m^3 kmol^{-1} s^{-1}$	*(R3-21)*
$N_2(A) + N_2 \rightarrow 2\,N_2$	2.2×10^5	$m^3 kmol^{-1} s^{-1}$	*(R3-22)*
$N_2(A) + N \rightarrow N_2 + N$	1.2×10^{10}	$m^3 kmol^{-1} s^{-1}$	*(R3-23)*
$N_2(B) + N_2 \rightarrow N_2(A) + N_2$	3.0×10^{10}	$m^3 kmol^{-1} s^{-1}$	*(R3-24)*
$N_2(B) \rightarrow N_2(A)$	1.5×10^5	$1/s$	*(R3-25)*
$N_2(a) + N_2 \rightarrow N_2(B) + N_2$	1.2×10^8	$m^3 kmol^{-1} s^{-1}$	*(R3-26)*
$N_2(C) \rightarrow N_2(B)$	3.0×10^7	$1/s$	*(R3-27)*
$N_2(C) + N_2 \rightarrow N_2(a) + N_2$	6×10^9	$m^3 kmol^{-1} s^{-1}$	*(R3-28)*
$N_2^+ + 2\,N_2 \rightarrow N_4^+ + N_2$	1.8×10^{13}	$m^6 kmol^{-2} s^{-1}$	*(R3-29)*
$N_4^+ + N_2 \rightarrow 2\,N_2 + N_2^+$	$1.5 \times 10^6 10^{0.0036(T_g-300)}$	$m^3 kmol^{-1} s^{-1}$	*(R3-30)*

Table 3.5 - Nitrogen non-thermal plasma at atmospheric pressure kinetic scheme, proposed by De Wilde et al. [158].

where θ is the reduced electric field (Td=10^{-21}Vm^2). The electron energy distribution can be calculated from collision cross-section data available in the literature [159] and solving the Boltzmann equation as described in the previous section. The units of the reaction rate coefficients depend on the order of the reaction, by considering the power-law equation.

According to Zhu et al. [160], the chemical reactions in a NO/N_2 non-thermal plasma system can be summarized as in Table 3.6:

Reaction	**Rate coefficient** $[cm^3 molecule^{-1} s^{-1}]$	at 298K	**#**
$N_2 + e^- \rightarrow N_2(a'1\Sigma_u^-) + e^-$			*(R3-31)*
$N_2(a'1\Sigma_u^-) + NO \rightarrow N + O + N_2$			*(R3-32)*
$N + NO \rightarrow N_2 + O$	$8.2 \times 10^{-11} e^{-3409/RT_g}$	2.1×10^{-11}	*(R3-33)*
$O + NO \rightarrow NO_2$	$3.02 \times 10^{-11} (T_g/298)^{-0.75}$	3.0×10^{-11}	*(R3-34)*
$O + NO_2 \rightarrow NO + O_2$	$6.51 \times 10^{-12} e^{998/RT_g}$	9.7×10^{-12}	*(R3-35)*
$N + NO_2 \rightarrow N_2O + O$	$5.8 \times 10^{-12} e^{1829/RT_g}$	1.2×10^{-11}	*(R3-36)*
$O + O_2 + M \rightarrow O_3 + M$	$5.6 \times 10^{-34} (300/T_g) 2.23[M]$	$1.3 \times 10^{-33}[M]$	*(R3-37)*
$NO + O_3 + M \rightarrow NO_2 + O_2 + M$	$1.0 \times 10^{-31} (300/T_g) 1.6[M]$	$1.3610^{-31}[M]$	*(R3-38)*
$O + O_3 \rightarrow 2\ O_2$	$8.0 \times 10^{-12} e^{-2060/T_g}$	8.0×10^{-15}	*(R3-39)*

Table 3.6 - NO in nitrogen non-thermal plasma at atmospheric pressure kinetic scheme [160].

R is the gas constant, that is proportional to the Boltzmann constant, expressed in $Jmol^{-1}K^{-1}$.

In nitrogen plasma, the NO dissociates in nitrogen and oxygen radicals as the reaction with either molecular and atomic nitrogen. The oxygen produced has a high oxidant capacity and oxidize NO to NO_2 mainly. It can also convert to O_2 according to (R3-35). Because of back conversion of NO_2 to NO by the atomic oxygen in (R3-35), not much NO_2 could be produced in the NO/N_2 system. Although the high reactivity of oxygen, the oxidated species are limited if the NO concentration is low, and they are proportional to the oxygen fed in the form of nitrogen oxide. For a very dilute concentration of NO in N_2, the kinetic energy of the electrons is deposited primarily into the major gas component, that is, nitrogen molecule. The most useful depositions of electron energy are the electron impact dissociation and excitation of N_2. Reaction (R3-33), in fact, is the primary elemental reaction for NO conversion in NO/N_2 system, and thereby, the concentration of NO converted depends on atomic nitrogen production yield and NO initial concentration. Penetrante et al. [106] calculated the production yield of atomic nitrogen as a function of the reduced electric field (θ = E/n) in gas discharges, based on experimental studies of N_2–electron interactions. For N_2 and airlike mixtures, the effective E/n is around $150\times10^{-17}Vcm^2$, which corresponds to an electron mean energy of about 4eV. For the electron impact dissociation of nitrogen (R3-14), Penetrante et al. [106] also calculated the number of dissociations and the rate coefficient in the function of the reduced electric field.

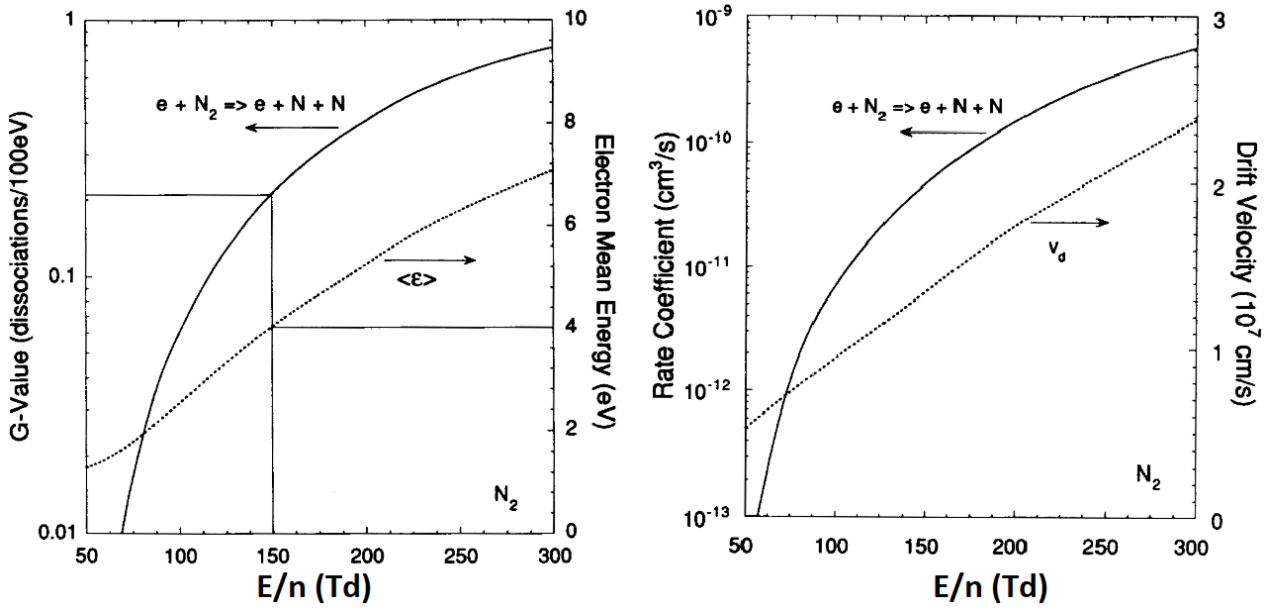

Figure 3.27 - Calculated G-value (left) and rate coefficient (right) for the electron impact dissociation of nitrogen in the function of the reduced electric field E/n [106].

Referring to the electron-impact dissociation of N_2, the G-Value corresponds to the number of dissociations per 100eV of energy input and it is proportional to the reduced electric field as well as the electron mean energy, as it is shown in Figure 3.27 (left). Also, the calculated N_2 electron-impact dissociation rate (in units $cm^3molecule^{-1}s^{-1}$) and the electron drift velocity in N_2 are proportional to the reduced electric field, as it is shown in Figure 3.27 (right). The data calculated by Penetrante et al. [106] have been validated from many authors in the following years for electron-impact dissociation of N_2 and could be used to infer the effective electron mean energy in an N_2 discharge plasma at atmospheric pressure. The rate coefficient for the reaction(R3-14) in table Table 3.5 (De Wilde et al. [158]) agrees with the data reported in Figure 3.27. For the reduced electric field of 150Td, e.g. the calculated rate constant from Table 3.5 is $1.76\times10^{8}m^3kmol^{-1}s^{-1}$ that correspond to $2.93\times10^{-11}cm^3molecule^{-1}s^{-1}$. Penetrante et al. obtained a NO_x reduction of about 100% in a DBD reactor at the input energy density of 100J/L; thus, almost the totality of the N radicals, resulting from the dissociation of N_2, is consumed predominantly by the reaction with NO molecules (R3-33) [106]. Among the NO_x species produced in the NO/N_2 plasma, there is N_2O that is a byproduct of NO conversion and is produced via (R3-36).

If the gas contains an initial concentration of O_2 different from zero, the generation of atomic oxygen is enhanced. A complex kinetic mechanism of 71 reactions for an $N_2/O_2/NO_x$ gas mixture atmospheric plasma has been proposed by Stefanović et al. [161]. With the increase in O_2 concentration, more

oxygen molecules would compete with nitrogen molecules for electrons and (R3-34) or (R3-38) becomes gradually dominant which would increase NO_2 selectivity, and hence the decrease of NO conversion to N_2 via *(R3-33)*. However, as we can see from the rates of *(R3-37)* and *(R3-39)* in Table 3.6, the formation of O_3 decreases a lot with the increase in temperature and the decomposition of O_3 to O_2 becomes significant as the temperature increases. Similar results were observed by Yan et al. [162]. They have found that the reduction process can be negligible if O_2 concentration is higher than 3.6%, which means that NO is completely converted into NO_2. This is due to the lower dissociation energy of O_2 (4.8 eV) than that of N_2 (9.2 eV). For common atmospheric pressure electrical discharge plasma, the average electron kinetic energy is relatively low (3–6 eV); under this condition, the rate for electron-impact dissociation of O_2 is much higher compared to that of N_2 as shown in Figure 3.28.

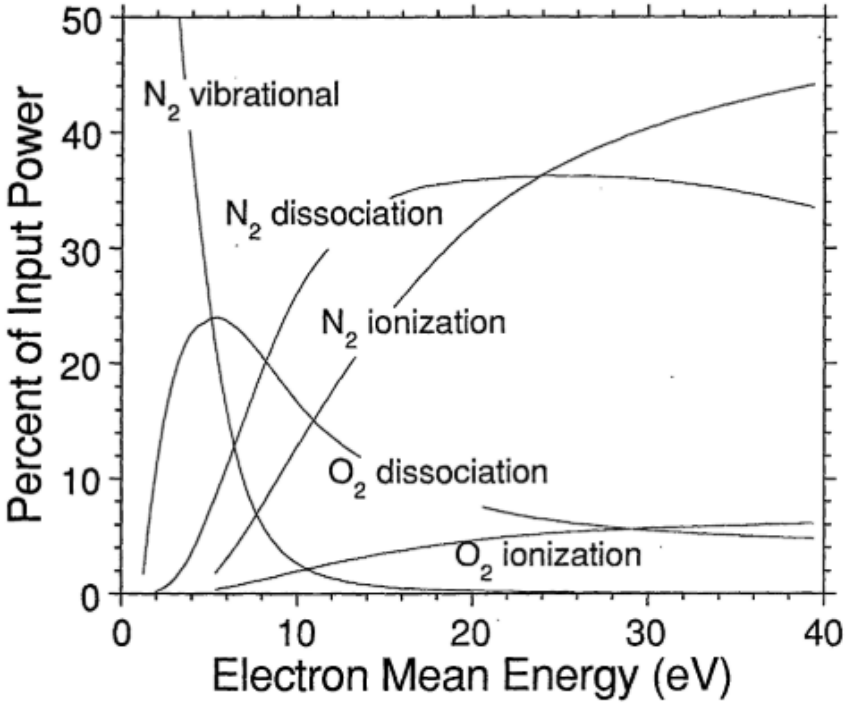

Figure 3.28 - Percentage of Input power consumed in the electron-impact processes leading to vibration excitation, dissociation and ionization of N_2 and O_2 in atmospheric-pressure dry air discharge [163].

From Figure 3.28, a large fraction of the input power is wasted in vibrational excitation of N_2 and a significant fraction goes into dissociation of O_2, in the range of 3-6eV (110-220Td). Only if the electron mean energy overtakes 9eV, the N_2 dissociation becomes favoured than O_2 dissociation, and when the electron mean energy reaches 11eV the N_2 ionization become favoured than O_2 dissociation too.

3.3Most innovative non-thermal plasma applications

Non-thermal plasma has been widely used for almost two hundred years. The first industrial applications of plasma electrical discharge were initiated by the brothers Siemens-Werner and William, who built the first ozonizer (1857) and the electric arc furnace (1878) [164]. So far, it is possible to state that plasma physics underlies numerous industrial applications and technological devices, including, selective inactivation of unhealthy cells, virus destruction, microelectronics, gas discharge lamps, water treatment, air cleaning (ESP, WESP, odour and VOC abatement), etc. Further the direct applications, the NTP has been also applied to catalyzed processes. The combination of Non-thermal plasma and heterogeneous catalysis is known as plasma catalysis. It represents a promising and emerging technology for environmental cleanup, energy conversion, and the synthesis of fuels and chemicals at ambient pressure and low temperatures. As an environmentally friendly new technology, NTP has been studied and successfully applied to limit the increasingly environmental pollutant emissions.

BIOCHEMICAL APPLICATIONS

Non-thermal plasma represents an effective source of oxidizing species which are able to kill micro-organisms without the use of high temperature or chemicals, moreover to destroy and decompose the micro-organisms. The first use of this technology in a medical device application occurred in 1995: it involved surface modification techniques and sterilization.

Sterilization of medical instruments contaminated with pathogens is a crucial step in preventing health risks. However current sterilization methods still have some disadvantages and bacterial spores and prions can easily resist against chemicals or physical treatments. For example, even if UV treatment is fast, low cost with no toxic residues and involves low temperatures, at the same time its efficiency of sterilization is poor and may damage the material. As well, chemical treatments are low temperature and effective, but involve the use of toxic gases that might be carcinogenic and flammable or induce unwanted biochemical changes. Therefore, plasma treatment is willing to be a valid alternative sterilization method. This mechanism of sterilization is based on the interaction between the reactive species generated in the plasma, such as oxygen radicals, with the cell walls or the DNA material of the germs. Many studies have investigated the germicidal power of NTP in atmospheric pressure [165]–[167]. Microbial decontamination is considered as the decomposition or removal of microorganisms, i.e., viruses, bacteria and fungi; prions are also included. The method of exposure may be direct, where the sample is in direct contact with the plasma, or semidirect, where

the sample is placed out of reach of short-living reactive species. In basic research, indirect exposure may also be interesting, where the discharge is closed in a transparent chamber, so the effect is caused by irradiation only. The microbicidal effect may be also “saved” in a medium, e.g., plasma-activated water. Two examples of the plasma effect on cells are shown in Figure 3.29.

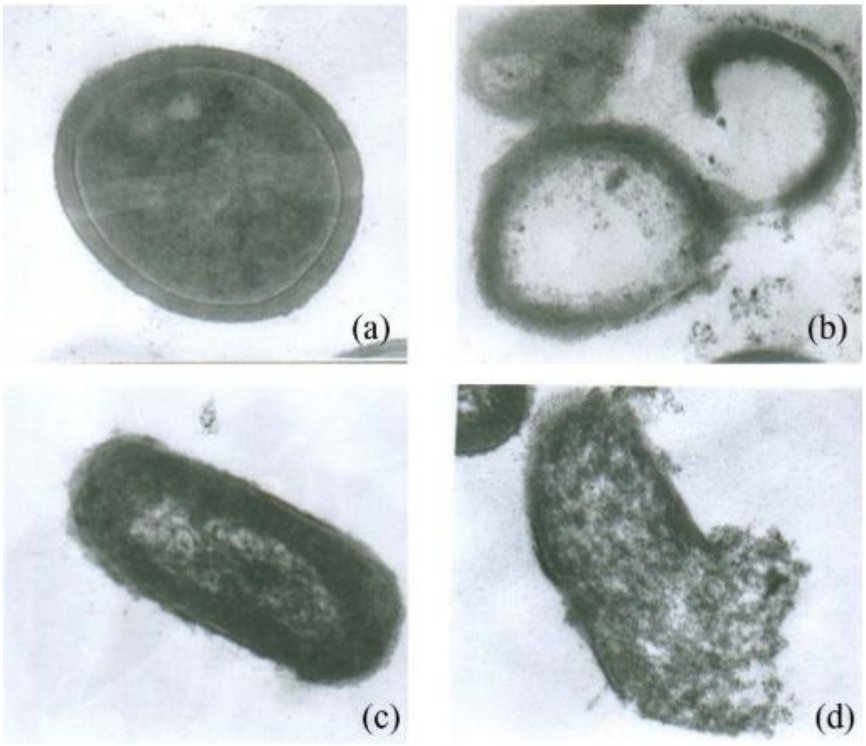

Figure 3.29 - TEM images before and after plasma treatment. S. aureus cells before plasma treatment (a) and after plasma treatment for 5s (b); E. coli cells before plasma treatment (c) and after plasma treatment for 5s (d) [165].

Before plasma treatment, the cell membrane was smooth, but after that, it turned significantly rough. It is clearly shown in Figure 3.29 that the membranes of both S. aureus and E. coli cells were ruptured, and some cytoplasm leaked outwards. From the TEM images, it is particularly intriguing that both the S. aureus and E. coli cells were killed by using atmospheric plasma.

NTP treatments have been investigated for coronaviruses also [168], [169]. Clack et al. attribute the bacteria and virus inactivation to either Reactive Oxygen Species (ROS), NO, NO_2, O_3 produced by the NTP. In particular, they found that the direct plasma is more effective than indirect plasma due to the high number of radicals and excited species with a low lifetime (O*; OH*; OH^-); However, the NTP power and the gas residence time must be controlled to reduce the emission of "stable" pollutants species (e.g. NO, NO_2, O_3). In such cases, a filter must be used to control their emission due to their dangerousness. Clack, for example, used an activated carbon filter at the NTP reactor outlet to control the emission of NO/NO_2, O_3 concentrations below the 500 ppb and 100 ppb respectively.

In 2020, many companies produced devices able to clean air from COVID-19. The company Jonixair e.g. has developed air filtration and sanitation devices with NTP technology, which are used for purification and decontamination of air and surfaces in all aeraulic systems.

Figure 3.30 - NTP-based device for air filtration and sanitation "Jonix cube", designed and produced by Jonixair S.r.l.

Jonix CUBE is a device that sanitises the air in the room in which it is located, eliminating bacteria, mould and viruses present in crowded but also domestic environments. This device uses an advanced oxidation process for the decontamination of air induced by non-thermal plasma. The department of Molecular Medicine of the University of Padua tested the NTP-technology used by Jonix CUBE devices; the results show that the device is capable of breaking down COVID-19, with a reduction of the viral load equal to 99.9999% in less than 30 minutes of exposure.

Another NTP application in the biochemical/biomedical field is the wound healing, especially for chronic wound, which can be infected with Staphylococcus, the most common detrimental bacteria hindering wound healing. The conventional effective therapy is to remove necrotic tissue and inactivate the microorganisms with antibacterial drugs. The use of NTP to treat chronic wounds is mainly based on its significant advantages in sterilization. Researchers show that a low dose of NTP treatment can induce the release of fibroblast growth factor 2 (FGF-2). It is an important signal for the growth factor of vascular endothelial and can induce the proliferation, migration and formation of endothelial cells [170].

PLASMA PRINTING

Besides paper, printing can be done on many other materials, like plastics, metal or glass. In the printing process of plastics, regardless of the substrate form (film, sheet or molded components), the ink does not penetrate the printing substrate but it is only fixed on its surface. As plastics are non-absorbent materials, the key determinant of printing is their surface free energy, which determines the wettability of the material and the adhesion of ink to the substrate.

Non-thermal plasma can modify the surface before the printing process or improve the print properties afterwards. Polymer ablation and grafting on polymer surfaces are the main two mechanisms of plasma treatment. Both processes run simultaneously, but to a different degree depending on the type of plasma, the material, and the conditions of the process. However, this treatment only affects the surface of the material; it is widely believed that changes are taking place in the top layer limited to 5-10 nm. Plasma activation used before the printing process is primarily intended to improve the hydrophilicity of the substrate and can be performed using such gases as He, Ar, N_2, NH_3, and O_2, etc. In addition, some types of plasma (e.g., Ar) can significantly change the roughness of the substrate [171].

The contact angle with water is the basic parameter used to assess the hydrophilicity or hydrophobicity of a material. In addition, its measurements are commonly used to evaluate the plasma activation of plastics. An example of Water Contact Angle (WCA) before and after the plasma jet modification is shown in Figure 3.31.

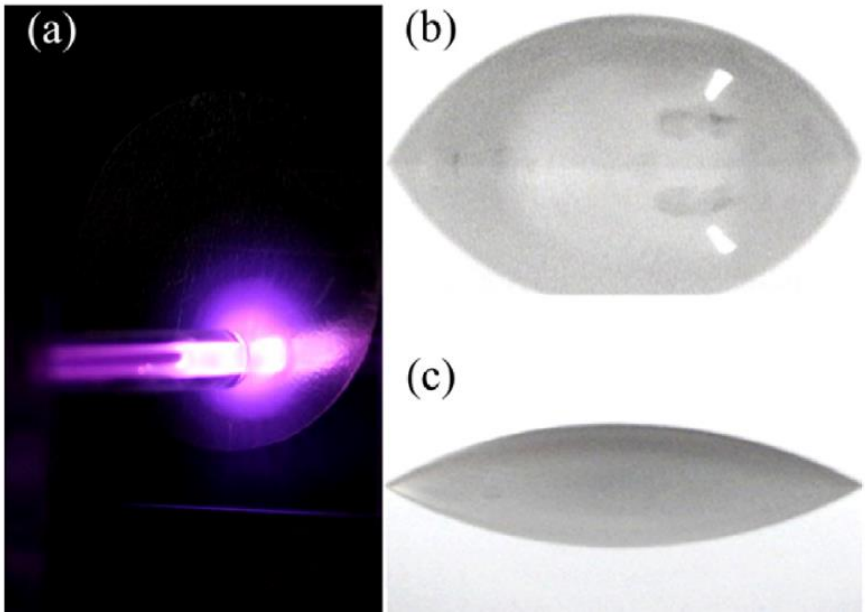

Figure 3.31 - Plasma jet picture (a); WCA before plasma jet modification (b), and after plasma jet modification (c) [172].

The WCA reduces as the effect of the plasma treatment. Materials for which the contact angle is less than 90° with water are considered to be hydrophilic and for values above, the material is said to be hydrophobic. The smaller the contact angle, the more easily the surface is wetted, and when the angle is close to 0°, the liquid properly dissolves over the surface [173]. In order to obtain high-quality prints, the surface of the substrate must be properly wetted by the ink that is available for the hydrophilic surface.

Chen et al. [174] noted as a result of activation of a polystyrene film with RF plasma with Ar that the contact angle of water was reduced from 88.9° to 14.3° degrees, proving that plasma treatment can get a high hydrophilic modification. The efficiency of the cold atmospheric pressure plasma with Ar on polyethylene film (LDPE) was significantly lower and the contact angle decreased from 85.2 only to 83 degrees, as it was found from Navaneetha et al. [175]. Wang et al. observed a maximum change in the contact angle from 69° to 32° degrees using a plasma jet with Ar on polymethyl methacrylate [172]. The contact angle decreased with the duration of the treatment up to the value of 32° achieved in the corresponding of 120s.

One of the ways to improve non-absorbent substrates' printability is to increase the surface free energy of the material by activating it. In the case of printing plastics with liquid inks, it is particularly important to increase the polar Surface Free Energy (SFE) component of the substrate. In addition to the water contact angle, contact angle measurements of diiodomethane are commonly performed in wettability studies. Unlike water, which is a very polar liquid, diiodomethane is a nonpolar liquid. The knowledge of contact angles with these fluids is commonly used to determine the values of SFE using the Owens-Wendt method [176].

PLASMA CATALYSIS

NTP has been presented as a mixture of radicals and charged particles that has great internal energy and they easily react to produce neutral or other charged species. The high energy content of plasma constituents particles can promote those chemical reactions that have great activation energy and thus they may not occur at room temperature and pressure. The NTP can be imaged as a catalyst that reduces the activation energy and encourages chemical reactions in mild conditions. The main difference between NTP and catalyst is that gas discharge is usually not selective. Although NTP presents appealing properties, such as low temperature, atmospheric pressure, compactness, low cost and a unique way to induce gas-phase reactions by electron collisions, the formation of unwanted chemical by-products and the poor energy efficiency still obstacle NTP industrial implementation.

To overcome these drawbacks, combining NTP with catalysts represents an effective way to improve the selectivity and the energy efficiency of chemical reactions, as it can merge the high selectivity of catalytic reactions with the low-temperature performance of plasma reactions in a compact reactor. Three different configurations can be adopted and they are shown in Figure 3.32:

- In-Plasma Catalysis (IPC);
- Post-Plasma Catalysis (PPC);
- Multistage.

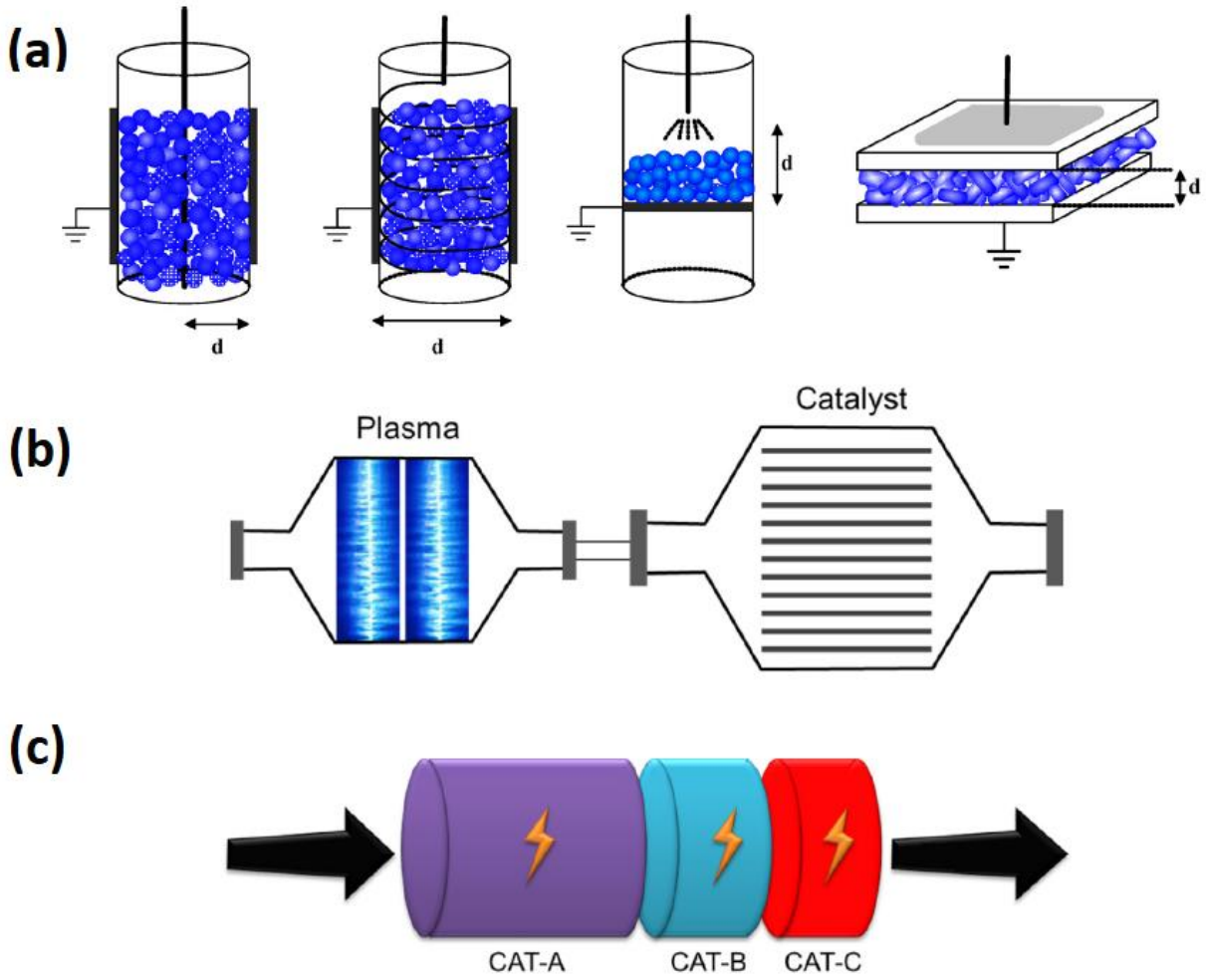

Figure 3.32 - NTP-catalyst classification: in-plasma catalysis (a), post-plasma catalysis (b), and multistage (c) [177].

IPC configuration consists of a single-stage system, where the catalyst is placed in the active plasma zone. The gas ionization occurs in the corresponding of the catalyst surface and also the adsorbed species are affected by the plasma radiation. In PPC configuration, the gas ionization occurs upstream the catalyst, that is placed soon after the plasma region. The catalyst sees an ionized gas and hence

lower energy is required for the catalyst chemical reactions. The catalyst can be active in a lower range of temperature compared to the process without gas ionization. The multistage configuration consists of a cascade of reactor units that can either be represented by IPCs or PPCs. The advantage of this technology is that each catalyst can implement a different function in the reaction, depending on its position.

Plasma reactors can vary in design and technology. The most common IPC reactors are packed DBD that are hence called "Packed Bed Plasma Reactor" (PBPR). The reactor presented in Figure 3.22 is hence filled with a catalyst in a place of a dielectric. Moreover, the catalyst can also cover the dielectric surface, thus reducing the pressure drop, as in Figure 3.33.

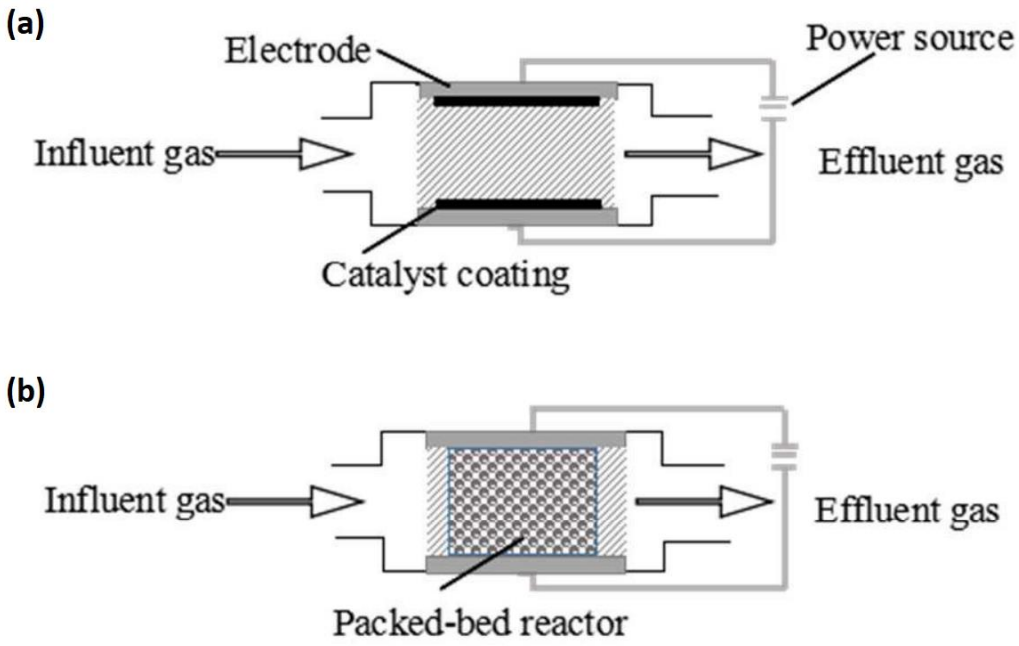

Figure 3.33 - IPC configurations: catalyst coating (a) and packed bed (b).

In the case of catalyst coating, the plasma occurs either in the gas gap and on the catalyst surface. The pressure drop decreases but the reactor must be longer to avoid the gas escape from it without react on the catalyst surface. The packed bed reactor, instead, has a lower void fraction and thus shorter reactors can be used; however, the pressure drop is much higher as the catalyst particle size decreases.

In such applications, the PPC configuration is preferred to IPC as the catalyst activity is indirectly dependent from the NTP reactor as the catalyst meets the ionized gas, but it is not exposed to the high-intensity electric field and hence a bombardment of electrons and ions. An example of PPC has been proposed in section 1.4.2.3 where the combination of the NTP to the SCR has been described as an alternative technique for the NO_x reduction (Figure 1.26). Moreover, many other processes

approach to this technology, as well as the abatement of Volatile Organic Compounds (VOCs). NTP in rich-oxygen air oxidize O_2 to O_3. The resulted gas has a high oxidising capacity that can break the VOC bonds, producing CO_2 and H_2O. Beside ozone direct reaction with hydrocarbons, the catalytic decomposition connected with the formation of an atomic O species represents a major oxidation pathway. Due to the long lifetime of O_3, this process is relevant for in-plasma catalysis. Hence, a catalyst for the selectivity O_3 decomposition to CO_2 can be placed downstream the plasma chamber [178].

Also, the NO_x conversion has been investigated in PPC configurations. Tran et al. have found that the γ-alumina impregnated with Indium downstream an NTP reactor allows the conversion of NO_x with an efficiency up to about 90% [179]. An appreciable efficiency has been achieved mixing the gas with hydrocarbons. Furthermore, the highest efficiency was obtained as the catalyst was placed in a furnace that sustained the temperature above the 550°C. Among the hydrocarbons, the propene showed the best performances.

4. EXPERIMENTAL CAMPAIGN ON ADSORPTION OF NO_X

In the adsorption experimental campaign, the effectiveness of granular activated carbons to adsorb NO_x was investigated. From the literature, the NOx adsorption was influenced by the presence of oxygen and the gas temperature. Hence, different operating conditions were investigated, and the experimental set-up was designed to monitor the emissions of NO and NO_2 from the adsorption of NO in N_2 and NO in O_2 and N_2. The adsorption was performed in a wide range of NO_x concentration at 30°C and 120°C, in order to simulate the conditions of interest for realistic application. The temperature of 30°C is representative of the adsorption at room temperature, while the adsorption at 120°C is the typical temperature of the gas before the chimney.

Two different adsorbent materials were used and the effect of the impregnation was discussed.

The content of this chapter can be summarized in:

- experimental set-up;
- materials used for the experimental investigation;
- methods for the analyses of the results;
- details of the NO_x adsorption experimental campaign and the operating protocols.

4.1Experimental set-up

Adsorption experimental campaign consisted of adsorption tests performed into a fixed bed reactor. The system built up was very flexible as the adsorption can be performed in the range of the pressure between 1-2 atm at 20-200°C. Furthermore, a wide range of gas composition may be tested.
The Process Flow Diagram of the experimental set-up is shown in Figure 4.1.

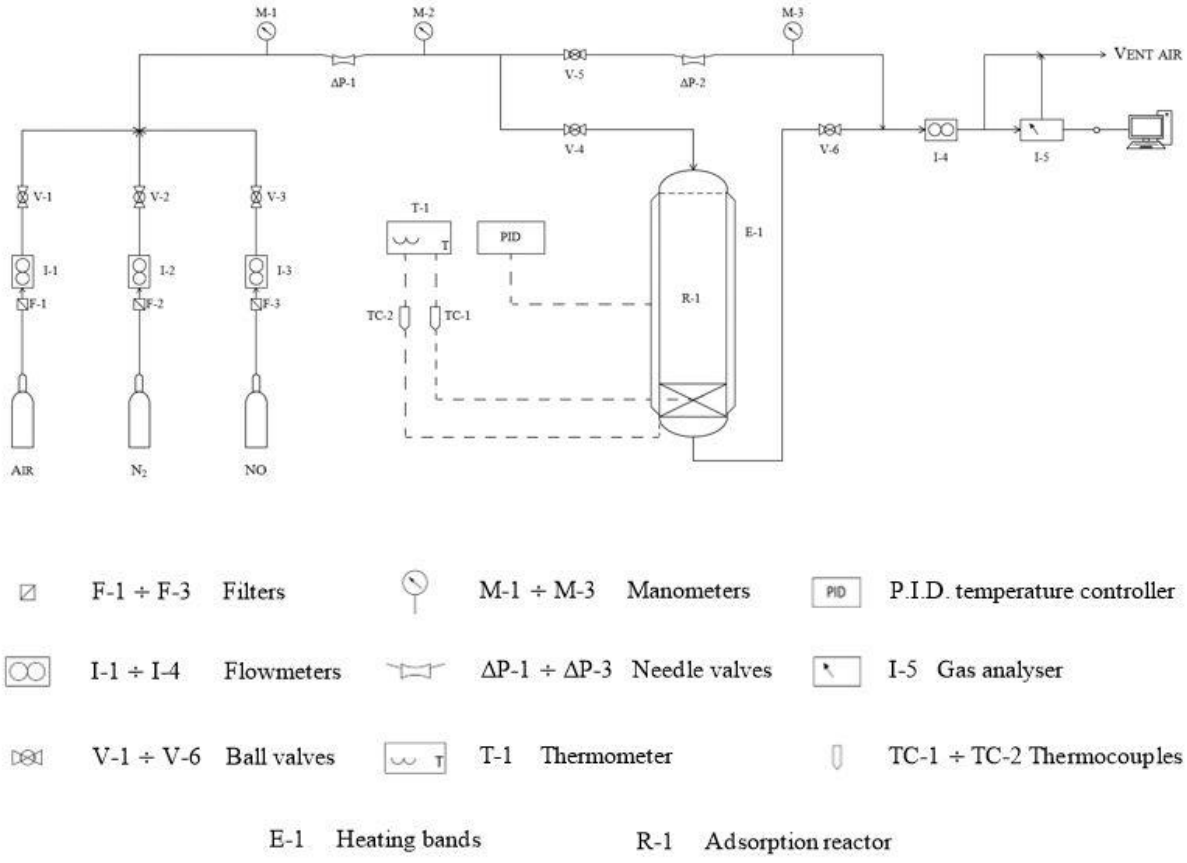

Figure 4.1 - Process Flow Diagram (PFD) of the Adsorption experimental campaign set-up.

The model flue gas used to carry out the experiments is produced by mixing three gas cylinders: air, nitrogen and NO diluted in N_2. Each gas-line coming from the cylinders was filtered (F-1, F-2, F-3) before entering the flowmeters (I-1, I-2, I-3). Then, the gas lines were mixed to equalize the gas concentration before the adsorption reactor (R-1). The valve ΔP-1 allowed to control the pressure that was measured by the manometer M-1. The adsorption reactor consisted of a packed bed column, thermally insulated from the external environment and equipped with a system of heating bands (E-1), which was meant to ensure a constant temperature of the packed bed during the experimental tests. The temperature of the bands was set by a P.I.D. controller, while the bed temperature and the reactor

external walls temperature were measured by the thermocouples TC-1 and TC-2, both connected to a thermometer (T-1). The pressure at the top and bottom of the packed-bed were measured by the manometers M-2 and M-3 respectively. The pressure at the end of the reactor was maintained at the value of 20mbar by the inner valve of the flow meter I-4, while the pressure drop inside the reactor depends mainly from the packed bed characteristics. In fact, the flow meter I-4 guaranteed both a bit overpressure and allowed measuring the flow rate assuming that no leakages were present into the reactor and piping system. The by-pass line, in parallel to the reactor, allowed to verify the flow rate and the gas composition before entering the reactor; the needle valve (ΔP-2) simulated the reactor drop pressure for the by-pass line. The total gas stream coming from the flowmeter I-4, was partially sent to a gas analyser (I-5), whose gas output was the ventilation system and whose digital signal output went to the monitor. The internal pump of the analyser was set to a flow rate of 1L/min (to optimise the analysis), the remaining was sent to the ventilation system. The overflow gas bypassed the analyser and achieved the fan directly. A picture of the plant is shown in Figure 4.2.

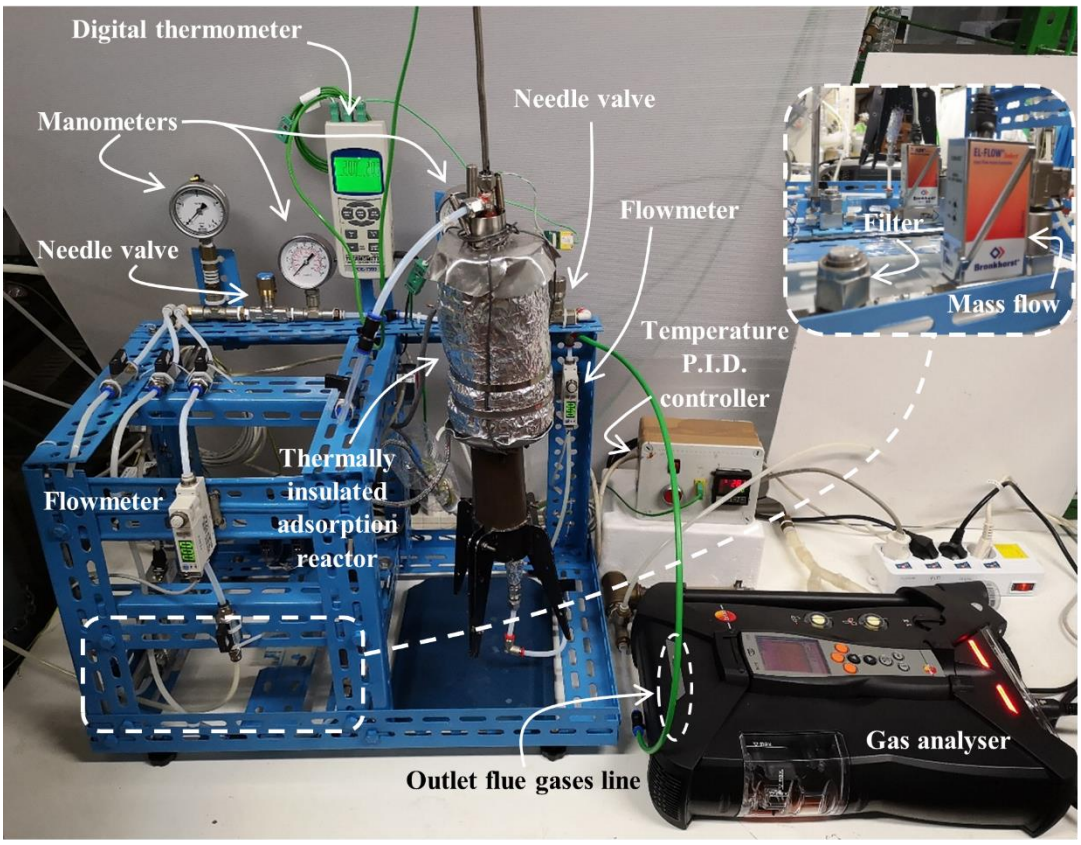

Figure 4.2 - Picture of the adsorption experimental campaign set-up.

4.1.1 Gas generation section

In this paragraph the gas generation section, used for the experimental campaign, is described in detail. Basically, the gas was produced from gas cylinders and the flow and the concentration was controlled by flow meters.

GAS CYLINDERS

The gas was generated from three gas cylinders shown in Figure 4.3.

Figure 4.3 - Gas cylinders containing 1000ppm of NO in N_2, Nitrogen 5.0 and Air UPP.

The gas cylinders consist of high-pressure cylinders containing the pure or special substances. The gas cylinders had the size of 50L and the pressure between 150 and 200bar. The high-pressure gas expanded to the pressure of 1-3 bar by a gas regulator, before being sent to the plants.
The simulated flue gas was generated by the mixing of three calibrated cylinders: NO (1007 ppm) in N_2, Nitrogen 5.0 and Air UPP.

FLOW METERS

The gas coming from the cylinders, after the expansion, was sent to mass flowmeters to adjust the flow rate. The flow wate was regulated by thermal mass flowmeters supplied by the Bronkhorst High-Tech company (model no. EL-FLOW Select series F-201CV), shown in Figure 4.4.

Figure 4.4 - EL-FLOW thermal mass flowmeter from Bronkhorst High-Tech.

The heart of the thermal mass flow meter/controller was the sensor, that consisted of a stainless-steel capillary tube with resistance thermometer elements. Part of the gas flowed through a bypass that allowed the control of the mass flow. The bypass consisted of two thermocouples in sequence and a heat ring between them. The controller warmed up the heating element and read the temperature of the thermocouples. The measured temperatures T1 and T2 drifted apart as the effect of the heat supplied; the temperature difference was directly proportional to mass flow through the sensor, by knowing the molecular weight of the gas and its thermal capacity. A schematic representation of the principle of working is shown in Figure 4.5.

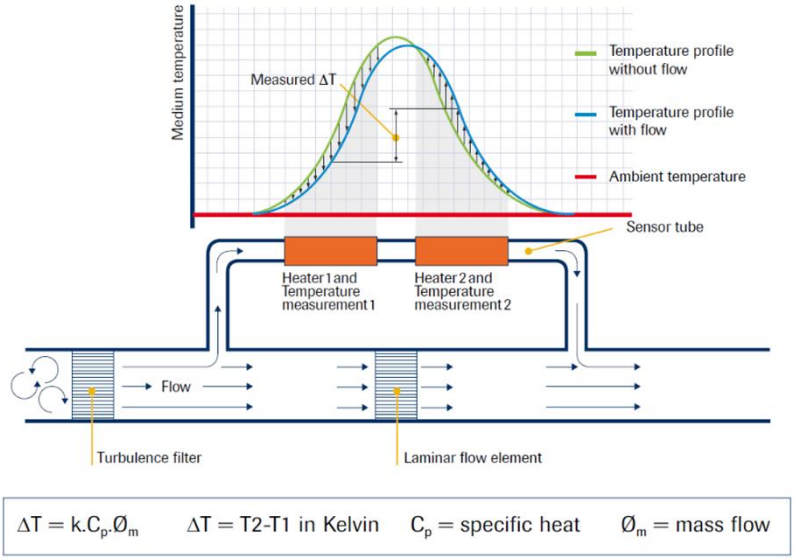

Figure 4.5 - Schematic representation of the principle of working of the thermal mass flowmeter.

The presence of the three cylinders and flowmeters allowed the easy modification of the gas composition to produce the desired inlet concentration. The model flue gas could either flush into the reactor or into the bypass before to enter the set up stack. In the downstream of the reactor, a gas analyser system held part of the gas to detect the composition before sending it in to the vent together with the rest of the gas.

4.1.2 Reactor section

The reactor for the adsorption tests consisted of a packed bed column, made of stainless steel AISI316. The reactor can be described focusing on three main areas:

- upper and lower sections;
- support grid for the solid adsorbent particles;
- junctions.

The upper and the lower sections were held together by a conic gas-tight thread, that was 2.8cm long to minimize leak issues. The adsorbent support grid was characterized by a mesh 350, which corresponds to a grid dimension of about 44μm; this choice consented the use of adsorbent materials of fine particle size, reducing the loss of the smallest grains. The full reactor (without the junctions) was about 14cm long, while its internal length was 10.7cm; the external diameter and the internal diameter were of 3 and 2cm respectively.
A picture of the reactor and a “dwg” drawing is shown in Figure 4.6.

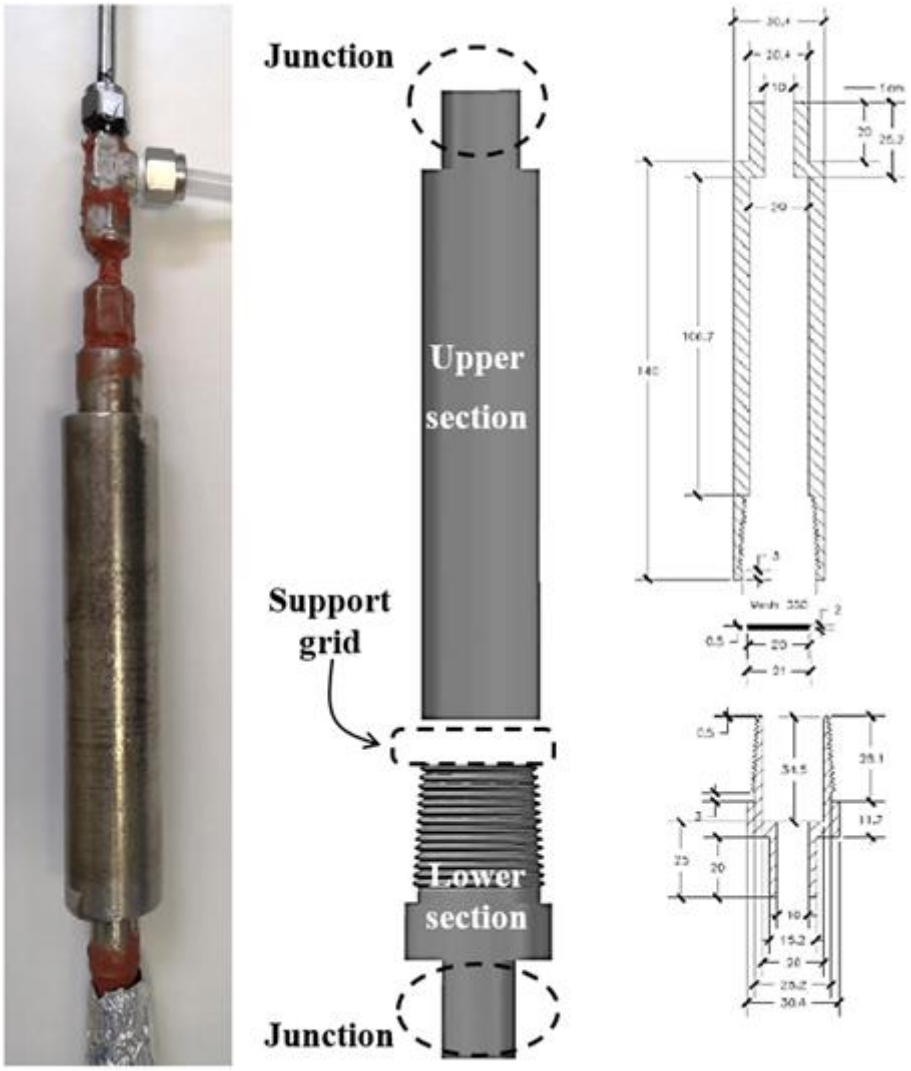

Figure 4.6 - Reactor for the adsorption tests: picture (left) 3D view middle, dimensioned "dwg" drawing (right).

The top of the reactor was connected with a Swagelok Tee union (Figure 4.6 left) to allow both the entrance of the gas and the insert of a thermocouple that fell into the reactor up to the packed bed.

The experimental set-up was equipped with two heating bands, connected in parallel each other to heat uniformly the whole column length. Furthermore, the reactor was wrapped with a thermal insulation, internally made of rock-wool and externally made of aluminium foils and it appeared as in Figure 4.7.

Figure 4.7 - Adsorption reactor insulated externally.

The insulation thickness was about 5 cm and it was calculated be enough to guarantee the isothermal process up to 200°C.

4.1.3 Auxiliary Instrumentations

TEMPERATURE CONTROL AND MONITORING

The reactor temperature was controlled by the use of a "P.I.D. controller" connected with two steel heating bands. The bands were connected in parallel and fixed around the reactor.

The reactor external wall temperature and the packed bed temperature were monitored by two K thermocouples, both connected to the digital thermometer PCE-T390.

The PID controller and the thermometer are shown in Figure 4.8.

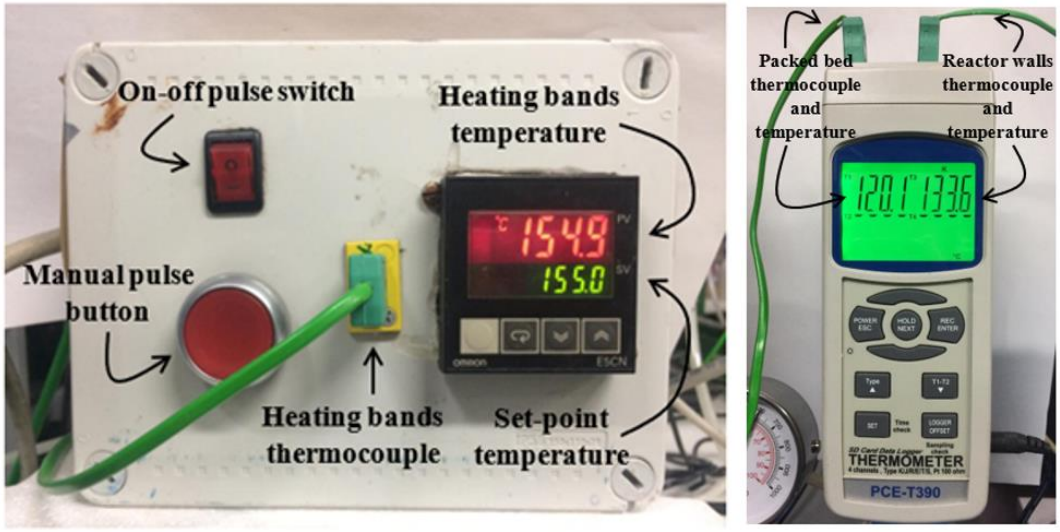

Figure 4.8 - P.I.D. temperature controller of heating bands (left), and thermometer (right).

GAS ANALYSER

The gas concentration was monitored using the Testo 350 that is shown in Figure 4.9.

Figure 4.9 - Testo 350 gas analyser.

The gas analyser supported electrochemical sensors for different substances. The analyser unit included 6 slots for gas sensors. The analyser units used during this experimental investigation included the NO, NO_2, O_2, SO_2 and two CO (low concentration) sensors as it is shown in Figure 4.10.

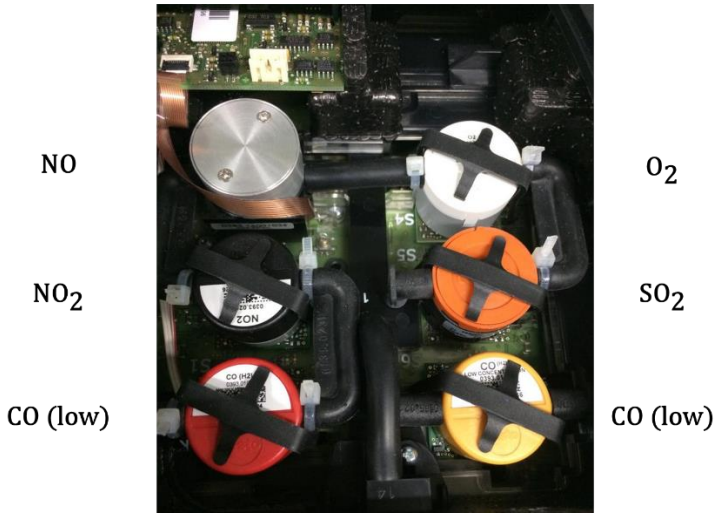

Figure 4.10 - Testo 350 gas sensors.

The only sensors used for our applications were those of NO and NO_2, as the model flue gas did not contain other species than that. Even the O_2 gas sensors should be helpful for monitoring the gas emissions to have a double check of the properly mixing of the gas cylinders. However, the data collected from that sensors was shaky due to the sensor damage during previous tests. However, the NO and NO_2 emissions were consistent with the calibrated gas cylinders.

The technical data of the NO and NO_2 sensors are summarized in Table 4.1.

Gas sensor	*Measurement range*	*Resolution*	*Accuracy*	*Response time (t_{90})*
NO	$0 - 4000\ ppm$	$1\ ppm$	$\pm 5\ ppm\ (0 - 99.9\ ppm)$ $\pm 5\%\ of\ m.v.\ (100 - 1999.9\ ppm)$ $\pm 10\%\ of\ m.v.\ (2000 - 4000\ ppm)$	$< 30\ s$
NO_2	$0 - 500\ ppm$	$0.1\ ppm$	$\pm 5\ ppm\ (0 - 99.9\ ppm)$ $\pm 5\%\ of\ m.v.\ (100 - 500\ ppm)$	$< 40\ s$

Table 4.1 - Technical data of the NO and NO_2 gas sensors.

An oscillation of ±5ppm from the real value can be observed in the range 0-99.9ppm for both the sensors; while the accuracy become ±5% of the measured value for higher concentration up to ±10% if the measured value of NO was in the range 2000-4000ppm. The response time t_{90} was the time needed to read the value with a precision of 90%.

In order to have an accurate response and a long sensor life, a fresh-air purge was required periodically: a purge valve mechanically opened the fresh-air gas path to remove flue gases from the analyser, regenerating the cells. Even the accuracy of the measurement was guaranteed by a periodic purge of fresh air through the analyser gas sensors to remove any gas residual from the

electrochemical cells. The recommended measurement period and purge time in function of the species concentration monitored are shown in Table 4.2.

Gas sensor	***Concentration*** [ppm]	***Recommended measurement period*** [min]	***Recommended rinse time*** [min]
NO	50	90	5
	100	60	5
	200	30	5
	500	20	10
	1000	10	10
	2000	10	20
	3000	5	30
	4000	5	30
NO_2	10	90	5
	20	60	5
	50	30	5
	100	20	10
	200	10	10
	500	10	20

Table 4.2 - Recommended measurement-rinse cycles.

Although the suggested recommended measurement period and rinse time, it had been decided to operate in precautionary conditions performing measurement for a maximum time of about 10 min, followed by a fresh-air purge from a minimum time of about 10 min for the lowest concentrations to a maximum time of about 30 min for the highest concentrations, even when the NO concentration was lower than 500ppm.

The analyser unit was connected to the computer and the experimental data were registered as concentration values over time.

The Testo 350 software registers the experimental data in terms of NO and NO_2 concentrations over time; this makes it possible to derive the breakthrough curves for the two species, gathering also kinetic information about the adsorption process. However, a discontinuous concentration profile over the time was taken from the monitoring of the gas concentration for long tests, due to the fresh-air purge. This makes the recording interrupted and hence it was impossible to calculate the amount

of NO_x adsorbed and/or desorbed without the full details of the curves. However, the variation of the concentrations with the time is quite slow (with the exception of the first minutes); hence it is possible to interpolate the data, drawing the breakthrough curve with a good approximation. An example of the approximated breakthrough curve is shown in Figure 4.11.

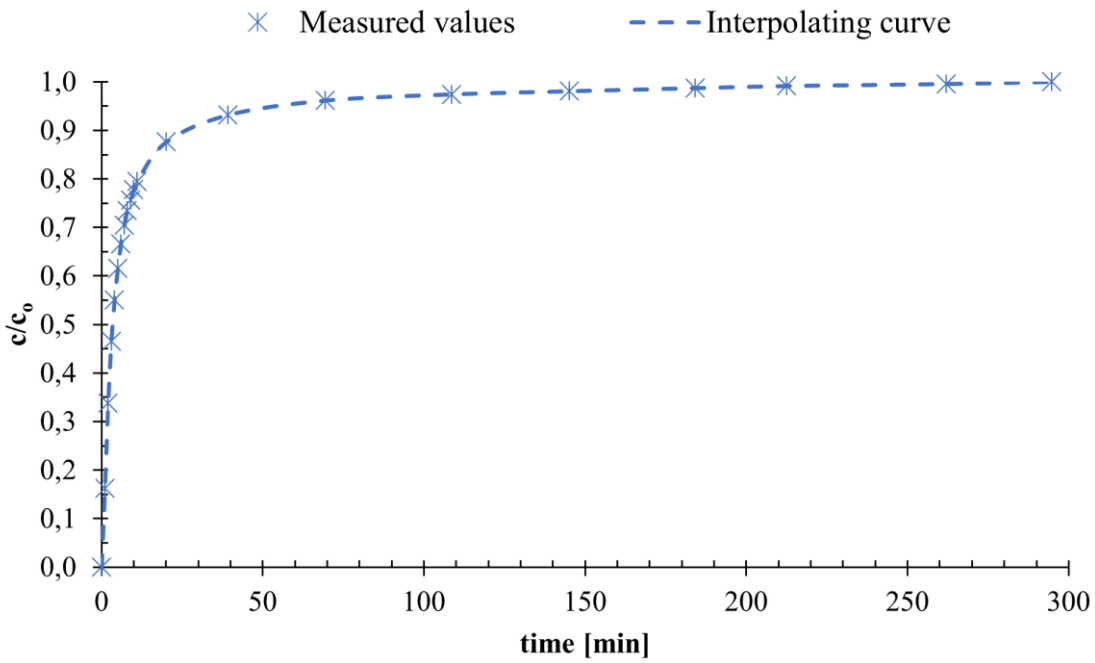

Figure 4.11 - Example of the NO_x breakthrough curve interpolation from the data recorded with testo 350.

In Figure 4.11 there are shown the data recorded by the testo 350 and they are represented by the blue stars. When the gas analysis was made after the purge stage, the concentration rose to the instantaneous value with an approximation of 90% in 30 seconds. The data each minute were taken in the first 10 minutes; after that, only the concentration value after 5 minutes of each recording was considered, in order to approximate the real value with a better accuracy. Collecting the values after 5 minutes from the recordings, it was possible to approximate the resulting curve, as the dashed blue line in Figure 4.11. Similar consideration can be made for the desorption curves, and hence the data are reported from the interpolation of the curves.

4.2Materials

The adsorbent used during the adsorption was Granular Activated Carbon (GAC) and Granular Activated Carbon impregnated with Copper (GAC-Cu). The adsorbent materials have been provided by the Activated Carbon Corporation in the form of microporous grains with a particle size 1.7÷3.35mm and a specific surface area of about 1000m^2/g. The carbon had an organic nature coming from coconut-shell, exhibiting no more than 3-5% ash content. The impregnated GAC contained about 5%$_{wt}$ of copper, mainly in the form of CuO and CuO_2 in traces. Both the GAC and GAC-Cu grains have been pounded and sieved to obtain desired particle size, which ranges between 300-400µm. The choice of the particle size was made to optimize the kinetics of the adsorption process, as it was described in Section 2.3

A picture of the commercial size and 300-400µm GAC-Cu is shown in Figure 4.12.

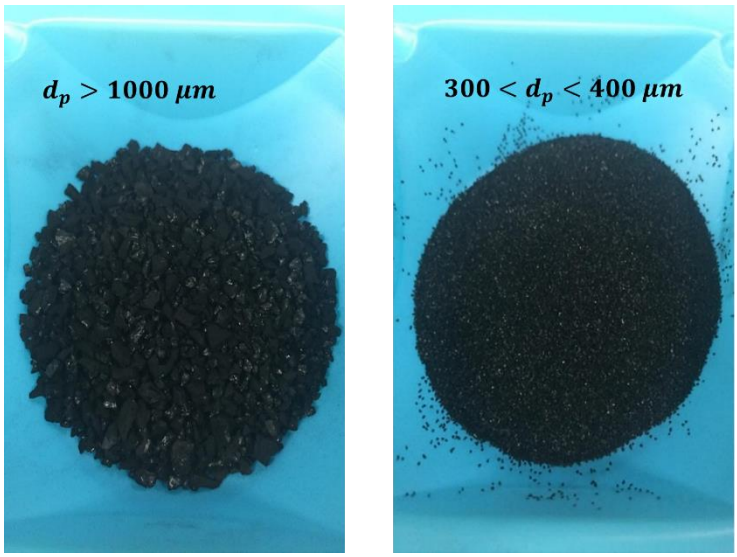

Figure 4.12 - GAC-Cu of the commercial size of 1.7÷3.35mm (left) and 300-400µm size (right).

4.3Methods of analysis and experimental schedule

From the interpolated curves it is possible to calculate the adsorption capacity that is proportional to the area on the left side of the curve, according to Equation (Eq. *2-25)*. From the selected values taken as it was shown in Figure 4.11, the adsorption capacities were calculated from a discretization of the integral in Equation (Eq. *2-25)*, considering the mean concentration of consecutive value analysed:

$$\omega(t) = \frac{u}{L_T \rho_b} \sum_{i=1}^{n-1} \left(c_o - \frac{c_i + c_{i+1}}{2} \right) \Delta t_i \qquad \textit{(Eq. 4-1)}$$

where the ratio out of the summation is also equivalent to the gas flow rate divided per the mass of the sorbent, while the summation is proportional to the area at the left of the curve.

The adsorption capacity was calculated from Equation (Eq. *4-1)* and it was measured in μmol/g or mmol/g in dependence of the scale of the values calculated.

It must be noted that ω is a function of the time and the adsorption capacity is representative of the equilibrium between the gas concentration and the adsorbed concentration. Although the equilibrium can be achieved only after an infinite time, the adsorption capacities were calculated as the saturation time was achieved. The adsorption process has been carried out until ~98% of the initial NO_x concentration has been reached, considering the adsorbent bed completely saturated. This means that the saturation time of the adsorption process has been defined as the time at which the concentration is 98% of the inlet concentration ($t_s=t_{98}$).

During the adsorption of NO in the presence of oxygen, some of the NO molecules were oxidized to NO_2. Hence, we assumed that the catalytic oxidation occurred with the same velocity during all the process. This assumption hypothesis was made on the performed tests as the adsorption of NO in the absence of oxygen occurred in a time greatly lower than the saturation time for the adsorption in the presence of oxygen. From the assumption, it is possible to consider the NO_x adsorption capacity as the sum of the NO and the NO_2 uptake capacities, where the NO and NO_2 initial concentrations are considered as their values in the steady state conditions. The NO and the NO_2 uptake capacities at the time t (ω^*_{NO} and $\omega^*_{NO_2}$, respectively) were calculated as the following equations:

$$\omega_{NO}^{*}(t) = \frac{u}{L_T \rho_b} \sum_{i=1}^{n-1} \left(c_{NO}^{SS} - \frac{c_{NO,i} + c_{NO,i+1}}{2} \right) \Delta t_i \qquad \textit{(Eq. 4-2)}$$

$$\omega_{NO_2}^{*}(t) = \frac{u}{L_T \rho_b} \sum_{i=1}^{n-1} \left(c_{NO_2}^{SS} - \frac{c_{NO_2,i} + c_{NO_2,i+1}}{2} \right) \Delta t_i \qquad \textit{(Eq. 4-3)}$$

It is important to note that the adsorption capacity is a function of the volumetric flow rate. The gas flow was controlled at the value of 1.88NL/min (at SATP), that correspond to the gas velocity of 0.1m/s. This means that the equivalent flow rate into the reactor is higher at high temperature, hence the spatial gas velocity is higher. The concentration, instead, is not affected by the changing of the temperature.

The experimental investigation has been carried out to determine the isotherms of NO_x adsorption onto two GACs and in presence of different O_2 concentrations. The experiments also allow to determine the dynamics of NO_x adsorption in a packed bed. All the adsorption tests have been performed on a packed bed, whose main features are summarized in Table 4.3.

Physical properties	Value
Mass [g]	2
Bed Diameter [cm]	2
Bed Length [cm]	1
Particle size [µm]	300-400
Bed porosity [-]	0.4
Specific surface area [m^2/g]	1000
Bulk density [g/L]	500

Table 4.3 - Packed bed features.

For the realization of the adsorption isotherms of NO in N_2, the influence of different adsorbate concentration has been indirectly investigated. The adsorption isotherms of NO in N_2 have been performed for both types of GAC (nonimpregnated and Cu-impregnated) by changing the NO concentration according to the shame reported in Table 4.4.

Adsorbent material	T [°C]	NO initial concentration [ppm]						
		50	100	150	200	250	300	400
GAC	30	X	X	X	X	X	X	X
	120	X		X		X		X
GAC-Cu	30	X	X	X	X	X	X	X
	120	X		X		X		X

Table 4.4 - Experimental programme for the adsorption of NO in N_2.

From the results of the experimental programme as in Table 4.4, the adsorption isotherms were calculated. The Langmuir model was used to fit the data as in Equation (Eq. *2-9)* and the determination coefficient was estimated.

The determination coefficient, R^2, is a measure of the accuracy of the model fitting. This coefficient is defined as the square of the correlation, R, between the predicted scores and the actual scores and it ranges from 0 to 1. The higher accuracy is given by R^2=1.

Another experimental campaign was performed to examine the effect of an oxidizing environment, by mixing the gas stream from the three cylinders. In this case a small amount of NO was oxidized to NO_2 (<1%), hence the benchmark inlet concentration is expressed in terms of total NO_x concentration (as sum of NO and NO_2). The total inlet gas flowrate was set to the same value of 1.88L/min and the NO_x concentration equal to 250ppm; while the O_2 concentration varied from 0% to 10%. The experimental programme for the adsorption test in presence of oxygen is reported in Table 4.5.

Adsorbent material	T [°C]	Oxygen concentration [%]			
		0	3	5	10
GAC	30	X	X	X	X
	120	X	X	X	X
GAC-Cu	30	X	X	X	X
	120	X	X	X	X

Table 4.5 - Experimental programme for the adsorption of NO in O_2 and N_2.

The operating protocol performed for the whole experimental investigation can be divided in two main stages: a plant preparatory stage and test execution stage.

The preparatory phase has been planned in order to optimize the execution of the adsorption tests and it is schematized as follows:

i. loading the reactor with a settled mass of the chosen adsorbent;
ii. heating the reactor to the desired operating temperature;
iii. flushing the reactor with a N_2 stream at the operating temperature for 15min to remove residual humidity from the adsorbent material;
iv. closing the reactor inlet and outlet valves, setting each gas stream flowrate by the flowmeters and checking the total NO_x concentration and total flow rate through the bypass line.

The adsorption tests have been carried out feeding the reactor with the gas sample in continuous mode, monitoring and recording the outlet NO and NO_2 concentrations by the Testo 350 gas analyser. The inlet total NO_x concentration has been occasionally monitored at the beginning and at the end of the test through the bypass line to the perform the tests correctly. At the time the saturation of the fixed bed is accomplished, the reactor inlet is closed and a last check of the inlet NO_x concentration is executed through the bypass line.

4.4Results of NO_x adsorption

Two kinds of activated carbons were investigated and the results are presented and discussed in this section. The experiments were duplicated for both Granular Activated Carbon (GAC) and Granular Activated Carbon impregnated with copper (GAC-Cu). The following features of the adsorption process have been evaluated:

i. effect of the NO_x concentration;
ii. effect of the O_2 concentration;
iii. effect of the operating temperature.

The analysis of the effect of the concentration of the adsorbate consists of a construction of adsorption breakthrough curves from which adsorption isotherms were also obtained. Unless otherwise indicated, all the breakthrough curves are reported in terms of c/c_o vs time, where c and c_o are the outlet and the inlet concentrations of the adsorbate. For calculation easiness and clarity, all the values of the adsorption capacity are expressed in terms of μmol of adsorbate per grams of solid adsorbent. Although the adsorption capacity is commonly expressed as mg/g, the NO adsorption process competes with the oxidation to NO_2. The produced NO_2 was partially trapped on the adsorbent surface, hence contributing to the NO_x adsorption. Being a great difference in molar weight of NO and NO_2, it was preferred to express the adsorption capacity as a function of the molar amount than weight.

Different adsorption models have been used to fit the experimental data. Since the highest fitting accuracy has been obtained with the Langmuir model, only the results related to this model have been reported.

The results will be shown separately for the GAC and the GAC-Cu and then a comparison between them will be made to discuss the effect of the impregnation.

4.4.1 NO_x adsorption over GAC

The effect of the initial NO_x (as NO) concentration in the inlet gas sample has been investigated in absence of oxygen at two different operating temperatures, i.e. 30 and 120°C, according to the experimental programme reported in Table 4.4. The kinetics and the thermodynamics of the adsorption were investigated, and the results are presented below. The calculated adsorption capacity is plotted in the function of the NO_x initial concentration, hence defining the adsorption isotherm curves for the adsorption of NO in N_2. Then the effect of oxygen in gas feed was analysed as well as the effect of the temperature.

4.4.1.1 Adsorption Isotherms

Many tests were performed at the same temperature and pressure by changing the gas composition. The adsorption capacity of GAC was evaluated for a gas stream made by NO balanced in N_2. It has been calculated from Equation (Eq. *4-1)*. The breakthrough curves for the feeding of 250ppm of NO in N_2 at 30°C and 120°C are shown in Figure 4.13.

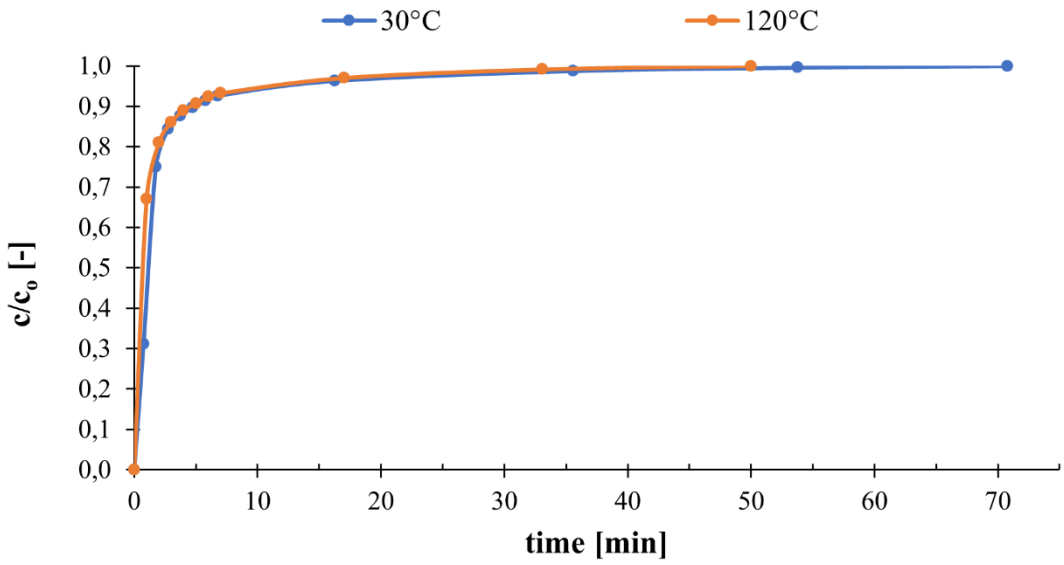

Figure 4.13 - Breakthrough curves for 250ppm of NO balanced in N_2 at 30°C (left) and 120°C (right), over GAC.

From Figure 4.13, it is possible to notice that the breakthrough curves present a very steep initial slope and do not have the classic sigmoidal shape shown in Figure 2.8. The value of c/c_o rapidly tends to 1, making it difficult to identify the breakthrough time t_b. The value of c/c0 rapidly tends to 1 and the slope of the breakthrough curve decreases over time. The trend of the curves at different concentrations is very similar; the curves become steeper and steeper as the NO inlet concentration increases. The curves are not reported here; however, two key parameters for the adsorption study have been considered: the saturation time (t_s=t_{98}) and the adsorption capacity. The data collected at different concentrations for the two investigated temperatures are shown in Table 4.6.

c_o [ppm]	T = 30°C		T = 120°C	
	t_s [min]	ω_{NO} [µmol/g]	t_s [min]	ω_{NO} [µmol/g]
50	37	15	50	16
100	39	21		
150	41	23	29	18
200	50	27		
250	36	28	30	22
300	30	28		
400	17	29	18	23

Table 4.6 - Saturation time and GAC adsorption capacity for NO in N_2 gas stream at different inlet concentrations, at 30°C (left) and 120°C (right).

From Table 4.6, it is possible to note that the saturation time increases with the NO concentration and then it decreases at higher concentrations, at 30°C; while the adsorption capacity rises fast with concentration at low values and then it slightly increases with concentration as it is higher than 200ppm.

The results at 120°C have some fluctuation in adsorption capacity as the heat generation system did not work properly, hence an oscillation of $\pm$10°C was observed during the tests. From the adsorption capacity collected in Table 4.6, it is possible to represent the adsorption capacity in the function of the NO initial concentration and hence fits the data with the mathematical models. Among the models presented in Section 2.2, the Langmuir model gives the best fitting of the results; hence the Equation (Eq. *2-9)* was used to fit the results.

The adsorption capacity in the function of the NO initial concentration, and the calculated adsorption isotherms are shown in Figure 4.14.

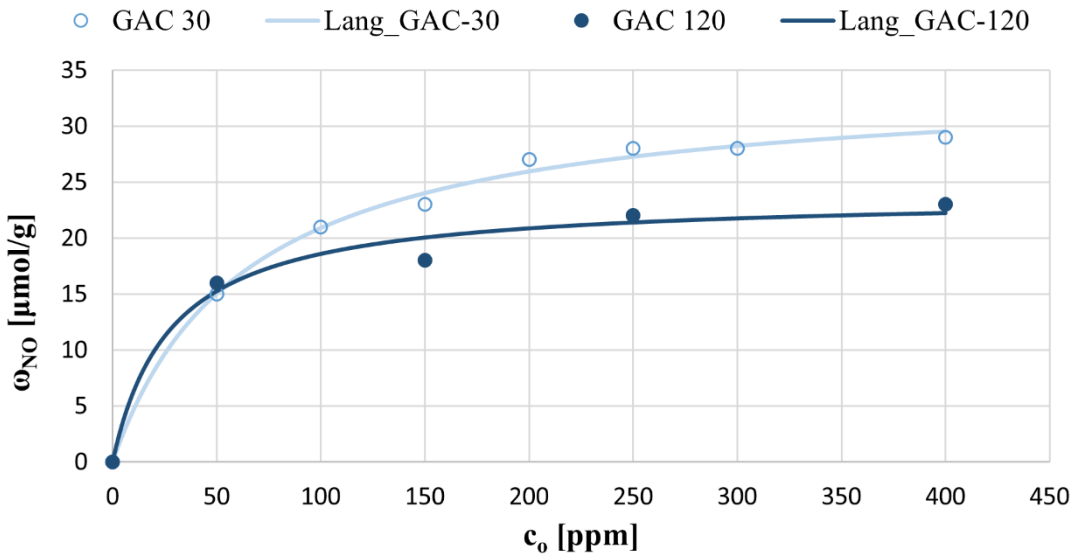

Figure 4.14 - Adsorption isotherms for NO in N_2 adsorption on GAC at 30°C and 120°C.

The experimental data show that the adsorption isotherm has an upward trend with the increasing feed concentration, approaching an asymptotic value. This trend is typical of the type I adsorption isotherms, called "favourable isotherms" and shown in Figure 2.4.

Since the adsorption is an exothermic process, it was expected that an increase in the operating temperature would lead to a lower NO adsorption. This trend suggests that there are some sites over the GAC that are not active at room temperature; while they become able to capture the NO molecules as the temperature increases.

From the fitting of the data shown in Figure 4.14, the parameters in the Langmuir equations and the determination coefficient were estimated (Table 4.7).

T [°C]	$K_L \cdot 10^2$ [-]	ω_{max} [µmol/g]	R^2 [-]
30	1.57	34.20	0.996
120	3.57	23.84	0.983

Table 4.7 – Langmuir parameters for the fitting of the adsorption isotherms for NO in N_2 adsorption on GAC at 30°C and 120°C.

The determination coefficient calculated for the fitting of the experimental data is close to 1 (Table 4.7). This means that the Langmuir model can be used with a good approximation to approximate the adsorption isotherms.

4.4.1.2 Effect of the O_2 concentration

The effect of oxygen concentration in the inlet gas sample has been investigated at room temperature (30°C) by fixing the inlet NO concentration equal to 250ppm and varying the O_2 concentration (3-10%). The experimental data have been reported in comparison to the related data for the adsorption in absence of O_2, presented in the previous section.

In the presence of O_2, it was observed that part of the NO reacts in the adsorbent bed converting to NO_2. The oxidation occurred with an efficiency of less than 1% in an empty reactor; while the efficiency increases significantly as the gas passed across the adsorbent bed. The oxidation is encouraged by the functional groups on the carbon surface and its rates depends on the gas residence time in the adsorbent bed reactor and the oxygen concentration. This means that the process involves simultaneously a co-adsorption of NO and O_2 and their reaction to produce NO_2, as it was found in the literature described in Section 2.4.1.

The first difference between the adsorption of NO in N_2 and in O_2/N_2 mixture was observed in the breakthrough curves for the adsorption of 250ppm of NO at different oxygen concentration, balanced in N_2 are shown in Figure 4.15.

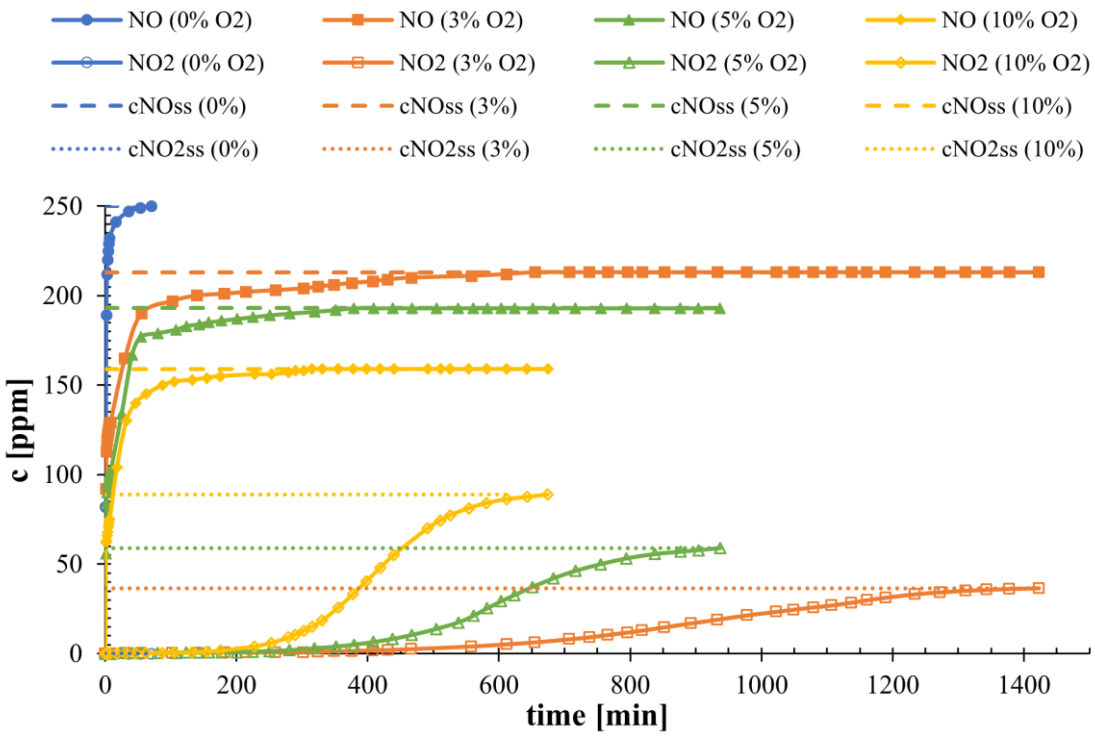

Figure 4.15 - NO and NO_2 breakthrough curves for the adsorption of 250ppm of NO in the presence of 0%, 3%, 5%, 10% of oxygen, balanced in N_2 on GAC at 30°C.

The NO and the NO_2 were monitored at the outlet of the adsorbed bed. The curves in Figure 4.15 are expressed as the pollutant concentration in the function of the time, and they are referred to the experiments performed at different oxygen concentration, collected in the same chart. They were not normalized to the initial concentration to appreciate the amount of NO_2 produced. It is possible to note that the oxidation of NO occurs even at low concentration of O_2 (3%). All the tests performed highlighted that the NO concentration rises until it reaches a steady-state level (c_{NO}^{ss}). In the meantime, the NO_2 concentration is almost zero until a few hundred minutes (exception for 0% of O_2). For longer times, the NO_2 concentration rises to a steady-state value ($c_{NO_2}^{ss}$) that is achieved after a few hours. The steady-state values change for NO and NO_2 as the oxygen content in the inlet changes; however, for each test, the sum of NO and NO_2 is equivalent to the inlet concentration of NO as the NO_2 achieves the stationary. From Figure 4.15, it is possible to note that the NO_2 produced was much higher as the oxygen content increases, thus evidencing a direct correlation between them; moreover, the saturation was achieved in a shorter time as the oxygen content increased. The shape of the NO_2 breakthrough curves is similar to the generic one, as it was shown in Figure 2.8.

The NO_x breakthrough curves were obtained from the sum of NO and NO_2 monitored concentration. The normalized curves were collected in one chart and they are shown in Figure 4.16.

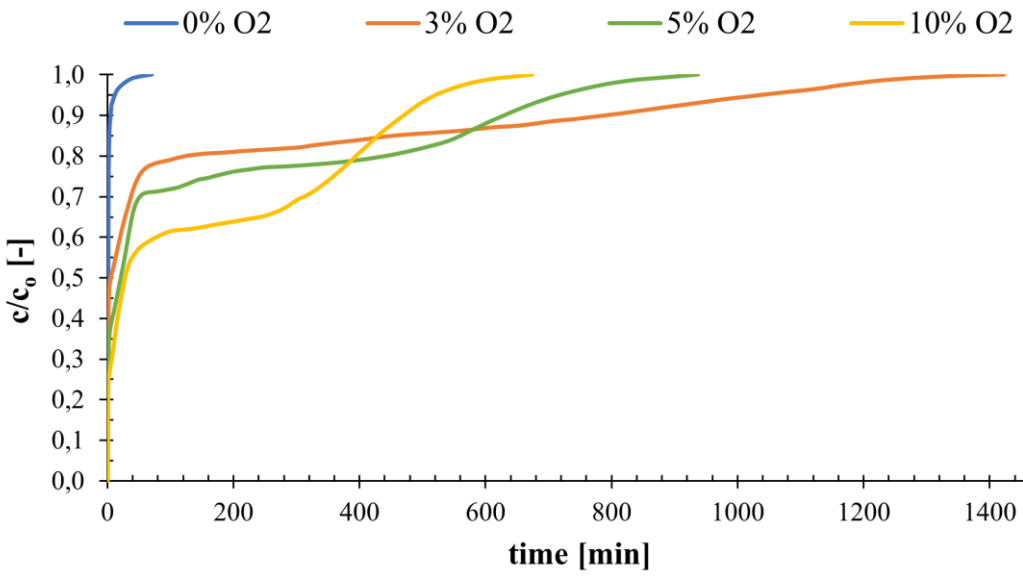

Figure 4.16 - NO_x breakthrough curves for the adsorption of 250ppm of NO in the presence of 0%, 3%, 5%, 10% of oxygen, balanced in N_2 on GAC at 30°C.

When no oxygen was content in the feed, the NO_x curve was equivalent to NO as the NO_2 was not detected. It is possible to note that the saturation time is greatly higher as the oxygen was fed; in

particular, it was maximum for 3% of oxygen fed, than 5% then 10%. This means that a great discontinuity can be observed between 0% and 3% of oxygen in the feed. Then the higher is the oxygen content, the lower is the NO concentration at the steady-state (from Figure 4.15), the higher is the concentration of NO_2 at the steady-state (from Figure 4.15), the lower is the saturation time (from Figure 4.16).

The GAC adsorption capacity for NO_x can be calculated from the data in Figure 4.16 that it will be the same as the adsorption capacity for NO only in the case of no oxygen fed. In addition to the adsorption capacity for NO_x, the equivalent uptake capacities for NO and NO_2 can be calculated by imaging an equivalent system in which the NO and NO_2 are fed with the same concentration as their steady-state concentrations respectively, as in Equations (Eq. *4-2)* and (Eq. *4-3).*

The saturation time, the adsorption capacity of NO_x and the equivalent uptake capacity for NO and NO_2 are reported in Table 4.8 for the tests as in Figure 4.15 and Figure 4.16.

O_2 [%]	NO_x		NO		NO_2	
	t_s [min]	ω_{NOx} [µmol/g]	t_s [min]	ω^*_{NO} [µmol/g]	t_s [min]	$\omega^*_{NO_2}$ [µmol/g]
0	36	28	36	28	-	-
3	1190	1634	408	311	1343	1323
5	810	1622	281	207	895	1415
10	578	1612	227	153	621	1459

Table 4.8 - Saturation times, adsorption capacities and equivalent uptake capacities for NO_x, NO and NO_2 in the presence of 0%, 3%, 5%, 10% of oxygen, balanced in N_2 on GAC at 30°C.

From Table 4.8 it is possible to note that the saturation time decreases with the oxygen concentration for either NO_x, NO, NO_2, except for the test in absence of oxygen. This means that the mass transfers will improves as the oxygen content in the feed increases. Being the physical properties constant in all the experiments, this result suggests a direct correlation between the mass transfers, the oxygen content and the oxidation yield. The literature suggests that the NO_x adsorption improves as the feed is contains either NO and O_2, as it was discussed in the section 2.4.1. The enhancement may be attributed to the higher adsorption capacity of carbon-based adsorbent for NO_2 rather than NO. The high efficient oxidation, increases the NO_2/NO rate, hence having a positive effect on the adsorption. Even if the NO_x adsorption does not change significantly with the O_2 feed concentration (Table 4.8), the saturation is achieved earlier. The higher conversion of NO to NO_2, increases the concentration

of the latter that has a higher affinity with the sorbent; hence, an increasing of the driving force occurs, with an improvement of the MTZ, and consequently the reduction of t* and ts, as it was discussed in Section 2.3.

4.4.1.3 Effect of the operating temperature

The adsorption is an exothermic process, hence the adsorption capacity decreases with the temperature, generally. This trend is verified for physical adsorptions as the active sites are not influenced by the temperature but only by the partial pressure of the adsorbate. However, such adsorbents could present on their surface functional groups that are inactive at low temperature; while they can link the adsorbate as the temperature rises. Is this the case of chemisorption and such examples were discussed in Section 2.4.2. This is the case of GAC. The adsorption isotherms at 30°C and 120°C calculated in Figure 4.14 show that the adsorption capacity is higher as the temperature increases in the range 50-400ppm of NO diluted in N_2.

When feed contains oxygen, the adsorption efficiency is worst at high temperature. The NO_x breakthrough curves for the adsorption of 250ppm of NO in the presence of 0%, 3%, 5%, 10% of oxygen, at 120°C, are shown in Figure 4.17.

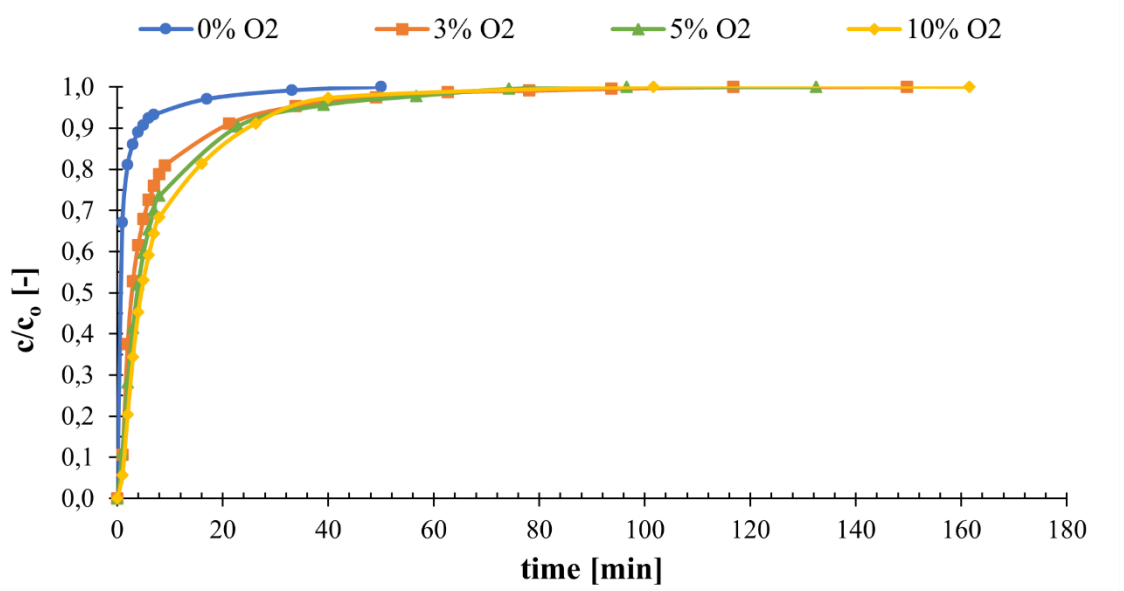

Figure 4.17 - NO_x breakthrough curves for the adsorption of 250ppm of NO in the presence of 0%, 3%, 5%, 10% of oxygen, balanced in N_2 on GAC at 120°C.

At high temperature, the oxidation of NO to NO_2 seems to be negligible as the NO_2 concentration in the outlet was always less than 1ppm; hence, the NO_x breakthrough curves are almost equivalent to those for NO. Compared to the breakthrough curve for NO in N_2, all the curves obtained in presence

of oxygen appear shifted rightward. Hence both the saturation time and the adsorption capacity increases with the oxygen content in the feed, as it is reported in Table 4.9.

O_2 [%]	**NO_x**	
	t_s [min]	**ω_{NOx} [µmol/g]**
0	30	22
3	51	73
5	57	83
10	55	93

Table 4.9 - Saturation times, adsorption capacities and equivalent uptake capacities for NO_x in the presence of 0%, 3%, 5%, 10% of oxygen, balanced in N_2 on GAC at 120°C.

The data in Table 4.9 are referred to the only NO_x, as the NO_2 was not relevant for all the tests performed at 120°C. The saturation times were almost equivalent for all the tests performed in the presence of oxygen and they were significantly higher than that obtained in absence of oxygen. The adsorption capacity increased a lot in the presence of oxygen but it slightly increased with the oxygen content above 3%, hence suggesting that part of NO was partially oxidized to NO_2, but the latter was not detected as the oxidation yield was below 1%. This suggest that the breakpoint of NO_2 might occur for a longer times; however, the experiments were stopped as the 98% of the inlet concentration was achieved. Therefore breakthrough of NO_2.

The NO_x adsorption capacities at 120°C have been compared with the related values calculated at 30°C, to evaluate the effect on temperature on the adsorption process when oxygen is fed. The results showed in Table 4.8 and Table 4.9 are collected in Figure 4.18.

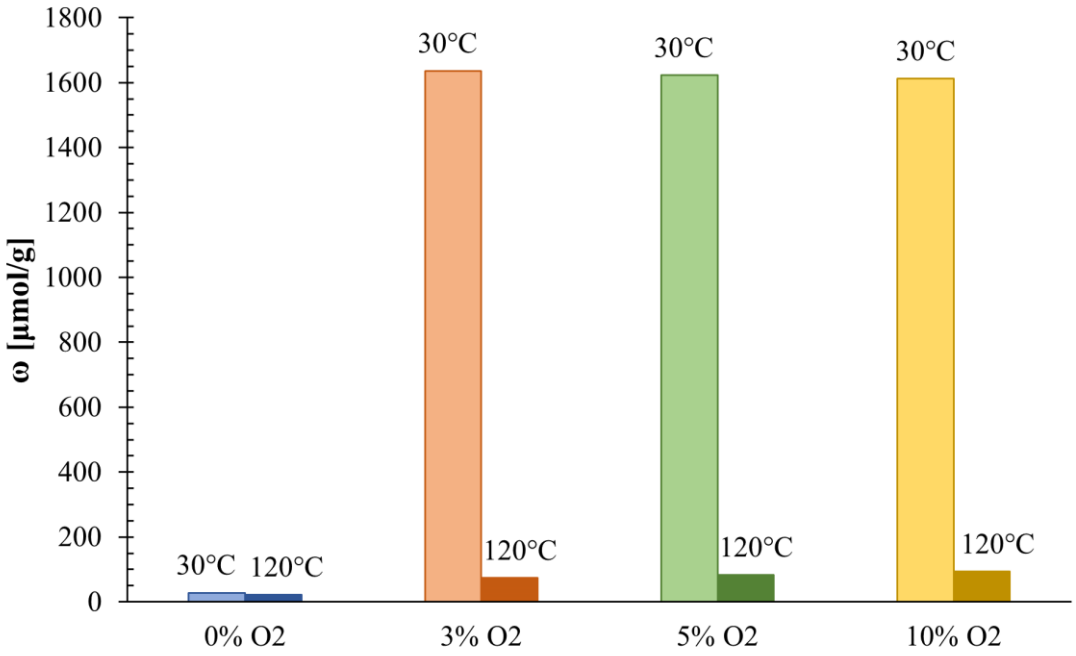

Figure 4.18 - GAC adsorption capacities for the adsorption of 250ppm of NO in the presence of 0%, 3%, 5%, 10% of oxygen, balanced in N_2 at 30°C and 120°C.

The presence of oxygen plays a positive role in the adsorption of NO_x on GAC either at 30°C and 120°C. However, the increment is much bigger at low temperature. A significantly increasing in the adsorption capacity between 0% and 3% of O_2 concentration can be observed both at 30°C and 120°C. Then, in the range of 3-10% of O_2, the adsorption capacity seems to be almost constant. This suggests that the oxidation of the sites participating in the NO_x adsorption (improving the uptake) almost saturated if more than 3% of O_2 was fed.

4.4.2 NO_x adsorption over GAC-Cu

The tests performed on the Granular Activated Carbon (GAC) were replicated on the (GAC-Cu), following the experimental programme reported in Table 4.5. In conformity with the previous section, the adsorption isotherms at 30°C and 120°C were defined for the adsorption of NO in N_2; then the effect of oxygen in gas feed was analysed as well as the effect of the temperature.

4.4.2.1 Adsorption Isotherms

Even in the case of the adsorption of NO in N_2 on GAC-Cu, the breakthrough curves present a very steep initial slope and do not have the classic sigmoidal shape shown in Figure 2.8. The trend of the curves at different concentrations is very similar; the curves become steeper as the NO inlet

concentration increases. Hence, the saturation time and the adsorption capacity have been calculated and the results are shown in Table 4.10.

c_o [ppm]	T = 30°C		T = 120°C	
	t_s [min]	ω_{NO} [µmol/g]	t_s [min]	ω_{NO} [µmol/g]
50	100	35	270	106
100	120	67		
150	170	91	134	120
200	130	111		
250	110	124	100	122
300	97	128		
400	90	135	70	127

Table 4.10 - Saturation time and GAC-Cu adsorption capacity for NO in N_2 gas stream at different inlet concentrations, at 30°C (left) and 120°C (right).

The trend of the saturation time is similar to that found for the GAC. The saturation time increases with the NO concentration and then it decreases at higher concentrations, at 30°C; while the adsorption capacity rises fast with concentration at low values and then it slightly increases for higher concentrations. At 120°C, instead, the saturation time decreased constantly, while the adsorption capacity increased as expected.

Again, the adsorption capacity was represented as a function of the inlet NO concentration, and the parameters of the Langmuir model were calculated. The adsorption isotherms at 30°C and 120°C are represented in Figure 4.19.

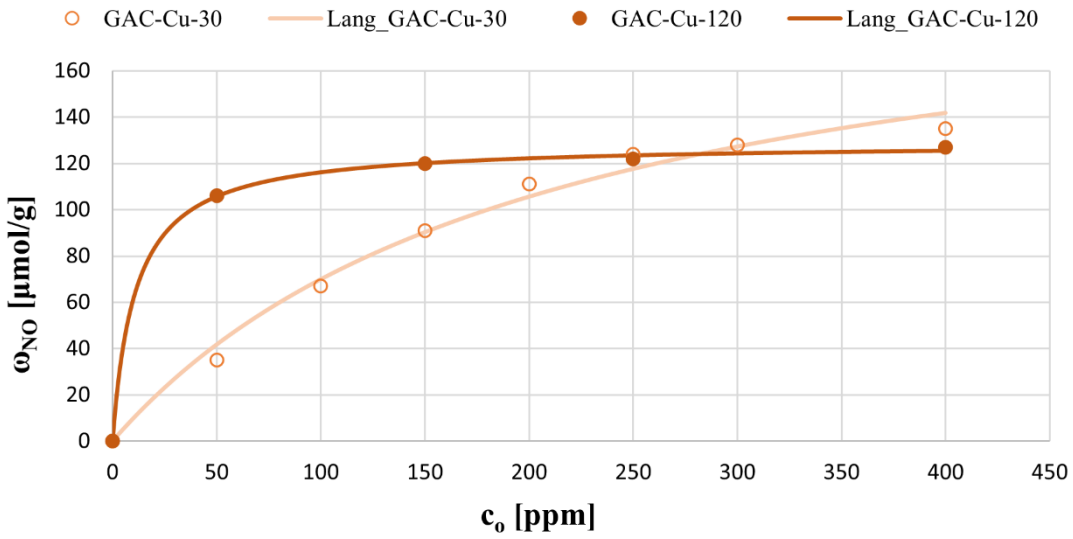

Figure 4.19 - Adsorption isotherms for NO in N_2 adsorption on GAC-Cu at 30°C and 120°C.

The adsorption capacity increases with a typical type I isotherm shapes and hence the Langmuir model can be proficiently applied. The estimated parameters in the Langmuir equations and the determination coefficient are shown in Table 4.11.

T [°C]	$K_L \cdot 10^2$ [-]	ω_{max} [µmol/g]	R^2 [-]
30	0.480	215	0.995
120	9.12	129	0.9996

Table 4.11 – Langmuir parameters for the fitting of the adsorption isotherms for NO in N_2 adsorption on GAC-Cu at 30°C and 120°C.

From Table 4.11, it is possible to note that the determination coefficient is very high, meaning that the Langmuir equation offer a good description to the experimental results.

The adsorption capacity is higher at 120°C than at 30°C in the range of low concentrations (50-250ppm) while it becomes comparable for higher concentrations. Further to the consideration made for GAC, the copper impregnation plays a positive role in NO_x adsorption as it was described by López et al. [134]. Reasonably, the temperature plays a major role in the activation of Cu, resulting in an enhancement of the process at higher temperatures.

4.4.2.2 Effect of the O_2 concentration

Even for the GAC-Cu, the effect of oxygen concentration in the inlet gas sample has been investigated at room temperature (30°C) by fixing the inlet NO concentration equal to 250ppm and varying the O_2 concentration (3-15%). The results have been analysed either in the kinetics and the thermodynamics.

The breakthrough curves for the adsorption of 250ppm of NO at different oxygen concentration, balanced in N_2 are shown in Figure 4.20.

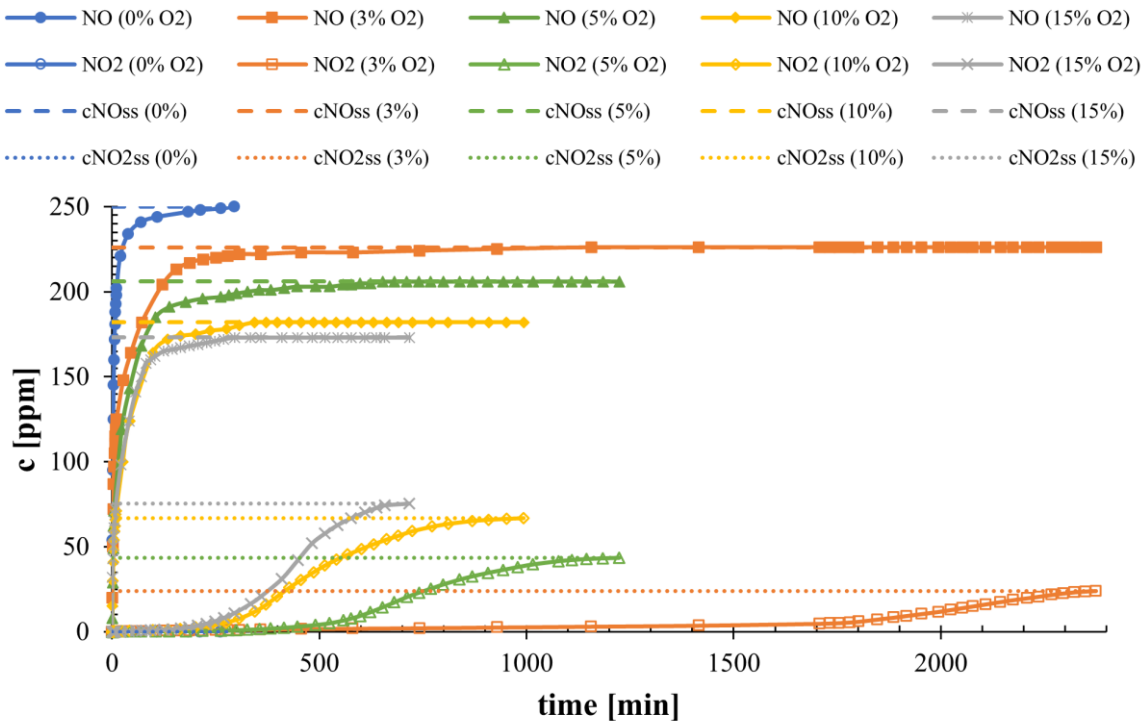

Figure 4.20 - NO and NO_2 breakthrough curves for the adsorption of 250ppm of NO in the presence of 0%, 3%, 5%, 10%, 15% of oxygen, balanced in N_2 on GAC-Cu at 30°C.

The NO and NO_2 breakthrough curves had a similar shape as in the case of GAC. Again, the NO_2 breakthrough curve achieved the saturation later than for the higher concentrations. The steady-state values change for NO and NO_2 as the oxygen content in the inlet changes. However, for each test, the sum of NO and NO_2 is equivalent to the inlet concentration of NO as the NO_2 achieves stationary conditions. The NO_2 produced was much higher as the oxygen content increases, thus evidencing a direct correlation between them; moreover, the saturation was achieved in a shorter time as the oxygen content increased. In addition, in the case of GAC-Cu, the NO_x adsorption in the case of 15% of oxygen in the feed was considered. The NO_2 concentration at the steady state was the highest and the saturation was achieved in a shorter time.

The saturation time, the adsorption capacity of NO_x and the equivalent uptake capacity for NO and NO_2 are reported in Table 4.12 for the tests as in Figure 4.20.

O_2 [%]	NO_x		NO		NO_2	
	t_s [min]	ω_{NOx} [µmol/g]	t_s [min]	ω^*_{NO} [µmol/g]	t_s [min]	$\omega^*_{NO_2}$ [µmol/g]
0	110	124	110	124	-	-
3	2190	2187	425	430	2340	1757
5	995	1698	400	410	1140	1288
10	752	1644	276	310	880	1334
15	610	1521	207	231	650	1290

Table 4.12 - Saturation times, adsorption capacities and equivalent uptake capacities for NO_x, NO and NO_2 in the presence of 0%, 3%, 5%, 10%, 15% of oxygen, balanced in N_2 on GAC-Cu at 30°C.

The saturation time decreases with the oxygen concentration for either NO_x, NO, NO_2, except for the test in absence of oxygen. The NO_x adsorption efficiency has a peak for the test with 3% of oxygen; it is about 1600% higher than in the absence of oxygen and about 43% higher than in the case of 15% of oxygen. In presence of oxygen, Cu can interact with both NO and O_2, as reported by López et al. [134]. Increasing the O_2 concentration in the gas sample, the interactions with NO are reduced and the overall NO_x adsorption capacity decreases. Furthermore, the authors proposed that Cu catalyses also the dissociative chemisorption of O_2 and the formation of NO_2 due to the oxidation reaction which occurs between NO and the oxygen groups formed on the surface of the carbon. It may be hypothesized that, at higher values of O_2 content, the copper is oxidized and its catalytic effect is reduced.

4.4.2.3 Effect of the operating temperature

The adsorption isotherms at 30°C and 120°C shown in Figure 4.19 indicate that the adsorption capacity is higher as the temperature increases in the range 50-250ppm for NO diluted in N_2, while it becomes comparable at higher NO concentrations.

When feed contains oxygen, the adsorption efficiency is worst at high temperature. The NO_x breakthrough curves for the adsorption of 250ppm of NO in the presence of up to 15% of oxygen, at 120°C, are shown in Figure 4.21.

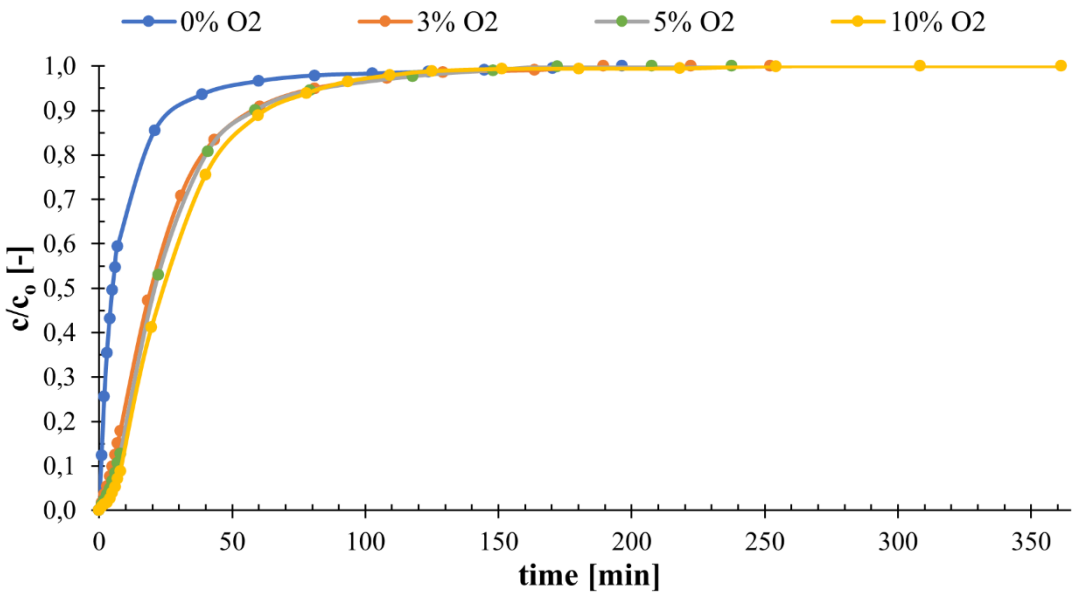

Figure 4.21 - NO_x breakthrough curves for the adsorption of 250ppm of NO in the presence of 0%, 3%, 5%, 10% of oxygen, balanced in N_2 on GAC-Cu at 120°C.

The NO_2 was not detected for all the tested inlet gas samples and, consequentially, the NO_x curves correspond to the NO curve. The absence of NO_2 in the gas stream leaving the column does not mean that no oxidation take place in the adsorbent bed. We instead believe that the higher temperature reduced the oxidation of NO_2 and the high levels of its adsorption capacity let the fixed bed remain below the breakpoint. The combined effects of the two phenomena lead to negligible values of NO_2 at the column exit.

Compared to the breakthrough curve for NO in N_2, all the curves obtained in the presence of oxygen appear shifted rightward. Moreover, the breakthrough curves for the adsorption with oxygen are almost perfectly coincident to each other and their shape appears more similar to a sigmoidal curve as the O_2 inlet concentration increases. Hence, both the saturation time and the adsorption capacity increases with the oxygen content in the feed, as it is reported in Table 4.13.

O_2 [%]	NO_x	
	t_s [min]	ω_{NOx} [µmol/g]
0	100	122
3	112	250
5	118	267
10	109	303

Table 4.13 - Saturation times, adsorption capacities and equivalent uptake capacities for NO_x in the presence of 0%, 3%, 5%, 10% of oxygen, balanced in N_2 on GAC-Cu at 120°C.

The data in Table 4.13 are referred to the NO_x, as the NO_2 was not relevant for all the tests performed at 120°C. The saturation times were almost equivalent for all the tests performed in the presence of oxygen and they were also comparable with that obtained in the absence of oxygen. However, the adsorption capacity increased to a great extent with 3% O_2, and then it increased almost linearly with the oxygen content.

The NO_x adsorption capacities at 120°C have been compared with the related values calculated at 30°C to evaluate the effect on temperature on the adsorption process when oxygen is fed. The results showed in Table 4.12 and Table 4.13 are collected in Figure 4.22.

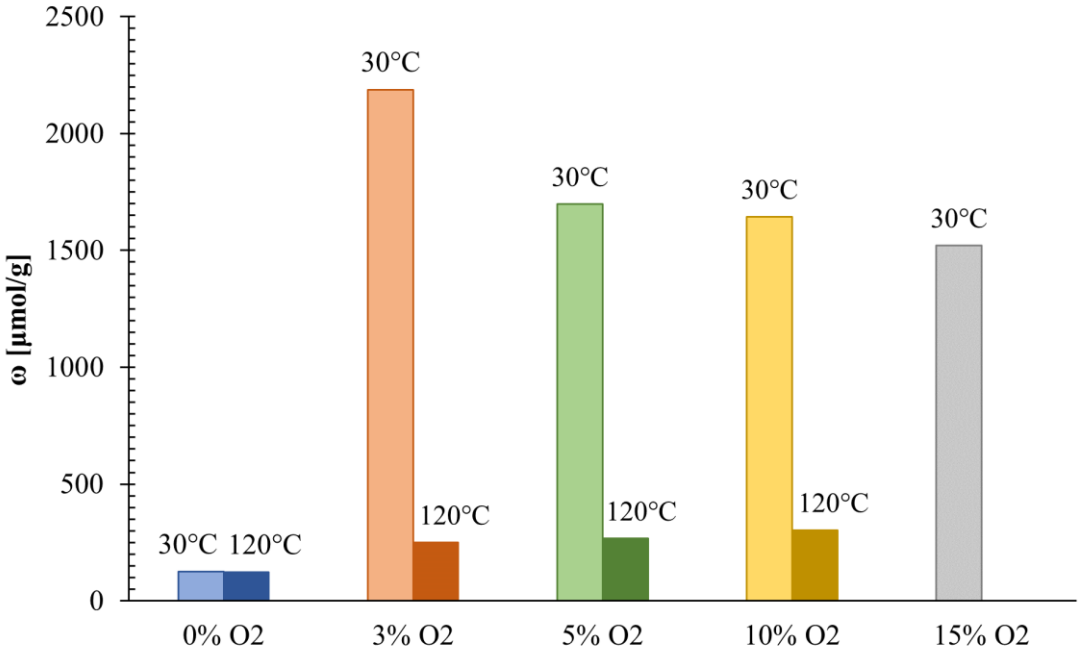

Figure 4.22 – GAC-Cu adsorption capacities for the adsorption of 250ppm of NO in the presence of 0%, 3%, 5%, 10%, 15% of oxygen, balanced in N_2 at 30°C and 120°C.

The presence of oxygen plays a positive role in the adsorption of NO_x on GAC either at 30°C and 120°C. However, the effect is much bigger at low temperature. A significantly increasing in the adsorption capacity between 0% and 3% of O_2 concentration can be observed both at 30°C and 120°C. Then, in the range of 3-15% of O_2, the adsorption capacity decreased at 30°C while it increased at 120°C, in the range of 3-10%. This behaviour is probably related to the role of surface groups present on the raw activated carbon and will be explained hereinafter.

4.4.3 Effect of the impregnation

This section is meant to investigate the effect of the activated carbon impregnation on the efficiency of the adsorption process. All the results reported in the previous sections for the GAC and the GAC-Cu will be presented as comparison of the two tested types of adsorbent. The effect of the impregnation will be discussed for the adsorption of NO in N_2 and the adsorption of NO in O_2 and N_2, separately.

4.4.3.1 Adsorption of NO in N_2

The results obtained for the adsorption of 250ppm of NO in N_2 at room temperature (30°C) for the two types of sorbents are reported in Figure 4.23.

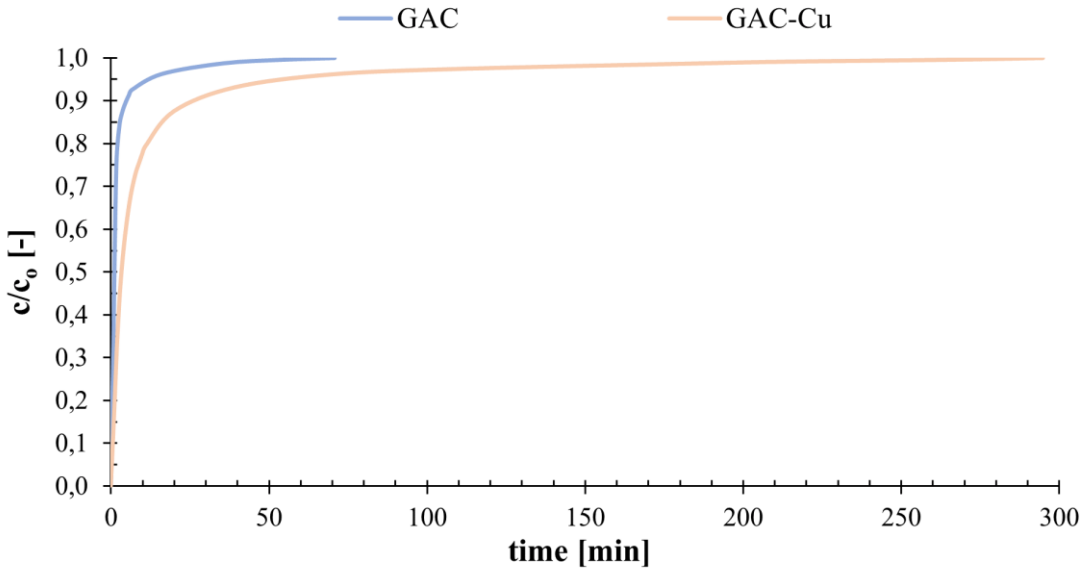

Figure 4.23 - Breakthrough curves for the adsorption of 250ppm of NO in N_2 on GAC and GAC-Cu, at 30°C.

The breakthrough curve associated to the adsorption on the Cu-impregnated GAC is always below that of raw GAC. Although the curves were obtained for 250ppm of NO in N_2, they are representative

of those others at different concentrations and the same considerations can be made for the concentrations 50, 100, 150, 200, 250, 300, 400 ppm of NO in N_2. Hence, in the range 50-400 ppm, the saturation time is always lower for the GAC than for the GAC-Cu. From Equation (Eq. *4-1)*, the first term is constant at fixed physical properties and initial concentration, while the summation is higher for the GAC-Cu. Hence a higher adsorption capacity may be predicted for GAC-Cu.

The saturation time and the NO_x adsorption isotherms at 30°C and 120°C for the two materials are compared in Table 4.14and Figure 4.24.

c_0 [ppm]	GAC (30°C)		GAC (120°C)		GAC-Cu (30°C)		GAC-Cu (120°C)	
	t_s [min]	ω_{NO} [µmol/g]	t_s [min]	ω_{NO} [µmol/g]	t_s [min]	ω_{NO} [µmol/g]	t_s [min]	ω_{NO} [µmol/g]
50	37	15	50	16	100	35	270	106
100	39	21			120	67		
150	41	23	29	18	170	91	134	120
200	50	27			130	111		
250	36	28	30	22	110	124	100	122
300	30	28			97	128		
400	17	29	18	23	90	135	70	127

Table 4.14 - Saturation times and adsorption capacities of GAC and GAC-Cu for NO in N_2 gas stream at different inlet concentrations, at 30°C (left) and 120°C (right).

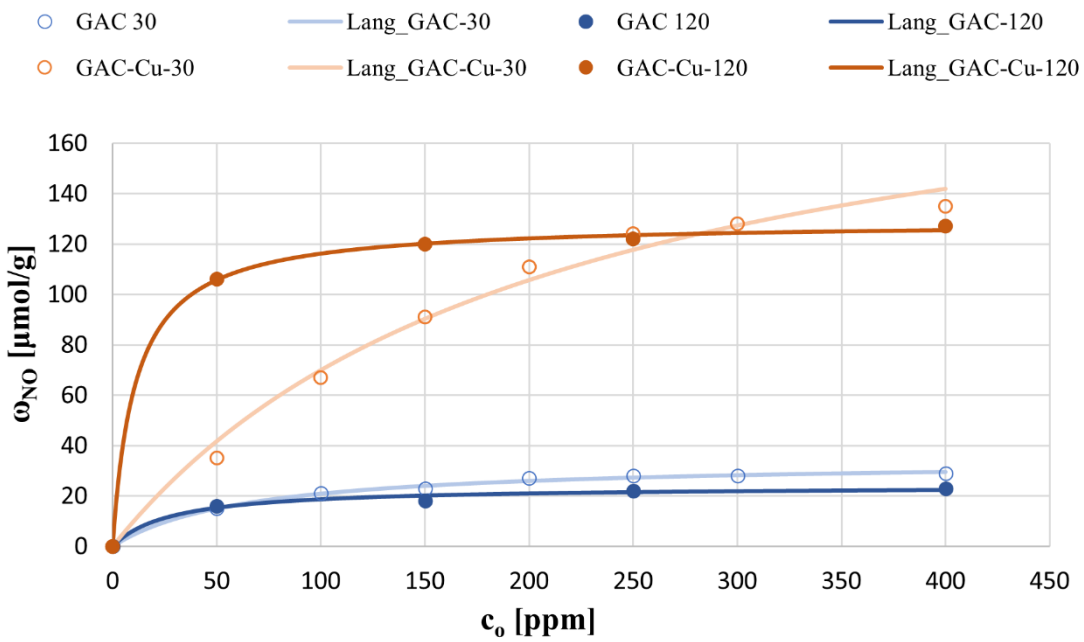

Figure 4.24 - Adsorption isotherms for NO in N_2 adsorption on GAC and GAC-Cu at 30°C and 120°C

From Table 4.14, it is possible to notice that the saturation time and the adsorption capacities for the GAC-Cu are always higher than those of the GAC.

For the adsorption of NO in N_2 at 30°C, the impregnation has a great positive effect on the performances of the adsorbent material in terms of adsorption capacity. This improvement become even more remarkable as the NO concentration in the inlet gas increases up to 250ppm; then it remains almost constant for higher concentrations. Even at 120°C, the impregnation has a positive effect on the adsorption capacity and the improvement is almost constant in the range 50-150ppm.

Many researchers showed that the impregnation of the sorbent can promote the adsorption of NO thanks to the generation of species with a higher affinity with the carbonaceous matrix. This improvement may be due to an interaction between the copper and the NO, that leads to the transfer of nitrogen and oxygen atoms on the carbon surface (dissociative chemisorption of NO) [134].

The improvement is more remarkable at 120°C than 30°C for low concentrations; the improvement is almost constant with the inlet concentration of NO, as it is higher than 250ppm.

4.4.3.2 Adsorption of NO in O_2 and N_2

The adsorption in presence of O_2 in the inlet gas samples revealed an increasing of the saturation time and the adsorption capacities, as shown in the previous sections. The comparison between the two sorbents have been reported hereinafter, referring to the effect of oxygen on the NO_x adsorption

capacities and the rate of the NO oxidation reaction to NO_2. The breakthrough curves for the adsorption of NO on GAC and GAC-Cu, for different oxygen contents, are reported in Figure 4.25.

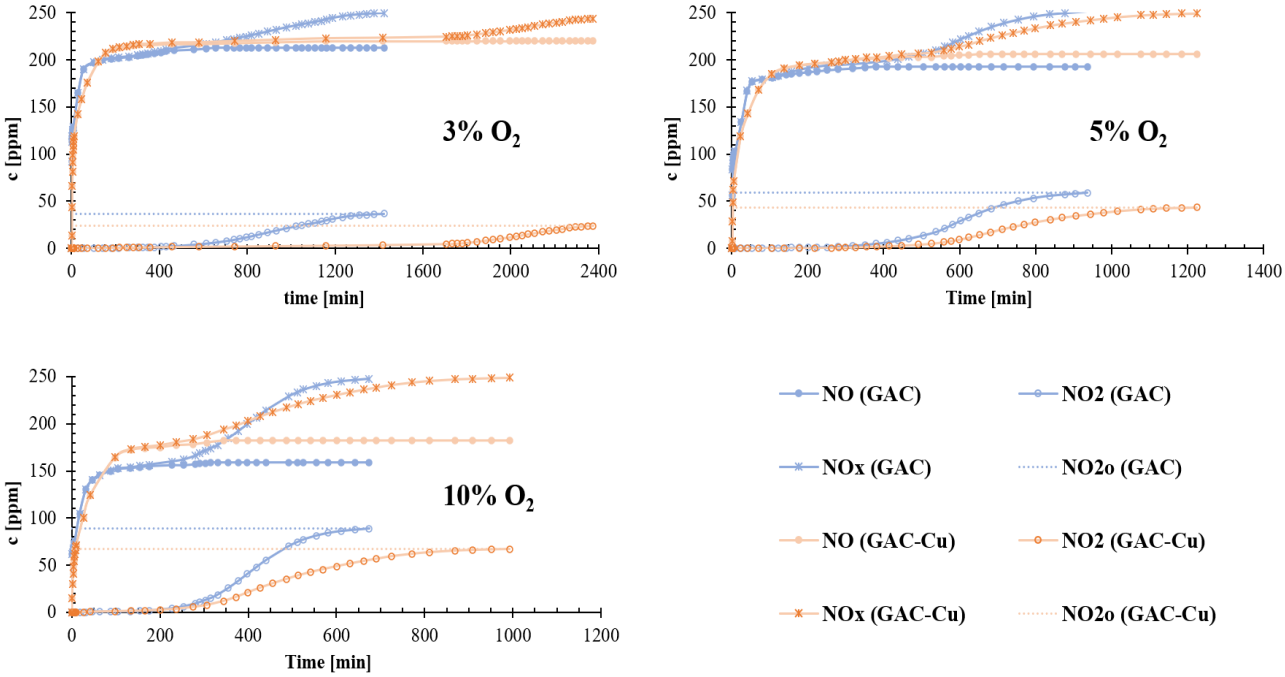

Figure 4.25 - NO and NO_2 breakthrough curves for the adsorption of 250ppm of NO in the presence of 0%, 3%, 5%, 10%, of oxygen, balanced in N_2 on GAC and GAC-Cu at 30°C.

The oxidation of NO occurs on both the GAC and the GAC-Cu surfaces, as discussed in the previous sections. This means the oxidation reaction is both due to the copper groups and to the other surface groups over the carbon. The oxidation has a positive effect either in the saturation times and the adsorption capacities. Table 4.15 collects the information provided in the previous sections, to observe the saturation times and the adsorption capacities for NO_x, as the function of the oxygen concentration and the gas temperature for both the materials.

O_2 [%]	GAC (30°C)		GAC-Cu (30°C)	
	t_s [min]	ω_{NOx} [µmol/g]	t_s [min]	ω_{NOx} [µmol/g]
0	36	28	110	124
3	1190	1634	2190	2187
5	810	1622	995	1698
10	578	1612	752	1644

Table 4.15 - Saturation times and adsorption capacities for NO_x, in the presence of 0%, 3%, 5%, 10% of oxygen, balanced in N_2 on GAC and GAC-Cu at 30°C.

Both the saturation times and the adsorption capacities are always higher for the GAC-Cu. This means that in addition to the functional groups can be found on GAC, copper plays a positive role in the NO_x adsorption. This effect is due to the further oxidation of NO to NO_2 in the GAC-Cu.

A clearer view of the comparison between the adsorption capacity of the two sorbents is given by the histogram in Figure 4.26.

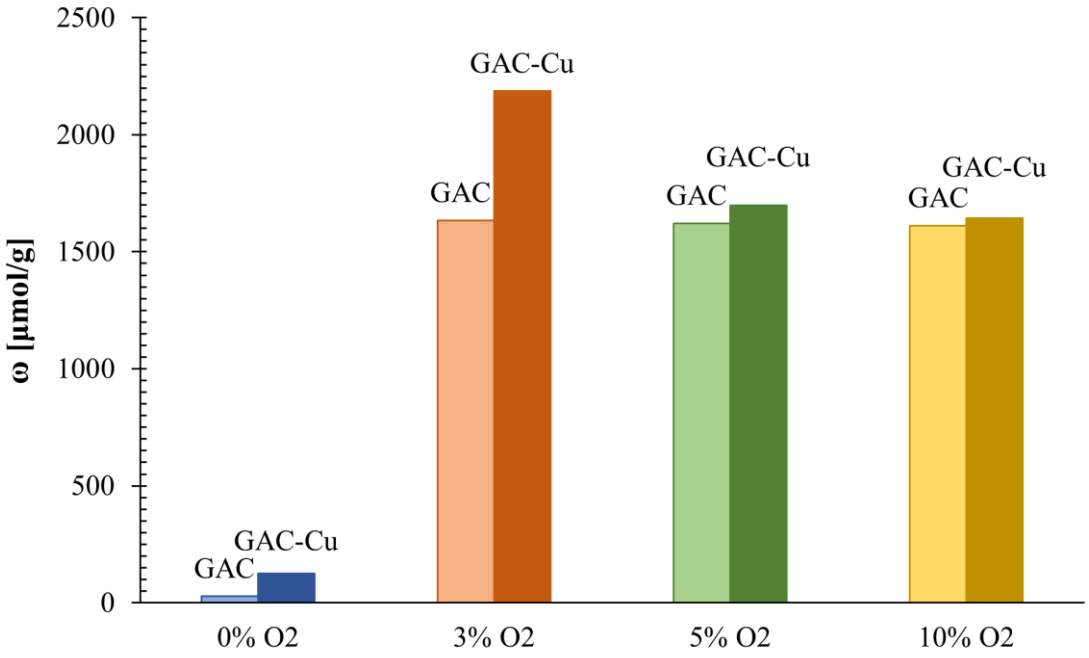

Figure 4.26 - GAC and GAC-Cu adsorption capacities for the adsorption of 250ppm of NO in the presence of 0%, 3%, 5%, 10% of oxygen, balanced in N_2 at 30°C.

For both adsorbent materials, it is clear that the oxygen has a positive effect on the overall NO_x removal. In fact, a drastic improvement of the adsorption capacity has been observed for the inlet gas samples which contain oxygen, as compared with the inlet gas sample without oxygen. Referring to

the adsorption in presence of oxygen, for the GAC-Cu, the NO_x adsorption capacity has a decreasing trend for increasing O_2 inlet concentration, while for the GAC these values all remain kind of constant. For low O_2 inlet concentrations, the GAC-Cu allows to obtain an adsorption capacity higher than the raw GAC, which suggests a catalytic effect of the impregnation. The positive effect of the copper is reduced at higher O_2 inlet concentrations and the value of the adsorption capacity tends to approach the value obtained with the non-impregnated GAC for 10% O_2. This result may be attributable to a deactivation of the copper sites due to an irreversible oxidation, which is enhanced at higher oxygen concentrations.

A similar analysis was made at 120°C. Table 4.16 collects the information provided in the previous sections to observe the saturation times and the adsorption capacities for NO_x as the function of the oxygen concentration and the gas temperature for both the materials.

O_2 [%]	**GAC (120°C)**		**GAC-Cu (120°C)**	
	t_s [min]	**ω_{NOx} [µmol/g]**	**t_s [min]**	**ω_{NOx} [µmol/g]**
0	30	22	100	122
3	51	73	112	250
5	57	83	118	267
10	55	93	109	303

Table 4.16 - Saturation times and adsorption capacities for NO_x, in the presence of 0%, 3%, 5%, 10% of oxygen, balanced in N_2 on GAC and GAC-Cu at 120°C.

Differently from the adsorption at room temperature, the saturation time was almost constant with the oxygen content for both the sorbents; however, the saturation time for GAC-Cu was twice those of GAC. The adsorption capacities were significantly higher for the GAC-Cu; a histogram of the values is reported in Figure 4.27.

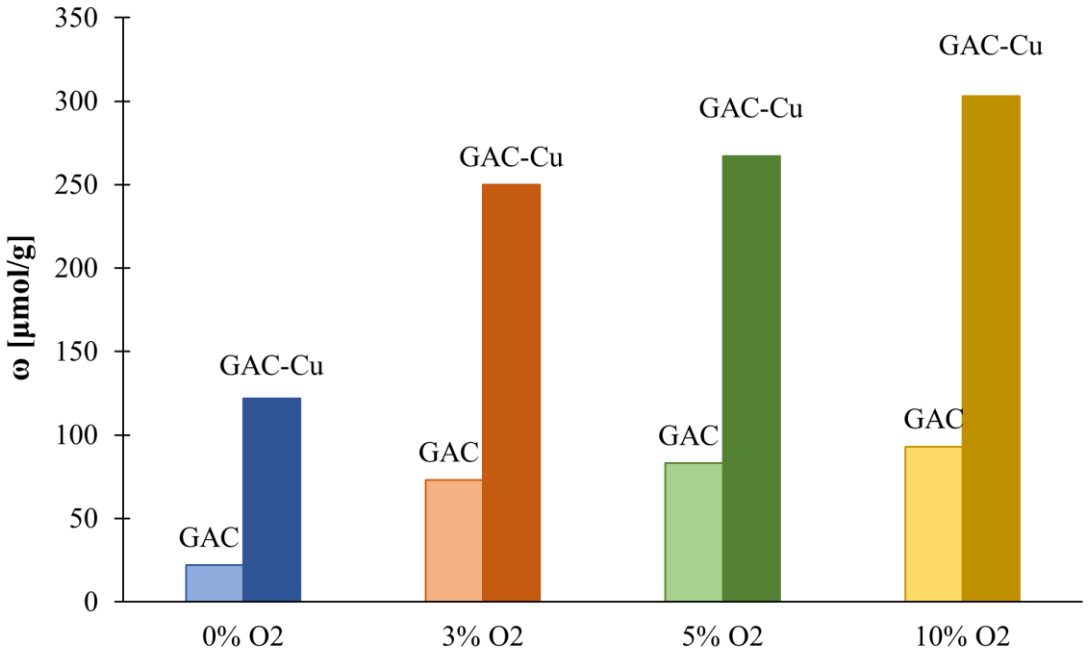

Figure 4.27 - GAC and GAC-Cu adsorption capacities for the adsorption of 250ppm of NO in the presence of 0%, 3%, 5%, 10% of oxygen, balanced in N_2 at 120°C.

The adsorption capacities present the same increasing trend with the O_2 inlet concentration for both types of carbon. Moreover, the differences between the value associated to the GAC-Cu and the GAC seem to remain almost constant as the O_2 concentration increases, in the range 3-10% of oxygen content.

4.4.4 Remarks of the adsorption campaign

The experiments revealed that in the absence of oxygen, the adsorption capacities of GAC and GAC-Cu can be predicted with Langmuir model with a good approximation. When 250ppm of NO were fed, GAC adsorbed about 22-28μmol/g of NO (660-840μg_{NO}/g) either at 30 and 120°C. Even GAC-Cu showed a similar adsorption capacity at the two temperatures; however, it could adsorb about 122-124μmol/g of NO (3.6-3.7mg_{NO}/g). The higher adsorption capacity of the impregnated sorbent may be attributed to the copper that catalyses a dissociative chemisorption of NO. Although the improvement in adsorption capacity for the impregnated sorbent, it is very low to make the process remarkable.

The presence of oxygen in the gas stream gives rise to the onset of NO oxidation processes over the carbon. Both the surface groups over the activated carbon and the copper sites over the impregnated carbon contributes to the NO oxidation. The adsorption capacity of NO_x over the activated carbon is

increased in presence of oxygen. However, the experiment revealed that copper groups are sensitive to oxygen content and gas temperature.

At 30°C, a peak of the adsorption capacity was observed as O_2 content was 3% both for GAC and GAC-Cu. About 1634 and 2187μmol/g (49 and 66 mg_{NO}/g) were captured on the surface of GAC and GAC-Cu respectively. A further increase in the oxygen content led to a significantly drop of the adsorption capacity of GAC-Cu, and a slight decrease for GAC. It was observed that the adsorption capacity at high concentration of O_2 (10%) was similar for the two sorbents (1612-1644μmol/g). This suggests that Cu groups, while having a role in increasing adsorption capacity for low oxygen gases, are deactivated in gas streams containing high percentage of oxygen (10%).

The higher temperature (120°C) inhibited the NO oxidation and the adsorption capacity decreased consequently, as the NO_x adsorption over activated carbons improves with the percentage of NO_2 in the gas stream. Even if the adsorption capacity drops at high temperature, there still be a positive effect of the oxygen and the copper impregnation. Both the GAC and GAC-Cu adsorption capacity increased from 22 to 93 μmol/g and from 122 to 303 μmol/g respectively, as the oxygen content increased from 0 to 10%. The copper played a positive role even at 120°C, improving the adsorption capacity of about 100μmol/g in the absence of oxygen and about 180-210μmol/g in the range of 3-10% of oxygen.

In summary, this study revealed that the uptake of NO over activated carbons, either impregnated or as-they-are, is a complex problem involving many concurring phenomena. In primis, the adsorption of NO, together with the oxidation of NO to NO_2 followed by a very high adsorption of this specimen. On the overall, this oxidation provides a significant improvement of the uptake capacity. While the extra costs of using an impregnating agent as Cu is a valid alternative to improve adsorption at low temperature, its effect is far less relevant for higher temperature and higher oxygen content. Both the sorbents showed a maximum adsorption capacity at 30°C and in the presence of 3% of oxygen; it was 1634μmol/g (49mg_{NO}/g or 75mg_{NO2}/g) and 2187μmol/g (66mg_{NO}/g or 101mg_{NO2}/g) for GAC and GAC-Cu respectively.

5. DIELECTRIC BARRIER DISCHARGE REACTORS FOR NO_X REMOVAL

In the literature, Dielectric Barrier Discharge (DBD) is the most common plasma technology for the reduction of NO_x in N_2 and O_2 [106], [107], [109], [111], [160]. DBD technology was investigated in this thesis and the effectiveness of NO_x reduction are here presented.

Numerical analyses have been performed to simulate the plasma condition in different DBD reactor designs. Two different configurations have been investigated and they consist of a single Dielectric Barrier Discharge (DBD) reactor and a two Dielectric Barriers Discharge (DBsD) reactor. Moreover, two different reactor sizes have been evaluated. A reactor of 2.2cm would simulate the average DBD reactor sizes can be found in the literature [147], while a reactor of 5cm was built up to accomplish the industrial requirements that would reduce the drop pressures of treatment units. Moreover, a threaded rod was used as inner electrode to enhance the electric field in the proximity of the tips of the thread, and hence encouraging the plasma generation.

The software COMSOL Multiphysics was used to estimate the electric field distribution in the designed reactors, by solving the electrostatics equations. Moreover, a complex model that couple the electrostatics equations and the nitrogen plasma chemistry was proposed for the promptest reactor for industrial applications, i.e. the reactor of 5cm with one dielectric layer.

An experimental campaign was performed to evaluate the effectiveness of the plasma reactors for the NO_x conversion. In particular, the reactor of 2.2cm having two dielectrics and the reactor of 5cm having one dielectric layer were investigated. The numerical analysis and the experimental results are presented in this chapter.

5.1 Numerical Analysis for DBD reactors

The software COMSOL Multiphysics has been used to explore the electric and chemical parameters involved in the DBD reactors. Two different physics were studied with COMSOL Multiphysics:

- Electrostatics physics;
- Plasma physics.

Electrostatics physics offer a simplified model that can be used to evaluate the electrical parameters e.g. electric potential and electric field, in the function of the geometry's design, the materials and the voltage applied. This model has been used to calculate these electric parameters and their distribution for the geometries tested experimentally.
Plasma physics include electrochemical reactions that participate in the distribution of the electric parameters. The electrons' impact and the generation of charged species affect the external electric field and determine a local electric field with a different distribution.

Space or time-dependent problems are usually expressed in terms of partial differential equations (PDEs). In most of the cases, PDEs cannot be solved analytically. Numerical methods, as the Finite Element Method (FEM), give an approximation of the solution to mathematical models using a discretization of the modelled domain and the dependent variables. The mathematical model is discretized into finite pieces called elements and different laws are applied on the single element. The truncation error introduced by the numerical model is defined as the difference between the solution of the numerical and the mathematical model. The numerical model is said consistent when the solution given is stable and the error approaches zero.
COMSOL Multiphysics is a finite element simulation software for modelling and numerical solving of physics and engineering processes, as well as coupled phenomena, or Multiphysics. COMSOL Multiphysics has a number of built-in set of equations with dedicated numerical methods that allow numerous solutions of specific physical problems, e.g. hydrodynamics, electrostatics, plasma, etc. These set of equations are called "physics" and can be coupled together to solve complex problems called "Multiphysics".
The software has a defined equation-based modelling approach. Assuming the generic dependent variable u, function of the three directions of the space and of the time, the generic coefficient form PDE used by COMSOL is:

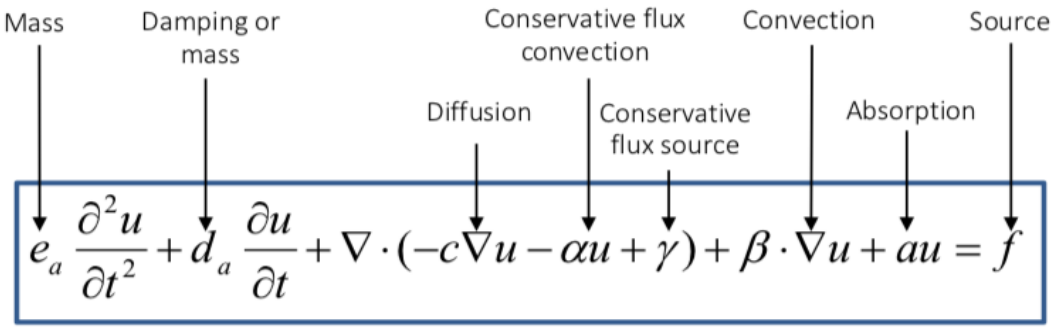

This PDE allows COMSOL to solve the equations of different physical process by specifying units for independent variables and the coefficients above.

In this mathematical approach, boundary conditions are required. These can be:

- Dirichlet conditions, which define a set a values (or a range of values) for the dependent variables;
- Neumann conditions, which prescribe a flux, i.e. a gradient of the dependent variable;
- Robin conditions, which define a relation between the variable and its gradient;

In this study, two built-in physics interfaces have been selected, Electrostatics (es) and Plasma (plas) with the relative governing equations and boundary conditions. The main equation solved in the two modules, the geometries designed and the results will be presented in the next paragraphs.

5.1.1 Electrostatics module

Electrostatics is the subfield of electromagnetics describing an electric field caused by static (non-moving) charges. In free space, with a space charge density ρ, the electric field E is related to ρ:

$$\nabla \cdot \boldsymbol{E} = \frac{\rho}{\varepsilon_0} \qquad \textit{(Eq. 5-1)}$$

where ε_o is the permittivity of vacuum (the predefined value is $8.854 \cdot 10^{12}$ [F/m]).
This relationship means that in the Electrostatics physics the space charge density behaves like a volume source. The charge-field relationship is not enough, but the following Maxwell's equation implies the additional requirement that the electric field is irrotational (or curl free):

$$\nabla \, x \, \boldsymbol{E} = 0 \qquad \textit{(Eq. 5-2)}$$

For an irrotational field **E**, a scalar potential exists, which leads to the definition of the electric potential V, as:

$$-\nabla V = \boldsymbol{E} \qquad \textit{(Eq. 5-3)}$$

So, the charge-field equation becomes:

$$-\nabla \cdot \nabla V = \frac{\rho}{\varepsilon_0} \qquad \textit{(Eq. 5-4)}$$

However, the electric field in a dielectric material is different from that of free space and the equation above needs to be solved integrating the effect of induced polarization by dielectrics.
A typical dielectric material does only have bound charges. At the microscopic level, these bound charges can be displaced by an external electric field and result in induced electric dipoles, which are pairs of positive and negative charges that align with the electric field to a certain extent. This creates an internal electric field that reduces the overall field within the dielectric itself.
To give a macroscopic idea of this phenomenon, a polarization vector field **P** and its charge density ρ_P are both introduced. They are related as follows:

$$\rho_P = -\nabla \cdot \boldsymbol{P} \qquad \textit{(Eq. 5-5)}$$

The polarization effects locally change the electric field, resulting in that:

$$\nabla \cdot \boldsymbol{E} = \frac{\rho + \rho_P}{\varepsilon_0} \qquad \textit{(Eq. 5-6)}$$

which can be also expressed:

$$\nabla \cdot (\varepsilon_0 \boldsymbol{E} + \boldsymbol{P}) = \rho \qquad \textit{(Eq. 5-7)}$$

At this point, a new fundamental quantity can be introduced: the electric displacement field **D**, defined as follows:

$$\boldsymbol{D} = \varepsilon_0 \boldsymbol{E} + \boldsymbol{P} \qquad \textit{(Eq. 5-8)}$$

Using this definition, the electrostatic equation, also known as Gauss's law, becomes:

$$\nabla \cdot \boldsymbol{D} = \rho \qquad \textit{(Eq. 5-9)}$$

Assuming the dielectric material as linear, the polarization vector field P is proportional to the electric field:

$$\boldsymbol{P} = \varepsilon_0 \chi_e \boldsymbol{E} \qquad \textit{(Eq. 5-10)}$$

where the constant of proportionality χ_e is the electric susceptibility. Combining this with the previous relationship between **D** and **E**, results in:

$$\boldsymbol{D} = \varepsilon_0 \boldsymbol{E} + \boldsymbol{P} = \varepsilon_0 \boldsymbol{E} + \varepsilon_0 \chi_e \boldsymbol{E} = \varepsilon_0 (1 + \chi_e) \boldsymbol{E} \qquad \textit{(Eq. 5-11)}$$

The quantity $(1 + \chi_e)$ is the relative permittivity of the dielectric material, ε_r. It quantifies how well a material is polarized in response to an applied electric field. The new constitutive relationship for linear dielectric materials gets:

$$\boldsymbol{D} = \varepsilon_0 \varepsilon_r \boldsymbol{E} \qquad \textit{(Eq. 5-12)}$$

The Gauss' law evaluates the electric field, as the electric potential is the dependent variable. Thus, the fundamental equation for Electrostatics in linear materials is:

$$-\nabla \cdot (\varepsilon_0 \varepsilon_r \nabla V) = \rho \qquad \textit{(Eq. 5-13)}$$

In COMSOL, the Gauss's law sets specific conditions on the divergence and curl of the electric field, respectively. At the material interfaces, the divergence condition is applied on the normal component of the field, the curl condition on the tangential component of the field.
Material interfaces represent discontinuities, and to understand what conditions to impose on boundaries, the corresponding integral forms are commonly used. The boundary formulations are then derived by taking the limit of a shrinking closed surface (Gauss's law), which enclose a portion of the material interface. The forms of the Gauss' law equation and the relative boundary condition are summarized as follows:

Differential Form	**Integral Form**	**Boundary Condition**
$\boldsymbol{\nabla \cdot D = \rho}$	$\oint \boldsymbol{D \cdot n}\, ds = Q$	$\boldsymbol{n \cdot (\mathbf{D_1} - \mathbf{D_2})} = \rho_s$
All field lines start and end on charges	The total flux through a closed surface equals its enclosed charge	The surface charge at a material interface equals the jump in the normal component of the displacement field

"*Charge Conservation*" is the main node of the Electrostatics Interface, used to define the equation for the conservation of the charge in a domain, according to the Gauss' law. This also specifies the constitutive relation for the electric displacement field and its associated properties such as the relative permittivity:

$$\boldsymbol{D} = \varepsilon_0 \varepsilon_r \boldsymbol{E} \qquad \textit{(Eq. 5-14)}$$

At a given electric potential, the dielectric material is polarized by the electric field and its surface accumulates an electric charge, resulting in a discontinuity of the electric displacement vectors on both sides of the dielectric interface. This phenomenon is described with the "*Surface Charge Accumulation*" boundary condition:

$$\boldsymbol{n} \cdot (\mathbf{D_1} - \mathbf{D_2}) = \rho_s \qquad \textit{(Eq. 5-15)}$$

where $\mathbf{D_1}$ and $\mathbf{D_2}$ are the electric displacement vectors on both sides (nitrogen side and dielectric side) of the insulation surface; ρ_s is the surface charge density, which can be computed by solving this distributed ODE on the boundary:

$$\frac{d\rho_s}{dt} = \boldsymbol{n} \cdot \boldsymbol{J_i} + \boldsymbol{n} \cdot \boldsymbol{J_e} \qquad \textit{(Eq. 5-16)}$$

where $\mathbf{n} \cdot \mathbf{J_i}$ is the normal component of the total ion current density on the wall and $\mathbf{n} \cdot \mathbf{J_e}$ is the normal component of the total electron current density on the wall, which are feature inputs.

Including the surface charge accumulation condition is relevant in COMSOL to describe the effect of the dielectric material on the electric field distortion (as said, the electric field is influenced by the induced polarization). However, in this simulation no reactions or species are introduced, so the right term of the equation is assumed as 0 and the surface charge is a constant. This allows to only focus on the electrical aspect of plasma and run the model without further complications due to the chemistry node.

The "*Zero Charge*" sets the condition of a charge null at the boundary so that:

$$\boldsymbol{n} \cdot \boldsymbol{D} = 0 \qquad \textit{(Eq. 5-17)}$$

This is the default boundary condition at exterior boundaries. At interior boundaries, it means that no displacement field can penetrate the boundary and that the electric potential is discontinuous across the boundary. It is also applicable at symmetry boundaries where the potential is known to be symmetric with respect to the boundary.

The "*Ground*" node implements ground (or zero potential) as the boundary condition.

The "*Terminal*" node provides a boundary or domain condition for connection to external circuits, to transmission lines, or with a specified voltage or charge.

5.1.1.1 Design of the reactors

DIELECTRIC BARRIER DISCHARGE REACTOR

The reactor was designed in COMSOL Multiphysics using a 2-D axisymmetric model. A higher dimension model would have been unpractical to study, due to the high computing time and memory required by the software at the conditions set in this work. Thus, the axial symmetry tool allows to simplify the 3-D geometry and represent a co-axial DBD, taking into account the radial component of this reactor. In this way, a first insight into the main electrical characteristics of the discharge is gained without excessive computation time.

The screw thread was simulated taking into account the standard tolerance of M5 construction design. The glass and the ground electrode were designed as rectangles, hence defining two tubes by their

revolution around the axis, while the gas gap was considered as the space between the glass and the screw thread.

The revolution of the geometry and a zoom of the screw thread are shown in Figure 5.1.

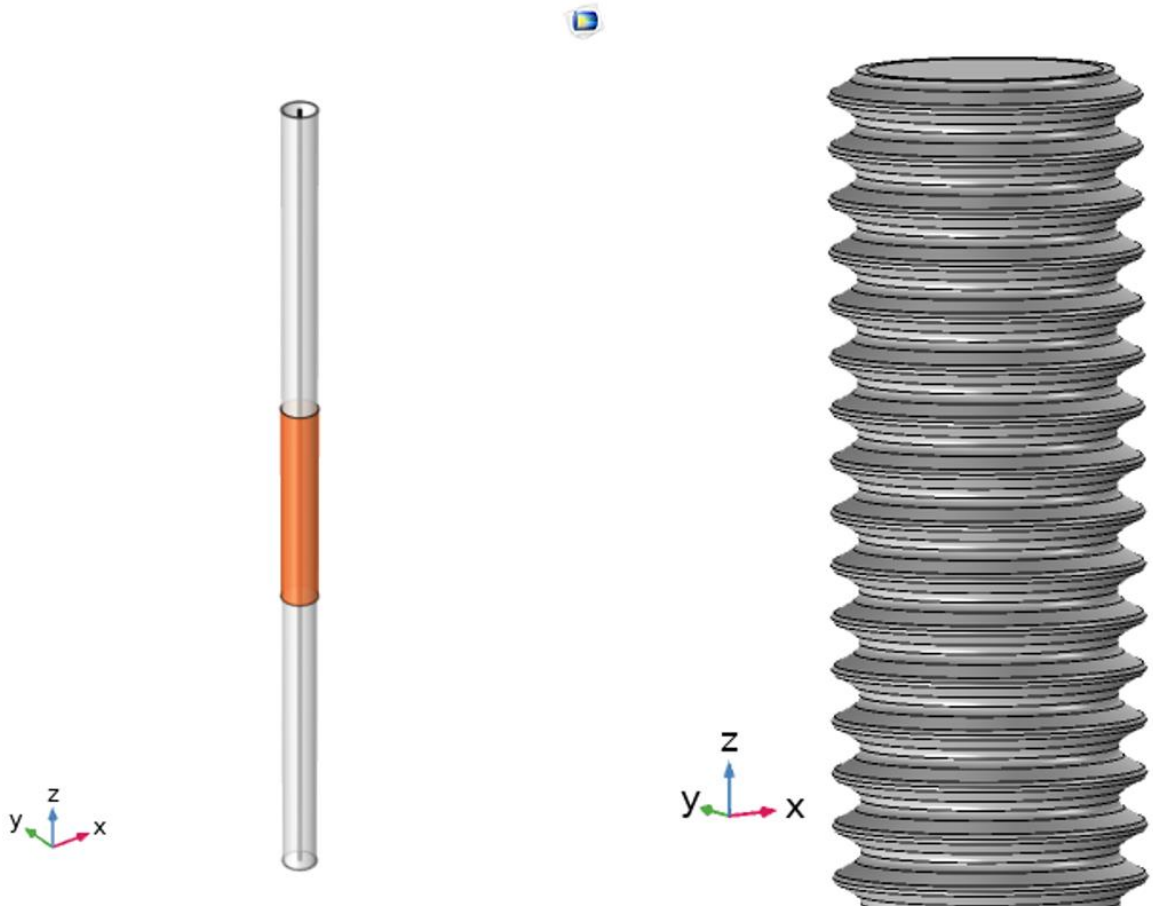

Figure 5.1 - Revolution of the 2D axial symmetric design of the DBD reactor having a screw thread as HV electrode (left) and zoom of the screw thread (right).

In Figure 5.1, the screw thread is represented in dark grey, the glass is transparent grey tube and the copper tube is shown in orange. Both the screw thread and the glass tube were of 1.2m long as the real reactor, and the copper tube was 30cm long with the thickness of 1.5mm. The thickness of the glass was of 2.5mm.

A zoom of the 2D axisymmetric geometry is shown in Figure 5.2.

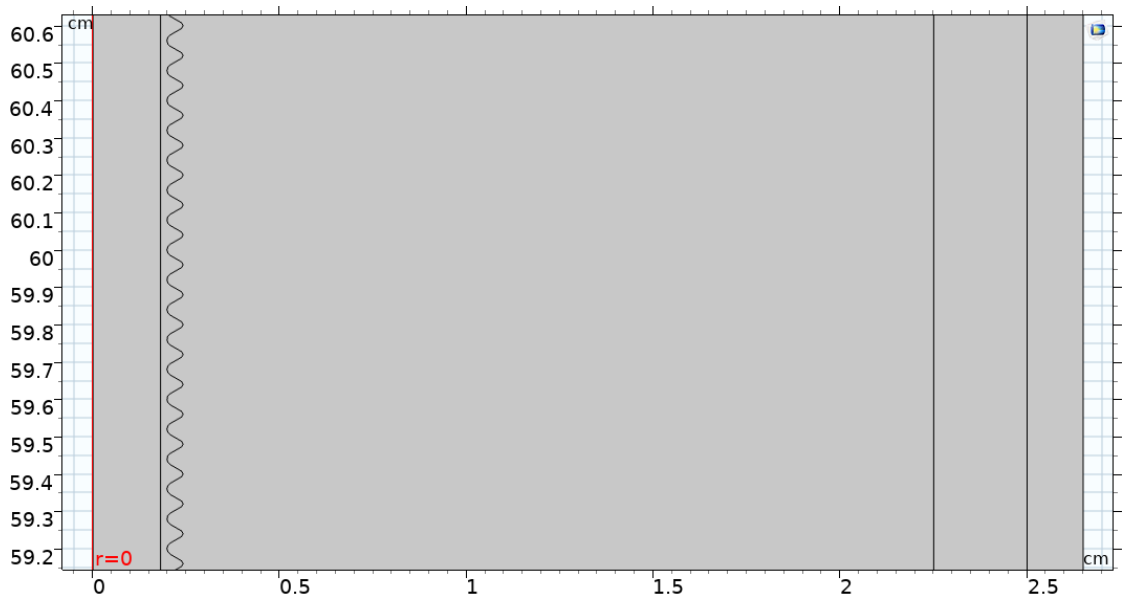

Figure 5.2 - Zoom of the 2D axisymmetric DBD of 5cm, in the middle of the reactor.

From Figure 5.2, it is possible to note the curve edges of the screw tips and the component sizes. Moving rightward, the vertical curves represent: the axis of symmetry (R=0), a form line for the construction of the rod (R≈0.18), the external surface of the rod (R≈0.22-0.24), the inner surface of the glass (R=2.25), the outer surface of the glass (R=2.5), the outer surface of the copper (2.65).

The results from the numerical analysis were plotted on the external surface of the reactor (3D plot) as in Figure 5.1 (left), on the corresponding of the yz cut-plane (2D plot), and at specific cut-lines (1D plots). An example of the yz cut-plane view is shown in Figure 5.3.

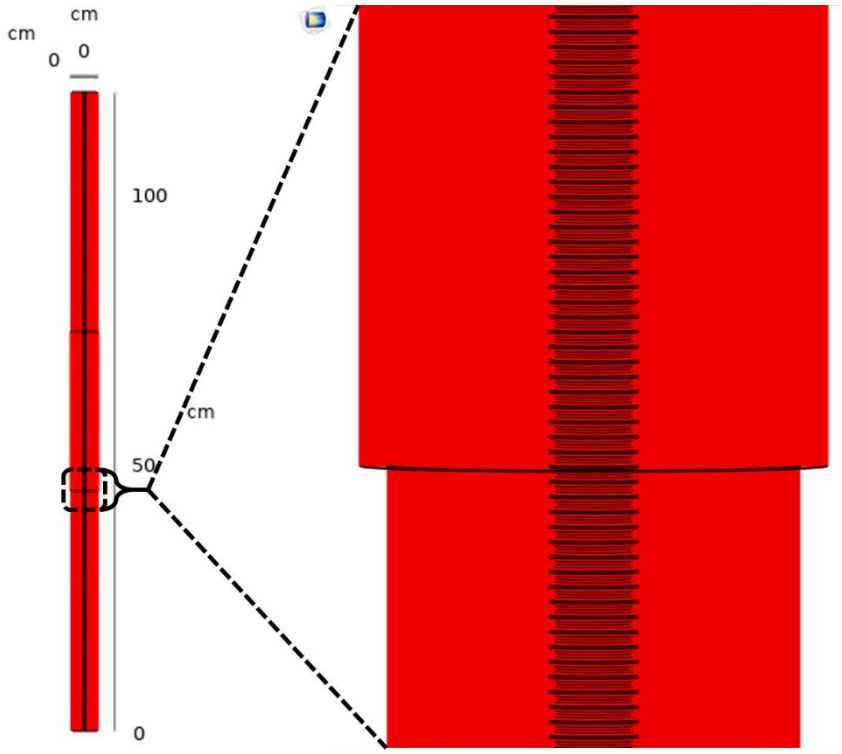

Figure 5.3 - yz cut-plane for the DBD reactor (left) and zoom in the proximity of the lower edge of the copper (right).

The cut-plane is represented in red while the cuts of the thread are represented with black lines.

For what concern the cut-lines, they can be divided in two groups: the radial cut-lines and the longitudinal cut-lines. The radial cut-lines were defined in the proximity of the middle of the reactor, in the proximity of the lower copper edge and in the proximity of 22.5cm quote that was denoted as outside of the plasma region. The three radial cutlines are shown in Figure 5.4.

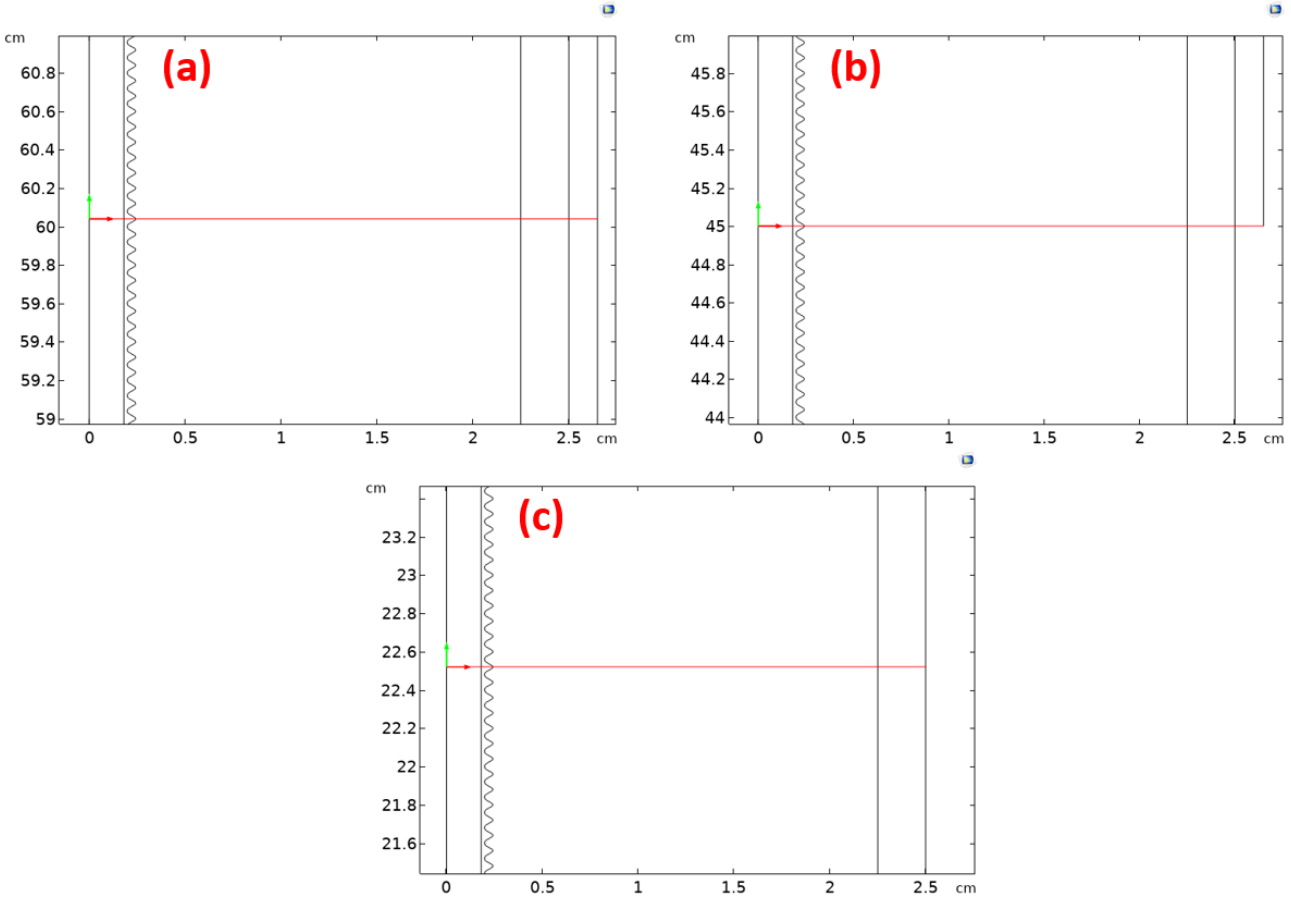

Figure 5.4 - Radial cut-lines for the DBD reactor in the proximity of: middle of the reactor (a), edge of the copper (b), outside from the plasma region (c)

The cut-lines were calculated in order to include the tips of the thread. In fact, in that region is supposed to be maximum the electric field as the edge effect. Also, the edge cut-line was designed in order to include both the tip of the electrode and the edge of the copper, for the reasons above. It must be remembered that the designed geometry was 2D with axial symmetry. Hence, the cutlines were considered in the 2D simplified geometry, considering the radius R=0 as the axis of symmetry.

The longitudinal cut-lines were designed to give a perception of the electric parameter distribution in the length and the radius of the reactor. The longitudinal cut-lines are shown in Figure 5.5.

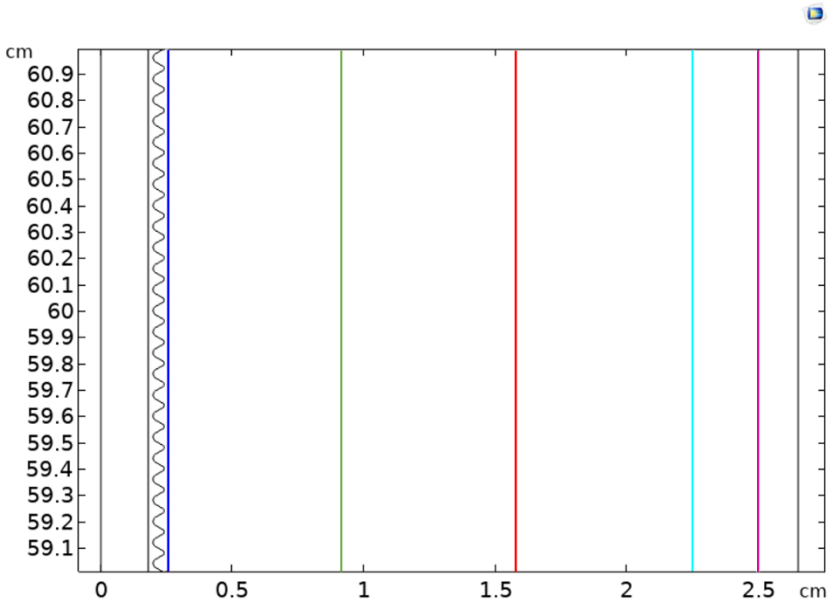

Figure 5.5 - Zoom of the longitudinal cut-lines for the DBD reactor at 2.5mm from the axis (blue), at 1/3 of the gas gap (green), at 2/3 of the gas gap (red), in the corresponding of the inner (azure) and outer (purple) surface of the glass.

The cut-line closest to the axis was designed at 2.5cm that corresponds to the nominal radius of the screw (blue line). However, due to the standard thread tolerance, the tips of the screw have a radius lower than that. Two longitudinal cut-lines were designed in the gas gap at 1/3 and 2/3 of the gap (green and red lines), and two cutlines were designed at both the surfaces of the glass (azure and purple lines).

A similar design was evaluated for the reactor having the glass tube 22mm OD and 2mm of thickness. The cut-plane and the cut-lines were designed as above. It must be considered that the radial cutlines are not influenced by the radial size of the reactor, while the longitudinal cut-lines were parametric with the radius, with the exception of the cut-line at 2.5mm; in fact, the rod radius did not change with the reactor tube. Hence, the cutlines designed were at 2.5mm radius, at 1/3 and 2/3 of the gas gap, and at the two sides of the glass.

Two Dielectric Barriers Discharge Reactor

In accordance with the experimental results, the two dielectric barriers discharge reactor was simulated with COMSOL Multiphysics; in particular, two different reactors were investigated by considering the reactor size of 5cm and 2.2cm. Starting from the geometries as they were described in the previous section, a quartz glass of 8mm OD, 1.5mm of thickness and 50 cm long was placed centred into the reactor, covering the screw. A zoom of the 2D axisymmetric geometry is shown in Figure 5.6.

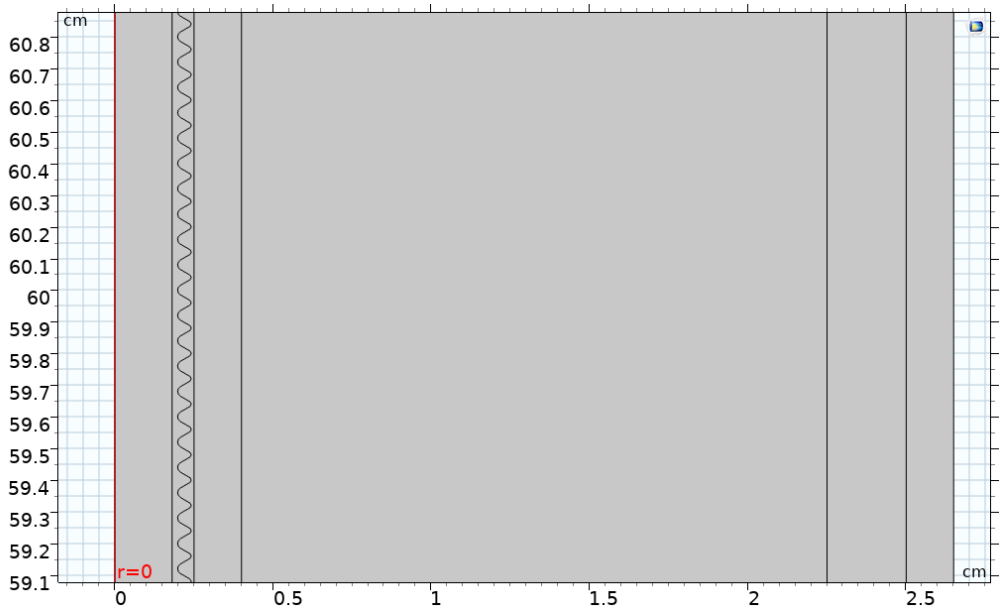

Figure 5.6 - Zoom of the 2D axisymmetric two DBsD of 5cm, in the middle of the reactor.

In this case, the quartz was represented by the rectangle within the radius of 2.5 and 4mm. The gas was declared for both the gaps between the screw and the quartz, and between the quartz and the silica glass. Even in this case, the cut-plane and the radial cut-lines did not change, while a further longitudinal cut-line was considered. All the longitudinal cut-lines are shown in Figure 5.7.

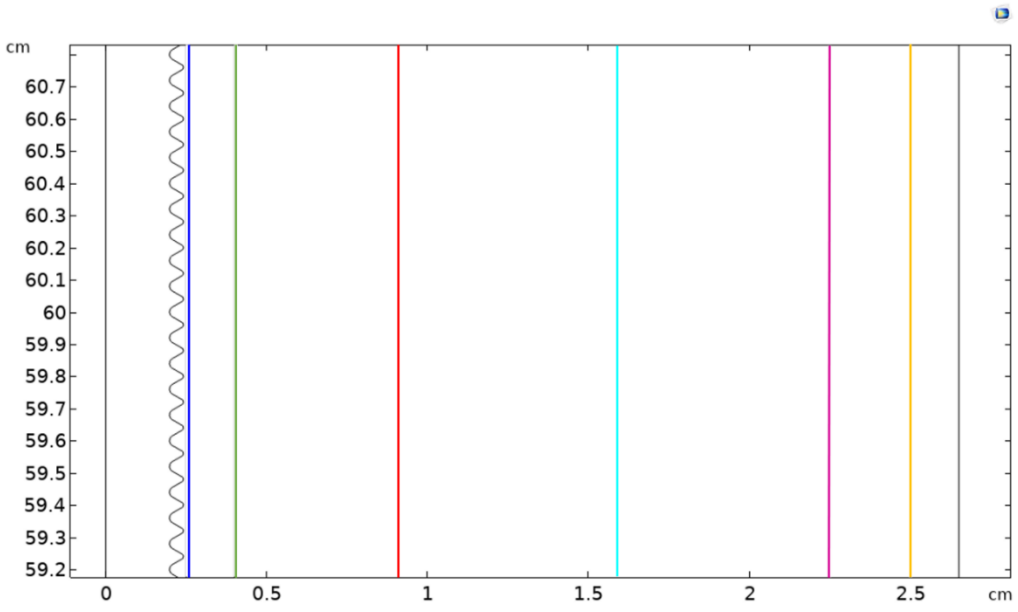

Figure 5.7 - Zoom of the longitudinal cut-lines for the two DBsD reactor at the inner (blue) and outer (green) surface of the quartz, at 1/3 (red) and 2/3 of the distance between the rod and the glass (azure), at the inner (purple) and outer (yellow) surface of the glass.

In conformity with the simulations of the DBD reactor, the longitudinal cut-lines were considered parametric with the radius in order to analyse the differences between the reactor of 5cm and that of 2.2cm.

5.1.1.2 Computational Mesh

In this model, a built-in triangular mesh was used overall. It comprises a set of triangles (typically in three dimensions) connected by their common edges or corners.

Meshing is a crucial part in the modelling: it is important to ensure the quality of the results in a reasonable time. Certainly, a fine mesh leads to more accurate results, but requires a longer computational time.

The strategy is to build a coarser mesh to save memory and customize the distribution and size of the elements depending on the domain. In the plasma region, the maximum element size was 0.08cm. In the corresponding of the screw thread surface, source of the electric field, and in the ground volume, a finer distribution was imposed, having a maximum element size of 0.03 cm. The computational mesh for the inner volume of the screw thread and the gas volume, out of the plasma region, was imposed with a maximum element size of 0.1cm.

An extremely fine computational mesh was designed in those regions where the electric parameters distribution had great oscillations, as in the proximity of the tips of the screw, the glass and the ground electrode. Due to the rectangular shape of the glass, a "*mapped*" computational mesh was designed in the corresponding of the silica and the quartz glasses. For the silica glasses, in the plasma region, 800 elements were imposed for the longitudinal direction with the growing ratio of 4 toward the centre of the reactor, while 16 elements were imposed for the radial direction with the growing ratio of 4 toward the two surfaces of the glass. Moreover, an extremely fine computational mesh was designed close to the radial cutlines in the gas volume. A number of 120 elements were imposed between the tips of the screw thread and the inner surface of the glass, with the growing ratio of 5 toward the edges. A zoom of the designed computational mesh for the DBD, in the centre of the reactor, is shown in Figure 5.8.

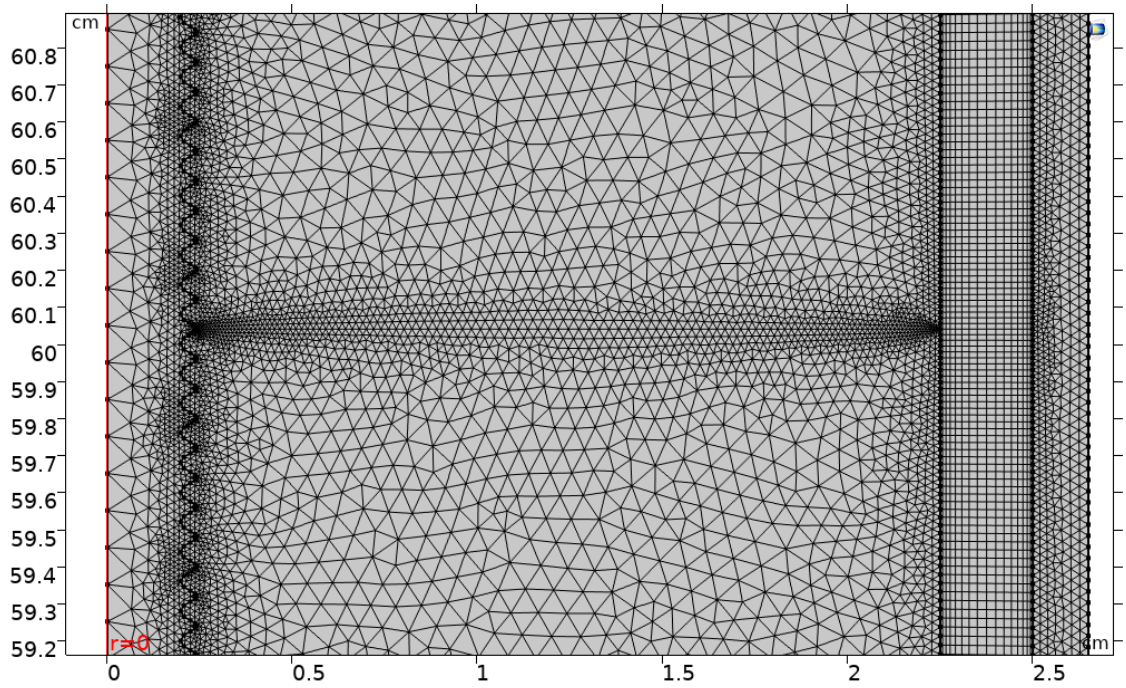

Figure 5.8 - Zoom of the computational mesh for the DBD reactor of 5cm.

From the Figure 5.8, it is possible to note the higher number of computational nodes in the proximity of the regions where higher oscillations of the electric parameters were expected.

In the geometry with two dielectrics, a “mapped” computational mesh was designed in the plasma region. A number of 80 elements were imposed for the radial direction with the growing ratio of 5 toward the surfaces of the glasses, for the 5cm reactor while 30 elements were imposed for the 2.2cm reactor. The number of elements in the quartz volume was the same as that in the silica glass, and further 5 elements were imposed between the thread tips and the quartz in the proximity of the cut-lines. Hence, the designed computational mesh for the two DBsD, in the centre of the reactor, appears as in Figure 5.9.

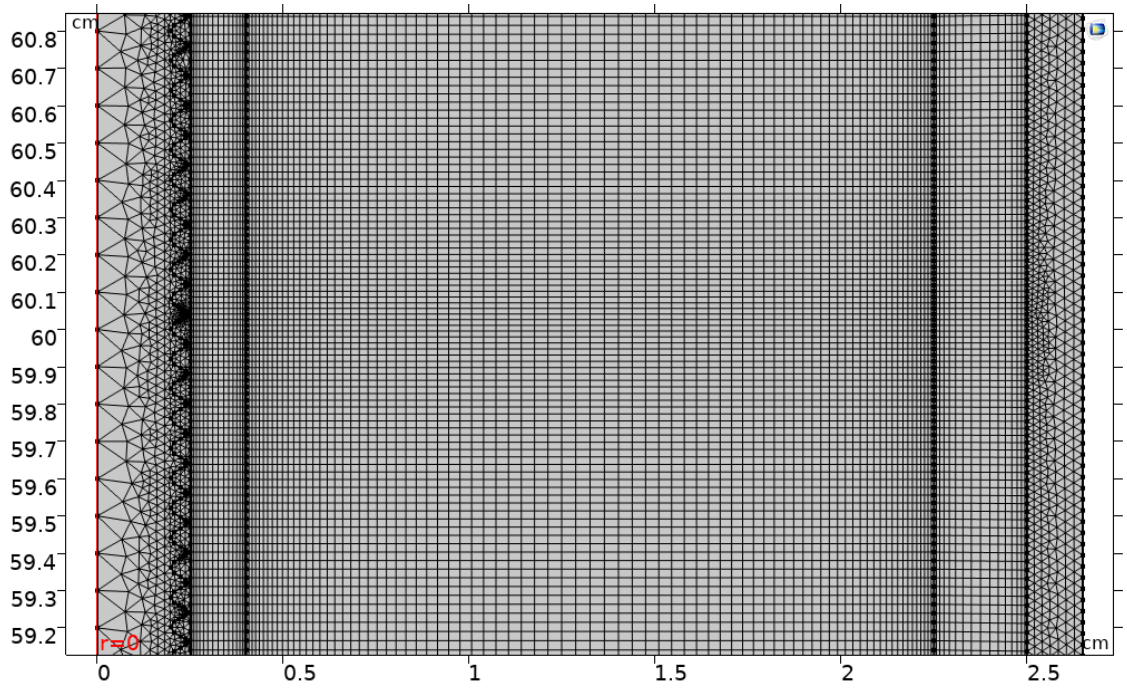

Figure 5.9 - Zoom of the computational mesh for the two DBsD reactor of 5cm.

5.1.1.3 Study and Solver set-up

The materials were taken from the COMSOL Multiphysics library. The screw thread was defined as Steel AISI 4340, the gas as pure nitrogen, the two tubes as quartz and silica glasses, the ground as copper. For the resolution of the electrostatics physics, the relative permittivity plays a key role, as it was discussed above. For each material, ε_r is provided:

- ε_r=1 for Nitrogen, Steel and Copper;
- ε_r=4.20 for Quartz Glass (dielectric);
- ε_r=3.75 for Silica Glass (dielectric).

The *Charge Conservation* condition, as in Equation (Eq. *5-14)*, was applied to all the geometry to calculate the electric field distribution both in the solid materials and in the gas.

A sinusoidal voltage was applied at the external surface of the screw thread (*Terminal* condition), as the function:

$$V_{app} = -V_0 \cdot \sin(\omega_0 \cdot t) \qquad \textit{(Eq. 5-18)}$$

Where V_o is the amplitude of the voltage applied, and ω_o is the angular frequency, that can be expressed as:

$$\omega_0 = 2\pi \cdot f_0 \qquad \textit{(Eq. 5-19)}$$

Where f_0 is the Radio Frequency (RF).
Unless otherwise specified, the voltage amplitude and the RF were fixed at the values of 20kV and 1kHz, respectively.
The *Ground* condition was applied to the edges of the copper.
All the other edges, with the exception of the axis of symmetry, were defined as *Zero Charge*.

COMSOL requires the initial value of the electric potential, as a first trial for a non-linear solver. The default value was 0V.

A time-dependent study was made. The time interval for the output was from 0 to $2/f_o$ (2 sine periods), with 24 number of instants per period; in fact, the solution was periodic from the second sine period, as the interference of the initial conditions quickly become negligible, and it extinguished in the first period.
COMSOL automatically detects the best solver without requiring any user interaction. For this simulation the MUMPS direct-solver was used. The direct solvers will use more memory than the iterative solvers but can be more robust. They are based on the lower-upper (LU) decomposition, that factors a matrix as the product of a lower triangular matrix and an upper triangular matrix.

5.1.1.4 Simulation results for the DBD reactors of 5cm

The electrostatics module was solved for the DBD and the DBsD. Both the reactors having 5cm and the 2.2cm as outer diameter have been investigated in the configurations with one and two dielectrics.

ONE DIELECTRIC BARRIER DISCHARGE

The geometry of the DBD reactor shown in Figure 5.1 was built in COMSOL. The sinusoidal voltage, as in Equation (Eq. *5-18)*, was declared on the rod surface. Unless otherwise indicated, the sinusoidal function amplitude was of 20kV and the frequency of 1kHz. The simulations were performed in the time range of 0-2ms as the electric parameters' distributions become independent from the initial values after the first cycle and they are periodic in the next sinusoidal periods. Hence, the study is focused on the time frame 1-2ms, where the voltage applied to the inner electrode is shown in Figure 5.10.

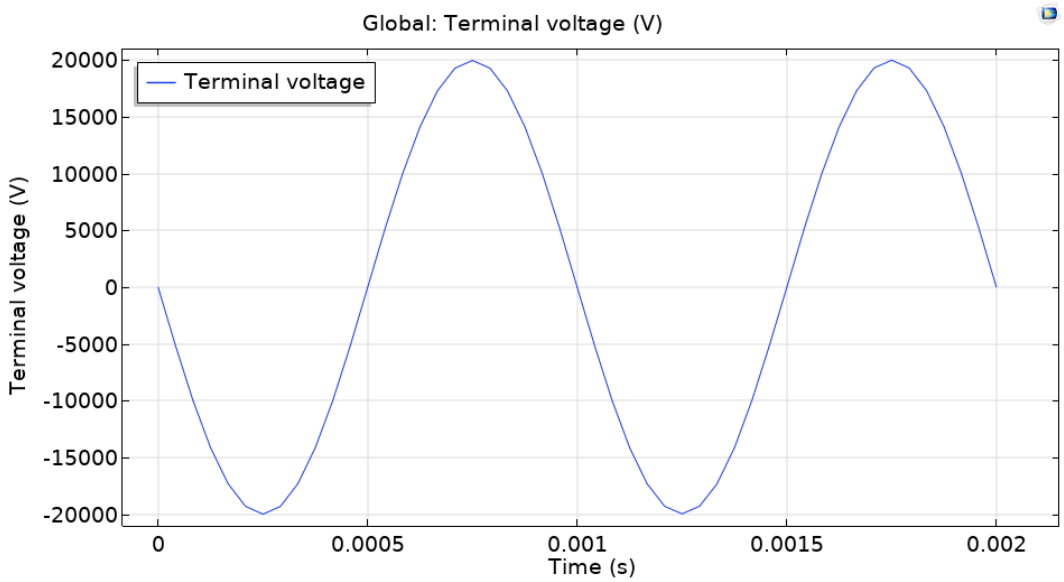

Figure 5.10 - Applied Voltage to the inner electrode surface with V_0=20kV and f =1kHz.

The sine wave is full developed in the range 1-2ms at 1.25ms and the maximum of 20kV at 1.75ms. The 3D view, showed in Figure 5.1, can be used to show the electric potential on the external surface of the reactor. The electric potential distributions on the external surface of the reactor at the instants 1.25 and 1.75ms are shown in Figure 5.11.

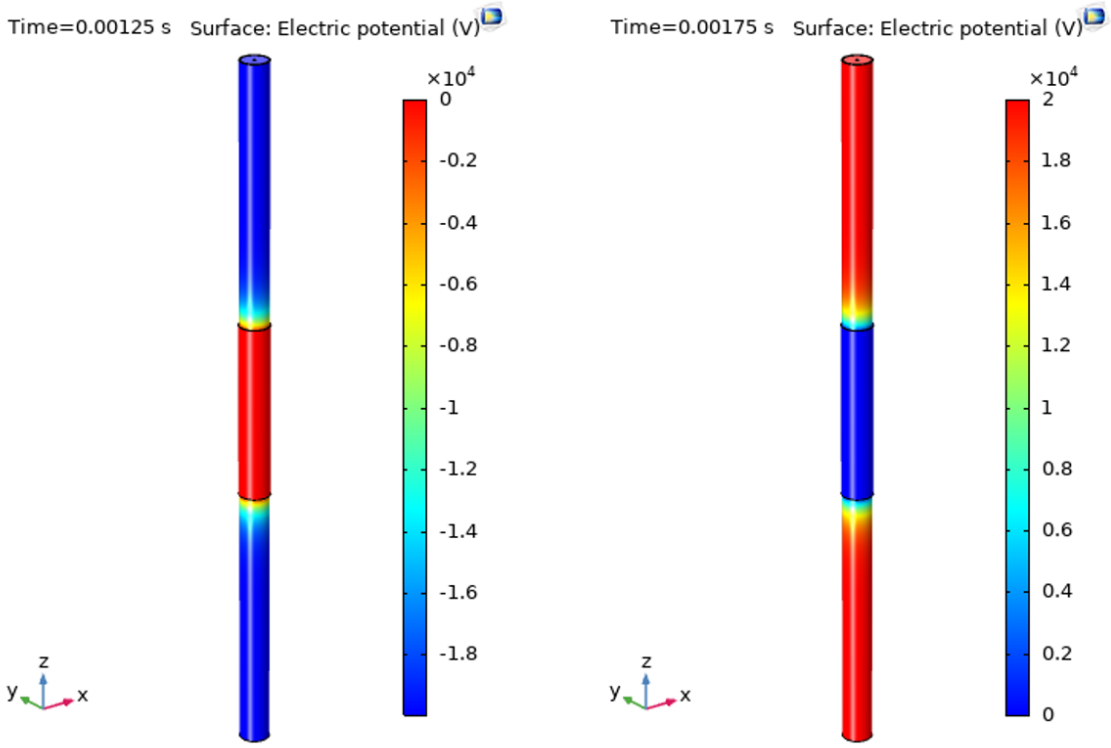

Figure 5.11 - Electric potential distribution in a 3D view of the DBD reactor of 5cm at 1.25ms (left) and 1.75ms (right).

When the voltage applied to the inner electrode achieves the minimum (at t=1.25ms), the electric potential on the external surface of the reactor has a gradient (Figure 5.11 left). It is equal to zero in the corresponding of the ground, while it decreases up to about -20kV, far from the ground. When the voltage applied to the inner electrode achieves the maximum (at t=1.75ms), the electric potential on the external surface is equal to zero in the corresponding of the ground, while it rises to about 20kV, far from the ground (Figure 5.11 right). These results suggest that a gradient of the electric potential occurs into the reactor, in the proximity of the ground quote. On the contrary, the electric potential seems to not be influenced by the ground, for the quote far enough from the ground.
The electric field norm on the external surface of the reactor is shown in Figure 5.12.

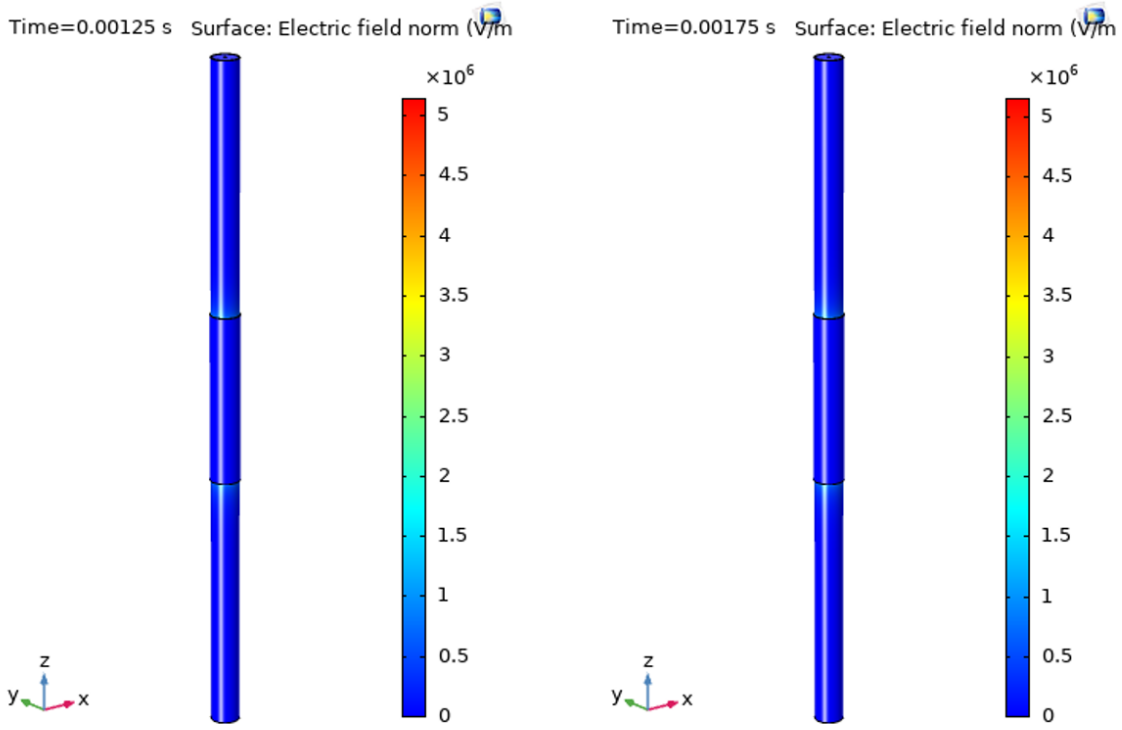

Figure 5.12 - Electric field norm distribution in a 3D view of the DBD reactor of 5cm at 1.25ms (left) and 1.75ms (right).

Although the scales of the electric field norm suggest that a gradient occur somewhere, it is not clear from Figure 5.12. A light azure can be observed in the proximity of the edges of the copper in contact with the glass, where the electric field norm increases.
Both the electric potential and the electric field norm can be evaluated into the reactor, plotting the variables on the cut-plane defined in Figure 5.3.
The electric potential and the electric field distributions on the 2D cut-plane, in the proximity of the ground electrode, are shown in Figure 5.13 and Figure 5.14 respectively.

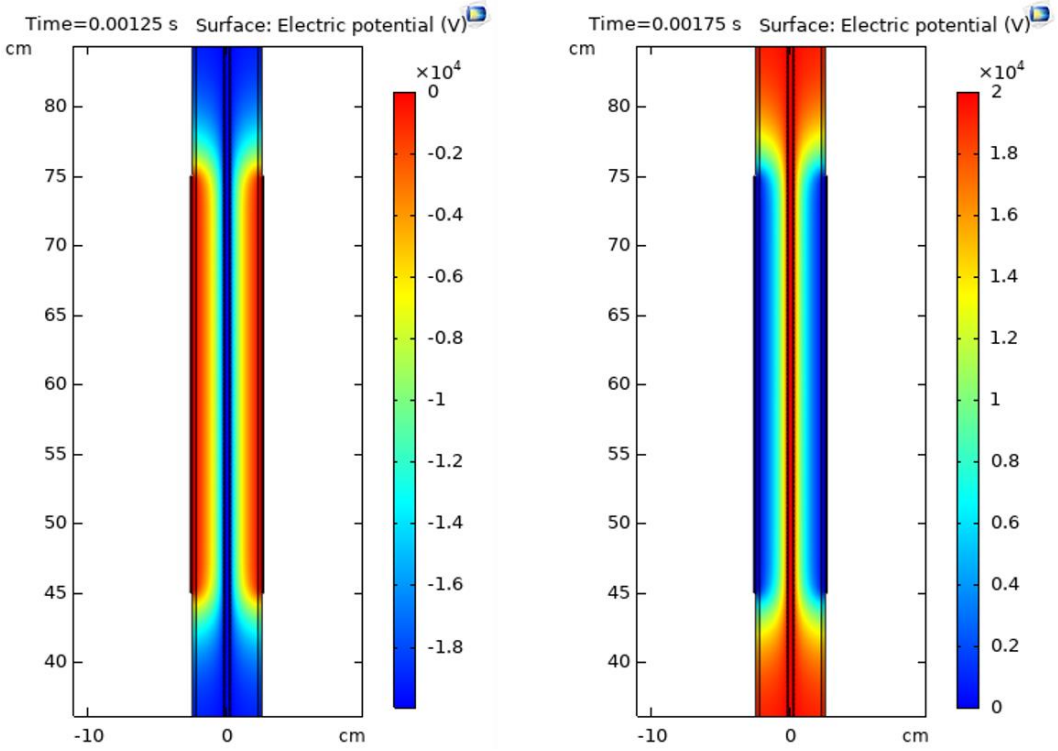

Figure 5.13 - Zoom of the electric potential distribution in a 2D view of the DBD reactor of 5cm at 1.25ms (left) and 1.75ms (right).

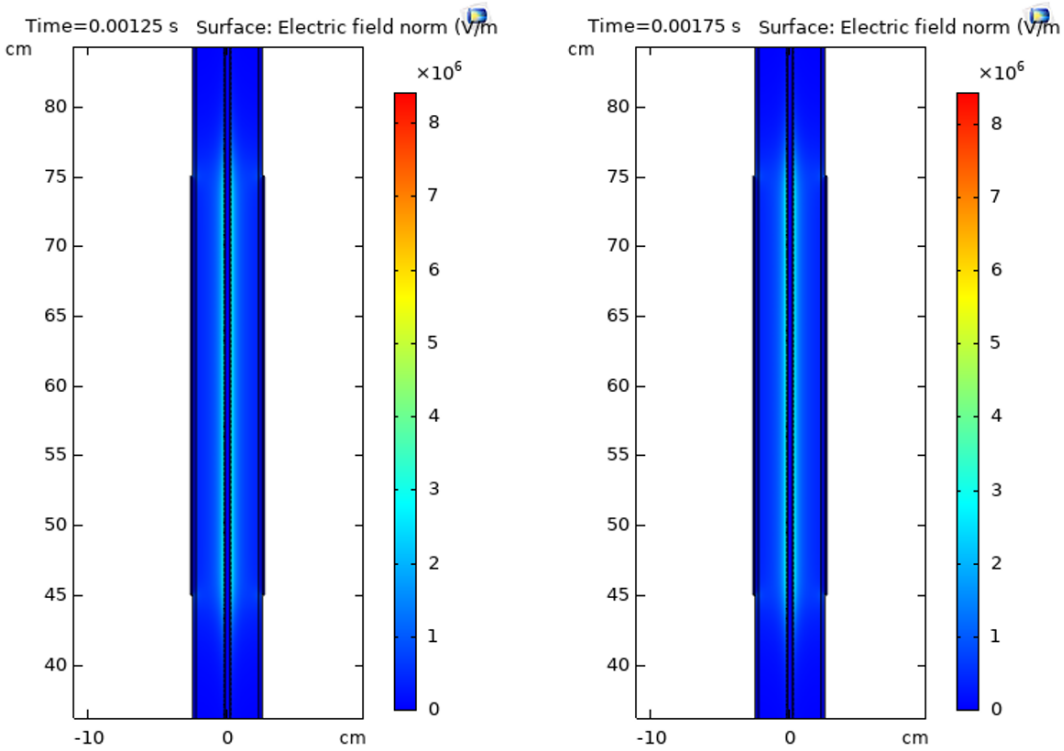

Figure 5.14 - Zoom of the electric field norm distribution in a 2D view of the DBD reactor of 5cm at 1.25ms (left) and 1.75ms (right).

Both the electric potential and the electric field norm gradients are radial, and they are more relevant in the proximity of the ground electrode quote. The voltage rises from the centre toward the ground

where it becomes zero, at the time 1.25ms (Figure 5.13 left). On the contrary, it decreases radially from 20kV to zero at 1.75ms (Figure 5.13 right). The electric potential gradient at 1.25ms is perfectly opposite to those at 1.75ms. This means that there is not a preferential way of discharge and the electric field distribution is equivalent at 1.25ms and 1.75ms as it is shown in Figure 5.14. While the electric potential varies linearly along the radius, the electric field norm decreases exponentially along the radius and hence it is not possible to appreciate the distribution and the peaks from the 2D cut-plane. Furthermore, the electric field norm is extremely high in the proximity of the thread tips, as it is shown in Figure 5.15.

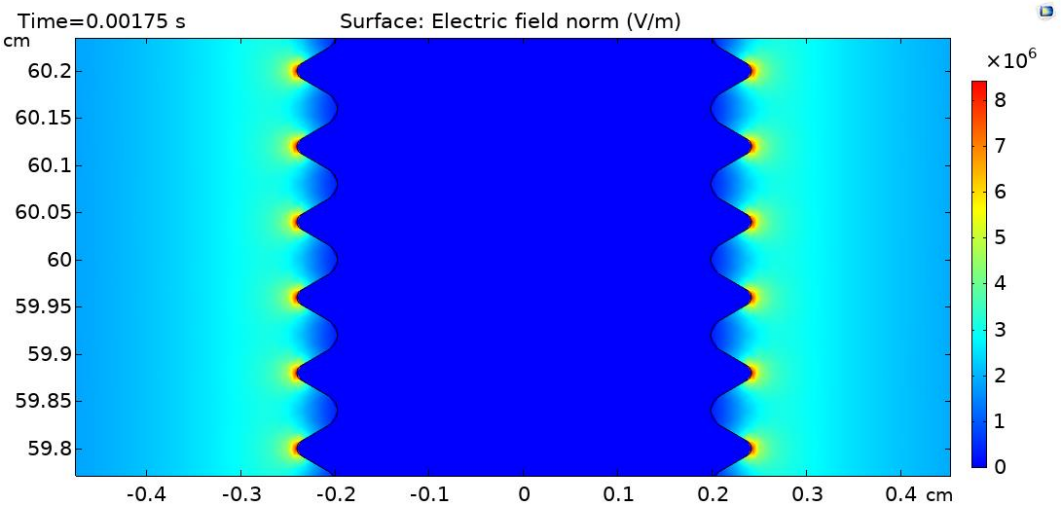

Figure 5.15 - Zoom on the thread tips of the electric field norm distribution in a 2D view of the DBD reactor of 5cm at 1.75ms.

The electric field norm is maximum as the electric potential achieves the peak (either negative or positive). The peak of the electric field can be seen in the proximity of the thread tips, for their sharp geometry; while it is significantly lower between the tips.

So far, the symmetry of the electric potential distribution has been described. The electric potential increases along the radius as the applied voltage is negative, while it decreases as the applied voltage change polarity. The absolute values of the electric potential coincide as the magnitude of the applied voltage is the same. This means that also the electric field norm is symmetric: the electric field distribution is periodic with period of 0.5ms and it does not change as the applied voltage change polarity (the electric field is always positive). Hence, the electric potential and the electric field norm can be evaluated in $1/4^{th}$ of the sine period and those others can be obtained for symmetry or equivalence.

A more accurate analysis can be made evaluating the electric parameters' values at the cut-lines. Looking at the results shown in Figure 5.11-Figure 5.15, it is possible to note that the electric

parameters' gradients drastically changes into the reactor in proximity of the ground quote. The electric potential and the electric field norm have been evaluated on the radial cut-lines shown in Figure 5.4. The results are shown in Figure 5.16.

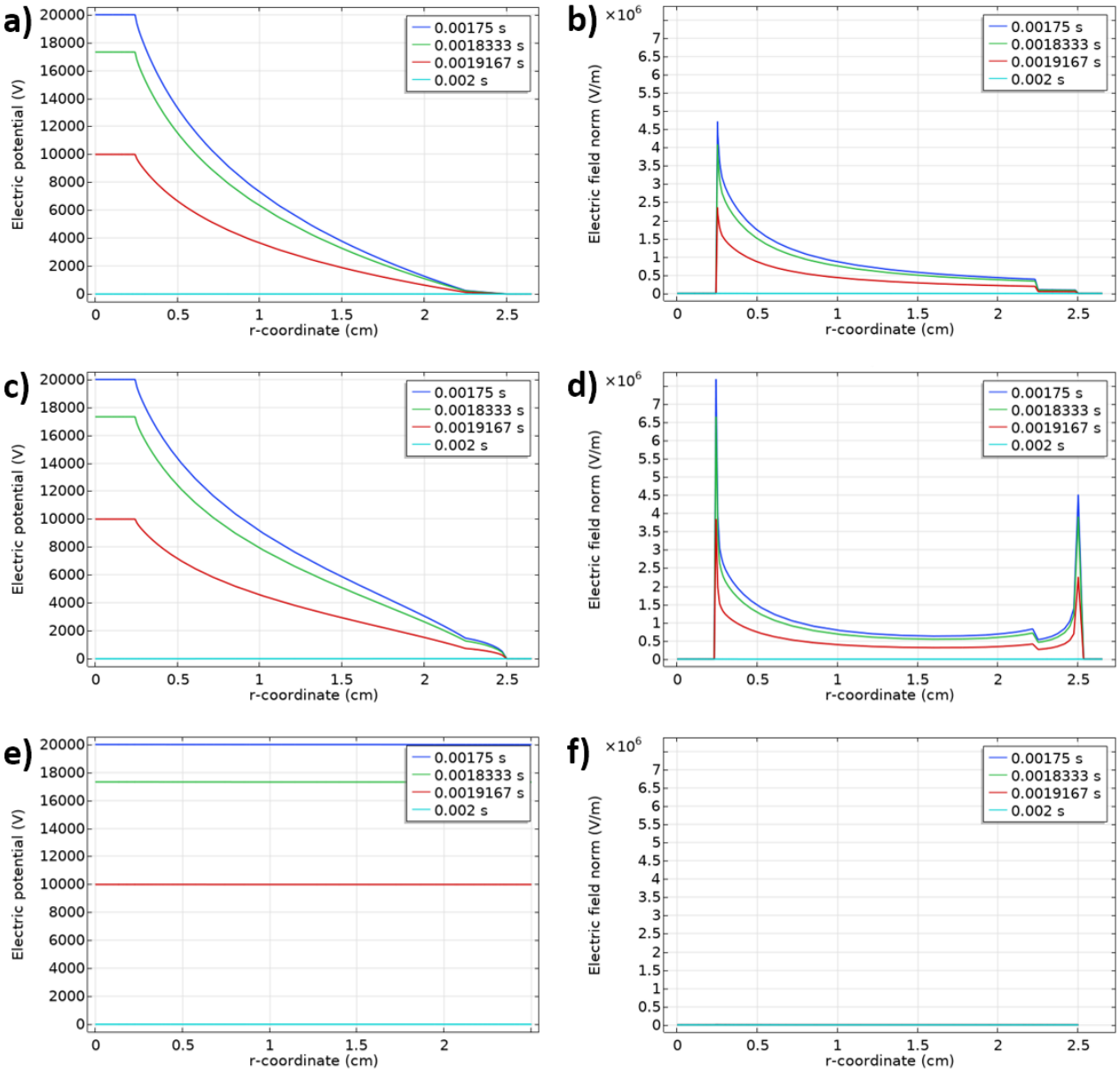

Figure 5.16 - Electric potential and electric field norm evaluated on radial cut-lines: in the middle of the reactor (a) and (b), in the corresponding of the ground edge (c) and (d), far from the ground (e) and (f), for the DBD reactor of of 5cm.

The electric potential in the middle of the reactor and at the corresponding of the ground edge decreases along the radius and it achieves the null voltage at the ground (Figure 5.16 a and c). The slope of the curves is a function of the relative permittivity of the medium. The electric potential decreases slower in the glass region than in the nitrogen gas. The electric potential in the glass at the

ground edge is higher than in the middle of the reactor due to the edge effect. In the case of the cut-line far from the ground, the electric potential remains constant along the radius (Figure 5.16 d). The results shown in Figure 5.16 can be compared with Figure 5.13 (right) at 1.75ms. The electric potential decreases as the applied voltage decreases (from 1.75ms to 2ms). At the time of 2ms, the applied voltage is zero and thus the potential remains almost constant as there is not any driving force. The electric field norm evaluated at the three cut-lines is shown in Figure 5.16 b, d, f. Again, these diagrams show that the electric field is higher as the applied voltage achieves the peak (1.75ms). The electric field is maximum in proximity of the rod surface, then it decreases exponentially moving along the radius in the gas gap. The discontinuity of the glass makes a ramp in the electric field between the gas and the glass. Then it decreases to zero on the external surface of the glass where the ground potential is assigned. Although the trend of the curves is similar in the middle of the reactor and at the ground edge, a second peak can be observed on the external surface of the glass for the ground edge cut-line (Figure 5.16 d). Again, this peak can be attributed to the edge effect. The edge effect affects also the first peak at the electrode surface; in fact, the electric field peak is higher on the ground edge cut-line than the middle cut-line. Although the order of magnitude is similar, the electric field peak in the middle of the reactor is about $4.7 \cdot 10^6$V/m; while it is about $7.7 \cdot 10^6$V/m for the ground edge cut-line. However, the peak values may depend on the computational mesh size. For what concerns the cut-line far from the electrode (Figure 5.16 f), the electric field is almost zero as the voltage applied is zero.

The radial cut-lines have been defined at strategical quotes to analyse the peaks of the electric potential and the electric field that could also represent the maximum values that can be found in the reactor. The data can be confirmed considering longitudinal cut-lines as they were presented in Figure 5.5. The electric potential and the electric field norm have been calculated on those cut-lines, and the results are shown in Figure 5.17.

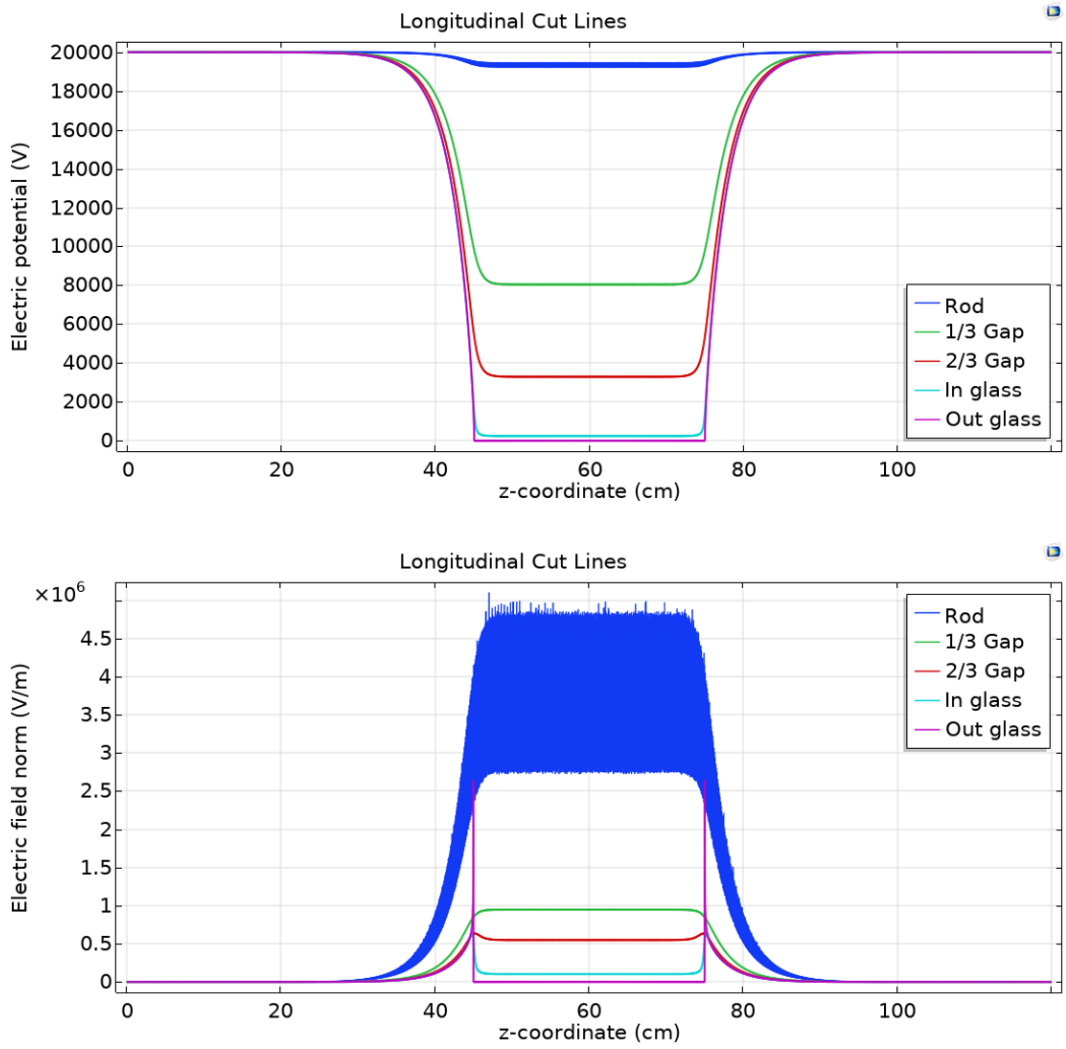

Figure 5.17 - Electric potential (top) and electric field norm (bottom) evaluated on longitudinal cut-lines: in the proximity of the rod, at 1/3 of the gap distance, at 2/3 of the gap distance, at the inner and outer surface of the glass; at 1.75ms.

The previous results shows that both the electric potential and the electric field norm have a maximum at the rod. Figure 5.17 shows the electric potential and the electric field norm at the time of 1.75ms, where the applied voltage achieves the peak of 20kV (Figure 5.10). The results showed in Figure 5.17 top, confirm that the electric potential decreases only in the region where the ground is placed (z=45-75cm) while it remains constant and equivalent to the applied voltage far from the ground. Moving from the rod surface toward the glass, the electric potential decreases constantly as it was observed in Figure 5.16 a and c. Figure 5.17 shows that the electric potential is constant at a fixed radius for all the length of the ground, while it rises above and below the ground length (z=0-45cm and z=75-120cm). It is possible to note from Figure 5.17 top that the electric potential in the proximity of the rod surface has weak oscillations due to the effect of the tips of the thread. This effect is more pronounced considering the electric field norm values. Figure 5.17 bottom shows that the electric

field norm varies in the range of 2.75-5·10^6V/m in the proximity of the rod surface and in proximity of the ground quote. The closer is the cut-line to the thread tips, the bigger is the fluctuation. However, irregular peaks can be recorded due to calculation errors closer to the tips. Even the electric field norm is gradually less affected by the ground moving longitudinally toward the two ends of the reactor. Focusing on the ground region (z=45-75cm), even the electric field norm is almost constant at a fixed radius (except for the blue line in the proximity of the rod). However, it is possible to note that in the proximity of the quotes z=45cm and z=75cm the electric field increases as the radius is closer to the ground. This result is consistent with the second peak found in the proximity of the ground in Figure 5.16 d. Again, this increase in the electric field norm can be attributed to the edge effect of the ground.

TWO DIELECTRIC BARRIERS DISCHARGE

In such realistic applications, the electrode exposed directly to the gas is covered by a dielectric layer. This strategy allows preventing the ageing of the electrode and its deterioration. The experimental investigation consisted of placing a quartz tube of 50cm in the middle of the reactor covering the rod electrode, as it is shown in Figure 5.46. The electric parameters such as the electric potential and the electric field are certainly affected by the introduction of new material in the discharge region. Hence, the results for the two dielectric barriers discharge reactor will be described in this section and the results will be compared to those obtained for the one dielectric barrier discharge reactor, described in the previous section. Only the results at 1.75ms will be described to simplify the visualization. In fact, the peaks of the electric potential and the electric field are expected at that time, since the maximum voltage of 20kV is applied, as it was confirmed in the previous section. The electric potential and the electric field distributions have been calculated and the results in a 2D view are reported in Figure 5.18.

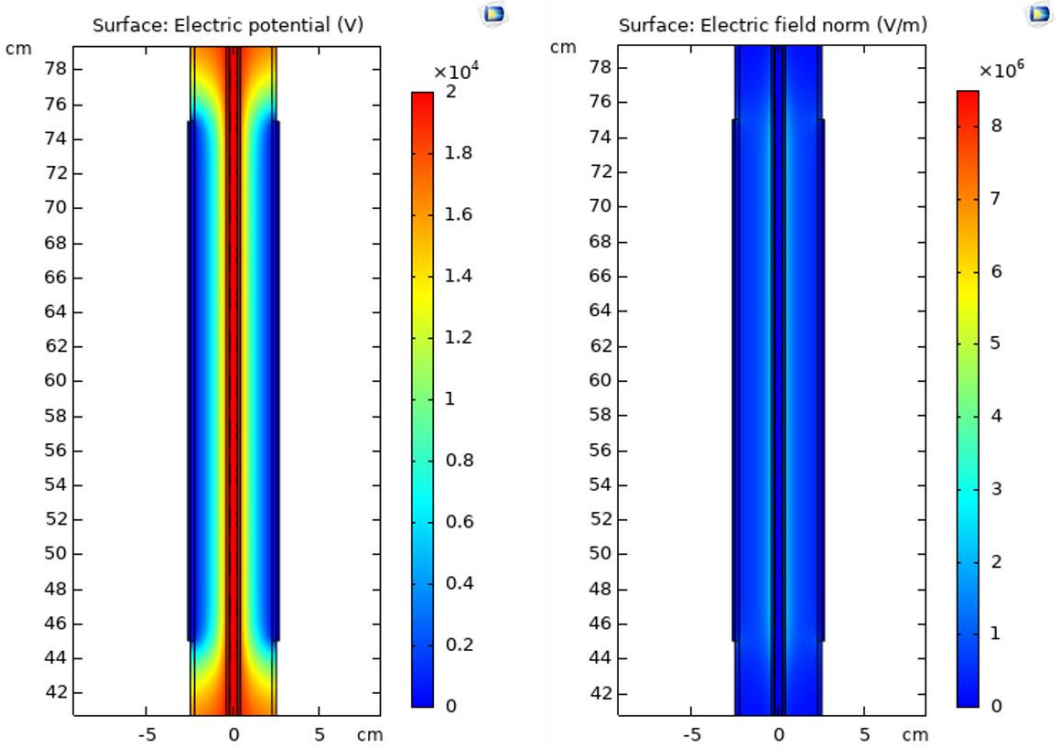

Figure 5.18 - Electric potential (left) and electric field norm (right) distributions in a two DBsD, of 5cm. 2D zoom view.

Again, the electric potential and the electric field decrease radially and the scales are similar to the results obtained in the case of the one dielectric barrier discharge (Figure 5.13 and Figure 5.14 right side). To better understand the influence of the dielectric, a zoom view in the proximity of the thread tips is reported for the electric field norm, in Figure 5.19.

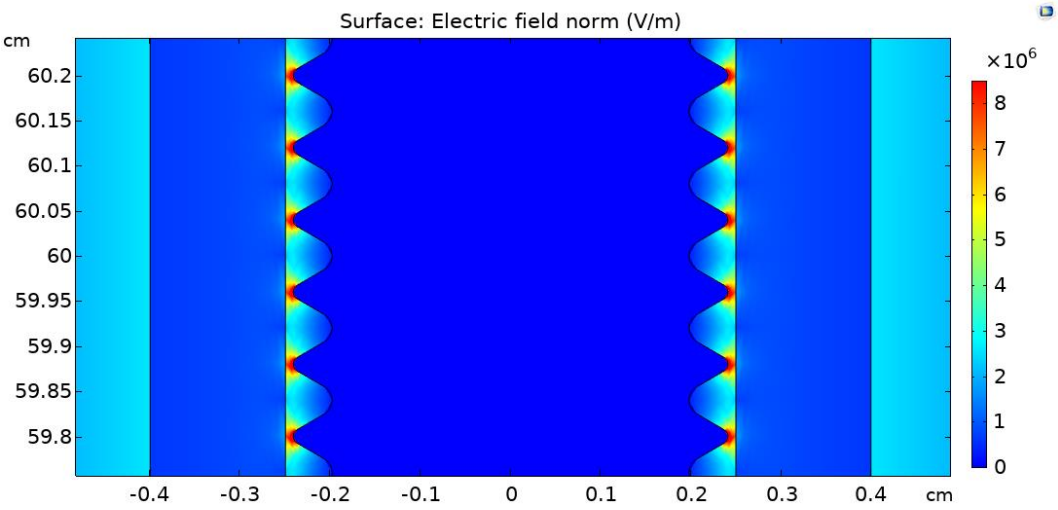

Figure 5.19 - Zoom on the thread tips of the electric field norm distribution in a 2D view of the two DBsD reactor of 5cm.

The electric field norm peaks are achieved in the proximity of the thread tips as in the DBD (Figure 5.15). However, the electric field decreases significantly into the dielectric layer and then rises again

on the external surface. The dielectric act as a ballast that buffers the electric field, neutralizing the effect of the tips. It has been demonstrated that replacing the threaded rod with a smooth rod having the same diameter the electric potential and the electric field on the external surface of the quartz were very similar. Hence, if the tips play a positive role in increasing the local electric field, the dielectric plays the role as a ballast that neutralize tip effect.

The electric potential and the electric field values can be appreciated with more accuracy, by plotting them in the function of the cut-lines, in conformity with Figure 5.16 and Figure 5.17. Again, the results at the instant 1.75ms will be described only. The electric potential and the electric field in the corresponding of the radial cut-lines are shown in Figure 5.20.

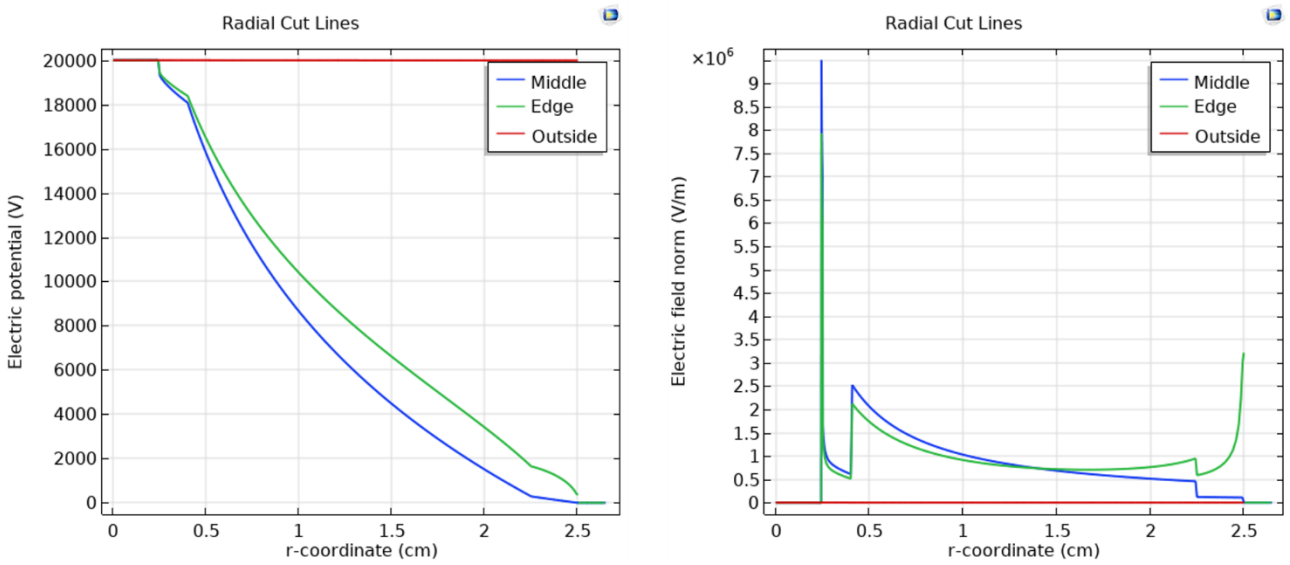

Figure 5.20 - Electric potential (left) and electric field norm (right) evaluated on radial cut-lines for the two DBsD reactor of 5cm.

The plots in Figure 5.20 confirm that the electric potential decreases radially from the rod electrode toward the ground electrode. Even in this case, the electric potential decreases faster in the middle, while it decreases with a lower slope in the proximityof the ground edge, as the edge effect. Even a different slope can be observed into the glass (r =2.25-2.5 cm) where it decreases faster for the edge line. Being the ground placed in the proximity of the outer surface of the glass, the potential displacement between the two sides of the glass is higher at the edge cut-lines than at the middle of the reactor. Overall, the trend is similar to that found in the case of the DBD reactor (Figure 5.16), except for the values in the proximity of the quartz glass. Having a relative permittivity higher than nitrogen, the quartz obstructs with less effectiveness the charge transport along the radius. Hence, the slope of the curves is lower in the corresponding of the quartz (r =0.25-0.4cm) than in the case of nitrogen (Figure 5.16).

A considerable difference in the electric field norm distribution can be observed between DBD and the two DBsD (Figure 5.16 and Figure 5.20). In the case of the two DBsD, the presence of quartz buffer the electric field and a new peak can be observed on the outer surface of the quartz. In fact, the electric field on both the sides of the quartz is higher than into the tube layer, and it is higher in the inner surface, as it was shown in Figure 5.19. For what concern the absolute values of the peaks, it must be taken into account that there is always an error due to size of the computational mesh and the tolerance. Although it is possible to estimate the order of magnitude, it is impossible to calculate the exact value of the electric field at the surfaces. Hence, there is a slight difference between the peaks calculated in the two DBsD reactor (Figure 5.20) and those calculated in the DBD reactor (Figure 5.16).

The electric potential and the electric field evaluated on the longitudinal cut-lines are shown in Figure 5.21. The cut-lines are those shown in Figure 5.7.

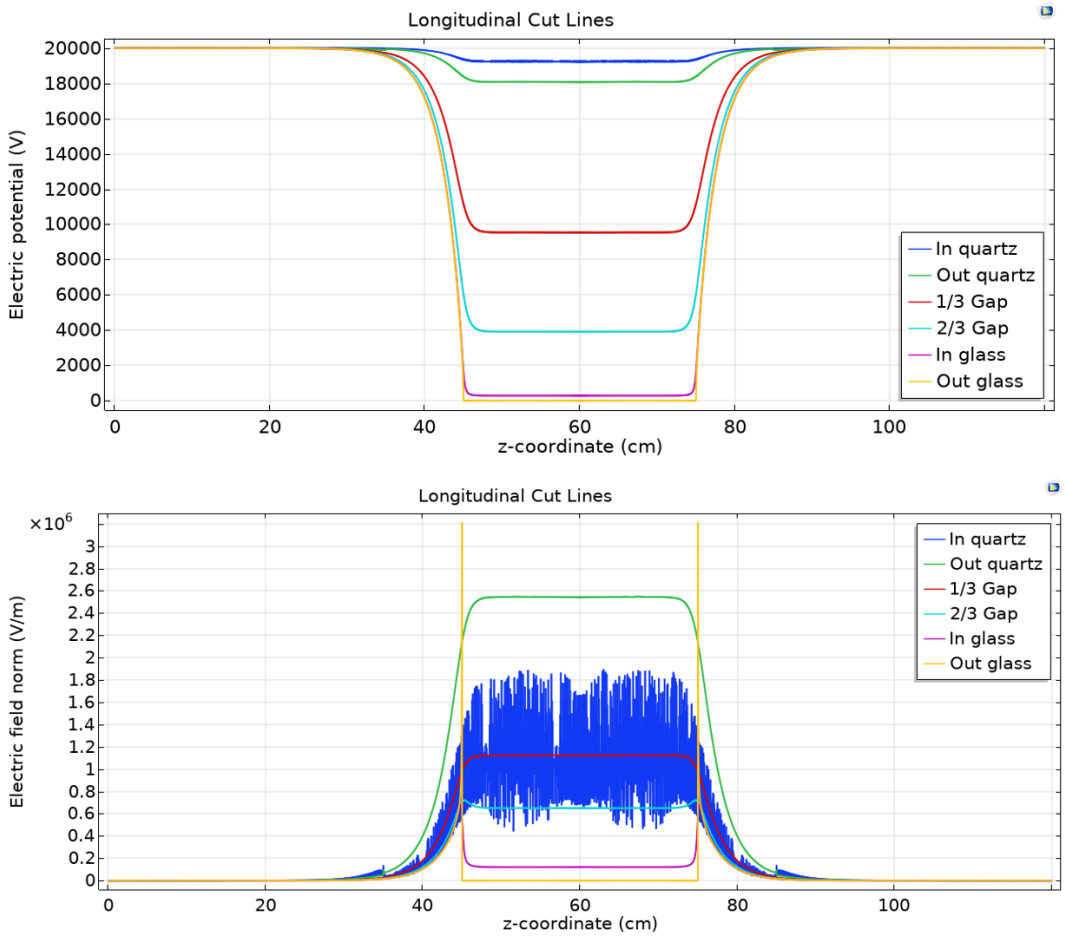

Figure 5.21 - Electric potential (top) and electric field norm (bottom) evaluated on the longitudinal cut-lines for the two DBsD reactor of 5cm.

The electric potential and the electric field norm distribution for the two DBsD configuration (Figure 5.21) are similar to those calculated in the case of the DBD (Figure 5.17). Even the fluctuation of the electric field in the proximity of the inner surface of the quartz is similar to those obtained in the DBD configuration, in the proximity of the rod. The electric field peaks in the proximity of the inner and outer surface of the quartz are lower than that showed in Figure 5.20 (right). This suggests that the peaks are achieved close to the surfaces. Again, peaks of the electric field can be observed on the outer surface of the glass, close to the ground edge.

5.1.1.5 Simulation results for the DBD reactors of 2.2cm

In conformity to the description of the 5cm reactor, both the one and two dielectric barriers discharge reactors will be described in this section for the reactor size of 2.2cm. Although the experimental results did not give an accurate description of the plasma promoted in the DBD reactor of 2.2cm, a wide range of tests were performed in the configuration with two dielectrics, as it was described in Section 5.1. Indeed, the plasma produced in the configuration with one dielectric was extremely heterogeneous as the high intensity of the electric field combined with the short gap distance. With this design, the imperfections and the impurities amplify the errors and localize the plasma in a small number of streamers.

Since the distribution of the electric potential and electric field norm are very similar for the reactors of 2.2cm and 5cm, there will be presented only the values on the cut-lines.

ONE DIELECTRIC BARRIER DISCHARGE

The electric potential and the electric field norm on the radial cut-lines are shown in Figure 5.22.

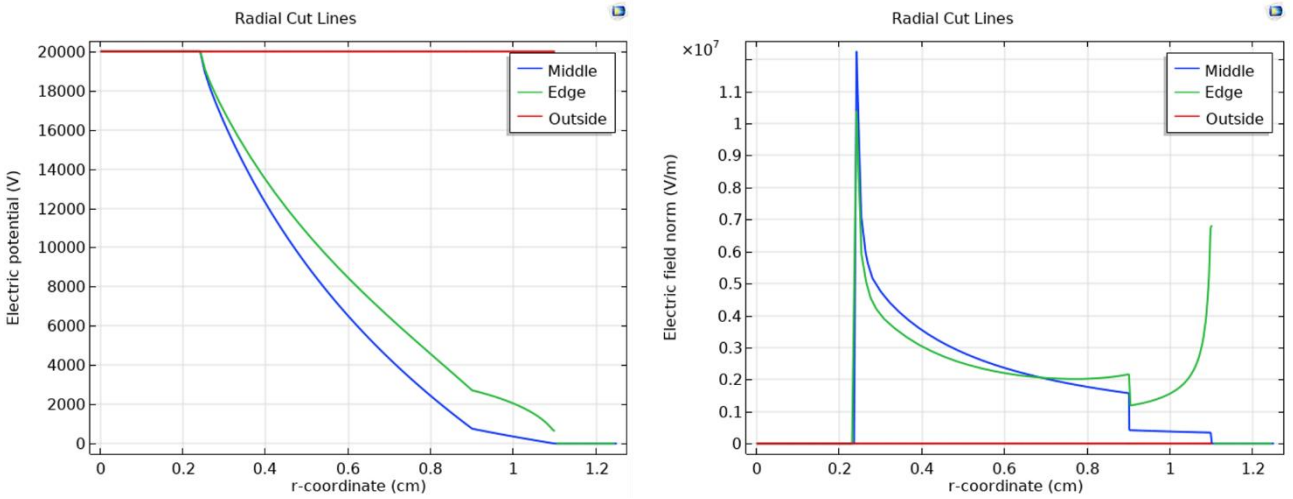

Figure 5.22 - Electric potential (left) and electric field norm (right) evaluated on radial cut-lines for the DBD reactor of 2.2cm.

The slopes of the curves are very similar to those described in the case of the one dielectric barrier discharge reactor of 5cm (Figure 5.16). The electric potential decreases along the radius in the plasma region and the slope of the curve is higher in the middle of the reactor rather than the edge of the ground. The electric potential far from the plasma region (red curve) is almost constant along the radius as the distance from the ground. Even the radial distributions of the electric field norm have a trend similar to those in Figure 5.16. However, the curves are higher for the reactor of 2.2cm, as a result of the lower distance between the electrodes, due to which the electric field norm is higher at fixed electric potential. Although it is difficult to calculate the exact value of the peak due to the limitation of the computational mesh size, it is possible to observe from the diagrams that they are about 1-1.2·10^7V/m for the reactor of 2.2cm (Figure 5.22), while they were of about 0.5-0.75·10^7V/m for the reactor of 5cm (Figure 5.16).

The increasing of the electric field norm can better be appreciated from the comparison of the longitudinal cut-lines. The electric potential and the electric field norm distribution along the longitudinal cut-lines are shown in Figure 5.23.

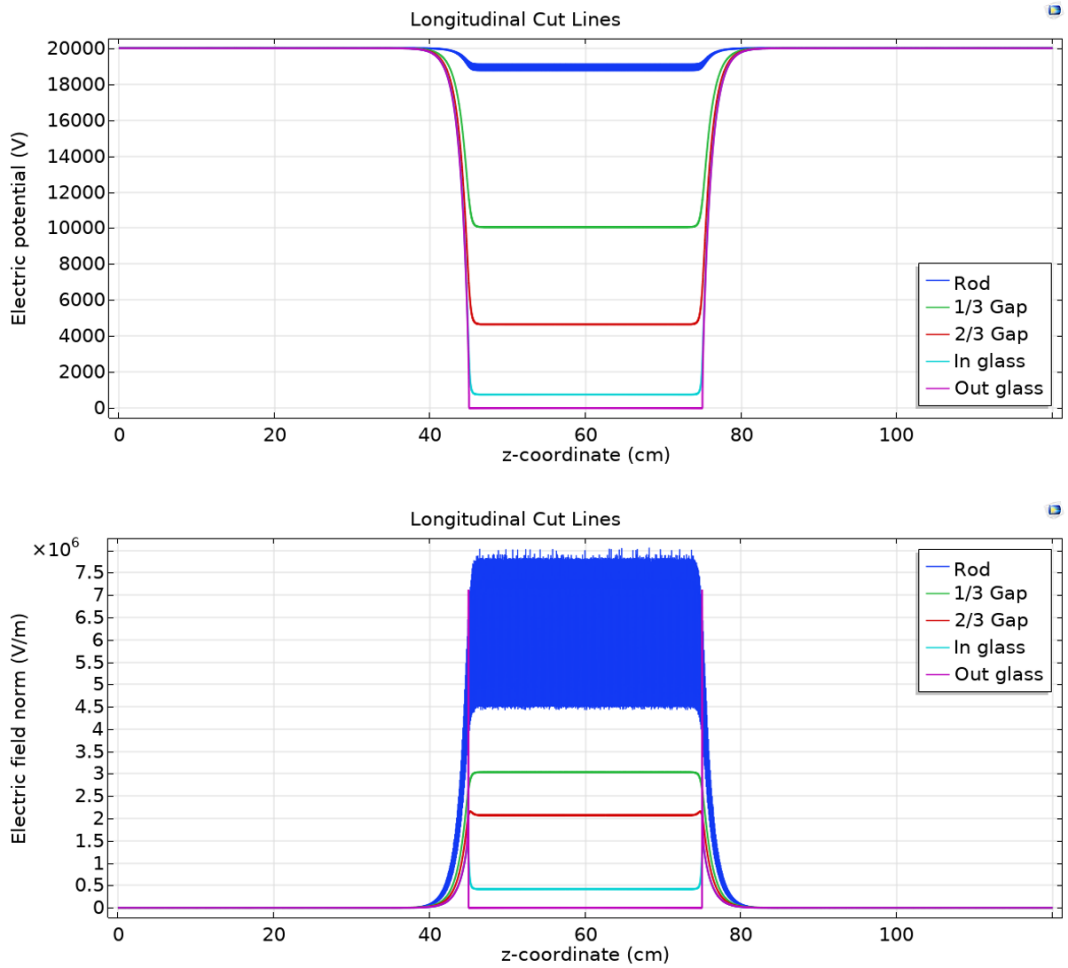

Figure 5.23 - Electric potential (top) and electric field norm (bottom) evaluated on the longitudinal cut-lines for the DBD reactor of 2.2cm.

The curves in Figure 5.23 were obtained for the one dielectric barrier discharge reactor of 2.2cm and they can be compared to the similar design reactor having a size of 5cm (Figure 5.17).

For what concern the electric field norm, from the comparison between the longitudinal cutlines for the two reactors (Figure 5.17 and Figure 5.23), it is clear that the peaks of the electric field norm are higher for the smaller reactor.

TWO DIELECTRIC BARRIERS DISCHARGE

In the two dielectric barriers discharge, the inner electrode influences the electric potential and the electric field norm, as it was discussed in Section 5.1.

The electric potential and the electric field norm distributions along the radial cut-lines and longitudinal cut-lines are shown in Figure 5.24 and Figure 5.25, respectively.

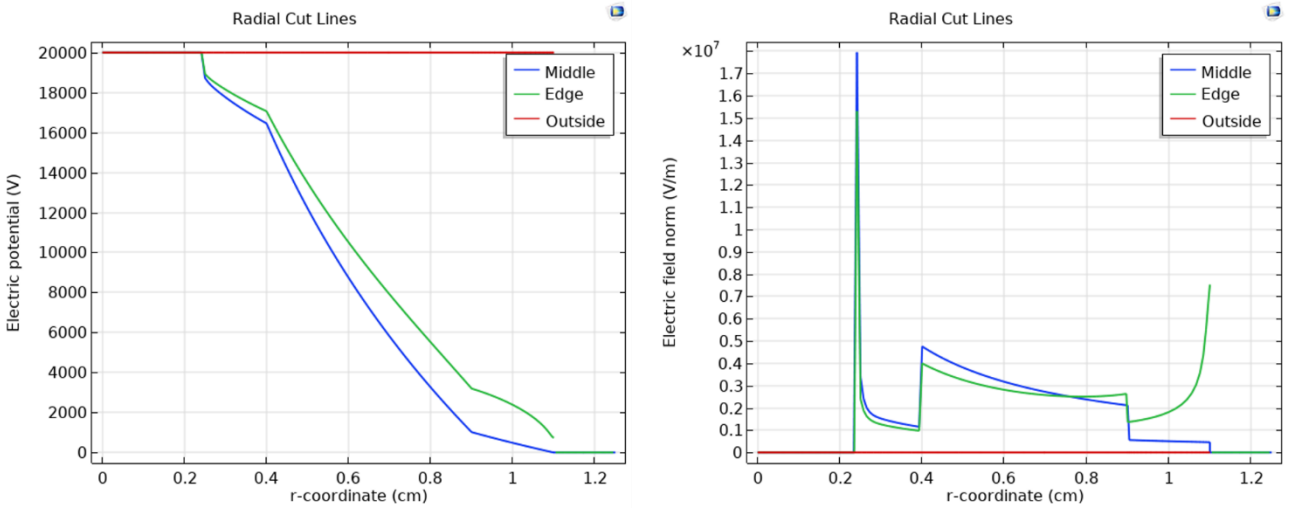

Figure 5.24 - Electric potential (left) and electric field norm (right) evaluated on radial cut-lines for the two DBsD reactor of 2.2cm.

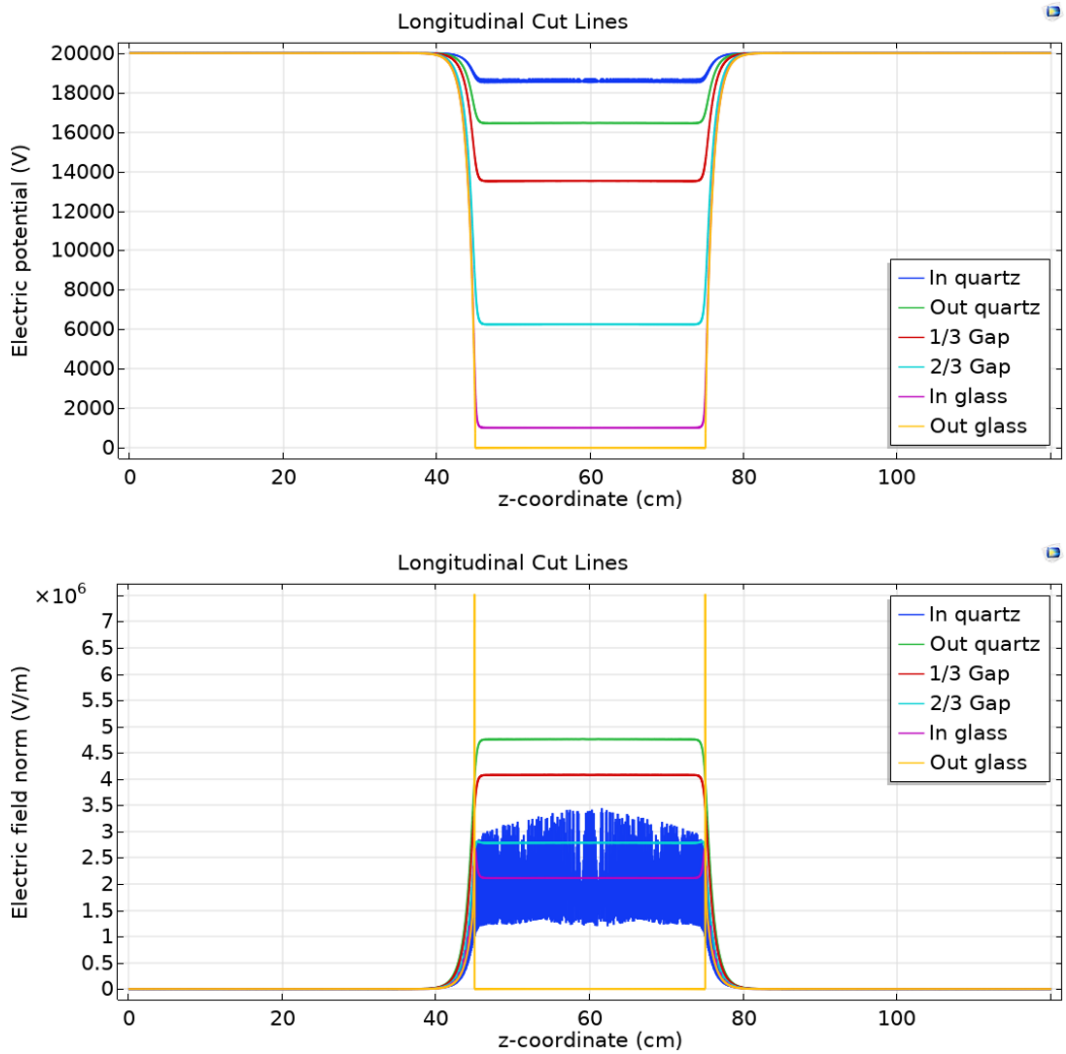

Figure 5.25 - Electric potential (top) and electric field norm (bottom) evaluated on the longitudinal cut-lines for the two DBsD reactor of 2.2cm.

Even in this case, the curves can be compared to those obtained for the reactor of 5cm in Figure 5.20 and Figure 5.21. Due to the lower gap distance in the 2.2cm reactor, the electric potential decreases with a higher derivative (absolute value). Even the difference of the electric potential at the two sides of both the dielectrics is higher for the smaller reactor. This high potential displacement could modify the internal structure of the dielectric, especially in the case of amorphous materials such as silica glass. Hence a dielectric breakdown may occur also in the dielectric causing an arc. For this reason, it is important to limit the voltage applied in smaller reactors to reduce the risk of electric arc.
Again, the electric field norm is higher in the case of the smaller reactor and the same considerations made for the comparison of the one dielectric barrier discharge reactors can be made for the two dielectric barriers discharge reactors.

5.1.2 Plasma module

The electric field generated by either the voltage applied and the small conductor curvature radius (inner electrode) causes the electron drift and ionization of the neutral gas. The resulting ions generate more electrons through secondary emission at the cathode surface. These electrons are accelerated through a small region away from the electrodes, where they can acquire significant energy from the electric field. This can lead to ionization, which creates new electron-ion pairs. The secondary ions will migrate towards the cathode where they eject more secondary electrons. This process is responsible for sustaining the discharge.

In the Plasma module, only the electron transport is modelled with a couple of drift-diffusion equations, one for the electron density and another one for the mean electron energy. These models are conservative as the transport of electrons is 3 order of magnitude faster than the other charged species. Convection of electrons due to fluid motion is not considered in the plasma model.

As assumptions, the drift-diffusion approximation is suitable when:

- the gas pressure is above about 10 mTorr (1.32 Pa), as in this case;
- the reduced electric field is typically less than 500 Townsends [Td];
- the number density of the charged species is much less than the number density of the background gas N_2 (in other words, the discharge must be "weakly ionized");
- the plasma state is collisional, which means that the mean free path between electrons and the background gas is much less than the characteristic dimension of the system.

Thus, the equation for the electron density is given by:

$$\frac{\partial n_e}{\partial t} + \nabla \cdot [-n_e(\mu_e \cdot \boldsymbol{E}) - \boldsymbol{D}_e \cdot \nabla n_e] = R_e \qquad \textit{(Eq. 5-20)}$$

where (the subscript $_e$ refers to an electron): n_e is the electron density [$1/m^3$]; R_e is either a source or sink of electrons [$1/m^3 \cdot s$]; μ_e is the electron mobility, which is either a scalar or tensor [$m^2/(V \cdot s)$]; **E** is the electric field [V/m]; $\mathbf{D}_e$ is the electron diffusivity which is either a scalar or a tensor [m^2/s].

On the other hand, the electron energy density is given by the following equation:

$$\frac{\partial n_\varepsilon}{\partial t} + \nabla \cdot [-n_\varepsilon(\mu_\varepsilon \cdot \boldsymbol{E}) - \boldsymbol{D}_\varepsilon \cdot \nabla n_\varepsilon] + \boldsymbol{E} \cdot [-n_e(\mu_e \cdot \boldsymbol{E}) - \boldsymbol{D}_e \cdot \nabla n_e] = S_{en} \qquad \textit{(Eq. 5-21)}$$

where (the subscript $_\varepsilon$ refers to the electron energy): n_ε is the electron energy density [V/m^3]; μ_ε is the electron energy mobility, which is either a scalar or tensor [m^2/(V·s)]; S_{en} is the energy loss/gain due to inelastic collisions [V/s·m^3].

From Equations (Eq. *5-20)* and (Eq. *5-21)*, the mean electron energy $\bar{\varepsilon}$ [V] is computed in COMSOL as:

$$\bar{\varepsilon} = \frac{n_\varepsilon}{n_e} \qquad \textit{(Eq. 5-22)}$$

So, the electron temperature [eV] can be defined as:

$$T_e = \frac{2}{3}\,\bar{\varepsilon} \qquad \textit{(Eq. 5-23)}$$

Only the electron mobility must be specified. This was taken from Kulikovsky [180]:

$$\mu_e = \frac{3.74 \cdot 10^{24}}{N}\left(\frac{E}{N}\right)^{-0.25} \qquad \textit{(Eq. 5-24)}$$

where N is the number density of the neutral gas [1/m^3] and E/N is the reduced electric field in Td[1Td = 10^{-21}V·m^2]. The electron diffusivity, the electron energy diffusivity and the electron energy mobility are automatically computed from the electron mobility using Einstein's relation for a Maxwellian EEDF:

$$\boldsymbol{D}_e = \mu_e T_e \qquad \textit{(Eq. 5-25)}$$

$$\boldsymbol{D}_\varepsilon = \mu_\varepsilon T_e \qquad \textit{(Eq. 5-26)}$$

$$\mu_\varepsilon = \frac{5}{3}\mu_e \qquad \textit{(Eq. 5-27)}$$

The *Wall* boundary condition is used to describe the behaviour of plasma in contact with a solid surface. Here, the exchange of electrons occurs through the following mechanisms:

- loss of electrons due to a net flux of electrons from the plasma bulk to the wall;
- loss of electrons due to the random motion of electrons within the mean free path of the wall;

- gain of electrons due to secondary emission; a wall emits an electron with some probability when it is struck by an ion or other excited species;
- gain of electrons due to thermionic emission.

The resulting equations for the normal component of the electron flux and the electron energy density at the wall are:

$$\boldsymbol{n} \cdot \boldsymbol{\Gamma}_e = \frac{1 - r_e}{1 + r_e}\left(\frac{1}{2} v_{e_{th}}\, n_e\right) - \sum \gamma_i (\boldsymbol{\Gamma_i} \cdot \boldsymbol{n}) \qquad \textit{(Eq. 5-28)}$$

$$\boldsymbol{n} \cdot \boldsymbol{\Gamma}_\varepsilon = \frac{1 - r_e}{1 + r_e}\left(\frac{5}{6} v_{e_{th}}\, n_\varepsilon\right) - \sum \varepsilon_i \gamma_i (\boldsymbol{\Gamma_i} \cdot \boldsymbol{n}) \qquad \textit{(Eq. 5-29)}$$

The first term on the right-hand side refers to the changes in the number and energy of electrons caused by the disappearance/rebound of electrons on the wall due to thermal motion, where r_e is the reflection coefficient, usually set to 0, and $v_{e_{th}}$ is the thermal velocity [m/s] defined as:

$$v_{e_{th}} = \sqrt{\frac{8 k_b T_e}{\pi m_e}} \qquad \textit{(Eq. 5-30)}$$

The second term is the electron quantity and the energy gain caused by secondary electron emissions, where γ_i is the secondary emission coefficient, Γ_i is the ion flux of the i^{th} positive ion species at the wall [$1/(m^2 s)$], and ε_i is the mean energy of the i^{th} species of secondary electrons [V].

The *Metal contact* condition is used to set the electric potential to the metal surface of the electrode.
The *Ground* condition implements ground as the boundary condition V=0.
The *Insulation* condition sets the normal component of the electron energy flux to zero:

$$\boldsymbol{n} \cdot \boldsymbol{\Gamma}_e = 0 \qquad \textit{(Eq. 5-31)}$$

Different from Electrostatics module, the *Charge Conservation* condition is used for the dielectric layer only, to define the constitutive relation between the electric displacement field and the electric field. The default one is chosen, based on the relative permittivity of the material:

$$\boldsymbol{D} = \varepsilon_0 \, \varepsilon_i \, \boldsymbol{E} \qquad \textit{(Eq. 5-32)}$$

where ε_o is the permittivity of free space and ε_i the relative permittivity of the material, i.e. the silica glass where ε_{glass}=4.8.

The surface of the dielectric medium will accumulate an electric charge, resulting in a discontinuity of the electric displacement vectors on both sides of the dielectric interface.

The *surface charge accumulation* condition is expressed as:

$$n \cdot (D_1 - D_2) = \sigma_s \qquad \textit{(Eq. 5-33)}$$

where D_1 and D_2 are, respectively, the electric displacement vectors on both sides (nitrogen side and dielectric side) of the insulation surface; σ_s is the surface charge density, which can be computed by solving the following equation on the surface:

$$\frac{d\sigma_s}{dt} = n \cdot J_i + n \cdot J_e \qquad \textit{(Eq. 5-34)}$$

where $n \cdot J_i$ is the normal component of the total ion current density at the wall and $n \cdot J_e$ is the normal component of the total electron current density at the wall.

The *periodic* condition consisted of the equivalence of the electric potential at the two sides of the edge:

$$V_{dst} = V_{src} \qquad \textit{(Eq. 5-35)}$$

5.1.2.1 Design of the reactors

Simplified geometries were considered to simulate the DBD reactor with plasma module. In fact, the computational costs greatly increased with the electrochemical coupled with the electrostatics study. Two different simplified geometries were proposed and investigated:

- 2D axisymmetric geometry;
- 1D axisymmetric geometry.

Both the simplified geometries would simulate the DBD reactor with the minimum computational cost.

TWO-DIMENSIONAL AXISYMMETRIC GEOMETRY

The simplified 2D axisymmetric geometry consisted of a portion of the DBD reactor in the corresponding of the plasma region, including one tip of the screw thread. In particular, the geometry was cut making it symmetric from the two sides of the cuts.

The designed 2D axisymmetric geometry is shown in Figure 5.26.

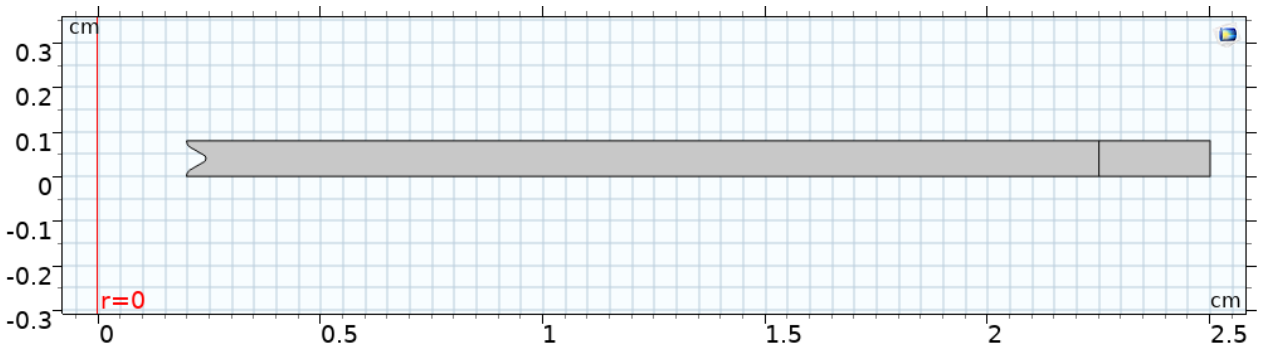

Figure 5.26 - 2D axisymmetric geometry - smallest independent part of the DBD reactor.

Figure 5.26 is representative of the DBD reactor, as it represents the smallest independent part of the plasma region in the DBD reactor. The DBD reactor can be built as the sequence of the parts as in Figure 5.26, overlapping the upper and the lower radii of the parts. Hence, the periodic condition was applied at the upper and the lower radii of the geometry. The tip was declared as metal contact and wall simultaneously. Even the inner dielectric (R=2.25cm) was declared as wall, while the outer surface was declared ground.

An radial cut-line was defined in the centre of the reactor cutting the tip in the middle, to evaluate the data in 1D plot, as it is shown in Figure 5.27.

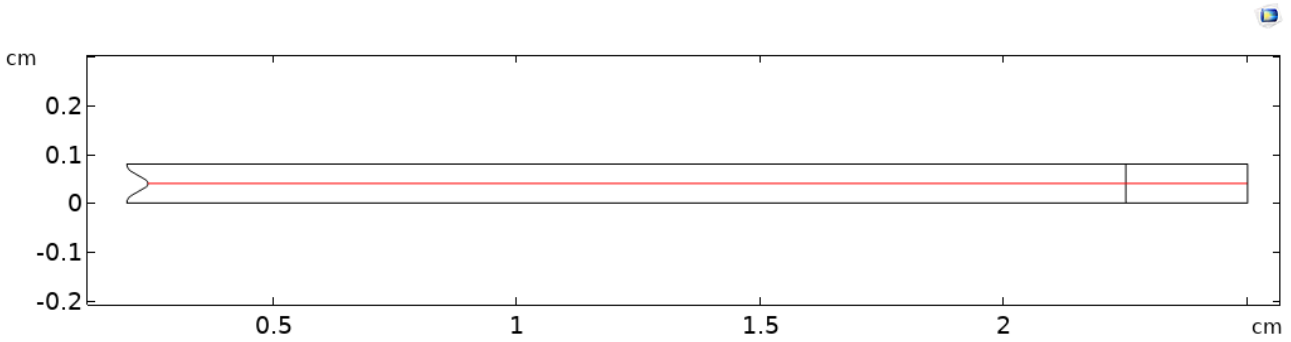

Figure 5.27 - Radial cut-line for the 2D axisymmetric geometry in the middle of the reactor.

In the corresponding of the middle of the geometry was expected the highest values of the electric parameters as the effect of the tip.

ONE-DIMENSIONAL AXISYMMETRIC GEOMETRY

The simplified 1D axisymmetric geometry is useful to simulate a cylindrical geometry, hence the tips of the screw thread cannot be evaluated. The designed line for the 5cm reactor is shown in Figure 5.28.

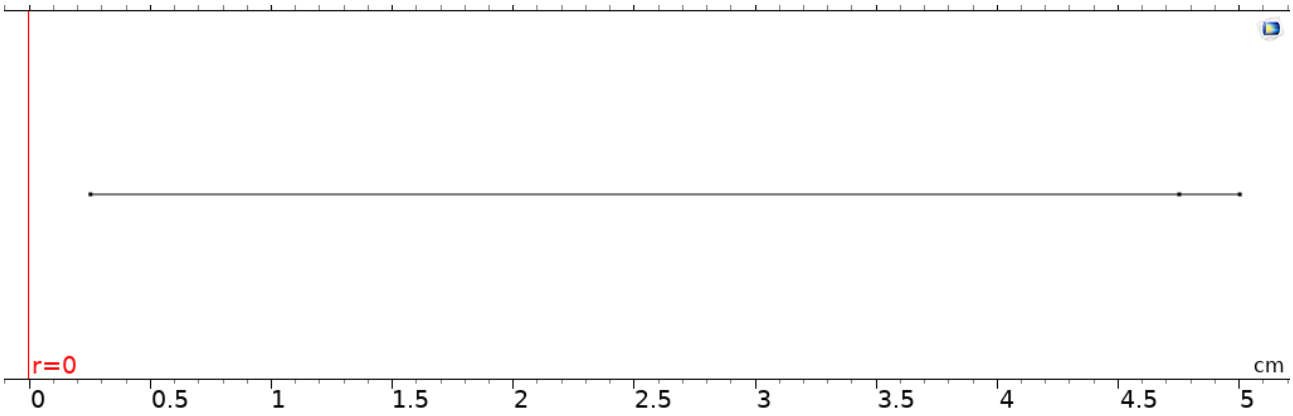

Figure 5.28 - 1D axisymmetric geometry; the node at R=0.25cm is representative of the electrode, the node at R=2.25cm represents the inner surface of the glass, the node at R=2.5cm represents the ground.

The plasma physics was imposed on the segment closest to the axis where the nitrogen gas was declared, while the segment between 2.25 and 2.5cm was declared as glass.

5.1.2.2 Computational Mesh

The complexity of the plasma module conflicted with the intention to simulate the reactor in the 2D geometry. Hence, further the simplification in the geometry, a simplified calculating mesh was required to reduce the numbers of calculating nodes. The highest oscillation was expected in the proximity of the electrode tip and close to the inner surface of the glass. Due to the rectangular shape of the reactor (except the electrode curve), a *mapped* mesh was defined in the middle of the reactor (R=0.328-2cm), imposing 80 elements for the radial direction with the growing ratio of 5 toward the edge of the reactor, and 6 elements for the longitudinal direction with the growing ratio of 2 toward the centre of the reactor. A *mapped* mesh was declared even for the terminal part of the reactor (R=2-2.25cm) and the glass (R=2.25-2.5cm), where the longitudinal elements were declared as before and the elements along the radius were 50 with the growing ratio of 2 toward the centre and, 20 elements with the growing ratio of 5 toward the edge, for the two mapped area respectively.

An extremely fine mapped area was designed in the proximity of the tip of the electrode for the radius in the range R=0.242-0.293cm, by imposing 20 elements along the radius with the growing ratio of 2 toward the tip and 21 elements for the longitudinal direction with the growing ratio of 5 toward the

centre of the reactor. The area between the extremely fine and the centre mapped mesh (R=0.293-0.328) was free triangular to balance the different number of elements, on the longitudinal direction, between the two mapped areas.

Lastly, a boundary layer mesh was declared in the area between the electrode (curve shape) and the extremely fine mapped area. Five boundary layers were designed on the curved electrode, with the stretching factor of 1.3 and the thickness adjustment factor of 1.4.

A zoom of the mesh on the two ends of the reactor is shown in Figure 5.29.

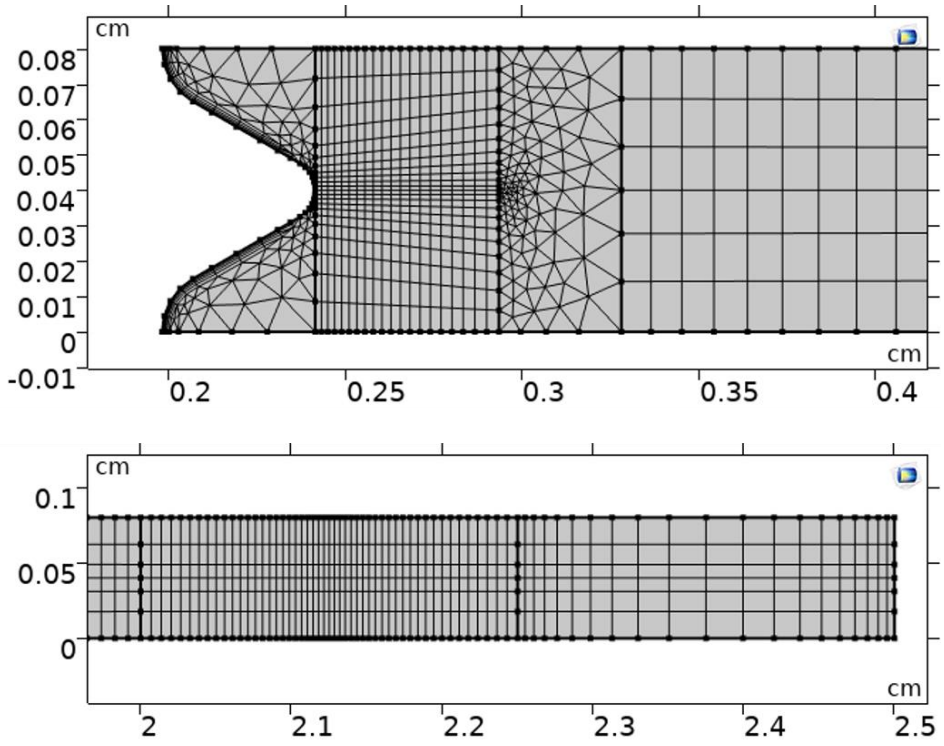

Figure 5.29 - Zoom of the designed mesh in the 2D axisymmetric simplified geometry in the proximity of the electrode (top) and the glass (bottom).

From Figure 5.29, it is possible to note that the designed calculating mesh is extremely fine in the proximity of the electrode and in the proximity of the tip, long the radius. Even the region close the inner surface of the dielectric was finer than the other areas as in that region the electric parameters supposed to have a great oscillations. In particular, it was observed that the parameters' peaks did not occur in the closest region of the glass, but 1-2mm far from that. Hence, the calculating mesh was designed as in Figure 5.29 bottom.

The calculating mesh for the 1D axisymmetric geometry was extremely simple as it consisted of distributing a number of elements along the line. A number of 50 elements with the growing ratio of

5 toward the edge was considered for the glass; while 800 elements with the same growing ratio were designed for the line representing the gas.
A zoom of the mesh on the two ends of the reactor is shown in Figure 5.30.

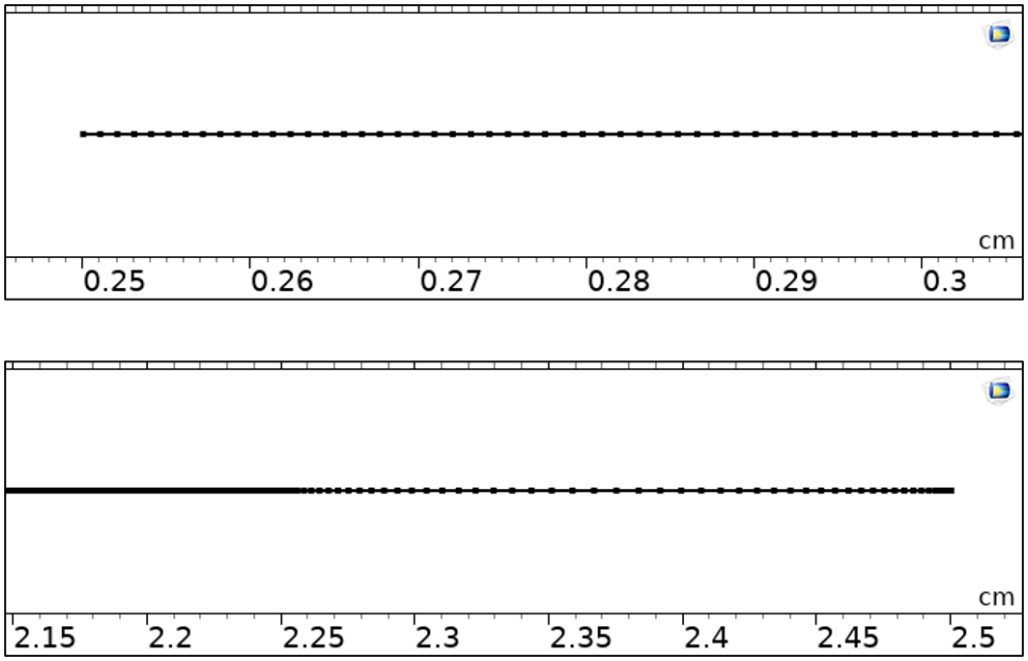

Figure 5.30 - Zoom of the designed mesh in the 1D axisymmetric simplified geometry in the proximity of the electrode (top) and the glass (bottom).

From the two axis scales in Figure 5.30, it is possible to appreciate the finer mesh designed in the corresponding of the gas line than the glass line.

In the case of the parametric study, the number of elements and their distribution for the glass did not change, while the number of elements increased of 80 elements per millimetre for the gas line, by maintaining the growing ratio at 5 toward the edge.

5.1.2.3 Nitrogen gas discharge

Plasma chemistry may be far complex to be modelled in COMSOL, since it involves many chemical reactions and species and sometimes their corresponding reaction rate coefficients are uncertain or even unknown at all. The plasma in the DBD reactor consisted of an ionized gas made of the radicals from NO_x and N_2. Tens of species might be detected in the gas ionized plasma, and the computational time increased exponentially with the number of species and reactions. Hence a simplified model including the faster and the more likely reactions is needed. Since the NO_x concentration in the tests performed was always lower than 0.05% and the rest was nitrogen, a simplified mechanism of

nitrogen gas discharge could be considered. This choice is conservative as the nitrogen gas molecules require a higher energy to be ionized and the even the kinetics is slower.
Among the mechanisms proposed for the N_2 plasma, the most relevant chemical reactions were considered from Table 3.4. The chemical reactions 1-5 and 7 were implemented.
This mechanism concerns reactions of ionization and excitation of the process gas N_2, mainly.
For each of the species introduced in this chemical system, the following information is required:

- the molecular weight of the species;
- the potential characteristic length of the species to compute the correct diffusivity and mobility;
- the potential energy minimum of the species, to compute the correct diffusivity and mobility.

N_2 was assumed as the background neutral gas and it was used as the mass constraint since its high mass fraction is not influenced by the production or reaction of the other species, which are in much lower concentrations. For this reason, in COMSOL a minimal number of species can be considered, as N_2, N_2^+, e^-, while the other ones do not chemically or electrically contribute to the overall gaseous density. Regarding the electrical contribute, the ions N_2^+ are necessary to balance the negative charge of the electrons so that the plasma is neutral.
Nitrogen atoms cannot be included in the group of species in COMSOL just considering the reactions in Table 5.1, otherwise the overall chemical system will evolve to the total conversion to nitrogen radicals. In fact, in the mechanism proposed by Moravej et al. [157], there is no reaction consuming atomic nitrogen. Hence, two further reactions were integrated to the Moravej et al. model, in accordance to the model proposed by De Wilde et al. in 2017 [158], as it was reported in Table 3.5. The nitrogen non-thermal plasma kinetic mechanism proposed and implemented in COMSOL Multiphysics is summarized in Table 5.1.

Reaction	Rate coefficient	Unit
$e^- + N_2 \rightarrow 2N + e^-$	$6.3 \cdot 10^{-6}\, T_e^{-1.6} e^{(-9.8/T_e)} \cdot N_A \cdot 10^{-6}$	$m^3/_{mol \cdot s}$
$e^- + N_2 \rightarrow N_2^+ + 2e^-$	$4.7 \cdot 10^{-13}\, T_e^{0.5}(1 + 0.13\, T_e) e^{-15.7/T_e} \cdot N_A \cdot 10^{-6}$	$m^3/_{mol \cdot s}$
$e^- + N_2 \rightarrow N^+ + N + 2e^-$	$4.0 \cdot 10^{-14}\, T_e^{0.5}(1 + 0.08\, T_e) e^{-25.5/T_e} \cdot N_A \cdot 10^{-6}$	$m^3/_{mol \cdot s}$
$e^- + N_2 \rightarrow N^* + N + e^-$	$2.6 \cdot 10^{-15}\, T_e^{0.5}(1 + 0.15\, T_e) e^{-13.3/T_e} \cdot N_A \cdot 10^{-6}$	$m^3/_{mol \cdot s}$
$e^- + N_2 \rightarrow N_2(A) + e^-$	$5.8 \cdot 10^{-13}\, T_e^{0.5}(1 + 0.29\, T_e) e^{-7.1/T_e} \cdot N_A \cdot 10^{-6}$	$m^3/_{mol \cdot s}$
$e^- + N_2^+ \rightarrow N^* + N$	$2.0 \cdot 10^{-7} \left(\frac{T_e}{0.03}\right)^{-0.39} \cdot N_A \cdot 10^{-6}$	$m^3/_{mol \cdot s}$
$2\,N \rightarrow N_2^+ + e^-$	6.0×10^5	$m^3/_{mol \cdot s}$
$2\,N + N_2 \rightarrow 2\,N_2$	$5.0 \times 10^{13} e^{(500/T_g)} \cdot 10^{-6}$	$m^6/_{mol^2 \cdot s}$

Table 5.1 - Nitrogen non-thermal plasma kinetic mechanism implemented in COMSOL Multiphysics.

where N_A is the Avogadro constant. From the implementation of the two last reactions in Table 5.1 to the Moravej et al. mechanism, the N atom can be involved as an active species in the plasma chemistry.

The rate coefficients are expressed as a function of the electron temperature T_e and they must be multiplied for the Avogadro constant N_A to be expressed in [cm^3/(mol·s)].

The kinetic constants integrate Equation (Eq. *5-20)*, as R_e is determined by:

$$R_e = \sum_{j=1}^{M} x_j k_j N n_e \qquad \textit{(Eq. 5-36)}$$

where M is the number of reactions that contribute to the growth or decay of the electron density, x_j is the mole fraction of the target species for reaction j, k_j is the rate coefficient for reaction j (i.e. [m^3/(mol·s)] for a first-order reaction), and N is the total neutral number density [1/m^3].

5.1.2.4 Study and Solver Set-Up

A sinusoidal voltage was applied at the inner electrode (Metal contact condition), as the Equation (Eq. *5-18),* in conformity with the electrostatics study. The voltage amplitude varied from 20 to 160kV at the frequency of 1kHz.

The electron density and energy equations were solved by imposing the electron transport as a function of the reduced electron mobility, as in the Equation (Eq. *5-24).*

Since the gas discharge is confined, it is assumed that when the ions reach the wall, they transfer charge to the surface and the charged particles transform into neutrals. Thus, in addition to the volumetric reactions, surface reactions are implemented to describe what happens when the ions and the electrons impact the cathode and the anode:

$$N_2^+ \rightarrow N_2 \qquad \textit{(Eq. 5-37)}$$

To set surface reactions in COMSOL, these require in input:

- the forward sticking coefficient, which describes the ratio of the number of atoms (or molecules) that adsorb, or "stick", to a surface to the total number of atoms that impinge upon that surface during the same period. This value is between 1 and 0 for all impinging atoms stick and none of the atoms sticks respectively. In the simulation it was set as 1;
- the secondary emission coefficient, defined as the number of secondary electrons emitted per primary ones. When a metal surface is bombarded by ions or electrons, these particles within the material may acquire sufficient kinetic energy to be emitted from the surface. The electrons or ions bombarding the surface are called primary, and the emitted ones are designated secondary. This value goes from 0 (no emission) to 1. For positive ions N_2^+, it was set to 0.01 on the high voltage electrode surface, while 10^{-6} on the dielectric surface;
- the mean energy of secondary electrons; most of the electrons would have energies peaking below 5eV. This value was set as 2.5eV.

The data was chosen in conformity with the COMSOL Multiphysics guide on Plasma module [181]. The environmental conditions were T=293.15 K and P=1 atm.

The initial parameters imposed were:

- the initial electric potential equal to 0 [V];
- the initial electron density equal to 10^{15} [$1/m^3$] (in conformity with the literature);
- the initial mean electron energy equal to 4 [V] (in conformity with the literature);
- the initial mole fraction of N equal to 10^{-6} [-]
- the initial mole fraction of the positive ions (N_2^+) from the electroneutrality constraint, to balance the negative charges and guarantee the neutral condition of plasma.

A time-dependent study was made. The time interval for the output was from 0 to $5/f_o$ (5 sine periods), with 12 number of instants per period; in fact, the solution was periodic from the fourth sine period, as the interference of the initial conditions extinguished after 4 periods, i.e. 4ms in the case of 1kHz. COMSOL automatically detects the best solver without requiring any user interaction. For this simulation the MUMPS direct-solver was used. The direct solvers will use more memory than the iterative solvers but can be more robust. They are based on the lower-upper (LU) decomposition, that factors a matrix as the product of a lower triangular matrix and an upper triangular matrix.

5.1.2.5 Simulation results

A 2D axial symmetric geometry and 1D axial symmetric geometry have been investigated in order to simplify the DBD reactor. The electric field norm, the electron density and their energy are here compared for the two different geometries. Moreover, two different variables were changed independently. From the literature the higher is the voltage applied, the higher is the plasma intensity; the bigger is the distance between the electrodes, the weaker is the plasma intensity. These results have been confirmed by experimental investigation and they would be here discussed, by the integration of numerical analysis.
The following four analysis have been made:

- 1D and 2D simplified geometries;
- Effect of the voltage applied for a fixed geometry;

COMPARISON OF ONE AND TWO-DIMENSIONAL SIMPLIFIED GEOMETRIES

The plasma physics module includes a high number of equations that solve either the Gauss's equations for the electric field distribution and the Boltzmann equations for the particles transport. These modelled equations are integrated by the rate coefficients of the electronic reactions that contribute to the electron density and their energy.

Due to the complexity of the model, which lead to a high computational time, simplified geometries of the DBD reactor shown in Figure 5.42 have been proposed, and they are shown in Figure 5.26 and Figure 5.28. The sinusoidal voltage, as in Equation (Eq. *5-18)*, was declared on the internal electrode, in conformity with the electrostatics study. The sine amplitude was 20kV and the frequency of 1kHz. Four sine cycles were needed to achieve independence from the initial conditions and the periodicity of parameters was observed in the following cycles. Hence, the results will be shown in the time range of 4-5ms and they are representative of one cycle of the periodic function.

As the effect of the applied voltage at the inner electrode surface, either the electric potential and the emitted current have a sine wave, as it is shown in Figure 5.31.

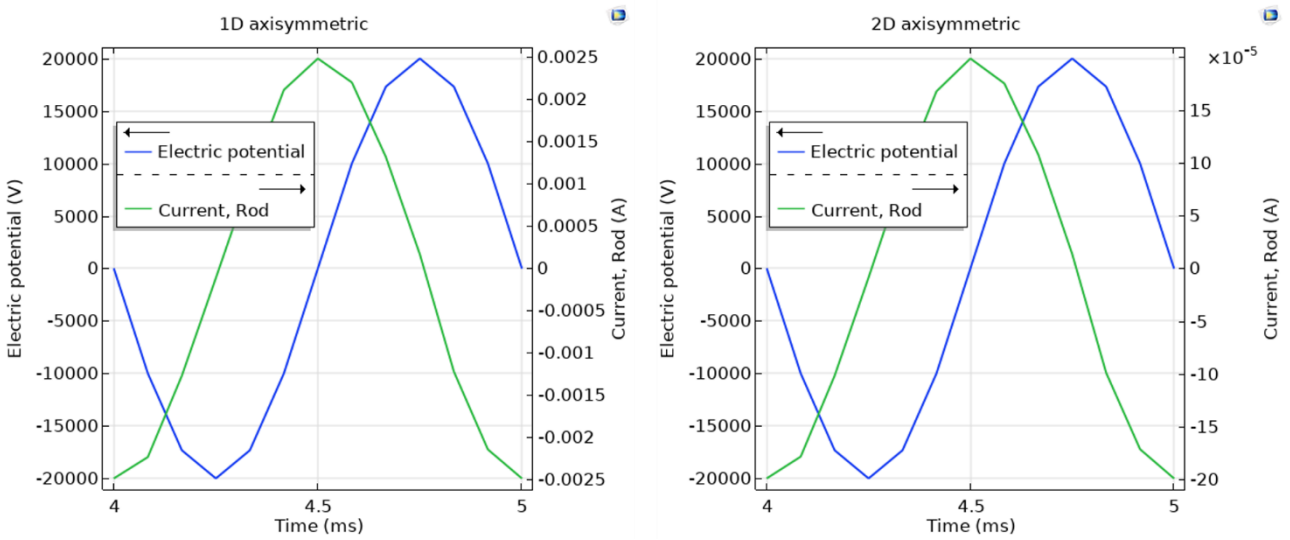

Figure 5.31 - Electric potential and current calculated at the inner electrode surface for the 1D (left) and the 2D (right) axisymmetric geometries.

The electric potential and the current are not in phase, but the current leads the voltage by ¼ of the cycle. This characteristic is typical of capacitors: the dielectric acts as a capacitor that accumulates the charge on its surface and then discharge as the polarity changes; the equivalent circuit was presented in Figure 3.19. Hence, the current peaks are representative either of charge starting from the inner electrode or charge accumulation close to the inner surface of the glass. The difference in current intensity between 1D and 2D axisymmetric configurations, in Figure 5.31, is due to the different shape of inner electrodes. The inner electrode in 1D axisymmetric geometry is represented by a point and it appears as a cylinder surface in a 3D revolution geometry. In the 2D axisymmetric geometry, the inner electrode is represented by a curve that has the shape of the thread tip. The non-uniformity of the 2D axisymmetric geometry makes the electron current density localized close to the tip and hence the current has a maximum on it, as it is shown in Figure 5.32 below. Hence, the current

displacement is mainly localized in the proximity of the tip, and the global current calculated at the inner electrode is overall lower than in the case of the 1D axisymmetric geometry.

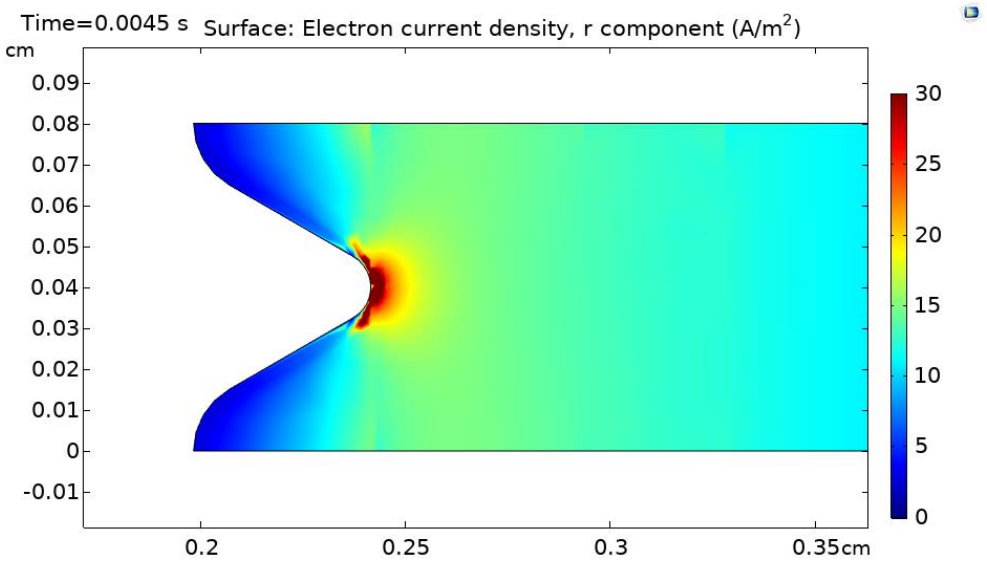

Figure 5.32 - Radial component of the electron current density in the proximity of the thread tip at 4.5ms for the 2D axisymmetric geometry.

The electron current density gives information about the displacement of the charge in the reactor. The peak in the proximity of the thread tip is easily explained by the edge effect that concentrates the charge in the proximity of the sharp point where the electric field is the highest. Due to the irregular distribution of the electric properties in the 2D axisymmetric geometry, a radial cut-line is defined at the tip quote, as it is shown in Figure 5.27.

The cut-line passing for the tip has a great interest for the high gradient of the electric properties. The parameters evaluated along the cut-line, are compared with those obtained in the 1D axisymmetric configuration.

The electron density in the 1D is compared with the trend of the cut-line, at the tip quote, of the 2D axisymmetric geometry in Figure 5.33.

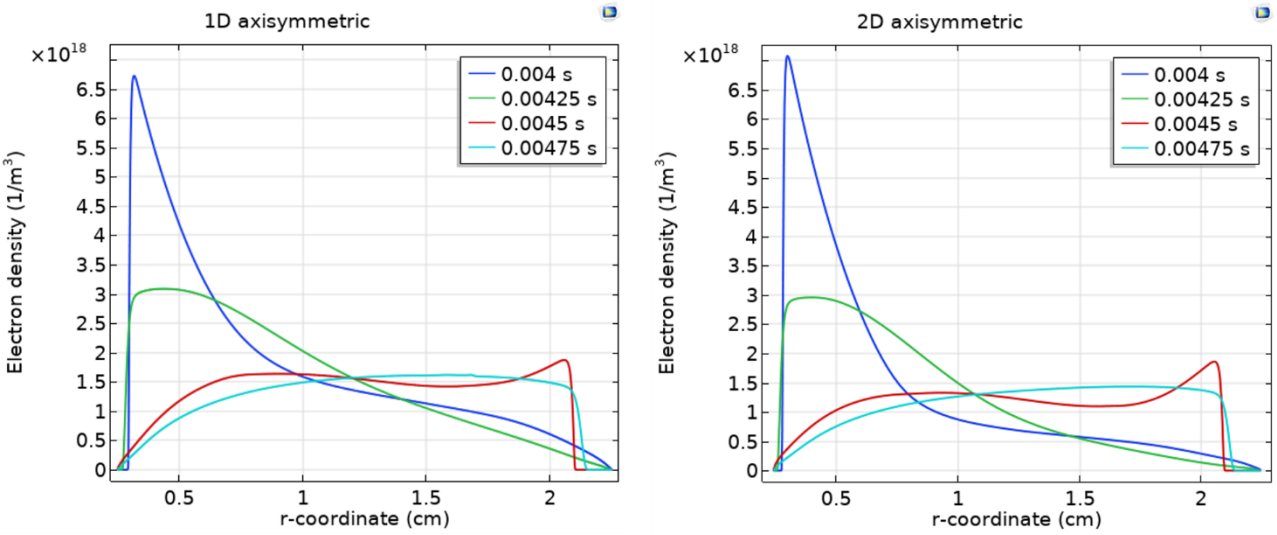

Figure 5.33 - Electron density calculated along the middle radius for the 1D (left) and the 2D (right) axisymmetric geometries.

Many peaks of the electron density can be observed along the radius and they move with the time from the inner electrode toward the glass. The position of the electron density peaks along the radius is correlated to the voltage applied, and hence to the current (and vice versa). The higher peak can be observed in the proximity of the inner electrode at the time of 4ms when a minimum of the current was measured (Figure 5.31). The electrons accumulate in the proximity of the inner electrode and they move in the direction of the glass as the current rises. At the time 4.25ms the peak decreases and the electron concentration spreads along the gas gap. When the current achieves a maximum (at 4.5ms), a peak of the electron density can be observed in the proximity of the inner surface of the glass. This peak is significantly lower than that obtained in the proximity of the inner electrode. This means that there is an accumulation of the electrons at the inner dielectric surface. Meanwhile the peak at the inner surface of the dielectric, the electron density is quite high along all the gas gap (red curves in Figure 5.33). The high concentration in the gas gap is representative of the microdischarges that occurred in the plasma region. When the voltage changes polarity, the current decreases and the electrons go back toward the inner electrode and hence the peak decreases. From Figure 5.33 it is possible to note that the trend of the curves is similar for the two geometries. The peak in the proximity of the inner electrode is slightly higher in the case of the 2D axisymmetric geometry, due to the tip effect. The peak at the inner surface of the dielectric at 4.5ms, instead, has the same value for the two geometries. In fact, the electrons that accumulate at the dielectric surface are far enough from the inner electrode to not be affected by its irregular shape.

The motion of electrons, as the effect of the imposed external electric field, can be understood better by calculating the electron density parametric in the time, for small intervals. The electron density along the radius for intervals of 0.1ms in the 1D axisymmetric geometry is shown in Figure 5.34

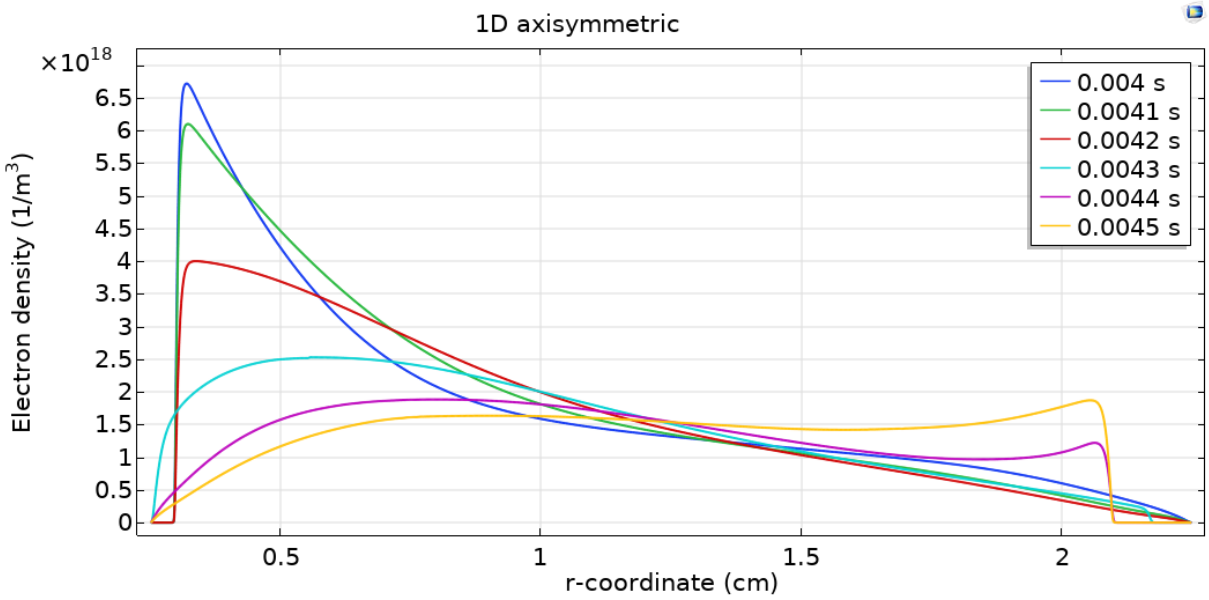

Figure 5.34 - Electron density calculated along the radius for the 1D axisymmetric geometry parametric in time, for the first half of the period.

The electron density peak, in the proximity of the inner electrode, decreases with the time in the first half of the period, while the electron density tail rises in the gas gap. Moving from 4.2 to 4.3ms, the peak in the proximity of the inner electrode disappears and the electron density is almost homogeneous along the radius. Moving from 4.3 to 4.4ms, a new peak appears on the opposite side, in proximity of the inner surface of the dielectric, and only at 4.5ms, the peak becomes higher than the mean electron density along the radius. The calculated electron density values in space and in time can indicate the electrons' motion in the gas gap. The shift of the peak and the oscillations of the electron density along the radius can be correlated to the movement of the electrons from one electrode toward the other. In particular, the electrons are produced with high intensity in the proximity of the inner electrode as the electric potential is zero and it has a negative derivative; while the electrons accumulate in the proximity of the inner surface of the dielectric as the electric potential is zero with a positive derivative. Although the electron density encourages the plasma as the high probability of electron collisions, it does not give information about the probability that those collisions could be effective. The electron energy in electron-particles collisions must be high enough to break the electrical bonds, promoting the conversion of neutral molecules to radicals or ion and electron pairs. The new electron, called secondary electron, participates in electrochemical reactions

in its movement toward the cathode. Hence, it is important to correlate the electron density to the electron energy in the gas ionization process. The electrochemical reactions, also, are correlated to the electron energy, as it is shown in Table 5.1.

The electron energy in the plasma region is commonly measured in electron temperature. In fact, the electrons can reach a temperature above tens of thousands of degrees. The electron temperature in the 1D and the 2D axisymmetric geometries have been calculated along the line and the cut-line respectively, and it is shown in Figure 5.35.

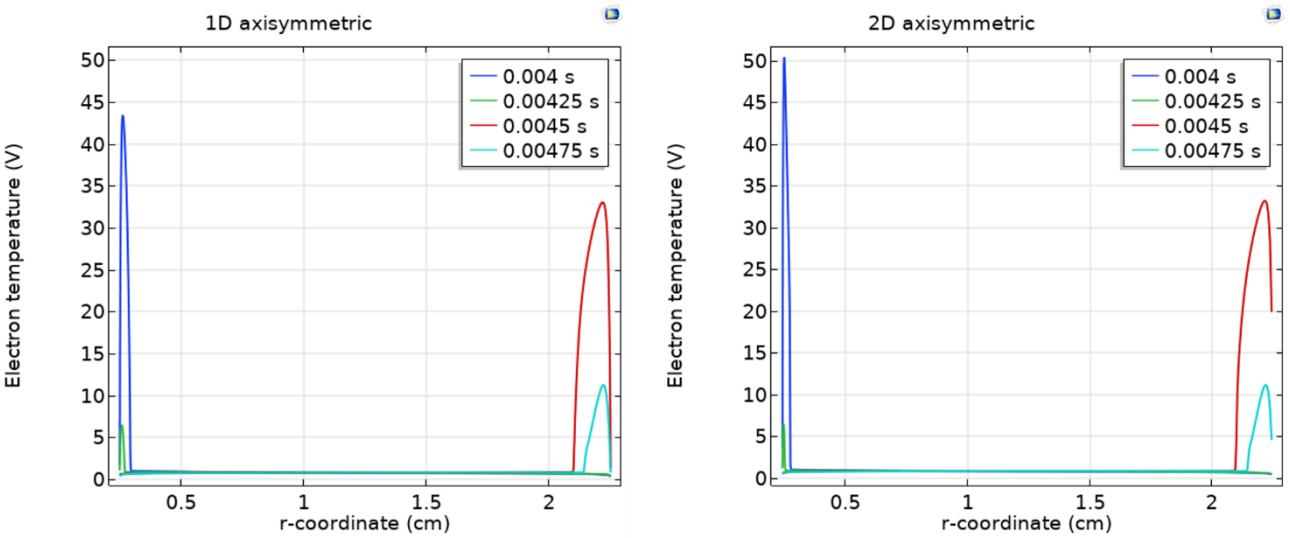

Figure 5.35 - Electron temperature calculated along the middle radius for the 1D (left) and the 2D (right) axisymmetric geometries.

As in the case of the electron density, even the energy of the electrons is proportional to the current and a peak of electron temperature can be observed in the proximity of the inner electrode at 4ms; while the peak move to the inner surface of the dielectric at 4.5ms, when the electric potential is zero and the current is maximum. Also, in the case of the electron temperature, the peak is higher in the proximity of the inner electrode than at the inner surface of the dielectric. From the comparison of the two geometries, it is possible to note that the peak in the proximity of the inner electrode is slightly higher in the case of the 2D axisymmetric geometry (Figure 5.35 right); while no change can be observed for the peak in the proximity of the dielectric. Even in the case of the electron density, the difference in the electron temperature values between the two geometries is negligible. On the contrary, a great difference can be appreciated between the electric field norm in the two geometries. The electric field norm in the 1D and the 2D axisymmetric geometries have been calculated along the line and the middle cut-line respectively, and it is shown in Figure 5.36

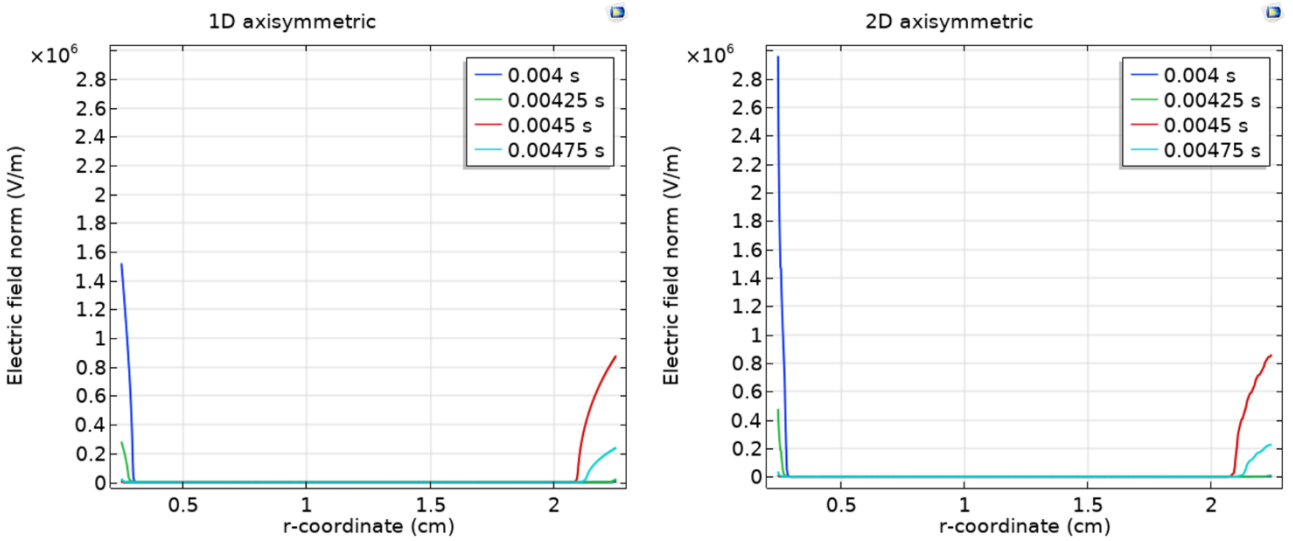

Figure 5.36 - Electric field norm calculated along the middle radius for the 1D (left) and the 2D (right) axisymmetric geometries.

Even the electric field norm is proportional to the current and a peak can be observed in the proximity of the inner electrode at 4ms; while the peak move to the inner surface of the dielectric at 4.5ms. Even in the case of the electric field, the peak is higher in the proximity of the inner electrode than at the inner surface of the dielectric. On the contrary to the other two parameters, the electric field peak near the inner electrode changes significantly with the geometry. The electric field in the proximity of the tip is about twice the electric field calculated in the 1D axisymmetric geometry. In the case of the electric field, the shape of the electrode and the tip effect make a great difference in the magnitude of the peak.

EFFECT OF THE VOLTAGE APPLIED FOR A FIXED GEOMETRY

The mathematical function of the applied voltage on the inner electrode influences either the electron density, the electron temperature and the electric field norm. The frequency of 1 kHz is small enough to make the electron motion independent from the applied voltage sine wave. The order of magnitude of the electron spatial velocity in a gas gap at atmospheric pressure is about nanoseconds. This is greatly faster than the time needed to change the polarity for the applied voltage (500ns). Although the results for different frequency are not reported because they are out of interest in our study, it can be demonstrated that higher frequency (e.g. GHz) reduce the peaks and they disappear as the frequency further increases. The effect is due to the comparable velocity between the electron mobility and the time of polarity inversion. The wave of electrons moving toward the glass meet the wave of electrons moving toward the inner electrode before it passes through the entire gap. Further

to the radio-frequency, the sine amplitude affects the applied voltage function and hence it contributes to the distribution of the electric parameters.

Two different amplitudes of the applied voltage have been simulated in the 1D axisymmetric configuration as shown in Figure 5.28. The electron density, the electron temperature and the electric field norm have been evaluated for applied voltage having 20 and 40kV amplitude peaks. The results are shown in Figure 5.37.

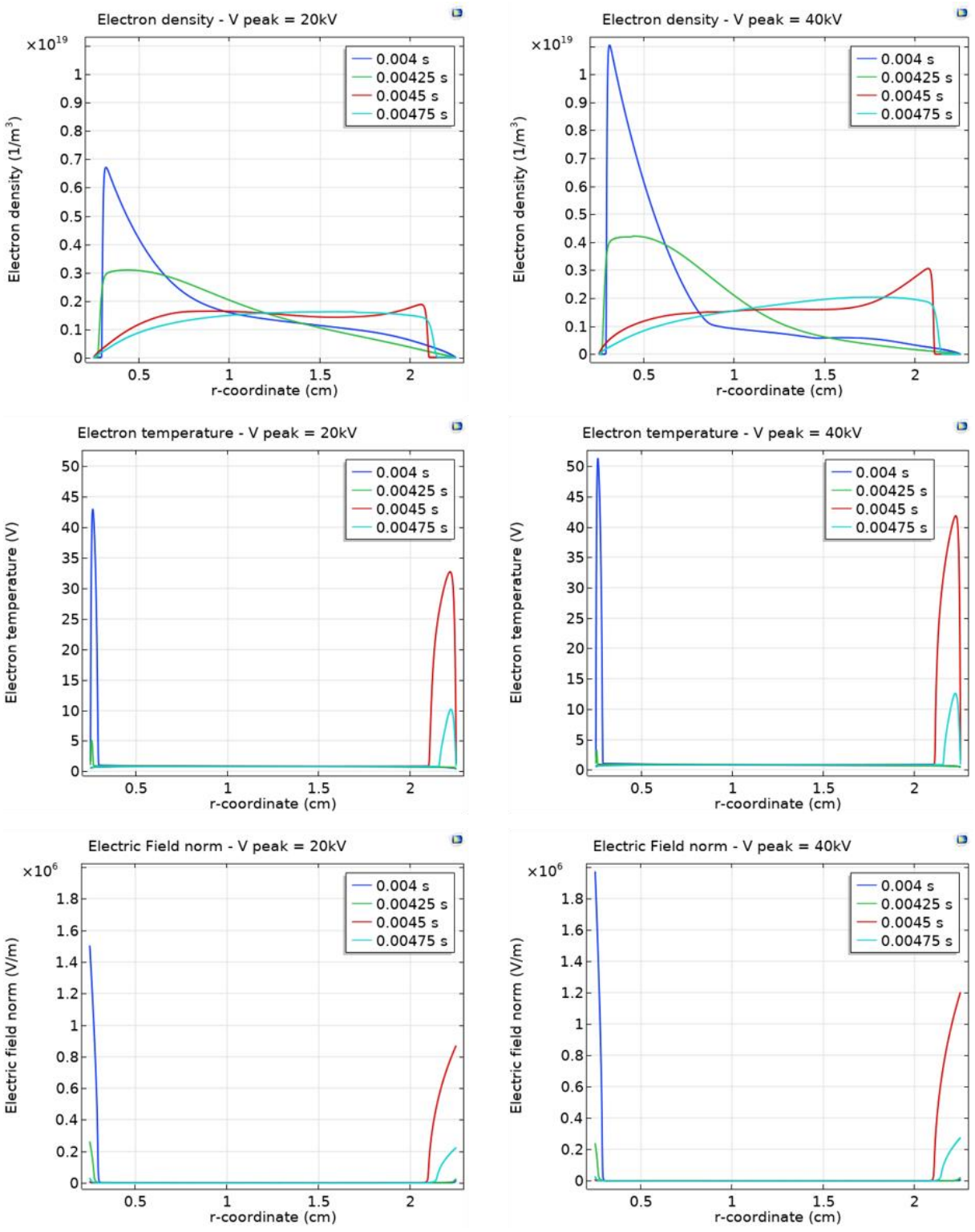

Figure 5.37 - Electron density (top), electron temperature (middle) and electric field norm (bottom) calculated along radius for the 1D axisymmetric geometry, for the applied voltage function having 20kV (left) and 40kV (right) amplitude.

The results in Figure 5.37 (left), are those already discussed in section 0 for the 1D axisymmetric geometry. Those on the right are analysed for the same geometry with a doubled voltage applied

(40kV peak). From Figure 5.37, it is possible to note that the shapes of the curves are similar for the two numerical analysis; hence, the same considerations made in the previous section can be made in the case of the applied voltage having 40kV peak. However, the peaks in the latter case are always higher than in the former. Doubling the applied voltage, the electron density peaks increase by almost 60-70%, where the electron temperature and the electric field norm increase by about 25-30%.

5.2 Experimental Investigation for DBD reactors

The experimental campaign concerns Non-Thermal Plasma (NTP) applications for NO_x removal in Dielectric Barrier Discharge (DBD) reactors. Two different DBD reactors were proposed and the comparison between one or two dielectric barriers discharge reactors was made. The effectiveness of the plasma for NO_x conversion was investigated in the function of the NO_x molar flow rate.

Among the reactors simulated and described in Section 5.1, the experimental campaign was focused on the two Dielectric Barriers Discharge (DBsD) of 2.2cm and the DBD of 5cm. In fact, the reactor of 5cm in the configuration with two dielectrics did not produce the plasma in the range of power supplied 10-20kV and 500-4000Hz. The ignition of the plasma did not occur as the low electric field produced in the two dielectric barriers discharge configuration. On the contrary the electric field was high enough to ignite and sustain the plasma in the reactor of 2.2cm, even in the case of double dielectric barriers discharge configuration, as it was discussed in Section 5.1.1. The reactor of 2.2cm in the configuration with one dielectric was low of interest for real applications. From preliminary tests performed, it was observed that localized streamers appeared in the region of the reactor where the tips of the threaded rod were sharper.

The content of this paragraph can be summarized in:

- experimental set-up;
- materials used for the experimental investigation;
- methods for the analyses of the results;
- details of the DBD investigation and the operating protocols;
- details of the cyclic tests structure and the operating protocols.

5.2.1 Experimental set-up

The Process Flow Diagram (PFD) of the DBD experimental setup is shown in Figure 5.38.

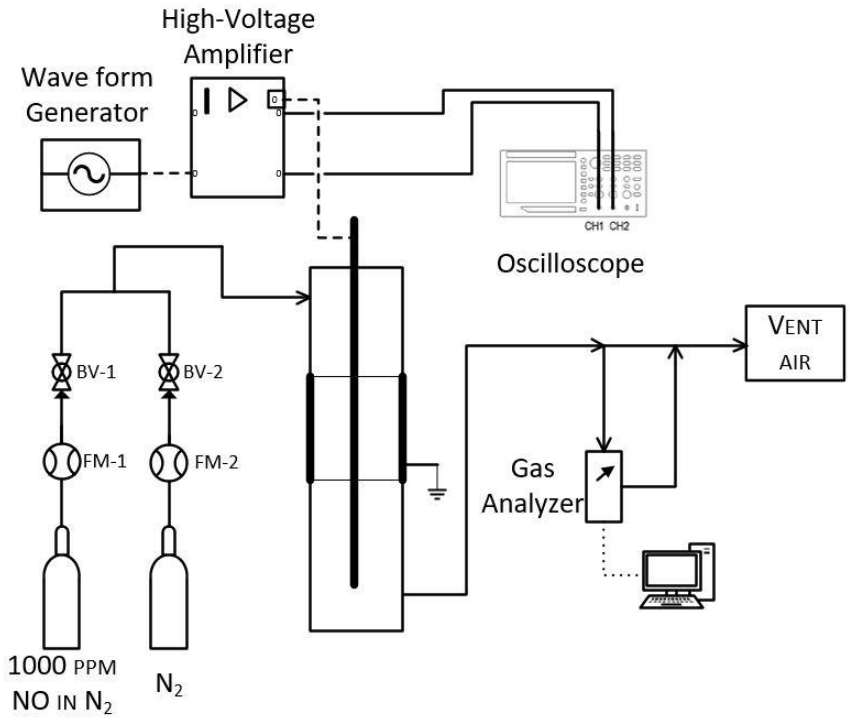

Figure 5.38 - Process Flow Diagram (PFD) of the DBD experimental campaign set-up.

The simulated flue gas was prepared from gas cylinders, whose flow and concentration were regulated by the flow meters FM-1 and, FM-2. The gas fed on the top of the plasma reactor and the exit gas was partially sent to the gas analyser and partly sent directly to the vent. The high voltage power supply was provided from the wave form generator whose signal was amplified by a high-voltage amplifier. The high voltage was connected with the inner electrode, while the metallic tube around the glass tube was grounded. An oscilloscope was used to read the current supplied to the HV electrode.

The overall experimental set-up, with the exception of the gas cylinders was supported by a portable trolley as it is shown in Figure 5.39.

Figure 5.39 - Portable trolley design for the DBD reactors.

Two DBD reactors of different sizes were held by a portable trolley that were able to support both the reactors and the electronic instrumentations.

A floor fan was used to circulate air and contain the temperature increase. Moreover, a thermocouple was used to measure the temperature on the outside electrode and to monitor the gas increasing temperature at the exit of the reactor. A picture of the plant is shown in Figure 5.40.

Figure 5.40 - Picture of the DBD and the PBPR set-up.

The gas generation section was similar to that of the adsorption experimental campaign and hence described in Section 4.1.1

5.2.1.1 Reactor section

In this section a focus on the reactors is reported. The NO_x reduction was performed in dielectric barrier discharge (DBD). Two cylindrical DBD reactor were designed and built. A schematic representation of the DBD reactors is shown in Figure 5.41.

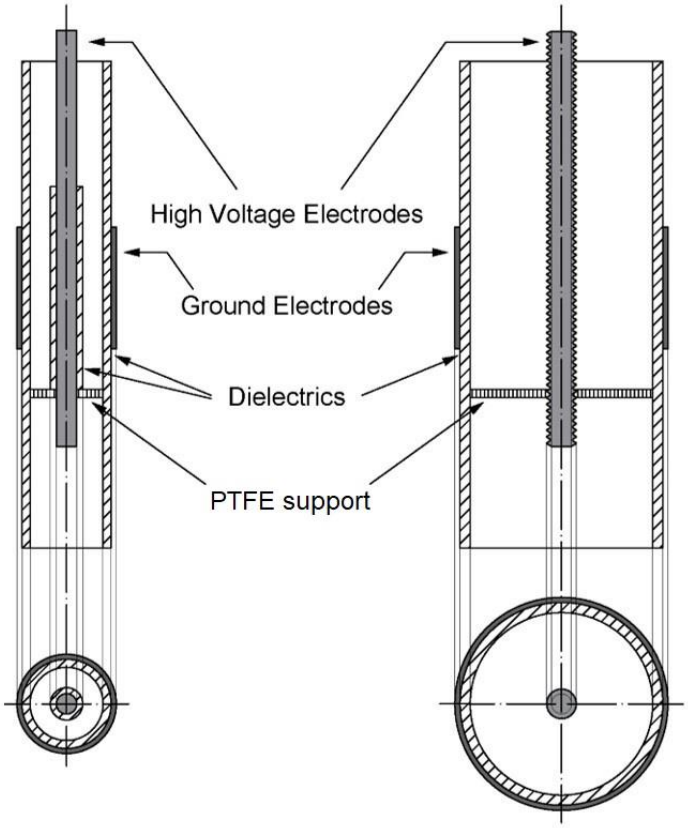

Figure 5.41 - Schematic representation of the DBD reactors designed.

The two reactors consisted of a two Dielectric Barriers Discharge (DBsD) reactor of 2.2cm (Figure 5.41 left) and a DBD reactor of 5cm (Figure 5.41 right). Both the reactors had a length of 1.2m, an inner electrode 1mt long and the ground electrode (outside) 30cm long. The high voltage electrode was centred by a PTFE support on the bottom and the gas connection on the top. The connections were the same as they were described in Figure 5.38. In the case of the two DBsD reactor, a further dielectric glass tube of 8mm was placed in the reactor, supported by the PTFE, and the electrode fitted in that.

The reactors are shown in Figure 5.42, before the trolley was assembled.

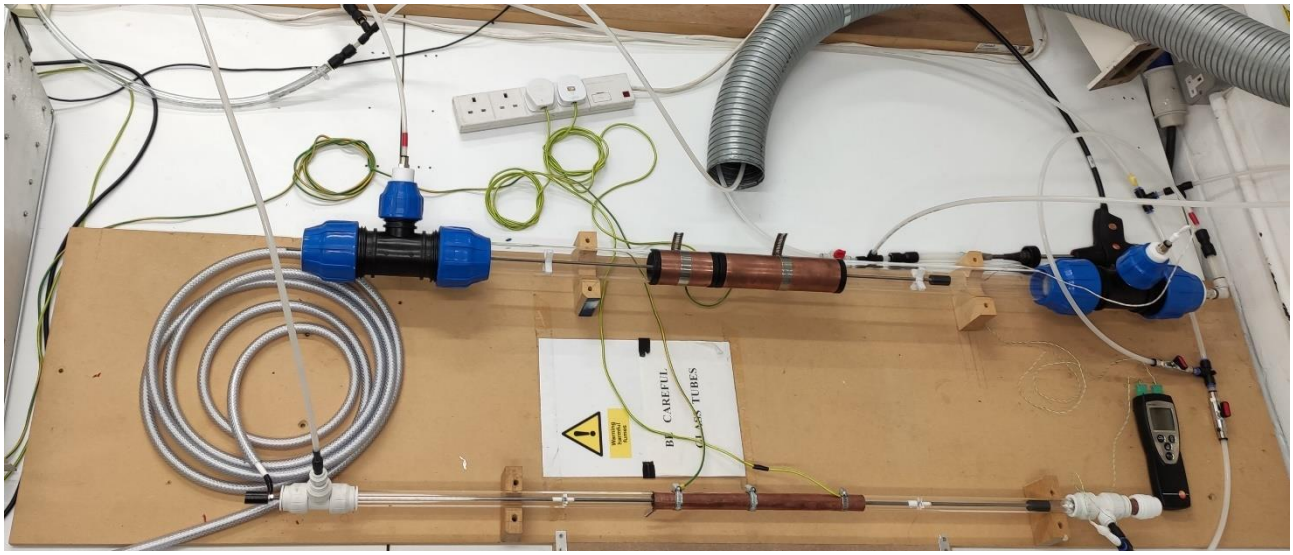

Figure 5.42 - Picture of the DBD and two DBsD reactors.

In Figure 5.42, the HV cable was connected to the two DBsD reactor, while the DBD was disconnected.

5.2.1.2 Auxiliary Instrumentations

The concentration of the flue gas was monitored with the Testo 350 analyser that was described in Section 4.1.3, having the same gas sensors configuration.
The other auxiliary instrumentations used for the plasma applications are here described.

TEMPERATURE CONTROL AND MONITORING

For what concern the DBD and the DBsD, the temperature in the corresponding of the plasma region could not be monitored as the interference with the strong electric field. Hence, the gas temperature was monitored at the exit of the reactors by the “Testo 720” Thermometer.
The thermometer and the installed thermocouples are shown in Figure 5.43.

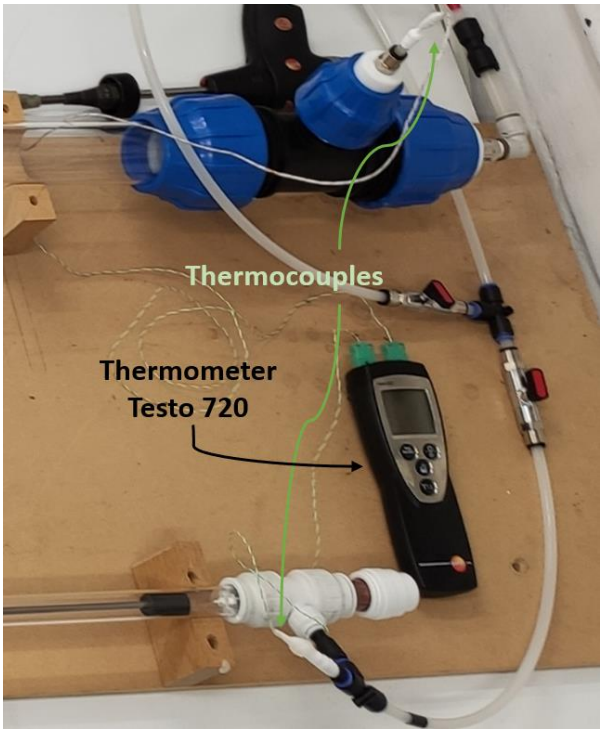

Figure 5.43 - Thermometer and thermocouples installed to the plasma reactors.

The Testo 720 has two inputs; hence, two different thermocouples can be monitored in simultaneously. Each thermocouple consisted of wires whose ends were weld each other and fixed in the centre of the reactors at the end of them.

ELECTRICAL SET-UP

The electrical set-up was made of a function generator, a high voltage amplifier and an oscilloscope. The function generator was the TG120 from Aim & Thurlby Thandar Instruments that allowed to generate a sine, square or triangle wave signal, at the frequency 0.2Hz to 20MHz, with the Voltage of 10mV to 20V pk-pk from 50Ω. The signal was amplified by the Trek Model 20/20C high-voltage power amplifier with the ratio $2000^{th}/1$, having the output voltage of ±20kV peak AC, and output current ±20mA peak AC. The oscilloscope Tektronix TBS1000B was used to monitor the power supplied. The oscilloscope registered and graphically displayed varying signal voltages, usually as a two-dimensional plot of one or more signals as a function of time, that was used to monitor the instantaneous voltage and current at the amplifier output.

The electrical set-up is shown in *Figure 5.44*.

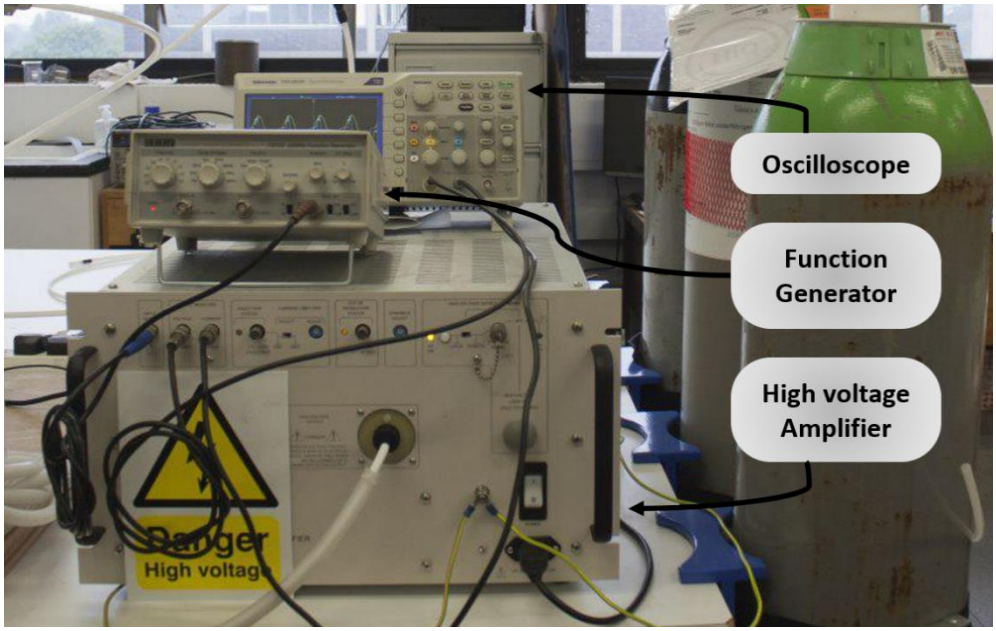

Figure 5.44 - Electrical set-up for the plasma generation: oscilloscope (top), function generator (middle), high voltage amplifier (bottom).

5.2.1.3 Materials

In this section, the most relevant materials and components used for the dielectric barrier discharge configurations are described.

GLASS TUBES

The DBD and the two DBsD reactors were made of glass tubes used as dielectric materials. The external tubes were made of borosilicate glass for its good insulator and for its transparency. In the case of the two dielectric barriers discharge reactor, the inner dielectric was a quartz tube. In fact, the higher purity of the quartz glass encouraged the equal distribution of the charged particles on the glass surface. Moreover, the tube was in a strict contact with the high voltage electrode, hence a higher electrical resistivity was required.

The physical properties of the borosilicate and quartz glass tubes adopted are described in Table 5.2.

Borosilicate Glass Tube &Rod 3.3			
Technical Data:			
Physical Property			
No.	Physical performance	Numerical Value	Unit
1	Coefficient of mean linear thermal expansion(20℃,300℃)	3.3±0.1	$10^{-6}K^{-1}$
2	Transformation temperature	525±15	℃
3	Softening point	820±10	℃
4	Working point	1260±20	℃
5	Density at 20℃	2.23±0.02	g/cm^3
6	Mean thermal conductivity(20℃-100℃)	1.2	w/m^2k
7	Refractive index	0.92	1
Main Composition			
SiO_2	B_2O_3	Na_2O+K_2O	Al_2O_3
81	13	4	2

Quartz Tube Properties

Mechanical Data	
Density	2.203 g/cm³
Mohs Hardness	5.5 … 6.5
Micro Hardness	8600 … 9800 N/mm²
Knoop Hardness	5800 … 6100 N/mm²
Modulus of elasticitiy (at 20°C)²	7.25 x 10^4 N/mm²
Modulus of torsion	3.0 x 10^4 N/mm²
Poisson's ratio	0.17
Compressive strength (approx.)	1150 N/mm²
Tensile strength (approx.)	50 N/mm²
Bending strength (approx.)	67 N/mm²
Torsional strength (approx.)	30 N/mm²
Sound velocity	5720 m/s

Thermal Data	electrically fused	flame fused	synthetic
Softening temperature °C	1710	1660	1600
Annealing temperature °C	1220	1160	1100
Strain temperature °C	1125	1070	1000
Max. working temp. continuous °C	1160	1110	950
Short-term °C	1300	1250	1200

Table 5.2 - Physical properties of the glass tubes made of borosilicate (left), and quartz (right).

A picture of the three glass tubes used is shown in Figure 5.45.

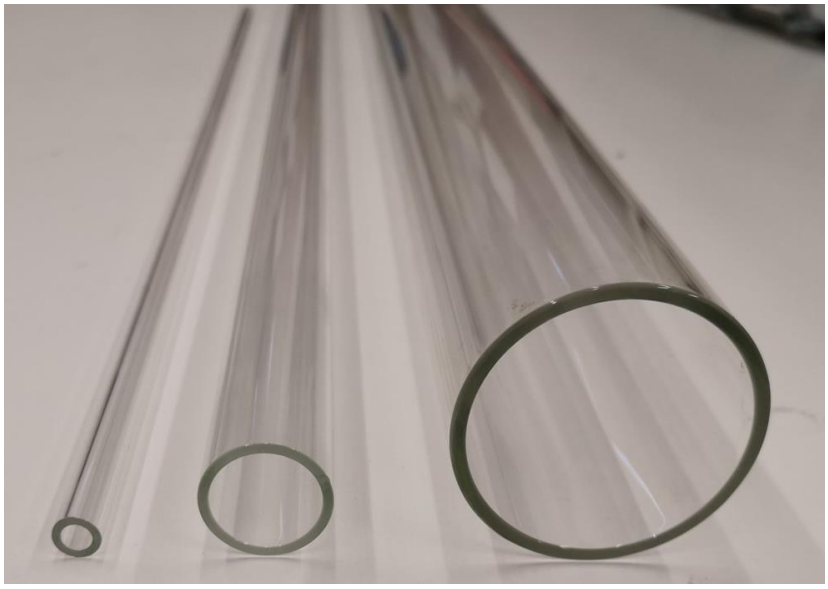

Figure 5.45 - Glass tube of 8mm OD and 1.5mm thickness (left), 22mm OD and 2mm thickness (middle), and 50mm OD and 2.5mm thickness (right).

The quartz tube of 8mm was used as inner dielectric for the two DBsD reactor, the glass tube of 2.2cm was used as outer dielectric for both the DBsD reactor, while the glass tube of 5cm was used as outer dielectric for the DBD reactor.

ELECTRODES

The high voltage and the ground electrodes were coaxial with the glass tubes and they were in the centre and out of the glass, respectively. The high voltage electrode consisted of a threaded rod standard size M5, 1m long, made of Stainless Steel. The ground for the 2.2cm tube was made with a copper sheet, 30cm long, wrapped around the glass tube and fixed with hose clamps, while the ground for the 5cm reactor consisted of a copper tube of standard size of 2 1/8".
A picture of the three electrodes is shown in Figure 5.46.

Figure 5.46 - Picture of electrodes: SS M5 threaded rod (left), wrapped copper sheet (middle), and copper tube of 2 1/8" (right).

In Figure 5.46, the threaded rod was diffed in the glass tube of 8mm to show how it appears in the case of the DBsD reactor.

PTFE SUPPORT

Particular attention was given to assure that the coaxial DBD reactor was perfectly symmetric with the electrode centred into the reactor. In fact, if it does not occur, the electrical resistance is not homogeneous and preferential discharges occur where the distance between the electrodes is lower.
The designed reactor used PTFE support to centre the inner electrode into the glass tube. The support should have a geometry that allowed the gas passing through it without high pressure drop. The picture of the PTFE support is shown in Figure 5.47.

Figure 5.47 - PTFE Support from the inner view of the reactor (left), in the reactor of 2.2cm (middle) and the reactor of 5cm (right) while they were operating.

The PTFE support was perfectly symmetric, and it had a thread in the centre for the rod (Figure 5.47 left). Figure 5.47 middle and right shows the support into the reactors while they were in operation. In the case of the DBD reactor (Figure 5.47 right), a further cylinder of POMC Acetal Plastic was screwed at the end of the rod to avoid unwanted corona discharge in the corresponding of the tips at the end of the rod (far from the plasma region).

The blue bright appearing in the DBsD reactor (Figure 5.47 middle) was due to the light exposure of the camera. Actually, the plasma brightness was purple as that can be seen in the DBD reactor (Figure 5.47 right)

5.2.1.4 Methods of analysis and experimental schedules

A Dielectric Barrier Discharge (DBD) reactor was used to reduce the NO_x as it was diluted in N_2. As the plasma was produced in the reactor, the NO_x emissions decreased as the effect of the reduction to N_2 and O_2.

Among the physiochemical factors, the NO_x reduction is a function of the gas pressure and temperature. Since the exposure to the plasma increases the wall temperatures gradually, even the gas temperature increases with the time; hence, it is not possible to identify a steady-state condition. The higher is the temperature (in a low range), the higher is the NO_x removal. The NO_x reduction yield was estimated at 3 minutes from the onset of the plasma, as it was observed that the slope of the NO_x emission curve exponentially decreased with the time. An example of the NO_x reduction in a DBD reactor is shown in Figure 5.48.

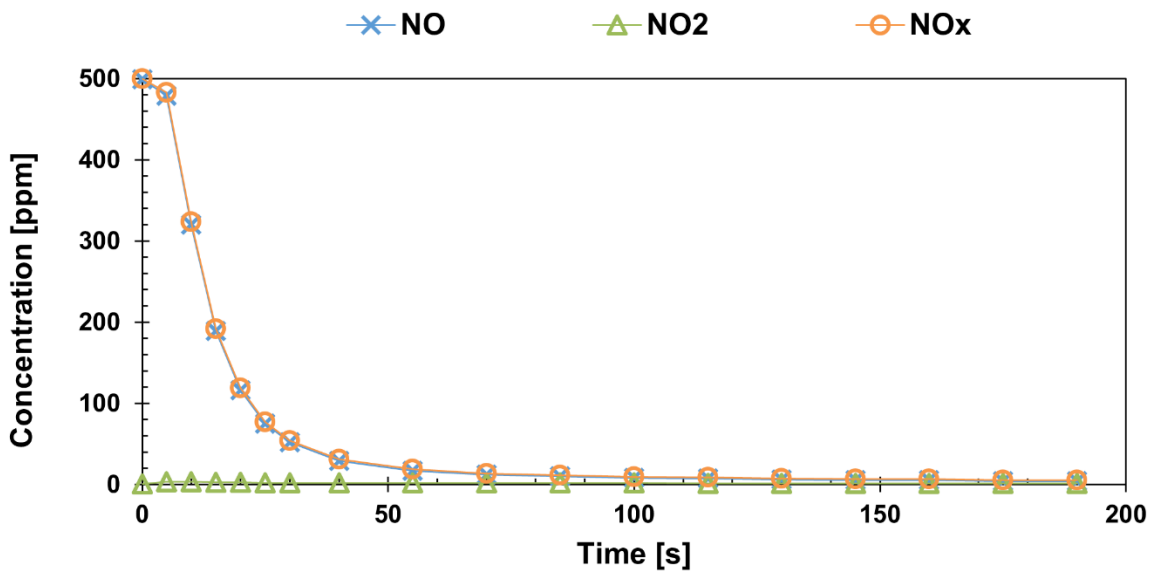

Figure 5.48 - Reduction of 500ppm of NO in N_2, as the effect of the plasma produced by applying 20kV at 1kHz to the DBD reactor.

From Figure 5.48, it is possible to notice the fast decreasing of the NO and NO_x emissions. The NO_2 was constantly negligible, as the NO was reduced rather than oxidized to NO_2. The concentrations at 180 seconds from the plasma generation were used to calculate the NO_x reduction yield:

$$\eta_{NO_x}(180s) = 1 - \frac{c_{NO_x 180}}{c^o_{NO_x}} \qquad (5.1)$$

where $c^o_{NO_x}$ is the initial concentration of NO_x and $c_{NO_x,180}$ is the NO_x concentration after 180s from the plasma ignition. The NO_x reduction yield was evaluated in each experiment where the effect of the gas velocity, the initial concentration, the applied voltage and the frequency was evaluated. For what concern the two dielectric barriers discharge (DBsD) reactor, different gas concentrations and gas velocity were investigated. The experimental programme at 19kV and 1kHz in the two DBsD reactor is shown in Table 5.3.

NO_x concentration	**Gas velocity [m/s]**											
	0.1	**0.2**	**0.3**	**0.4**	**0.5**	**0.6**	**0.7**	**0.8**	**0.9**	**1.0**	**1.1**	**1.2**
80 ppm	X	X	X	X	X	X	X	X	X	X	X	X
250 ppm	X	X	X	X	X	X	X	X				
500 ppm	X	X	X	X								

Table 5.3 - Experimental programme for the two DBsD reactor, supplying 19kV at 1kHz.

For what concern the NO_x initial concentration of 80ppm, others potentials were tested at different frequencies. The results reported in this thesis for the feed of 80ppm will consider 19kV at 500Hz, 19kV at 1kHz, 20kV at 1kHz. The experimental programme at 80ppm is shown in Table 5.4.

Power supply	Gas velocity [m/s]											
	0.1	**0.2**	**0.3**	**0.4**	**0.5**	**0.6**	**0.7**	**0.8**	**0.9**	**1.0**	**1.1**	**1.2**
19kV - 500Hz	X	X	X	X	X	X	X	X	X	X		
19kV - 1kHz	X	X	X	X	X	X	X	X	X	X	X	X
20kV - 1kHz	X	X	X	X	X	X	X	X	X	X	X	X

Table 5.4 - Experimental programme for the conversion of 80ppm in the two DBsD reactor.

Although the amplifier might supply 20kV (40kV pk/pk), most of the experiments were performed at 19kV for safety reasons. However, some spot tests were performed at 20kV to evaluate the effect of the potential on NO_x removal efficiency.

Further to the tests performed on the two DBsD reactor, the DBD reactor with the screw thread was investigated. In this thesis we reported the tests performed by supplying 19kV at 1kHz only.

The experimental programme for of the tests on the DBD reactor is shown in Table 5.5.

NO_x concentration	Gas velocity [m/s]		
	0.1	**0.2**	**0.3**
80 ppm	X	X	X
250 ppm		X	
500 ppm		X	

Table 5.5 - Experimental programme for the DBD reactor, supplying 19kV at 1kHz.

The maximum gas velocity considered in the DBD was of 0.3m/s as the bigger cross sectional area of the reactor. Indeed, the velocity of 0.3m/s was equivalent to about 28NL/min that was the maximum flow rate we were able to simulate in lab-scale.

A comparison between the two configurations, in terms of effectiveness, cannot be easily made as the different cross-sectional area of the reactor. The NO molar flow rate was defined as:

$$Q'_{NO} = c^0_{NO} \cdot Q_{tot} \qquad (5.2)$$

where Q_{tot} was the total flow rate and c^0_{NO} was the initial concentration of NO. The NO molar flow rate allowed to estimate the effectiveness of the plasma in the function of the amount of NO fed in the reactor per unit time. The efficiency was evaluated according to the Equation (5.1).

The operating protocol consisted of mixing the gas up to the desired concentration, then the plasma was applied for 3 minutes and the NO_x concentration before the plasma and the concentration after 3 minutes were considered.

5.1Results of the NO_x reduction in the DBD reactors

NO_x reduction in a dielectric barrier discharge was investigated using two different designs: a dielectric barrier discharge (DBD) reactor and a two dielectric barriers discharge (DBsD) reactor. The two reactors have been described in Section 5.2.1.1; while the methods of analysis can be found in Section 5.2.1.4. Most of the tests were performed in the two dielectric barriers discharge as it was easier simulate a wide range of gas velocities and compositions.

When the plasma occurs on almost pure nitrogen gas, the dissociation of molecules takes place. The nitrogen radicals produced from the dissociation react with the other molecules like NO to convert them into N_2 and O_2 e.g. Hence, the NO_x molecules' concentration decreases as the effect of their conversion, as in Figure 5.48.

The capability to reduce NO to N_2 and O_2 depends on many variables: the NO concentration, the gas flow rate (proportional to the gas residence time), the voltage applied and the frequency. The effect of these variables was investigated separately, and the results are shown in this section. The NO_x reduction yield was estimated as in Equation (5.1) for each test.

For what concern the gas features, the NO_x reduction efficiency in the configuration with two dielectrics for 250ppm of NO in N_2 exposed to a plasma promoted by the supply of 19kV (38kVpk/pk) at 1kHz, in the function of the spatial gas velocity is shown in Figure 5.49.

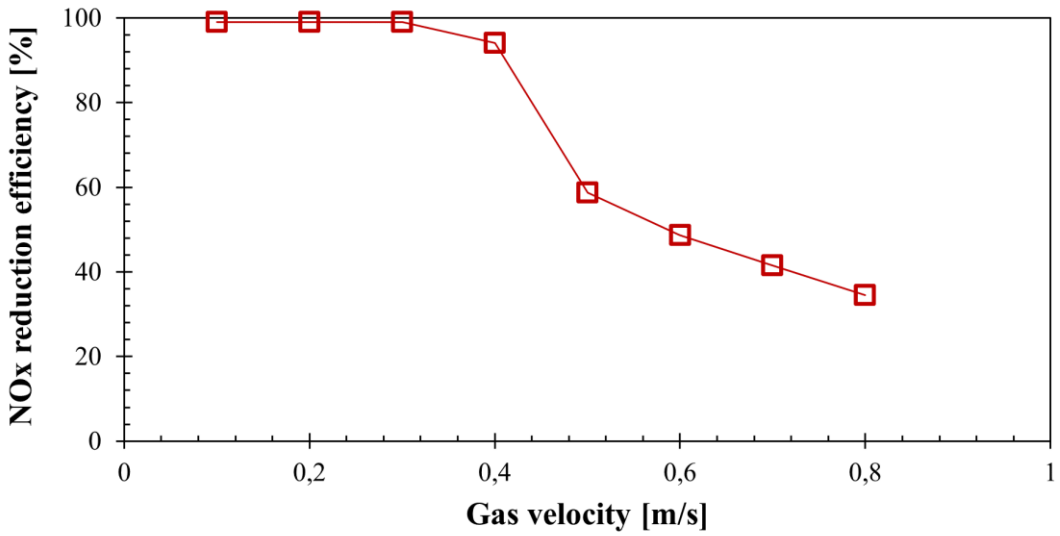

Figure 5.49 – NO_x reduction efficiency for the reduction of 250ppm of NO in N_2, supplying 19kV at 1kHz to the DBsD reactor.

An efficiency of about 100% was obtained as the gas velocity was below 0.3m/s, that corresponds to a gas residence time in plasma region of 1s. The NO_x reduction efficiency decreased with the increasing of the gas velocity. The higher is the gas velocity, the lower is the gas residence time in the plasma region, the higher is the number of NO_x molecules passing through the plasma region per unit of time while, the plasma energy remained constant.

There exists a direct correlation between the discharge power and the NO_x conversion efficiency in a NTP reactor, in accordance with Mihalcioiu et al. [108]. Hence, at fixed plasma energy, the higher is the NO_x flow rate in the plasma reactor, the lower is the NO_x reduction efficiency. The NO_x flow rate can be controlled by either the gas flow rate, as in Figure 5.49, or by changing the NO_x composition in the inlet gas. An example of the effect of the NO_x gas composition can be found in Figure 5.50.

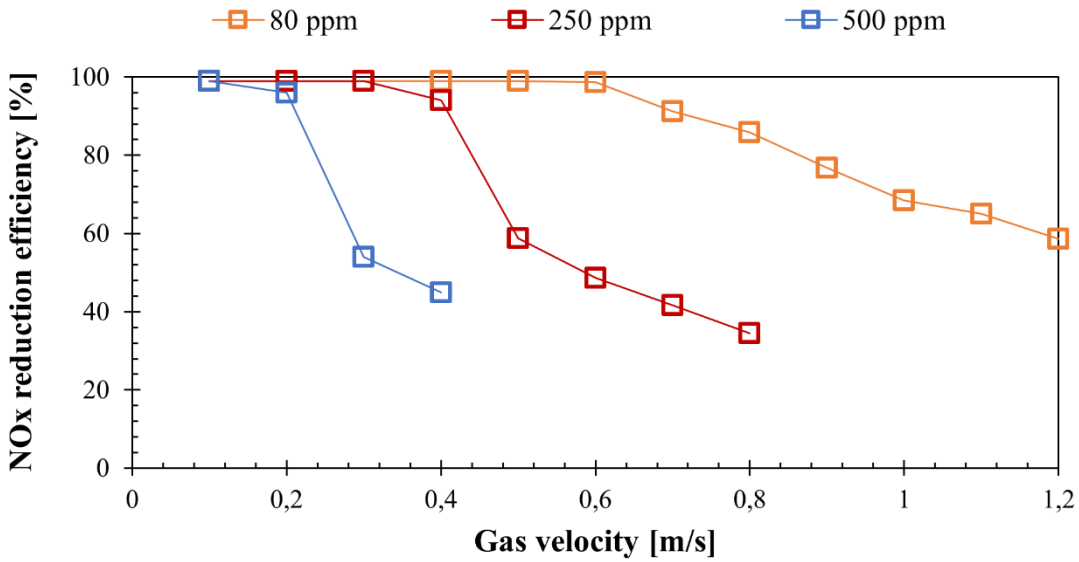

Figure 5.50 - NO_x reduction efficiency for the reduction of 80, 250 or 500ppm of NO in N_2, supplying 19kV at 1kHz to the DBsD reactor.

A higher concentration of NO_x in the gas leads to a lower amount of NO_x converted, as the plasma energy remained constant. From Figure 5.50, it is possible to note that the NO_x reduction efficiency decreased from 99% to 45% as the NO concentration in the inlet gas increased from 80 to 500ppm, at the gas velocity of 0.4m/s; or (which is the same thing) an efficiency of 55-60% was obtained from a gas at the velocity of 0.3, 0.5 and 1.2 m/s, as the NO_x concentration in the inlet was of 500, 250 and 80ppm respectively, by supplying a voltage of 19kV at 1kHz.

So far, the NTP energy in the plasma reactor was considered constant as the potential applied was the same. This is an approximation that is conservative if the plasma energy is calculated in a quiet gas. When the gas velocity increases, the ions and radicals produced in the plasma region swept away out from the high electric field region. The higher is the gas velocity, the lower is the amount of the charged species in the plasma region, hence a lower amount of current can be transferred in the gas gap, with the consequence of a lower power supplied. However, for our calculation we can approximate the plasma power constant with the gas velocity.

Once the effect of the gas velocity and the gas composition on the NO_x reduction efficiency have been described, at a fixed plasma power, it could be interesting to understand how the electric potential and the frequency affect the plasma power and hence the NO_x removal efficiency. The effect of the applied voltage to the NO_x reduction efficiency can be observed in Figure 5.51.

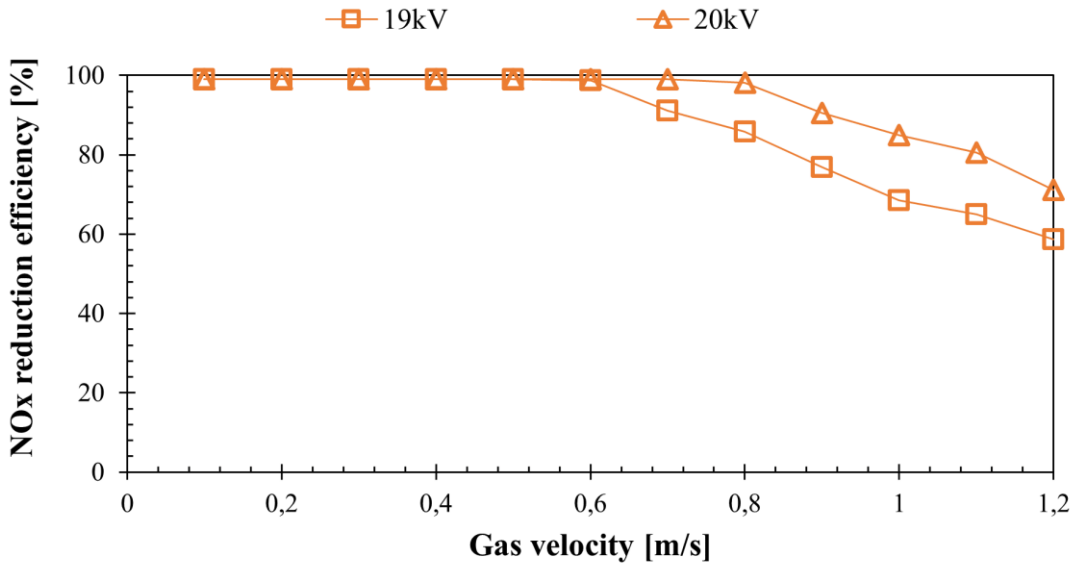

Figure 5.51 - NO_x reduction efficiency for the reduction of 80ppm of NO in N_2, supplying 19kV and 20kV at 1kHz to the DBsD reactor.

Figure 5.51 shows the NO_x reduction efficiency of 80ppm of NO in N_2 calculated as the electric potential of 19kV and 20kV were applied at the fixed frequency of 1kHz. Even at 20kV, the NO_x reduction efficiency decreases with the gas velocity and the trend of the curve is very similar to that at 19kV. The efficiency at 20kV was always higher and the curve seems to be shifted above the curve at 19kV. The reduction efficiency for the treatment using 20 instead of 19kV was about 20% higher, in the range 0.8-1.2m/s. This result confirms that the higher is the plasma power, the higher is the NO_x conversion. A higher electric potential provided a higher amount of energy and hence a higher plasma power.

Further to the applied voltage, the frequency plays a key role in the plasma power. If the frequency is too low, the charges stored in the corresponding of the dielectric surface dissipate and the plasma power decreases. If the frequency is too high, the polarity could change before the charged particles across the gas gap and hence only a small number of electrons across the gap and transfer the charges. At extremely high frequency, the plasma could extinguish. Referring to the data shown in Figure 5.50 and Figure 5.51, the NO_x reduction efficiency for the removal of 80ppm of NO in N_2 by applying 19kV to the two DBsD reactor was analysed by imposing the frequency of 500Hz and the results were compared to those obtained at 1kHz. The NO_x reduction efficiencies for the two frequencies are shown in Figure 5.52.

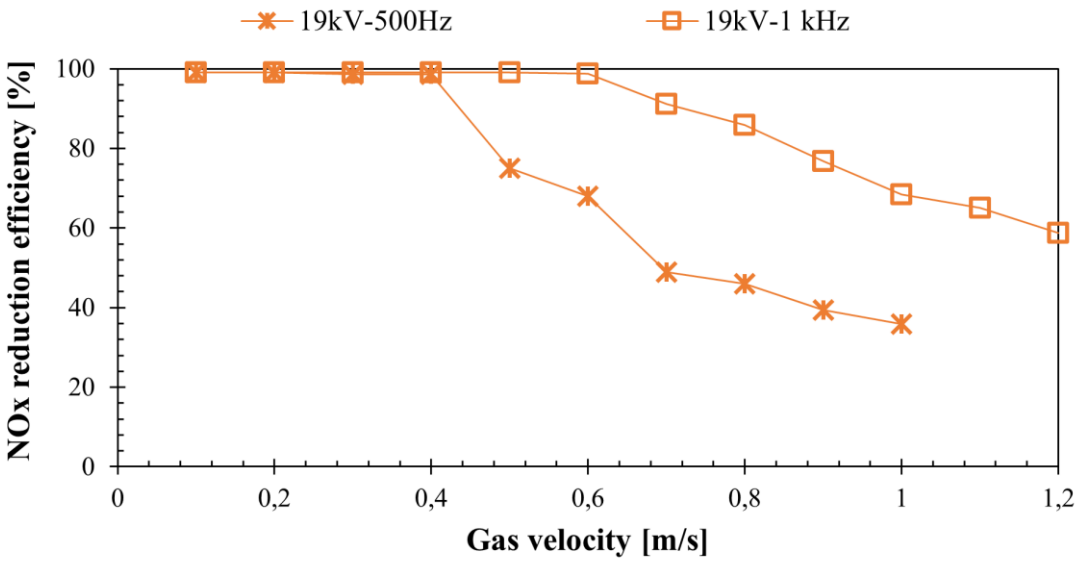

Figure 5.52 - NO_x reduction efficiency for the reduction of 80ppm of NO in N_2, supplying 19kVat 500Hz and 1kHz to the DBsD reactor.

The frequency of 500Hz had a negative effect to the NO_x reduction efficiency. A further reduction of 30-40%, of the NO fed, was obtained as the voltage was applied at the frequency of 1kHz. Also, the light emitted by the plasma produced at 1kHz was brighter than that at 500Hz. Although the power supply allowed to sustain the electric potential of 19kV at higher frequencies, the limit of 1kHz was imposed for safety reasons in laboratory tests. It must be considered that, further to the electrical aspects, the dielectric exposed to a bombardment of electrons at high frequency increases its surface temperature. The increasing of the gas temperature leads to a rearrangement of the internal structure of the glass that can be penetrate by the current promoting the dielectric breakdown. This phenomenon likely occurs to amorphous materials such as silica glass.

The NO_x removal efficiency in the function of the NO molar flow rate, obtained in the two DBsD reactor, was compared with that obtained in the DBD reactor (Figure 5.42) and the results are shown in Figure 5.53.

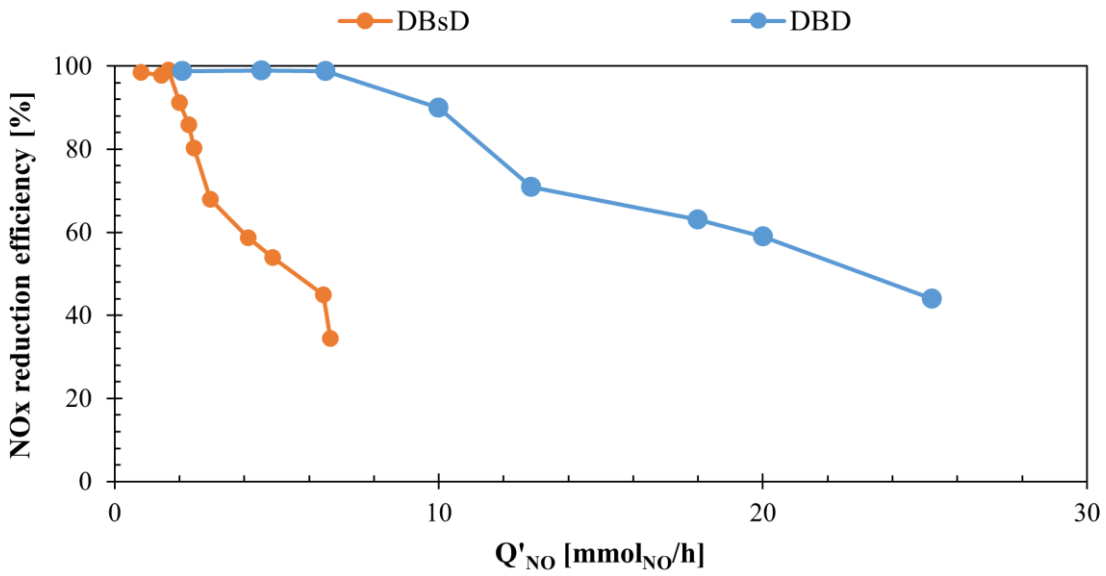

Figure 5.53 - NO_x reduction efficiency for the reduction of NO supplying 19kVat 1kHz to the two DBsD (2.2cm) and the DBD (5cm) reactors, as the function of the NO molar flow rate.

The NO conversion efficiency was always higher for the one dielectric barrier reactor than the configuration with the two dielectric barriers. This result can be attributed to the higher diameter of the one dielectric barrier reactor that allows a lower gas velocity by maintaining the same NO mass flow. The NO conversion efficiency remained constant at the value of 99% when the NO molar flow was lower than 6mmol$_{NO}$/h (for the one dielectric barrier configuration) that corresponds to about 80ppm of NO and the flow rate of about 28NL/min e.g. The efficiency decreased as the NO mass flow increased and it achieved the value of about 40% when the molar flow was 25mmol$_{NO}$/h that corresponds to about 500ppm and the flow rate of 18NL/min e.g. The two dielectric barrier configurations could achieve the same efficiency only under a lower NO mass flow. The efficiency was 99% as the NO mass flow was lower than 2mmol$_{NO}$/h; while it achieved the efficiency of about 40% as the NO mass flow was 4mmol$_{NO}$/h.

The plasma generated in the two dielectric barriers reactor appeared to be extremely thin streamers in the gas gap. The streamers spread all along the length of the electrode and were homogeneously distributed. The larger the reactor diameter, the lower the electric field in the gas gap.

The screw thread electrode used in the one dielectric barrier reactor was chosen to improve the electric field. The sharp edges of the screw thread electrode produced a localized high-intensity electric field, which is similar to the tip of a needle that encourages the plasma production. The localized high-intensity electric field near the sharp edges increases the electron energy and produces a high number of secondary electrons that develops to promote electron avalanche before it develops into streamers.

The plasma generated in the one dielectric barrier reactor configuration appeared as a series of pulsed streamers that started from the HV electrode and travelled toward the glass inner surface (dielectric barrier). The streamers branched out radially from the sharp edges and they were more scattered. These streamers were thicker for the one dielectric barrier reactor configuration than in the two dielectric barriers reactor. The presence of ramified streamers promoted a higher NO conversion due to the high plasma volume generated. Although, the plasma volume did not correspond to the totality of the gas volume as in the two dielectric barriers reactor configuration, the plasma power supposed to be higher and hence the high number of active species produced in the plasma streamers could react downstream the streamers converting the NO_x in the gas phase.

6. PROOF OF THE CONCEPT OF NO_X ADSORPTION AND NTP DESORPTION-REDUCTION PROCESS

A proof of the concept of the NO_x adsorption and NTP Desorption-Reduction process was performed in a lab-scale reactor. A small amount of sorbent was used for the NO_x adsorption and regeneration in a Packed Bed Plasma Reactor (PBPR).

Cyclic tests have been performed with the scope to analyse the NO and the NO_2 emissions from the adsorption stage at the exit evaluating a potential reduction of the NO_x emissions (compared to the previous adsorption) and consequently a constant amount of adsorbed NO_x cycle after cycle. This will demonstrate the capability to regenerate a certain amount of reversible active sites on the sorbent surface.

Two different sorbent granulometries have been tested in this experimental campaign. The adsorption and NTP desorption-reduction tests were performed on:

i. GAC-Cu of 0.3-0.6mm as the granular size;
ii. GAC-Cu of 1.5-3mm as the granular size.

This chapter includes:

- Experimental set-up;
- Methods of analysis and experimental schedules;
- Experimental results.

6.1 Experimental set-up

The experimental set-up for the cyclic tests of NO_x adsorption and NTP desorption and reduction was very similar to that for the NO_x reduction shown in Figure 5.38 by including an air gas cylinder and replacing the DBD reactor with the PBPR.

The Process Flow Diagram (PFD) of the DBD experimental setup is shown in Figure 6.1.

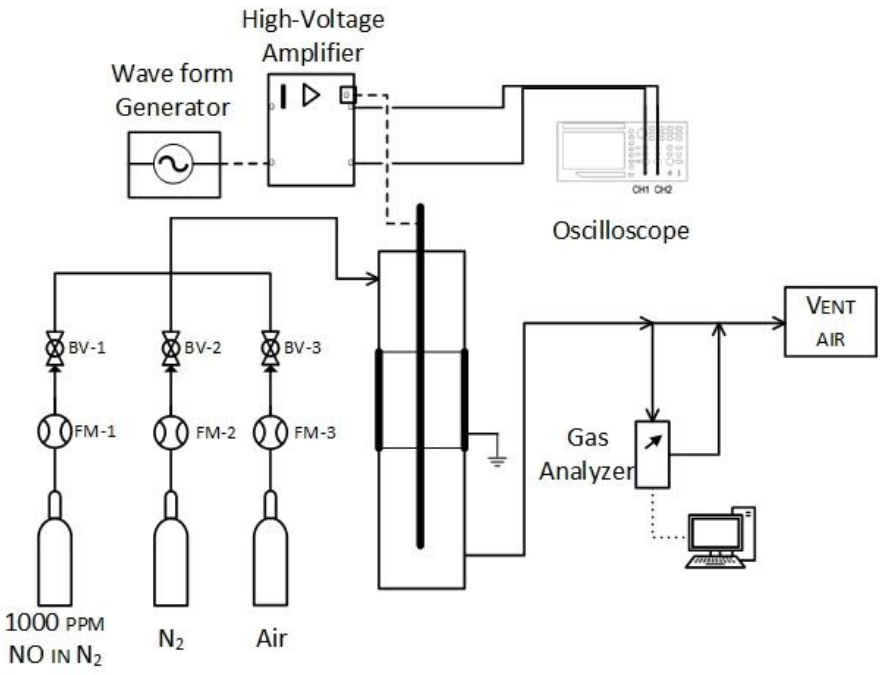

Figure 6.1 - Process Flow Diagram (PFD) of the PBPR experimental campaign set-up.

The simulated flue gas was prepared from gas cylinders, whose flow and concentration were regulated by the flow meters FM-1, FM-2 and FM-3. The reactor was supported by the portable trolley shown in Figure 5.39 as it has the same size of the DBsD reactor of 2.2cm.

The Packed Bed Plasma Reactor (PBPR) consisted a glass tube of a packed with adsorbent material and having the threaded rod (HV electrode) centred into the reactor. The borosilicate glass tube was the same of the DBsD reactor of 2.2cm, 2mm of thickness and 1.2m long as it was shown in Figure 5.45 middle. A M5 threaded rod 1m long was centred into the reactor and held by the PTFE supports, as they were shown in Figure 5.47. A copper sheet of 5cm long was used as ground. It wrapped around the glass tube and it was placed in the middle of it.

The cyclic tests of adsorption and NTP desorption-reduction were performed using a GAC-Cu having the same nature of that described in Section 4.2. Two different granulometries were considered: crushed grans of 0.3-0.6mm size and the commercial size one (1.7÷3.35mm). The plasma reactor was

packed with sorbent and the whole length of the ground was filled with it. The total length of 5 cm corresponded to about 7.5g of sorbent grans.

A picture of the PBPR, while it was operating, is shown in Figure 6.2.

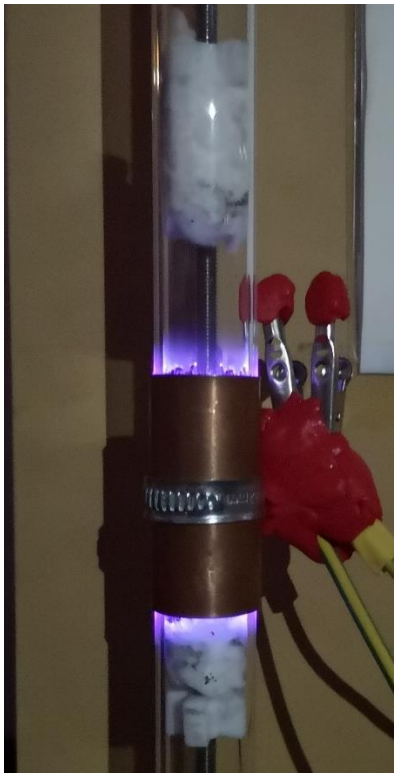

Figure 6.2 - Picture of the Packed Bed Plasma Reactor (PBPR), while it was operating.

From Figure 6.2 it is possible to note the glass wool that was place above and below the adsorbent bed to uniform the gas flux. The purple light from the inner of the reactor was due to the gas streamers appearing between the adsorbent grains as the plasma took place.

6.2 Methods of analysis and experimental schedules

The process consisted in the two stages in which the NO_x adsorbed on the adsorbent material (1st stage) and a pure nitrogen gas was flushed into the plasma reactor promoting the NO_x desorption and reduction (2nd stage).

The methods for the calculation of the amount of NO_x adsorbed were described in Section 4.3; however, in cyclic tests the adsorbent was not exposed to the gas up to the saturation, but the adsorption was interrupted before this condition. In this case, it is not possible to define the adsorption capacity in the saturation condition; however, it is possible to calculate the amount of adsorbate trapped on the sorbent surface up to that time. This amount, divided per the grams of adsorbent was calculated as in the Equation (Eq. *4-1)*, up to a time lower than the saturation time. In order to distinguish the adsorption capacity and the amount adsorbed up to a specific condition, the latter will be expressed as ω_t, where t represents the duration of the adsorption in minutes.

Similar considerations could be made for the calculation of the desorption capacities. Starting from the Equation (Eq. *4-1)*, it is possible to consider the amount of NO_x desorbed proportional to the flow rate and to the area below the desorption curve. Hence, the amounts of NO_x desorbed per grams of adsorbent was calculated as:

$$\sigma(t) = \frac{u}{L_T \rho_b} \sum_{i=1}^{n-1} \left(\frac{c_{NO_x,i} + c_{NO_x,i+1}}{2} \right) \Delta t_i \qquad \textit{(Eq. 6-1)}$$

The first member of the equation remains the same of the adsorption capacity, while the member in the summation is complementary to the initial concentration of NO_x.

Proof of the concept of the NO_x adsorption and NTP Desorption-Reduction process was demonstrated by performing cyclic tests of adsorption and NTP desorption-reduction. The cyclic tests consisted in the adsorption of NO_x, from a modelled flue gas, followed by the desorption in N_2. The desorption occurred either in the presence and in the absence of the plasma as the external electric field was applied or not. Before the cycles, long preliminary adsorption was performed to achieve a partial saturation of the adsorbent, as it was demonstrated that the adsorption was not effective on the NO adsorbed. Hence, two different targets were considered: NO_2 breakpoint and NO_2 emission in the range of 5-10%. Although a feeding consisted of NO in O_2 and N_2, part of the NO was oxidized to NO_2 and the concentrations rose with the time as the adsorption occurred. For each adsorbent sample, the following tests were performed:

α. adsorption up to the NO_2 breakpoint (≈1ppm);
β. seven cycles of adsorption-desorption;
γ. adsorption up to the NO_2 concentration in the range of 5-10%;
δ. seven cycles of adsorption-desorption.

The tests were performed on GAC-Cu. Two different granulometry were considered: 0.3-0.6mm and 1.5-3mm. The former would be as similar as possible to the size of the adsorbent tested during the adsorption experimental campaign, as in Table 4.3; the latter is the average size of the GAC-Cu commercialized.
The adsorption and desorption tests were performed according to Table 6.1 and they were the same for the two granulometries.

test	cycles	Adsorption		Desorption	
		Feed	duration	Feed	duration
α	-	250ppm NO 10% O_2 Balanced N_2		-	-
β	0	250ppm NO 10% O_2 Balanced N_2	20 min	N_2	20 min
	1-6	250ppm NO 10% O_2 Balanced N_2	20 min	N_2 with plasma 18kV at 1kHz	20 min
γ	-	250ppm NO 10% O_2 Balanced N_2			
δ	0	250ppm NO 10% O_2 Balanced N_2	20 min	N_2	20 min
	1-6	250ppm NO 10% O_2 Balanced N_2	20 min	N_2 with plasma 18kV at 1kHz	20 min

Table 6.1 - Experimental schedule for the adsorption and desorption tests on GAC-Cu

The cyclic tests expressed with β and δ in Table 6.1 will be discussed in details in the results of this thesis. Each test will be described with the notation "i.j" where i represents the set of experiments, j represents the number of the cycle.

The cycle called 0 was representative of the adsorption and the desorption that occurred in nitrogen without applying an external electric field and hence in the absence of the plasma. In the cycles 1-6, the desorption occurred at 18kV and 1kHz applied to the high voltage electrode. The nitrogen flushed into the reactor carrying out the NO_x desorbed. Either the adsorption and the desorption occurred by fixing the gas velocity at 0.1m/s corresponding to the gas flow rate of about 1.4L/min.
The amount of NO_x adsorbed and desorbed was calculated according to Equations (Eq. *4-1)* and (Eq. *6-1)*, respectively.

6.3 Results of the NO_x adsorption and NTP desorption-reduction

The experimental results for the NO_x adsorption and NTP desorption and reduction will be presented are presented in this section and they are summarized in two groups:

- Cyclic tests on GAC-Cu d_p=0.3-0.6mm;
- Cyclic tests on GAC-Cu d_p=1.7-3.35mm;

The tests performed were similar for the two size of carbons and they will consist of the adsorption of NO up to the NO_2 breakpoint condition. Then, the sorbent was treated in cyclic tests of adsorption and regeneration having the duration of 20 minutes each.

The first cyclic tests were performed as soon as the NO_2 achieved the breakpoint condition. Then the adsorption was prolonged until the emission of NO_2 was about 6-8% of inlet NO_x concentration. These two sets of tests allowed to calculate the amount of NO_x adsorbed in each cycle and hence on the effectiveness of the regeneration stage.

6.3.1 Cyclic tests on GAC-Cu, d_p=0.3-0.6mm

The adsorption of NO_x was performed on 7.5g of GAC-Cu (d_p=0.3-0.6) corresponding to 5cm length of packed bed reactor, as in Figure 6.2. The breakthrough curve for the adsorption of 250ppm of NO in 10% O_2, balanced in N_2, is shown in Figure 6.3.

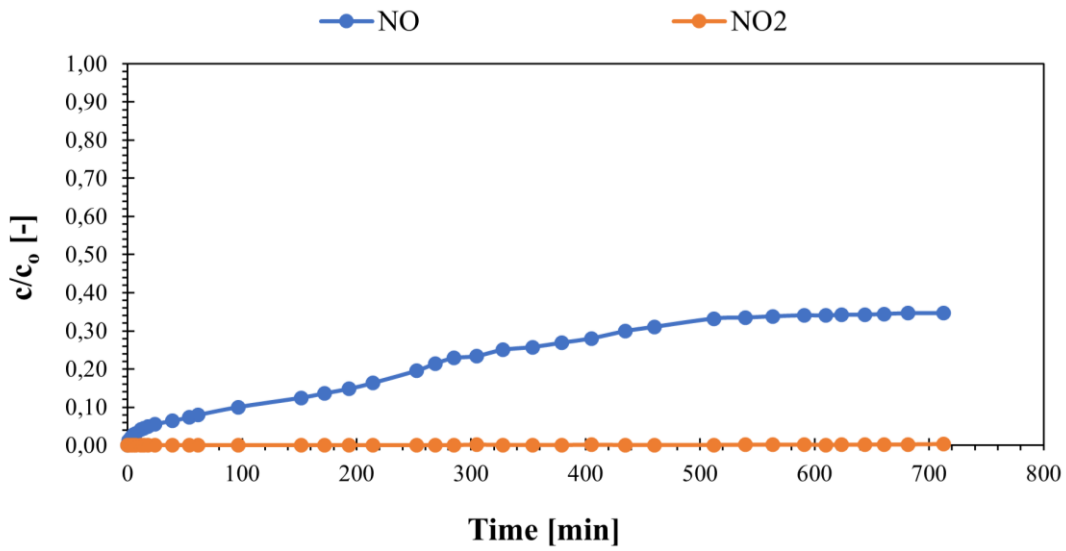

Figure 6.3 - NO and NO_2 breakthrough curves up to the NO_2 breakpoint, for the adsorption of 250ppm of NO in 10% O_2, balanced in N_2, on GAC-Cu (d_p=0.3-0.6mm).

The NO breakthrough curve is similar to those obtained in the adsorption campaign whose results was shown in Section 4.4. The NO concentration quickly rose as the adsorption started, then it slightly increases with the time. Meanwhile the adsorption occurred, the oxidation of NO to NO_2 took place and hence the NO_2 adsorption, as it was discussed for the adsorption campaign results.
When the NO_2 achieved the concentration of 1ppm, the adsorption was stopped, and the adsorbent was exposed to cyclic tests as in Table 6.1. The adsorption i.0 duration was of 20 minutes and it occurred soon after the adsorption in Figure 6.3. The adsorption 0 is shown in Figure 6.4.

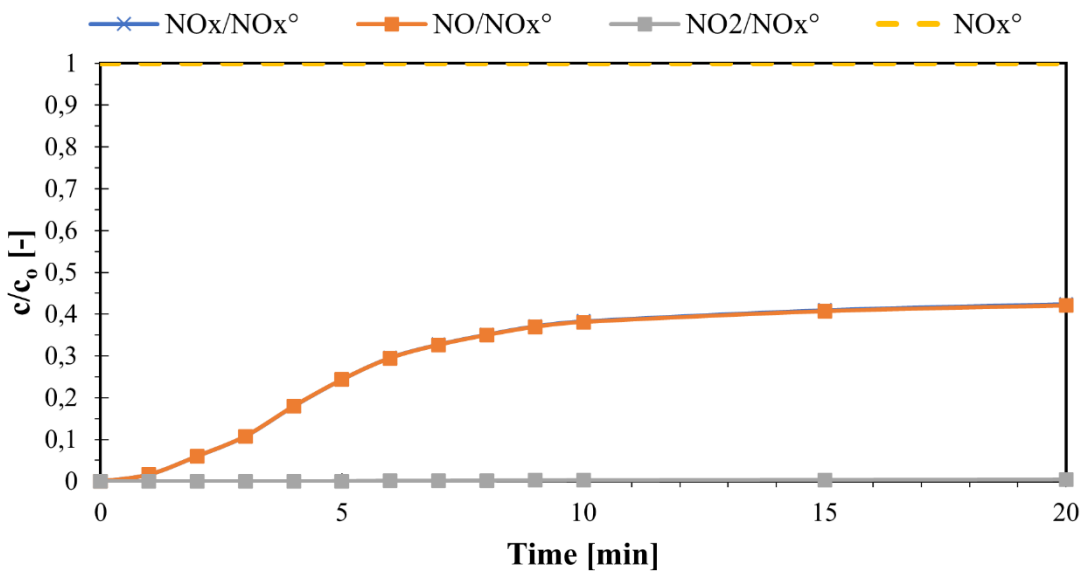

Figure 6.4 – NO, NO_2 and NO_x breakthrough curves for the adsorption i.0 on GAC-Cu (d_p=0.3-0.6mm).

Since the sorbent sites were partially occupied by NO_x, the NO at the reactor exit achieved the highest concentration as in Figure 6.3, in 20 minutes. This breakthrough curve represents the reference for the cyclic tests. It was demonstrated in the adsorption experimental campaign that the NO_2 gives the highest contribution to the adsorption capacity. The breakpoint condition for NO_2 represents the beginning of the sigmoidal NO_2 curve, as in Figure 4.20. In Figure 4.20, NO achieved the stationary condition at the value of about 180ppm that corresponds to about 72% of the feed. In the case of the adsorption i.0 (Figure 6.4), the stationary condition was achieved for a smaller percentage. The difference of the two NO steady-state values, and hence of the NO_2 steady-state values, is mainly correlated to the two different design of the reactors (Figure 4.6 and Figure 6.2), the sorbent size and the reactor length. The reactor for the cyclic tests has the high voltage electrode along the axis and hence the wall effect is higher, influencing negatively the fluid distribution in the sorbent bed. However, the higher range of the sorbent size and the higher reactor length, encourage the flux

distribution in the packed bed and increase the gas residence time, respectively. The latter aspects increase the time of contact between the gas molecules and the solid surface, hence increasing the probability of NO oxidation of functionalized active sites.

The desorption i.0 followed the adsorption i.0 and the detected emissions at the reactor exit are shown in Figure 6.5.

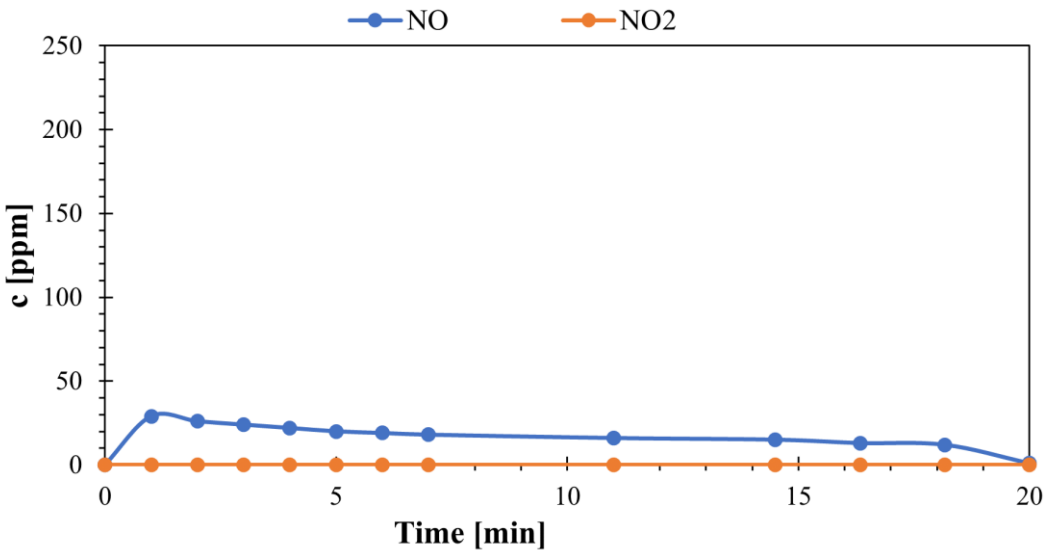

Figure 6.5 - NO and NO_2 emissions for the desorption i.0 on GAC-Cu (dp=0.3-0.6mm).

The desorption i.0 occurred using N_2 as carrier gas, in absence of any electric field, as it was described in Table 6.1. The desorption curves, shown in Figure 6.5, has a peak for the NO emission that occurred in the first minutes (40ppm), then it slowly decreased up to 16ppm after 20min. The NO_2 emission, instead, was always zero. From Figure 6.4 and Figure 6.5, it is possible to calculate the amount of the NO_x adsorbed and the amount desorbed during the adsorption and desorption stages, respectively.

The amount of NO_x adsorbed during adsorption i.0 and the amount of NO_x desorbed during desorption i.0 were calculated according to Equation (Eq. *4-1)* and (Eq. *6-1)*, and they were 26.7 µmol/g and 3.9 µmol/g , respectively. The difference between the amount adsorbed and the amount desorbed means that NO_x was still partially adsorbed on the sorbent surface.

After the desorption i.0, the adsorption i.1 was performed, in accordance with Table 6.1. The breakthrough curves for adsorption i.0 and i.1 were compared and they are shown in Figure 6.6

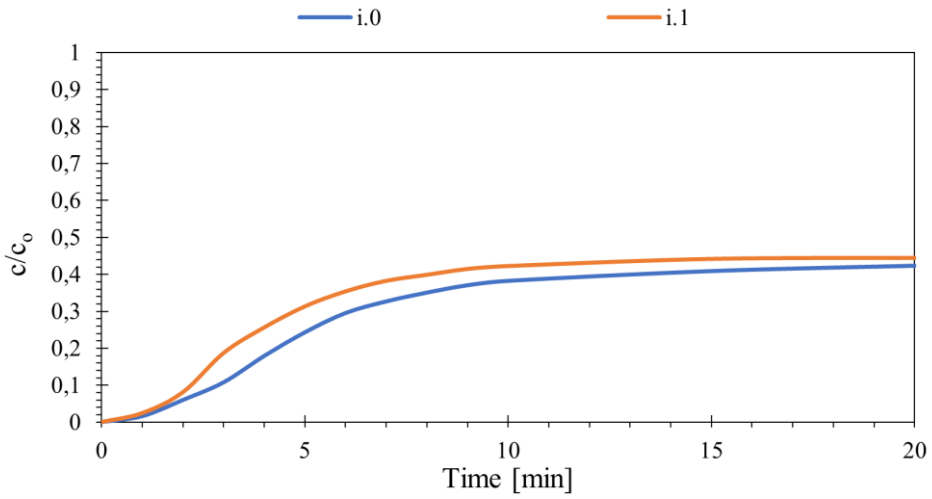

Figure 6.6 - NO_x breakthrough curves for the adsorption i.0 and i.1 on GAC-Cu (d_p=0.3-0.6mm).

The shape of the breakthrough curve in adsorption i.1 is similar to that in adsorption i.0, but the curve was always above the previous. This result confirms what said before: the desorption in N_2 at room temperature was not 100% effectiveness and the adsorption worsened from adsorption i.0 to that i.1. This result was deductible both from the highest emissions in the i.1 adsorption (Figure 6.6) and from the adsorbed amount that decreased from 26.7 to 24.6µmol/g

From the cycle i.1, the desorption occurred by applying a high voltage electric field, in accordance with Table 6.1. The concentrations of NO and NO_2 were monitored out of the reactor during the desorption plasma assisted and the curves are shown in Figure 6.7.

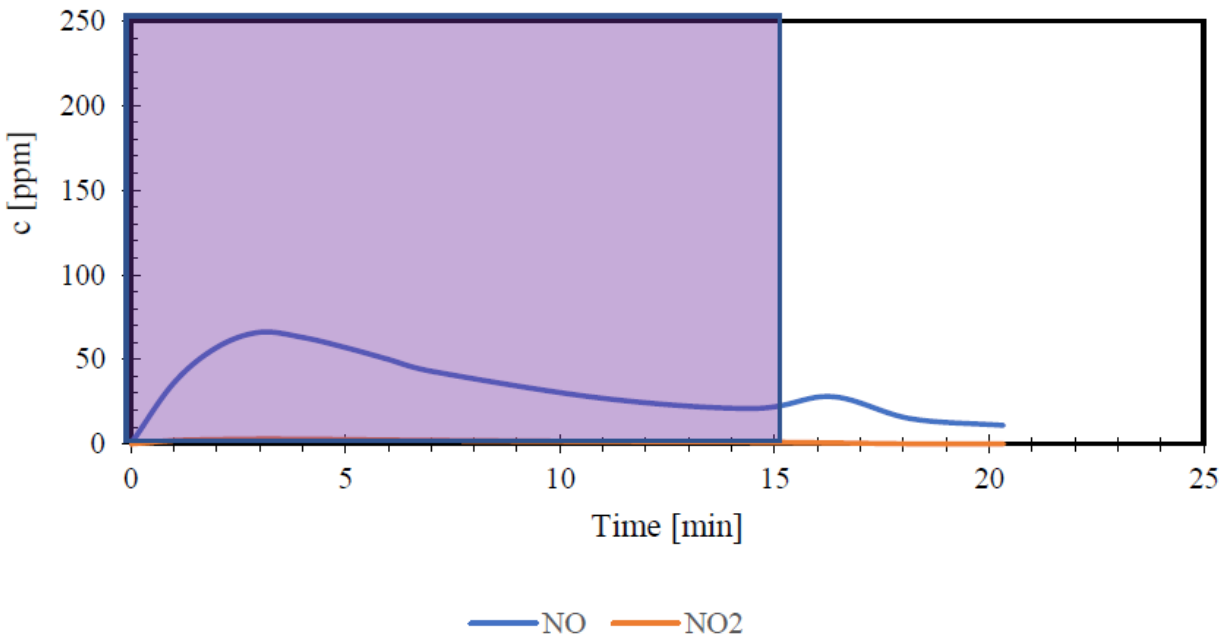

Figure 6.7 - NO and NO_2 emissions for the desorption i.1 on GAC-Cu (dp=0.3-0.6mm); 32kV at 1kHz was applied for the first 15min.

In desorption i.2, non-thermal plasma was generated with a voltage of 32 kV and a frequency of 1 kHz for 15 minutes (violet area); in the last the plasma was switched off and only N_2 continued to flush, to blown away traces of the radicals produced during the plasma application from the sorbent and to stabilize the inside reactor temperature at the operative conditions required to carry the subsequent adsorption test of the cycle. During the desorption plasma assisted, the emission of NO_2 was almost constant, always. The NO concentration rose up to almost 80ppm, then it dropped to 30ppm in the last phase of the desorption with plasma. The second peak during the N_2 flushing was due to the NO_x desorbed during the plasma effect. Again, the amount of NO_x desorbed (5.5µmol/g) was lower than the amount adsorbed during the last adsorption (i.1); this suggests that the i.1 desorption was not 100% effective for sorbent regeneration. The proof of this could be made from the comparison between the previous and the following adsorption.

The breakthrough curves for the first three adsorptions are shown in Figure 6.8.

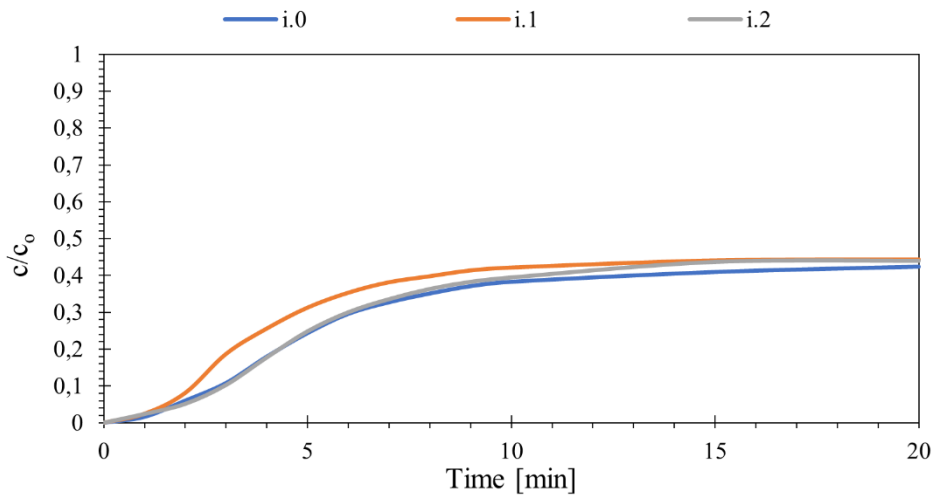

Figure 6.8 - NO_x breakthrough curves for the adsorption i.0-2 on GAC-Cu (dp=0.3-0.6mm).

Moving from adsorption i.1 to i.2, the NO_x emission was always lower; hence, the adsorption improved. The amount adsorbed increased from 24.6µmol/g to 26.4µmol/g. This result was unpredicted as from a mass balance on the amount adsorbed in cycle 1 and the amount desorbed from the same cycle, there should be an accumulation of NO_x on the sorbent surface. The increased amount of NO adsorbed in cycle 2 means that more active sites were available as the effect of the plasma. This effect could be attributed to the plasma reduction of desorbed NO_x. In Section 5.1, it was demonstrated that the NO_x, diluted in N_2, could be reduced with an efficiency close to 100% as the electric field produced was high enough. In the packed bed, the NO_x desorbed moved from the solid surface to the gas bulk, made of N_2 gas discharge species. Hence the molecules of NO_x desorbed might convert as the high intensity of the electric field inter and intra-particles. The NO_x reduction cannot be observed experimentally as it occurred in the corresponding and/or downstream the packed bed. Hence, the amount of NO_x detected at the exit of the reactor could represent a fraction of the effective amount of NO_x desorbed. Being the curve i.2 always lower than i.1 in Figure 6.8, the amount of NO_x desorbed in cycle 1 should be higher than the amount adsorbed in same cycle. In fact, if the amount adsorbed and desorbed were equivalent, the curves of the consecutive adsorption should coincide and the amount adsorbed in the two cycles should be the same. In the next cycle, the adsorption curve further decreased, and then it remained almost equivalent in the following cycles. The breakthrough curves for the cycles i.1-6 are shown in Figure 6.9.

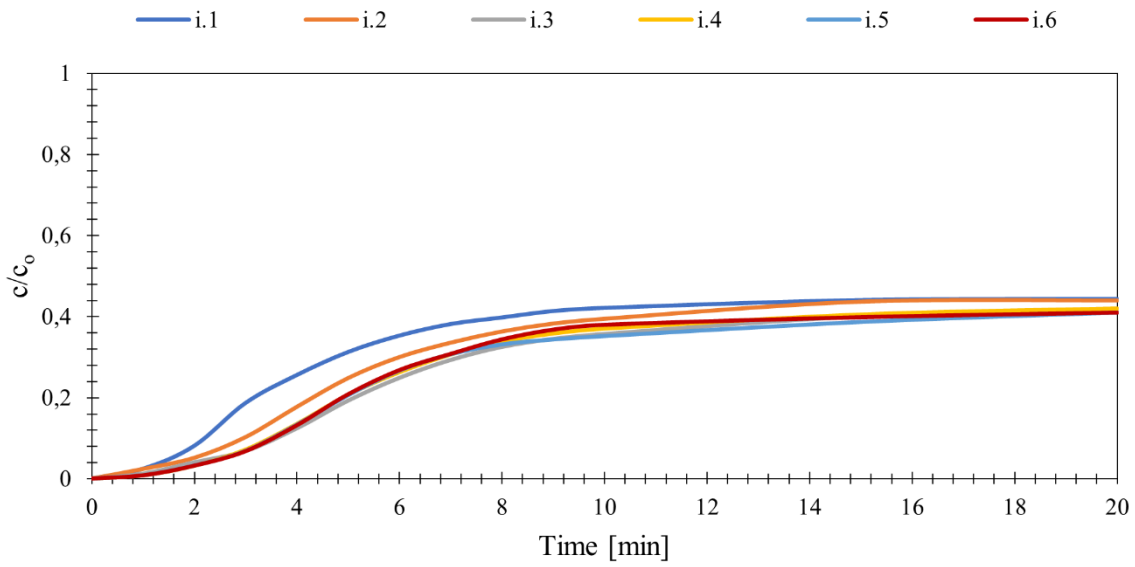

Figure 6.9 - NO_x breakthrough curves for the adsorption i.1-6 on GAC-Cu (dp=0.3-0.6mm).

From Figure 6.9, it is possible to notice that the curves were very similar for the cycles i.3-6. This means that the plasma-assisted desorption was effective and the adsorbent was regenerated enough to guarantee a constant emission. The NO_2 curves were not reported as they were always lower than 1% of the NO inlet concentration. Even the desorption curves were very similar for the cycles i.1-6; hence they were not reported here. Moreover, they will not give any added value as they are not representative of the amount of NO_x desorbed, for the reasons described before.

The amount of NO_x adsorbed and desorbed, in each cycle, are reported in Table 6.2.

Cycle	$\omega_{20}^{NO_x}$ [µmol/g]	$\sigma_{20}^{NO_x}$ [µmol/g]
i.0	26.7	3.9
i.1	24.6	5.5
i.2	26.4	4.7
i.3	27.2	4.7
i.4	27.2	5.2
i.5	27.1	5.1
i.6	27.1	-

Table 6.2 - Amount of NO_x adsorbed and desorbed for the cycles i.0-6 on GAC-Cu (dp=0.3-0.6mm).

From Table 6.2, it is possible to notice that the amount of NO_x desorbed in the cycle i.0 was about 7 times lower than the amount of NO_x previously adsorbed (in the same cycle). This means that part of the NO_x was still adsorbed, and the desorption was not really effectiveness. As a proof of that, the following adsorption (i.1) showed a lower amount of NO_x adsorbed in the same 20 minutes, as it was predictable from Figure 6.6, where NO_x concentration was always higher for the adsorption i.1 than that of i.0. Although the following desorption i.1-i.5 were still greatly lower than the amount of NO_x adsorbed (of 5-6 times), the specific amount adsorbed in the cycle i.2 was higher than the previous as well as i.3, then it remained almost constant at the value of 27μmol/g. This result cannot be explained from a mass balance as there seems to not be an accumulation of NO_x on the adsorbent. In fact, a further accumulation of adsorbed NO_x cycle after cycle should reduce the driving force and hence the outlet concentration of NO_x should increase with the cycle. On the contrary, the concentration decreased with the cycles and then remained almost constant from the adsorption i.3, as it was shown in Figure 6.9. This result was explained by the NO_x reduction that occurred simultaneously with the desorption as was discussed before; hence, the amount of NO_x adsorbed in each cycle was almost constant for the cycles i.3-i.6.

A second set of experiments were performed as the NO_2 concentration achieved the value of about 6% of the total NO_x inlet concentration, as it was discussed in Section 6.2.
The breakthrough curves for adsorption ii.0 and ii.1 are shown in Figure 6.10.

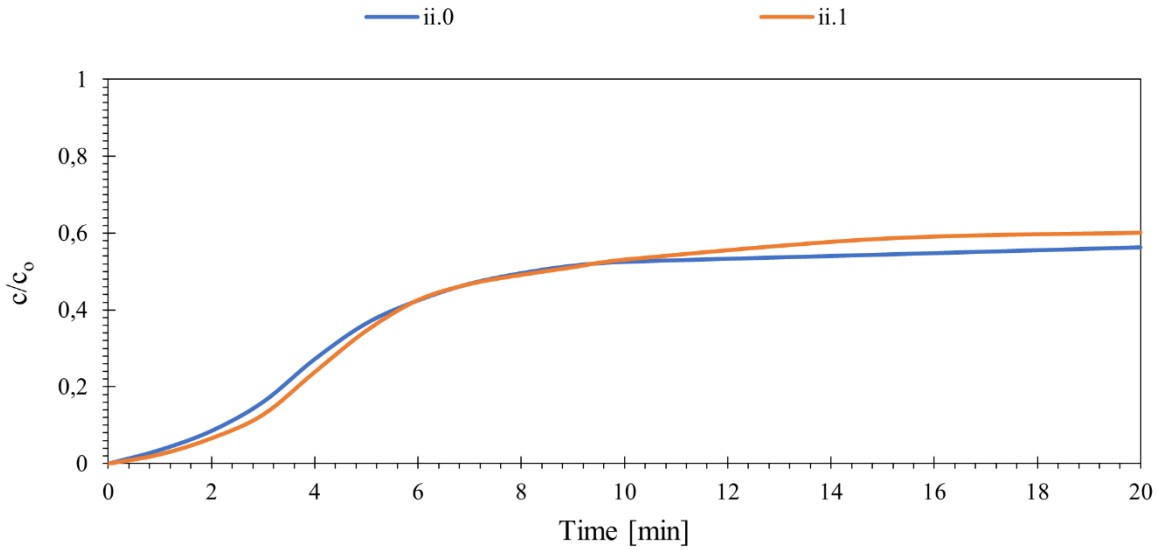

Figure 6.10 - NO_x breakthrough curves for the adsorption ii.0 and ii.1 on GAC-Cu (d_p=0.3-0.6mm).

The shape of the breakthrough curve in adsorption ii.1 is very similar to that in adsorption ii.0; The NO_x concentration in the adsorption ii.1 becomes slightly higher in the last 10 minutes, compared to ii.0. However, the difference in the NO_x concentration between the two adsorption is smaller than in the previous set of experiments (Figure 6.6). From the cycle ii.1, the desorption occurred by applying a high voltage electric field, and the regeneration occurred with a higher efficiency, as it was found before. A comparison between the first three adsorption breakthrough curves was made and the results are shown in Figure 6.11.

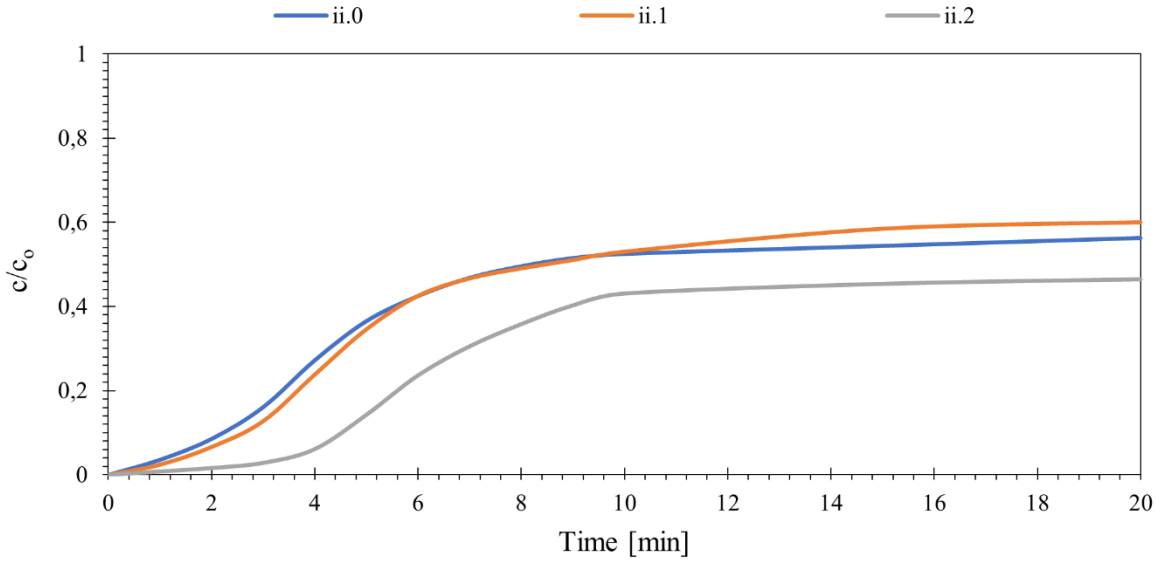

Figure 6.11 - NO_x breakthrough curves for the adsorption ii.0-2 on GAC-Cu (dp=0.3-0.6mm).

Moving from adsorption ii.1 to ii.2, the NO_x emission was significantly lower; hence, the adsorption improved. The improvement was greatly higher than those observed in the first set of experiments (Figure 6.8). The NO_x concentration was also lower than that in adsorption ii.0. This means that a huge amount of NO_x was desorbed, and it was greatly higher than the amount of NO_x adsorbed in the previous adsorption cycle.

In the next cycle, the adsorption curves did not decrease as in the previous set of experiments. The breakthrough curves for the cycles ii.1-6 are shown in Figure 6.12.

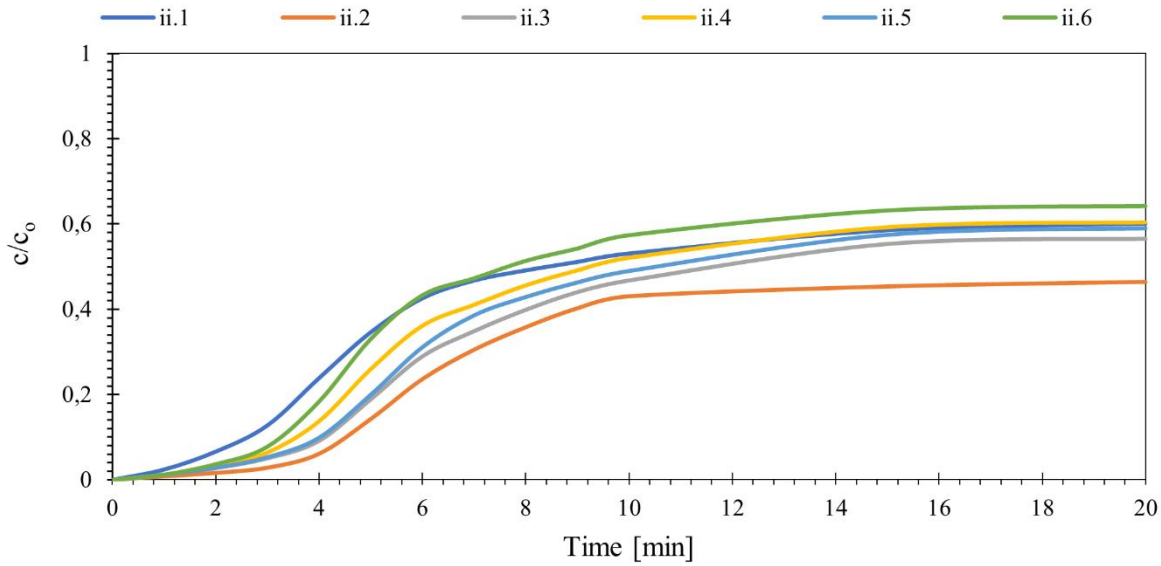

Figure 6.12 - NO_x breakthrough curves for the adsorption ii.1-6 on GAC-Cu (dp=0.3-0.6mm).

From Figure 6.12, it is possible to notice that the curves were very similar for the cycles ii.3-6; however, the NO_x emission was higher than the adsorption in cycle ii.2. This means that moving from cycle ii.2 to ii.3, the adsorption worsened. Hence, the desorption ii.2 was not so effective as in desorption i.2. The highest percentage of the adsorption capacity was attributed to the NO_2 adsorption as it was demonstrated in the previous experimental campaign (Chapter 4). To further investigated this phenomenon, the trend of the NO_2 breakthrough curves are shown in Figure 6.13.

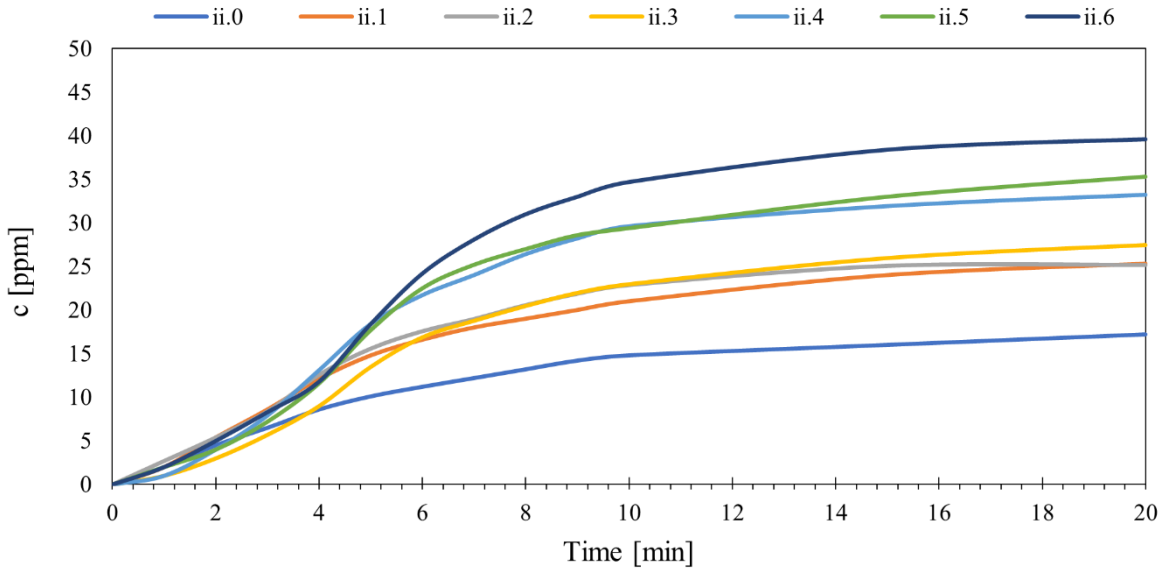

Figure 6.13 – NO_2 breakthrough curves for the adsorption ii.0-6 on GAC-Cu (dp=0.3-0.6mm).

Although there are some fluctuations in the NO_2 concentration profile in the different cycles, it is possible to note an overall increasing trend in the NO_2 concentration with the cycles. The breakthrough curve in adsorption ii.6 is always above the other curves, and the NO_2 concentration was greatly higher of those in adsorption ii.0 and ii.1, e.g. It is possible to suppose that, although the desorption with plasma is effective, it is not strong enough to release completely the amount of NO_x adsorbed in the previous adsorption. The increasing in NO_2 concentration should lead to a slower saturation of the sorbent cycle after cycle. In conformity with the previous set of experiments, the amount of NO_x adsorbed and desorbed in each cycle are reported in Table 6.3; furthermore, they are also reported the peaks of the NO_2 concentrations achieved after 20 minutes of adsorption, for each cycle.

Cycle	$\omega_{20}^{NO_x}$ [µmol/g]	$[NO_2]_{max}$	$\sigma_{20}^{NO_x}$ [µmol/g]
ii.0	21.2	17	4.2
ii.1	21.4	25	6
ii.2	23.1	25	5.7
ii.3	22.2	28	5.9
ii.4	21.7	33	6.1
ii.5	21.9	35	5.8
ii.6	21.3	40	-

Table 6.3 - Amount of NO_x adsorbed and desorbed for the cycles ii.0-6 on GAC-Cu, and the peaks of the NO_2 achieved in the adsorptions (dp=0.3-0.6mm).

Even from the amount of NO_x adsorbed it is possible to note the reduction of the calculated value cycle after cycle. The only improvement was observed from the adsorption ii.1 to the adsorption ii.2 as the effect of the plasma for the first time. Then, the specific amount of NO_x adsorbed decreased from 23.1 to 21.3µmol/g in the last 4 cycles.

6.3.2 Cyclic tests on GAC-Cu, d_p=1.5-3mm

The experiments performed in Section 6.3.2 were replicated here by using a GAC-Cu for the commercialized size of 1.5-3mm. Although the bigger size would reduce the mass transfer, the sorbent has two main advantage: it was not modified during crushing required to achieve the desired size range, and the wide size distribution of the sorbent grains should enhance the plasma discharges.

The breakthrough curves were analysed to make a comparison with the previous cyclic tests. Once the NO_2 achieved the concentration of 1ppm, the adsorption was stopped, and the adsorbent was exposed to cyclic tests as it was summarized in Table 6.1.

The NO_x breakthrough curves for the adsorptions iii.0-2 are shown in Figure 6.14.

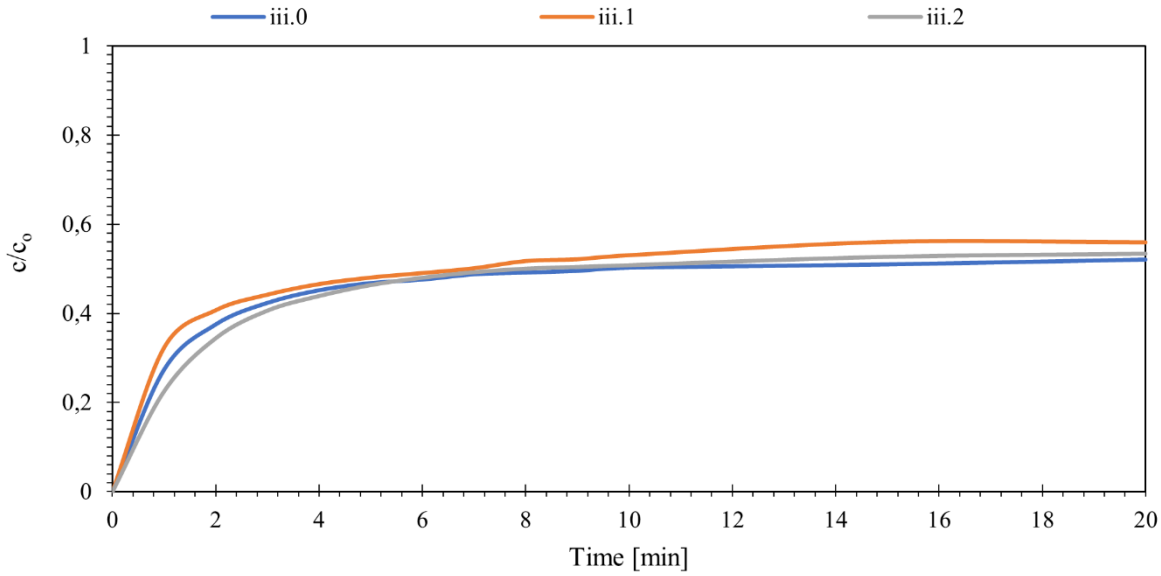

Figure 6.14 - NO_x breakthrough curves for the adsorption iii.0-2 on GAC-Cu (dp=1.5-3mm).

The NO_x breakthrough curves for the first three adsorption were very similar. From the comparison with the breakthrough curves obtained with the 0.3-0.6mm GAC-Cu, the curves in Figure 6.14 have a higher slope in the first minutes, indicating a weak mass transfer and a high bypass of the gas in the packed bed, as it was discussed in the adsorption experimental campaign (Chapter 4). For this reason, the considerations could be made in the set of tests iii are weak and with low interest.

In any case, the experimental adsorption curves for the cycles iii.1-6 were detected, and they are shown in Figure 6.15

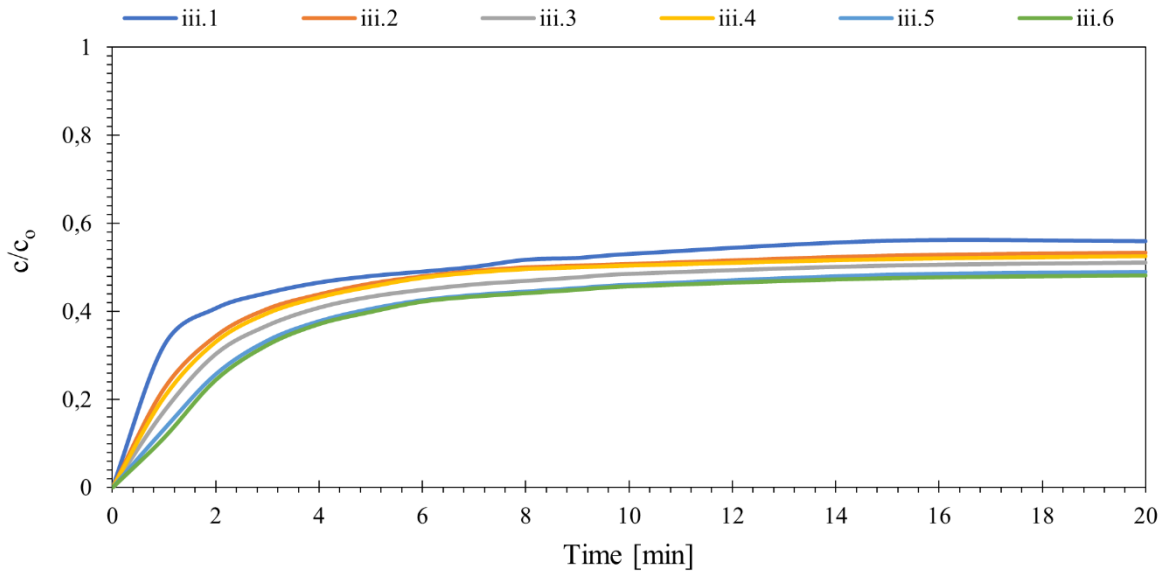

Figure 6.15 - NO_x breakthrough curves for the adsorption iii.1-6 on GAC-Cu (dp=1.5-3mm).

The breakthrough curves for the adsorptions in the cycles 1-6 were almost overlapped and indicating that the amount of NO_x adsorbed in the previous adsorption was desorbed by the following desorption. However, we believe that this condition would not be representative for the cyclic tests as the fluid dynamics did not allow to make a good analysis of the adsorption process.

The amount of NO_x adsorbed and desorbed in each cycle were calculated, and the values are reported in Table 6.4.

Cycle	$\omega_{20}^{NO_x}$ [µmol/g]	$\sigma_{20}^{NO_x}$ [µmol/g]
iii.0	19.8	3.1
iii.1	19.5	4.2
iii.2	20.0	4.1
iii.3	20.4	3.7
iii.4	20.1	4.1
iii.5	20.7	4.0
iii.6	20.8	-

Table 6.4 - Amount of NO_x adsorbed and desorbed for the cycles iii.0-6 on GAC-Cu (dp=1.5-3mm).

In the case of the granular size of 1.5-3mm, the specific amount of NO_x adsorbed cycle after cycle slightly increased as the plasma-assisted desorption occurred. Although the amount of NO_x adsorbed

in one cycle was lower than the similar adsorption tests using granular sizes of 0.3-0.6mm, the improvement of more than 1μmol/g was observed from cycle 1 to cycle 6.
The lower amount of NO_x adsorbed in the cycles iii.1-6 than the cycles i.1-6, was due to the higher amount of gas that bypass the adsorbent grains as the low ratio between the reactor diameter and the granular size.

A second set of experiments were performed as the NO_2 concentration achieved the value of about 8% of the total NO_x inlet concentration, as it was discussed in Section 6.2.
The breakthrough curves for adsorption iv.0-2 are shown in Figure 6.16.

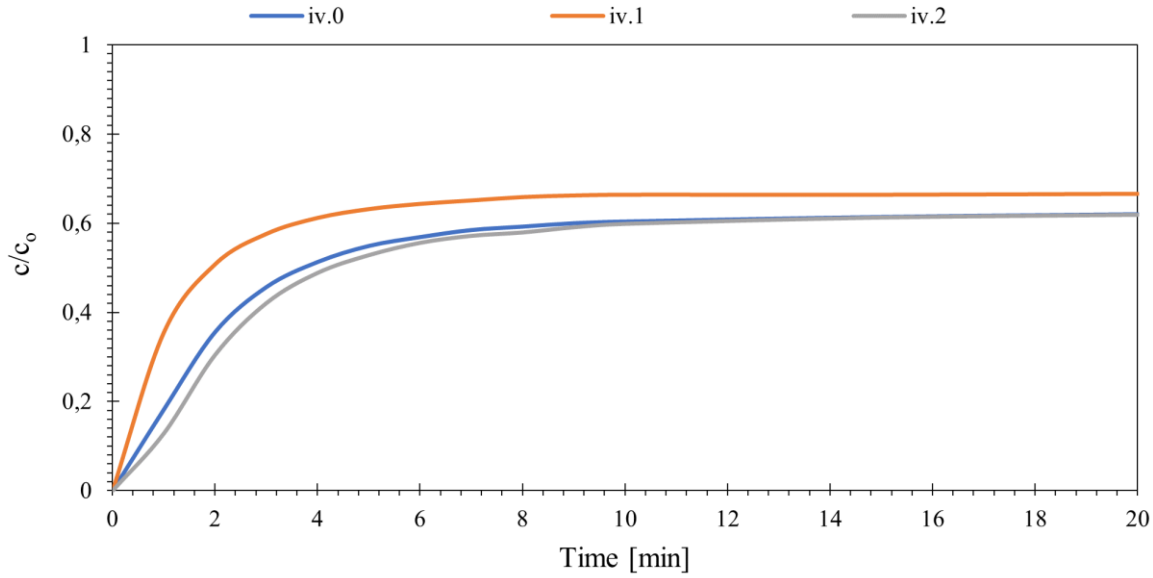

Figure 6.16 - NO_x breakthrough curves for the adsorption iv.0-2 on GAC-Cu (d_p=1.5-3mm).

The NO_x breakthrough in the cycle iv.1 was significantly higher than that in the previous cycle. This means that the desorption with N_2 was not effective and the following adsorption showed a higher emission. On the contrary, a relevant drop of the NO_x breakthrough curve was observed in the adsorption iv.2. NO_x emission in the adsorption iv.2 was also lower than that in the adsorption iv.0. This means that the plasma-assisted desorption had a great effectiveness to the NO_x desorption at this stage. The breakthrough curves in the next adsorption cycles are shown in Figure 6.17.

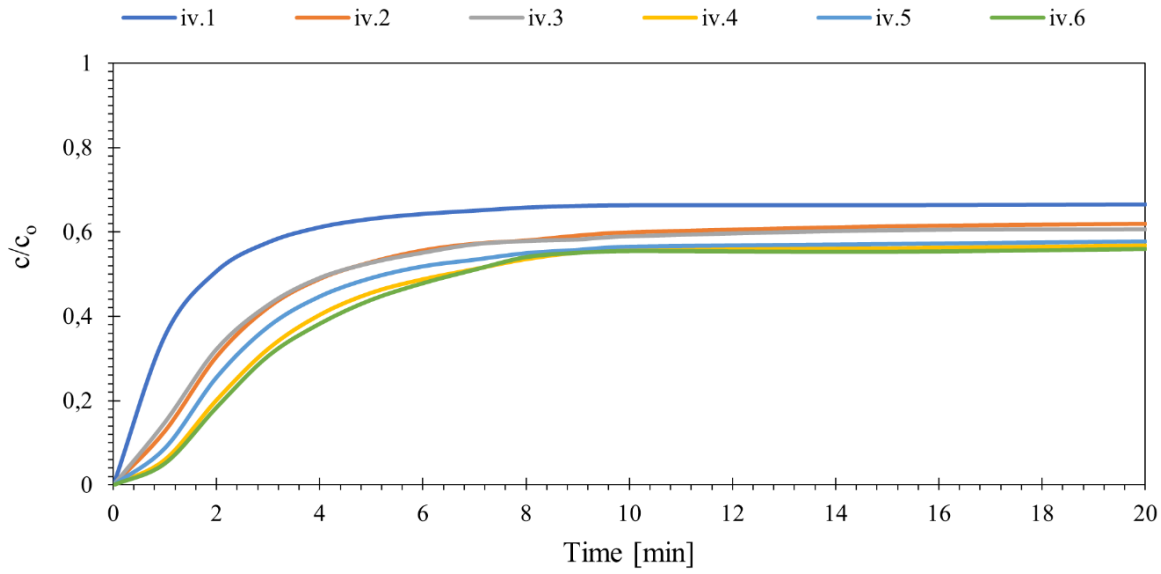

Figure 6.17 - NO_x breakthrough curves for the adsorption iv.1-6 on GAC-Cu (dp=1.5-3mm).

The NO_x breakthrough curves had a similar shape and their values were very similar in each cycle. A relatively big step can be observed between the 3rd and the 4th cycle; however, the breakthrough curves can be considered almost equivalent. Even if they were almost constant, we can observe that the curves slightly dropped cycle after cycle, with the only exception of cycle 5, that was then overtook by the breakthrough in the cycle 6, which was the lowest of all. In addition to the NO_x breakthrough curves, it could be interesting to look at the NO_2 breakthrough curves that are shown in Figure 6.18.

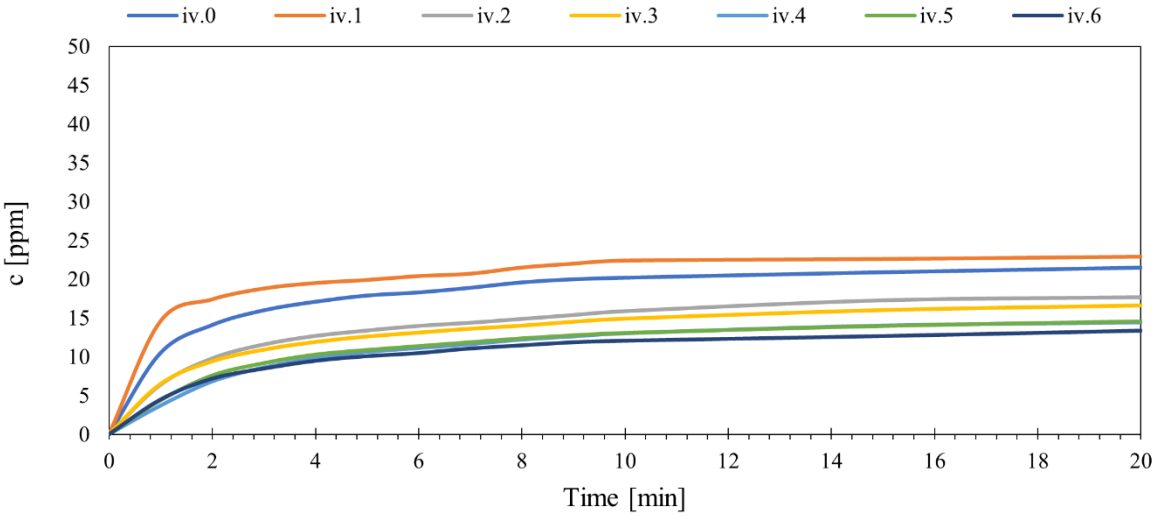

Figure 6.18 – NO_2 breakthrough curves for the adsorption iv.0-6 on GAC-Cu (dp=1.5-3mm).

From Figure 6.18, it is possible to notice that the NO_2 concentration constantly dropped cycle after cycle, with the only exception of cycle 1 that followed the desorption in the absence of the plasma. This trend makes evident the importance of the plasma in Nitrogen desorption at room temperature

and it highlights the effectiveness of the plasma-assisted desorption. Both the NO_x and the NO_2 emissions decreased with the cycles, with the only exception of cycle 5, where the NO_x and NO_2 concentration slightly increased.

In addition to the breakthrough curves, the amount of NO_x adsorbed and desorbed, in each cycle, were calculated and they are reported in Table 6.5; furthermore, they are also reported the peaks of the NO_2 concentrations achieved after 20 minutes of adsorption, for each cycle.

Cycle	$\omega_{20}^{NO_x}$ [µmol/g]	$[NO_2]_{max}$	$\sigma_{20}^{NO_x}$ [µmol/g]
iv.0	19.6	22	3.7
iv.1	18.5	23	4.7
iv.2	19.8	18	4.6
iv.3	19.8	17	5.0
iv.4	20.5	14	4.6
iv.5	20.1	15	4.9
iv.6	20.6	13	-

Table 6.5 - Amount of NO_x adsorbed and desorbed for the cycles iv.0-6 on GAC-Cu, and the peaks of the NO_2 achieved in the adsorptions (dp=1.5-3mm).

The amount of NO_x adsorbed increased from cycle iv.1 to cycle iv.6. This means that even after the NO_2 breakpoint, the desorption was effective and the sorbent capacity to adsorb NO_x was restored. It is important to note that although the adsorbent exceeded the NO_2 breakpoint, the amount of NO_x adsorbed in one cycle (e.g. iv.6) was similar to the amount adsorbed in one cycle before the NO_2 breakpoint (e.g. iii.5). This result demonstrated that although the effectiveness of the process decreased as the adsorbent of a commercial size was used (lower amount of NO_x adsorbed per cycle), due to the worst distribution of the gas in the packed bed, the amount of NO_x adsorbed cycle after cycles was maintained almost constant.

We believe that the decreasing of the NO_2 concentration cycle after cycle, shown in Figure 6.18 and reported in Table 6.5 is directly correlated to the capability of the system to restore the adsorption capacity. It must be taken in mind that the cycles iv.1-6, was preceded by a long adsorption test until the concentration of NO_2 rose up to 22ppm. Hence, there was still a higher amount of NO_x already adsorbed before cycles and we suppose that those molecules could be partially and slowly desorbed if further cycles

7. CONCLUSIONS

The NO_x adsorption and NTP desorption-reduction process has been proposed as an alternative technology to retrofit existing plants where SCR units cannot be adopted. The granular activated carbon impregnated with copper (GAC-Cu) was selected as the high performance in NO_x adsorption and the positive role the copper could play even during the plasma-assisted sorbent regeneration. The adsorption tests were performed either at 30°C and 120°C in the presence and the absence of oxygen. When the adsorption of NO was performed in N_2, the adsorption isotherms were estimated using the Langmuir model. In the absence of oxygen, a higher adsorption capacity of GAC-Cu was calculated at 120°C at low NO concentration (50ppm), while at 250ppm of NO the adsorption capacities were similar for the two temperatures and it was equal to about 122$\mu mol_{NO}/g$ (3.7mg_{NO}/g). The adsorption capacity increased greatly when O_2 was added to the gas. A peak of 66mg_{NO}/g was obtained as the oxygen content was of 3% at 30°C. The improvement was attributed to the NO oxidation to NO_2 that occurred on specific functional groups of the carbon. Since the carbon capacity to adsorb NO_2 is higher than NO, it plays a positive role in the NO_x adsorption. Further to the functional groups, the copper played a positive role in the NO_x adsorption, as it was demonstrated from a comparison with the non-impregnated carbon.

In the second part of the thesis, the Dielectric Barrier Discharge technology was investigated for NO_x reduction. A preliminary numerical analysis was performed to investigate the electric field distribution in a Dielectric Barrier Discharge (DBD) and two Dielectric Barriers Discharge (DBsD) reactors. Both the configurations were evaluated for a 2.2cm and a 5cm reactors.

Although the resolution of the Gauss' Law and the Faraday's Law coupled to the charge conservation was not accurate enough to simulate the plasma power, the electrostatics study was performed to simulate the electric field norm in the proximity of the gas boundaries where the onset of the plasma takes place. It was demonstrated that, in accordance with the literature, the presence of the dielectric reduces the electric field, hence the configuration with two dielectrics has a lower peak of the electric field that represents the onset of the plasma. On the contrary, the configuration with one dielectric and the threaded rod, has a peak of the electric field greatly higher. Although it is complex to calculate the exact value of the peak, it was observed that the electric field at 2.5mm from the axis (choice conservative) was about $2.75 \div 5 \cdot 10^6$V/m for the reactor of 5cm with one dielectric; while the same reactor having the inner dielectric also, had an electric field of about $2.5 \cdot 10^6$V/m at outer surface of the inner dielectric. For what concern the reactor of 2.2cm, the electric field norm was of

$4.5 \div 8 \cdot 10^6$V/m in the configuration with one dielectric and $4.75 \cdot 10^6$V/m in the configuration with two dielectrics.

In addition to the electrostatic study, the plasma chemistry was coupled in COMSOL Multiphysics. Nitrogen plasma chemistry was integrated and the Boltzmann Equation for the calculation of the electrons drift diffusion were coupled to the electrostatics study. Since the complexity of the problem, the geometry was simplified in 1D axisymmetric. The simplification did not affect greatly the electron density and the electron temperature, while the electric field decreased of almost 50%. The peaks of the electron density ($6.7 \div 7 \cdot 10^{18}$1/m), electron temperature (43÷50eV) and electric field norm ($1.5 \div 3 \cdot 10^6$V/m) were observed in the proximity of the inner electrode, and they are consistent with the literature.

Two different DBD reactors were tested for the NO_x reduction: two dielectric barriers discharge reactor of outer diameter of 2.2cm and a one dielectric barrier discharge reactor of outer diameter of 5cm. The experiments showed that it is possible to reduce NO_x emissions with an efficiency of 99%. NO_x removal efficiency decreased as the NO concentration in the inlet gas and the gas flow rate increased. The removal efficiency increased about 20% when the applied potential increased from 19 to 20kV (38kV and 40kV pk/pk). Likewise, the conversion efficiency increased by 30-40% when the frequency of the applied potential was increased from 500 to 1000 Hz. From the comparison between the two designs, it was demonstrated that the NO_x removal efficiency was always higher for the geometry having one dielectric barrier and the screw thread as a high voltage electrode. In particular, the efficiency of 99% was achieved as the NO molar flow increased up to $2 mmol_{NO}/h$, using the configuration with two dielectric barriers; while the same efficiency was achieved in the dielectric barrier discharge reactor as the NO molar flow was three times higher.

From the cyclic tests that would simulate the continuous process of NO_x adsorption and NTP desorption-reduction. The results highlighted that the NO_x regeneration cannot be easily analysed before the NO_2 breakthrough. Indeed, the NO concentration remained constant for a long time and the breakthrough curves cycle after cycle were overlapped. The NO_x emissions coincided with NO as the NO_2 concentration in the outlet was negligible. Hence, also the NO_x breakthrough curves were similar for the cyclic tests.

When the NO_2 emissions exceeded the breakthrough condition, e.g. NO_2 concentration higher than 6-8% of the NO feed, the NO_x concentration varied cycle after cycle. It was observed that the NO_x concentration slightly increased with the cycles when the sorbent having granular size of .3-0.6mm was used. In particular, the NO_2 emission increased from 6% to 16% after 6 cycles. In the case of the

sorbent having granular size of 1.7÷3.35mm, the NO_x emissions decreased with the cycles. In particular, the NO_2 emissions decreased from 8% to 5% after 6 cycles. The decreasing in the NO_2 and hence NO_x emissions suggests that the amount of nitrogen oxides desorbed during the sorbent regeneration was higher than the amount adsorbed during a cycle.

The proof of the concept demonstrated the effectiveness of the adsorption and NTP sorbent regeneration in a 2.2cm reactor, while an efficiency of about 100% of the NO_x reduction was achieved in a 5cm DBD reactor.

REFERENCES

[1] Environmental Protection Agency (EPA), "Nitrogen oxides (NOx), why and how they are controlled," *Epa-456/F-99-006R*, no. November, p. 48, 1999.

[2] Z. Tan *et al.*, "Exploring ozone pollution in Chengdu, southwestern China: A case study from radical chemistry to O3-VOC-NOx sensitivity," *Sci. Total Environ.*, vol. 636, pp. 775–786, 2018.

[3] V. Grewe *et al.*, "Origin and variability of upper tropospheric nitrogen oxides and ozone at northern mid-latitudes," *Atmos. Environ.*, vol. 35, no. 20, pp. 3421–3433, 2001.

[4] SCOEL/SUM/89, "Recommendation from the Scientific Committee on Occupational Exposure Limits for Nitrogen Monoxide," *Employment, Soc. Aff. Incl. - Eur. Comm.*, 2014.

[5] J. M. Fukuto, J. Y. Cho, and C. H. Switzer, "The Chemical Properties of Nitric Oxide and Related Nitrogen Oxides," *Nitric Oxide*, no. 1996, pp. 23–40, 2000.

[6] Y. B. Zeldovich, P. Y. Sadovnikov, and D. A. Frank-Kamenetskii, "Oxidation of Nitrogen in Combustion," *Acad. Sci. USSR, Inst. Chem. Physics, Moscow-leningr.*, 1947.

[7] O. T. K. Svoboda, 1. Cennak, "NOx CHEMISTRY AND EMISSIONS - I," in *Pollutants from Combustion - Formation and Impact on Atmospheric Chemistry*, 2000, pp. 145–163.

[8] SCOEL/SUM/53, "Recommendation from the Scientific Committee on Occupational Exposure Limits for Nitrogen Dioxide," *Employment, Soc. Aff. Incl. - Eur. Comm.*, 2014.

[9] W. S. Epling, L. E. Campbell, A. Yezerets, N. W. Currier, and J. E. Parks, "Overview of the Fundamental Reactions and Degradation Mechanisms of NOx Storage/Reduction Catalysts," *Catal. Rev. - Sci. Eng.*, vol. 46, no. 2, pp. 163–245, 2004.

[10] H. Tsukahara, T. Ishida, and M. Mayumi, "Gas-phase oxidation of nitric oxide: Chemical kinetics and rate constant," *Nitric Oxide - Biol. Chem.*, vol. 3, no. 3, pp. 191–198, 1999.

[11] L. S. Kassel, "The theory of third-order gas reactions," *J. Phys. Chem.*, vol. 34, no. 8, pp. 1777–1796, 1930.

[12] W. P. L. Carter, “Development of ozone reactivity scales for volatile organic compounds,” *J. Air Waste Manag. Assoc.*, vol. 44, no. 7, pp. 881–899, 1994.

[13] D. J. Jacob, “Heterogeneous chemistry and tropospheric ozone,” *Atmos. Environ.*, vol. 34, no. 12–14, pp. 2131–2159, 2000.

[14] J. M. Roberts, “The atmospheric chemistry of organic nitrates,” *Atmos. Environ. Part A, Gen. Top.*, vol. 24, no. 2, pp. 243–287, 1990.

[15] R. Price, D; Birnbaum, R; Batiuk, R; McCullough, M; Smith, “Nitrogen oxides: Impacts on public health and the environment,” *Environmental Protection Agency, Washington, DC (United States). Office of Air and Radiation*. 1997.

[16] P. De Voogt, *Reviews of Environmental Contamination and Toxicology*, vol. 242. 2017.

[17] Health and Safety Authority (H&SA), “2020 Code of Practice for the Safety, Health and Welfare at Work Regulations,” *Chem. Agents Code Pract. 2020*, 2020.

[18] E. J. Bucsela, K. E. Pickering, D. J. Allen, R. H. Holzworth, and N. A. Krotkov, “Midlatitude Lightning NOx Production Efficiency Inferred From OMI and WWLLN Data,” *J. Geophys. Res. Atmos.*, vol. 124, no. 23, pp. 13475–13497, 2019.

[19] G. C. M. Vinken, K. F. Boersma, J. D. Maasakkers, M. Adon, and R. V. Martin, “Worldwide biogenic soil NOx emissions inferred from OMI NO2 observations,” *Atmos. Chem. Phys.*, vol. 14, no. 18, pp. 10363–10381, 2014.

[20] C. E. Liaskos, D. J. Allen, and K. E. Pickering, “Journal of Geophysical Research : Atmospheres by replay simulations with GEOS-5,” pp. 8512–8534, 2015.

[21] S. J. Hall, P. A. Matson, and P. M. Roth, “NOx emissions from soil: Implications for air quality modeling in agricultural regions,” *Annu. Rev. Energy Environ.*, vol. 21, no. 1, pp. 311–346, 1996.

[22] S. Rasouli, J. K. Whalen, and C. A. Madramootoo, “Review: Reducing residual soil nitrogen losses from agroecosystems for surface water protection in Quebec and Ontario, Canada: Best management practices, policies and perspectives,” *Can. J. Soil Sci.*, vol. 94, no. 2, pp. 109–

127, 2014.

[23] Organization for Economic Co-operation and Development (OECD), “Emissions of Air Pollutants,” *https://stats.oecd.org/Index.aspx?DataSetCode=AIR_EMISSIONS*, 2020. .

[24] S. Saint Akadiri, F. V. Bekun, E. Taheri, and A. C. Akadiri, “Carbon emissions, energy consumption and economic growth: A causality evidence,” *Int. J. Energy Technol. Policy*, vol. 15, no. 2–3, pp. 320–336, 2019.

[25] U. Berardi, “A cross-country comparison of the building energy consumptions and their trends,” *Resour. Conserv. Recycl.*, vol. 123, pp. 230–241, 2017.

[26] I. V. Provornaya, I. V. Filimonova, L. V. Eder, V. Y. Nemov, and E. A. Zemnukhova, “Formation of energy policy in Europe, taking into account trends in the global market,” *Energy Reports*, vol. 6, pp. 599–603, 2020.

[27] W. World Health Organization, “WHO Air quality guidelines for particulate matter, ozone, nitrogen dioxide and sulfur dioxide: Global update 2005,” pp. 1–21, 2005.

[28] European Environmental Agency, *European Environmental Agency. Air quality in Europe — 2019 report*, no. 10. 2019.

[29] E. E. A. (EEA), “National Emission Ceilings Directive emissions data viewer 1990-2018,” *https://www.eea.europa.eu/data-and-maps/dashboards/necd-directive-data-viewer-3*, 1964. .

[30] W. M. Colton, “The outlook for energy: A view to 2030,” *Exxonmob. 2010 Energy Outlook*, pp. 1–9, 2011.

[31] World Energy Council, *Global Transport Scenarios 2050*. 2011.

[32] G. Kalghatgi, “Development of Fuel/Engine Systems—The Way Forward to Sustainable Transport,” *Engineering*, vol. 5, no. 3, pp. 510–518, 2019.

[33] A. Joshi, “Review of Vehicle Engine Efficiency and Emissions,” *SAE Int. J. Adv. Curr. Pract. Mobil.*, 2020.

[34] A. Walker, “Future Challenges and Incoming Solutions in Emission Control for Heavy Duty

Diesel Vehicles," *Top. Catal.*, vol. 59, no. 8–9, pp. 695–707, 2016.

[35] "https://eippcb.jrc.ec.europa.eu/reference/," 2010. .

[36] F. Schorcht, I. Kourti, B. M. Scalet, S. Roudier, and L. D. Sancho, *Best Available Techniques (BAT) Reference Document for the Production of Cement, Lime and Magnesium Oxide*. 2013.

[37] F. NEUWAHL, G. CUSANO, J. G. BENAVIDES, S. HOLBROOK, and R. Serge, "Best Available Techniques (BAT) Reference Document for Waste Treatment Industries," *Ind. Emiss. Dir. 2010/75/EU (Integrated Pollut. Prev. Control. Frederik*, pp. 1–764, 2019.

[38] C. F. Edwards and P. J. Goix, "Effect of fuel gas composition and excess air on VOC emissions from a small-scale, industrial-style burner," *Combust. Sci. Technol.*, vol. 116–117, no. 1–6, pp. 375–397, 1996.

[39] C. W. Siegmund and D. W. Turner, "NOx EMISSIONS FROM INDUSTRIAL BOILERS: POTENTIAL CONTROL METHODS.," *ASME Pap*, no. 73-IPWR-10, pp. 1–6, 1973.

[40] J. A. Wünning and J. G. Wünning, "Flameless oxidation to reduce thermal no-formation," *Prog. Energy Combust. Sci.*, vol. 23, no. 1, pp. 81–94, 1997.

[41] A. Cavaliere and M. De Joannon, *Mild combustion*, vol. 30, no. 4. 2004.

[42] R. Verschaeren, W. Schaepdryver, T. Serruys, M. Bastiaen, L. Vervaeke, and S. Verhelst, "Experimental study of NOx reduction on a medium speed heavy duty diesel engine by the application of EGR (exhaust gas recirculation) and Miller timing," *Energy*, vol. 76, no. x, pp. 614–621, 2014.

[43] G. H. Abd-Alla, "Using exhaust gas recirculation in internal combustion engines: A review," *Energy Convers. Manag.*, vol. 43, no. 8, pp. 1027–1042, 2002.

[44] B. Shi, J. Hu, H. Peng, and S. Ishizuka, "Effects of internal flue gas recirculation rate on the NOx emission in a methane/air premixed flame," *Combust. Flame*, vol. 188, no. x, pp. 199–211, 2018.

[45] Z. Zhang and L. Li, "Investigation of in-cylinder steam injection in a turbocharged diesel engine for waste heat recovery and NOx emission control," *Energies*, vol. 11, no. 4, 2018.

[46] G. Gonca, “Investigation of the effects of steam injection on performance and NO emissions of a diesel engine running with ethanol-diesel blend,” *Energy Convers. Manag.*, vol. 77, pp. 450–457, 2014.

[47] A. Parlak *et al.*, “New method to reduce NOx emissions of diesel engines: Electronically controlled steam injection system,” *J. Energy Inst.*, vol. 85, no. 3, pp. 135–139, 2012.

[48] C. Sayin, “Engine performance and exhaust gas emissions of methanol and ethanol-diesel blends,” *Fuel*, vol. 89, no. 11, pp. 3410–3415, 2010.

[49] M. Mbarawa, B. E. Milton, R. T. Casey, and H. Miao, “Fuel injection characteristics of diesel-stimulated natural gas combustion,” *Int. J. Energy Res.*, vol. 23, no. 15, pp. 1359–1371, 1999.

[50] Ö. Can, I. Çelikten, and N. Usta, “Effects of ethanol addition on performance and emissions of a turbocharged indirect injection Diesel engine running at different injection pressures,” *Energy Convers. Manag.*, vol. 45, no. 15–16, pp. 2429–2440, 2004.

[51] B. Schreiner, L. Rangmark, T. Ekman, and A. Gusberti, “LOW-NOx- BURNER - US 10,352,555 B2,” 2015.

[52] J. Colannino, “LOW NOx BURNER - US 10,753,605 B2,” 2020.

[53] D. W. Karkow, I. A. Krichtafovich, J. Colannino, and C. A. Wiklof, “SELECTABLE DILUTION LOW NOx BURNER - US 9,803,855 B2,” 2017.

[54] S. Desi-Seulean, J. Ejdrygiewicz, and D. Neufeldt, “LOW NOx BURNER - US 9,920,927 B2,” 2018.

[55] J. M. Kasper, C. A. C. Iii, and C. D. Cooper, “Control of Nitrogen Oxide Emissions by Hydrogen Peroxide-Enhanced Gas-Phase Oxidation Of Nitric Oxide,” *J. Air Waste Manag. Assoc.*, vol. 46, no. 2, pp. 127–133, 1996.

[56] I. Liémans, B. Alban, J. P. Tranier, and D. Thomas, “SOx and NOx absorption based removal into acidic conditions for the flue gas treatment in oxy-fuel combustion,” *Energy Procedia*, vol. 4, pp. 2847–2854, 2011.

[57] L. Wang, W. Zhao, and Z. Wu, “Simultaneous absorption of NO and SO2 by Fe(II)-EDTA

combined with Na2SO3 solution," *Chem. Eng. J.*, vol. 132, no. 1–3, pp. 227–232, 2007.

[58] H. S. Zhu, Y. P. Mao, X. J. Yang, Y. Chen, X. L. Long, and W. K. Yuan, "Simultaneous absorption of NO and SO2 into FeII-EDTA solution coupled with the FeII-EDTA regeneration catalyzed by activated carbon," *Sep. Purif. Technol.*, vol. 74, no. 1, pp. 1–6, 2010.

[59] H. Chu, T. W. Chien, and B. W. Twu, "The absorption kinetics of NO in NaClO2/NaOH solutions," *J. Hazard. Mater.*, vol. 84, no. 2–3, pp. 241–252, 2001.

[60] H. K. Lee, B. R. Deshwal, and K. S. Yoo, "Simultaneous removal of SO2 and NO by sodium chlorite solution in wetted-wall column," *Korean J. Chem. Eng.*, vol. 22, no. 2, pp. 208–213, 2005.

[61] Z. Wang and Z. Wang, "Mass Transfer-Reaction Kinetics Study on Absorption of NO with Dual Oxidants (H2O2/S2O82-)," *Ind. Eng. Chem. Res.*, vol. 54, no. 41, pp. 9905–9912, 2015.

[62] N. E. Khan and Y. G. Adewuyi, "Absorption and oxidation of nitric oxide (NO) by aqueous solutions of sodium persulfate in a bubble column reactor," *Ind. Eng. Chem. Res.*, vol. 49, no. 18, pp. 8749–8760, 2010.

[63] V. K. Sharma, "Potassium ferrate(VI): An environmentally friendly oxidant," *Adv. Environ. Res.*, vol. 6, no. 2, pp. 143–156, 2002.

[64] Y. Zhao, Y. Han, T. Guo, and T. Ma, "Simultaneous removal of SO2, NO and Hg0 from flue gas by ferrate (VI) solution," *Energy*, vol. 67, pp. 652–658, 2014.

[65] J. L. Zhu, Y. H. Wang, J. C. Zhang, and R. Y. Ma, "Experimental investigation of adsorption of NO and SO2 on modified activated carbon sorbent from flue gases," *Energy Convers. Manag.*, vol. 46, no. 13–14, pp. 2173–2184, 2005.

[66] H. Yi *et al.*, "Simultaneous removal of SO2, NO, and CO2 on metal-modified coconut shell activated carbon," *Water. Air. Soil Pollut.*, vol. 225, no. 5, 2014.

[67] W. J. Zhang, S. Rabiei, a. Bagreev, M. S. Zhuang, and F. Rasouli, "Study of NO adsorption on activated carbons," *Appl. Catal. B Environ.*, vol. 83, pp. 63–71, 2008.

[68] Y. W. Lee, D. K. Choi, and J. W. Park, "Characteristics of NOx adsorption and surface

chemistry on impregnated activated carbon," *Sep. Sci. Technol.*, vol. 37, no. 4, pp. 937–956, 2002.

[69] T. E. Green and C. N. Hinshelwood, "CCXXIV.—The catalytic decomposition of nitric oxide at the surface of platinum," *J. Chem. Soc.*, pp. 1709–1713, 1926.

[70] M. Iwamoto, H. Yahiro, K. Tanda, N. Mizuno, Y. Mine, and S. Kagawa, "Removal of nitrogen monoxide through a novel catalytic process. 1. Decomposition on excessively copper ion exchanged ZSM-5 zeolites," *J. Phys. Chem.*, vol. 95, no. 9, pp. 3727–3730, 1991.

[71] A. Ogata, A. Obuchi, K. Mizuno, A. Ohi, H. Aoyama, and H. Ohuchi, "Enhancement effect of Mg2+ ion on direct nitric oxide decomposition over supported palladium catalysts," *Appl. Catal.*, vol. 65, no. 2, 1990.

[72] H. Hamada, Y. Kintaichi, M. Sasaki, and T. Ito, "Silver-promoted Cobalt Oxide Catalysts for Direct Decomposition of Nitrogen Monoxide," *Chem. Soc. Japan*, pp. 1069–1070, 1990.

[73] H. M. Zhang, Y. Shimizu, Y. Teraoka, N. Miura, and N. Yamazoe, "Oxygen sorption and catalytic properties of La1-xSrxCo1-yFeyO3 Perovskite-type oxides," *J. Catal.*, vol. 121, no. 2, pp. 432–440, 1990.

[74] Y. Teraoka, K. I. Torigoshi, H. Yamaguchi, T. Ikeda, and S. Kagawa, "Direct decomposition of nitric oxide over stannate pyrochlore oxides: Relationship between solid-state chemistry and catalytic activity," *J. Mol. Catal. A Chem.*, vol. 155, no. 1–2, pp. 73–80, 2000.

[75] N. Imanaka, T. Masui, and H. Masaki, "Direct decomposition of nitric oxide over C-type cubic (Gd 1-x-yyxBay)2O3-y, solid solutions," *Adv. Mater.*, vol. 19, no. 21, pp. 3660–3663, 2007.

[76] Z. Liu and S. Ihl Woo, "Recent advances in catalytic DeNOX Science and Technology," *Catal. Rev. - Sci. Eng.*, vol. 48, no. 1, pp. 43–89, 2006.

[77] N. Imanaka and T. Masui, "Advances in direct NOx decomposition catalysts," *Appl. Catal. A Gen.*, vol. 431–432, pp. 1–8, 2012.

[78] F. Garin, "Mechanism of NOx decomposition," *Appl. Catal. A Gen.*, vol. 222, no. 1–2, pp. 183–219, 2001.

[79] K. Goto, H. Matsumoto, and T. Ishihara, "Direct decomposition of NO on Ba/Ba-Y-O catalyst," *Top. Catal.*, vol. 52, no. 13–20, pp. 1776–1780, 2009.

[80] J. O. L. Wendt, C. V. Sternling, and M. A. Matovich, "Reduction of sulfur trioxide and nitrogen oxides by secondary fuel injection," *Symp. Combust.*, vol. 14, no. 1, pp. 897–904, 1973.

[81] M. Tayyeb Javed, N. Irfan, and B. M. Gibbs, "Control of combustion-generated nitrogen oxides by selective non-catalytic reduction," *J. Environ. Manage.*, vol. 83, no. 3, pp. 251–289, 2007.

[82] S. Salimian and R. K. Hanson, "A kinetic study of no removal from combustion gases by injection of NHi-Containing Compounds," *Combust. Sci. Technol.*, vol. 23, no. 5–6, pp. 225–230, 1980.

[83] S. L. Chen, J. A. Cole, M. P. Heap, J. C. Kramlich, J. M. Mccarthy, and D. W. Pershing, "Advanced NOx reduction processes using -NH and -CN compounds in conjunction with staged air addition," *Symp. Combust.*, vol. 22, no. 1, pp. 1135–1145, 1989.

[84] Z. Hu, E. Jiang, and X. Ma, "Numerical simulation on operating parameters of SNCR process in a municipal solid waste incinerator," *Fuel*, vol. 245, no. August 2018, pp. 160–173, 2019.

[85] O. Finnerman, N. Guo, N. Razmjoo, M. Strand, and H. Ström, "Reactor modelling assessment for urea-SNCR applications," *Int. J. Numer. Methods Heat Fluid Flow*, vol. 27, no. 7, pp. 1395–1411, 2017.

[86] J. L. Sorrels, "Chapter 1 - Selective Non-Catalytic Reduction," *Air Econ. Gr. - U.S. EPA Form 2220-1.(Rev. 4-77)*, 2019.

[87] J. L. Sorrels, "Chapter 2 Selective Catalytic Reduction," *Air Econ. Gr. - U.S. EPA Form 2220-1.(Rev. 4-77)*, no. May 2016, 2016.

[88] C. J. G. Van Der Grift, A. F. Woldhuis, and O. L. Maaskant, "The Shell DENOX system for low temperature NOx removal," *Catal. Today*, vol. 27, no. 1–2, pp. 23–27, 1996.

[89] J. E. Cichanowicz, "Current Capital Cost and Cost-Effectiveness of Power Plant Emissions Control Technologies," *Util. Air Regul. Gr. - Exhib. No. GLF-41*, 2010.

[90] G. Liu and P. X. Gao, "A review of NOx storage/reduction catalysts: Mechanism, materials and degradation studies," *Catal. Sci. Technol.*, vol. 1, no. 4, pp. 552–568, 2011.

[91] P. Svedberg, E. Jobson, S. Erkfeldt, B. Andersson, M. Larsson, and M. Skoglundh, "Influence of the storage material on the storage of NOx at low temperatures," *Top. Catal.*, vol. 30–31, no. x, pp. 199–206, 2004.

[92] Z. Zhou, M. P. Harold, and D. Luss, "Comparison of Pt-BaO/Al2O3 and Pt-CeO2/Al2O3 for NOx storage and reduction: Impact of cycling frequency," *Appl. Catal. B Environ.*, vol. 255, no. May, 2019.

[93] Y. Su, K. S. Kabin, M. P. Harold, and M. D. Amiridis, "Reactor and in situ FTIR studies of Pt/BaO/Al2O3 and Pd/BaO/Al2O3 NOx storage and reduction (NSR) catalysts," *Appl. Catal. B Environ.*, vol. 71, no. 3–4, pp. 207–215, 2007.

[94] I. Nova *et al.*, "NOx adsorption study over Pt-Ba/alumina catalysts: FT-IR and pulse experiments," *J. Catal.*, vol. 222, no. 2, pp. 377–388, 2004.

[95] Z. Say, O. Mihai, M. Tohumeken, K. E. Ercan, L. Olsson, and E. Ozensoy, "Sulfur-tolerant BaO/ZrO2/TiO2/Al2O3 quaternary mixed oxides for deNOX catalysis," *Catal. Sci. Technol.*, vol. 7, no. 1, pp. 133–144, 2017.

[96] Y. Sun Mok and E. Young Yoon, "Effect of ozone injection on the catalytic reduction of nitrogen oxides," *Ozone Sci. Eng.*, vol. 28, no. 2, pp. 105–110, 2006.

[97] M. Koebel, M. Elsener, and M. Kleemann, "Urea-SCR: a promising technique to reduce NOx emissions from automotive diesel engines," *Catal. Today*, vol. 59, no. 3, pp. 335–345, 2000.

[98] Y. S. Mok and I. S. Nam, "Reduction of nitrogen oxides by ozonization-catalysis hybrid process," *Korean J. Chem. Eng.*, vol. 21, no. 5, pp. 976–982, 2004.

[99] R. Ono and T. Oda, "Ozone production process in pulsed positive dielectric barrier discharge," *J. Phys. D. Appl. Phys.*, vol. 40, no. 1, pp. 176–182, 2007.

[100] S.-L. Park, J.-D. Moon, S.-H. Lee, and S.-Y. Shin, "Effective ozone generation utilizing a meshed-plate electrode in a dielectric-barrier discharge type ozone generator," *J. Electrostat.*,

vol. 64, no. 5, pp. 275–282, 2006.

[101] I. Jõgi, K. Erme, E. Levoll, J. Raud, and E. Stamate, "Plasma and catalyst for the oxidation of NOx," *Plasma Sources Sci. Technol.*, vol. 27, no. 3, 2018.

[102] D. Ye, D. Gao, G. Yu, X. Shen, and F. Gu, "An investigation of the treatment of particulate matter from gasoline engine exhaust using non-thermal plasma," *J. Hazard. Mater.*, vol. 127, no. 1–3, pp. 149–155, 2005.

[103] M. Babaie *et al.*, "Performance evaluation of non-thermal plasma on particulate matter, ozone and CO2 correlation for diesel exhaust emission reduction," *Chem. Eng. J.*, vol. 276, no. x, pp. 240–248, 2015.

[104] Y. S. Mok and Y. J. Huh, "Simultaneous removal of nitrogen oxides and particulate matters from diesel engine exhaust using dielectric barrier discharge and catalysis hybrid system," *Plasma Chem. Plasma Process.*, vol. 25, no. 6, pp. 625–639, 2005.

[105] Y. Zhang *et al.*, "The byproduct generation analysis of the NO_x conversion process in dielectric barrier discharge plasma," *RSC Adv.*, vol. 6, no. 68, pp. 63946–63953, 2016.

[106] B. M. Penetrante, M. C. Hsiao, B. T. Merritt, G. E. Vogtlin, and P. H. Wallman, "Comparison of Electrical Discharge Techniques for Nonthermal Plasma Processing of NO in N2," *IEEE Trans. Plasma Sci.*, vol. 23, no. 4, pp. 679–687, 1995.

[107] B. M. Penetrante *et al.*, "Pulsed corona and dielectric-barrier discharge processing of NO in N2," *Appl. Phys. Lett.*, vol. 68, no. 26, pp. 3719–3721, 1996.

[108] A. Mihalcioiu, K. Yoshida, M. Okubo, T. Kuroki, and T. Yamamoto, "Design factors for NOx reduction in nitrogen plasma," *IEEE Trans. Ind. Appl.*, vol. 46, no. 6, pp. 2151–2156, 2010.

[109] Z. Liu, Y. Cai, J. Wang, C. Sun, and W. Han, "A study on coaxial type DBD decomposing NO/N2 mixture gas by optical emission spectrum," *Proc. - 2012 5th Int. Conf. Intell. Comput. Technol. Autom. ICICTA 2012*, pp. 657–661, 2012.

[110] M. Okubo, G. Tanioka, T. Kuroki, and T. Yamamoto, "Adsorption and Nonthermal Plasma Desorption Process for Concentrating NO x in Flue Exhaust Gas," vol. 00, no. x, pp. 698–705,

2001.

[111] M. Okubo, M. Inoue, T. Kuroki, and T. Yamamoto, “NOx reduction aftertreatment system using nitrogen nonthermal plasma desorption,” *IEEE Trans. Ind. Appl.*, vol. 41, no. 4, pp. 891–899, 2005.

[112] Q. Yu, H. Wang, T. Liu, L. Xiao, X. Jiang, and X. Zheng, “High-efficiency removal of NOx using a combined adsorption-discharge plasma catalytic process,” *Environ. Sci. Technol.*, vol. 46, no. 4, pp. 2337–2344, 2012.

[113] K. Skalska, J. S. Miller, and S. Ledakowicz, “Trends in NOx abatement: A review,” *Sci. Total Environ.*, vol. 408, no. 19, pp. 3976–3989, 2010.

[114] A. Dąbrowski, “Adsorption - From theory to practice,” *Adv. Colloid Interface Sci.*, vol. 93, no. 1–3, pp. 135–224, 2001.

[115] D. H. Everett and L. Butterworths, “International union of pure and applied chemistry division of physical chemistry. Manual of symbols and terminology for physicochemical quantities and units . Appendix II: Definitions, Terminology and Symbols in Colloid and Surface Chemistry PART I,” pp. 579–638, 1972.

[116] C. Tien, *INTRODUCTION TO ADSORPTION - Basics, Analysis, and Applications*. Elsevier, 2019.

[117] P. N. Cheremisinoff and F. Ellerbusch, *Carbon adsorption handbook*. 1978.

[118] R. T. Yang, *Adsorbents: Fundamentals and Applications*. John Wiley & Sons, 2003.

[119] D. D. Do, *Adsorption Analysis: Equilibria and Kinetics*, vol. 2, no. Imperial College Press. 1998.

[120] C. R. Girish, “Various impregnation methods used for the surface modification of the adsorbent: A review,” *Int. J. Eng. Technol.*, vol. 7, no. 4.7 Special Issue 7, pp. 330–334, 2018.

[121] D. M. Ruthven, *Principles of adsorption and adsorption processes*. John Wiley & Sons, 1984.

[122] R. Zsigmondy, “uber die Struktur des Gels der Kieselsaure. Theorie der Entwasserung.,” 1911.

[123] J. M. Haynes, “Pore size analysis according to the Kelvin equation,” *Matériaux Constr.*, vol. 6, no. 3, pp. 209–213, 1973.

[124] M. Naderi, “Surface Area: Brunauer-Emmett-Teller (BET),” in *Progress in Filtration and Separation*, Elsevier Ltd, 2015, pp. 585–608.

[125] H. A. Jakobsen, *Chemical Reactor Modeling - Multiphase Reactive Flows*. 2008.

[126] W. L. McCabe, J. C. Smith, and P. Harriott, “Adsorption,” in *Unit operations of Chemical Engineering - Fifth Edition*, McGraw-Hill, 1993, pp. 810–837.

[127] D. W. Green and R. H. Perry, *Perry’s Chemical Engineers’ Handbook*, vol. 8th. 2008.

[128] M. Suzuki, “Kinetics of Adsorption in a Column- Breakthrough Curves,” in *Adsorption Engineering*, Elsevier, 1990, pp. 151–186.

[129] L. Largitte and R. Pasquier, “A review of the kinetics adsorption models and their application to the adsorption of lead by an activated carbon,” *Chem. Eng. Res. Des.*, vol. 109, pp. 495–504, 2016.

[130] T. L. P. Dantas *et al.*, “Modeling of the fixed-bed adsorption of carbon dioxide and a carbon dioxidenitrogen mixture on zeolite 13X,” *Brazilian J. Chem. Eng.*, vol. 28, no. 3, pp. 533–544, 2011.

[131] A. M. Rubel, M. L. Stewar, and J. M. Stencel, “Activated carbon for control of nitrogen oxide emissions,” *J. Mater. Res.*, vol. 10, no. 3, pp. 562–567, 1995.

[132] Y. Kong and C. Y. Cha, “NOx adsorption on char in presence of oxygen and moisture,” *Carbon N. Y.*, vol. 34, no. 8, pp. 1027–1033, 1996.

[133] J. K. Neathery, A. M. Rubel, and J. M. Stencel, “Uptake of NOx by activated carbons: Bench-scale and pilot-plant testing,” *Carbon N. Y.*, vol. 35, no. 9, pp. 1321–1327, 1997.

[134] D. López, R. Buitrago, A. Sepúlveda-Escribano, F. Rodríguez-Reinoso, and F. Mondragon, “Low-temperature catalytic adsorption of NO on activated carbon materials,” *Langmuir*, vol. 23, no. 24, pp. 12131–12137, 2007.

[135] W. Klose and S. Rincón, "Adsorption and reaction of NO on activated carbon in the presence of oxygen and water vapour," *Fuel*, vol. 86, no. 1–2, pp. 203–209, 2007.

[136] S. Sumathi, S. Bhatia, K. T. Lee, and A. R. Mohamed, "SO2 and NO simultaneous removal from simulated flue gas over cerium-supported palm shell activated at lower temperatures-role of cerium on NO removal," *Energy and Fuels*, vol. 24, no. 1, pp. 427–431, 2010.

[137] Y. Takeuchi, K. Yanagisawa, Y. Tanaka, and N. Tsuruoka, "Removal of nitrogen oxides from air by chemicals-impregnated carbons," *Korean J. Chem. Eng.*, vol. 14, no. 5, pp. 377–381, 1997.

[138] P. Davini, "SO2 and NOx adsorption properties of activated carbons obtained from a pitch containing iron derivatives," *Carbon N. Y.*, vol. 39, no. 14, pp. 2173–2179, 2001.

[139] S. Sumathi, S. Bhatia, K. T. Lee, and A. R. Mohamed, "Performance of an activated carbon made from waste palm shell in simultaneous adsorption of soxand NOxof flue gas at low temperature," *Sci. China, Ser. E Technol. Sci.*, vol. 52, no. 1, pp. 198–203, 2009.

[140] D. Xiao, *Gas Discharge and Gas Insulation*. 2016.

[141] Y. P. Raizer, "Breakdown of Gases in Fields of Various Frequency Ranges," in *Gas Discharge Physics*, J. E. Allen, Ed. Springer-Verlag, 1991.

[142] W. Grassi and D. Testi, "Induction of waves on a horizontal water film by an impinging corona wind," *IEEE Trans. Dielectr. Electr. Insul.*, vol. 16, no. 2, pp. 377–385, 2009.

[143] G. Levitin, K. Reinhardt, and D. W. Hess, "Plasma Cleaning for Electronic, Photonic, Biological, and Archeological Applications," in *Developments in Surface Contamination and Cleaning: Contaminant Removal and Monitoring*, Elsevier, 2013, pp. 55–121.

[144] P. Yan *et al.*, "Characteristics of negative DC corona discharge in a wire-plate configuration at high temperatures," *Sep. Purif. Technol.*, vol. 139, pp. 5–13, 2015.

[145] A. Villot *et al.*, "Separation of particles from syngas at high-temperatures with an electrostatic precipitator," *Sep. Purif. Technol.*, vol. 92, pp. 181–190, 2012.

[146] V. I. Gibalov and G. J. Pietsch, "The development of dielectric barrier discharges in gas gaps

and on surfaces," *J. Phys. D. Appl. Phys.*, vol. 33, no. 20, pp. 2618–2636, 2000.

[147] U. Kogelschatz, "Dielectric-barrier Discharges : Their History, Discharge Physics, and Industrial Applications," *Plasma Chem. Plasma Process.*, vol. 23, no. 1, pp. 1–46, 2003.

[148] A. M. Fridman, *Plasma Chemistry*. Cambridge University press, 2008.

[149] U. Kogelschatz, "Filamentary, patterned, and diffuse barrier discharges," *IEEE Trans. Plasma Sci.*, vol. 30, no. 4 I, pp. 1400–1408, 2002.

[150] M. Mehdizadeh, "Plasma applicators at RF and microwave frequencies," in *Microwave/RF Applicators and Probes for Material Heating, Sensing, and Plasma Generation*, Second Edi., Elsevier, 2015, pp. 335–363.

[151] H. Deutsch, F. X. Bronold, and K. Becker, "Calculation of electron-impact ionization cross sections: Bottom-up inductive vs. top-down deductive approaches," *Int. J. Mass Spectrom.*, vol. 365–366, pp. 128–139, 2014.

[152] H. Friedrich, *Theoretical atomic physics*, Fourth Edi. Springer, 2017.

[153] E. F. Greene and A. Kuppermann, "Chemical reaction cross sections and rate constants," *J. Chem. Educ.*, vol. 45, no. 6, pp. 361–369, 1968.

[154] G. J. M. Hagelaar and L. C. Pitchford, "Solving the Boltzmann equation to obtain electron transport coefficients and rate coefficients for fluid models," *Plasma Sources Sci. Technol.*, vol. 14, no. 4, pp. 722–733, 2005.

[155] W. Van Gaens and A. Bogaerts, "Kinetic modelling for an atmospheric pressure argon plasma jet in humid air," *J. Phys. D. Appl. Phys.*, vol. 46, no. 27, 2013.

[156] I. A. Kossyi, A. Y. Kostinsky, A. A. Matveyev, and V. P. Silakov, "Kinetic scheme of the non-equilibrium discharge in nitrogen-oxygen mixtures," *Plasma Sources Sci. Technol.*, vol. 1, no. 3, pp. 207–220, 1992.

[157] M. Moravej, X. Yang, M. Barankin, J. Penelon, S. E. Babayan, and R. F. Hicks, "Properties of an atmospheric pressure radio-frequency argon and nitrogen plasma," *Plasma Sources Sci. Technol.*, vol. 15, no. 2, pp. 204–210, 2006.

[158] J. De Wilde, C. Lorant, and P. Descamps, "2D modeling and simulation of the flow dynamics, electric field and reactions in a low-temperature, atmospheric-pressure nitrogen plasma sharp-end plate-to-plane configuration and CVD reactor," *J. Phys. D. Appl. Phys.*, vol. 50, no. 13, 2017.

[159] Y. Itikawa, "Cross sections for electron collisions with nitrogen molecules," *J. Phys. Chem. Ref. Data*, vol. 35, no. 1, pp. 31–53, 2006.

[160] A. M. Zhu, Q. Sun, J. H. Niu, Y. Xu, and Z. M. Song, "Conversion of NO in NO/N2, NO/O2/N2, NO/C2H4/N2 and NO/C2H4/O2/N2 systems by dielectric barrier discharge plasmas," *Plasma Chem. Plasma Process.*, vol. 25, no. 4, pp. 371–386, 2005.

[161] I. Stefanović, N. K. Bibinov, A. A. Deryugin, I. P. Vinogradov, A. P. Napartovich, and K. Wiesemann, "Kinetics of ozone and nitric oxides in dielectric barrier discharges in O2/NOx and N2/O2/NOx mixtures," *Plasma Sources Sci. Technol.*, vol. 10, pp. 406–416, 2001.

[162] K. Yan, S. Kanazawa, T. Ohkubo, and Y. Nomoto, "Oxidation and reduction processes during NOx removal with corona-induced nonthermal plasma," *Plasma Chem. Plasma Process.*, vol. 19, no. 3, pp. 421–443, 1999.

[163] B. M. Penetrante, J. N. Bardsley, and M. C. Hsiao, "Kinetic analysis of non-thermal plasmas used for pollution control," *Japanese J. Appl. Physics, Part 1 Regul. Pap. Short Notes Rev. Pap.*, vol. 36, no. 7 SUPPL. B, pp. 5007–5017, 1997.

[164] W. Siemens, "Ueber die elektrostatische Induction und die Verzögerung des Stroms in Flaschendrähten," *Ann. Phys.*, vol. 178, no. 9, pp. 66–122, 1857.

[165] Y. Ma, G. J. Zhang, X. M. Shi, G. M. Xu, and Y. Yang, "Chemical mechanisms of bacterial inactivation using dielectric barrier discharge plasma in atmospheric air," *IEEE Trans. Plasma Sci.*, vol. 36, no. 4 PART 3, pp. 1615–1620, 2008.

[166] T. G. Klämpfl *et al.*, "Cold atmospheric air plasma sterilization against spores and other microorganisms of clinical interest," *Appl. Environ. Microbiol.*, vol. 78, no. 15, pp. 5077–5082, 2012.

[167] V. Scholtz, J. Pazlarova, H. Souskova, J. Khun, and J. Julak, "Nonthermal plasma - A tool for

decontamination and disinfection," *Biotechnol. Adv.*, vol. 33, no. 6, pp. 1108–1119, 2015.

[168] H. L. Clack and K. R. Wigginton, "Process for electro-hydrodynamically enhanced destruction of chemical air contaminants and airborne inactivation of biological agents," US 2018/0117209 A1, 2018.

[169] H. L. Clack, K. R. Wigginton, and A. S. Lauring, "Production of immune-response-stimulating aerosols by non-thermal plasma treatment of airborne pathogens," US 2020/0016286 A1, 2020.

[170] B. Liu, "Non-thermal atmospheric pressure plasma interacting with water for biological applications," p. 248 pages, 2019.

[171] J. Izdebska-Podsiadły, "Application of Plasma in Printed Surfaces and Print Quality," in *Non-Thermal Plasma Technology for Polymeric Materials*, 2019, pp. 159–191.

[172] R. Wang, Y. Shen, C. Zhang, P. Yan, and T. Shao, "Comparison between helium and argon plasma jets on improving the hydrophilic property of PMMA surface," *Appl. Surf. Sci.*, vol. 367, pp. 401–406, 2016.

[173] D. Tian, Y. Song, and L. Jiang, "Patterning of controllable surface wettability for printing techniques," *Chem. Soc. Rev.*, vol. 42, no. 12, pp. 5184–5209, 2013.

[174] Y. Chen, Q. Gao, H. Wan, J. Yi, Y. Wei, and P. Liu, "Surface modification and biocompatible improvement of polystyrene film by Ar, O 2 and Ar + O 2 plasma," *Appl. Surf. Sci.*, vol. 265, pp. 452–457, 2013.

[175] K. Navaneetha Pandiyaraj *et al.*, "Effect of cold atmospheric pressure plasma gas composition on the surface and cyto-compatible properties of low density polyethylene (LDPE) films," *Curr. Appl. Phys.*, vol. 16, no. 7, pp. 784–792, 2016.

[176] M. Żenkiewicz, "Methods for the calculation of surface free energy of solids," *J. Achiev. Mater. Manuf. Eng.*, vol. 24, no. 1, pp. 137–145, 2007.

[177] H. H. Kim, Y. Teramoto, N. Negishi, and A. Ogata, "A multidisciplinary approach to understand the interactions of nonthermal plasma and catalyst: A review," *Catal. Today*, vol.

256, no. Part 1, pp. 13–22, 2015.

[178] U. Roland, F. Holzer, and F. D. Kopinke, “Combination of non-thermal plasma and heterogeneous catalysis for oxidation of volatile organic compounds: Part 2. Ozone decomposition and deactivation of γ-Al2O3,” *Appl. Catal. B Environ.*, vol. 58, no. 3–4, pp. 217–226, 2005.

[179] D. N. Tran, C. L. Aardahl, K. G. Rappe, P. W. Park, and C. L. Boyer, “Reduction of NOx by plasma-facilitated catalysis over In-doped γ-alumina,” *Appl. Catal. B Environ.*, vol. 48, no. 2, pp. 155–164, 2004.

[180] A. A. Kulikovsky, “Positive streamer between parallel plate electrodes in atmospheric pressure air,” *J. Phys. D. Appl. Phys.*, vol. 30, no. 3, pp. 441–450, 1997.

[181] U. G.- COMSOL, “Plasma Module,” *Part number: CM021401*, 2018. [Online]. Available: https://doc.comsol.com/5.4/doc/com.comsol.help.plasma/PlasmaModuleUsersGuide.pdf.